



# On the interactions between urban structures and air flows: A numerical study of the effects of urban morphology on the building wind environment and the related building energy loads

Lucie Merlier

## ► To cite this version:

Lucie Merlier. On the interactions between urban structures and air flows: A numerical study of the effects of urban morphology on the building wind environment and the related building energy loads. Fluids mechanics [physics.class-ph]. INSA de Lyon, 2015. English. NNT : 2015ISAL0070 . tel-01368556

**HAL Id: tel-01368556**

**<https://theses.hal.science/tel-01368556>**

Submitted on 19 Sep 2016

**HAL** is a multi-disciplinary open access archive for the deposit and dissemination of scientific research documents, whether they are published or not. The documents may come from teaching and research institutions in France or abroad, or from public or private research centers.

L'archive ouverte pluridisciplinaire **HAL**, est destinée au dépôt et à la diffusion de documents scientifiques de niveau recherche, publiés ou non, émanant des établissements d'enseignement et de recherche français ou étrangers, des laboratoires publics ou privés.

Numéro d'ordre: 2015-ISAL-0070

Année: 2015

Thèse

**ON THE INTERACTIONS BETWEEN URBAN STRUCTURES  
AND AIR FLOWS:  
A NUMERICAL STUDY OF THE EFFECTS OF URBAN MORPHOLOGY  
ON THE BUILDING WIND ENVIRONMENT  
AND THE RELATED BUILDING ENERGY LOADS**

Soutenue devant:

**L'Institut National des Sciences Appliquées de Lyon (INSA Lyon)**

Pour obtenir: **le grade de docteur**

**Formation doctorale:** Génie Civil

**Ecole doctorale:** MEGA

Mécanique, Energétique, Génie Civil Acoustique

**Laboratoire d'accueil:** CETHIL, UMR 5008

Centre d'Energétique et de Thermique de Lyon

Par: **Lucie MERLIER**

Soutenue le 4 septembre 2015 devant la commission d'examen.

Jury:

Bert BLOCKEN	Professeur, BPS - TU Eindhoven	Rapporteur
Julien HANS	Directeur adjoint, Dpt. Energie & Environnement - CSTB	Co-encadrant
Frédéric KUZNIK	Professeur, CETHIL - INSA de Lyon	Directeur de thèse
Peter MOONEN	Professeur, LFC-R - Univ. de Pau et pays de l'Adour	Examineur
Marjorie MUSY	Ingénieure de recherche HDR, CRENAU-IRSTV Nantes	Rapporteur
Christian OBRECHT	Maître de conférences, CETHIL - INSA de Lyon	Invité
Gilles RUSAOUËN	Maître de conférences, CETHIL - Univ. de Lyon	Co-encadrant
Pierre SAGAUT	Professeur, M2P2 UMR 7340 - Univ. de Aix Marseille	Examineur

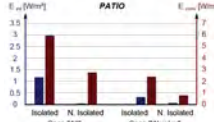
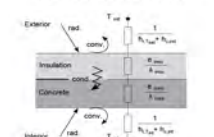
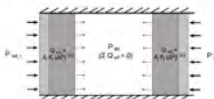
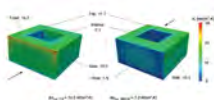
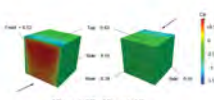
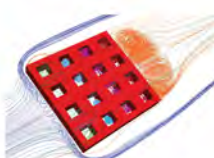
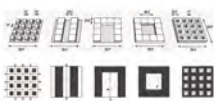
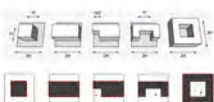
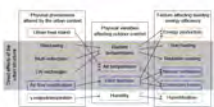
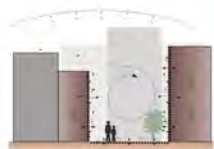


## INSA Direction de la Recherche - Liste des Écoles Doctorales

SIGLE	ÉCOLE DOCTORALE	NOM ET COORDONNÉES DU RESPONSABLE
<b>CHIMIE</b> EDA 206	<b>CHIMIE DE LYON</b> <a href="http://www.edchimie-lyon.fr">http://www.edchimie-lyon.fr</a> Sec. : Renée EL MELHEM Bât. Blaise Pascal 3ème étage Tél. : 04 72 43 80 46 Insa : R. GOURDON <a href="mailto:secretariat@edchimie-lyon.fr">secretariat@edchimie-lyon.fr</a>	<b>M. Jean-Marc LANCELIN</b> Université de Lyon - Collège Doctoral Bât. ESCPE 43 bd du 11 novembre 1918 69622 VILLEURBANNE Cedex Tél. : 04 72 43 13 95 <a href="mailto:directeur@edchimie-lyon.fr">directeur@edchimie-lyon.fr</a>
<b>E.E.A.</b> EDA 160	<b>ÉLECTRONIQUE, ÉLECTROTECHNIQUE, AUTOMATIQUE</b> <a href="http://edeea.ec-lyon.fr">http://edeea.ec-lyon.fr</a> Sec. : M. C. HAVGOUDOUKIAN <a href="mailto:ecole-doctorale.eea@ec-lyon.fr">ecole-doctorale.eea@ec-lyon.fr</a>	<b>M. Gérard SCORLETTI</b> École Centrale de Lyon 36, avenue Guy de Collongue 69134 ECULLY Tél. : 04 72 18 60 97 / Fax. : 04 78 43 37 17 <a href="mailto:gerard.scorletti@ec-lyon.fr">gerard.scorletti@ec-lyon.fr</a>
<b>E2M2</b> EDA 341	<b>ÉVOLUTION, ÉCOSYSTEME, MICROBIOLOGIE, MODÉLISATION</b> <a href="http://e2m2.universite-lyon.fr">http://e2m2.universite-lyon.fr</a> Sec. : Bât. Atrium - UCB Lyon I Tél. : 04 72 44 83 62 Insa : S. REVERCHON <a href="mailto:secretariat.e2m2@univ-lyon1.fr">secretariat.e2m2@univ-lyon1.fr</a>	<b>M. Fabrice CORDEY</b> Laboratoire de Géologie de Lyon Université Claude Bernard Lyon I Bât. Géode - Bureau 225 43, bvd du 11 novembre 1918 69622 VILLEURBANNE Cedex Tél. : 04 72 44 83 74 <a href="mailto:fabrice.cordey@univ-lyon1.fr">fabrice.cordey@univ-lyon1.fr</a>
<b>EDISS</b> EDA 205	<b>INTERDISCIPLINAIRE SCIENCES-SANTÉ</b> <a href="http://ediss-lyon.fr">http://ediss-lyon.fr</a> Bât. Atrium - UCB Lyon I Tél. : 04 72 44 83 62 <a href="mailto:infomaths@univ-lyon1.fr">infomaths@univ-lyon1.fr</a>	<b>Mme Emmanuelle CANET-SOULAS</b> INSERM U1060, CarMeN lab, Univ. Lyon I Bâtiment IMBL 11, avenue Jean Capelle 69621 VILLEURBANNE Cedex Tél. : 04 72 11 90 13 <a href="mailto:emmanuelle.canet@univ-lyon1.fr">emmanuelle.canet@univ-lyon1.fr</a>
<b>INFOMATHS</b> EDA 512	<b>INFORMATIQUE ET MATHÉMATIQUES</b> <a href="http://infomaths.univ-lyon1.fr">http://infomaths.univ-lyon1.fr</a> Sec. : Renée EL MELHEM Bât. Blaise Pascal - 3ème étage <a href="mailto:infomaths@univ-lyon1.fr">infomaths@univ-lyon1.fr</a>	<b>Mme Sylvie CALABRETTO</b> LIRIS - INSA de Lyon - Bât. Blaise Pascal 7, avenue Jean Capelle 69622 VILLEURBANNE Cedex Tél. : 04 72 43 80 46 / Fax. : 04 72 43 16 87 <a href="mailto:sylvie.calabretto@insa-lyon.fr">sylvie.calabretto@insa-lyon.fr</a>
<b>Matériaux</b> EDA 034	<b>MATÉRIAUX DE LYON</b> <a href="http://ed34.universite-lyon.fr">http://ed34.universite-lyon.fr</a> Sec. : M. LABOUNE-DAHMANI Bât. Direction - 1er étage Tél. : 04 72 43 71 70 <a href="mailto:ed.materiaux@insa-lyon.fr">ed.materiaux@insa-lyon.fr</a>	<b>M. Jean-Yves BUFFIERE</b> MATEIS - INSA de Lyon - Bât. Saint Exupéry 7, avenue Jean Capelle 69621 VILLEURBANNE Cedex Tél. : 04 72 43 71 70 / Fax. : 04 72 43 85 28 <a href="mailto:ed.materiaux@insa-lyon.fr">ed.materiaux@insa-lyon.fr</a>
<b>MEGA</b> EDA 162	<b>MÉCANIQUE, ÉNERGÉTIQUE, GÉNIE CIVIL, ACOUSTIQUE</b> <a href="http://mega.universite-lyon.fr">http://mega.universite-lyon.fr</a> Sec. : M. LABOUNE-DAHMANI Bât. Direction - 1er étage Tél. : 04 72 43 71 70 <a href="mailto:mega@insa-lyon.fr">mega@insa-lyon.fr</a>	<b>M. Philippe BOISSE</b> LAMCOS - INSA de Lyon Bât. Jacquard 25 bis, avenue Jean Capelle 69621 VILLEURBANNE Cedex Tél. : 04 72 43 71 70 / Fax. : 04 72 43 72 37 <a href="mailto:philippe.boisse@insa-lyon.fr">philippe.boisse@insa-lyon.fr</a>
<b>ScSo</b> EDA 483	<b>AMÉNAGEMENT, URBANISME, ARCHÉOLOGIE, SCIENCES POLITIQUES, SOCIOLOGIE, ANTHROPOLOGIE</b> <a href="http://recherche.univ-lyon2.fr/scso/">http://recherche.univ-lyon2.fr/scso/</a> Sec. : Viviane POLSINELLI Brigitte DUBOIS Insa : Jean-Yves TOUSSAINT <a href="mailto:viviane.polsinelli@univ-lyon2.fr">viviane.polsinelli@univ-lyon2.fr</a>	<b>Mme Isabelle VON BUELTZINGLOEWEN</b> Université Lyon II 86, rue Pasteur 69365 LYON Cedex 07 Tél. : 04 78 77 23 86 / Fax. : 04 37 28 04 48 <a href="mailto:isavonb@dbmail.com">isavonb@dbmail.com</a>







Ph.D. Thesis:

## Interactions between urban structures and air flows:

Numerical study of the effects of urban morphology on the building wind environment and the related building energy loads

Par : **Lucie MERLIER**

Soutenue le: **04 septembre 2015**

Équipe encadrante:

Pr. Frédéric KUZNIK (Directeur)

MCF. Gilles RUSAOUËN, Dr. Julien HANS

Rapporteurs:

Pr. Bert BLOCKEN, Dr. Marjorie MUSY

Examineurs:

Pr. Peter MOONEN, Pr. Pierre SAGAUT

(Président), MCF. Christian OBRECHT (Invité)



*Có công mài sắt có ngày nên kim.*  
- Vietnamese citation -

# Acknowledgements

First of all, I would like to thank my family for their every day support during these last three years, and during these last 29 years actually. Thank you very much Mum, Dad and Sweetie! And thank you Benjamin for your support and help and for your understanding of the hazards of a Ph.D. student mood... (I am glad you are nearly an urban physics expert now!)

I would also like to sincerely thank my supervisors Frédéric Kuznik, Gilles Rusaouën and Julien Hans, as well as Jean-Jacques Roux and Serge Salat for their valuable advice and the discussions we had during my Ph.D. thesis and before. I also wanted to warmly thank Christian Obrecht, for his help in proof checking my manuscript and all the valuable scientific, methodological and typographic advice he gave me, as well as for his perfectionism, coffees, funny T-shirts... 42 to sum up!

Thank you very much to all the members of the jury too, Bert Blocken, Marjorie Musy, Pierre Sagaut and Peter Moonen for agreeing to review and discuss my first real work as a researcher, yet an apprentice. I am very glad and honored you participated on my jury. Your comments and advice on my work will certainly be of the utmost importance for my future carrier, during which, hopefully, I will be able to discuss urban physics issues with you again.

I also wanted to express my gratefulness to all the persons I met during my Ph.D., who took some of their precious time to discuss my work and give me helpful advice, even though I already mentioned some of them in the previous paragraph, especially Thijs Defraeye, Peter Moonen, Bert Blocken, Emmanuel Bozonnet and Darren Robinson.

I am also grateful to the CETHIL and the CSTB for providing the financial support without which this project would not have existed. Thank you to the CETHIL members for their warm welcome during these last few years, especially Dany and Jocelyn, the directors of the lab, for making my thesis possible and their consideration for Ph.D. students. I also wanted to thank Loic for making me appreciate SSH, command lines and the other “dark sides” of my work, as well as for still talking to me despite all my requests; Eric and Etienne, for their dynamic help on Paraview, Stéphane for his precious beamer templates; and Florence, Corrine(s), Christine, Rémy and Marilyn for their administrative support.

Warmest thanks to all the Ph.D. students, post-docs and interns of the lab too, especially Romain, Sébastien, Carolina and my work guard teddy Furby with whom I mostly shared my office, Damien, Auline, Benjamin, Leon, Kim, Christophe, Philémon, Rémi, Ali, Roula, both Matthieu(s), Virginie, Céline, Quentin, Sylvain, Wei and Zakaria, as well as the senior members, especially Stéphane(s), Olivier(s), Jacques, Damien, Agnès, Abdelkrim, Ronnie, M’hamed, Magda, Joel and the others. A friendly though also to the GCU students I had during these last years, and who made me realize how exciting teaching is.

My very best regards go to Sami for its unfaltering support, advice and joyfull motivation, as well as to Léo for its valuable help and communicative enthusiasm during my Ph.D.. Real thanks too for their patience when thoroughly proof-reading parts of my manuscript, although it deals with quite a different scientific subject from theirs.

I won't forget my other very good friends: Perrinette, Justine, Aude-Marie, Laureline, David, Florence, Noëlie, Céline, Sébastien, Agnès, Noura and Dimitris, who are always there to discuss and share their time (and food) with me.

As I also met a lot of kind persons during my curriculum, I would like to thank my teachers of the GCU department, INSA Lyon, ENSAL and IUL, and my colleagues and friends: coTP, Capi, Nico, Farid, Thomas, Théo, Anna, Sara and of course (L.)A.N.E.!

And I cannot end these acknowledgments without mentioning my sporty regards to my previous and present “energetic” colleagues, who taught me the taste of effort and perseverance. Thank you Robi at first, and my basket-ball team mates of the EStLeu, BCErmont, CMGarges, AS INSA basket and the CASI-basket team of course, and also thanks to my training partners at the gym for, among other things, all those intense moments of Xycling...

# Abstract

The rapid urban population growth involves a fast development of urban areas and increases the energy demand and greenhouse gas emissions. Hence, problems related to citizen's well-being, global warming and natural resources depletion emerge. Buildings represent 32 % of the total final energy consumption in the world. They have an impact on urban micro-climates and energy balance, which reciprocally condition the building energy demand and citizens' health and comfort. The bio-climatic design of urban areas appears as critical for preserving citizens' living conditions while improving building energy efficiency and conservation. However, such integrated urban approaches require an in-depth knowledge of the interplay between urban structures, aerodynamic processes and thermal exchanges.

This thesis is an exploratory study that lays the scientific and methodological foundations of a transverse approach for studying urban energy and bio-climatic issues. This approach involves concepts and tools of building and urban physics as well as urban planning and architecture. It addresses the relations between urban morphology and aerodynamic processes, and studies their effects on the building energy loads due to infiltration and convective heat losses.

This thesis is divided into three main parts. The first part synthesizes the specificities of urban aerodynamics and urban physics, and analyzes existing urban fabrics from a morphological point of view. Generic typologies of isolated buildings and urban blocks for small scale aerodynamic studies are deduced. The second part validates the computational fluid dynamics (CFD) model (steady RANS RSM) against detailed experimental and numerical data, and presents the numerical experiments performed on the different morphological types. Mean flow structures that develop according to the construction shape and built environment, as well as pressure distribution on the building outer walls are examined. The last part couples heat and air fluxes to evaluate the contribution of urban air flows on the building energy loads. The improvement brought by CFD to the assessment of building convective heat transfers is verified by comparing numerical results to experimental data, detailed numerical studies and standard correlations. An enhanced temperature wall-function adapted for forced convection problems is adjusted to the model based on existing studies, and the convective heat transfers distribution on building facades is analyzed. Finally, the building energy loads due to air infiltration and heat transmission are estimated for typical constructions and compared to standard values.

The results of this thesis show strong effects of the topology and dimensionality of constructions and urban structures on the development of recirculation phenomena within the urban canopy layer. The related aerodynamic conditions yield heterogeneous pressure and convective heat transfer intensities and distributions on building facades, which depend upon the considered built morphology. Their effects on building energy loads are logically particularly important in absolute value for buildings that are neither insulated nor air tight. Nonetheless, the estimates of the building energy needs based on standard or simulated pressure and convective heat transfer coefficients often show substantial deviation. Focusing on the relative contribution of the built

structure, the effects of the aerodynamic context appear more influential for insulated buildings. Essentially, switching from an exposed to a sheltered building may decrease the energy needs per surface unit of floor due to air infiltration and heat transmission through outer walls by 18 % up to 47 % according to simulation.

Hence, the methodology developed in this thesis integrates different urban factors to examine their mutual effects toward a more sustainable urban development. Results highlight the relevance of implementing an integrated and detailed approach of urban physics to better understand the building energy behavior. Nonetheless, the generalization of such an approach using usual CFD tools requires substantial computational resources. Recently developed models and computational techniques as well as dedicated full-scale experiments appear therefore promising.

**Keywords:**

Urban morphology, Urban aerodynamics, Building physics, Computational Fluid Dynamics, Infiltration, Convective heat transfers.



# Résumé

Le développement urbain contribue fortement à l'augmentation de la demande énergétique et des émissions de gaz à effet de serre. Dans le même temps, les conditions de vie des citadins, le réchauffement climatique et la raréfaction des ressources naturelles deviennent problématiques. Les bâtiments consomment 32 % de l'énergie finale mondiale. Ils modifient également le bilan énergétique et les micro-climats urbains. Ces micro-climats affectent en retour les sollicitations thermiques des bâtiments ainsi que les ambiances urbaines. L'approche bioclimatique de la construction apparaît donc être une solution d'avenir pour améliorer la performance énergétique du bâti et favoriser de bonnes conditions de vie en ville. Cependant, une telle approche requiert une connaissance fine des interrelations entre les environnements bâtis, les phénomènes aérodynamiques et les échanges thermiques se développant en milieu urbain.

L'étude exploratoire développée dans cette thèse pose les bases scientifiques et méthodologiques d'une approche transversale visant à étudier l'énergie urbaine et le bio-climatisme. Elle fait appel à des concepts et des outils empruntés à l'architecture et l'urbanisme d'une part, et à la physique du bâtiment et de la ville d'autre part. Cette thèse étudie plus particulièrement les relations entre la morphologie urbaine et les processus aérodynamiques qui se développent dans la canopée urbaine et leurs effets sur la demande énergétique des bâtiments induite par les infiltrations d'air et les échanges thermiques convectifs.

Cette thèse se compose de trois parties principales. Dans un premier temps, les spécificités de l'aérodynamique et de la physique urbaines sont synthétisées et la morphologie de tissus urbains réels est analysée. Une typologie générique de bâtiments isolés et une autre d'îlots urbains en sont déduites. Dans un second temps et afin d'étudier ensuite les écoulements d'air en milieu bâti, le modèle de mécanique des fluides numérique est validé par comparaison des prédictions du modèle avec des résultats expérimentaux et numériques détaillés. Des expérimentations numériques sont ensuite réalisées sur les différents types morphologiques. Les écoulements moyens sont analysés dans leurs rapports avec la morphologie bâtie, et la distribution des coefficients de pression sur les façades des bâtiments est analysée. Dans un troisième temps, les échanges thermiques sont couplés aux processus aérodynamiques. L'amélioration des estimations des échanges convectifs des bâtiments grâce à la mécanique des fluides numérique est vérifiée par comparaison des résultats de simulation avec des données expérimentales et numériques, ainsi qu'avec les valeurs standard généralement considérées en ingénierie du bâtiment. Une adaptation des fonctions de paroi relatives au transfert thermique est proposée sur la base d'études existantes, et la distribution des échanges convectifs sur les façades de bâtiments est analysée. Enfin, la demande énergétique des bâtiments due aux infiltrations d'air et à la transmission de chaleur au travers de leur enveloppe est estimée pour différents types morphologiques, et comparée avec les valeurs estimées suivant une approche réglementaire.

Les résultats de cette thèse mettent en évidence les effets des propriétés topologiques et métriques des bâtiments et ensembles bâtis sur le développement de recirculations d'air dans la canopée urbaine. Les conditions aérodynamiques en résultant induisent une distribution et intensité hétérogènes des coefficients de pression et d'échange convectif sur les façades des bâtiments. Ces conditions influent notablement sur le comportement thermique des bâtiments non isolés et perméables à l'air. Par ailleurs, l'estimation de leur demande énergétique diffère de façon substantielle suivant si celle-ci est basée sur les valeurs simulées ou standard des coefficients de pression et d'échange convectif. Cependant, si l'on s'intéresse à la contribution relative de la structure bâtie, l'influence des conditions aérodynamiques sur la demande énergétique des bâtiments apparaît plus importante pour les bâtiments isolés thermiquement. Selon les résultats de simulation, la différence entre la demande énergétique, rapportée à l'unité de surface de plancher, due aux infiltrations d'air et pertes thermiques au travers de l'enveloppe peut varier de 18 % à 47 % suivant si le bâtiment est isolé ou situé dans un environnement bâti.

Ainsi, la méthodologie que cette thèse développe intègre différents facteurs de l'environnement urbain (morphologie, vent) pour en étudier leurs effets mutuels dans un souci de développement urbain durable. Les résultats obtenus soulignent l'intérêt de développer une telle approche intégrée et détaillée relevant de la physique urbaine pour mieux comprendre le comportement énergétique des bâtiments. Cependant, la généralisation de cette approche nécessiterait des moyens de calculs très importants. Les méthodes et techniques de calculs nouvellement développées ainsi que des études expérimentales dédiées en site réel apparaissent donc incontournables pour porter cette démarche plus loin.

#### **Mots-clefs:**

Morphologie urbaine, Aérodynamique urbaine, Physique du bâtiment, Mécanique des fluides numérique, Infiltrations d'air, Transferts de chaleur convectifs.



# Long Résumé

*Cette thèse a été réalisée au CETHIL-UMR 5008, sous la direction et l'encadrement de F. KUZNIK (Pr, CETHIL), G. RUSAOUËN (MCF, CETHIL) et J. HANS (Dr, CSTB). Ont également participé à l'encadrement de ces travaux J.J. ROUX (Pr, CETHIL) et S. SALAT (Dr, IMUSC).*

## Introduction

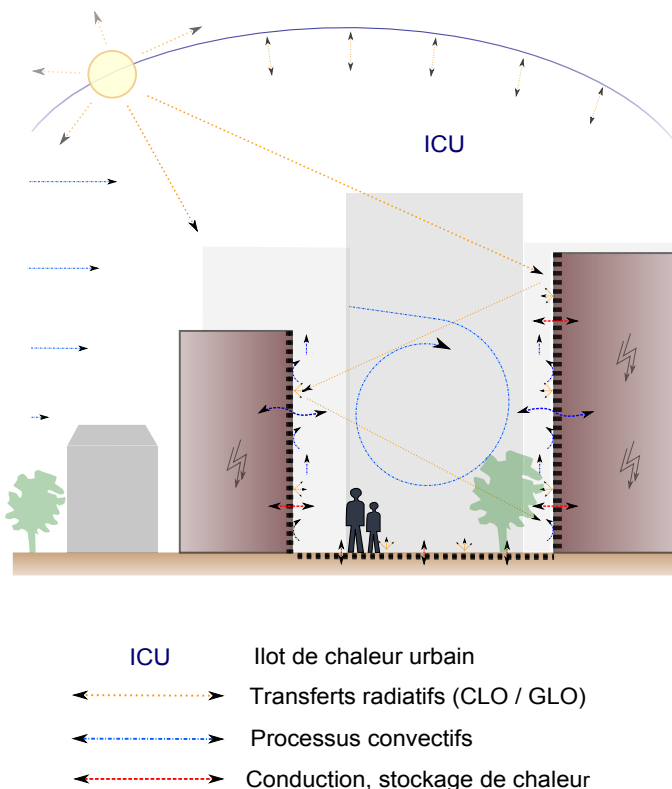
Le secteur du bâtiment représente 35 % de la consommation d'énergie finale dans le monde et ce ratio atteint 44 % en France (ADEME, 2013a; IEA, 2010). Dans le contexte actuel de raréfaction des ressources naturelles et de crise environnementale, améliorer la sobriété et l'efficacité énergétique des bâtiments et de nos villes se révèle être un levier d'action des plus importants. Par ailleurs, en France, plus de la moitié de la consommation énergétique de bâtiments est utilisée pour garantir des ambiances intérieures thermiquement confortables (CEREN, 2014). S'il s'agit principalement de chauffer les bâtiments, la climatisation a connu un très fort développement ces dernières années, notamment du fait des fortes vagues de chaleur dont la fréquence augmente. Bien que ne faisant pas appel à des solutions technologiques de pointe, mais reposant sur une synergie entre le bâtiment et son environnement, la gestion bioclimatique des espaces bâtis et urbains apparaît ainsi comme une solution d'avenir pour répondre aux enjeux du développement durable.

Dans ce contexte, l'étude exploratoire développée dans cette thèse pose les bases scientifiques et méthodologiques d'une approche transversale visant à étudier l'énergétique urbaine et le bioclimatisme. Elle fait appel à des concepts et des outils empruntés à l'architecture et l'urbanisme d'une part, et à la physique du bâtiment et de la ville d'autre part. Cette thèse étudie plus particulièrement les relations entre la morphologie urbaine et les processus aérodynamiques qui se développent autour des constructions, ainsi que leurs effets sur la demande énergétique des bâtiments induite par les infiltrations d'air et les échanges thermiques convectifs.

Cette thèse se compose de trois parties. Premièrement, les spécificités de l'aérodynamique et de la physique urbaines sont synthétisées et la morphologie de tissus urbains réels est analysée. Une typologie générique de bâtiments isolés et une autre d'îlots urbains en sont déduites. En second lieu, le modèle de mécanique des fluides numérique est validé par comparaison avec des résultats expérimentaux et numériques détaillés. Des expérimentations numériques sont réalisées sur les différents types morphologiques. Les écoulements moyens sont analysés dans leurs rapports avec la morphologie bâtie, et la distribution des coefficients de pression ( $C_p$ ) sur les façades des bâtiments est analysée. Dans un troisième temps, les échanges thermiques sont couplés aux processus aérodynamiques. Une adaptation des fonctions de paroi relatives au transfert thermique est alors proposée sur la base d'études existantes, et la distribution des coefficients d'échanges convectifs ( $h_{c,w}$ ) sur les façades de bâtiments est analysée. La demande énergétique des bâtiments due aux infiltrations d'air et à la transmission de chaleur au travers de leur enveloppe est finalement estimée pour différents types morphologiques, et comparée avec les valeurs estimées suivant une approche réglementaire.

# 1. Bases de l'étude

## 1.1. Phénoménologie et cadre de la thèse

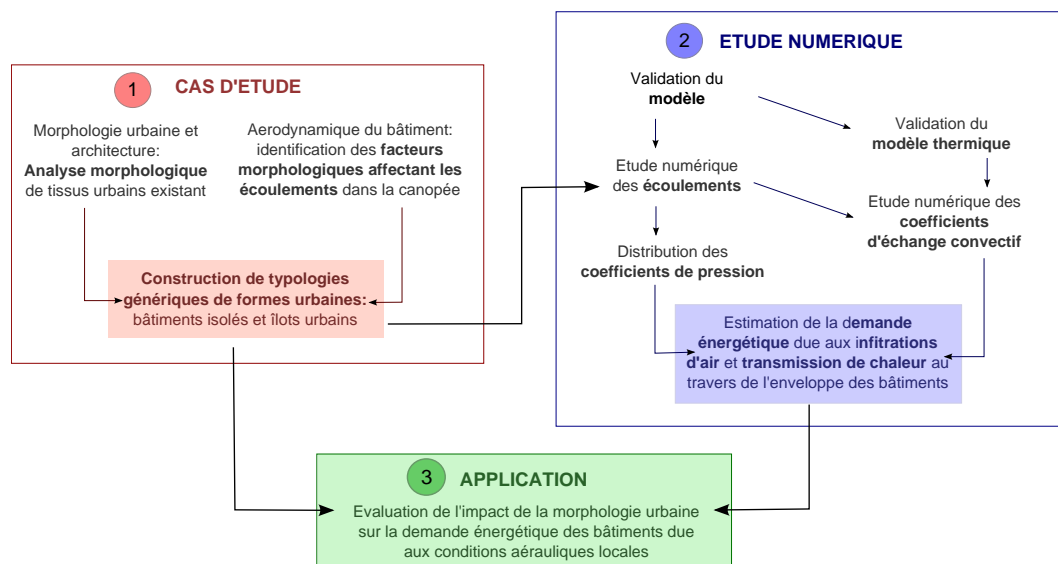


$\alpha$ . Micro-climats urbains et échanges thermo-aérodynamiques entre le bâtiment et son environnement

Le comportement énergétique des bâtiments dépend fortement des conditions ambiantales et donc des micro-climats locaux. Ces micro-climats dépendent eux-mêmes des interactions entre les bâtiments et le climat urbain plus général. Plus spécifiquement, les conditions thermo-aérodynamiques locales affectent les transferts de chaleur au travers de l'enveloppe des constructions de par les transferts radiatifs et convectifs spécifiques qu'elles créent, mais également les infiltrations d'air et le potentiel de ventilation naturelle des bâtiments (Fig.  $\alpha$ ). Réciproquement, les constructions affectent leur environnement, en créant notamment des masques solaires et des circulations aérodynamiques particulières. Ils participent plus généralement à créer le phénomène d'îlot de chaleur urbain (ICU).

Différentes études ont montré l'influence considérable de l'environnement urbain sur la demande énergétique des constructions comparé à une configuration de bâtiment isolé (Allegri et al., 2012b; Bouyer et al., 2011). Les effets radiatifs sont montrés fondamentaux mais les effets liés aux circulations d'air, i.e. les échanges convectifs et la ventilation naturelle, sont aussi des facteurs importants, surtout en saison chaude. En effet, l'environnement urbain provoque en général une diminution des vitesses de vent du fait de la présence de multiples obstacles, et conduit à des températures d'air plus chaudes, surtout en soirée. S'ajoute à ces transferts de chaleur par convection et à la ventilation, les infiltrations d'air, dont la connaissance et les effets sur le comportement énergétique des bâtiments restent aujourd'hui limités.

La connaissance des conditions aérodynamiques locales urbaines est donc une problématique scientifique à fort enjeu, d'autant plus que la ventilation des espaces urbains semble être un des moyens les plus efficaces pour atténuer l'effet d'ICU (Givoni, 1998). Cependant, les phénomènes en jeu sont très complexes. Les bâtiments sont en général des obstacles rigides à angles saillants qui engendrent des phénomènes complexes de séparation d'écoulement aux arêtes. Par ailleurs, des recirculations interagissant avec les structures d'écoulement avoisinantes et aux différentes échelles, sont créées en fonction des propriétés générales de la ville, mais également en fonction de la morphologie bâtie locale. La connaissance des phénomènes convectifs est d'autant plus complexe que la turbulence demeure encore aujourd'hui un problème scientifique ouvert.



### β. Méthodologie d'étude

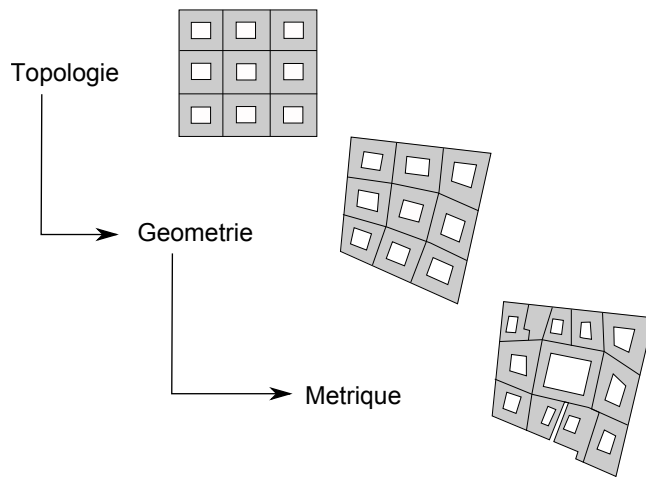
L'objectif de cette thèse est d'apporter des connaissances relatives à l'influence de la morphologie bâtie sur les mécanismes aérodynamiques et convectifs se développant en milieu urbain en régime de convection forcée. Plus précisément, cette thèse vise à apporter des éléments de réponse aux questions suivantes:

- *Quelles sont les principales structures d'écoulement qui se développent aux abords des bâtiments en fonction de la morphologie bâtie?*
- *Comment ces structures d'écoulement particulières affectent-elles les sollicitations énergétiques des bâtiments dues aux infiltrations d'air et transferts thermiques convectifs?*

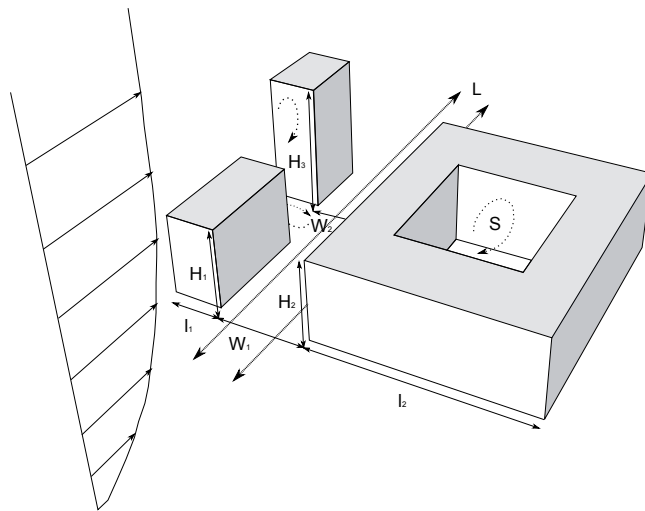
D'un point de vue urbanistique, il s'agit donc d'étudier l'influence de la morphologie bâtie sur les conditions aérauliques dans l'environnement proche des constructions afin de promouvoir une conception intégrée des bâtiments et des quartiers. D'un point de vue physique, il s'agit d'analyser les processus aérodynamiques se développant dans l'environnement proche des constructions et leur impact sur les sollicitations thermo-aérauliques de bâtiments. Pour ce faire une méthodologie transdisciplinaire composée de trois blocs principaux a été développée (Fig β.).

(1) Le premier bloc de travail inclut une analyse morphologique de tissus urbains traditionnels existant situés sur différents continents. L'objectif est de mettre en évidence leurs points communs ou principales différences, et éventuellement des stratégies bioclimatiques. Cette analyse se superpose à une identification des principaux facteurs morphologiques affectant les structures d'écoulement dans la canopée urbaine basée sur une revue détaillée de littérature, permettant ainsi la définition des cas d'étude. (2) Le second bloc de travail, le plus conséquent, développe l'approche numérique. Il intègre les validations des modèles aérodynamiques et thermiques, nécessaires à la réalisation des simulations, à l'étude des structures 3D d'écoulement et à l'analyse des distributions des  $C_p$  et  $h_{c,w}$  sur les façades des bâtiments types dans leur rapport à la morphologie bâtie. (3) Le troisième bloc de travail utilise les résultats obtenus pour évaluer la demande énergétique des bâtiments due aux infiltrations d'air et à la transmission de chaleur au travers de l'enveloppe en fonction des structures d'écoulement identifiées et donc de la morphologie bâtie. Ces résultats sont ensuite discutés dans leurs différences par rapport aux valeurs couramment estimées en ingénierie physique du bâtiment.

## 1.2. Construction des cas d'étude



γ. Paramètres morphologiques des formes bâties.



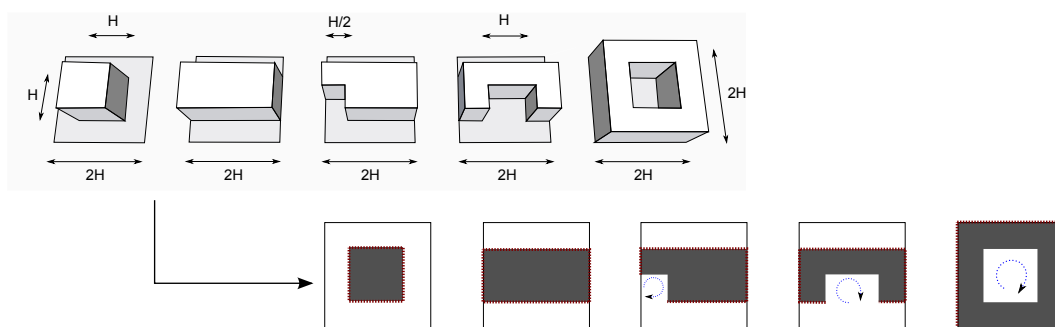
δ. Paramètres morphologiques affectant les structures d'écoulement en milieu urbain à l'échelle du îlot.

Des tissus urbains très divers existent dans le monde, compte tenu des différents contextes climatiques et culturels régionaux. En particulier, des tissus continus ou non, formés de blocs compacts ou articulés autour de cours, aux tracés organiques ou orthogonaux, ou présentant des granulométries homogènes ou variées existent. Leurs formes bâties peuvent être étudiées objectivement en termes de topologie, géométrie et de métrique (Fig. γ), permettant ainsi de tendre vers une classification des formes (Burdet, 2011).

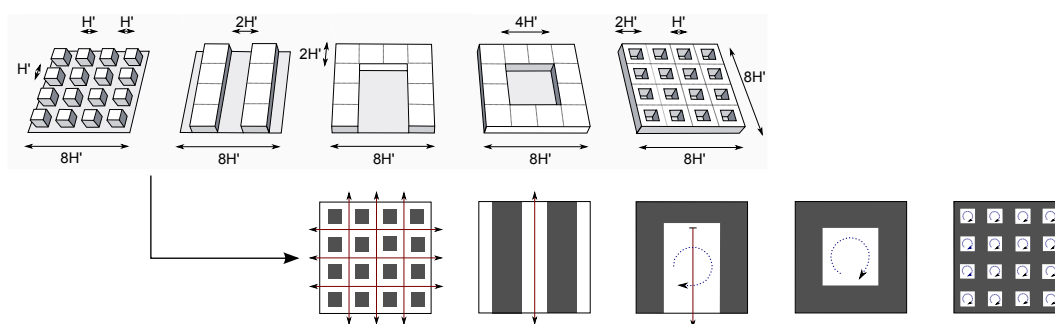
Pour étudier ces aspects morphologiques, les échelles du quartier et de l'îlot urbain sont particulièrement pertinentes. Ces échelles sont également celles où s'observent les processus aérauliques affectant la demande énergétique des bâtiments. Une revue bibliographique détaillée des approches bioclimatiques des tissus urbains et des indicateurs morphométriques urbains caractérisant ces processus aérodynamiques a mis en évidence l'influence de deux familles de facteurs morphologiques sur le développement de structures d'écoulement particulières: la rugosité et la porosité (Fig. δ).

A l'échelle de l'îlot, la rugosité urbaine fait référence à des propriétés de distribution verticale des éléments bâtis en termes de hauteur moyenne et d'ouverture au ciel des tissus. La rugosité urbaine affecte donc les échanges entre l'intérieur de la canopée et l'air susjacent. La porosité urbaine fait référence à la distribution et aux propriétés horizontales des vides urbains au sein de la canopée, c'est à dire aux propriétés morphologiques conduisant à la création de circulations d'air privilégiées, de blocage des écoulements et au développement de recirculations. Elle traduit donc des propriétés de continuité horizontale, d'orientation et de taille des vides urbains, qui font directement référence aux caractéristiques topologiques, géométriques et métriques permettant l'analyse morphologique des tissus. C'est donc sur cette base de critères hiérarchisés que les différents tissus urbains<sup>1</sup> ont été analysés et abstraits afin de former les deux typologies d'étude, chacune composée de cinq types génériques.

<sup>1</sup>tissus étudiés dans (Firley and Stahl, 2010; Salat, 2011).



ε. Typologie générique de bâtiments isolés



ζ. Typologie générique d'îlots urbains.

La typologie de bâtiments isolés intègre le cube, le pavé, le bâtiment en L, le bâtiment en U et le bâtiment à cour / patio (Fig. ε). Une progression peut être observée du cube vers le patio: le bâtiment voit sa compacité diminuer au profit de l'émergence d'une cour intérieure. Par ailleurs, le cube et le patio sont les négatifs l'un de l'autre. Cette typologie permet en particulier d'examiner les structures d'écoulement qui se développent autour d'un bâtiment compact et leur altération par la présence de cours semi ou totalement fermées. Les conditions aérauliques au sein d'une cour fermée, typique de nombreuses architectures traditionnelles peuvent également être mis en évidence.

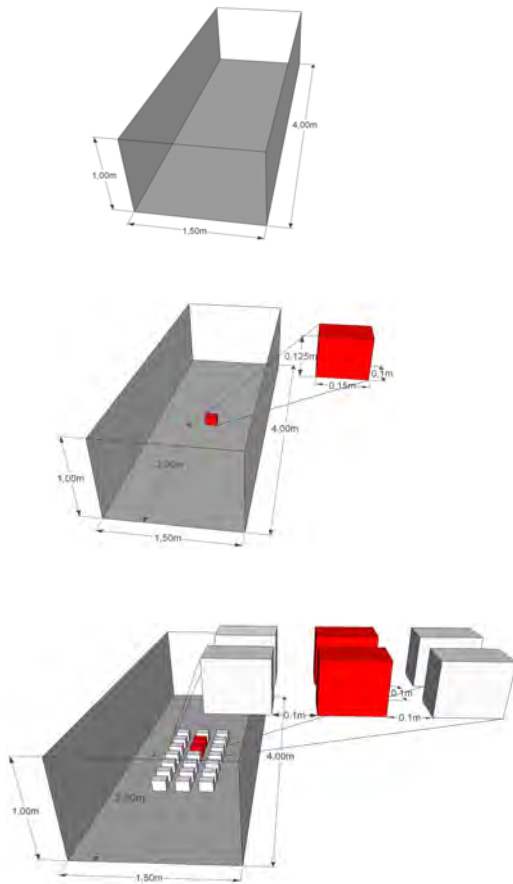
La typologie d'îlots urbains intègre le réseau de cubes, les bâtiments en bande, l'îlot en U, l'îlot fermé et le réseau continu de bâtiments à cour (Fig. ζ). Une progression peut également être observée du réseau de cubes au réseau de patios: l'îlot urbain, initialement traversant dans les deux directions du plan horizontal voit les limites de son vide progressivement se refermer, et des cours intérieures émergent. Les réseaux de cubes et de patios sont les négatifs l'un de l'autre et présentent les structures les plus fractales. Cette typologie permet non seulement l'étude des écoulements se développant à l'intérieur des îlots, et plus particulièrement l'évolution des recirculations au sein des réseaux de constructions, mais également de mettre en évidence l'effet de l'ensemble de la structure bâtie sur les écoulements se développant autour de l'îlot.

Le fait que les cas d'étude soient génériques est restrictif. Cela implique de nombreuses simplifications, notamment au regard du caractère orthogonal des formes et de leur faible rugosité. Cependant, ceci est nécessaire afin de conserver leur représentativité et de pouvoir mettre directement en relation les formes avec les flux étudiés. Par ailleurs, chaque type peut ensuite être complexifié pour se rapprocher des formes bâties réelles, sans créer de nouveaux types tels que définis dans ce travail.



## 2. Etude numérique de l'aérodynamique

### 2.1. Validation du modèle de dynamique des fluides

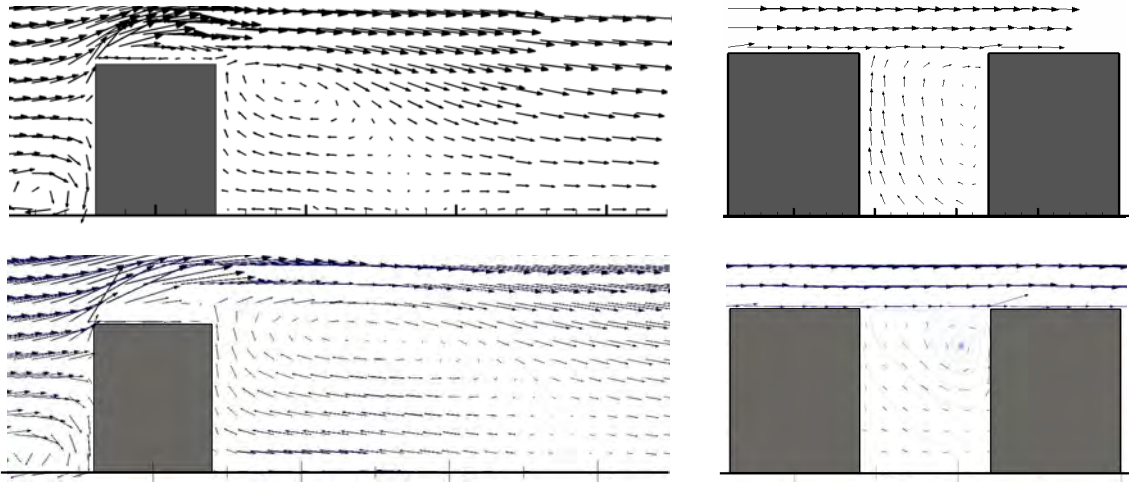


η. Configurations physiques étudiées pour la validation du modèle

L'approche numérique développée dans cette thèse repose sur la méthode dite "Steady RANS". Le champ moyen de vitesse est résolu alors que les effets de la turbulence sont modélisés en se plaçant en régime permanent. Cette méthode fait donc l'hypothèse de l'existence d'un champ aérodynamique moyen au sens de la décomposition de Reynolds des équations de Navier-Stokes. Cette approche nécessite l'utilisation de modèles de turbulence, dont les principaux peuvent être classés en deux familles: ceux qui font l'hypothèse d'une turbulence isotrope (e.g. les modèles type  $k-\epsilon$ ) ou qui prennent en compte l'anisotropie de la turbulence (modèles aux tensions de Reynolds, RSM). Si les modèles steady RANS sont réputés efficaces pour de nombreuses utilisations industrielles et pour prédire les zones de grandes vitesses en milieu urbain, ils sont en général incapables de reproduire précisément les phénomènes transitoires de séparation / réattachement et les recirculations des écoulements. Cependant, l'objectif du travail n'étant pas de prédire précisément les phénomènes mais d'identifier et comprendre les mécanismes en jeu en utilisant des ressources informatiques raisonnables, l'utilisation de ces modèles se justifie en première approche.

Afin d'évaluer les incertitudes sur les résultats de simulation et de définir leur domaine de validité, les performances des modèles  $k-\epsilon$  réalisable (R $k-\epsilon$ ) et RSM ont été évaluées par comparaison avec des données expérimentales et numériques détaillées. Comme recommandé dans la littérature, trois configurations ont été étudiées: un domaine vide, vérifiant la cohérence du profil de vent incident, un obstacle isolé à angles saillants, i.e. un pavé, et une configuration multi-obstacles, en l'occurrence un réseau de pavés (Fig. η). Chacune de ces configurations a été étudiée en soufflerie (CEDVAL, 2013) et a été reproduite par simulation aux grandes échelles (LES) avec la méthode de Boltzmann sur gaz réseau (LBM) (Obrecht et al., 2014).

Les simulations RANS ont été réalisées avec le logiciel Ansys Fluent version 14.5 (Ansys Fluent, 2013b). Le domaine reproduit la section test expérimentale et le profil de vent incident a été modélisé par simulation préliminaire d'un long domaine vide. Des fonctions de parois standard modélisent le comportement de l'écoulement proche des parois et les gradients longitudinaux sont supposés nuls en sortie du domaine. Les parois verticales et supérieure du domaine ainsi que les faces des obstacles sont supposées non glissantes et lisses, tandis que le sol est considéré rugueux ou lisse. L'analyse des résultats est faite pour le plan médian vertical du domaine.



10. Champs de vitesse moyenne pour l'obstacle isolé et le canyon. Haut: expérience; bas: simulation RSM.

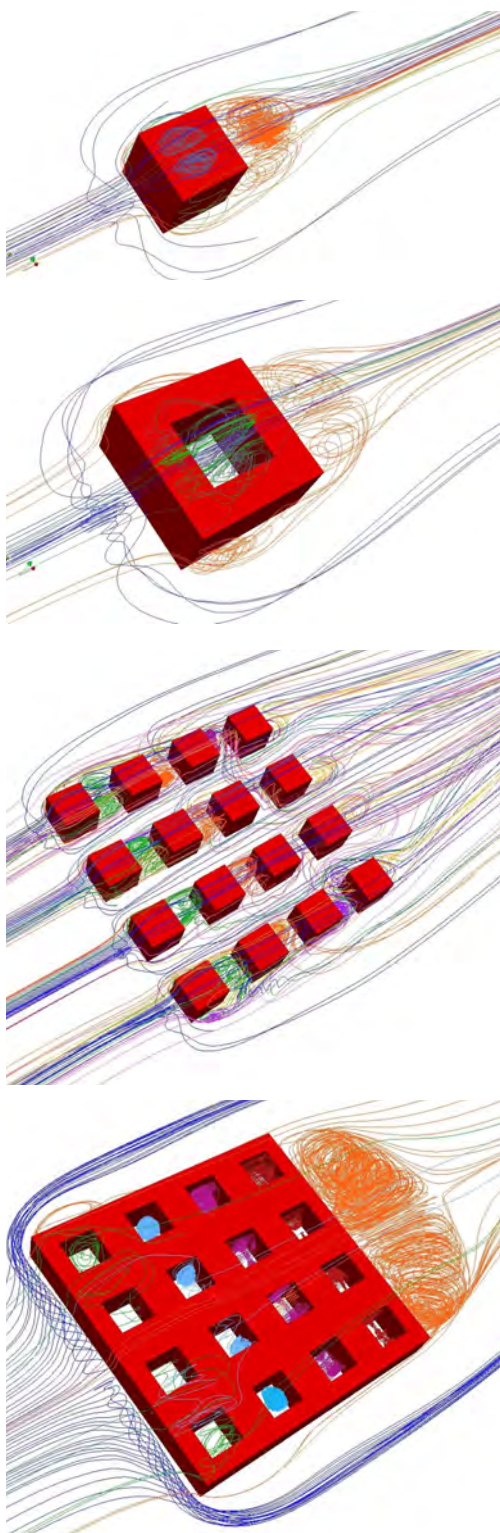
Les résultats montrent qu'un profil de vent incident cohérent peut être obtenu grâce à la simulation préliminaire d'un tunnel vide suffisamment long et présentant les mêmes conditions aux limites (sauf d'entrée) que le domaine d'étude final. En effet, le profil de vent moyen obtenu correspond à celui de l'expérience. En revanche, la modification des conditions aux limites (notamment de rugosité) entre la simulation préliminaire et la finale engendre le développement de gradients longitudinaux. La couche limite simulée n'est alors plus à l'équilibre, et le modèle numérique n'est souvent plus représentatif de la physique à modéliser. Ceci peut impacter les structures d'écoulement simulées autour des obstacles.

Chacun des modèles RANS reproduit les principales recirculations se développant autour de l'obstacle isolé: le vortex amont, celle se développant à la séparation de l'écoulement de l'arête supérieure amont de l'obstacle et celle de derrière (Fig. 10 haut). Cependant, dans le cas rugueux, le modèle RSM prédit la recirculation amont légèrement trop en amont et semble moins bien reproduire la recirculation supérieure que le modèle  $Rk-\epsilon$ . En revanche, bien que prédite plus longue qu'observée expérimentalement, la recirculation arrière est mieux reproduite par le modèle RSM que par le  $Rk-\epsilon$ . Dans le cas lisse, les résultats du modèle RSM sont plus proches de ceux des simulations LBM LES que ne le sont ceux du modèle  $Rk-\epsilon$ .

L'analyse de ces résultats souligne également le manque de représentativité physique des exploitations 2D. Si elles sont plus faciles à quantifier, les données 2D ne permettent généralement pas de comprendre correctement les écoulements 3D complexes se développant autour des obstacles. Une méthode d'analyse 3D est donc à développer pour pouvoir répondre à cet objectif.

Considérant le cas multi-obstacles, le vortex se développant dans le canyon est reproduit par le modèle RSM mais pas par le  $Rk-\epsilon$  (Fig. 10 bas). Notons en outre que l'expérience rapporte un caractère fortement instationnaire de l'écoulement, nécessitant des durées de moyennage importants. Ceci explique très probablement les résultats des simulations RSM. Si le modèle reproduit le vortex, les profils de vitesse moyenne ne se stabilisent pas en fonction du nombre d'itérations; et ce, quel que soit la résolution du maillage. Ceci questionne la pertinence de l'utilisation courante des modèles de type steady RANS pour l'étude d'écoulements urbains. Cependant, étant capable de reproduire les principaux phénomènes aérodynamiques se développant autour d'obstacles à angles saillants, le modèle RSM est retenu pour la suite de l'étude.

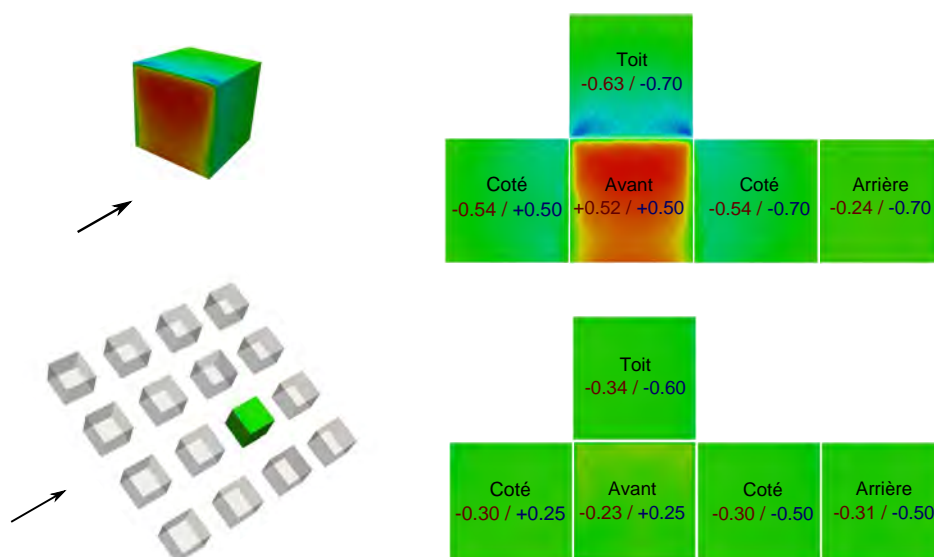
## 2.2. Etude des écoulements autour des cas d'étude



ι. Exemples d'écoulements moyens 3D simulés pour types morphologiques basés sur le cube et le patio.

Les expérimentations numériques ont été réalisées pour les différents types morphologiques définis en se basant sur les conclusions de la phase de validation aérodynamique et les recommandations de la littérature. Compte tenu des dimensions des bâtiments et îlots urbains, deux tailles de domaine ont été considérées. Le profil de vent d'entrée a été défini par simulation préliminaire d'un long domaine vide au sol rugueux. La vitesse du vent à 10 m est de  $4.3 \text{ m} \cdot \text{s}^{-1}$ . Différentes orientations du vent ont été testées suivant la symétrie des obstacles, mais toujours avec une incidence perpendiculaire aux faces principales du ceux-ci.

Les structures d'écoulement basiques, i.e. la recirculation en fer à cheval, les recirculations se développant au niveau des arêtes amont de l'obstacle et le vortex aval en forme d'arche, se développent autour du cube. Ces structures d'écoulement se retrouvent également autour du bâtiment patio, bien que modifiées. La recirculation arrière est plus importante, principalement du fait de la plus grande largeur de l'obstacle. Il en est de même pour les autres bâtiments présentant une large empreinte au sol extérieure. En revanche, l'augmentation de la longueur des obstacles tend à diminuer, dans une moindre mesure, la taille de la recirculation avale. La présence d'une cour crée des recirculations intérieures particulières, qui diffèrent suivant leur ouverture. Des vortex en forme de tubes verticaux peuvent apparaître dans les cours amont des bâtiments en L, alors qu'une recirculation relativement indépendante et d'axe horizontal est formée dans le patio. Les structures d'écoulement formées dans les cours situées sur les parties aval des obstacles ou centrées en amont des bâtiments isolés se confondent en général avec les circulations "basiques" se développant autour des constructions, conduisant à une amplification ou une déformation de celles-ci, notamment lorsque le bâtiment est asymétrique par rapport à l'incidence du vent. Le réattachement ou non de l'écoulement sur les faces des obstacles influe également sur la forme du sillage proche.



κ. Distribution et  $C_p$  moyen par face pour le cube isolé ou non. Rouge: simulation; Bleu: standard.

Les grandes dimensions des cours des îlots en U ou à cour fermée conduisent généralement à la formation de structures d'écoulement relativement indépendantes. Les vides traversant parallèles au vent induisent des circulations d'air privilégiées tandis qu'un écoulement très complexe est observé dans la rue canyon formée par les bâtiments en bande placés perpendiculairement au vent. Dans les vides intérieurs protégés du vent (derrière les cubes et dans les patios), des recirculations se forment. Leur forme varie en fonction de leur distance à la limite amont de l'îlot. Si les structures d'écoulement se développant autour des cubes de première ligne ressemblent beaucoup à celles observées pour le cas isolé, elles se déforment ensuite du fait des masques aérodynamiques et des flux latéraux convergents. Des structures d'écoulement particulières se développent dans la première ligne de patios du fait de la formation d'une bulle de séparation supérieure à l'échelle du bloc. L'écoulement réattachant en aval, des recirculations proches de celle observée dans le cas du patio isolé se développent ensuite.

La topologie et les dimensions des différents types morphologiques créent donc des structures d'écoulement très locales, et les recirculations sont en général de relativement faible vitesse. Cependant, la porosité des structures bâties peut engendrer quelques survitesses, notamment aux coins amont des obstacles.

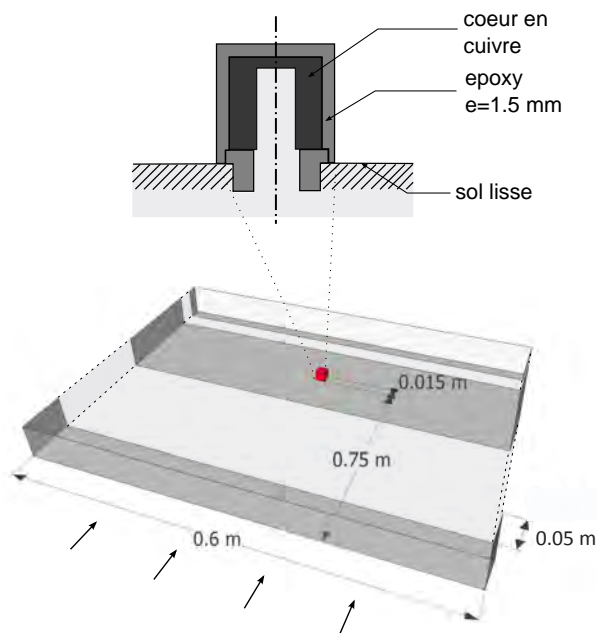
La distribution des  $C_p$  a été évaluée pour le cube, le patio, le réseau de cubes ainsi que le réseau de patios (exemples en Fig. κ). Le développement de zones d'impact ou de recirculation sur les façades des constructions conduit à des  $C_p$  moyens très hétérogènes. D'après les résultats de simulation, seules les faces directement au vent sont caractérisées par des  $C_p$  positifs, alors que les zones de séparation présentent les dépressions les plus importantes. De forts gradients sont observés sur ces faces, particulièrement sur les toits des bâtiments exposés au vent. Les  $C_p$  à l'intérieur des patios sont fortement corrélés à ceux observés au dessus, et sont relativement homogènes sur les différentes faces. Par contre, les  $C_p$  varient considérablement en fonction de la distance à la face avant des constructions. En effet, la bulle de séparation formée sur la partie amont des constructions conduit à des  $C_p$  négatifs très importants.

Ces résultats diffèrent de ceux qui peuvent être dérivés de la RT 2012 (CSTB, 2012a). Conventionnellement, la moitié des faces des bâtiments est caractérisée par des  $C_p$  moyens positifs et la diminution de leur intensité n'est pas aussi importante que simulée lorsque des masques au vent sont présents.

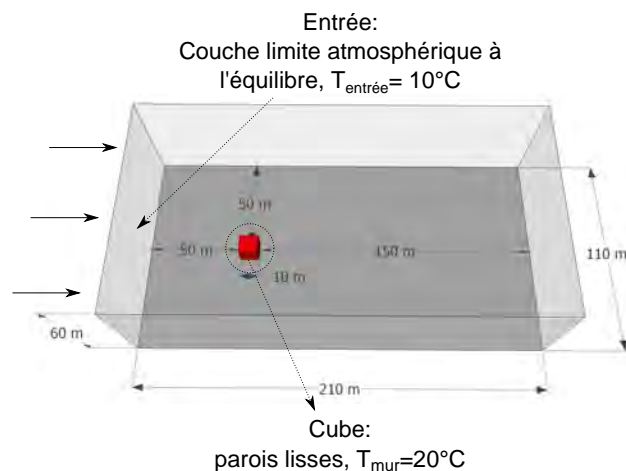


### 3. Effet du vent sur le bilan thermique des bâtiments

#### 3.1. Etude des coefficients d'échange convectif extérieurs



λ. Configuration physique utilisée pour la validation du modèle thermique (bas Reynolds).



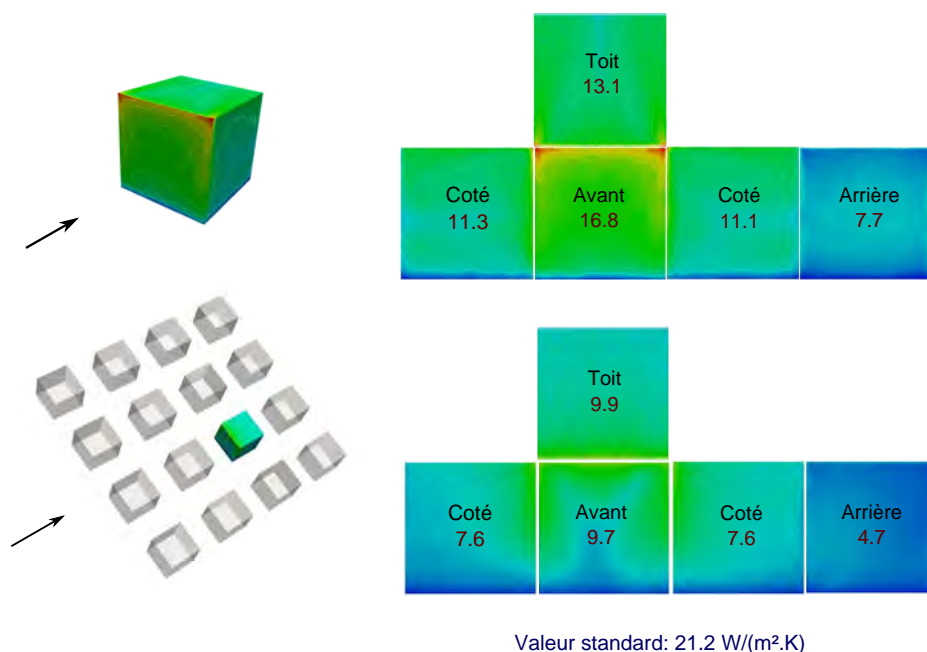
μ. Cas test utilisé pour l'évaluation des fonctions de paroi pour la température.

Un modèle de transfert thermique a été couplé au modèle aérodynamique dans Fluent. La validation du modèle aérodynamique ne permettant pas de garantir la validité des transferts de chaleur calculés aux parois, une étude dédiée a été réalisée. Ni les transferts radiatifs ni la flottabilité ne sont considérés (convection forcée prédominante).

Premièrement, la précision des modèles RSM et  $Rk-\epsilon$  a été évaluée par comparaison des  $h_{c,w}$  simulés avec des données expérimentales (Meinders et al., 1999) et numériques (Defraeye et al., 2010) de référence pour un cube de 1.5 cm placé dans une couche limite en développement (Fig. λ). Bien que peu représentatif des problématiques urbaines, ce cas d'étude permet d'utiliser un modèle bas Reynolds en proche paroi, qui résout la couche limite.

Les modèles prédisent bien la distribution de  $h_{c,w}$  sur la face avant de l'obstacle et de façon satisfaisante sur la face arrière, où une légère différence entre les deux modèles est cependant observée. En revanche, les prédictions diffèrent considérablement entre elles et par rapport à l'expérience sur les autres faces, où les phénomènes de séparation / réattachement se développent physiquement. De plus, les profils de  $h_{c,w}$  simulés avec le modèle RSM ne se stabilisent pas sur les faces latérales du cube, pour lesquelles l'expérience rapporte, là encore, des phénomènes fortement instationnaires.

Comme il est généralement impossible d'utiliser un modèle bas Reynolds pour les problèmes de physique du bâtiment, une seconde étude a évalué la validité des fonctions de paroi pour la température couplées au modèle RSM ou  $Rk-\epsilon$ . Pour ce faire, un bâtiment cubique théorique de 10 m placé dans une couche limite atmosphérique a été modélisé (Fig. μ), et les résultats comparés avec des résultats numériques de référence obtenus avec le modèle  $Rk-\epsilon$  et une approche bas Reynolds (Defraeye, 2009).



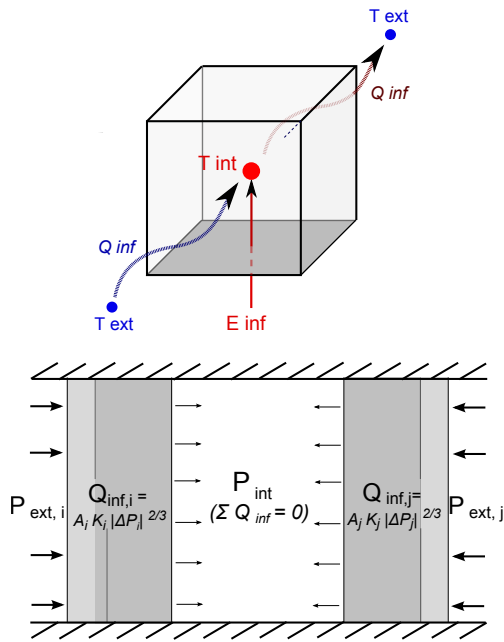
$\nu$ . Distribution et  $h_{c,w}$  moyen par face pour le cube isolé ou non. Rouge: simulation; Bleu: standard.

Les simulations mettent en évidence une sur-estimation considérable des  $h_{c,w}$  prédits par les fonctions de paroi standard, confirmant les résultats de la littérature. Cependant, il est possible de modifier celles-ci afin de se rapprocher des résultats de modélisation bas Reynolds. En particulier, une bonne correspondance est obtenue en modifiant la valeur de  $Pr_{t,w}$  de 0.85 par défaut à 1.95 avec un modèle  $k-\varepsilon$  (Defraeye et al., 2011a). Ceci ne permet cependant pas d'obtenir des prédictions satisfaisantes avec le modèle RSM. Une optimisation du  $Pr_{t,w}$  a donc été réalisée, montrant une bonne performance du modèle pour  $Pr_{t,w} = 1.55$ .

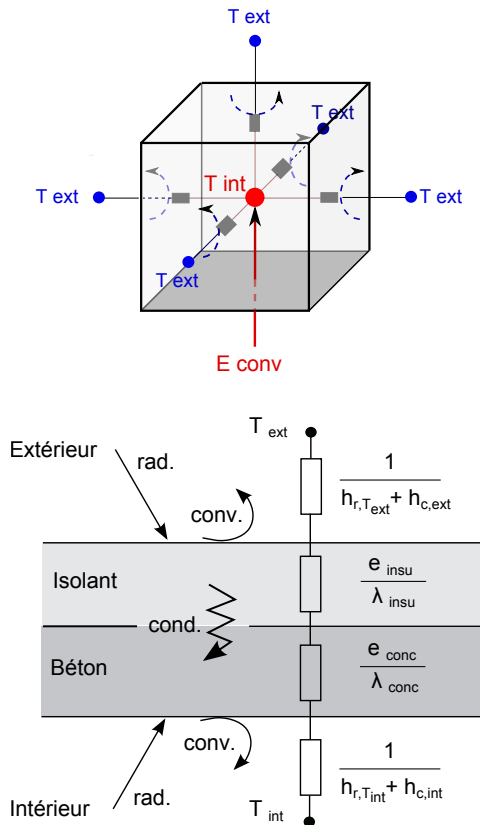
Les simulations couplées ont ensuite été réalisées pour le cube, le patio, le réseau de cubes et le réseau de patios en intégrant cette fonction de paroi adaptée pour la température. Une différence de 5 °C entre la température d'air de référence et les parois des types est considérée (cas de convection forcée). Le développement de zones d'impact ou de recirculation derrière les constructions conduit à des distributions de  $h_{c,w}$  très hétérogènes. D'après les résultats de simulation (exemples en Fig.  $\nu$ ), les faces directement au vent présentent les  $h_{c,w}$  les plus importants, alors que les zones sous le vent présentent les  $h_{c,w}$  les plus faibles, de l'ordre de la moitié de ceux observés pour les faces avant. Les valeurs de  $h_{c,w}$  à l'intérieur des patios sont similaires à celles observées pour les faces arrières des constructions, ce qui s'explique par le développement de recirculations de grande taille. Par ailleurs, la distribution de  $h_{c,w}$  est relativement homogène sur les différentes faces de la cour à l'exception de la partie supérieure de la face au vent. Cette homogénéité s'observe également pour les différents patios du réseau de patios. Au contraire, des variations de  $h_{c,w}$  moyen sont observées à au sein du réseau de cubes, particulièrement entre les faces avant et arrière des cubes, la ligne de cube de tête se comportant de façon relativement similaire au cube isolé.

Ces résultats diffèrent de ceux qui peuvent être généralement dérivés de la RT 2012 (CSTB, 2012b). En effet, ne disposant généralement pas d'information sur la vitesse de vent local, les  $h_{c,w}$  moyens sur les surfaces sont souvent estimés en considérant  $U_{10}$ . Cette simplification conduit à une estimation uniforme des  $h_{c,w}$  sur toutes les façades des constructions qui s'avère par ailleurs être plus élevée que le plus grand  $h_{c,w}$  moyen simulé pour les faces au vent.

### 3.2. Effets du vent sur la demande énergétique des bâtiments due aux infiltrations d'air et transmission de chaleur au travers de l'enveloppe



$\pi$ . Infiltration d'air et bilan de masse.



$\xi$ . Bilan thermique et transmission de chaleur dans les parois.

Afin d'évaluer l'effet des conditions aérodynamiques locales induites par les formes bâties sur le bilan thermo-aérodynamique des constructions, la demande énergétique de chauffage due aux infiltrations d'air et transmission de chaleur au travers de l'enveloppe de bâtiments a été évaluée pour une différence de température de  $10^{\circ}\text{C}$ . Des bâtiments cubiques ou à cour, isolés ou non, constitués uniquement de parois opaques et présentant de bonnes ou mauvaises performances (isolation thermique et d'étanchéité à l'air) ont été étudiés. Pour ce faire, les méthodologies proposées par les annexes de la RT 2012 ont été appliquées en considérant les  $C_p$  et  $h_{c,w}$  déduits des simulations ou leurs valeurs classiques. Les demandes énergétiques ont été estimées en effectuant le bilan de masse (Fig.  $\pi$ ) et de chaleur (Fig.  $\xi$ ) des volumes intérieurs, considérés à température et pression constantes et uniformes.

La demande énergétique ramenée à l'unité de surface de plancher d'un bâtiment non isolé et perméable à l'air est d'un ordre de grandeur supérieur à celle d'un bâtiment performant. La part liée aux infiltrations d'air est en général plus faible que celle liée à la transmission de chaleur, mais sa contribution est relativement importante pour les bâtiments bien isolés thermiquement. Si les bâtiments bien étanches à l'air sont caractérisés par une demande énergétique liée aux infiltrations très faible, celle-ci, tout comme celle estimée pour des bâtiments perméables à l'air est très dépendante des conditions de pression sur les façades. D'après les simulations, passer d'une configuration de cube exposé à protégé du vent peut réduire la demande énergétique liée aux infiltrations d'air de plus de 80%. De façon générale, la considération des valeurs standards de  $C_p$  au lieu des valeurs simulées conduit à une estimation plus importante des débits d'infiltration. De plus, compte tenu de la distribution conventionnelle des  $C_p$  et de leur plus faible réduction induite par la présence de masques, cette diminution des débits d'infiltration est estimée moindre en suivant une approche standard.

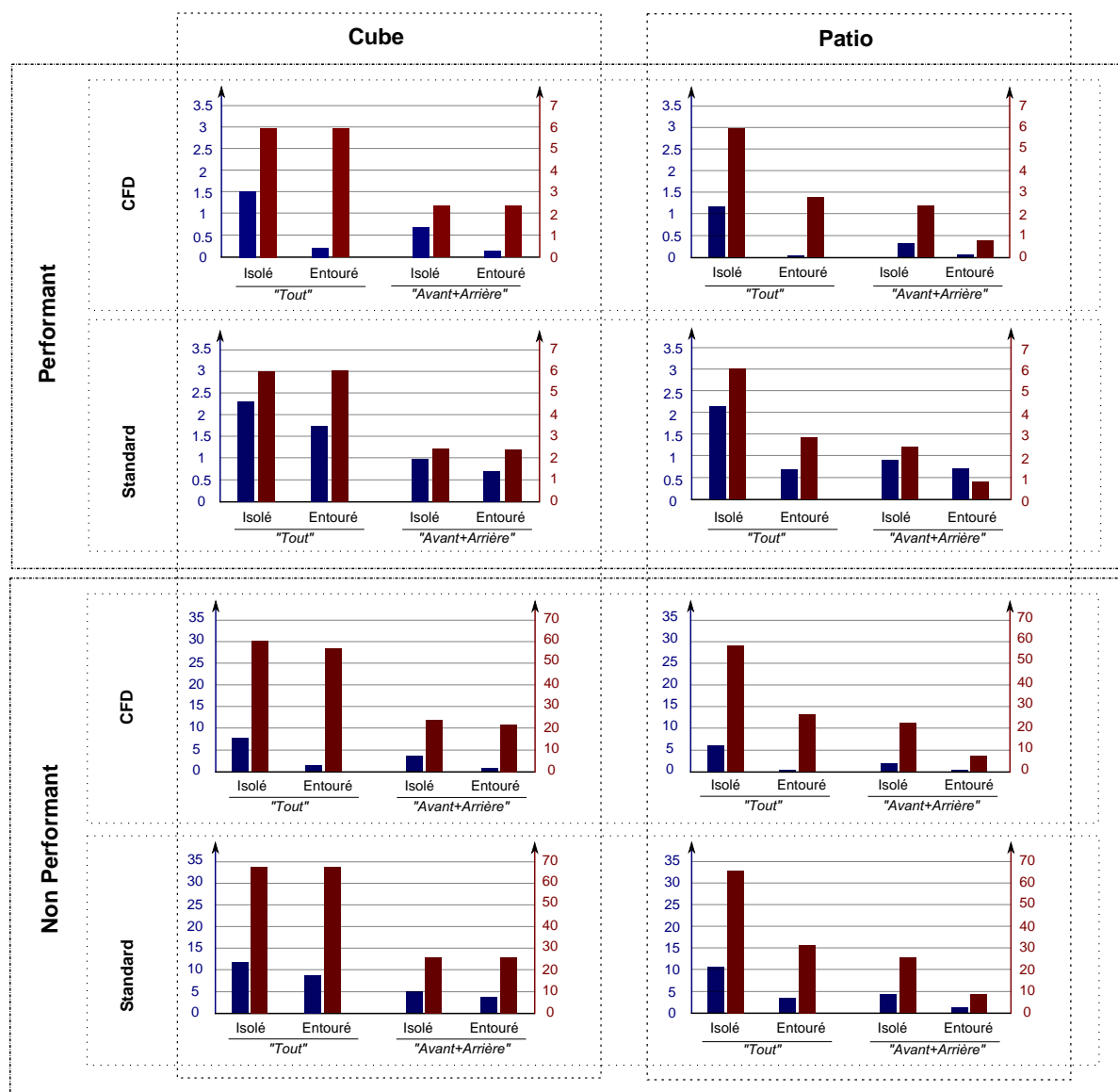


Fig. 10. Demande énergétique  $[W \cdot m^{-2}]$  liée aux infiltrations d'air et transmission de chaleur au travers de l'enveloppe des cubes et patios isolés ou non. Bleu: infiltration d'air; rouge: transmission de chaleur.

La transmission de chaleur au travers des parois est peu sensible aux différences de coefficients d'échanges convectifs, voire même insensible dans le cas de bâtiments fortement isolés thermiquement. La demande énergétique liée aux pertes thermiques par conduction / convection au travers des parois opaques est estimée constante, et plus importante que simulée, par l'approche standard du fait de la valeur supposée unique de  $h_{c,w}$ . Les différences observées entre le patio isolé ou non sont liées à la diminution de la surface active d'enveloppe entre les deux types.

Ainsi, la demande énergétique liée aux infiltrations d'air est très dépendante des conditions aérodynamiques locales qui dépendent de l'environnement bâti, i.e. exposition ou masque au vent, alors que les transferts de chaleur par transmission au sein des parois y sont peu voire pas sensibles (Fig. 10). Ceux-ci dépendent directement de la surface active de l'enveloppe. Cependant, les différences d'échanges convectifs seraient certainement estimées plus importantes si des parois vitrées et des systèmes actifs intégrés aux façades étaient considérés.



## Conclusions et perspectives

Les résultats de cette thèse mettent en évidence les effets des propriétés topologiques et métriques des bâtiments et ensembles bâtis sur le développement de recirculations d'air autour des constructions. Les conditions aérodynamiques en résultant induisent une distribution et intensité hétérogènes de  $C_p$  et  $h_{c,w}$  sur les façades des bâtiments. Ces conditions influent notablement sur le comportement thermique des bâtiments non isolés et perméables à l'air. Par ailleurs, l'estimation de leur demande énergétique diffère de façon substantielle suivant si celle-ci est basée sur les valeurs simulées ou standard de  $C_p$  et  $h_{c,w}$ . Cependant, si l'on s'intéresse à la contribution relative de la structure bâtie, l'influence des conditions aérodynamiques sur la demande énergétique des bâtiments apparaît relativement plus importante pour les bâtiments isolés thermiquement. Selon les résultats de simulation, la différence entre la demande énergétique, rapportée à l'unité de surface de plancher, due aux infiltrations d'air et pertes thermiques au travers de l'enveloppe peut varier de 18 % à 47 % suivant si le bâtiment est isolé ou situé dans un environnement bâti.

Ainsi, la méthodologie que cette thèse développe intègre différents facteurs de l'environnement urbain (morphologie, vent) pour en étudier leurs effets mutuels dans un souci de développement urbain durable. Les résultats obtenus soulignent l'intérêt de développer une telle approche intégrée et détaillée relevant de la physique urbaine pour mieux comprendre le comportement énergétique des bâtiments.

Cependant, la généralisation de cette approche nécessiterait des moyens de calculs très importants. Par ailleurs, la méthodologie développée dans ce travail implique de nombreuses simplifications, en termes de physique (bâtiments types orthogonaux constitués de parois opaques lisses et uniformes, convection forcée, direction et vitesse du vent imposée, etc.) et de modélisation. En effet, les méthodes steady RANS utilisées, y compris celles intégrant un modèle RSM, ne permettent pas reproduire précisément les recirculations et ne prédisent pas les phénomènes stationnaires. Or, ces phénomènes sont primordiaux dans la définition des  $C_p$  et  $h_{c,w}$  sur les façades des constructions. De même, si les transferts convectifs ont été estimés à l'aide d'une fonction de parois adaptée pour la température, celle-ci n'a été validée que pour les faces avant (et arrière) de constructions isolées. Elle ne garantit pas la précision des transferts convectifs estimés sur les autres faces ou dans d'autres configurations.

Ainsi, si l'étude exploratoire développée dans cette thèse a permis de répondre aux objectifs de recherche initiaux, à savoir mettre en évidence et mieux comprendre certains phénomènes physiques se développant en milieu urbain et leur potentiel impact sur le comportement thermo-aéraulique des bâtiments, des méthodes de calculs plus détaillées seraient nécessaires pour garantir des résultats plus précis. Cependant, ce type d'étude nécessiterait des moyens informatiques très importants. Les méthodes et techniques de calculs nouvellement développées ainsi que des études expérimentales dédiées en site réel se révèlent donc être incontournables pour porter cette démarche plus loin.

### *Principales contributions de la thèse*

- Construction de deux typologies génériques de structures bâties basées sur une analyse détaillée des principaux facteurs affectant les processus aérodynamiques moyens à l'échelle de l'îlot urbain.
- Identification de structures d'écoulements 3D se développant en fonction des propriétés morphologiques des structures bâties.
- Mise en évidence de la distribution des  $C_p$  sur les façades bâtiments en fonction des écoulements 3D locaux.
- Développement d'une fonction de paroi pour la température adaptée au modèle RANS RSM en régime permanent.
- Mise en évidence de la distribution des  $h_{c,w}$  sur les façades bâtiments en fonction des écoulements 3D locaux.
- Estimation de l'influence de la structure bâtie sur les sollicitations thermiques du bâtiment liées aux écoulements locaux en termes d'infiltration d'air et d'échanges convectifs.
- Estimation de l'incertitude liée à l'utilisation de valeurs standard de  $C_p$  et  $h_{c,w}$  lors de l'estimation de la demande énergétique des bâtiments due aux infiltrations d'air et transmission de chaleur au travers de l'enveloppe.



---

# Contents

Acknowledgments	viii
Abstract	x
Résumé	xii
Long Résumé	xv
Contents	xxxi
List of figures	xxxvi
List of tables	xlili
Introduction	1
I Fundamentals and preliminary work	5
1 Phenomenological foundations and outline of the thesis	7
1.1 Phenomenological background . . . . .	8
1.1.1 The atmospheric and urban boundary layers . . . . .	8
1.1.2 The urban energy balance . . . . .	13
1.1.3 Effects of urban micro-climates on the outdoor comfort and building energy loads . . . . .	17
1.2 Introduction to urban physics and aerodynamics . . . . .	20
1.2.1 Urban physics and building physics . . . . .	20

---

1.2.2	Existing techniques to study urban air flows . . . . .	23
1.2.3	Overview of noteworthy urban flow patterns . . . . .	26
1.3	Problem formulation and outline of the thesis . . . . .	34
1.3.1	Motivation and scope of the work . . . . .	34
1.3.2	Problem formulation and expected outcomes . . . . .	37
1.3.3	Methodology . . . . .	37
1.4	Summary . . . . .	39
<b>2</b>	<b>Design of generic typologies of urban structures for small scale aerodynamic (and bio-climatic) studies</b>	<b>41</b>
2.1	Urban morphologies: characterization and models . . . . .	42
2.1.1	Description and analysis of urban morphologies . . . . .	42
2.1.2	Bioclimatic approaches of urban forms . . . . .	45
2.2	Urban morpho-metric indicators (UMMIs) addressing thermo-aeraulic exchanges .	49
2.2.1	UMMIs addressing the openness of city toward the sun, sky and atmosphere	50
2.2.2	UMMIs mainly addressing aerodynamic processes . . . . .	51
2.2.3	UMMIs addressing the ability of a building to interact with its outdoors . . .	53
2.3	Synthesis of the morphological factors affecting urban air and heat fluxes . . . . .	53
2.3.1	Main morphological factors affecting urban air flows . . . . .	53
2.3.2	Main morphological factors affecting urban and building heat transfers . . .	55
2.4	Design of urban form typologies . . . . .	57
2.4.1	Design methodology . . . . .	57
2.4.2	Proposed typologies of isolated buildings and urban blocks . . . . .	60
2.4.3	Discussion of the typologies . . . . .	63
2.5	Summary . . . . .	63
<b>II</b>	<b>Computational fluid dynamics for the understanding of urban air flow patterns</b>	<b>65</b>
<b>3</b>	<b>CFD modeling and validation study</b>	<b>67</b>
3.1	Theoretical background and best practices . . . . .	68

---

3.1.1	Introduction to urban fluid mechanics for turbulent flows . . . . .	68
3.1.2	Usual CFD approaches in environmental wind engineering . . . . .	70
3.1.3	State of the art of steady RANS modeling for building aerodynamics . . . . .	76
3.2	Validation test cases . . . . .	79
3.2.1	Reference wind-tunnel tests . . . . .	79
3.2.2	Reference LBM LES simulations . . . . .	81
3.2.3	Steady RANS models . . . . .	82
3.3	Comparison between numerical results and experimental data . . . . .	85
3.3.1	The modeled boundary layer . . . . .	85
3.3.2	The rectangular block . . . . .	86
3.3.3	The array of rectangular blocks . . . . .	92
3.4	Model accuracy and reliability . . . . .	96
3.4.1	Accuracy of the computational methods . . . . .	96
3.4.2	ABL and roughness modeling effects . . . . .	97
3.5	Synthesis of the settings to be used in actual models . . . . .	100
3.6	Summary . . . . .	101
<b>4</b>	<b>Numerical study of the urban morphology effects on air flow patterns</b>	<b>103</b>
4.1	General model settings and modeled ABL . . . . .	104
4.1.1	General settings . . . . .	104
4.1.2	The ABL . . . . .	105
4.2	CFD modeling of the isolated building types . . . . .	106
4.2.1	Specific settings of the model . . . . .	106
4.2.2	Simulation results . . . . .	108
4.3	CFD modeling of the urban block types . . . . .	115
4.3.1	Specific settings of the model . . . . .	115
4.3.2	Simulation results . . . . .	116
4.4	Effects of urban morphological features on air flows . . . . .	126
4.4.1	Analysis of the external flows patterns: topology and size effects . . . . .	126
4.4.2	Analysis of the inner flows patterns: effects of topology and orientation . . . . .	130

---

4.5	Analysis of the pressure distribution on facades . . . . .	135
4.5.1	Physical background and applications . . . . .	135
4.5.2	Pressure distribution on isolated buildings . . . . .	136
4.5.3	Pressure distribution in arrays . . . . .	139
4.6	Summary . . . . .	142
<b>III</b>	<b>Effects of urban air flows on the building energy balance</b>	<b>143</b>
<b>5</b>	<b>Numerical study of the urban morphology effects on the building external convective heat transfer</b>	<b>145</b>
5.1	Theoretical background . . . . .	146
5.1.1	Physical basis . . . . .	146
5.1.2	Usual convective heat transfer correlations for building physics . . . . .	147
5.1.3	Improving of the estimations of building external convective heat transfer using CFD . . . . .	149
5.2	Validation study . . . . .	155
5.2.1	Evaluation of the accuracy of CFD in modeling convective heat transfers . . . . .	155
5.2.2	Performance of wall-functions in modeling convective heat transfer . . . . .	162
5.3	Analysis of $h_{c,w}$ distribution on building facades . . . . .	174
5.3.1	Settings of the coupled thermal and aerodynamic model . . . . .	174
5.3.2	Distribution of the convective heat transfers on isolated buildings . . . . .	176
5.3.3	Distribution of the convective heat transfers in arrays . . . . .	177
5.4	Summary . . . . .	180
<b>6</b>	<b>Urban morphology, air flows and building energy loads - Synthesis and discussion</b>	<b>181</b>
6.1	Effects of urban morphology on air infiltration through the building envelope . . . . .	182
6.1.1	Discussion . . . . .	182
6.1.2	Case studies . . . . .	185
6.2	Effects of urban morphology on the building external convective heat losses . . . . .	194
6.2.1	Discussion . . . . .	194
6.2.2	Case studies . . . . .	199

6.3	Effects of urban air flows on building energy loads due to air infiltration and heat transmission . . . . .	206
6.3.1	Relative contribution of air infiltration and heat transmission to the building energy loads . . . . .	206
6.3.2	Analysis of the effects of the building topology and urban context on the building energy loads induced by external air flows . . . . .	211
6.4	Summary . . . . .	214
<b>Conclusions and perspectives</b>		<b>215</b>
<b>Bibliography</b>		<b>221</b>
<b>Appendices</b>		<b>231</b>
<b>Appendices of Part 1</b>		<b>A. 1</b>
A	Classification of the terrain categories - power law profile . . . . .	A. 2
B	Urban morphological properties and urban flow regimes . . . . .	A. 3
C	Properties of the scales related to urban physics . . . . .	A. 4
D	Overview of the archetypes used in urban physics . . . . .	A. 5
D.1	Archetypes of street canyons . . . . .	A. 5
D.2	Urban archetypes based on pavilions, terraces and courts . . . . .	A. 5
D.3	Typical building arrangements for the study of street level dispersion processes . . . . .	A. 6
E	Local climate zones . . . . .	A. 7
F	Formulae of the urban morpho-metric indicators . . . . .	A. 8
F.1	UMMIs principally related to the openness of urban structures toward the sun, the sky and the atmosphere . . . . .	A. 8
F.2	UMMIs mostly related to unbuilt volumes and urban roughness, addressing aerodynamic issues . . . . .	A. 9
F.3	UMMIs mainly related to the architectural properties of buildings and their interface with the outdoors . . . . .	A. 11



<b>Appendices of Part 2</b>	<b>A. 13</b>
G RANS transport equations for the momentum . . . . .	A. 15
H Wall-functions . . . . .	A. 20
I Usual inlet conditions for steady RANS methods . . . . .	A. 22
J Blasius wind-tunnel . . . . .	A. 23
K Discussion of the approach flow profiles . . . . .	A. 24
L Complements to the case study A1-1 . . . . .	A. 28
M Levels of the scaled residuals reached at the end of simulations . . . . .	A. 29
N Aerodynamic results for the isolated building types . . . . .	A. 30
O Aerodynamic results for the urban block types . . . . .	A. 70
P 2D internal recirculation phenomena for the cube and the continuous patio arrays .	A. 84
Q Distribution of $C_p$ on the building surfaces . . . . .	A. 86
<b>Appendices of Part 3</b>	<b>A. 97</b>
R Comparison of $T_w$ profiles around the small cube . . . . .	A. 99
S Optimization of $Pr_{t,w}$ for the RSM . . . . .	A. 101
T Applicability of the revised customized temperature wall-function for the RSM for high $z^*$ . . . . .	A. 102
U Distribution of $h_{c,w}$ on the building surfaces . . . . .	A. 104
V Configurations studied to evaluate the energy needs . . . . .	A. 109
W Computation of $P_{int}$ and estimation of $E_{inf}$ . . . . .	A. 110
X Comparison of the building energy needs due to air infiltration or heat transmission through the building envelope . . . . .	A. 114
Y Comparison of the total building energy needs due to infiltration and heat transmission through the building envelope . . . . .	A. 117

# List of Figures

1	Interactions between natural and anthropogenic factors contributing to the development of complex aerodynamic and thermal processes in cities: effects on urban micro-climates, citizen's health and well being as well as building energy loads. . . .	4
1.1	Structure of the ABL. (Adapted from ( <a href="#">Oke, 1987</a> )) . . . . .	9
1.2	Mean wind profile depending on the land use. (Based on ( <a href="#">Blocken and Stathopoulos, 2013</a> ; <a href="#">Oke, 2006a</a> ), and ( <a href="#">Gandemer, 1976</a> ) cited in ( <a href="#">Bouyer, 2009</a> )) . . . . .	9
1.3	Physical heat fluxes contributing to the urban energy balance. (Adapted from ( <a href="#">Oke, 1987</a> )) . . . . .	14
1.4	The UHI phenomenon: evolution of the air temperature from the countryside to the city center. (Adapted from ( <a href="#">Oke, 1987</a> )) . . . . .	16
1.5	Physical processes and exchanges occurring between a city and its environment and in an urban canyon. . . . .	18
1.6	Effects of urban structures on the physical parameters determining the urban outdoor comfort and affecting the building energy balance. . . . .	20
1.7	Correspondence and imbrication of the spatial scales, disciplines, physical phenomena and main models related to urban physics. (Based on ( <a href="#">Blocken, 2013</a> ; <a href="#">Bitter and Hanna, 2003</a> ) and ( <a href="#">Schlünzen et al., 2011</a> ) cited in ( <a href="#">Blocken, 2014a</a> )) . . . . .	22
1.8	Adjustment of the mean wind profile from meteorological stations (open rural areas) to urban locations: terrain and design related contributions. (Based on ( <a href="#">Blocken and Stathopoulos, 2013</a> ; <a href="#">Bottema, 1999</a> )) . . . . .	24
1.9	Flow structures around an isolated high cuboidal obstacle. (Adapted from ( <a href="#">Beranek, 1984b</a> )) . . . . .	27
1.10	Flow patterns around obstacles of different shapes and for different wind incidences. (Based on ( <a href="#">Brown and DeKay, 2000</a> )) . . . . .	27
1.11	Flow regimes in an urban context depending on canyon aspect ratio (H/W). (Adapted from ( <a href="#">Oke, 1987</a> )) . . . . .	29

1.12 Occurrence of urban flow regimes in an urban-like context as well as ventilation effectiveness depending on the plan density. (Adapted from ( <a href="#">Brown and DeKay, 2000</a> )) . . . . .	29
1.13 Urban air flow anomalies affecting the pedestrian wind comfort due to particular building and urban layouts. (Adapted from ( <a href="#">Gandemer, 1975</a> )) . . . . .	32
1.14 Inter-relations between the factors affecting urban micro-climates and the building energy consumption. (Based on ( <a href="#">Ratti et al., 2005</a> )) . . . . .	35
1.15 Motivation, problem and the expected outcomes of the thesis. . . . .	38
1.16 Summary of the five steps methodology developed by the thesis. . . . .	40
2.1 Characterization of the main urban spatial scales in urban morphology analysis. (Based on ( <a href="#">Salat, 2011</a> )) . . . . .	43
2.2 Schematic illustration of some UMMIs addressing the openness of the city to the sun, sky and atmosphere. . . . .	50
2.3 Schematic illustration of some UMMIs addressing aerodynamic processes. . . . .	51
2.4 Main morphological factors affecting urban aerodynamic processes. . . . .	54
2.5 Main morphological factors affecting building heat transfers. . . . .	56
2.6 Examples of urban fabrics studied. (From ( <a href="#">Firley and Stahl, 2010</a> )) . . . . .	58
2.7 Summary of the design methodology of the generic isolated building and urban block typologies for small scale aerodynamic (and micro-climatic) studies. . . . .	60
2.8 3D and plan views of the five types composing the typology of generic isolated buildings: emergence of a courtyard. Height of each type: $H$ . . . . .	61
2.9 3D and plan views of the five types composing the typology of generic urban blocks. Height of each type: $H'$ . . . . .	62
3.1 CFD methods: hierarchy, main assumptions and applicability. (Based on ( <a href="#">Blocken, 2013</a> ; <a href="#">Sagaut et al., 2013</a> )) . . . . .	69
3.2 Best practice guidelines for the CFD modeling of the pedestrian wind environment around buildings. . . . .	78
3.3 Reference wind-tunnel model: the isolated rectangular block (A1-1 case). . . . .	80
3.4 Reference wind-tunnel model: the array of rectangular blocks (B1-1 case). . . . .	81
3.5 Comparison between the experimental approach flow and the numerical incident mean flow profiles depending on the computational approach and bottom boundary condition. . . . .	86

3.6	Comparison of the mean velocity field for the A1-1 case. . . . .	88
3.7	Comparison between the numerical and experimental characteristics of the flow structures around the obstacle. . . . .	89
3.8	Comparison of the $U$ -profiles around the obstacle. . . . .	90
3.9	Comparison of the $W$ -profiles around the obstacle. . . . .	91
3.10	Comparison of the mean flow fields and 2D mean velocity streamlines between the fifth and the sixth blocks of the B1-1 case. . . . .	93
3.11	Comparison of $U$ -profiles within the canyon. . . . .	94
4.1	$U$ -profile of the approach flow used for the actual simulations. . . . .	106
4.2	Computational domain and number of cells used to model the isolated building types. . . . .	107
4.3	Schemes and names of the different configurations tested (isolated types). . . . .	107
4.4	Aerodynamic results for the cube. . . . .	110
4.5	Aerodynamic results for the cuboid. . . . .	111
4.6	Aerodynamic results for the cuboid: orientation effects. . . . .	111
4.7	Aerodynamic results for the L building. . . . .	112
4.8	Aerodynamic results for the L building: orientation effects. . . . .	112
4.9	Aerodynamic results for the U building. . . . .	113
4.10	Aerodynamic results for the U building: orientation effects. . . . .	113
4.11	Aerodynamic results for the patio. . . . .	114
4.12	Computational domain and number of cells used to model the urban block types. . . . .	116
4.13	Schemes and names of the different configurations tested (urban block types). . . . .	116
4.14	Aerodynamic results for the cube array. . . . .	119
4.15	Aerodynamic results for the row block 1. . . . .	120
4.16	Aerodynamic results for the row block 2. . . . .	121
4.17	Aerodynamic results for the U block 1. . . . .	122
4.18	Aerodynamic results for the U block 2. . . . .	123
4.19	Aerodynamic results for the enclosed block. . . . .	124
4.20	Aerodynamic results for the continuous patio array. . . . .	125
4.21	2D mean velocity streamlines around the cube and the cuboid 1. . . . .	127

4.22	2D comparison between the flow structures in the theoretical symmetry plane of the courts of the patio, enclosed block, U building 3 and U block 2. . . . .	132
4.23	2D streamwise evolution of the internal recirculation phenomena through the cube and continuous patio arrays. . . . .	132
4.24	Distribution and surface averaged value of $C_p$ for each face of the cube envelope. .	137
4.25	Distribution and surface averaged value of $C_p$ for each face of the patio envelope. .	137
4.26	Distribution and surface averaged of $C_p$ for the cube array. . . . .	140
4.27	Distribution and surface averaged of $C_p$ for the continuous patio array. . . . .	140
5.1	Distribution of the coefficient A and exponent B characterizing the $h_{c,w}-U_{10}$ correlation derived by Defraeye et al. (2011b). . . . .	152
5.2	Bases of the customized temperature wall-function. (Based on (Defraeye et al., 2011a,b)) . . . . .	154
5.3	Reference experimental configuration. (Based on (Meinders et al., 1999)) . . . . .	156
5.4	Computational model used for the first part of the thermal model validation study.	157
5.5	Comparison of the numerical and experimental $h_{c,w}$ profiles around the small cube: effects of the turbulence model. . . . .	159
5.6	Computational model used for the second part of the thermal model validation study.	163
5.7	Comparison of the $h_{c,w}$ profiles around the cube: effects of the turbulence model and near-wall treatment. . . . .	165
5.8	Comparison of the $h_{c,w}$ profiles obtained using the optimized $Pr_{t,w}$ value together with the appropriate turbulence model. . . . .	167
5.9	Comparison between vertical $h_{c,w}$ profiles simulated using the original or the revised customized temperature wall-function together with the appropriate turbulence model and the LRNM results of Defraeye (2009) for $U_{10} = 0.5 \text{ m} \cdot \text{s}^{-1}$ . . . . .	168
5.10	Comparison of the distributions of $z^*$ on the front and rear faces of the cube in cases of $U_{10} = 0.5$ or $5 \text{ m} \cdot \text{s}^{-1}$ . . . . .	169
5.11	Comparison between the distributions of $h_{c,w}$ simulated using the revised customized temperature wall-function for the RSM on the front and rear faces of the cube in cases of $U_{10} = 0.5$ or $5 \text{ m} \cdot \text{s}^{-1}$ . . . . .	170
5.12	Comparison between the simulated $h_{c,w}$ profiles using the original and revised customized temperature wall-function together with the appropriate turbulence model with reference LRNM data of Defraeye (2009) for $U_{10} = 5 \text{ m} \cdot \text{s}^{-1}$ . . . . .	172
5.13	Settings of the actual thermal model. . . . .	175

5.14	Distribution and surface averaged values of $h_{c,w}$ for each face of the cube. . . . .	176
5.15	Distribution and surface averaged values of $h_{c,w}$ for each face of the patio. . . . .	176
5.16	Distribution and surface averaged $h_{c,w}$ values for the cube array. . . . .	178
5.17	Distribution and surface averaged $h_{c,w}$ values for the continuous patio array. . . . .	178
6.1	Comparison between the generic surface averaged $C_p$ values provided by the Th-BCE rules ( <a href="#">CSTB, 2012a</a> ) and the simulated surface averaged $C_p$ values for an isolated 10 m high cubical building. . . . .	184
6.2	Comparison between the generic surface averaged $h_{c,w}$ values provided by the Th-U rules ( <a href="#">CSTB, 2012b</a> ) and the simulated surface averaged $h_{c,w}$ values for an isolated 10 m high cubical building. . . . .	196
6.3	Electrical analogy for 1D heat transfers through a wall. . . . .	196
6.4	Comparison of the energy needs per $m^2$ of floor area ( $E_{i+c,m^2}$ ) differentiated depending on $E_{inf,m^2}$ or $E_{conv,m^2}$ for the cubical building located either in an open terrain or in a theoretical urban environment. . . . .	208
6.5	Comparison of the energy needs per $m^2$ of floor area ( $E_{i+c,m^2}$ ) differentiated depending on $E_{inf,m^2}$ or $E_{conv,m^2}$ for the patio building located either in an open terrain or in a theoretical urban environment. . . . .	209
a.1	Wind profiles depending on the landscape. (Based on ( <a href="#">Gandemer, 1976</a> ).) . . . . .	A. 2
a.2	Urban morphological properties and urban flow regimes. (Based on ( <a href="#">Grimmond and Oke, 1999</a> ; <a href="#">Oke, 1988</a> )) . . . . .	A. 3
a.3	Spatial and temporal scales of the different aerodynamic phenomena related to urban physics. (From ( <a href="#">Oke, 2006b</a> )) . . . . .	A. 4
a.4	Different types street canyons. (From ( <a href="#">Kastner-Klein et al., 2004</a> )) . . . . .	A. 5
a.5	Urban archetypes based on pavilions, terraces and courts. (From ( <a href="#">Steemers et al., 1997</a> )) . . . . .	A. 5
a.6	Local climate zones (LCZs). (From ( <a href="#">Stewart and Oke, 2012</a> )) . . . . .	A. 7
a.7	Law-of-the-wall giving the mean velocity profile as a function of the distance to the wall, plotted in a semi-log scale. (Adapted from ( <a href="#">Ansys Fluent, 2013a</a> ).) . . . . .	A. 20
a.8	Sketch of the Blasius wind-tunnel. (Adapted from ( <a href="#">Meteorological Institute of Hamburg, 2013</a> ).) . . . . .	A. 23
a.9	Fitting of the experimental approach flow. . . . .	A. 25
a.10	Fitting of the steady RANS approach flow. . . . .	A. 26

a.11 Fitting of the approach flow for the actual simulations. . . . .	A. 27
a.12 Identification of the flow structures (Adapted from <a href="#">Meroney et al. (1999)</a> ). . . . .	A. 28
a.13 Top bubbles simulated by the steady RANS $Rk-\epsilon$ and RSM turbulence models for the case A1-1. . . . .	A. 28
a.14 2D internal recirculation phenomena developing in each row of the cube array. . . . .	A. 84
a.15 2D internal recirculation phenomena developing in each row of the continuous patio array. . . . .	A. 85
a.16 Distribution of the surface averaged $C_p$ for the cube and the patio. . . . .	A. 86
a.17 Specification of the indexes for the cube array. . . . .	A. 87
a.18 $C_p$ distribution and surface averaged mean $C_p$ by faces for the cubes 1-1, 2-2, 3-1 and 4-2 of the cube array. . . . .	A. 88
a.19 Specification of the indexes for the continuous patio array. . . . .	A. 89
a.20 $C_p$ distribution and surface averaged mean $C_p$ by faces for the patios 1-1, 2-2, 3-1 and 4-2 of the continuous patio array. . . . .	A. 90
a.21 Comparison of the approach flows used to determine the $C_p$ . . . . .	A. 92
a.22 Wind-tunnel based $C_p$ distributions and surface averaged values for isolated flat-roofed buildings. (Adapted from ( <a href="#">TPU, 2003</a> )) . . . . .	A. 94
a.23 Wind-tunnel based $C_p$ distributions and surface averaged values for an element of an array and an isolated flat-roofed buildings. (Adapted from ( <a href="#">TPU, 2003</a> )) . . . . .	A. 95
a.24 Comparison of the simulated $T_w$ profiles with predictions obtained using different $k-\epsilon$ models by <a href="#">Seeta Ratnam and Vengadesan (2008)</a> . . . . .	A. 99
a.25 Comparison of the simulated $T_w$ profiles with predictions obtained using different $k-\omega$ models by <a href="#">Seeta Ratnam and Vengadesan (2008)</a> . . . . .	A. 99
a.26 Comparison of the numerical and experimental $T_w$ profiles: influence of the turbulence model, convergence study for the RSM and effects of the near wall treatment. . . . .	A. 100
a.27 Optimization of $Pr_{t,w}$ for RSM-based temperature wall-function. . . . .	A. 101
a.28 Comparison of the $h_{c,w}$ profiles for $U_{10} = 0.5 \text{ m}\cdot\text{s}^{-1}$ . . . . .	A. 102
a.29 Comparison of the $h_{c,w}$ profiles for $U_{10} = 5 \text{ m}\cdot\text{s}^{-1}$ . . . . .	A. 103
a.30 Distribution of $h_{c,w}$ for the cube and the patio. . . . .	A. 104
a.31 Specification of the indexes for the cube array. . . . .	A. 105

---

a.32 $h_{c,w}$ distribution and surface averaged $h_{c,w}$ by faces for the cubes 1-1, 2-2, 3-1 and 4-2 of the cube array. . . . .	A. 106
a.33 Specification of the indexes for the continuous patio array. . . . .	A. 107
a.34 $h_{c,w}$ distribution and surface averaged mean $h_{c,w}$ by faces for the patios 1-1, 2-2, 3-1 and 4-2 of the continuous patio array. . . . .	A. 108
a.35 Isolated and non-isolated cubes and patios, cases “All” and “Lw+Ww”. . . . .	A. 109
a.36 Comparison of the total energy needs ( $E_{i+c,tot}$ ) differentiated depending on $E_{inf,tot}$ or $E_{conv,tot}$ for the cubical building located either in an open terrain or in a theoretical urban environment. . . . .	A. 120
a.37 Comparison of the total energy needs ( $E_{i+c,tot}$ ) differentiated depending on $E_{inf,tot}$ or $E_{conv,tot}$ for the patio building located either in an open terrain or in a theoretical urban environment. . . . .	A. 121





# List of Tables

1.1	Updated Davenport's classification of effective terrain roughness: Increase of the aerodynamic roughness length value ( $z_0$ ) from flat and smooth landscapes to densely built and chaotic urban areas. (From ( <a href="#">Wieringa et al., 2001</a> )) . . . . .	12
1.2	Urban factors and physical processes influencing the UHI effect: contribution of the urban structure, materials and anthropogenic direct sources. (Based on ( <a href="#">Oke, 1987</a> )) . . . . .	16
1.3	Advantages and drawbacks of full-scale study, wind-tunnel testing and CFD modeling.	25
2.1	Urban climate zones (UCZs): "Simplified classification of distinct urban forms arranged in approximate decreasing order of their ability to impact local climate". (From ( <a href="#">Oke, 2006a</a> )) . . . . .	47
2.2	Classification of UMMIs with respect to their link with air flows and heat fluxes. . .	49
2.3	Relations between urban roughness and porosity with aerodynamic processes. . . .	55
2.4	Relations between the urban fabric and heat transfers. . . . .	57
2.5	Morphological characteristics of the isolated building types. . . . .	61
2.6	Morphological characteristics of the urban blocks types. . . . .	62
3.1	Origin and sources of errors and uncertainties in CFD models. (Adapted from ( <a href="#">COST-Action and 732, 2007</a> )) . . . . .	77
4.1	General model settings to be used in the CFD simulations. . . . .	105
4.2	Location of flow structures around the rectangular-shaped types in the plane $y=0m$ .	127
5.1	Coefficients related to the $h_{c,w}-U_{10}$ correlations of <a href="#">Liu et al. (2015)</a> . . . . .	153
5.2	Comparison of the surface averaged $h_{c,w}$ [ $W \cdot m^{-2} \cdot K^{-1}$ ] values for the front face of a building estimated using different models available in literature. . . . .	153
5.3	Thermal properties of the model used. . . . .	157

5.4	Comparison of the surface averaged $h_{c,w}$ computed using the reference $h_{c,w}-U_{10}$ correlation of Defraeye et al. (2010) or estimated using CFD simulations for the cube in cases of $U_{10} = 0.5 \text{ m} \cdot \text{s}^{-1}$ and $U_{10} = 5 \text{ m} \cdot \text{s}^{-1}$ . . . . .	172
6.1	$C_p$ values given by the Th-BCE appendix for crossing building zones (CSTB, 2012a). Windward and leeward faces are conventionally distributed. . . . .	183
6.2	Comparison by face of the generic surface averaged $C_p$ values (and the corresponding $P_{ext}$ [Pa]) provided by the Th-BCE rules (CSTB, 2012a) or simulated (Sec. 4.5) in cases of 10 m high isolated and non-isolated buildings (cubes or patios). . . . .	186
6.3	Synthesis of the physical parameters used in the computations of $Q_{inf}$ and $E_{inf}$ . . . . .	189
6.4	Comparison of $P_{int}$ [Pa], $Q_{inf,m^2}$ [ $\text{m}^3 \cdot \text{h}^{-1} \cdot \text{m}_{env}^{-2}$ ] and $E_{inf,m^2}$ [ $\text{W} \cdot \text{m}_{floor}^{-2}$ ] calculated using the Th-BCE or the simulated $C_p$ values for buildings located in different urban configurations. . . . .	190
6.5	Evaluation of the effects of the building topology and urban morphology on $E_{inf,m^2}$ [ $\text{W} \cdot \text{m}_{floor}^{-2}$ ] according to the Th-BCE rules or simulation results. . . . .	192
6.6	Standard $h_{c,int}$ values used in the computations. . . . .	196
6.7	Standard $h_{rad}$ values used in the computations. . . . .	196
6.8	Comparison by face of the generic surface averaged $h_{c,w}$ values [ $\text{W} \cdot \text{m}^{-2} \cdot \text{K}^{-1}$ ] (and the corresponding $R_{th}$ [ $\text{m}^2 \cdot \text{K} \cdot \text{W}^{-1}$ ]) provided by the Th-U rules (CSTB, 2012b) or simulated (Sec. 5.3) in cases of 10 m high isolated and non-isolated buildings (cubes or patios). . . . .	198
6.9	Synthesis of the physical parameters used in the computations of $U_{env}$ and $E_{conv}$ . . . . .	200
6.10	Comparison of $U_{env}$ [ $\text{W} \cdot \text{m}^{-2} \cdot \text{K}^{-1}$ ] and $E_{conv}$ [ $\text{W} \cdot \text{m}_{floor}^{-2}$ ] calculated using the Th-BCE or the simulated $h_{c,w}$ values for buildings located in different urban configurations. . . . .	202
6.11	Comparison between $E_{conv}$ [ $\text{W} \cdot \text{m}_{floor}^{-2}$ ] for different urban configurations: effects of the building topology and urban morphology. . . . .	203
6.12	Comparison between the $E_{i+c,m^2}$ [ $\text{W} \cdot \text{m}_{floor}^{-2}$ ] estimated using the standard or simulated values of $C_p$ and $h_{c,w}$ in cases of an isolated and a non-isolated buildings that are insulated and air-tight or not. . . . .	207
6.13	Evaluation of the effects of the building topology and urban morphology on the energy needs due to thermal transmission through the envelope ( $E_{conv}$ [ $\text{W} \cdot \text{m}_{floor}^{-2}$ ]) according to the Th-BCE rules or simulation results. . . . .	212
a.1	Atmospheric boundary layer parameters and power law. (Adapted from (ASHRAE, 2005)) . . . . .	A. 2

a.2	Detailed spatial scales of the UCL. (From (Oke, 2006b)) . . . . .	A. 4
a.3	Typical building arrangements for the study of street level dispersion processes. (From (Theurer, 1999)) . . . . .	A. 6
a.4	Main characteristics of the flow structures around the obstacle for the case A1-1. . .	A. 28
a.5	Levels of the scaled residuals reached at the end of simulations. . . . .	A. 29
a.6	Surface averaged $C_p$ for each face the cube array. . . . .	A. 87
a.7	Surface averaged $C_p$ for each face the patio array. . . . .	A. 89
a.8	Comparison between the numerical and experimental surface averaged $C_p$ for the four case studies. . . . .	A. 93
a.9	Surface averaged $h_{c,w}$ for each face of the cube array. . . . .	A. 105
a.10	Surface averaged $h_{c,w}$ for each face of the continuous patio array. . . . .	A. 107
a.11	Comparison of the envelope and floor areas of the isolated and non-isolated cube and patio types. . . . .	A. 109
a.12	Comparison of $P_{int}$ [Pa], $Q_{inf}$ [ $\text{m}^3 \cdot \text{s}^{-1}$ ] and $E_{inf}$ [W] for patios that are located in different urban configurations. . . . .	A. 114
a.13	Comparison of the wall thermal transmittivity ( $U_{env}$ [ $\text{W} \cdot \text{m}^{-2} \cdot \text{K}^{-1}$ ]) and the related energy needs ( $E_{conv,tot}$ [W]) for insulated or a non-insulated buildings (cube / patio) located different urban configurations (isolated / in a group of buildings). . . . .	A. 115
a.14	Comparison between $E_{inf,tot}$ [W] different urban configurations: effects of the building topology and urban morphology. . . . .	A. 116
a.15	Comparison between $E_{conv,tot}$ [W] different urban configurations: effects of the building topology and urban morphology. . . . .	A. 116
a.16	Comparison of $E_{inf,tot}$ , $E_{conv,tot}$ and $E_{i+c,tot}$ for an isolated and a non-isolated cubes, which present high or low levels of insulation and air tightness. . . . .	A. 117
a.17	Comparison of $E_{inf,tot}$ , $E_{conv,tot}$ and $E_{i+c,tot}$ for an isolated and a non-isolated pa- tios, which present high or low levels of insulation and air tightness. . . . .	A. 118
a.18	Comparison between the $E_{tot}$ [W] estimated using the standard or simulated values of $C_p$ and $h_{c,w}$ in cases of an isolated or a non-isolated building that is insulated and air-tight or not. . . . .	A. 119
a.19	Comparison between $E_{i+c,tot}$ [kW] for different built morphologies. . . . .	A. 122



# Nomenclature

## Abbreviations: general

Chap.	Chapter
Fig.	Figure
Sec.	Section
Tab.	Table

## Abbreviations: specific

2D/3D	Two / Three Dimensional
ABL	Atmospheric Boundary Layer
CFD	Computational Fluid Dynamics
CPU	Central Processing Unit
GHG	Green-House Gases
GPU	Graphics Processing Unit
HVAC	Heat Ventilation Air Conditioning
ISL	Inertial Sub-Layer
LBM	Lattice Boltzmann Method
LES	Large Eddy Simulation
NS	Navier–Stokes
LRNM	Low Reynolds Number Modeling
PBL	Planetary Boundary Layer
RANS	Reynolds Averaged Navier–Stokes
$Rk-\varepsilon$	Realizable $k-\varepsilon$ model
RSM	Reynolds Stress Model
RSL	Roughness Sub-Layer
$Sk-\varepsilon$	Standard $k-\varepsilon$ model
UBL	Urban Boundary Layer
UCL	Urban Canopy Layer
UHI	Urban Heat Island
UMMI	Urban Morpho-Metric Indicator

**Symbols**

$C$	Thermal capacity	$[\text{J} \cdot \text{kg}^{-1} \cdot \text{K}^{-1}]$
$C_p$	Pressure coefficient	$[-]$
$e$	Wall thickness	$[\text{m}]$
$E_{inf}$	Energy needs due to air infiltration	$[\text{W}]$
$E_{conv}$	Energy needs due to heat transmission	$[\text{W}]$
$E_{i+c}$	Combined energy needs due to air infiltration and heat transmission	$[\text{W}]$
$g$	Gravitational acceleration	$[\text{m} \cdot \text{s}^{-2}]$
$h_w$	Total surface heat transfer coefficient	$[\text{W} \cdot \text{m}^{-2} \cdot \text{K}^{-1}]$
$h_{c,w}$	Convective heat transfer coefficient	$[\text{W} \cdot \text{m}^{-2} \cdot \text{K}^{-1}]$
$h_{rad}$	Radiative heat transfer coefficient	$[\text{W} \cdot \text{m}^{-2} \cdot \text{K}^{-1}]$
$k$	Turbulent kinetic energy	$[\text{m}^2 \cdot \text{s}^{-2}]$
$k_s$	Equivalent roughness height	$[\text{m}]$
$p$	Pressure	$[\text{Pa}]$
$q_w$	Total surface heat flux per surface unit	$[\text{W} \cdot \text{m}^{-2}]$
$q_{c,w}$	Convective heat flux per surface unit	$[\text{W} \cdot \text{m}^{-2}]$
$R_{th}$	Total thermal resistance of a wall	$[\text{m}^2 \cdot \text{K} \cdot \text{W}^{-1}]$
$U_{env}$	Thermal transmittivity of the building envelope	$[\text{W} \cdot \text{m}^{-2} \cdot \text{K}^{-1}]$
$u^*$	Friction velocity	$[\text{m} \cdot \text{s}^{-1}]$
$U, V, W$	Mean velocity vector components	$[\text{m} \cdot \text{s}^{-1}]$
$u', v', w'$	Fluctuating velocity vector components	$[\text{m} \cdot \text{s}^{-1}]$
$u'u', v'v', w'w'$	Reynolds stresses	$[\text{m}^2 \cdot \text{s}^{-2}]$
$u'v', v'w', u'w'$		
$z_0$	Aerodynamic roughness length	$[\text{m}]$
$z_D$	Zero displacement height	$[\text{m}]$

**Greek symbols**

$\alpha$	Power law exponent	$[-]$
$\beta$	Thermal expansion coefficient	$[\text{K}^{-1}]$
$\delta$	Boundary layer thickness	$[\text{m}]$
$\varepsilon$	Turbulence dissipation rate	$[\text{m}^2 \cdot \text{s}^{-3}]$
$\lambda$	Thermal conductivity	$[\text{W} \cdot \text{m}^{-1} \cdot \text{K}^{-1}]$
$\mu$	Dynamic viscosity	$[\text{kg} \cdot \text{m}^{-1} \cdot \text{s}^{-1}]$
$\nu$	Kinematic viscosity	$[\text{m}^2 \cdot \text{s}^{-1}]$
$\rho$	Density	$[\text{kg} \cdot \text{m}^{-3}]$

## Subscripts

$c$	convective
$w$	wall
$F-R$	front-rear
$F-S$	front-side
$Ww-Lw$	windward-leeward
$H$	horizontal
$V$	vertical
$conv$	transmission
$inf$	infiltration
$m^2$	per surface unit
$tot$	total
$insul$	insulation
$conc$	concrete

## Dimensionless numbers

$Gr$	Grashof number	$\frac{g \beta \Delta T L_c^3 \rho^2}{\mu^2}$
$Ma$	Mach number	$\frac{U}{c}$
$Re$	Reynolds number	$\frac{U \times L_c}{\nu}$
$Ri$	Richardson number	$\frac{g \beta (T - T_{ref}) L}{U^2}$
$T^*$	Dimensionless temperature	$\frac{(T_w - T_p) \rho C C_\mu^{1/4} k_p^{1/2}}{q_w}$
$z^+$	Dimensionless wall unit	$\frac{\rho u_t z}{\mu}$
$z^*$	Dimensionless wall unit based on $k$	$\frac{\rho C_\mu^{1/4} k_p^{1/2} z_p}{\mu}$





# Introduction

## Context: complex-cities and environmental problems

Cities are almost artificial environments that are built in given natural contexts. Their shape and development are determined by the combination of different interacting factors. In particular, the natural context defines the overall geographical and climatic conditions in which they can evolve. It also determines the amount of available resources that could be transformed and used by cities to work, and the potential to clean wastes. Urban activities and the city's life create internal and external fluxes as well as tangible objects. These fluxes can be material or immaterial and urban objects may be consumer goods, industrial and mobility facilities, or dwellings and other buildings. These products of human activities, and more generally the urban development, are fostered by the demographic, social, economic, technical and technological evolutions and are constrained by the available natural resources.

Between 1970 and 2013, the world population has been nearly multiplied by a factor two to reach 7.2 billion people. Predictions forecast a 33.3 % additional increase by 2025 ([INSEE, 2012](#)). In parallel, the urban population has significantly grown. In 1990, 2 out of 10 people lived in urban areas and in 2010, the ratio overcame 5 out of 10. The urban population is expected to double in 2050, with 6.4 billion of citizens instead of 3.4 billion ([WHO and GHO, 2013](#)). This fast and important growth of urban population involves a significant increase of the energy needs and natural resources consumption, as well as heat releases, waste production and green-house gas (GHG) emissions. This also substantially affects urban micro-climates. These modifications give rise to major problems as the increased environmental footprint of cities is very likely to impact on the global warming. According to the [GIEC \(2013\)](#), an increase of about 0.75 °C of the mean temperature at the surface of the Earth was observed between 1950 and 2005. This trend is even more worrying as scenarios expect another 0.5 to 3.7 °C increasing of the Earth surface temperature between 2005 and 2100. These warmer temperatures intensify in turn environmental and urban risks.

The building sector holds for 7.8 % of the total GHG emissions, non considering the emission from the electricity use (data 2004 ([IPCC, 2007](#))) and for 35 % of the world final energy consumption (data 2010, ([IEA, 2010](#))). In France, the residential / tertiary sector represents 22 % of the CO<sub>2</sub> emissions (data 2011, ([ADEME, 2013b](#))) and 44.5 % of the final energy consumption (data 2012, [ADEME \(2013a\)](#)). These data place buildings at the first energy consumption sector, on top of other consumption posts such as transports and industries. As this energy is mostly used to provide comfortable indoor conditions, an integrated design and retrofitting of built areas is a key point of any energy saving and GHG emission reduction strategy.

These environmental issues, and more generally sustainable urban development challenges,

are not only critical to Western European and Northern American countries. In developing countries, the number of urban residents is forecasted to at least double between 2009 and 2050, whereas it is expected to remain stable in high income countries (WHO and GHO, 2013). Moreover, the artificial air conditioning is often not possible in these countries due to economic constraints. Hence, urban environmental and energy challenges are also of uttermost importance in developing countries, which are places of a very fast urban growth.

### **Background and motivation: toward sustainable cities**

Following the Kyoto protocol (1997), the “20-20-20 target” (2007) translates the European environmental goals in terms of climate change mitigation and energy consumption reduction. The key objectives for 2020 are a 20% reduction of the GHG emissions in comparison with 1990, a 20% increase of the energy consumption issued from renewable sources, and a 20% improvement of the energy efficiency (European-Commission, 2014). In order to reach this last objective, the energy efficiency plan and directive was created in 2011. It emphasizes the necessity to act on lowering the energy consumption in the construction sector and to implement strategies for reducing the final energy consumption in buildings (European Union, 2011).

In France, the application of the European “20-20-20 target” extends the factor 4 commitments undertaken in 2003. As GHG significantly affect the global warming, the aim was to divide by a factor 4 their emissions in 2050 in comparison with 1990. Concerning the building sector, regulations were established to promote building energy efficiency and reduce the building total energy consumption by 30% in 2050. In particular, the recent thermal regulation 2012 (RT 2012) fixes ambitious objectives in terms of building energy efficiency and conservation. A threshold value of  $50 \text{ kWh} \cdot \text{m}^{-2} \cdot \text{an}^{-1}$  for the primary energy consumption was set for new residential buildings (MEEDDM, 2010). However, the related indicators of building energy performance are often understood as absolute measures of the building energy efficiency. But, in built-up areas, its effective efficiency is very dependent on the adequateness of its design with its immediate environment. The interactions between sun beams, air flows and buildings determine to a large extent the very local micro-climatic conditions, which define in turn the effective thermal and aer-audic solicitations that act on the building envelope. These conditions can substantially change the building thermal behavior from one configuration to another, especially in urban contexts.

Furthermore, the urban growth and public awareness to environmental problems give rise to new contexts for urban developments. The development and retrofitting of urban areas together with the increase in urban densities make current design practices evolve. Sustainable neighborhoods that include comfortable outdoor spaces are yet increasingly considered rather than only isolated buildings. This trend is well illustrated by the increasing number of new eco-neighborhoods. From a bio-climatic and energy points of view, their integrated design implies to work simultaneously with the natural phenomena, their modifications by the urban context, their effects on the thermal behavior of buildings and the energy management. Designing effective energy efficient urban areas and buildings requires thus to understand the interplay between the very local micro-climatic phenomena and the buildings heat and mass fluxes.

---

## Study overview

Aiming at promoting energy efficient buildings and urban environments, the issues outlined above are central concerns for the Building physics group of the CETHIL<sup>2</sup> and the Energy and environment department of the CSTB.<sup>3</sup> Both research teams work on several aspects of the building thermal behavior and develop methods, models and tools to study, design, retrofit and manage buildings in order to improve and assess their operative energy performance. For this purpose, realistic boundary conditions are needed to accurately integrate the different physical exchanges of buildings and understand their thermal and aerodynamic behaviors. The knowledge of the physical processes occurring at the building interface is therefore required. This implies to understand the interactions between buildings and the physical phenomena that develop at the upper scales of the urban block and the city, which are highly affected by the urban three dimensional (3D) morphological properties.

This CETHIL / CSTB work aims at investigating how urban structures affect the very local urban micro-climatic conditions. It focuses on the aerodynamic phenomena and convective heat transfers that develop in the vicinity of buildings envelope and in their close environment. As outlined in Fig. 1 among the other urban micro-climatic factors, this work especially addresses the effects of the urban morphological properties on the developing air flow structures, and their coupling with the building ventilation potential, infiltration and thermal loads.

An original approach linking distinct disciplines, namely urban planning and architecture, as well as urban and building physics, is designed and implemented in this study. This exploratory study more precisely links concepts and tools from the urban morphology analysis, environmental wind engineering and building physics. Numerical experiments are undertaken on generic urban structures that have been specifically designed for this purpose. The actual objective is to identify the mean air flow patterns that develop around buildings according to the surrounding urban design and to assess the related infiltration and convective heat exchanges.

This thesis is structured into three main parts. The first part lays the foundations of the study. The physical processes of interest are reviewed, the problem and the methodology are detailed and the design of the case studies is reported. The second part addresses the aerodynamic study, which is carried out by means of computational fluid dynamics (CFD) simulations. The validation study is developed and the mean flow fields around the different case studies are analyzed. The third part deals with the impacts of urban aerodynamics on the building energy loads. Building convective heat transfers are studied using a coupled computational approach. The validation of the model is described, and the building convective heat exchanges are examined. The effects of the urban flow patterns on the building energy loads due to air infiltration and convective heat losses are then discussed. Finally, the main results as well as the perspectives of this work are synthesized in the conclusion.

---

<sup>2</sup>CETHIL: Center for thermal and energy sciences of Lyon, <http://cethil.insa-lyon.fr/>

<sup>3</sup>CSTB: French scientific and technical center for buildings, <http://www.cstb.fr/>

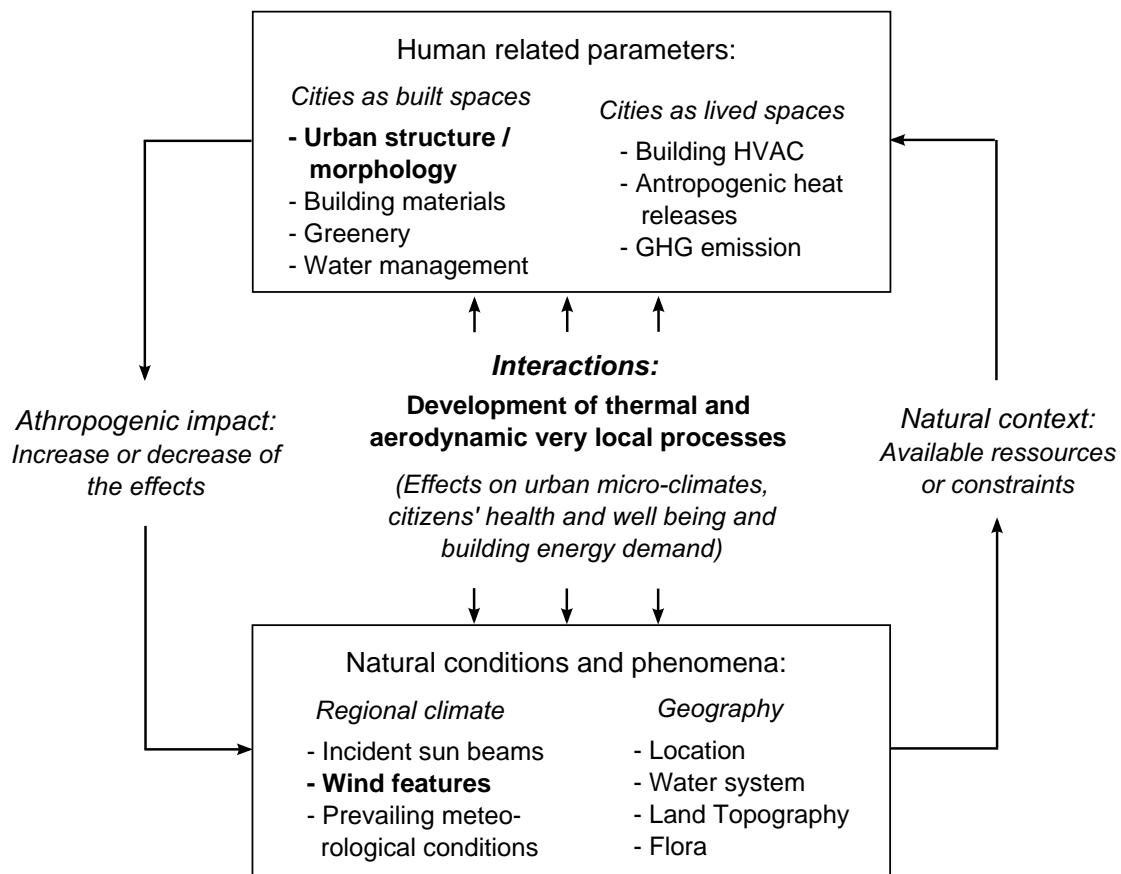


Figure 1: Interactions between natural and anthropogenic factors contributing to the development of complex aerodynamic and thermal processes in cities: effects on urban micro-climates, citizen's health and well being as well as building energy loads.

## **Part I**

# **Fundamentals and preliminary work**



# Chapter 1

## Phenomenological foundations and outline of the thesis

This chapter presents the prerequisites of the current study. The main physical structures and processes involved in the determination of urban micro-climates are briefly reviewed. Urban physics is introduced as the engineering discipline studying these phenomena, along with building physics. On this basis and considering the current environmental and energy challenges, the scope, problem and methodology of the thesis are outlined.

### Contents

---

<b>1.1 Phenomenological background . . . . .</b>	<b>8</b>
1.1.1 The atmospheric and urban boundary layers . . . . .	8
1.1.2 The urban energy balance . . . . .	13
1.1.3 Effects of urban micro-climates on the outdoor comfort and building energy loads . . . . .	17
<b>1.2 Introduction to urban physics and aerodynamics . . . . .</b>	<b>20</b>
1.2.1 Urban physics and building physics . . . . .	20
1.2.2 Existing techniques to study urban air flows . . . . .	23
1.2.3 Overview of noteworthy urban flow patterns . . . . .	26
<b>1.3 Problem formulation and outline of the thesis . . . . .</b>	<b>34</b>
1.3.1 Motivation and scope of the work . . . . .	34
1.3.2 Problem formulation and expected outcomes . . . . .	37
1.3.3 Methodology . . . . .	37
<b>1.4 Summary . . . . .</b>	<b>39</b>

---



## 1.1 Phenomenological background

### 1.1.1 The atmospheric and urban boundary layers

The lower part of the atmosphere is called the planetary boundary layer (PBL) or atmospheric boundary layer (ABL). It extends from the ground up to  $10^2$  to  $10^3$  m depending on the atmospheric stability. There, air flows are disturbed by the Earth surface on a diurnal time scale as thermal and mechanical processes develop due to the sun heating and friction on the Earth surface. The ABL is characterized by its turbulent behavior and the vertical mixing that occurs. These properties differ from those of the above free atmosphere, where geostrophic winds are almost laminar and horizontal. As less thermally induced turbulence phenomena occur, the ABL is generally thinner by night (Blocken, 2014b; Oke, 1987).

The urban boundary layer (UBL) develops within the ABL when air flows from the countryside encounter an urban area. It modifies the ABL properties as an internal boundary layer develops. Wind experiences a vertical motion when impinging on and flowing over buildings and other urban obstacles, and the air is generally heated because of urban higher temperatures. This can lead to the formation of a dome over the city. By daytime, these processes increase both the mechanical and thermal convection (Oke, 1987).

Fig. 1.1(a) shows the two main layers that compose the UBL (Oke, 1987). The upper one is called the mixing layer. Due to the fact that the effects of natural convection decrease slower with height than those of forced convection, this layer is dominated by thermal processes, especially during daytime.

The lower part of the UBL, about 10 % of its depth, is called the surface layer. It is located near the ground and directly undergoes the effects of the underlying urban elements. Due to the urban obstacles and increased roughness, the flow experiences a relatively large drag force (Britter and Hanna, 2003), which decreases the horizontal wind speed. As a consequence and on average, a lower horizontal wind speed is observed inside and above cities as compared to the countryside wind speed at the same height. However, when regional winds are weak, a thermally induced upwards air motion can develop above the city, which could initiate a centripetal air motion from the countryside.

In a surface layer and according to the Monin-Obukhov's similarity theory, the horizontal mean wind flow profile can be modeled by a logarithmic law,<sup>1</sup> which depends on the roughness of the Earth surface and the atmospheric stability (Britter and Hanna, 2003; Oke, 2006b), as follows:

$$U(z) = \frac{u^*}{\kappa} \times \ln \left( \frac{z - z_D}{z_0} + \Psi_M \frac{z}{L} \right) \quad (1.1)$$

---

<sup>1</sup>In this equation  $\Psi_M$  is a dimensionless function representing the modification of the wind profile curvature away from the neutral profile (stable or unstable conditions), and  $L$  is the Obukhov's stability length, whose formulation is:  $L = -u^{*3} / [\kappa (g/\theta_v) Q_H]$ , with  $g$  the gravitational acceleration,  $\theta_v$  the virtual potential temperature and  $Q_H$  the turbulent sensible heat flux (Oke, 2006a).

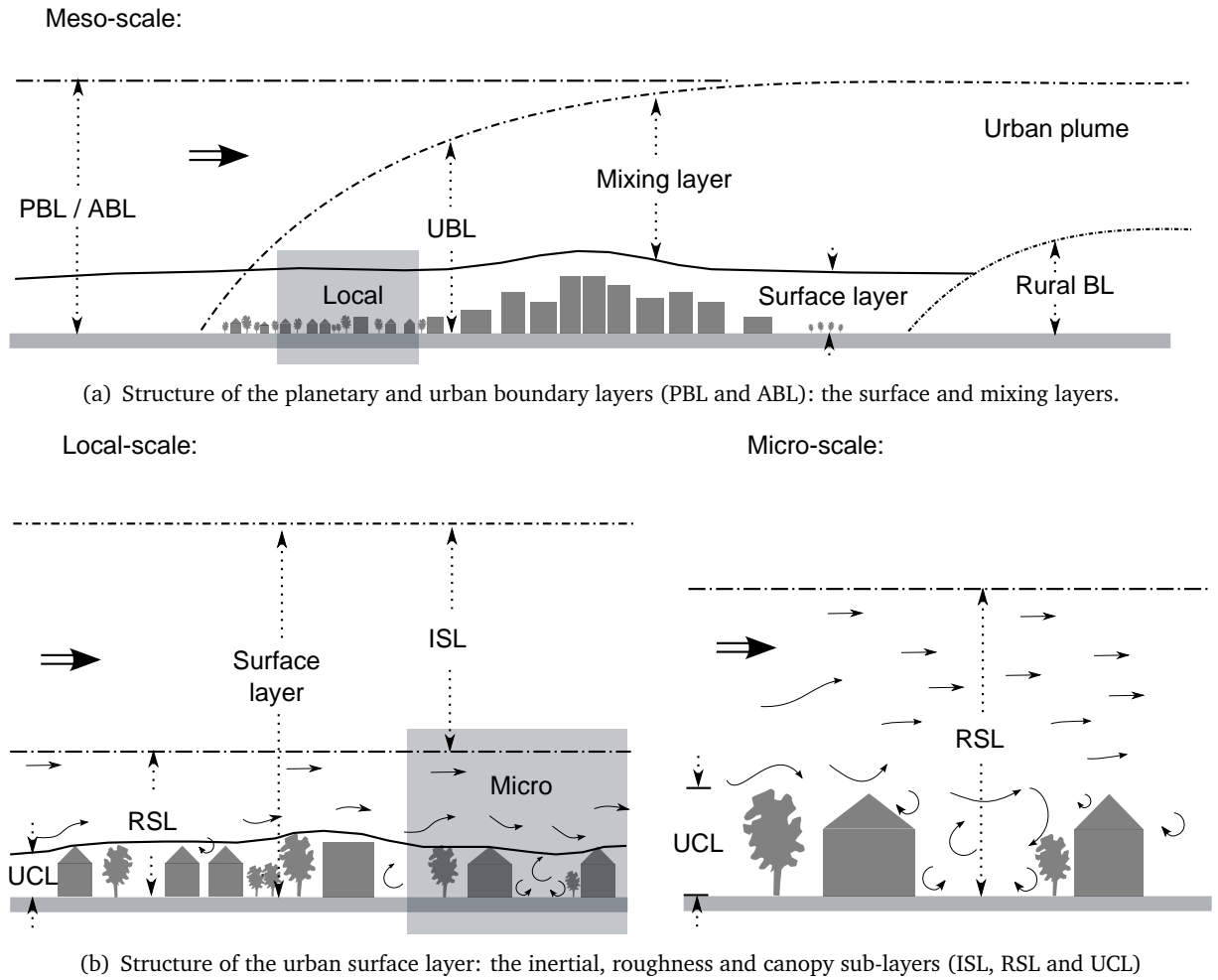


Figure 1.1: Structure of the ABL. (Adapted from (Oke, 1987))

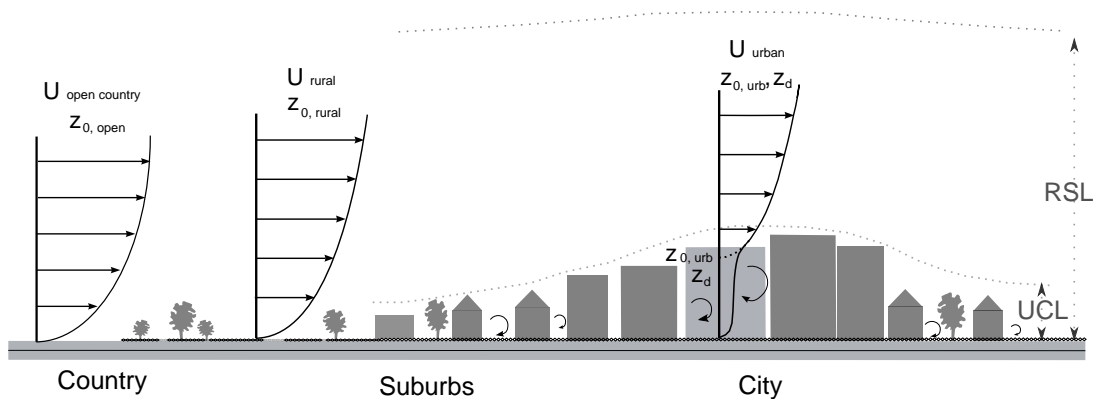


Figure 1.2: Mean wind profile depending on the land use. (Based on (Blocken and Stathopoulos, 2013; Oke, 2006a), and (Gandemer, 1976) cited in (Bouyer, 2009))

$$\text{with: } \begin{cases} U(z) : \text{the horizontal mean velocity at height } z \text{ [m} \cdot \text{s}^{-1}\text{]}, \\ u^* : \text{the friction velocity [m} \cdot \text{s}^{-1}\text{]}, \\ \kappa = 0.418 : \text{the von Kármán constant,} \\ z : \text{the height [m]}, \\ z_0 : \text{the roughness length, depending on the terrain roughness class (see Tab. 1.1) [m]}, \\ z_D : \text{the surface displacement length, depending on the surface properties [m]}, \\ \Psi_M \frac{z}{L} : \text{the universal dimensionless function, which accounts for the effects of the} \\ \quad \text{atmospheric stability.} \end{cases}$$

In a neutrally stratified surface layer, i.e. without significant effects of thermal processes, the universal dimensionless function equals zero. As a consequence, the formulation of the mean wind profile is simpler ([Bitter and Hanna, 2003](#)):

$$U(z) = \frac{u^*}{\kappa} \times \ln \left( \frac{z - z_D}{z_0} \right) \quad (1.2)$$

$$\text{with: } \begin{cases} U(z) : \text{the horizontal mean velocity at height } z \text{ [m} \cdot \text{s}^{-1}\text{]}, \\ u^* : \text{the friction velocity [m} \cdot \text{s}^{-1}\text{]}, \\ \kappa : \text{the von Kármán constant,} \\ z : \text{the height [m]}, \\ z_0 : \text{the roughness length [m]}, \\ z_D : \text{the zero displacement height [m]}. \end{cases}$$

The logarithmic formulation of the ABL wind profile was mainly used by meteorologists and benefits from a theoretical background. However, engineers used to consider a power law profile to model the ABL wind profile under neutrally stratified atmospheric conditions:

$$U(z) = U_{ref} \times \left( \frac{z}{z_{ref}} \right)^\alpha \quad (1.3)$$

$$\text{with: } \begin{cases} U_{ref} : \text{the horizontal mean velocity at height } z_{ref} \text{ [m} \cdot \text{s}^{-1}\text{]}, \\ z_{ref} : \text{the reference height [m]}, \\ \alpha : \text{the power law exponent, depending on the terrain type (see Appendix A).} \end{cases}$$

This formulation is still often used as in the [ASHRAE \(2005\)](#).

Due to the modification of the bottom boundary condition in cities as compared to an open rural configuration, the logarithmic law that describes a countryside wind profile is altered. The profile concavity is generally lower over cities as friction increases, and the profile intercept is higher. This means that the theoretical height of zero wind speed is located above the ground level

because of the roughness elements. Turbulence intensities are also higher. These modifications are generally translated by a higher value of the displacement height  $z_D$  as well as the roughness length  $z_0$ <sup>2</sup> (Oke, 1987), as shown in Fig. 1.2. The correspondence between the values of  $z_0$  and the type of terrain,<sup>3</sup> i.e. the type of country or city, is given in the Davenport's classification, which has been modified by Wieringa et al. (2001). This revised classification includes more data about rough and inhomogeneous rural and urban areas. This classification is given in Tab. 1.1. For an open rural landscape  $z_0$  equals 0.03 m, whereas for a chaotic and densely built-up area such as a city center,  $z_0$  may exceed 2 m. Appendix A gives another classification of terrain types, which are related to  $\alpha$ . For an open landscape  $\alpha = 0.1$  and for a densely built city  $\alpha = 0.33$ . Similar to  $z_0$ , the value of  $\alpha$  increases with roughness.

As shown in Fig. 1.1(b), the urban surface layer can itself be divided into three main sub-layers (Oke, 1987):

- the urban inertial sub-layer (ISL);
- the urban roughness sub-layer (RSL);
- and the urban canopy layer (UCL).

The ISL is the highest layer. It makes the transition between the inner and the outer surface layer. This layer is also called equilibrium boundary layer as the mean flow is horizontally homogeneous and the Reynolds fluxes are constant. In this area, the flow has adapted to the integrated effects of the city (Britter and Hanna, 2003) and behaves as if it was streaming over an homogeneous surface. The profiles of the mean flow and other atmospheric physical variables follow the theoretical logarithmic law (Barlow and Coceal, 2009).

The RSL extends from the ground to typically three or five times the building height depending on the urban configuration (Barlow and Coceal, 2009). The rougher the urban area, the thicker the RSL. In this sub-layer, the flow is not horizontally homogeneous and is affected by wake interference. The flow is still adjusting to the effects of urban elements. Turbulent diffusive processes are important for heat and momentum transfers (Oke, 1987). For a relative homogeneous canopy, the maximum shear stress is observed around the mean building height. It decreases then down in the UCL. When the roughness is increased, the maximum shear stress is reduced, and occurs higher than the mean building height (Britter and Hanna, 2003). Note that different studies showed that a logarithmic law can model the horizontally averaged properties of the flow in this layer down to 1.5 or 1.8 times the mean building height (Britter and Hanna, 2003; Cheng and Castro, 2002; Kastner Klein et al., 2000).

---

<sup>2</sup> $z_D$  represents the height of the equivalent ground surface, where the mean momentum sink for the flow is located. Not considering  $z_D$ ,  $z_0$  corresponds to the height where the theoretical mean wind speed is zero. A greater value of  $z_0$  translates the increase of turbulence intensity as well as the frictional influence due to the surface properties.  $z_0$  increases with urban density up to a maximum. It decreases then because the interference between individual wakes smoothes the turbulence production (Oke, 1988). For rough and densely built cities,  $z_0$  corresponds to the additional roughness provided by tall elements (Grimmond and Oke, 1999).

A representation of the evolution of  $z_D$  and  $z_0$  against the urban density is given in Appendix B.

<sup>3</sup>The term landscape is also often used in literature instead of terrain.

Rough. class	$z_0$ (m)	Landscape description
1. "Sea"	0.0002	Open sea or lake (irrespective of wave size), tidal flat, snow covered flat plain, featureless desert, tarmac or concrete, with a free fetch of several kilometers.
2. "Smooth"	0.005	Featureless land surface without any noticeable obstacles and with negligible vegetation, e.g. beaches, pack ice without large ridges, marsh and snow covered or fallow open country.
3. "Open"	0.03	Level country with low vegetation (e.g. grass) and isolated obstacles with separations of at least 50 obstacle heights; e.g. grazing land without wind breaks, heather, moor or tundra, runway area of airports. Ice with ridges across-wind.
4. "Roughly open"	0.10	Cultivated or natural area with low crops or plants cover, or moderately open country with occasional obstacles (e.g. low hedges, isolated low buildings or trees) at relative horizontal distances of at least 20 obstacle heights.
5. "Rough"	0.25	Cultivated or natural area with high crops or crops of varying height, and scattered obstacles at relative distances of 12 to 15 obstacle heights for porous objects (e.g. shelterbelts) or 8 to 12 obstacle heights for low solid objects (e.g. buildings). <i>Analysis may need <math>z_D</math>.</i>
6. "Very rough"	0.5	Intensively cultivated landscape with many rather large obstacle groups (large farms, clumps of forest) separated by open space of about 8 obstacle heights. Low densely planted major vegetation like bushland, orchards, young forest. Also, area moderately covered by low buildings with inter-spaces of 3 to 7 building heights and no high trees. <i>Analysis requires <math>z_D</math>.</i>
7. "Skimming"	1.0	Landscapes regularly covered with similar size large obstacles, with open spaces of the same order of magnitude as obstacle heights; e.g. mature regular forests, densely built-up area without much building height variation. <i>Analysis requires <math>z_D</math>.</i>
8. "Chaotic"	$\geq 2$	City centers with mixture of low rise and high rise buildings or large forests of irregular height with many clearings. <i>Analysis by wind-tunnel advised.</i>

Table 1.1: Updated Davenport's classification of effective terrain roughness: Increase of the aerodynamic roughness length value ( $z_0$ ) from flat and smooth landscapes to densely built and chaotic urban areas. (From (Wieringa et al., 2001))

The UCL is the lower sub-division of the urban surface layer and is more specifically studied in this thesis. Its height is typically the building's height. Inside, the averaged wind speed is more uniform than above, except near the ground, where the wind speed is zero (Britter and Hanna, 2003). Air flows are locally affected by the urban 3D and morphological properties and can be significantly influenced by local thermal processes as well. The physical phenomena that develop are complex, with small time scales. For very dense cities, turbulence may be produced at the top of the canopy, where the above flow interacts with building roofs. Turbulence is then advected downwards in the UCL. When the flow through the canopy generates turbulence, the effective turbulence level in the UCL is comparable to that above (Britter and Hanna, 2003).

The complex and interacting micro-scale processes that operate between the different roughness elements of the UCL determine its climate (Oke, 1987). As these very local processes are conditioned by their immediate environment, a wide diversity of very local micro-climatic conditions are produced.

In case of forced convection, the interactions between the mean flows and urban obstacles lead to the mechanical development of turbulence and intricate aerodynamic phenomena. Separated and reversed flows, wakes and other recirculation phenomena around each building interfere with those of other buildings and more or less interact with the above flow (see Sec. 1.2.3). These specific aerodynamic conditions induce different ventilation regimes, which alter urban heat transfers and pollutant transport.

In case of mixed or natural convection, i.e. when thermal effects are substantial, buoyancy yields thermally induced air motions and turbulence development. In these cases, differences in air densities due to temperature gradients contribute to drive the flow. This may generate new vortices and modify the flow and temperature fields within the UCL, especially in low wind speed zones. It can thus affect the urban internal and external heat and mass fluxes. On larger scales, it can modify the stability of the boundary layer.

### 1.1.2 The urban energy balance

The energy balance of a given urban surface is basically obtained by summing up all the energy input and output fluxes as well as the change of energy storage that occur within it. The urban surface is understood here as an active surface, i.e. as a "layer where the majority of the energy is absorbed, reflected and emitted, where the main transformations of energy and mass occur, where the precipitation is intercepted and where the major portion of drag on air flow is exerted" (Oke, 1987). As a consequence, the urban surface is thick and encompasses an urban fragment with some part of its underlying ground<sup>4</sup> and above air (see Fig 1.3).

According to Oke (1987) and Britter and Hanna (2003), the following input and output fluxes determine the surface energy budget:

---

<sup>4</sup>The part of the ground generally considered goes from the ground surface down to 1 to 2 m deep. This corresponds to the depth of the ground that experiences significant diurnal variations.

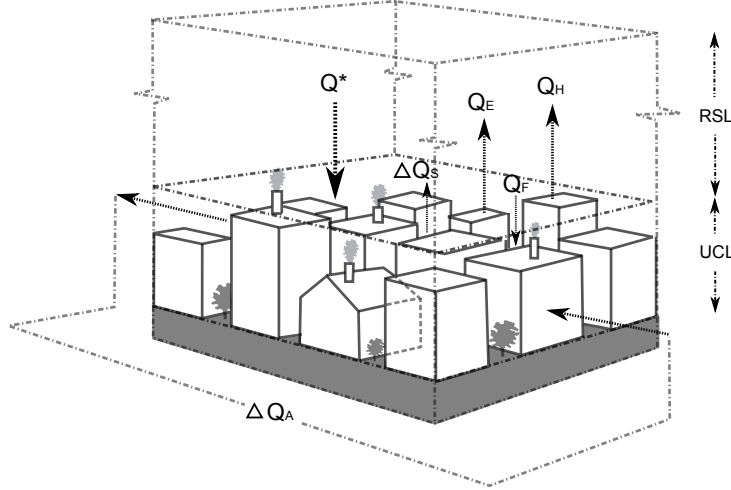


Figure 1.3: Physical heat fluxes contributing to the urban energy balance. (Adapted from (Oke, 1987))

- the all-wave net radiative flux ( $Q^*$ ), which includes the incoming short-wave radiation from the sun as well as the long-wave radiation exchanges between urban surfaces and the sky and the atmosphere;
- the anthropogenic heat fluxes that are produced by citizens' activities ( $Q_F$ );
- the relative loss of sensible heat due to the vertical turbulent heat flux ( $Q_H$ ), which cools down the surface layer during the day;
- the vertical latent heat loss due to evaporation ( $Q_E$ ), which cools down the surface layer;
- the net change in heat within the surface layer ( $\Delta Q_S$ ), due to the energy storage or discharge in or from the ground, building materials and air volume;
- and the net horizontal advected flux of sensible and latent heat ( $\Delta Q_A$ ), due to winds.

On this basis, the expression of the urban energy balance is given by (Oke, 1987):

$$Q^* + Q_F = Q_H + Q_E + \Delta Q_S + \Delta Q_A \quad (1.4)$$

with:  $\left\{ \begin{array}{l} Q^* : \text{the net all-wave radiative flux,} \\ Q_F : \text{the anthropogenic heat flux associated with combustion,} \\ Q_H : \text{the turbulent sensible heat flux,} \\ Q_E : \text{the turbulent latent heat flux,} \\ \Delta Q_S : \text{the storage of heat in urban materials and the air,} \\ \Delta Q_A : \text{the net horizontal advected flux of sensible and latent heat.} \end{array} \right.$

The urban energy balance varies on a diurnal time scale and depends on the surrounding environmental and meteorological conditions as well as the urban features of the volume considered. On the one hand, external relative inputs are conditioned by the regional climate, which is modified by the prevailing meteorological conditions as well as the surrounding topography

and land use. The corresponding boundary conditions determine the total amount of sunlight, radiation, moisture and winds that enter or leave the urban surface. On the other hand, the fluxes that develop inside the volume involve convective and radiative exchanges between the buildings, other urban surfaces and their environment, as well as heat storage in thermal masses and latent heat transfers. Anthropogenic factors come in addition to these physical exchanges by generally creating extra heat and moisture sources.

These energy internal fluxes depend on three main urban factors:<sup>5</sup>

- the shape and relative layout of buildings and open spaces;
- the design and thermal properties of urban materials and greenery;
- and the building heat losses as well as other anthropogenic heat and mass releases.

Tab. 1.2 sums up these factors and their corresponding effects.

The design and thermo-physical properties of urban materials as well as greenery influence both the heat and mass exchanges and storage within the UCL. As urban materials are mostly impervious and highly capacitive, they amplify the water-proofing and the thermal admittance of urban areas. This decreases evapo-transpiration and increases the sensible heat storage in urban masses. This stored heat is then released to the surrounding environment.

Building losses and other anthropogenic heat and mass releases, e.g. from traffic, combustion and technical systems, alter the sensible and latent energy balance by creating additional sources. They warm up the surrounding air and structures. In addition, airborne pollutants intensify the radiative absorption and emission phenomena. Particles increase long-wave radiation from the sky but might not have significant effects within the UCL (Oke, 1987).

These urban related factors impact on the sensible and latent heat transfers as well as the convective and turbulent advective processes that develop in cities. These effects make the urban energy fluxes much more complex than those of rural areas. By intensifying the urban heat storage during the day and slowing down heat dissipation especially during the night because of the thermal mass and 3D morphology, they contribute to generate the urban heat island (UHI) phenomenon (Oke, 1987). The UHI phenomenon is defined by an increase of the urban mean temperature compared to that of the country.<sup>6</sup> Fig. 1.4 shows the corresponding air temperature profile from the countryside to city centers. Note that surface temperatures are sometimes considered as well.

---

<sup>5</sup>These factors could also be organized into four categories that together determine the urban internal fluxes and more generally the urban climate (Oke, 2006b):

- the “urban structure”, which refers to the dimensions and spacing of the buildings and streets;
- the “urban cover”, which refers to the imperviousness of the urban surface;
- the “urban fabric”, which refers to the nature of materials (artificial or natural);
- and the “urban metabolism”, which refers to the anthropogenic heat, water and pollutant emissions.

<sup>6</sup>As the UHI intensity is determined by the geometrical and urban planning features of a city as well as human activities, a more accurate way to define the UHI is to refer to local climate zones (LCZs) (Stewart and Oke, 2012). Indeed, the terms “urban” and “rural” can describe a wide diversity of landscapes, which could have only very few in common. A better characterization of the UHI effects could therefore be achieved by specifying the type of land use or built environment, and the land cover.



Urban factors	Physical consequence	Impact on the energy budget
Urban morphology (Urban structure)	↗ surface area and multiple reflections	↗ absorption of short-wave radiation
	↘ openness to the sky (sky view factor)	↘ heat loss from long-wave radiation
	↘ mean wind speed	↘ total turbulent heat transport
Urban materials (Urban cover and fabric)	↗ thermal admittance	↗ sensible heat storage
	↗ water proofing	↘ evapo-transpiration
Anthropogenic releases (Urban metabolism)	↗ absorption and reemission by pollutant	↗ long-wave radiation from the sky
	↗ building and traffic heat loss	↗ heat sources

Table 1.2: Urban factors and physical processes influencing the UHI effect: contribution of the urban structure, materials and anthropogenic direct sources. (Based on (Oke, 1987))

↗: increase of, ↘: decrease of.

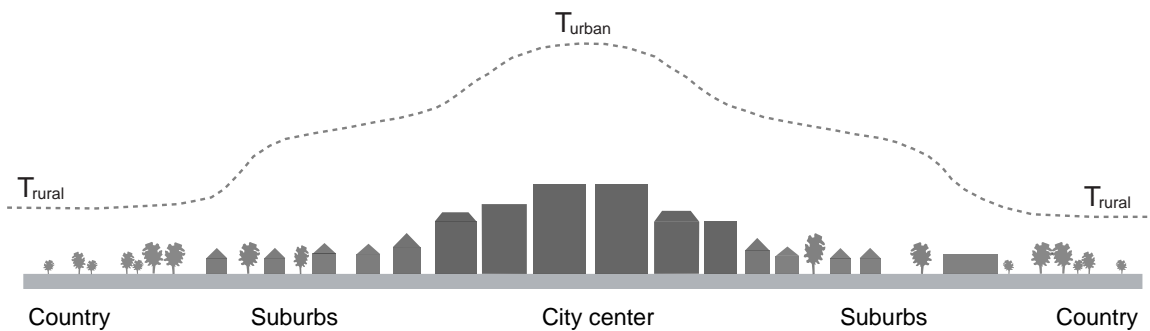


Figure 1.4: The UHI phenomenon: evolution of the air temperature from the countryside to the city center. (Adapted from (Oke, 1987))

The UHI influence can be felt up to  $10^4$  to  $2 \times 10^4$  m out of the city. The UHI intensity is generally 2 or 3 °C (Bitter and Hanna, 2003), but it depends on the city's features and context. According to studies reviewed by Santamouris (2014), the mean annual UHI intensity is 1.4 °C in Melbourne, Australia, and 2 °C in London, United Kingdom. Its average maximum is about 7 °C in Athens, Greece and 3 °C in Bahrain. Other examples of maximum UHI intensities are given in Memon et al. (2009) for cities located all over the world, showing values up to 10 °C in Hong Kong and 12 °C in Łódź, Poland. The UHI phenomenon substantially varies on a diurnal time scale. Its intensity is generally lower, and even negative, during the morning / midday and maximum during the night, especially under calm and clear atmospheric conditions. These variations are due to the uneven distribution of the different above-mentioned energy fluxes over the day (Memon et al., 2009; Oke, 1987). For example, in Paris, France, an averaged 2.5 °C positive temperature difference is generally observed between the downtown and the surrounding rural areas. A 8.1 °C difference can nevertheless be observed during summer nights (APUR, 2012). In Basel, Switzerland, the monthly averaged UHI intensity based on measurements taken between 1999 and 2001 equals 1.8 °C in the late evening, but is close to 0 °C in the late morning (Allegrini

et al., 2012b). In the urban area of Hong Kong, the diurnal variation over the year 2005 was of 3 °C with a minimum after noon and a maximum during the night (Memon et al., 2009).

### 1.1.3 Effects of urban micro-climates on the outdoor comfort and building energy loads

Urban micro-climates, which are the result of the complex urban energy balance, affect citizen's health and comfort as well as building energy loads. Thus, the UHI affects both urban environmental and social matters. It can be beneficial in cold climates and winter but harmful in hot regions and during summers. Warmer ambient outdoor temperatures alter the citizens' thermal stress as well as the building energy demand by increasing or reducing the need of artificial air conditioning. According to Santamouris (2014), the UHI effect decreases the residential total energy demand in cold zones. Conversely, in hot zones, the increase of the cooling demand is much more important than the reduction of the heat demand. Moreover, the increased use of artificial cooling during hot seasons affects the ambient thermal conditions, as air conditioning devices release heat in the surrounding streets, which increases the building cooling loads (Bozonnet, 2006), and energy transformation can emit pollutants. Warmer temperatures also affect citizen's health and comfort by intensifying the magnitude or the duration of heat waves with the maintaining of high temperatures during nights. The local meteorological conditions can be altered as well, through secondary effects or a change in the precipitation patterns (Rasheed, 2009).

At a smaller scale and neglecting latent heat transfers, Fig. 1.5 summarizes the physical phenomena developing around and in an urban canyon. These heat exchanges are decisive in determining urban micro-climates. The surrounding urban structure determines the obstruction of incident sun beams, which limits the sun heating and the natural lighting of the shadowed urban areas and buildings. Radiative heat exchanges between the numerous facing surfaces and with the sky are also impacted on, including multi-reflections of incoming radiation, the exchanges of long-wave radiation between urban surfaces of different temperatures and the emission of long-wave radiation by urban surfaces toward the sky. Urban structures also modify urban air flows. They generally decrease air flow speeds, increase turbulence intensities and form vortices with very local features (see Sec. 1.2.3). Moreover, the potential of evaporative cooling of urban areas is generally reduced because of the surface imperviousness and weak greenery (see Sec. 1.1.2).

These specific alterations of the radiative exchanges, wind conditions and latent heat transfers impact on the outdoor pedestrian comfort. More precisely, they impact on the outdoor thermal environment, as in addition to physical factors, the notion of comfort implies physiological and psychological aspects. Four environmental parameters determine the experienced thermal environment (Ramponi, 2013):

- the mean radiant temperature, which affects radiative heat transfers;
- the air temperature, which affects convective heat transfers and latent energy exchanges;
- humidity, which affects latent heat transfers;
- and the wind speed, which mainly affects convective heat transfers.

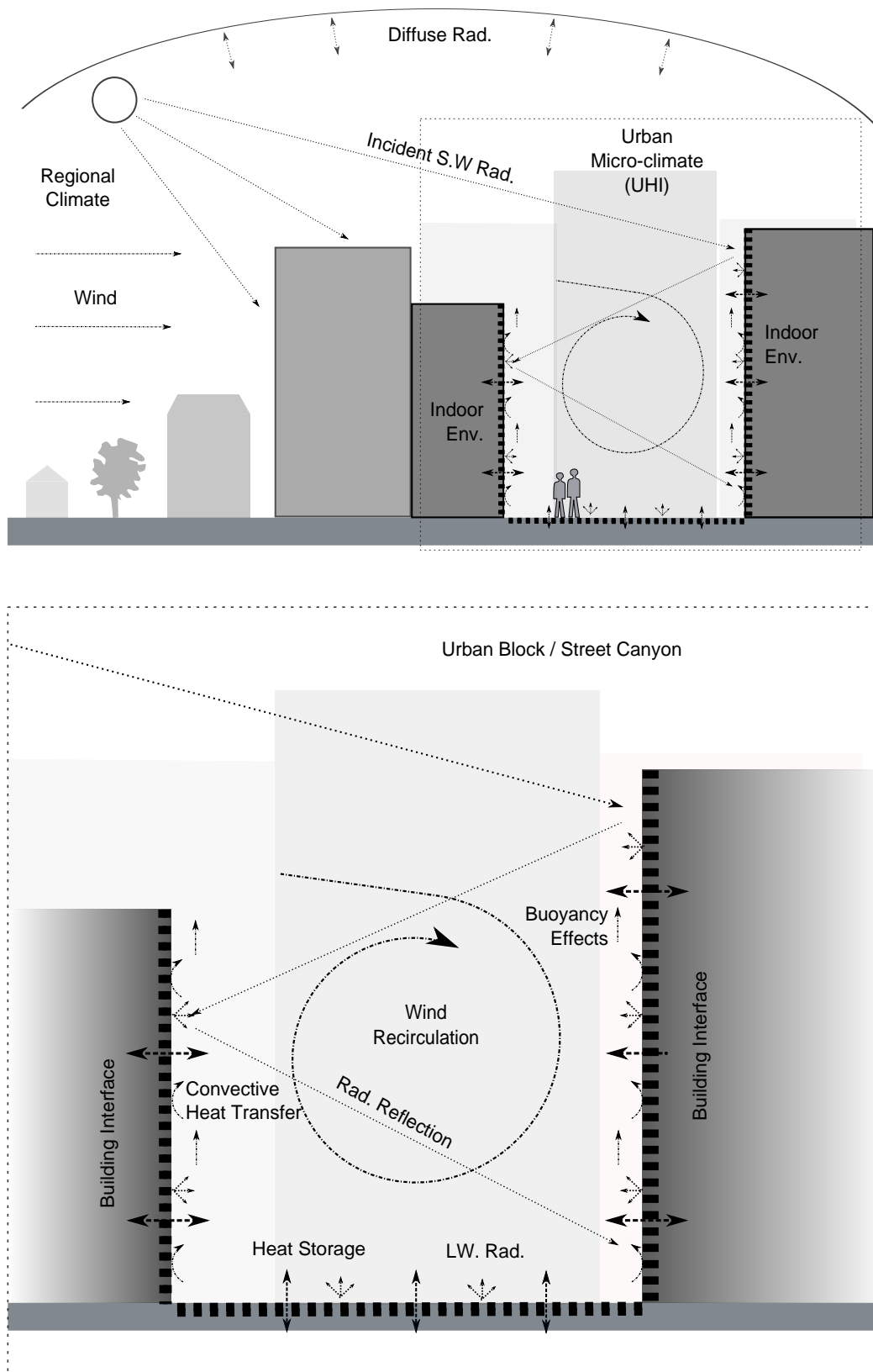


Figure 1.5: Physical processes and exchanges occurring between a city and its environment and in an urban canyon.

The mean radiant temperature is directly impacted on by the solar access of urban spaces as well as the surface temperature of building facades and other urban surfaces. Indeed, the sun heating, shadowing, multi-reflections and long-wave radiation emission by surrounding urban surfaces determine the radiative budget of a surface. In addition to the urban layout, the albedo of urban surfaces is a key parameter that determines radiative heat fluxes and surface temperatures. Note that further than the mean radiant temperature, differences in urban surface temperatures may substantially affect the urban comfort.

The air temperature is mostly determined by the season, meteorological conditions and hour of the day. However, it is also affected by the urban heat island effect, urban surface temperatures, anthropogenic heat releases as well as the ability of urban air flows to remove heat from urban areas. This advective heat removal is improved in case of high wind speeds or high turbulence intensities.

Humidity depends on the meteorological conditions and geographic context but it is also strongly related to the urban surface imperviousness and greenery. These factors determine the evapo-transpiration potential in urban areas. However, they do not directly depend on the urban structure but more on the urban planning. Human releases also affect the humidity level.

Neglecting the effects of trees, urban wind speeds are mainly altered by general urban structure and the presence of still and sharp-edged obstacles. The general urban structure alters incident winds in terms of mean speed, direction and turbulence intensity. Buildings create sheltered zones or accelerated streams. Beyond their effects on thermal comfort, winds also alter the pedestrian comfort as urban mean flow speeds and turbulence levels can be high and strongly vary on very small time and spatial scales. This can restrict or forbid some activities. It might even create dangerous conditions. In order to evaluate the acceptability of such wind-induced mechanical effects on pedestrian comfort and safety, effective wind speed thresholds and probabilities of exceeding them are often considered<sup>7</sup> (Stathopoulos, 2006).

As shown in Fig. 1.6, radiant and air temperatures, humidity and air flows also impact on the building energy balance. On the one hand, the passive solar heating of buildings can be reduced due to numerous urban obstructions that produce shade. On the other hand, their potential radiative cooling is also generally restricted because of the limited sky view factor (see Sec. 2.2.1). Moreover, multi-reflections can warm-up shadowed facades. Natural ventilation as well as convective heat exchanges are also often reduced because of the lower urban wind speeds and the development of recirculation phenomena (see Sec. 5.1.1).

The respective and total influence of these physical parameters on the building energy demand were investigated by Bozonnet (2006), Bouyer et al. (2011) and Allegrini et al. (2012b) using numerical approaches. A 35 % increase in the energy demand of a building located in a street canyon in Athens was assessed by Bozonnet (2006), accounting for the UHI and thermo-aeraulic

---

<sup>7</sup>According to (Bottema, 1993) cited by Blocken (2014b), a dis-comfortable zone in terms of wind effects occur when the effective wind speed,  $U_c = U + \sigma_U$ , overcomes  $6 \text{ m} \cdot \text{s}^{-1}$  more than 10 % of time. To define wind danger, turbulence and gusts are much more important and areas are considered dangerous when  $U_D = U + 3\sigma_U$  overcomes  $15 \text{ m} \cdot \text{s}^{-1}$  more than 1 % of time.

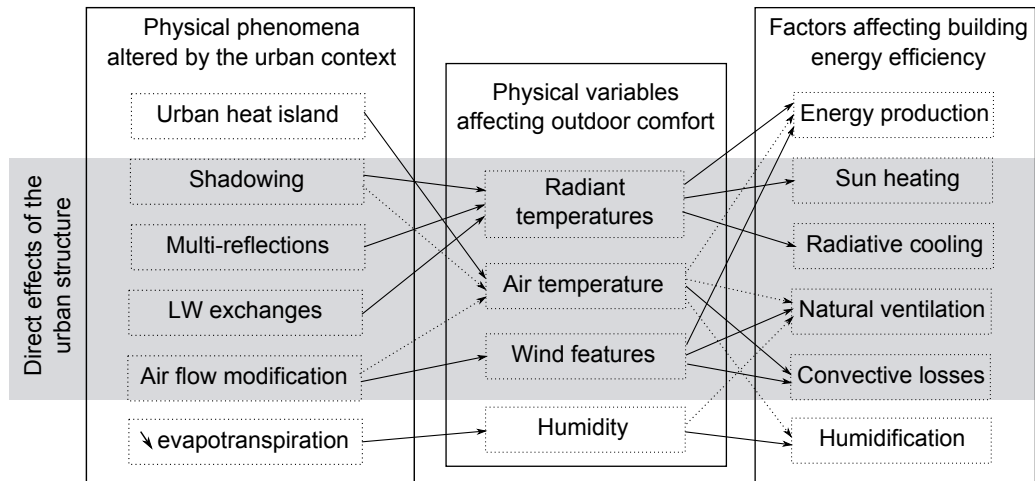


Figure 1.6: Effects of urban structures on the physical parameters determining the urban outdoor comfort and affecting the building energy balance.

transfers that develop in the street canyon. For an urban block located in Lyon, France, and as compared to a stand alone building with theoretical urban masks, [Bouyer et al. \(2011\)](#) computed a 28 % increase in the building sensible loads for heating during one week in winter and a 42 % increase of the sensible cooling loads for one week in summer. This increase of the building energy loads was assessed taking into account realistic solar masks, infra-red exchanges and specific convective heat transfers. [Allegrini et al. \(2012b\)](#) investigated the combined effects of radiative multi-reflections, adapted convective heat exchanges as well as the UHI effect on the building energy demand in the case of an idealized street canyon located in Basel, Switzerland. Results showed a multiplication by a factor 8 of the annual building energy demand for cooling and reduction of 20 % for heating, in the case of an office and residential building and in comparison with a isolated rural building.

The three above-mentioned works demonstrate the substantial effect of the urban context on the building energy balance. The urban context modifies the heat and air fluxes around and at building outer walls in comparison with an isolated building configuration, and thus impacts the building thermo-aeraulic solicitations. Therefore, considering the effects of the urban environment on the very local thermal and aerodynamic conditions appears necessary when aiming at designing comfortable urban areas and assessing the effective thermal behavior and energy performance of buildings.

## 1.2 Introduction to urban physics and aerodynamics

### 1.2.1 Urban physics and building physics

Urban physics is an engineering discipline that is strongly linked with building physics. In fact, it can be understood as a part of building physics, as the *building physics of outdoors*. According to [Blocken \(2012\)](#), “building physics is the study of the physical behavior of buildings and building

components, including the transfer of heat and mass, acoustics, lighting, energy and the indoor and outdoor environment. It is aimed at improving health, comfort and productivity taking into account energetic, ecological and economic constraints.” As such, building physics addresses three main fields of study, namely: the indoor environment, the building envelope and the outdoor environment.

Urban physics refers to the last point: the outdoor environment. Extending the previous definition to urban physics, it can be understood as “the study of the physical aspects of the outdoor urban environment, including the transfer of heat and mass, acoustics, lighting and energy, and their interaction with the indoor environment and the building envelope. It is aimed at improving outdoor and indoor health, comfort, productivity and sustainability taking into account energetic, ecological and economics constraints” (Blocken, 2012). As such, it includes different concepts and tools from physics, environmental chemistry, aerodynamics, meteorology and statistics (Moonen et al., 2012a).

Focusing on the lower part of the UBL, the practical application fields of urban physics are linked with the effects of urbanization and global warming on the urban micro-climate and citizens (Carmeliet, 2015). The related topics include, among others, the UHI effect, the pedestrian wind and thermal comfort and building heat transfer. As seen in the previous sections (see Sec. 1.1.2 and 1.1.3), those subjects have in common the fact that they depend on the interactions between air flows, heat fluxes and solid masses. Particle dispersion, wind driven rain, wind energy or sound propagation in urban areas are other possible application fields of urban physics (Blocken, 2013; Moonen, 2013).

Fig. 1.7 shows the imbrication of the different spatial scales related to urban physics. These scales are nested between the material and human scale on the lower boundary ( $L < 1$  m), and the meso-scale on the upper one ( $L > 10^4$  m) (Blocken, 2013). Spatial scales covered by urban physics extend thus from the component and building scales ( $L < 10$  m, time scale smaller than one hour) to the micro-scale ( $L < 10^4$  m, time scale of one day). The former especially involves building wakes and heat transfers, which are processes developing in the vicinity of buildings due to their shape and thermo-physical properties. The later is related to the UHI phenomenon and refers to the micro-scale climatology.

For specific analysis, especially with respect to urban aerodynamics, urban physics’ spatial scales are often divided into four sub-scales, which actually almost correspond to usual urban scales<sup>8</sup> (see Sec. 2.1.1) (Britter and Hanna, 2003):

- the regional scale ( $< 10^5$  or  $2 \times 10^5$  m), which is affected by the effects of the whole urban area, especially those induced by the UHI;
- the city scale ( $< 10^4$  or  $2 \times 10^4$  m), in which the averaged effects of buildings or other urban elements result in a general behavior. Specificities of the flow structures within the UCL are thus smoothed out;

---

<sup>8</sup>Note that Oke (2006b) provides a further detailed division of urban scales (UCL units). They are presented in Appendix C.

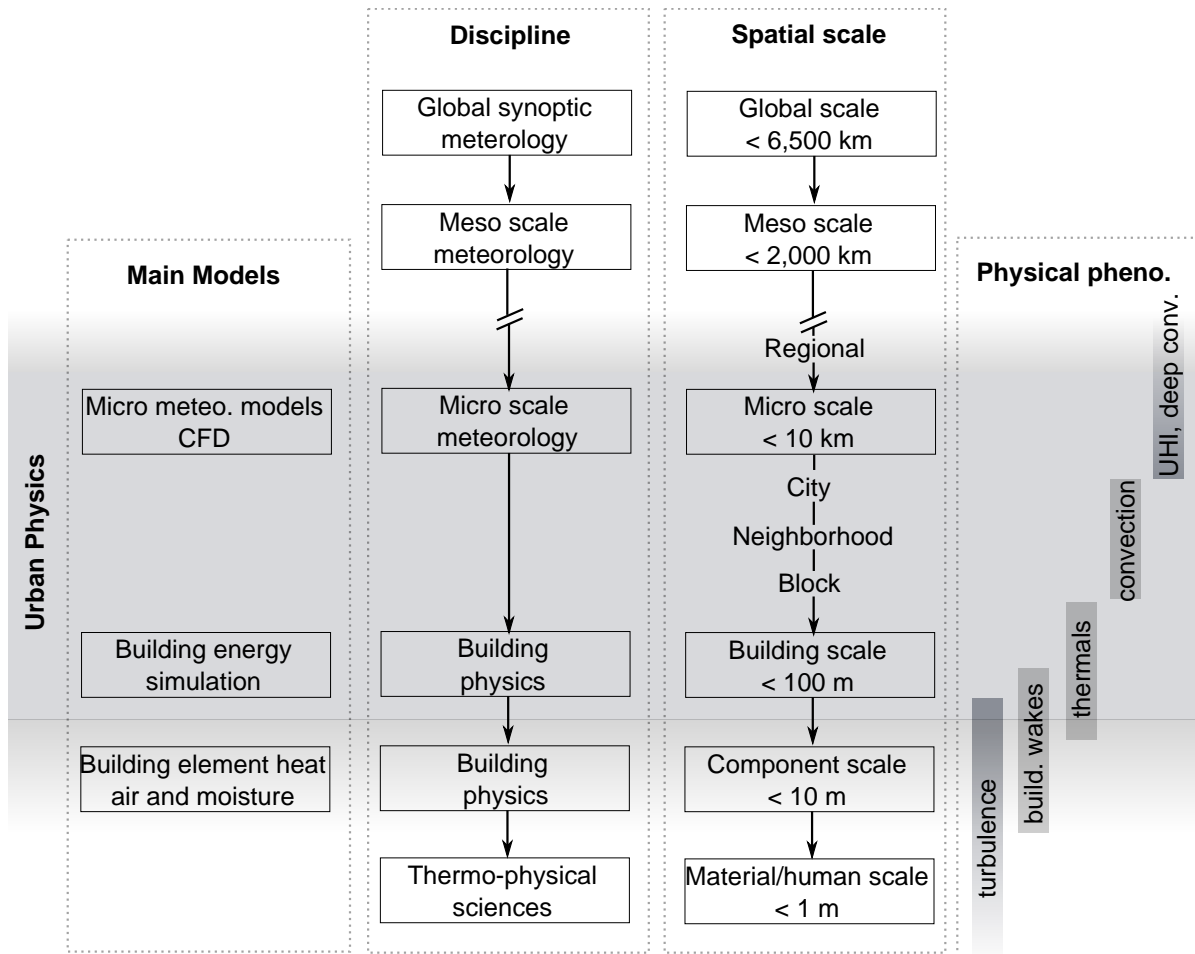


Figure 1.7: Correspondence and imbrication of the spatial scales, disciplines, physical phenomena and main models related to urban physics. (Based on (Blocken, 2013; Britter and Hanna, 2003) and (Schlünzen et al., 2011) cited in (Blocken, 2014a))

For completeness, another representation of the time and spatial scales that are related to urban physical phenomena is given in Appendix C. (Oke, 2006b).

- the neighborhood scale ( $< 10^3$  or  $2 \times 10^3$  m), in which a statistical approach can still be implemented but where the flow behavior inside the UCL becomes important, especially in its differences from one neighborhood to another;
- and the street canyon scale ( $< 10^2$  or  $2 \times 10^2$  m), which addresses the flow behavior and structures around buildings, in streets or intersections.

Physical phenomena developing on these scales are inter-related and interact with each other. As a consequence, the conditions in the upper and lower scales should be considered when investigating a physical phenomenon that is more specifically associated with one spatial scale. As determining boundary conditions, they both condition the processes under study.<sup>9</sup>

<sup>9</sup>These complex interactions justify the development of multi-scale models as explained in (Rasheed, 2009). In such approaches, the upper scale generally provides boundary conditions, while the lower one provides sources or sink terms (momentum, heat) and is parameterized.



This nesting of interacting scales is particularly important for urban meteorology and physics as shown in Fig. 1.1(a) and Fig. 1.1(b). In particular, the related aerodynamic processes are critical as ventilation and convective processes significantly impact on the UHI, the outdoor pedestrian comfort and the building thermal behavior. However, studying aerodynamic processes is challenging because, in addition to the complexity of the interactions between buildings, the surrounding air and the remainder of the atmosphere, turbulence remains an open problem while having significant consequences in terms of flow behavior and convective exchanges. Indeed, turbulence intensifies the mixing of the different variables such as particles, momentum and heat and it is highly dissipative. However, its behavior is irregular, apparently chaotic and random. It is generally associated with high levels of vorticity fluctuation (Lesieur, 1994; Robinson, 2011). The understanding of its mechanisms as well as its effects on the mean flow are therefore complex.

### 1.2.2 Existing techniques to study urban air flows

As described in Sec. 1.1.1, wind speeds in the UCL are significantly reduced on average as compared to rural areas and turbulence intensities are higher. This alteration of the averaged wind speed is due to the presence of numerous roughness elements in cities, especially buildings. They are almost stiff and sharp-edged solid masses, which are often positioned close to each other. Therefore, they create particular and local aerodynamic phenomena. On the contrary, meteorological stations are generally located in airports, which are large open spaces located in rural areas. As they undergo relatively undisturbed flows, traditional meteorological data are generally not relevant to describe air flows within and above the UCL.

According to Blocken and Carmeliet (2004); Bottema (1999) and as shown on Fig. 1.8, characterizing the aerodynamic conditions at a particular place within the UCL requires to modify twice usual meteorological data. The first modification is the change of  $U_{meteo}$  into  $U_0$ . This translates the alteration of the mean flow between the meteorological station and the surroundings of the location of interest. This modification is due to the general properties of the terrain (upstream fetch). This can be achieved by modifying the aerodynamic properties of the mean wind profile, especially  $z_0$ . The second modification aims to describe the effective air flows ( $U$ ) that occur within the location of interest. It is the one addressed in this thesis.  $U$  depends on the local 3D configuration and potentially thermal characteristics of the local urban design. As each configuration is unique, flow fields are very case-specific and almost no universal behavior applies despite some trends can be *a priori* expected.

In order to study urban air flows in terms of mean velocity and turbulence features, three techniques are mostly used in environmental wind engineering. From the most expensive to the most cost effective, they are (Blocken, 2014b; Moonen et al., 2012a):

- full-scale survey or field campaign;
- physical modeling or wind-tunnel testing;
- and numerical approaches, especially computational fluid dynamics (CFD) modeling.



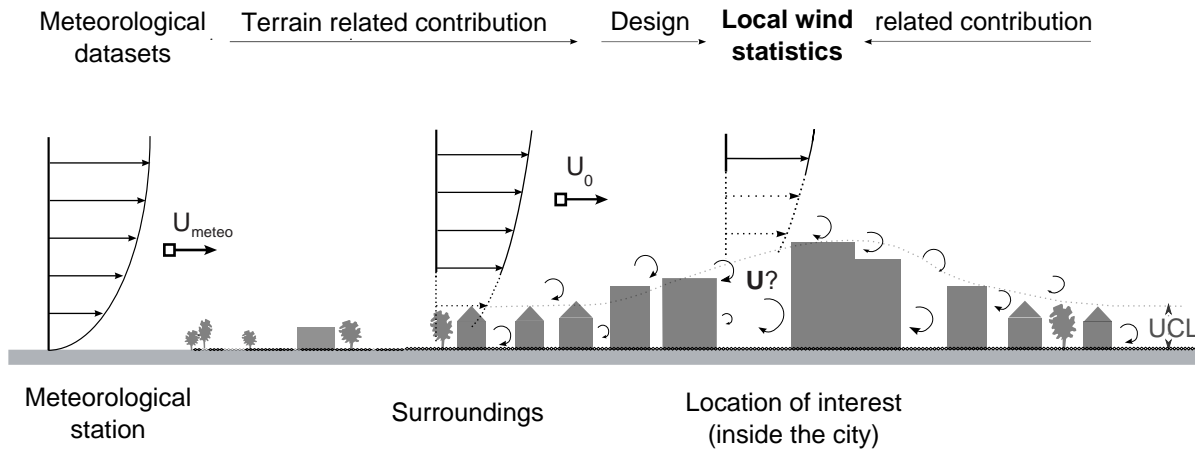


Figure 1.8: Adjustment of the mean wind profile from meteorological stations (open rural areas) to urban locations: terrain and design related contributions. (Based on (Blocken and Stathopoulos, 2013; Bottema, 1999))

Each of these techniques has specific advantages and limitations. Their respective advantages and drawbacks are summarized in Tab. 1.3.

Full-scale studies are generally carried out in real urban environments. This technique is the only one that integrates all the physical and geometrical complexity of the urban environment. It includes the details of urban design, material features, anthropogenic sources, temperature gradients, aerodynamic processes, all turbulence scales and so on. All of these factors influence the air flow field and its effects on pedestrian comfort, particle dispersion and buildings loads. However, such on-site surveys suffer from the inherent ill-definition and variability of the boundary conditions and the fact that only some discrete measurements can be taken. Moreover, unless taken over a very long period, these measurements are almost snapshots of the real conditions. As a consequence, data post-processing and interpretation can be difficult.

Reduced-scale tests are generally undertaken in atmospheric wind-tunnels. These experimental facilities are generally quite long as the approach flow modeling is very demanding (Blocken, 2014b). The targeted approach flow generally corresponds to an equilibrium ABL in terms of mean wind speed and turbulence profiles. For urban and building aerodynamic purposes, the range of the model scale is 1 : 75 to 1 : 400. In comparison with full-scale studies, boundary conditions can be controlled and measured, and tests can be run several times. Very high resolution measurements and some field data can be taken. Wind-tunnel tests are therefore suitable to provide extensive and high quality data. Moreover, experiments can be undertaken during the design process of architectural projects in order to evaluate the aerodynamic consequences of a new urban development and to support its design. Nevertheless, reducing the geometric scale of the model leads to some caveats. Some geometrical details are simplified because of manufacturing constraints and similarity criteria have to be matched in order to be representative of the real urban conditions. This implies that the dimensionless numbers characterizing the test should match the real ones, especially the Reynolds ( $Re$ ) and the Grashoff ( $Gr$ ) numbers. Since these numbers have very high values at full-scale, it is almost impossible to meet these requirements.

	Advantages	Drawbacks
Field study	<ul style="list-style-type: none"> <li>- Measure reality</li> <li>- Account for all the geometric complexity</li> <li>- Account for all the physical complexity</li> </ul>	<ul style="list-style-type: none"> <li>- Take discrete measures</li> <li>- Expensive and difficult to undertake</li> <li>- Undefined and unsteady boundary conditions</li> </ul>
Wind tunnel test	<ul style="list-style-type: none"> <li>- Can provide some field data</li> <li>- Control over boundary conditions</li> </ul>	<ul style="list-style-type: none"> <li>- Respect similarity criteria</li> <li>- Generally model isothermal conditions</li> </ul>
CFD modeling	<ul style="list-style-type: none"> <li>- Versatile</li> <li>- Provide whole field data</li> <li>- Relatively low cost</li> </ul>	<ul style="list-style-type: none"> <li>- Rely on turbulence models</li> <li>- Need to be validated</li> <li>- Need to be verified</li> </ul>

Table 1.3: Advantages and drawbacks of full-scale study, wind-tunnel testing and CFD modeling.

For this reason, wind-tunnel tests are generally based on the Reynolds number independence assumption and are generally carried out under isothermal and neutrally stratified conditions.

Due to the rapid development of computational capabilities, CFD simulations are increasingly used<sup>10</sup> (Blocken, 2014a). In such computational approaches, boundary conditions are controlled and models can be full-scale so that no similarity requirement has to be matched. Whole field data are computed and there is no theoretical limit for the dimensions and complexity of the urban model. Parametric studies can be carried out and simulations can be run during the design process of architectural projects. These features make numerical experiments very powerful and efficient for many urban applications. Nevertheless, computational models that could be used in environmental wind engineering are based on physical, mathematical and numerical assumptions as well as empirical constants (see Sec. 3.1.2). In addition, numerical predictions are very sensitive to the modeling strategy and the input parameters that are defined by the modeler. This can significantly compromise the accuracy of simulation. Therefore, models have to be carefully validated by comparison with experimental data sets in order to assess the model uncertainties, and verified to estimate errors.

The respective features of each investigation technique make them highly complementary. Numerical predictions can provide insights on the relevant measurement locations for a full-scale survey as well as whole field data where field studies only get discrete measurements. Numerical simulations can also supplement wind-tunnel studies when the Reynolds number independence cannot be achieved, and include heat transfers to evaluate buoyancy effects when thermal effects cannot be physically modeled. Experiments provide in turn essential data for the validation of numerical models, which is a necessary step to ensure the reliability of the computational study. Hence, since the development of computational approaches, both an experimental and a numerical approaches are often used to study urban flow characteristics, and especially the flow features in the UCL.

<sup>10</sup>As CFD studies are generally time consuming, simplified approaches suitable for urban environmental studies using zonal models have been developed (Bozonnet, 2006).

### 1.2.3 Overview of noteworthy urban flow patterns

Due to the complex shape of cities, urban very local aerodynamic conditions are highly complex. To better understand urban air flows, several wind-tunnel tests have been carried out over the last decades. More recently, CFD studies were also performed. Most of the results presented hereafter correspond to wind-tunnel experiments.

Fig. 1.9 shows that even only considering the simple configuration of an isolated cuboid obstacle standing perpendicular to the incident flow without any thermal effects, intricate recirculation phenomena already develop. The flow around the obstacle is characterized by separation at the obstacle edges and vortex shedding downstream (Peterka et al., 1985). More precisely, when the flow impinges on its frontal face, it is stopped and deviated. An over-pressure zone is created. In case of high-rise building, a significant part of the flow is deflected downwards, which induces high wind speeds at ground level. Upstream the building, a standing vortex develops and a horseshoe vortex is formed. The flow passing from this upwind region on the building sides is accelerated (corner streams). The remaining part of the incident flow is deviated upwards and goes above the roof, or laterally on the sides with an increased speed. Because of the non-aerodynamic shape of buildings, which have sharp edges, flow detaches at corners and reattaches (or not) on the top and side faces, which are under-pressure regions. Downstream the building, an under-pressure zone also takes place and a reversed flow (arch vortex) develops in the cavity zone. In an horizontal plane, two counter-rotative vortices are produced. All of these vortices and recirculation phenomena are transient and characterized by increased turbulence as part of the kinetic energy of the incident flow is transformed into turbulent kinetic energy. The wake carrying the residual turbulence persists a long time until the flow comes back to its initial state.

Increasing the geometric complexity of such an isolated obstacle by adding a recess in its plane yields new recirculation phenomena within the recesses and downwind. Considering such generic shapes, Fig. 1.10 compares the main flow structures around square, rectangle, U-shaped and L-shaped obstacles for an horizontal plane. It can be seen that low pressure zones downstream obstacles or within recesses lead to the formation of reversed flows and vortices. In case of normal wind incidence and cuboid obstacles, the extent of the cavity zone depends on the width and length of the obstacles. The larger the obstacle, the longer the cavity zone (case b), whereas the longer the obstacle, the shorter the cavity zone (case d). Flow fields become more complex when the shape of the obstacle shows protrusions, especially in case of asymmetric configurations (cases i-l). The development of recirculation phenomena in semi-enclosed courts (in the L-shaped and U-shaped obstacles) depends on their openness and their orientation in relation to the incident flow. This determines if courts experience over- or under-pressure, and thus the flow pattern that develops inside (cases e-l). The presence of protrusion also generally decreases the cavity zone length as compared to what happens downstream a rectangular obstacle. When obstacles lay oblique in relation to the mean flow direction, asymmetric and seemingly larger downstream recirculation phenomena in the spanwise direction occur. The obstacle relative dimensions, the presence of semi-enclosed spaces as well as the wind incidence angle appear thus to be critical in determining the flow structures around an isolated obstacle.

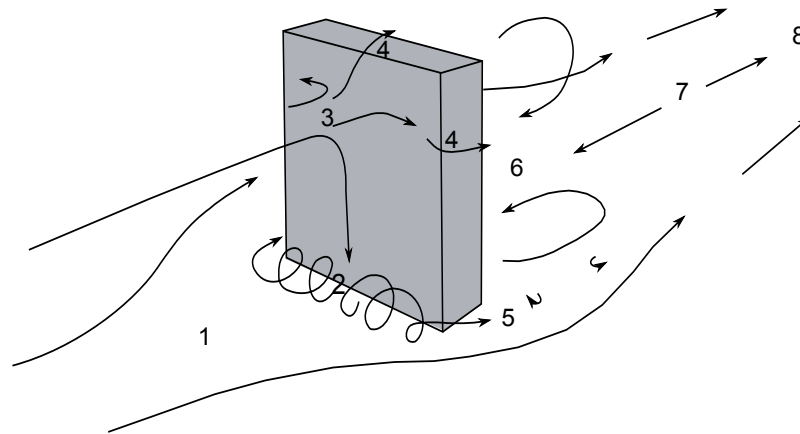
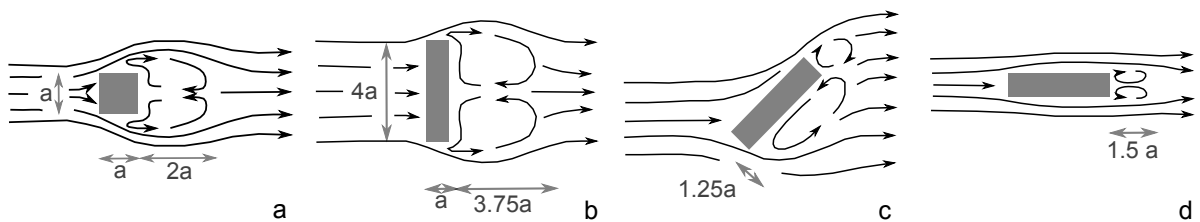


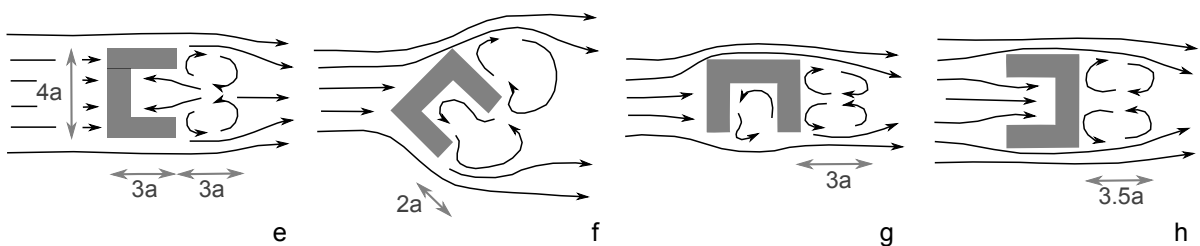
Figure 1.9: Flow structures around an isolated high cuboidal obstacle. (Adapted from (Beranek, 1984b))

- |   |                                      |
|---|--------------------------------------|
| 1: upstream stagnation region,              | 2: standing/horseshoe vortex,        |
| 3: stagnation point on the windward facade, | 4: flow separation at sharp corners, |
| 5: corner streams,                          | 6: cavity zone,                      |
| 7: downstream stagnation region,            | 8: far wake.                         |

Rectangular-shaped obstacles:



U-shaped obstacle:



L-shaped obstacle:

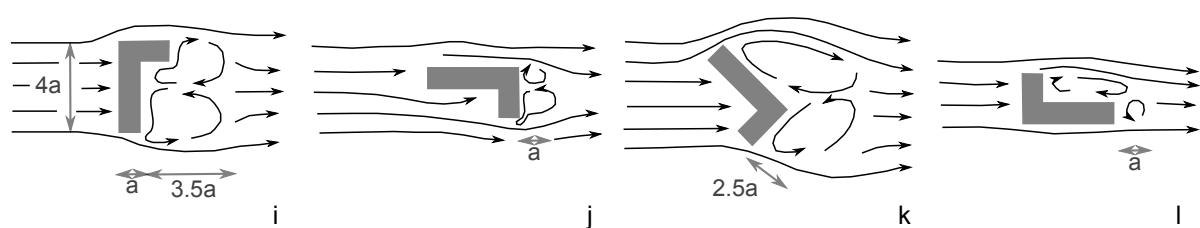


Figure 1.10: Flow patterns around obstacles of different shapes and for different wind incidences. (Based on (Brown and DeKay, 2000))

Considering an urban canyon,<sup>11</sup> both the upwind and the downwind obstacles can affect the inner flow structures. These inner flow structures differently interfere with the surrounding flows depending on the relative dimensions of the canyon and obstacles. This property is generally characterized by the aspect ratio or  $H/W$ ,  $H$  being the building height and  $W$  the canyon width. For a wind incidence normal in relation to the urban canyon axis, Fig. 1.11 illustrates the three flow regimes that can occur (Oke, 1987):

- the isolated roughness flow regime;
- the wake interference regime;
- and the skimming flow regime.

According to Oke (1987), the isolated roughness flow regime occurs when buildings are widely spaced, i.e. when  $H/W < 0.4$  for cubic buildings and  $H/W < 0.3$  for rows. In such a configuration, the shear layer has room to reattach downwind the former obstacle and before being disturbed by the following one. When obstacles are closer, i.e. for  $H/W < 0.7$  for cubes and  $H/W < 0.65$  for rows, the flow in the canyon substantially increases in complexity as the recirculation phenomena that are produced by each obstacle interfere with each other. This is the wake interference regime. When buildings are even closer, the skimming flow regime develops. A vortex is formed in the cavity, which corresponds to the lee eddy found in the cavity zone of isolated buildings. This recirculation is driven by the above flow and is reinforced by the presence of the downwind obstacle, which deflects the flow downwards. These three flow regimes condition the exchanges between the UCL and the air aloft and are related to the urban canopy roughness (see Fig. 1.12 and Appendix B). As a result, they are critical in determining the general ventilation potential and aerodynamic properties of urban areas.

When focusing on urban canyons, the most documented and simplest urban model is the urban street canyon. This almost 2D form represents a configuration where the lengths of the bordering buildings are much higher than the height and width of the canyon. Accordingly with the different aforementioned urban flow regimes, for sufficiently high wind speeds above the street and  $H/W \approx 1$ , a recirculation develops in the canyon. It is driven by the momentum transport from the above shear layer. The vortex is asymmetric and unsteady, as it is more concentrated on the downwind side of the canyon. In comparison with the top wind speed, recirculation velocities are of order  $1/3$  to  $1/2$  and turbulence levels are of about  $1/10$ . For low  $H/W$ , the shear flow can reattach on the floor in the canyon. For high  $H/W$ , a second counter rotating vortex can develop below the main recirculation (Britter and Hanna, 2003).

Nevertheless, it is worth mentioning that considering regular street canyons, three models that exhibit different flow characteristics are usually studied (Kastner-Klein et al., 2004). Appendix D.1 gives their respective schemes. The isolated street canyon composed of two juxtaposed rows is the most basic model but is subjected to an undisturbed upstream fetch. As a consequence, it is not representative of realistic urban conditions. In addition, the inner flow structures are greatly

---

<sup>11</sup>A canyon is defined as an urban unit that encompasses the wall and ground between two adjacent buildings so that it has three sides with active surfaces and three open sides (Oke, 1987). As an urban canyon, it is generally considered as a part of a network, often a regular array of identical long rows or cubes.

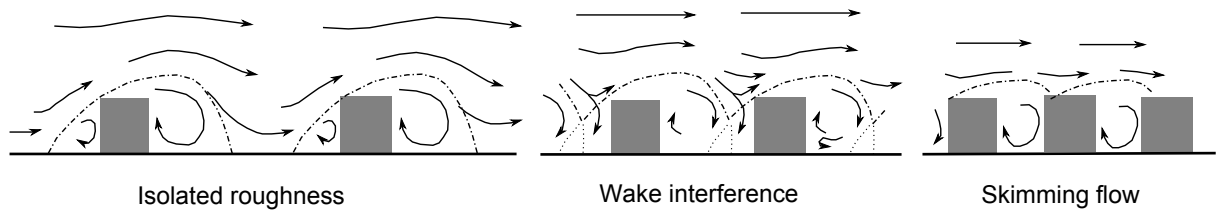


Figure 1.11: Flow regimes in an urban context depending on canyon aspect ratio ( $H/W$ ). (Adapted from (Oke, 1987))

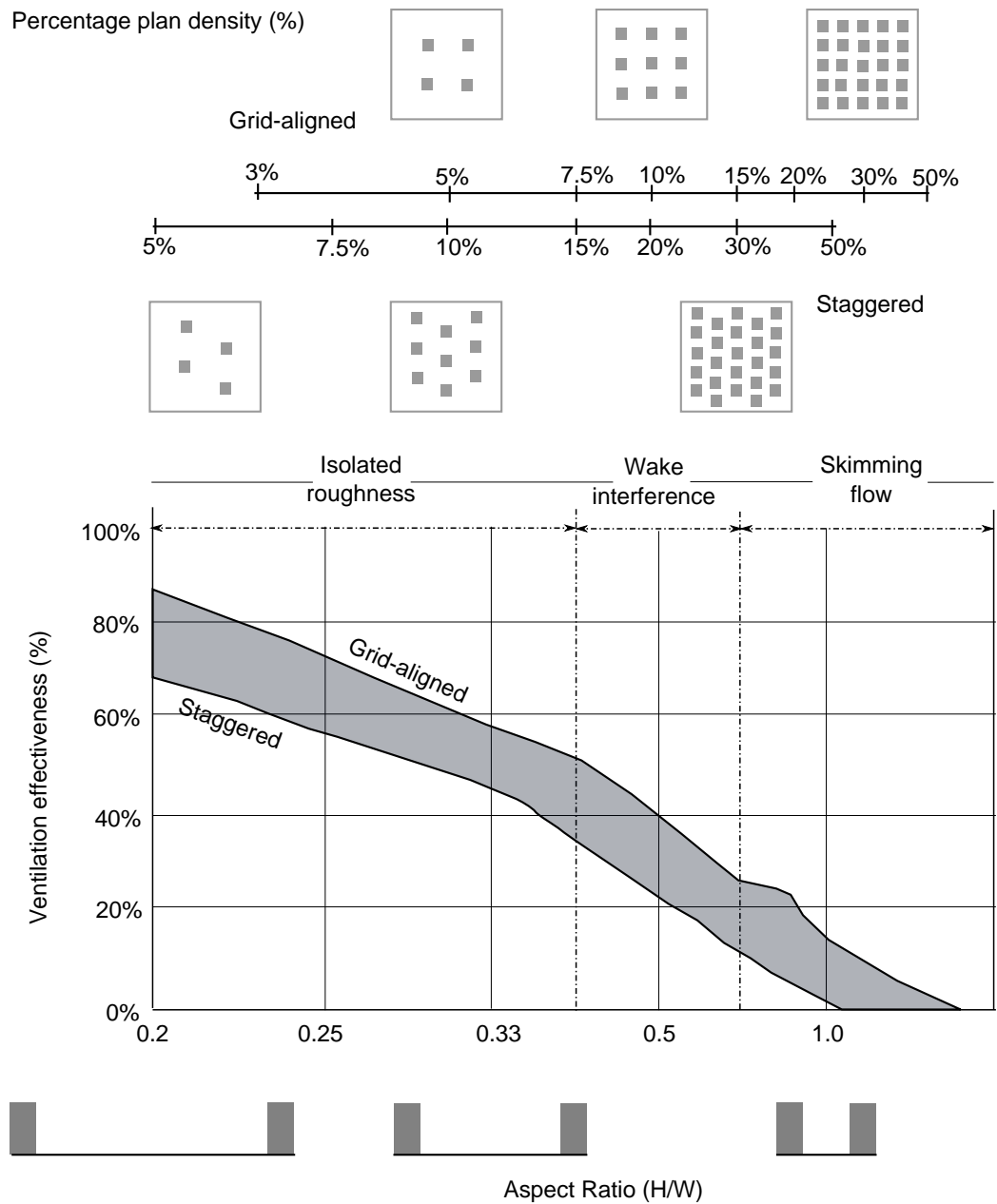


Figure 1.12: Occurrence of urban flow regimes in an urban-like context as well as ventilation effectiveness depending on the plan density. (Adapted from (Brown and DeKay, 2000))

determined by the flow separation at the upwind edge of the upstream building. Modeling a cavity, i.e. a hollow area within a flat plate, avoids the development of the flow separation at the upstream edge of the first row. Nevertheless, it does not integrate the effects of the urban fetch. Considering rows of streets canyons may overcome this limitation. In the first rows, flow features are still substantially affected by the flow separation at the upstream edge of the leading obstacle. Then, the flow becomes self similar, as the above flow has adapted to the underlying structure.

Hence, examining solely very simple 2D and regular configurations with several obstacles rather than an isolated obstacle highlights more complex flow fields. This is mainly because of two reasons. First, upstream obstacles modify the incident flow arriving in, or flowing over an urban open space. Secondly, nearby obstacles alter the flow patterns in the UCL, especially in their wakes. The resulting aerodynamic conditions are complex and affect the flow-induced forces on constructions, including the drag force. Hence, these interference effects depend on the upstream terrain properties, and the geometry and arrangement of the obstacles (Khanduri et al., 1998).

To represent 3D urban-like configurations, arrays of identical cuboids immersed in a boundary layer are often considered. For regular arrays of cubical obstacles with  $H/W = 1$  and a normal wind incidence, two main flow patterns occur (Coceal et al., 2014):

- recirculation phenomena associated with low velocities develop between obstacles;
- and channeling flows, which are generally characterized by faster velocities, develop along streets parallel to the mean flow.

Nonetheless, flow patterns and likewise ventilation patterns of such arrays vary depending on their layout.

Still in case of a normal incident flow, Fig. 1.12 shows that the building and urban ventilation effectiveness of such urban-like configurations depends on the plan density (Ramponi and Blocken, 2012) and the alignment of the obstacles (Golany, 1996; Hu and Yoshie, 2013). As the horizontal blocking effect increases for higher densities and staggered arrays, the ventilation effectiveness decreases. Moreover, given a certain density, randomizing the obstacles height increases the “roughness efficiency” of the canopy. This effect can significantly affect the surface layer structure, possibly to the point of inertial sub-layer squeezing (Cheng and Castro, 2002).

Aerodynamic features of six other urban archetypes have been studied by Steemers et al. (1997). These archetypes are based on three original urban forms,<sup>12</sup> namely the pavilion or tower, the street and the court. These generic urban forms are given in Appendix D.2. Results of expended polystyrene bead dispersion tests show that street canyons (terraces) form direct and effective air paths when they are aligned with the wind incidence, but cross flows and turbulence can modify the ventilation effectiveness. Conversely, courts and enclosed areas, as well as streets (terraces) normal to the wind incidence are less disturbed by the incident flow. This behavior may be explained by the development of internal recirculation phenomena in such confined spaces.

---

<sup>12</sup>These forms were defined by the Martin Center for Architecture and Urban Studies: <http://www.martincentre.arct.cam.ac.uk/>



As a partial conclusion, switching from cases of isolated buildings to cases of building groups highlights the development of different flow patterns and aerodynamic phenomena within the UCL. Those are not only dependent on the morphological properties of each obstacle, whose shape can already lead to specific flow patterns, especially when courts are present. The buildings layout is decisive as well, as the resulting morphological properties of outdoor spaces create specific flow patterns and ventilation regimes. Furthermore, recirculation phenomena and wakes interfere in complex configuration yielding intricate flow patterns.

In addition to the building overall shapes and layouts, many other factors impact on urban flow patterns. Architectural details are one of them. In particular, pitched roofs on buildings bordering a street canyon can prevent the development of the street canyon vortex ([Kastner-Klein et al., 2004](#)). Thermal effects due to the heating of urban surfaces can also modify the theoretical flow structure in a street canyon and may lead to the development of an additional vortex in the lower part of the canyon ([Allegrini et al., 2013](#); [Kovar-Panskus et al., 2002](#)). Flow patterns obviously depend on the wind direction as well. Considering the simple case of a cube array and a wind incidence oblique ( $45^\circ$ ) in relation to the main direction of the array, recirculation phenomena behind each face of the cubes develop. These vortices are symmetric with respect to the diagonal line of the model ([Coceal et al., 2014](#)) and deviate from those observed in case of a wind incidence perpendicular to the buildings.

Furthermore, it is worth mentioning that the different flow structures described above are related to mean flow patterns. Instantaneous flow patterns significantly differ from the mean ones even considering steady state boundary conditions. Typically, in a symmetric configuration, the instantaneous flow is asymmetric. Still in the case of a symmetric cube array, wind vectors along the streets change continuously and unpredictably, especially around intersections ([Coceal et al., 2014](#)).

Hence, urban flows are very difficult to describe and understand in complex configurations even when the approach flow is well-defined. It is however possible to identify some typical urban configurations that are linked with specific aerodynamic conditions. Based on wind-tunnel studies of several urban configurations, [Gandemer \(1975\)](#) identified aerodynamic anomalies that affect the pedestrian comfort.<sup>13</sup> These anomalies characterize some flow patterns related to typical building or urban configurations, which generally lead to substantially accelerated flows or sheltered regions. In addition to the standing vortex, corner and wake effects described above for the isolated building configuration, Fig. 1.13 illustrates these different anomalies and the following list briefly reviews them.

- The passage effect occurs when there is an open hallway the bottom of a building. The flow is concentrated in the passage and forms a jet that produces an accelerated flow within and downstream the passage. Note that this effect was also studied in details by [Beranek \(1984a\)](#) and [Blocken et al. \(2004\)](#).

---

<sup>13</sup>Note that for an isolated high-rise building, discomfort mainly depends on its dimensions. Its height is the most determining factor, and its width is the less influential ([Beranek, 1984a](#)).



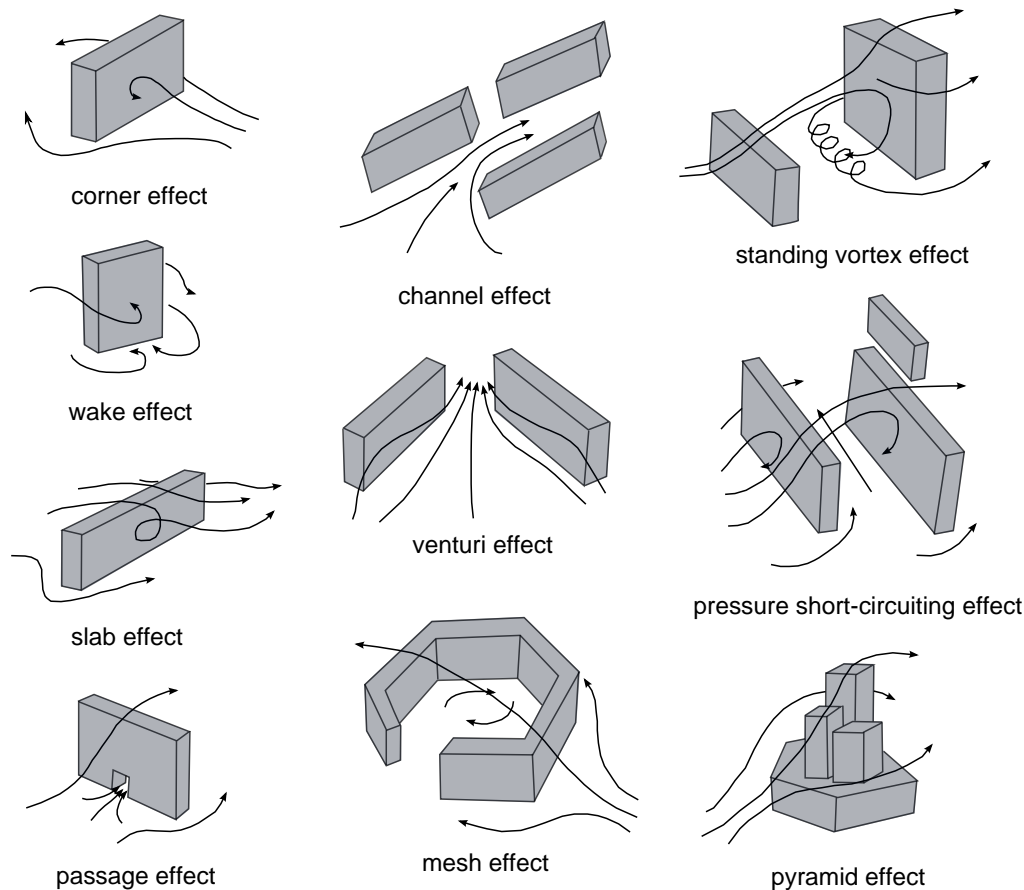


Figure 1.13: Urban air flow anomalies affecting the pedestrian wind comfort due to particular building and urban layouts. (Adapted from (Gandemer, 1975))

- The slab effect occurs depending on the relative obstacle size with respect to the wind turbulence scale. The worse wind conditions are produced when the slab is oriented at  $45^\circ$  in relation to the mean flow incidence. A swirled flow circulation is formed downstream the obstacle, which induces accelerated flow speeds.
- The channel effect occurs when the building layout forms an almost continuous path that is open on its top. This configuration can amplify the effects of another anomaly, but does not generally create specific aerodynamic conditions by itself.
- The so-called venturi effect occurs when the building layout is funnel-shaped, with an acute or right angle. Accelerated flows are mainly produced in the bottleneck. Several conditions should be satisfied to form such an anomaly.<sup>14</sup> Note that this effect is also discussed in Beranek (1984a) and Blocken et al. (2008). Indeed, wind-tunnel and CFD studies recently indicated that such an effect does not occur between convergent buildings. In such a configuration, the upstream over-pressure zone deflects a part of the flow upwards and on the sides of the group of buildings. Hence, the so-called venturi effect does likely not occur between buildings as open and not confined flows are involved.

---

<sup>14</sup>Conditions are a building height greater than 15 m, a total building length greater than  $10^2$  m, an unobstructed upstream and downstream zones and a bottleneck equal to 2 or 3 times the building height (Gandemer, 1975).

- The mesh effect occurs when a building layout forms an almost enclosed courtyard. It is generally characterized by inside sheltered conditions, as it could be either fled over or penetrated by the wind depending on its size. Note that [Beranek \(1984a\)](#) highlights some inner flow structures for almost square meshes opened on their corners.
- The pressure short-circuiting effect occurs when the layout of large buildings that are perpendicular to the wind is staggered. It is characterized by an accelerated flow that transversely links the two zones of different pressures. More generally, according to [Beranek \(1984a\)](#), when long buildings are parallel to each other and perpendicular to the flow incidence, strong transverse flow occur, which increases discomfort. Conversely, when buildings stand perpendicular to each other, discomfort rather corresponds to the superimposition of the basic conditions that develop around single buildings.
- The pyramid effect occurs in case of a compact building layout with several terraces. Although this shape is rather aerodynamic, terraces can experience accelerated wind speeds.
- The mask effect is due to the presence of the upstream buildings, which generally shelter urban spaces. In case of an homogeneous layout, the first  $2 \times 10^2$  m are the most impacted by aerodynamic changes.

Other studies carried out for existing urban configurations emphasize the complexity of the flow structures that develop in a real urban context. For example, the DAPPLE project ([DAPPLE, 2002-2010](#)) investigated the flow field at an intersection in London, United Kingdom, using the three techniques described in Sec. 1.2.2. Results highlight that 3D flows inside and around the intersection are strongly affected by the urban configuration as well as the wind incidence. Complex flows develop, especially upstream the intersection. The increased geometric complexity enhances the mixing due to the development and merging of different vortical flow structures and channeling flows from the different streets. In comparison with a typical idealized street canyon intersection, flows were significantly impacted on by the presence of two towers. Moreover, the asymmetric urban geometry enhanced the interactions between the UCL and the air flow aloft as compared to an idealized skimming flow regime ([Carpentieri and Robins, 2009](#); [Carpentieri et al., 2009](#)). Because of the heterogeneous urban structure, simulated exchange velocities are often higher than twice that of an homogeneous configuration characterized by the same plan density ([Panagiotou et al., 2013](#)). [Kastner-Klein et al. \(2004\)](#); [Kastner Klein et al. \(2000\)](#) extensively investigated the flow structures in a street canyon located in an inner-city area in Nantes, France. Wind-tunnel results showed that despite the presence of pitched roofs, a weak vortex developed in the street canyon. Two types of flow patterns were identified in the UCL. The first is characteristic of a street canyon flow with an almost zero or negative velocity. The other is characteristic of flows in open squares or street crossings, which shows higher mean and turbulent velocities. The flow field was found to be very heterogeneous in space and substantially affected by differences in building densities. The JU2003 project ([JU2003, 2003](#)) carried out full- and reduced-scales experiments for the central business district of Oklahoma city, USA. Results highlighted the critical impact of the particular structure of buildings and gaps between blocks on air flows. Strong vertical air flows were observed in the wake of tall buildings and in street canyons.

Moreover, flow patterns were found to be highly intermittent (in reality) and very sensitive to little changes in the wind incidence (Leitl and Schatzmann, 2005).

These few exemplar studies illustrate the diversity and the intricacy of the flow structures that can occur inside the UCL due to the heterogeneity and complexity of real urban configurations. Findings of such studies are hard to compare and synthesize to build general statements on the effective urban flow patterns that develop in the UCL, as they integrate too much complexity parameters, including the pressure-gradient wind features, the upstream terrain and characteristics, the local urban arrangement as well as building architectural details.<sup>15</sup> This is generally why generic urban configurations are considered in more fundamental studies. Thanks to the simplification of the urban configurations, some basic flow features as well as relations between morphological parameters and flow patterns can be extensively examined.

## 1.3 Problem formulation and outline of the thesis

### 1.3.1 Motivation and scope of the work

As demonstrated by Rogers (2000) and Salat (2011), the concept of urban sustainability and its environmental implications involve many different factors. They especially include economy, equity, mobility, well being, land use, environment and energy. All but the two last of these topics go beyond the scope of this thesis but are important to keep in mind because they have significant implications on cities' forms as well as on the way in which cities might be understood and analyzed.

Considering the rapid urbanization in developing countries and the substantial contribution of the building sector in the world final energy consumption, some fields of action are critical for any sustainable urban development plan. They especially include the protection of citizen's living conditions, the bio-climatic design of urban spaces as well as the improvement of the building energy efficiency and conservation. The integrated design of urban areas would not only reduce the direct energy consumption as it could also reduce the embedded energy of cities by providing some design guidelines and differentiate the needs of the different parts of a building or neighborhood. This could also contribute to save some motorized commutes if adapted cities, especially in terms of density, pleasant outdoor spaces as well as comfortable buildings are designed so that people would less often take their car to spend their free time out of the city (Maizia, 2010).

Sec. 1.1.2 shows that several interacting factors contribute to determine urban micro-climates and the building energy performance. As shown in Fig. 1.14, they include:

- the enlarged environment of the urban area, i.e. the regional climate, the surrounding geography and land use;

---

<sup>15</sup>Moreover, these studies generally focus on dispersion processes, and do not primarily examine the mean flow structures.

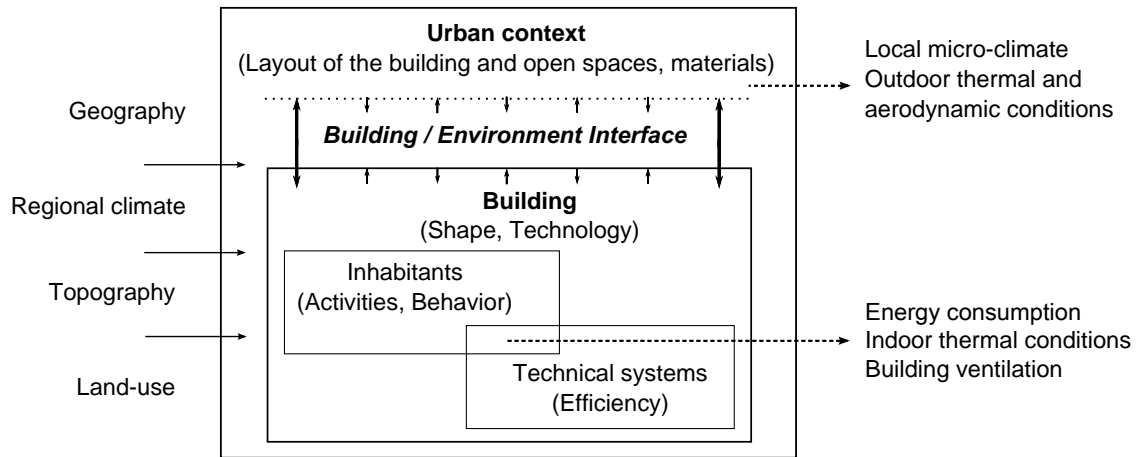


Figure 1.14: Inter-relations between the factors affecting urban micro-climates and the building energy consumption. (Based on (Ratti et al., 2005))

- the urban context, especially in terms of morphology and thermo-physical properties of materials;
- the building design, including its shape, technology and the characteristics of its envelope;
- the management and efficiency of technical systems;
- and the behavior and activities of inhabitants.

Sec. 1.1.3 reviews how the urban context determines the urban outdoor thermal and wind environment and to which extent it might affect the bio-climatic potential and energy demand of buildings. In comparison with an open rural configuration, built structures modify the energy balance of urban spaces and buildings in terms of radiative and convective fluxes. Radiative fluxes involve sun heating, shading, multi-reflections and exchanges between urban surfaces and the sky. Convective processes are related to the effects induced by air flows, including the natural ventilation potential, convective heat exchanges as well as infiltration for buildings. The UHI effect and the limited evaporative cooling also contribute to alter the urban thermal conditions. Hence, a better knowledge of the urban very local micro-climatic conditions would contribute to assess better the outdoor thermal and wind comforts and provide more relevant boundary conditions for usual building energy models. This can significantly improve the assessment of building energy loads, the implementation of passive and active strategies and support the design of comfortable and energy efficient urban areas.<sup>16</sup>

According to Givoni (1998), urban air flows constitute the most effective means to improve urban comfort and energy consumption with respect to the urban morphology, even if the radiative balance may have a greater impact on the thermal comfort and building energy loads (Allegrini

<sup>16</sup>More generally than CFD studies of urban air flows, urban micro-climate and their effects on building energy behaviors can be studied using numerical simulations as well. Such approaches enable a wide diversity of phenomena to be investigated in an analytic, coupled or systemic way. The corresponding numerical models differ by the considered scale, physical phenomena and complexity. Several of such computational methods, linked with sustainable urban development issues are reviewed in Robinson (2011). For urban physics, usual numerical approaches use thermo-radiative, CFD, micro-climatic and building energy simulations, or couplings of them.

et al., 2012b; Bouyer, 2009; Huang, 2010). Allegrini et al. (2015) also stressed the importance of urban air flows in determining the urban micro-climates when dealing with urban morphology. However, as highlighted in Sec. 1.2.3, air flows in cities are very complex. Hence, this thesis addresses the direct effects of the interactions between the urban structures and the physical processes that occur within the UCL. This thesis studies more particularly the effects of the urban local design on the aerodynamic processes that develop in the building close environment in case of forced convection. The implications of these aerodynamic processes on the building energy balance are examined in return in terms of infiltration flows and convective heat exchanges. As a consequence, the street canyon or building scale is considered, which practically corresponds to the urban block scale too (see Sec. 2.1.1).

The relations between urban forms and physical processes in the UCL were discussed about 15 years ago. The corresponding studies were mainly based on empirical and experimental considerations as well as some early numerical simulations. Especially, Steemers et al. (1997) studied the relationship between typical urban forms and their environmental characteristics (see Sec. 1.2.3), including the solar access and air flows to estimate their implications in terms of energy use. Givoni (1998) discussed the relationships between the features of the urban and building design with respect to climatic purposes, and especially how urban features can improve the thermal comfort in different climates. Brown and DeKay (2000) focused on energy with an architectural point of view and investigated the effects of urban forms on physical processes. These last works resulted in the creation of tools and guidelines for several steps of the architectural design process, mainly toward a better management and use the solar and ventilation potentials in buildings and neighborhoods.

Nowadays, such issues are reconsidered mainly using detailed computational approaches. For example, using generic arrays of buildings, Huang (2010) developed a methodology to better design urban districts from a morphological and climatic points of view, in order to enhance the building energy efficiency. Athamena (2012) studied the effects of the design of some French eco-neighborhoods that are characterized by their specific cross forms, on outdoor thermal comfort. Allegrini et al. (2015) studied the influence of urban morphology on the micro-climate on the neighborhood scale. Less focused on urban morphology issues but rather on the effects of the very local urban micro-climate, Allegrini et al. (2012b); Bouyer et al. (2011); Bozonnet (2006) addressed the influence of the urban environment on the building energy demand (Sec. 1.1.3). Note that in addition to the impact of the built environment, most of these studies highlighted the significant contribution of greenery on thermal comfort and building energy loads.

These latter studies demonstrate the increasing awareness of the scientific community about the need to work on integrated and micro-climatic approaches of urban forms to answer the current environmental and energy challenges. However, to the best of our knowledge, contemporary studies still mainly focus on the outdoor climate or the radiative effects on the thermal comfort or building energy demand. They also mainly consider some specific case studies or arrays of cuboids. When focusing on urban aerodynamics, ventilation and dispersion processes as well as wind comfort are often addressed. Real urban configurations, street canyons or cube

arrays are generally considered. No generic and systematic study based on the examination of worldwide urban fabrics was fulfilled to investigate the relations between urban forms and aerodynamic / convective processes, in order to examine the effects of these processes on the building energy balance in terms of infiltration and convective heat transfers.

### 1.3.2 Problem formulation and expected outcomes

The aim of this thesis is to bring new knowledge concerning the effects of urban morphology on the aerodynamic and convective mechanisms that develop within cities in case of forced convection. More precisely, this thesis aims at providing answers to the two following questions:

*What are the flow patterns that develop close to buildings according to the local urban morphology?*

*How do these specific flow structures affect the building energy loads due to infiltration air flows and convective heat fluxes?*

From an urban planning perspective, the main aim is to study the influence of urban morphology on aerodynamic conditions in the building close environment in order to promote a more integrated design of urban neighborhoods and buildings. From an urban physics point of view, the aim is to analyze the aerodynamic processes that develop in the building close environment and study their impact on the building air infiltration and thermal stresses. As this is an exploratory study, these questions are conjoint with some underlying methodological issues, especially the choice of the case studies and tools. These fundamental choices determine the scope of applicability of the findings.

The expected outcomes of the thesis are theoretic as well as applied. From an academic research perspective, they will contribute to a better understanding of the complex physical mechanisms that develop within the UCL. From an operational standpoint the aim is to identify some basic flow structures that develop next to buildings according to the local urban morphology and their potential effects on the building energy demand. This thesis will also provide information relative to the wind conditions in outdoor urban spaces, which significantly impact on the pedestrian comfort, and discuss the usual boundary conditions that are used in building energy models in terms of mean pressure distribution and convective heat transfer on the building envelope.

### 1.3.3 Methodology

To tackle the scientific and operational objectives outlined above, this thesis develops a transverse methodology that combines an architectural and a physical approach. As shown in Fig. 1.16, the methodology is composed of three main parts, which are supported by a literature review and concluded by a synthetic discussion of the work. The sequencing of the three main parts almost corresponds to the outline of the manuscript.

Preliminarily, the general background of the methodology, which consists of a literature review, lays the foundations of the work. Two disciplinary fields are involved: urban morphology

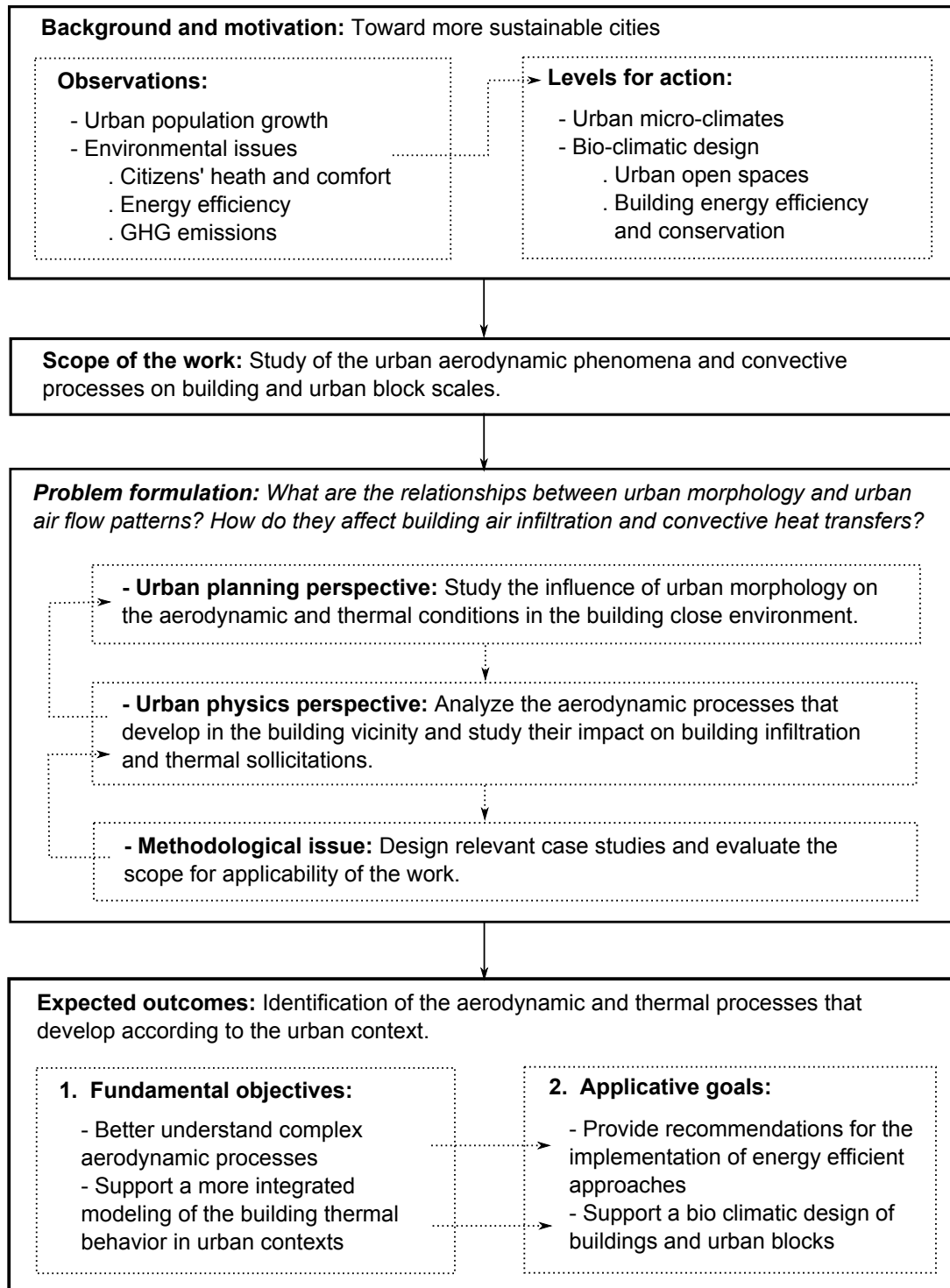


Figure 1.15: Motivation, problem and the expected outcomes of the thesis.

analysis and urban physics. Their main subjects of study, specific practices and investigation tools are especially examined. This literature survey extends all along the work to support the implementation of the different methodological steps.

In the first step, a morphological analysis of existing urban fabrics is combined with a bioclimatic and physical approach of cities. The crossing of these approaches highlights the morphological features that particularly affect urban aerodynamic processes and provides the required elements to outline the physical scope of the study. On this basis, two generic typologies of urban structures are designed: an isolated building and an urban block typologies.

The second step is the aerodynamic study. Numerical experiments are undertaken using CFD. The model is validated by comparison with detailed experimental data sets and numerical predictions. This preliminary and necessary phase is critical to define the modeling strategy and settings to be used. It also stresses the related methodological challenges. Then, CFD simulations are performed for the different types. The analysis of the predicted flow fields highlights the physical processes and phenomena that develop around the generic constructions according to the morphological configuration. This provides information on the outdoor mean aerodynamic conditions, which can be related to the outdoor urban comfort, as well as the pressure distribution on the building facades, which would further inform on building infiltration processes.

In the third step, the effects of urban morphology on the building energy loads are examined. Convective heat transfers are firstly integrated to the aerodynamic model using the internal coupling available in the CFD software. Again, the model is validated by comparison with reference experimental data and detailed numerical studies. Cases of predominant forced convection are investigated. Convective heat transfer coefficients on the different building outer walls are analyzed, and their links with the corresponding flow structures are investigated. Focusing on building energy efficiency problems, the energy demand of typical buildings due to air infiltration and heat transmission through the envelope is examined. The improvement brought by the use of more accurate boundary conditions compared to usual engineering practices is evaluated.

To conclude the work, the methodological and physical results are synthesized. The study's scope of applicability and scientific contribution, as well as its strengths, possible improvements and perspectives are discussed.

## 1.4 Summary

Urban micro-climates are determined by complex interactions between the prevailing weather conditions, the urban structure and human activities. Their effects on the UHI, the outdoor thermal comfort and building energy loads are substantial. Because of the complexity of recirculation and turbulence phenomena as well as urban forms, urban air flows are difficult to assess and understand, while being essential for many applications. Hence, this thesis addresses the effects of the urban local design on the flow structures that develop within the UCL and their effects on building air infiltrations as well as convective heat transfers. A transverse approach linking urban morphology analysis and urban physics concepts and tools is therefore developed.



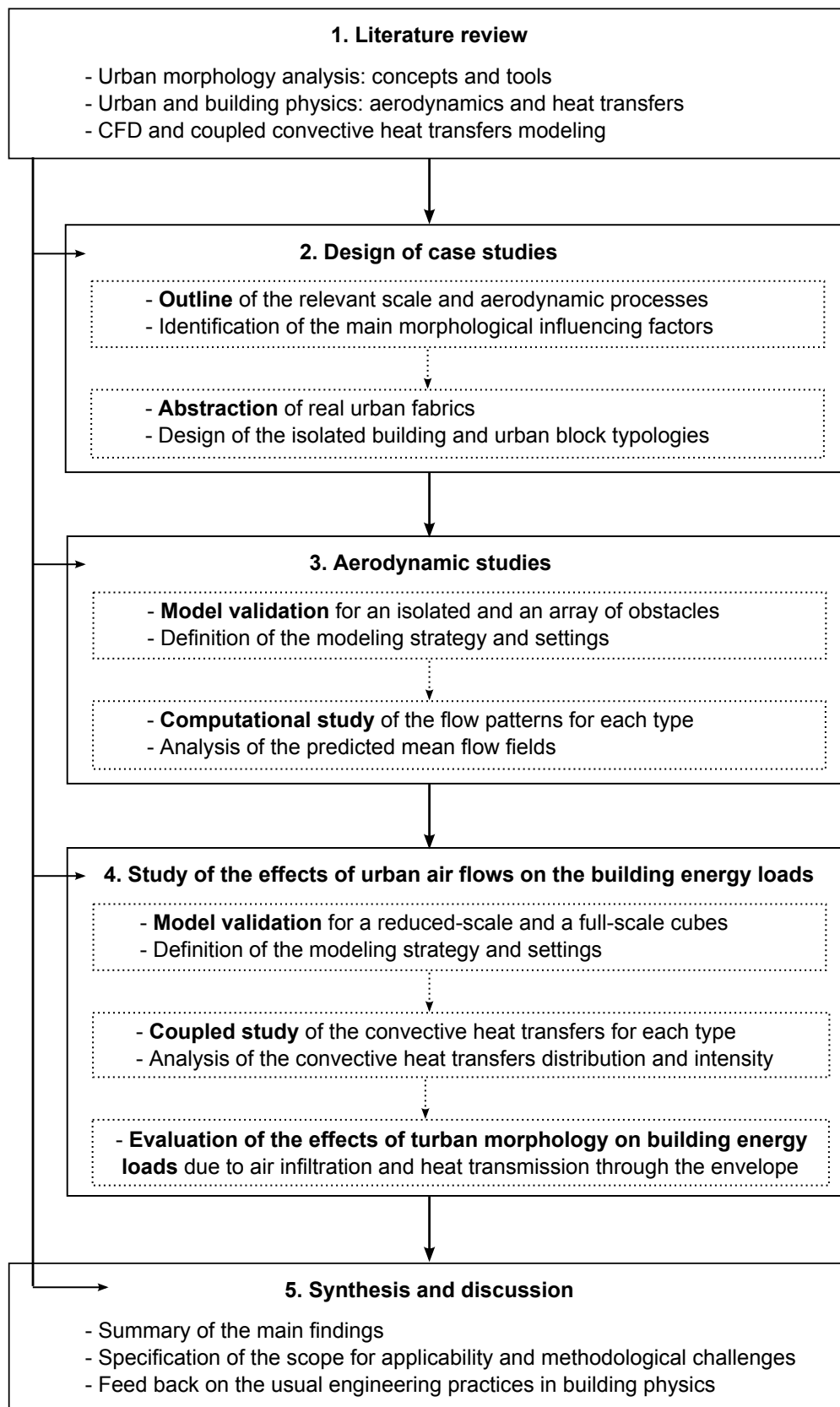


Figure 1.16: Summary of the five steps methodology developed by the thesis.

## Chapter 2

# Design of generic typologies of urban structures for small scale aerodynamic (and bio-climatic) studies

This chapter develops the transverse approach used to design the case studies addressed in this thesis. It introduces concepts and tools from the urban morphology and architectural analysis, and combines them with a bio-climatic and physical points of view. In particular, morphological parameters affecting urban air flows and heat fluxes are reviewed, and a morphological analysis and abstraction of existing urban fabrics are performed. This provides the materials for the design of two generic typologies of urban structures: one of isolated buildings and one of urban blocks.

### Contents

<b>2.1 Urban morphologies: characterization and models . . . . .</b>	<b>42</b>
2.1.1 Description and analysis of urban morphologies . . . . .	42
2.1.2 Bioclimatic approaches of urban forms . . . . .	45
<b>2.2 Urban morpho-metric indicators (UMMIs) addressing thermo-aeraulic exchanges</b>	<b>49</b>
2.2.1 UMMIs addressing the openness of city toward the sun, sky and atmosphere .	50
2.2.2 UMMIs mainly addressing aerodynamic processes . . . . .	51
2.2.3 UMMIs addressing the ability of a building to interact with its outdoors . . . .	53
<b>2.3 Synthesis of the morphological factors affecting urban air and heat fluxes . . . .</b>	<b>53</b>
2.3.1 Main morphological factors affecting urban air flows . . . . .	53
2.3.2 Main morphological factors affecting urban and building heat transfers . . . .	55
<b>2.4 Design of urban form typologies . . . . .</b>	<b>57</b>
2.4.1 Design methodology . . . . .	57
2.4.2 Proposed typologies of isolated buildings and urban blocks . . . . .	60
2.4.2.1 Proposed typology of isolated buildings . . . . .	60
2.4.2.2 Proposed typology of urban blocks . . . . .	61
2.4.3 Discussion of the typologies . . . . .	63
<b>2.5 Summary . . . . .</b>	<b>63</b>

## 2.1 Urban morphologies: characterization and models

### 2.1.1 Description and analysis of urban morphologies

The term *urban morphology* can address the social structure of the population, the urban landscape, the street network of the city, the plots division of lands, or the urban composition in terms of solid masses and empty spaces from an environmental point of view (Lévy, 2005). In this thesis, following the definition given by Steemers et al. (2004), urban morphology is understood as the 3D form of a group of buildings and the space they create,<sup>1</sup> i.e. in its tangible and physical dimensions. Thus, it corresponds to a description of the city as an interactive system of buildings, streets and open spaces. The urban form is thus considered at a specific moment, *as a static and material configuration composed of a relative arrangement of solid masses and unbuilt volumes*.

Between the micro-scale and the building-scale as defined in Sec. 1.2.1, five structural urban spatial scales can be distinguished for urban analysis purposes (Salat, 2011). They are:

- the city scale, whose size is highly variable, depending on the local administrative definition;
- the district scale, whose typical size is 800 m × 800 m in Europe and twice this size in North America (its perimeter depends on historical or urban criteria);
- the neighborhood scale, whose typical size is determined by the urban fabric. It is 200 m × 200 m in Europe and 400 m × 400 m in North America;
- the block scale, whose boundaries are defined by streets. Its typical size is roughly 100 m × 100 m, but is very dependent on the local architecture, size and contiguity of buildings;
- and the building scale, whose size is variable, depending on the building type and its relations with the nearby buildings.

These spatial scales are comparable with the city, neighborhood and street canyon scales defined in Sec. 1.2, but exhibit two additional intermediate scales: the district and the block scales. Fig. 2.1 summarizes these urban spatial scales, their main properties and the morphological features that can be analyzed at each scale.

According to Salat (2011), on the one hand, connectivity and structural aspects are more related to the city and the district scales, which correspond to the macroscopic level (Adolphe, 2001a). At the comprehensive scale of the city, general features can be assessed and compared with other cities. Note that for analysis purposes, administrative boundaries are often meaningless. Connectivity and distribution, especially of the road network, may mainly be studied. At the district scale, the diversity and heterogeneity in distributions as well as the structure, complexity and connectivity of the street network can be studied inside the district boundaries or compared with others. On the other hand, morphological aspects as understood in this thesis are more related to the neighborhood, block and building scales, which correspond to the microscopic

---

<sup>1</sup>Originally: “La forme tridimensionnelle d’un groupe de bâtiments ainsi que les espaces qu’ils créent.”

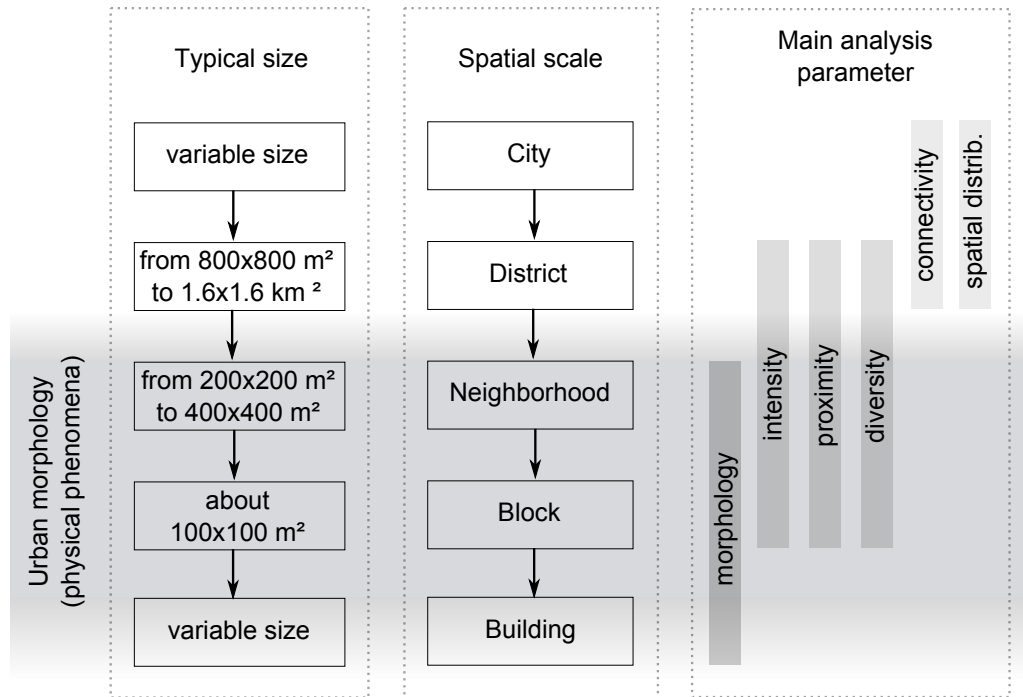


Figure 2.1: Characterization of the main urban spatial scales in urban morphology analysis. (Based on (Salat, 2011))

level (Adolphe, 2001a). At the neighborhood scale, the links between morphological parameters and physical processes that develop within the UCL can be studied as well as segregation and proximity matters. At the block and building scales, diversity and morphology parameters are of particular relevance. Elementary energy needs or thermal behaviors can be assessed. For homogeneous urban fabrics, these results can be extended or aggregated to upper scales. Note that the block and building scales coincide sometimes, as the building can sometimes be itself defined as a block (e.g. for towers), included in a block, or be an indivisible part of a continuous block (e.g. in the Hausmannian Paris).

As can be seen in Firley and Stahl (2010) and Salat (2011) among others, a wide diversity of urban fabrics exist all over the world, depending on the local geographic, climatic and cultural contexts. It is particularly the case for traditional urban fabrics. To characterize them, housing types or urban types are often used. Housing types generally account for the morphological features of dwellings and distinguish single- or multi-family types. For example, Firley and Stahl (2010) differentiate courtyard houses and row houses as single family housing types, and compounds and apartments buildings as multi-family housing types. Givoni (1998) distinguishes single family detached houses, town (row) houses, multi-storey apartments buildings with long corridors or stair cases, as well as high rise tower buildings. Urban types distinguish urban patterns, that often correspond to different periods of edification. In addition to street features, the structure of urban blocks differs. For example, Panerai et al. (2006) identifies five types of Western European urban blocks in order to represent and discuss the consequences of their evolution from the traditional to the modern patterns. These urban block types go from the Hausmannian block to the Housing Unit of Le Corbusier, via the Megablocks in Amsterdam. Extending this historical

approach, [Athamena \(2012\)](#) distinguishes four urban types according to their morphological and historical features. They are:

- compact blocks, which include the traditional and the Hausmannian blocks;
- pavilion housing estates, which include city gardens and park subdivisions;
- vertical and repetitive blocks, e.g. Housing Units of Le Corbusier and large housing estates;
- and open blocks, such as the ones created by de Portzamparc.

These housing and urban types are meaningful as they directly refer to specific building or urban patterns. They are generally related to the compactness of urban forms and refer to the relation that exists between buildings and outdoor spaces. These can be totally external, attached, semi-enclosed or totally included and enclosed inside buildings or urban blocks. However, these types are almost qualitative even if each one has some similar morphological features, and their definition criteria are not systematic.

A more quantitative characterization of urban forms uses indicators, such as the urban density or building coverage ratio, or the floor area ratio. An extensive list of such indicators for urban block and street metrics is given in [Hermosilla et al. \(2014\)](#). If used together with building or urban types, these indicators can qualify an urban pattern in an almost comprehensive way. However, they do not enable the setting up of a systematic and comprehensive classification of urban fabrics based on rather objective criteria.

Hence, in order to initiate the establishment of a taxonomy of urban forms, the Urban morphology laboratory of the CSTB and [Burdet \(2011\)](#) proposed a set of criteria to describe and classify urban patterns in a general and objective manner. The analysis and characterization of limits are essential in this urban morphology description process. Three categories of morphological parameters are addressed.

- Topology describes discontinuities in the urban texture, especially the presence or absence of courts. Connectedness and void openness as well as the relative positioning of buildings and type of spatial arrangements belong to this class of descriptors.
- Geometry characterizes the conformation of urban elements, i.e. the urban fabric shape, and deals with orthogonality, straightness, convexity and direction parameters.
- Finally, dimensionality is mostly related to the fractal depth of urban components and involves scales, measurements and ratios.

These classes of morphological parameters are particularly relevant when used at the neighborhood scale or smaller scales. They are mainly related to each other following a hierarchical order given that a dimensional analysis can mainly be applied on a given geometric configuration, which can itself mostly be applied on a given topological configuration ([Burdet, 2011](#)). Note that these morphological attributes were also considered by [Groleau and Marenne \(1995\)](#) to analyze and differentiate urban forms and structures in order to classify them as well.

### 2.1.2 Bioclimatic approaches of urban forms

As understood in bio-climatology for living beings, a bio-climatic approach of building and urban areas refers to the study of heat and mass exchanges between buildings and their environment (Larousse, 2014). The usual extension of this concept characterizes the ability of a building or an urban area to optimize its use of solar energy and natural ventilation in order to provide comfortable indoor or outdoor conditions. From a morphological perspective, and adapting the definition given by Lévy (2005), approaching an urban form as a bio-climatic form means considering it in its environmental dimension as an urban micro-climate, both in terms of its geographical variation by neighborhood and in its diversity linked to urban fabric patterns (opened / closed / semi-open), with regard to the site (water, topography, greenery) as well as its orientation towards the sun and the winds.<sup>2</sup>

Sec. 1.1.2 describes the different ways in which urban structures affect air flows and thermal transfers. The physical processes involved are the solar heating of urban surfaces and the other radiative exchanges between urban surfaces and the sky, air exchanges throughout the upper limit of the urban canopy layer, as well as the radiative and convective exchanges that occur in the UCL between buildings, streets and other outdoor spaces. To relate the effects of a particular urban structure and its morphological features with these physical processes, three main approaches are usually implemented in literature. They consist of:

- characterizing existing urban configurations, which may mainly be done from the block to the district scale;
- studying generic urban types that have previously been defined, which may mainly be done from the block to the neighborhood scale as well;
- and defining categories of typical urban configurations with respect to their expected micro-climatic, thermal or aerodynamic effects. This may be done at the district scale to consider averaged effects, or on the urban block or building scales to focus on specific physical phenomena.

The former method often attempts to relate urban layouts to a bio-climatic potential (Adolphe, 2001b) or an energy consumption level (Ratti et al., 2005; Salat, 2011; Steemers et al., 1997). Quantitative morpho-metric indicators (see Sec. 2.2) are often used. These indicators inform on the potential bio-climatic behavior of a given urban area, e.g. on the effects of urban forms on the received solar energy or the modification of winds in an open space. Used as parameters into simplified equations, these indicators can also inform on an energy consumption level for heating. Such an approach does not consider the physics in detail but rather some simplified relations in order to provide material for comparisons (Steemers et al., 2004).

---

<sup>2</sup>Originally: “dans sa dimension environnementale, comme micro-climat (urbain), tant dans ses variations géographiques par quartier, que dans sa diversité liée aux types de tissus (ouvert / fermé / semi-ouvert), selon l’orientation (héliothermique), selon le site (eau, relief, végétation). (Lévy, 2005)

Another approach based on the analysis of existing urban configurations consists in characterizing climatopes in order to provide design guidelines for the urban development. According to [Scherer et al. \(1999\)](#), climatopes can be defined as “areas of characteristic combinations of climatic factors and of similar relative significance for their surroundings, operating on a spatial scale of several tenths to hundreds of meters”. In this approach, each area is characterized by an areal type, which characterizes the land-use structure (e.g. dense urban housing), and a ventilation class (e.g. terrain-induced ventilation path or reduced ventilation). Ventilation classes refer to characteristic combinations of climatic factors controlling local and regional aerodynamic processes that result in typical ventilation patterns. This climatope approach was especially applied on the area of Basel, Switzerland. Following a similar approach, [Acero et al. \(2013\)](#) mapped the city of Bilbao, Spain. Using spatial information, climate measurements and knowing the specific urban climate, the thermal loads and dynamic potential of different urban zones were assessed. Thermal loads refer to the stored heat intensity, surface fraction and the presence of vegetation. The dynamic potential accounts for the air ventilation and exchange capacity and is based on ventilation paths and slopes.

Unlike the analysis of existing urban areas and thanks to their relative simplicity, the study of archetypes enables straightforward comparisons, detailed investigations of the different physical phenomena and parametric studies to be made. As a consequence, fundamental mechanisms can be highlighted and useful basis for further more complex studies can be provided. Using such an approach and some morpho-metric indicators, [Steemers et al. \(1997\)](#) analyzed the implications of urban morphology in terms of solar availability, wind conditions and dispersion. These archetypes are pavilions, slabs, terraces, terrace-courts, pavilion courts and courts (see Sec. 1.2.3 and Appendix D). [Ratti et al. \(2003\)](#) reduced then the scope down to three of these archetypes, which were compared for their environmental performance in a hot and arid climate: the traditional Arabic courtyard, the micro-pavilion and the bigger pavilion. These studies highlighted the different behaviors of compact or detached forms, as well as the particular case of courtyards, which experience very specific internal thermal and aerodynamic conditions. Considering arrays of slabs, pavilions and courts, and varying their layouts and heights, [Huang \(2010\)](#) examined the effects of urban morphology on the building energy performance.

Extending the two above-mentioned approaches and providing for a wider applicability, some categorizations of urban configurations with respect to their thermal performance or micro-climatic effects have been established. Considering the evolution of urban forms from indigenous to modern patterns, [Golany \(1996\)](#) distinguished the compact, dispersed and clustered forms. Each of them constitutes a more or less adapted solution to specific climatic issues.

From another perspective and based on the identification of significant land uses that may affect urban micro-climates as well as urban thermal zones that are related to the urban geometry, street configuration and construction materials, [Oke \(2006a\)](#) designed a typology of urban zones. These urban climate zones (UCZs) are expected to have substantial effects on the urban climate. These UCZs are correlated with different roughness classes, structures (in terms of street aspect ratio, building height and density), covers (surface imperviousness) and metabolisms (land use

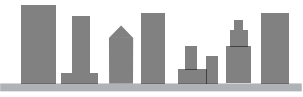






Urban climate zone (UCZ)	Image	Rough. class	Aspect ratio	% Imperv.
1. Intensely developed urban with detached close-set high-rise buildings with cladding, e.g. downtown towers.		8	> 2	> 90 %
2. Intensely developed, high density urban with 2 to 5 storey, attached or very close-set buildings often of brick or stone, e.g. old city core.		7	1.0 to 2.5	> 85 %
3. Highly developed, medium density urban with row or detached but close-set houses, stores and apartments e.g. urban housing.		7	0.5 to 1.5	70 to 85 %
4. Highly developed, low or medium density urban with large low buildings and paved parking, e.g. shopping mall, warehouses.		5	0.05 to 0.2	70 to 95 %
5. Medium development, low density suburban with 1 or 2 storey houses, e.g. suburban housing.		6	0.2 to 0.6, up to > 1 depends on trees	< 40 %
6. Mixed use with large buildings in open landscape, e.g. institutions such as hospital, university, airport.		5	0.1 to 0.5, depends on trees	< 40 %
7. Semi-rural development, scattered houses in natural or agricultural area, e.g. farms, estates.		4	> 0.05 depends on trees	< 10 %

Table 2.1: Urban climate zones (UCZs): “Simplified classification of distinct urban forms arranged in approximate decreasing order of their ability to impact local climate”. (From (Oke, 2006a))



or human activities). They cover a large diversity of landscapes as they go from semi-rural developments in natural areas to intensely developed city centers with towers. Tab. 2.1 details these UCZs.

[Stewart and Oke \(2012\)](#) refined the UCZs in order to represent better the urban and rural types that are related with specific temperature levels. Based on temperature measurements, a typology of local climate zones (LCZs) was established. Each LCZ is characterized by its temperature regime and refers to a local scale unit (about 1 km<sup>2</sup> according to [Oke \(2006b\)](#)). On the basis of these LCZs, the UHI effect can be better characterized and urban built types can be linked with expected micro-climatic properties. The classification of the LCZs distinguishes ten built types. They are characterized by their typical sky view factor (Sec. 2.2.1), aspect ratio, height, ratio of built surface and relative surface imperviousness as well as roughness class. These built types can be associated with seven land covers to better evaluate their potential climatic effects. These LCZs are detailed in Appendix E. Note that aerodynamic criteria should be considered to complete this approach, in addition to temperature related parameters.

Focusing on street level dispersion processes, which are more correlated with aerodynamic processes, [Theurer \(1999\)](#) proposed a classification of typical building arrangements and green spaces. Appendix D.3 describes these types. In association with recommended morpho-metric parameters, such as the aspect ratio or the building spacing as well as roof shapes, these typical urban layouts could be used in wind-tunnel or numerical studies. Based on German patterns, the identified building arrangements and green spaces are:

- single- or double-family buildings of 1 to 2 stories;
- dense urban developments, residential and commercial, with 1 to 3 stories;
- building rows, building blocks of 2 to 4 stories;
- block edge buildings (enclosed blocks), with 2 to 4 stories.
- city centers;
- commercial areas;
- industrial areas;
- green areas with few trees;
- and parks with trees, forest areas.

The three above mentioned approaches that either address real urban fabrics, consider generic urban forms or design typical urban categories with respect to their bio-climatic effects are complementary. They can more or less account for the details of physics or urban characteristics, and have different fields of application. In particular, the study of representative generic urban forms or general categories enables a wider scope of applicability of the findings. Furthermore, a better understanding of the physical processes with respect to the urban configuration can be achieved using simplified generic urban forms.

## 2.2 Urban morpho-metric indicators (UMMIs) addressing thermo-aeraulic exchanges

Complementary to usual urban metric indicators, specific urban morpho-metric indicators (UMMIs) are often used to characterize urban forms from a bio-climatic point of view. As they characterize urban morphological properties, most of them address both thermal and aerodynamic trends to some level. UMMIs thus inform on how a certain morphological feature may affect energy and air exchanges in an urban context.

Thanks to their quite simple formulation, such indicators can generally be easily understood and allow for straightforward parametric studies and comparisons. Their scope for use is very large as they can be applied to any kind of urban pattern and require no significant computational resources.

In order to identify the morphological factors that affect aerodynamic processes and energy exchanges in the UCL, a selection of such UMMIs is given hereafter with some explanatory schemes and descriptions. Tab. 2.2 synthesizes the different UMMIs with respect to their links with aerodynamics or heat transfers. Appendix F provides most of their formulae. Other urban form factors in relation to urban archetypes can be found in [Huang \(2010\)](#); [Huang et al. \(2008\)](#).

	Unbuilt Volumes		Built Volumes
Air Flows	Porosity Sinuosity	Variance Mean rugosity Passage Ratio Blockage Ratio Frontal Area Ratio W/S Plan Areal Fraction Aspect Ratio Sky View Factor Occlusivity UHA	
Thermal Exchanges			Form Factor Contiguity
Building Performance		Passive Volume Ratio	Size Factor

Table 2.2: Classification of UMMIs with respect to their link with air flows and heat fluxes.

### 2.2.1 UMMIs addressing the openness of city toward the sun, sky and atmosphere

By determining the capacity of an urban area to receive short-wave radiation from the sun, exchange long-wave radiation with the sky as well as to interact with the air flows aloft the canopy, the following UMMIs address both aerodynamic and thermal processes:

- the aspect ratio of canyons (Oke, 1987, 1988; Steemers et al., 1997);
- the sky view factor (Oke, 1987, 1988; Ratti et al., 2003; Robinson, 2006; Steemers et al., 1997);
- the oclusivity (Adolphe, 2001b) or rate of reduction built floor area with height (Steemers et al., 1997);
- and the urban horizon angle (Ratti et al., 2005).

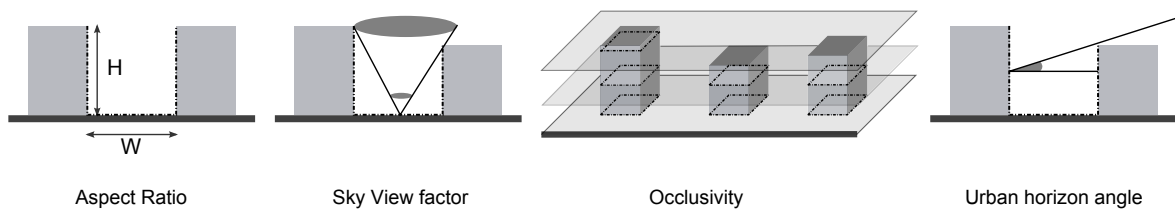


Figure 2.2: Schematic illustration of some UMMIs addressing the openness of the city to the sun, sky and atmosphere.

The aspect ratio ( $H/W$ ) is a 2D indicator, which evaluates the relative dimensions of a canyon in a vertical plane. Its value gives information on the ability of the canyon to receive sun beams or to be shadowed, as well as to release long-wave radiation to the sky. It also provides information about the expected air flow regime taking place within this space, generally considering a perpendicular wind incidence. A variant of this indicator is proposed in Ratti et al. (2006) to account for asymmetric configurations and a wider range of orientations.

The sky view factor (SVF) at ground level gives a measure of the openness of an urban fabric to the sky and the atmosphere, thus informing on its potential exchanges with the part of the atmosphere located above. It gives the portion of the sky that is viewed from a point located on the ground with respect to the total hemisphere.

The oclusivity or rate of reduction built floor area with height provides an integrated indication of the distribution of built perimeters, accounting for the three dimensions of the space. When the built volume decreases with height, physical exchanges with the sun, the sky and the atmosphere are promoted.

The urban horizon angle (UHA) corresponds to the angle formed by an horizontal line passing through the middle of a vertical surface, and the line passing by the same point and the mean surrounding roof tops. It provides information about on the relative obstruction of a surface and gives an indication on the potential radiative exchanges that can occur between the surface and the other urban surfaces, the sky and the sun, as well as the potential exposure of the surface to the free flow.

### 2.2.2 UMMIs mainly addressing aerodynamic processes

Indicators addressing urban aerodynamic processes mostly characterize open volumes in terms of their relative dimensions in relation with the buildings as well as the urban roughness. They can be related to the ventilation potential and flow regimes in the UCL on the microscopic level, or the overall urban aerodynamic drag and mean wind modification on the macroscopic level. From the ones usable at the smaller scales to those applicable on larger scales, the related UMMIs are:

- the length to height ratio ( $L/H$ ) (Oke, 1988) or length to width ratio ( $L/W$ ) (Kastner-Klein et al., 2004) of street canyons;
- the  $W/S$  ratio of passage between two buildings (Blocken et al., 2007a);
- the blockage ratio (BR) (Brown and DeKay, 2000) and the passage ratio (PR) (Hu and Yoshie, 2013);
- the frontal area ratio (Grimmond and Oke, 1999);
- the mean porosity (Adolphe, 2001b);
- the sinuosity (Adolphe, 2001a,b);
- the plan areal fraction (Grimmond and Oke, 1999);
- the absolute rugosity or canopy mean height (Adolphe, 2001b);
- the relative rugosity (Adolphe, 2001a), and the permeability (Steemers et al., 1997) / variance (Ratti et al., 2006);
- and the roughness length ( $z_0$  and zero displacement height  $z_D$ ) (Grimmond and Oke, 1999).

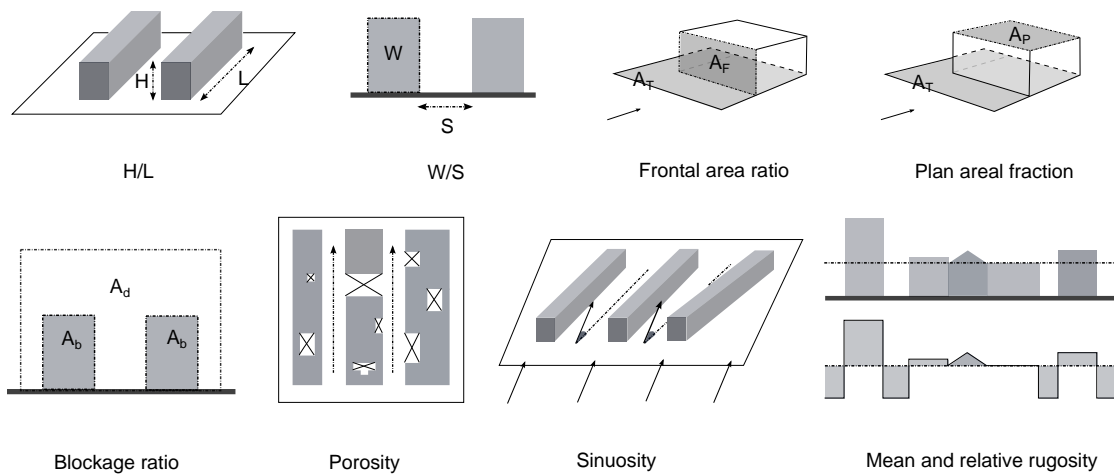


Figure 2.3: Schematic illustration of some UMMIs addressing aerodynamic processes.

The length to width ratio ( $L/W$ ) completes  $H/W$  as it evaluates relative dimensions of a street canyon in the streamwise plane.  $L/H$  is related to  $L/W$  through  $H/W$ . In addition to  $H/W$ , these ratios inform on the flow regime taking place in an urban street canyon, accounting for the effects of the additional horizontal flows coming from the sides.

The W/S ratio is a dimensionless factor that characterizes the relative proportion of a passage width with respect to the building influence scale (S), with S depending on the dimensions of the building windward facade. As this ratio increases, the resistance, interaction or isolated flow regimes develop between buildings, as a result of the development of corner streams.

The blockage ratio (BR) is a 2D indicator that evaluates the proportion of the span wise section of the flow that is obstructed by built elements.<sup>3</sup> Typically, it informs on the blocking effect encountered by the wind as it impinges on a built area. Extending this notion and W/S, the passage ratio (PR) evaluates the ventilation efficiency of a cuboid array as a function of the width of the windward facades and the spacing between obstacles. The higher its value, the more efficient the ventilation.

In the same perspective, the frontal area ratio ( $\lambda_F$ ) evaluates the ratio between the frontal area of a built structure with respect to its total plot area. The higher this ratio, the higher the blocking effect.

The mean porosity extends the concepts of blockage ratio and frontal area ratio as it characterizes the proportion of useful open volume according to the total urban volume in order to evaluate its effects on the pressure-gradient flow, considering streets parallel to the mean flow. It takes into account the rectangular shape of streets and other open spaces which are located within the canopy layer but ignore semi-enclosed or enclosed courtyards as well as streets perpendicular to the mean flow.

The sinuosity completes the mean porosity as it measures the angle between the streets and the mean wind direction. Thus, it indicates the potential of the street network to disturb the pressure-gradient flow due to its orientation.

The plan area fraction ( $\lambda_p$ ) is generally understood as the measure of the built density. It is also often called the packing density of urban elements. It evaluates the area of built roughness elements with respect to the total plot area. As this ratio increases from zero to about 0.5, the urban roughness increases. For higher values, roughness decreases as the skimming flow regime occurs (Appendix B).

The absolute rugosity or canopy mean height informs on the overall effect of an urban area on the change in the mean wind profile.

The relative rugosity and the permeability / variance provide directional information on the relative regularity and smoothness of an urban texture by evaluating the mean square deviation of the canopy's height. It gives information on the direction of the most effective ventilation.

As discussed in Sec. 1.1.1, the roughness length and zero displacement height inform on the general effects of an urban area on the mean wind profile modification on large scales. Their values mainly depend on the mean building height, the coverage ratio and the frontal area ratio. More details can be found in [Grimmond and Oke \(1999\)](#).

---

<sup>3</sup>This indicator is often adapted to be used in CFD and wind tunnel modeling as a quality indicator for the domain section with respect to the front size of the obstacle (see Sec. 3.1.2.2).

### 2.2.3 UMMIs addressing the ability of a building to interact with its outdoors

These indicators address the building thermal exchanges through its envelope as well as the potential for natural ventilation and infiltration. These processes depend on the characteristics of the interface between the building and its immediate environment, and in particular of its area. They mainly refer to the building scale. The main indicators are:

- the building volumetric compactness or surface to volume ratio ( $S/V$ ) ([Adolphe, 2001b](#); [Ratti et al., 2005](#); [Salat, 2011](#); [Steemers et al., 1997](#));
- the passive volume ratio ([Ratti et al., 2005](#); [Salat, 2011](#); [Steemers et al., 1997](#));
- and the contiguity ([Adolphe, 2001b](#)).

The building volumetric compactness or surface to volume ratio ( $S/V$ ) should be decomposed into two parts, namely the building form and the building size factors. The form factor is a dimensionless value characterizing a shape. It is given by the ratio of the envelope area over the built volume to the power of  $2/3$ . The higher the value, the more physical exchanges may occur through the building envelope as the building becomes less compact. The size factor gives the typical length of a facade of the building or the typical distance between a point to the envelope. The greater this distance is, the more artificial lighting and mechanical ventilation are generally needed.

The passive volume ratio evaluates the proportion of the building volume that is located less than two times the floor height ( $\approx 6$  m) from the facade. This volume may benefit from natural lighting and ventilation, but this greatly depends on the facade orientation and design. As it is an indicator of building width, it can be linked to the size and the form factors.

The contiguity measures the proportion of building facade which is not directly in contact with the outside, but adjacent to another built volume (not a buffer zone). Those walls cannot take part in the exchanges between the building and its external environment.

## 2.3 Synthesis of the morphological factors affecting urban air and heat fluxes

### 2.3.1 Main morphological factors affecting urban air flows

According to Sec. 1.1.1 and Sec. 1.2.3, the findings of the studies synthesized in Sec. 2.1.2 and the review of the UMMIs addressing urban aerodynamics given in Sec. 2.2.2, three main effects of the urban structure on air flows can be distinguished.

- The first effect refers to spatial scales larger than the neighborhood (macroscopic level). It addresses the aggregated effects of the UCL on the mean wind profile.

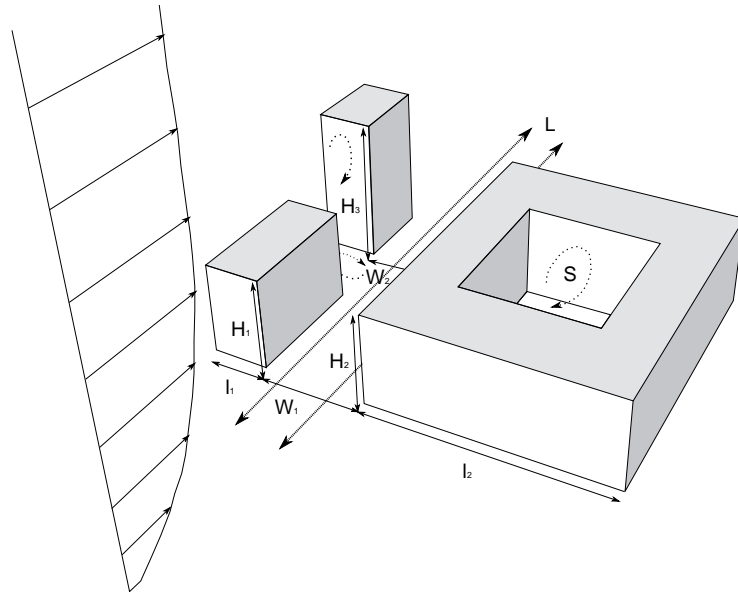


Figure 2.4: Main morphological factors affecting urban aerodynamic processes.

- The second effect refers to spatial scales smaller than the neighborhood (microscopic level). It addresses the direct exchanges and interactions that can occur between the flow patterns developing inside the UCL and the above free flow, i.e. the potential exchanges through the urban canopy;<sup>4</sup>
- The third effect also refers to spatial scales smaller than the neighborhood. It addresses the UCL's internal flows, i.e. inner flow paths and recirculation phenomena.

Of course, this decomposition is rather arbitrary as all these aerodynamic processes and phenomena are closely linked with each other.

The general modification of the wind profile by urban areas depends on the urban overall structure and especially of its density and regularity in terms of the street network and building heights. Because of the drag force experienced by the mean flow due to friction on this active surface, the pressure-gradient flow is altered. So does the mean velocity profile. This adjustment can be translated by a modification of  $z_0$  and  $z_D$  as discussed in Sec. 1.1.1.

Flow modifications are conditioned by the averaged effects of two main urban factors, which determine the flow features on smaller scales: the urban roughness and urban porosity. The definitions of these concepts extend the ones considered by [Adolphe \(2001a\)](#) as these concepts are actually morphological factors and not indicators. Moreover, they are defined at the street canyon and block scales. Fig. 2.4 synthesizes their related urban morphological parameters. Tab. 2.3 summarizes the small scale aerodynamic processes involved as well as their related urban morphological features.

<sup>4</sup>These exchanges are related to the concept of breathability as defined by [Neophytou \(2015\)](#).


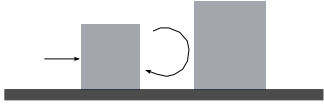
	Urban roughness: external exchanges through the canopy 	Urban porosity: internal flow paths and recirculation phenomena 
Physical processes involved	<ul style="list-style-type: none"> <li>- Flow driven from above</li> <li>- Free flow penetration</li> <li>- Additional air supply</li> </ul>	<ul style="list-style-type: none"> <li>- Aerodynamic drag</li> <li>- Flow channeling or blockage</li> <li>- Flow interference</li> </ul>
Main morphological features	<ul style="list-style-type: none"> <li>- Openness to the atmosphere</li> <li>- Dimensions / buildings</li> <li>- Canopy's heterogeneity</li> </ul>	<ul style="list-style-type: none"> <li>- Horizontal openness</li> <li>- Connectedness</li> <li>- Geometry</li> </ul>

Table 2.3: Relations between urban roughness and porosity with aerodynamic processes.

Urban roughness mainly depends on the openness of the urban fabric to the above atmosphere and the distribution of building heights. It also conditions the vertical exchanges through the canopy. It determines the potential of the free flow to penetrate the UCL or the development of above flow-driven internal recirculation phenomena (such as in the skimming flow regime). It also determines the potential additional air supply due to higher urban obstacles, which induce downward flows. Urban roughness conditions the mechanical development of turbulence due to shear stress or flow separation processes as well, which can substantially improve turbulent exchanges between the UCL and the air above. Thus, urban roughness mainly refers to geometric and dimensional parameters.

Urban porosity addresses the potential horizontal exchanges inside the UCL. It conditions flow paths, interference effects or flow entrapment. Therefore, it determines the capacity of the flow to circulate through the UCL in an almost horizontal way. These internal flows can be channeled, deviated, swirled or blocked depending on the features of the network of open spaces, which may differ by its orientation, continuity, connectedness and width, as well as the overall geometry and layout of buildings. Hence, urban porosity mainly depends on topological, geometric and dimensional parameters as these parameters are essential in shaping these internal flow patterns.

Hence, urban roughness and porosity condition the aerodynamic phenomena that develop inside the UCL. They are especially critical in shaping the air flow structures developing in streets, intersections, squares and courts. They also greatly contribute to determine the relative wind velocities and turbulence intensities in these different outdoor spaces.

### 2.3.2 Main morphological factors affecting urban and building heat transfers

According to Sec. 1.1.2 as well as the review of the UMMIs addressing the openness of urban fabrics toward the sun and the sky (Sec. 2.2.1) and the potential of buildings to exchange with their environment (Sec. 2.2.3), three main categories of heat transfer can be distinguished:



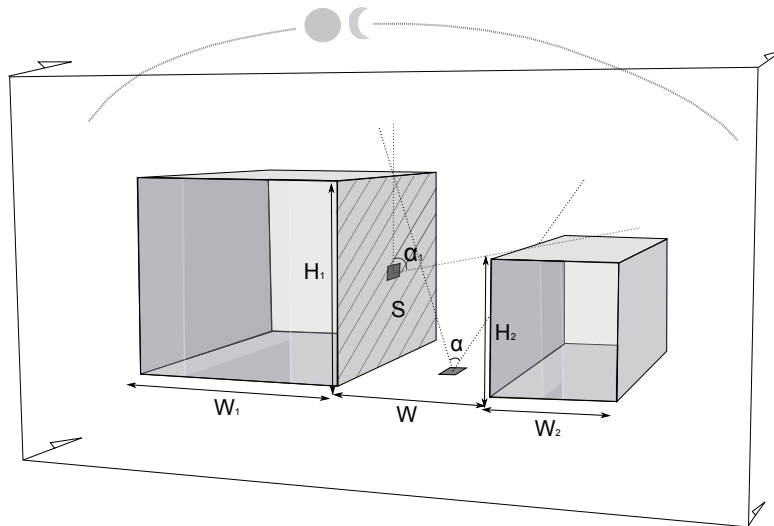


Figure 2.5: Main morphological factors affecting building heat transfers.

- the external energy exchanges, i.e. the heat transfers that develop between the UCL and the sky and the sun (as well as those due to air flows);
- the internal energy exchanges, i.e. the heat exchanges between urban surfaces;
- and the thermal exchanges occurring at the building interface with the outdoors, determining the building energy balance.

This classification is still arbitrary as all the related energy exchanges are correlated.

The UCL external exchanges are mostly related to the potential of sun heating and radiative cooling of urban surfaces. These exchanges depend on the openness of the urban texture toward the sun and the sky as well as on the orientation of the urban surfaces in relation to the sun position. These parameters determine the solar exposure or sun shading of urban surfaces. They also condition the potential amount of long-wave radiation that can be released by warm urban surfaces to the cool sky by night.

The internal heat exchanges that develop between urban surfaces involve multi-reflections of incident solar radiation as well as long-wave radiation transfers between surfaces of different temperatures. Only considering the urban structure, these exchanges depend on the total (unfolded) surface area, including building walls and outdoor floors, as well as the form factors between these surfaces. Note that these form factors are complementary to the openness of urban surfaces to the sky.

The building energy balance is influenced by the envelope area, as well as the building width. Only considering morphological parameters, the envelope area determines the potential convective and radiative heat transfers that can occur between the building and its immediate environment. These exchanges are intensified in case of highly glazed buildings. It also determines the potential for natural wind-driven ventilation and infiltration, as larger envelope areas provides larger room to place openings and leaks. The building width conditions the potential of the building to use passive energy inputs as well as to benefit from natural lighting.

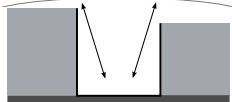
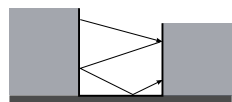
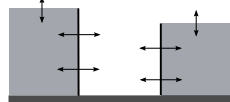
	External exchanges with the sky and the sun 	Internal exchanges between urban surfaces 	Building energy efficiency 
Physical processes involved	<ul style="list-style-type: none"> <li>- Sun heating</li> <li>- Radiative cooling</li> <li>(- Convection)</li> </ul>	<ul style="list-style-type: none"> <li>- Multi-reflections</li> <li>- Radiative trapping</li> <li>- Absorption</li> </ul>	<ul style="list-style-type: none"> <li>- Convective and radiative transfers</li> <li>- Natural ventilation</li> </ul>
Main morphological features	<ul style="list-style-type: none"> <li>- Openness to the sky and the sun</li> <li>- Orientation</li> </ul>	<ul style="list-style-type: none"> <li>- Unfolded area of urban surfaces</li> <li>- Form factors</li> </ul>	<ul style="list-style-type: none"> <li>- Interface area / envelope</li> <li>- Building width</li> </ul>

Table 2.4: Relations between the urban fabric and heat transfers.

Hence, small scales urban thermal exchanges mostly depend on the openness and orientation of urban textures in relation to the sky and their reciprocal relative obstruction levels, as well as the area of urban surfaces. Fig. 2.5 synthesizes the related urban morphological parameters. Tab. 2.4 summarizes the physical processes involved in these internal and external radiative exchanges and the building energy efficiency, as well as their related morphological factors.

## 2.4 Design of urban form typologies

### 2.4.1 Design methodology

The aim of this methodology is primarily to design a typology of urban structures in order to link them with typical flow patterns occurring within the UCL. Considering the complexity of aerodynamic phenomena and the multiplicity of architectural features and details that affect flow structures, generic case studies are considered. Such an approach has a wide scope for applicability and representativeness, despite involving a substantial simplification of urban forms and some arbitrary choices. As presented in Sec. 1.2, the building or street canyon / urban block scales are relevant for studying very local physical phenomena. Based on the literature review presented above, this approach could be further extended to more general micro-climatic issues.

The second objective of the approach is to try to account for the wide variety of urban fabrics that exist around the world. There is a need for several real urban textures to be analyzed, and not only the occidental and modern ones. Studying developing countries is important as they are subject to a very fast urban growth. Furthermore, cities in these countries are home to very diverse ways of life and are located in contrasting climates. This involves particular urban and architectural challenges given that healthy ambient conditions should be ensured, while the artificial air conditioning is often not possible. Analyzing their vernacular urban forms can thus highlight efficient bio-climatic strategies (Golany, 1996). The corpus of urban fabrics we considered is therefore based on Firley and Stahl (2010), in which thirty real urban fabrics corresponding to urban neighborhoods of the late XVIII to the early XX centuries that are located

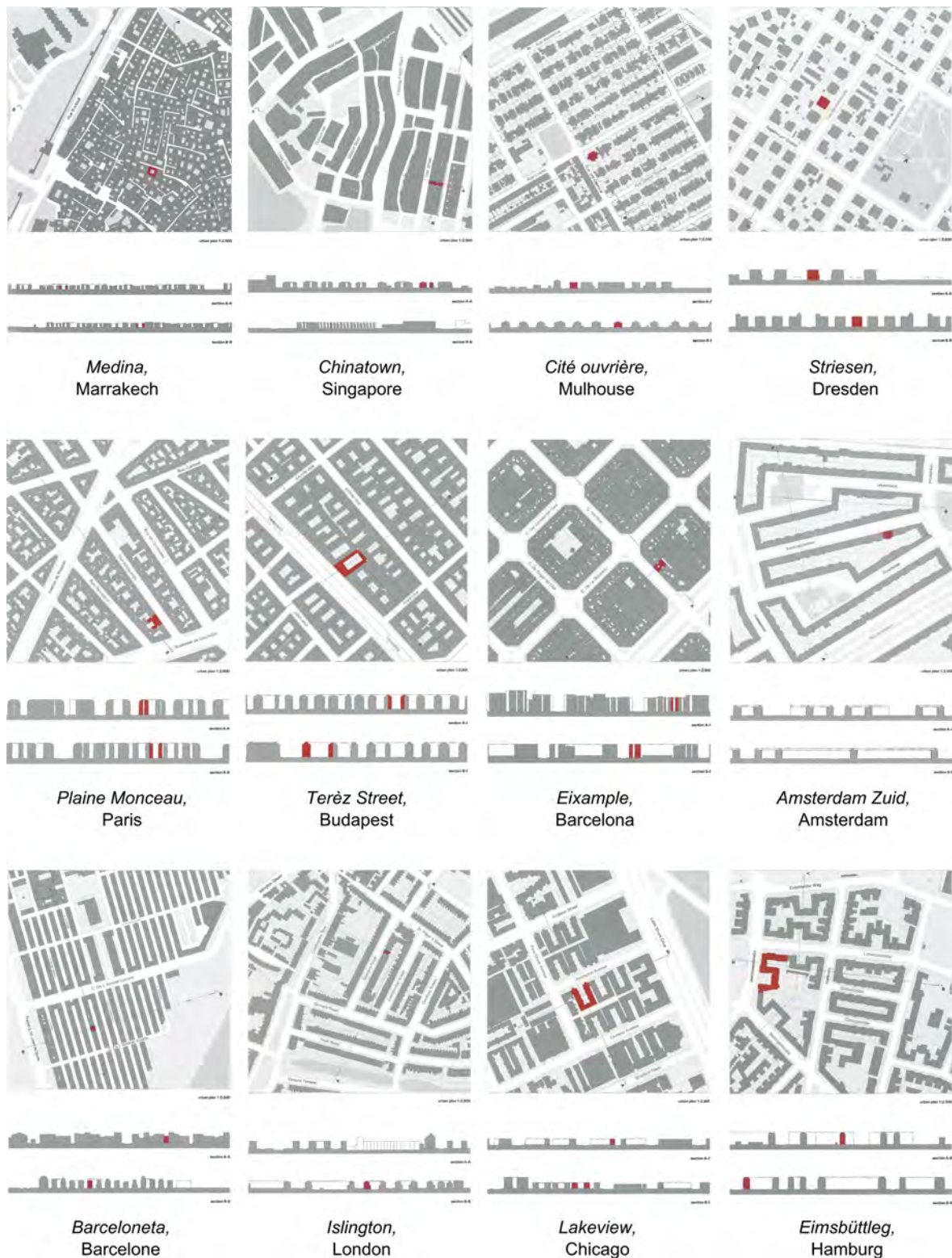


Figure 2.6: Examples of urban fabrics studied. (From (Firley and Stahl, 2010))

around the world are reviewed. Fig. 2.6 shows some examples of these urban fabrics. These neighborhoods are mostly composed of housing and are fairly homogeneous. [Firley and Stahl \(2010\)](#) carried out a spatial analysis at medium scale, which mostly dealt with the spatial organization and the relationships that exist between the dwellings and their surrounding courts and streets as well as the status of open spaces. This analysis could be further extended to examine the micro-climatic features of these urban spaces with respect to their morphological properties, to highlight how they could promote or restrict social practices.

Hence, the different urban fabrics were analyzed considering:

- the physical processes involved in determining urban air flows inside the UCL (Sec. 1.1.1 and 1.2.3);
- the relevancy of the building and street canyon as well as urban block scales to study small scale urban flow structures (Sec. 1.2 and 2.1.1);
- the main morphological factors affecting urban internal aerodynamic processes synthesized in Sec. 2.3.1;
- the corpus of worldwide traditional neighborhoods given in [Firley and Stahl \(2010\)](#) and the importance of courtyards in traditional as well as some contemporary urban patterns;
- and the three main categories of criteria suitable for the urban morphology analysis defined by [Burdet \(2011\)](#) (Sec. 2.1.1).

Their main morphological features were identified in order to highlight some common texture properties and to initiate a semi-empirical classification of urban forms. The approach focuses primarily on the topological features of urban forms. The existence of courts, the openness and the connectedness of outdoor spaces, as well as their orientation and distribution are particularly examined. As outdoor and built volumes reciprocally define themselves, these parameters correspond to the compactness, continuity and the fractality of the buildings shapes and layouts.

Two typologies of five generic buildings and urban blocks were designed. Fig. 2.7 synthesizes the general design methodology. A typical length has been kept constant for all types within the two typologies rather than retaining the built volume or the total built area constants.

Note that because of the different considered criteria (morphology or spatial configuration) and although they may have similar abstracted shapes, some urban patterns could not be attributed to the same class in our typologies as they are in [Firley and Stahl \(2010\)](#). Moreover, traditional and century-old urban fabrics do generally not correspond to idealized master plans, but testify to processes of many decades of increasing complexity, even if they may have followed an initial urban master plan (as Cerda's blocks in Barcelona, Spain), or have been subject to great urban modifications (such as the Hausmannian Paris, France). In addition, cities may not necessarily have had planning rules, or these may be relatively recent so that older neighborhoods might have freely developed. As a consequence, when examining a real urban fabric at the block or neighborhood scale, it is often not possible to classify it as fitting only one of the defined types. However, such configurations can generally be understood as combinations or hybridizations of the basic morphological types.

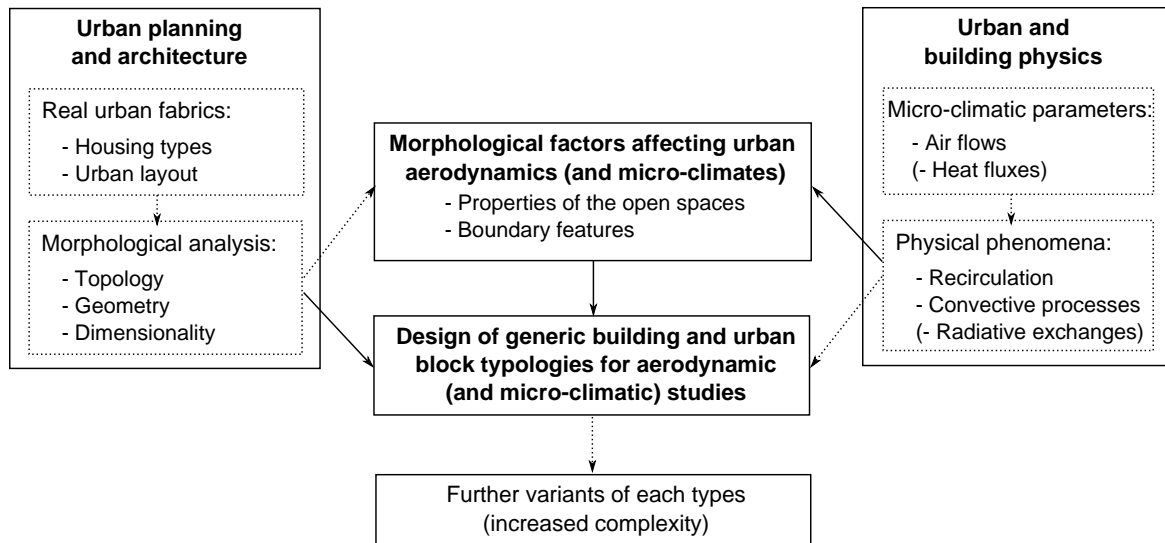


Figure 2.7: Summary of the design methodology of the generic isolated building and urban block typologies for small scale aerodynamic (and micro-climatic) studies.

## 2.4.2 Proposed typologies of isolated buildings and urban blocks

### 2.4.2.1 Proposed typology of isolated buildings

Five types of isolated buildings compose the isolated building typology. Fig. 2.8 and Tab. 2.5 give their representations and main morphological characteristics respectively. For this first typology, the typical horizontal length is  $2H$ , with  $H$  being the obstacle height. From the most to the least compact, the five isolated building types are:

- the cube;
- the cuboid;
- the L building;
- the U building;
- and the patio building (named patio hereafter).

The typology shows decreasing compactness from the cube to the patio, which corresponds to the appearance of a court. Initially the courtyard merely intersects with the obstacle. It becomes progressively more integrated, until it is totally contained inside. Thus, for the cube and the cuboid, the outdoor volume is external to the obstacle and totally open. Then, the number of edges is increased throughout the typology. The edges correspond to the limits of the void and characterize its concavity. In the patio type, the courtyard is totally enclosed. The two extremes of the typology, namely the cube and the patio, are negative images of each other.

With this first typology, the influence of the building shape itself can be analyzed, especially with regard to its relative dimension and orientation as well as the existence and position of a courtyard. This later design feature is key in many urban developments while producing specific internal wind and thermal conditions (Givoni, 1998).



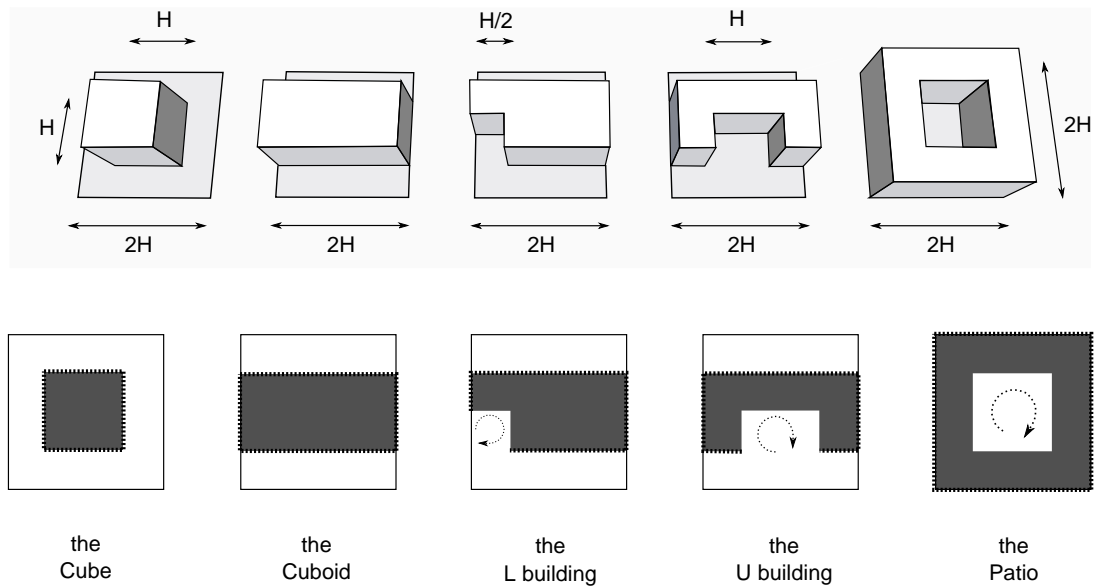


Figure 2.8: 3D and plan views of the five types composing the typology of generic isolated buildings: emergence of a courtyard. Height of each type:  $H$ .

	Cube	Cuboid	" L "	" U "	Patio
Floor Area [ $H^2$ ]	1	2	1.75	1.5	3
Volume [ $H^3$ ]	1	2	1.75	1.5	3
Envelope Area [ $H^2$ ]	5	8	7.75	8.5	15
Compactness Factor [ $H^{-1}$ ]	5	4	4.43	5.67	5
1/Size Factor [ $H$ ]	1	1.26	1.21	1.14	1.44
Shape Factor [—]	5	5.04	5.34	6.49	7.21
Mean horiz. side length [ $H$ ]	1	1.5	1	0.9	1.5
Nb. of horiz. sym. planes	4	2	0	1	4
Nb. of horiz. open sides of the court	-	-	2	1	0

Table 2.5: Morphological characteristics of the isolated building types.

Nb: Number, horiz.: horizontal, sym.: symmetry.

#### 2.4.2.2 Proposed typology of urban blocks

Five types of urban blocks compose this second typology. Fig. 2.9 and Tab. 2.6 give their representations and main morphological characteristics respectively. The typical horizontal length of a block is taken to be  $8H'$ ,  $H'$  being the obstacle height. From the two types with (horizontally) open voids to those that include enclosed courtyards, the five urban block types are:

- the cube array;
- the row block;
- the U block;
- the enclosed block;
- and the continuous patio array.

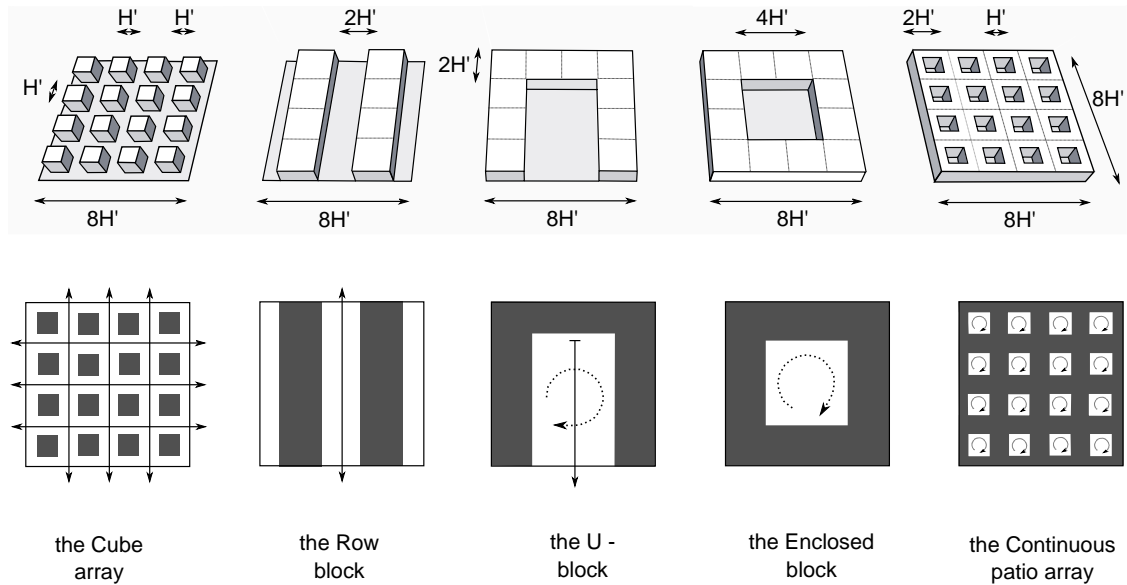


Figure 2.9: 3D and plan views of the five types composing the typology of generic urban blocks. Height of each type:  $H'$ .

	Cube array	Row block	U block	Encl. block	Patio array
Floor Area [ $H^2$ ]	16 or 1	32 or 16	40	48	48
Volume [ $H^3$ ]	16 or 1	32 or 16	40	48	48
Envelope Area [ $H^2$ ]	80 or 5	72 or 36	84	96	144
Compactness Factor [ $H^{-1}$ ]	5 or 5	2.25 or 2.25	2.1	2	3
1/Size Factor [ $H$ ]	2.52 or 1	3.17 or 2.51	3.42	3.63	3.63
Shape Factor [—]	12.6 or 5	7.14 or 5.67	7.18	7.27	10.9
Mean horiz side length [ $H$ ]	1	5	5.5	6	1.41
Nb. of hori. sym. planes	4	2	1	4	4
Void connectedness	conn.	s. conn.	s. conn.	s. conn.	not conn.
Nb. of horiz open directions	4	2	1	0	0
Void aspect ratio	1	0.5	0.25	0.25	1

Table 2.6: Morphological characteristics of the urban blocks types.

Nb: Number, horiz.: horizontal, sym: symmetry, conn.: connected, s. conn.: simply connected. When two values are given, they respectively refer to the whole built volume and a built unit.

A progression can also be identified in this typology, moving from the cube array to the continuous patio array. The unbuilt volume of the cube array is not simply connected, but continuous and open on both axes of the horizontal plane. Then, the unbuilt volume progressively becomes less open on the horizontal plane. It becomes larger and, for the row block, it crosses the block along one axis. It loses then step by step its horizontal openness (through the U block and enclosed block types) until it becomes a network of small enclosed courtyards in the continuous patio array. As the built volume increases in continuity, the open space gradually loses its openness and unity. Spaces located between the built volumes are smaller (higher aspect ratio) in the two extreme cases than in the three stages in between. The structure of the extreme cases is more fractal, and they are negative images of each other.

With this second typology, the effects of the block relative composition, openness and fractality on the inner flow structures can be examined. Differences in their flow structures due to the presence of several obstacles as opposed to an isolated obstacle configuration (interference effects) can also be studied. The effect of the overall group on the upper scale of the entire urban block, especially with regard to its porosity, can be examined as well.

### 2.4.3 Discussion of the typologies

Abstracting urban fabrics to design generic typologies necessarily produces simplified urban types. In the current case, the types are regular, orthogonal and straight-shaped. As a consequence, some main morphological features that characterize real urban patterns are neglected despite being critical in determining urban flow patterns. Some arbitrary choices were made, such as working with a typical length and a constant height and not a constant built volume or footprint. Nevertheless, even though very restrictive, such choices are necessary when working on generic forms in order to provide a basis for a wide scope for further developments and parametric studies.

Neglecting variations in height allows a first planar comparison of morphological configurations. However, considering a constant height involves substantial limitations. Essentially, the improvement of vertical mixing due to an increase in the canopy roughness is overlooked. Another consequence is that the U and the enclosed blocks have an aspect ratio of 0.25, which seems rather low when compared to real dense urban fabrics. Nonetheless, as these continuous built volumes have similar topological features as the U building and the patio, for which the aspect ratio value is 1, they can be studied in parallel and compared to these single building types.

Other important morphological parameters that are not taken into account in these types include the variation of the urban densities as well as the alignment staggering of arrays, which substantially affect urban aerodynamics processes (see Sec. 1.2.3). Nevertheless, due to the fact that they increase the geometric complexity without creating new morphological classes as defined in our typologies, the modification of the obstacle heights and canyon aspect ratios, the staggering of array's layout and other geometrical declinations as well as the modification of the typical lengths and dimensions are kept as subsequent variants for each type.

## 2.5 Summary

A transverse and semi-empirical approach is developed for designing generic urban typologies suitable for small scales urban aerodynamic studies. Air flows within the UCL are especially targeted, so the building and urban block scales are considered. Based on a literature review, the main morphological factors that are key for urban aerodynamics are identified. These factors are linked to the properties of urban open spaces in terms of topology, geometry and dimensionality. By combining these initial results with a morphological analysis and abstraction of worldwide traditional urban fabrics, two generic typologies of urban forms are designed: one of isolated buildings and one of urban blocks.



Five types compose each typology:

- the cube, the cuboid, the L the U and the patio, for the isolated building types;
- the cube array, the row block, the U block, the enclosed block and the continuous patio array, for the urban block types.

These typologies are composed of regular and orthogonal forms to keep their genericity, and thus allowing a wide scope for use, a high level of representativeness and further detailed investigations. The complexity of each type could be then increased in terms of relative dimensions, obstacles height and arrangement of building groups. Homogeneity, symmetry, straightness and the extent of each type can also be modified so that parametric studies on specific morphological features may be performed.

——— *Main contribution of this chapter:* ———

- *Design two generic typologies of built structures based on a detailed analysis of the main factors affecting urban aerodynamic processes on the urban block scale.*

## **Part II**

# **Computational fluid dynamics for the understanding of urban air flow patterns**



# Chapter 3

## CFD modeling and validation study

As an essential and time-consuming step of any CFD study, this chapter presents the validation of the aerodynamic model, with some preliminary considerations on urban fluid mechanics and literature recommendations for CFD studies. The validation study is reported for a free ABL, an isolated sharp-edged rectangular block and an array of rectangular blocks. Simulation results are compared to detailed experimental data as well as computational predictions and are discussed with respect to the available literature. On this basis, the actual modeling strategy is defined.

### Contents

<b>3.1 Theoretical background and best practices</b>	<b>68</b>
3.1.1 Introduction to urban fluid mechanics for turbulent flows	68
3.1.2 Usual CFD approaches in environmental wind engineering	70
3.1.2.1 CFD models based on the Navier–Stokes equations	70
3.1.2.2 Steady RANS models	71
3.1.2.3 Near wall treatment	74
3.1.3 State of the art of steady RANS modeling for building aerodynamics	76
3.1.3.1 Best practices: modeling and validation	76
3.1.3.2 Performance and applicability	78
<b>3.2 Validation test cases</b>	<b>79</b>
3.2.1 Reference wind-tunnel tests	79
3.2.2 Reference LBM LES simulations	81
3.2.3 Steady RANS models	82
<b>3.3 Comparison between numerical results and experimental data</b>	<b>85</b>
3.3.1 The modeled boundary layer	85
3.3.2 The rectangular block	86
3.3.3 The array of rectangular blocks	92
<b>3.4 Model accuracy and reliability</b>	<b>96</b>
3.4.1 Accuracy of the computational methods	96
3.4.2 ABL and roughness modeling effects	97
<b>3.5 Synthesis of the settings to be used in actual models</b>	<b>100</b>
<b>3.6 Summary</b>	<b>101</b>

### 3.1 Theoretical background and best practices

#### 3.1.1 Introduction to urban fluid mechanics for turbulent flows

To express the different equations, the following notations are introduced:

- $i, j, k \in \{1, 2, 3\}$ : spatial subscripts;
- $x_i$ : the spatial coordinates;
- $u_i$ ;  $p$ ;  $T$ : the instantaneous velocity, pressure and temperature variables;
- $g_i$ : the gravitational acceleration;
- the Einstein's notation (implicit summation on  $i, j$  or  $k$ ).

Assuming the continuum hypothesis and an incompressible Newtonian fluid, the instantaneous flow behavior can be described by three governing equations, which are simplified versions of the general Navier–Stokes (NS) equations. They enforce conservation laws for the mass, momentum and energy respectively.

The continuity equation or conservation equation for the mass is given by:

$$\frac{\partial u_i}{\partial x_i} = 0 \quad (3.1)$$

The conservation equation for the momentum corresponds to the application of the second law of Newton for a finite volume of fluid. It gives the fluid's acceleration as a function of the external forces that act on it. These forces include the effects of the pressure ( $p$ ), viscosity ( $\nu$ ) and gravity ( $g_i$ ). The corresponding equation is:

$$\frac{\partial u_i}{\partial t} + u_j \frac{\partial u_i}{\partial x_j} = -\frac{1}{\rho} \frac{\partial p}{\partial x_i} + \nu \frac{\partial^2 u_i}{\partial x_j^2} + g_i \quad (3.2)$$

with:  $\begin{cases} p : \text{the pressure [Pa]}, \\ \rho : \text{the fluid density [kg} \cdot \text{m}^{-3}\text{]}, \\ g_i : \text{the gravitational acceleration [m} \cdot \text{s}^{-2}\text{]}. \end{cases}$

Similarly, the conservation equation for the energy is given by:

$$\frac{\partial T}{\partial t} + u_i \frac{\partial T}{\partial x_i} = \frac{\lambda}{\rho C} \frac{\partial^2 T}{\partial x_j^2} \quad (3.3)$$

with:  $\begin{cases} T : \text{the temperature [K]}, \\ \lambda : \text{the thermal conductivity [W} \cdot \text{m}^{-1} \cdot \text{K}^{-1}\text{]}, \\ C : \text{the thermal capacity [J} \cdot \text{kg}^{-1} \cdot \text{K}^{-1}\text{]}. \end{cases}$

This system of five deterministic equations carries five unknowns, namely  $u_i$ ,  $p$  and  $T$ . However in practice, this system of equations can only be analytically solved for some very simple cases. Indeed, flows characterized by Reynolds numbers higher than a critical Reynolds number show a very complex behavior, with the development of turbulence. The critical Reynolds number depends on the addressed configuration.

Turbulent flows show changes of scales, which may be related to the non-linear term of Eq.3.2. Assuming that flows are effectively governed by the NS equations, the eventual flow depends on the initial and boundary conditions, whose effects on the solution are increased tenfold by the non-linearity of the equations. Hence, turbulence is still an open problem and it is still not possible to predict a realistic solution to the NS equations for complex and high Reynolds number flows.

Computational fluid dynamics (CFD) is a numerical approach that is often used to study flows. Because of problems involved by turbulence and the non-linearity of the NS equations, different CFD methods exist. They differ by their physical accuracy and applicability. More specifically, three main groups of methods exist. From the most exact method to the one characterized by the highest degree of turbulence modeling, they are:

- the direct numerical simulation (DNS) method;
- the large eddy simulation (LES) method;
- and the Reynolds averaged NS (RANS) method.

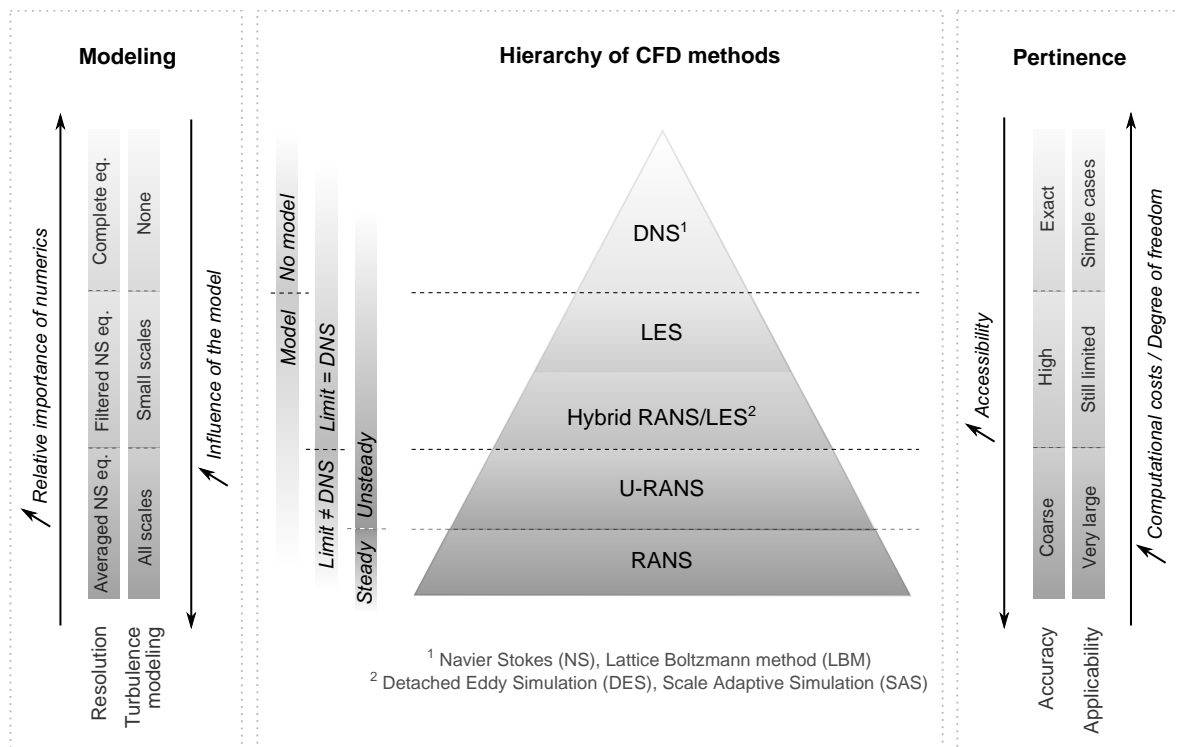


Figure 3.1: CFD methods: hierarchy, main assumptions and applicability. (Based on (Blocken, 2013; Sagaut et al., 2013))

Based on [Sagaut et al. \(2013\)](#) and [Blocken \(2013\)](#), Fig. 3.1 hierarchies these different CFD methods and synthesizes their main properties. The next section further develops the properties of these CFD methods from urban environmental engineering perspective. Note that the scope of Fig. 3.1 is extended to other CFD methods than those based on the NS equations to better position the different approaches.

### 3.1.2 Usual CFD approaches in environmental wind engineering

#### 3.1.2.1 CFD models based on the Navier–Stokes equations

Usual CFD methods use control volumes to compute flows. It is based on a decomposition of the computational domain into a 3D mesh. Governing equations are discretized into these control volumes and linearized. Discretization in time also occurs for transient models. In order to solve the linearized equations, numerical schemes are used and the computation generally relies on iterative processes (for more details, see [Ansys Fluent, 2013a](#)) for example).

Because of the non-linearity of the NS equations, performing computations without using a turbulence model can hardly be achieved to study urban problems. Such an approach is called DNS. It solves all the turbulence scales down to the Kolmogorov scales. However, it necessitates huge computational resources. Therefore, it is currently unfeasible to use this method for urban problems as the Reynolds number often exceeds  $10^6$ , meaning that the flow is fully turbulent. To the best of our knowledge, such an approach has only been carried out for urban-like flows with a Reynolds number roughly equal to the ones modeled in wind-tunnel tests, i.e. about two orders of magnitude smaller than at full-scale.

The LES method is based on filtered time-dependent NS equations. The turbulence scales smaller than a given size and down to the dissipative eddies are modeled using a sub-grid scale model. The corresponding threshold size is generally linked to the mesh size. Larger flow structures, i.e. the dynamic of large eddies, are directly solved. These eddies are the most energetic ones and depend on the model geometry. They are thus very specific to a given problem. This CFD method is more and more used in environmental wind engineering, especially for research purposes as important fluctuating flow features are computed. This provides highly valuable information especially for dispersion studies. However, it still requires significant computational resources when used to solve complex turbulent urban flows.

RANS methods only solve the mean flow. All the turbulence scales are modeled. Turbulence effects on the mean flow are taken into account thanks to turbulence models. These models were originally designed for industrial problems, which involved confined and high speed flows. More details about usual turbulence models are given in the following section (Sec. 3.1.2.2). These approaches can solve both unsteady (URANS methods) or steady state (steady RANS methods) flows, but steady RANS studies are the most frequently performed. They have widely been used in environmental wind engineering and many other engineering applications as they are generally known to be efficient: they can be used on almost any geometric model, most of the time requiring

reasonable computational resources. Note that RANS methods can sometimes be used together with LES (hybrid RANS-LES methods).

The different levels of turbulence modeling (DNS, LES, RANS) involve different levels of accuracy of the computed flows. However, the more accurate the computational method is, the more computational resources are required. As a consequence, computations of turbulent flows generally rely on simple models and are substantially uncertain (see Sec. 3.1.3.2). They are nonetheless useful as they can inform on the nature of turbulence and on its statistical properties in terms on mean and fluctuating features (Lesieur, 1994).

### 3.1.2.2 Steady RANS models

#### RANS equations

In order to overcome problems linked with the turbulence modeling, a statistical description of turbulent flows is often used. The different physical variables involved ( $u_i$ ,  $p$  and  $T$ ) are decomposed into a mean ( $\overline{u_i}$ ,  $\overline{p}$  and  $\overline{T}$ ) and a fluctuating ( $u'_i$ ,  $p'$  and  $T'$ ) parts as follows:

$$u_i = \overline{u_i} + u'_i \quad (3.4)$$

$$p = \overline{p} + p' \quad (3.5)$$

$$T = \overline{T} + T' \quad (3.6)$$

Note that mean values can correspond to an ensemble or a time averaging (ergodic assumption). This method is called the Reynolds decomposition.

Using this decomposition, the RANS versions of Eq. 3.1, Eq. 3.2 and Eq. 3.3 become:

$$\frac{\partial \overline{u_i}}{\partial x_i} = 0 \quad (3.7)$$

$$\frac{\partial \overline{u_i}}{\partial t} + \overline{u_j} \frac{\partial \overline{u_i}}{\partial x_j} + \frac{\partial \overline{u'_i u'_j}}{\partial x_j} = -\frac{1}{\rho} \frac{\partial \overline{p}}{\partial x_i} + \nu \frac{\partial^2 \overline{u_i}}{\partial x_j^2} + g_i \quad (3.8)$$

$$\frac{\partial \overline{T}}{\partial t} + \overline{u_j} \frac{\partial \overline{T}}{\partial x_j} + \frac{\partial \overline{u'_j T'}}{\partial x_j} = \frac{\lambda}{\rho C_p} \frac{\partial^2 \overline{T}}{\partial x_j^2} \quad (3.9)$$

The RANS momentum equation introduces new unknowns.  $\overline{u'_i u'_j}$  are called the Reynolds stresses and together form the Reynolds stress tensor ( $\tau_{ij}$ ). This tensor is symmetric so that there are only six independent unknowns and not nine.  $\overline{u'_j T'}$  is the turbulent heat flux. These two terms translate the effects of fluctuations on the mean flow. Thus, the RANS equations form an under-constrained system as there are more unknowns than equations. Eq. 3.8 and Eq. 3.9 (Appendix G) show that the determination of the mean velocity ( $\overline{u_i}$ , first order) necessitates the knowledge of the Reynolds stress tensor ( $\overline{u'_i u'_j}$ , second order) and the determination of  $\overline{u'_i u'_j}$  neces-



sitates the knowledge of  $\overline{u'_i u'_j u'_k}$  (third order). Hence, because of the non-linearity of the momentum conservation equation, the  $n$ -th order correlation is always coupled with the  $(n+1)$ -th order correlation. As a consequence, resolving independently the  $n$ -th and  $(n+1)$ -th orders equations requires assumptions about the unknowns, especially for  $\overline{u'_i}$  and for  $\overline{u'_i u'_j}$ . Therefore, RANS computational methods are based on turbulence models. The Reynolds heat flux is generally modeled similarly. Two categories of RANS turbulence models are generally used.

- First order models carry two additional equations. They generally take into account an equation for the turbulent kinetic energy ( $k$ ) and another for the dissipation rate ( $\varepsilon$ ) or the specific dissipation rate ( $\omega$ ). The corresponding models are called  $k$ - $\varepsilon$  and  $k$ - $\omega$  models.
- Second order models carry seven additional equations. They take into account an equation for each Reynolds stress and another one for  $\varepsilon$ . Corresponding models are called  $\overline{u'_i u'_j}$ - $\varepsilon$  or Reynolds stress models (RSM).

### The Boussinesq assumption

The Boussinesq assumption makes the analogy between the molecular viscosity and a turbulent viscosity. To model the effects of fluctuations on the mean flow, this model considers a turbulent viscosity, or eddy viscosity:  $\mu_t$ .  $\mu_t$  links the Reynolds flux to the mean velocity gradient. This term assumes that the Reynolds stress tensor ( $\tau_{ij}$ ) is a linear function of the trace-less mean strain rate tensor ( $S_{ij}^*$ ). Hence, this model does not involve differential equations but an algebraic equation, as follows (Ansys Fluent, 2013a):

$$-\rho \overline{u'_i u'_j} = \mu_t \left( \frac{\partial \overline{u_i}}{\partial x_j} + \frac{\partial \overline{u_j}}{\partial x_i} \right) - \frac{2}{3} \rho k \delta_{ij} \quad \equiv \quad \tau_{ij} = 2\mu_t S_{ij}^* - \frac{2}{3} \rho k \delta_{ij} \quad (3.10)$$

The temperature fluctuation  $T'$  is assumed advected like the velocity fluctuation  $u'_j$ .  $\overline{u'_j T'}$  is thus related to the mean temperature gradient by a linear function, whose slope depends on  $\mu_t$ :

$$-\overline{u'_j T'} = \frac{\mu_t}{Pr_t} \frac{\partial \overline{T}}{\partial x_j} \quad (3.11)$$

with  $Pr_t$ : the turbulent Prandtl number.

In order to solve the mean velocity and temperature fields, turbulence models based on the Boussinesq assumption aim thus to express  $\mu_t$  as a function of the other problem unknowns.

### $k$ - $\varepsilon$ models

First order models only consider the turbulent kinetic energy  $k = \overline{u'_i u'_i}$  and therefore the diagonal elements of the Reynolds stress tensor. In particular,  $k$ - $\varepsilon$  models are semi-empirical and rely on phenomenological considerations and empiricism (Ansys Fluent, 2013a). In the standard  $k$ - $\varepsilon$  ( $Sk$ - $\varepsilon$ ) model, the transport equation for  $k$  is derived from the exact equation, whereas the transport equation for  $\varepsilon$  differs from the exact one. Appendix G gives the corresponding equations. This class of models is suitable for use only for fully turbulent flows, in which cases the effects of molecular viscosity are negligible.

This model benefits from a good numerical stability and is easy to implement. The equation for the mean velocity is structured as the usual NS equation. However,  $\mu_t$  is assumed as an isotropic scalar quantity. Estimating correctly its value is challenging as it is a *a priori* variable. In  $k$ - $\varepsilon$  models, this term is a function of  $k$  and  $\varepsilon$ :

$$\mu_t = \rho C_\mu \frac{k^2}{\varepsilon} \quad (3.12)$$

With:  $\left\{ \begin{array}{l} \mu_t : \text{the turbulent viscosity } [\text{s}^{-1}], \\ C_\mu : \text{a model parameter}, \\ k : \text{the turbulent kinetic energy } [\text{m}^2 \cdot \text{s}^{-2}], \\ \varepsilon : \text{the turbulent dissipation rate } [\text{m}^3 \cdot \text{s}^{-2}]. \end{array} \right.$

The  $Sk$ - $\varepsilon$  model assumes a constant value for  $C_\mu$ , which can lead to some mathematical and numerical inconsistencies. Therefore, different variants were proposed to improve its performance. The realizable  $k$ - $\varepsilon$  ( $Rk$ - $\varepsilon$ ) model is one of them and considers  $C_\mu$  variable. In addition, the equation for  $\varepsilon$  derives from the exact equation for the mean square velocity fluctuation ([Ansys Fluent, 2013a](#)). Appendix G gives the corresponding equations. Due to its improved formulation compared to the  $Sk$ - $\varepsilon$  model, the  $Rk$ - $\varepsilon$  model satisfies some mathematical constraints, and is theoretically in better agreement with physics. According to [Ansys Fluent \(2013a\)](#), the  $Rk$ - $\varepsilon$  model performs better than the  $Sk$ - $\varepsilon$  in cases of channel, boundary layers and separated flows.

### Reynolds stress models

As an alternative approach to isotropic turbulence models, second order models take into account the turbulence anisotropy by solving an equation for each independent term of the Reynolds stress tensor. Appendix G provides the corresponding equations. Six terms are involved, each of which translating a specific phenomenon such as production or dissipation. Half of the exact equation terms (Eq. .38) are solved, whereas the remaining terms are modeled in order to close the system of equations. Because of their more detailed formulation, second order turbulence models are theoretically more accurate than two-equations models. According to [Ansys Fluent \(2013a\)](#), such models perform better than first order models when turbulence anisotropy substantially affects the mean flow, such as in swirling flows or stress driven secondary flows. However, literature shows that they do not necessarily give better results than simpler models due to the assumptions made in the modeled terms of the equation.

Despite some well known limits,  $k$ - $\varepsilon$  models are far more often used than the RSM in environmental wind engineering as they are generally understood to be quite efficient, more stable and require less computational resources. Their specific accuracy is discussed in Sec. 3.1.3.2.

Hereafter, the Cartesian coordinate system is considered, and the following notations are used:

- $x, y, z$ : the spatial coordinates, corresponding to the above mentioned  $x_i$  ( $x$  oriented stream-wise,  $y$  spanwise and  $z$  upwards);

- $U, V, W$ : the mean velocity components respective to the  $x, y$  and  $z$  directions and corresponding to  $\overline{u_i}$ ;
- $k$ : the turbulent kinetic energy;
- and  $\varepsilon$ : the turbulent dissipation rate.

### 3.1.2.3 Near wall treatment

In addition to the mass flow modeling, additional laws are required to describe the flow behavior at the domain boundaries, and especially near walls. The different flow variables experience large gradients in these regions. Based on experimental observations, Appendix H.1 gives the law-of-the-wall that governs the evolution of the momentum next to a non-slipping wall depending on the dimensionless wall unit ( $z^+$ ), which depends on the friction velocity  $u_t$  according to:

$$z^+ = \frac{\rho u_t z}{\mu} = \frac{z}{\nu} \sqrt{\frac{\tau_w}{\rho}} \quad (3.13)$$

with:  $\left\{ \begin{array}{l} \rho : \text{the fluid density } [\text{kg} \cdot \text{m}^{-3}], \\ u_t = \sqrt{\frac{\tau_w}{\rho}} \text{ the friction velocity } [\text{m} \cdot \text{s}^{-1}], \\ \tau_w : \text{the wall shear stress } [\text{N} \cdot \text{m}^{-2}], \\ z : \text{the distance to the wall } [\text{m}], \\ \mu : \text{the fluid dynamic viscosity } [\text{kg} \cdot \text{m}^{-1} \cdot \text{s}^{-1}]. \end{array} \right.$

The boundary layer velocity profile evolves as a function of  $z^+$  from a linear correlation close to the surface, i.e. in the laminar region of the flow ( $z^+ < 4$ ), to a logarithmic correlation in the turbulent region of the flow ( $z^+ > 50$ ). In between ( $4 \leq z^+ \leq 50$ ), a buffer zone is observed.

CFD models consider the height of the first cell ( $z_p$ ) to evaluate  $z^+$  and thus the flow regime to model. However, in the commercial software Ansys Fluent,<sup>1</sup>  $z^*$  is considered rather than  $z^+$ . Its formulation is given by (Ansys Fluent, 2013a):

$$z^* = \frac{\rho C_\mu^{1/4} k_p^{1/2} z_p}{\mu} = \frac{u^* z_p}{\nu} \quad (3.14)$$

with:  $\left\{ \begin{array}{l} \rho : \text{the fluid density } [\text{kg} \cdot \text{m}^{-3}], \\ u^* = C_\mu^{1/4} k_p^{1/2} : \text{the friction velocity based on } k [\text{m} \cdot \text{s}^{-1}], \\ C_\mu = \text{a model parameter}, \\ k_p : \text{the turbulent kinetic energy in the first cell } [\text{m}^2 \cdot \text{s}^{-2}], \\ z_p : \text{the first cell height (middle) } [\text{m}], \\ \mu : \text{the fluid dynamic viscosity } [\text{kg} \cdot \text{m}^{-1} \cdot \text{s}^{-1}]. \end{array} \right.$

---

<sup>1</sup><http://www.ansys.com/Products/Simulation+Technology/Fluid+Dynamics/Fluid+Dynamics+Products/ANSYS+Fluent>

As it takes into account the turbulent kinetic energy at the first cell ( $k_p$ ) and not  $\mu_t$ ,  $z^*$  differs from the usual  $z^+$ . For an equilibrium boundary layer, the difference between  $z^+$  and  $z^*$  is negligible and  $\sqrt{\tau_w/\rho} \approx C_\mu^{1/4} k^{1/2}$ . However, according to Defraeye et al. (2012),  $\tau_w$  can become zero in stagnation and reattachment points. Consequently,  $z^+$  becomes 0, which may be problematic for the design of the mesh and the computation of near-wall flow properties using wall-functions if based on  $z^+$ .

Very fine meshes may involve very small values of  $z^*$ , i.e  $z^* \approx 1$ . In such configurations, a low Reynolds number modeling (LRNM) approach may apply and the flow can be solved down to the wall. This approach involves a modification of the turbulence model as the laminar flow region close to the wall is solved.

For urban applications, it is generally not possible to use such fine grids as the depth of the laminar boundary layer is about  $10^{-4}$  m (Blocken, 2014b). In urban models,  $z^+$  or  $z^*$  values are much higher and often overcome  $5 \times 10^2$  even  $1 \times 10^3$ . Such cases require the use of wall-functions, which generally use a semi-empirical formulas to bridge the viscous and buffer sub-layers that are located between the wall and the fully turbulent region of the boundary layer. Wall-functions are based on the law-of-the-wall and apply for mean velocities and other passive scalars. Other formulas are involved for near wall turbulent quantities (Ansys Fluent, 2013a). Wall-functions should preferably be used for  $5 \times 10^1 \leq z^* \leq 5 \times 10^2$  to  $10^3$ . Although being derived and primarily designed for equilibrium boundary layers, they were shown to perform satisfactorily when used around sharp-edged bluff bodies as well. This is because such complex flows mainly depend on the macroscopic mass flow behavior.

Several models of wall-functions exist, but the most used are standard wall-functions. To compute the velocity at the first cell ( $U_p$ ), Fluent uses the dimensionless velocity formulation ( $U^*$ ) given by:

$$U^* = \frac{U_p C_\mu^{1/4} k_p^{1/2}}{\tau_w/\rho} = \frac{U_p u_p^*}{u_{t,p}^2} \quad (3.15)$$

To integrate the different flow regimes, the correlation used to compute  $U^*$  depends on  $z^*$ . A laminar linear relationship applies for low  $z^*$  while a logarithmic law is considered for higher  $z^*$ . The correlations used are respectively (Ansys Fluent, 2013a):

- For  $z^* < 11.25$ :

$$U^* = z^* \quad (3.16)$$

- For  $z^* > 11.25$ :

$$U^* = \frac{1}{\kappa} \times \ln(E z^*) \quad (3.17)$$

with:  $\begin{cases} \kappa = 0.418 : \text{the von Kármán constant,} \\ E \approx 9.74 : \text{the smooth log-law constant according to Appendix H.} \end{cases}$

Note that Eq. 3.16 and Eq. 3.17 are valid for smooth walls. To account for wall roughness, Fluent implements the equivalent sand grain model. According to experiments undertaken for roughened pipes, roughness effects do not change the slope of the log-law-of-the-wall, but modify its intercept. As a consequence an additional term is considered in the wall-function. The correlation actually used when  $z^* > 11.25$  (Ansys Fluent, 2013b) is thus:

$$U^* = \frac{1}{\kappa} \times \ln(E z^*) - \Delta B \quad (3.18)$$

$\Delta B$  is a roughness function that was found to be well correlated with the physical roughness height  $K_s$ . For more details, Appendix H.2 develops its expression depending on the flow regime.

### 3.1.3 State of the art of steady RANS modeling for building aerodynamics

#### 3.1.3.1 Best practices: modeling and validation

Usual RANS approaches are based on some physical, mathematical and numerical assumptions, and use empirical constants and relationships. These models were not primarily developed for urban environmental studies but for industrial applications involving quite high Mach numbers ( $Ma$ ) and confined flows. Moreover, outcomes are very sensitive to the modeling strategy and input parameters that are set by the modeler. In particular, inaccuracies in CFD models can be related to the overall model settings and assumptions, including the computational method, turbulence model, the inflow and boundary conditions as well as the physical accuracy of the model. Additional errors occur because of the numerical resolution of the flow, which uses spatial and temporal discretizations and different numerical resolution schemes. Tab. 3.1 synthesizes these different sources of uncertainties and errors. As a consequence, models have to be carefully validated and verified before being used to produce reliable results (Schatzmann and Leitl, 2011).

As performing reliable CFD studies using steady RANS models for urban environmental purposes is not straightforward although rather easily accessible, best practice guidelines were established in order to help modelers. Guidance especially addresses pedestrian level wind conditions. They were either based on literature reviews (COST-Action and 732, 2007), specific benchmarks (Tominaga et al., 2008), or expertise (Blocken, 2014b; Blocken and Gualtieri, 2012).

These best practices guidelines include recommendations about the domain size, mesh resolution, turbulence model, boundary conditions, numerical schemes and convergence criteria to be used as well as advice relative to the validation study. A synthesis of some of them is given hereafter. Fig. 3.2 synthesizes recommendations relative to the modeling of the computational domain.

- The domain should be extended by 5 H upstream, from the sides and above the model, and 15 H downstream, H being the obstacle height. Moreover, the total blockage ratio ( $BR_{tot}$ ) should be less than 5 % and the directional  $BR_{dir}$  (vertical:  $BR_v$ , horizontal:  $BR_H$ ) should preferably respect the relative dimensions of the model, with  $BR_H, BR_v \leq 17$  to 22 %.

Type	Uncertainties linked with the physical modeling	Errors due to the numerical resolution
Origin	Assumptions and simplifications done in the mathematical description of the physical problem.	Assumptions and simplifications done in the numerical resolution of the mathematical problem.
Sources	<ul style="list-style-type: none"> <li>- Physical simplification,</li> <li>- Use of previous data,</li> <li>- Geometric boundary conditions,</li> <li>- Physical boundary conditions,</li> <li>- Initialization.</li> </ul>	<ul style="list-style-type: none"> <li>- Computational implementation,</li> <li>- Numerical rounds-off,</li> <li>- Spatial discretization,</li> <li>- Temporal discretization,</li> <li>- Iterative convergence, residuals.</li> </ul>

Table 3.1: Origin and sources of errors and uncertainties in CFD models. (Adapted from (COST-Action and 732, 2007))

- The mesh should be refined in regions where high flow gradients occur, and the minimum grid resolution requires that the building length scale is divided into ten cells. The evaluation height should be located in the third cell from the ground at least, and the stretching ratio between two consecutive cells should not overcome 1.3. A grid sensitivity analysis has to be also performed to assess the effects of the spatial discretization on the solution.
- Because the  $Sk-\varepsilon$  model cannot properly reproduce the separated and reversed flows on the roof, revised  $k-\varepsilon$  models and differential stress models should preferably be used.
- Consistent inflow and domain boundary conditions, especially at the bottom of the computational domain, should be used to ensure the quality of the modeled ABL. Recommendations given by Richards and Hoxey (1993) and Richards and Norris (2011) can be used. Appendix I gives the related inflow conditions. Other inflow conditions were proposed by Tominaga et al. (2008). For the downstream boundary condition, a zero normal gradient for all variables should preferably be set. If the domain is large enough, the effects of the lateral and top boundary conditions on the computation results are negligible. Symmetry conditions can be specified.
- First order upwind numerical schemes are too diffusive to produce sufficiently accurate results. Consequently, higher numerical schemes have to be used to compute the solution.
- Further than checking the drop in scaled residuals as usually proposed by commercial softwares, the iterative convergence of the solver should be confirmed by monitoring some flow variables or examining specific contours at different steps of the computation to verify that the solution does not change anymore.
- A validation study for at least one case of single building as well as one case of a group of buildings (building complex) should be performed. The best way would be to compare numerical results with corresponding experimental data if possible.

The validation step is particularly demanding. It basically consists of a detailed comparison between numerical predictions and experimental data. In order to be valuable for model validation, experimental data sets have to respect completeness and accuracy requirements (Leitl,

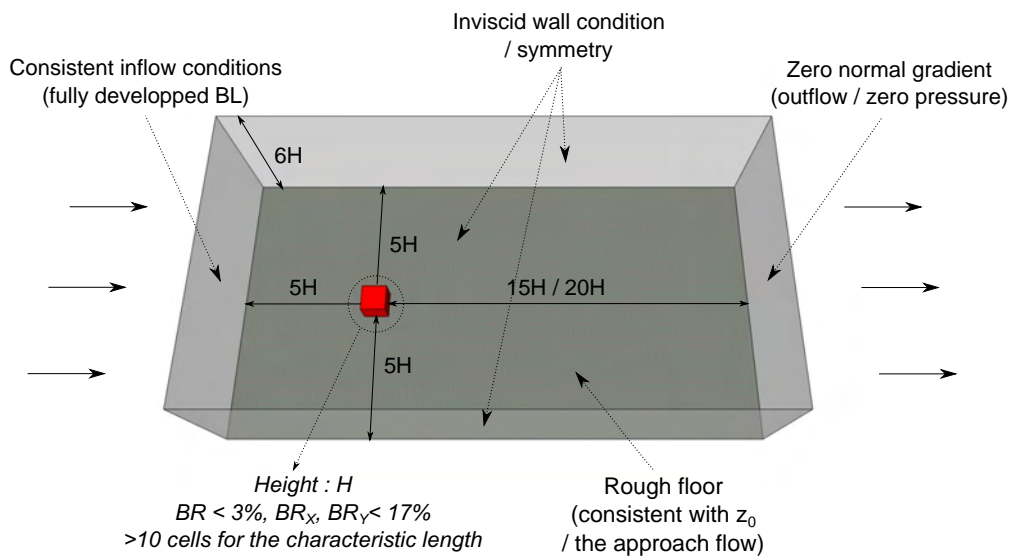


Figure 3.2: Best practice guidelines for the CFD modeling of the pedestrian wind environment around buildings.

2000). As shown in Sec. 1.2.2, reduced-scale wind-tunnel tests can provide high quality data sets for this purpose. These include, among others, the providing of detailed data of mean velocity components and turbulence properties for the approach flow, a comprehensive and high resolution flow field around obstacles, as well as concentration values for dispersion models.

If any wind-tunnel experiment or experimental reference exist for the configuration under investigation, it is possible to carry out a sub-configuration model validation. This technique compares the model outputs for different physical configurations that are together representative of the actual model (Blocken and Carmeliet, 2008). For each sub-configuration, some detailed experimental data sets are generally available as they mostly refer to generic building or urban configurations such as isolated cubes or cuboids, street canyons or arrays of cuboids.

### 3.1.3.2 Performance and applicability

Urban CFD studies often aim at investigating wind conditions at pedestrian level (Stathopoulos, 2006) or dispersion processes within the urban canopy layer (Coccal et al., 2014; Lateb et al., 2010). They can also provide more appropriate boundary conditions for building energy models (Allegrini et al., 2012a; Bouyer et al., 2011) and information about the natural ventilation of buildings and urban blocks (Hooff and Blocken, 2010; Moonen et al., 2011). They are therefore useful for many urban problems. However, because of their intrinsic physical and mathematical assumptions, steady RANS models present some significant limitations.

Even considering revised turbulence models such as the  $Rk-\varepsilon$  model, they generally fail to reproduce well the cavity zone downstream obstacles. Reattachment zones are simulated further downstream than experimentally observed (see Sec. 3.4). Furthermore, considering different geometric models including complex urban configurations, Yoshie et al. (2007) and Tominaga



and Stathopoulos (2010) showed that if two equations models satisfactorily perform in predicting high wind speed regions, they are generally not accurate in reproducing recirculation phenomena in the wake of buildings. This may be due to their incapacity to reproduce the vortex shedding. In addition, RANS models assume the existence of a mean flow in a statistical sense, which might not be effective in complex configurations. The distinction between long time scale turbulence phenomena and mean flow structures is also not obvious.

Steady RANS models make thus important assumptions on the flow behavior although flow unsteadiness and other turbulent features were shown to affect different aerodynamic processes. These processes especially include the ventilation potential of urban spaces (Moonen et al., 2012b), dispersion problems (Gorlé et al., 2010; Gousseau et al., 2011; Tominaga and Stathopoulos, 2010, 2011) and structural wind loads (Stathopoulos, 2006). The fluctuating contribution on these processes is not reproduced by steady RANS models. Therefore steady RANS methods might not be sufficiently accurate for the study of some urban problems. However, it is worth mentioning that most of the different studies dealing with the performance of steady RANS models and comparing their accuracy with e.g. LES predictions consider  $k-\epsilon$  models and not RSM, while flow anisotropy is often stressed to be important (Gorlé et al., 2010; Panagiotou et al., 2013). According to their formulation, second order turbulence models might provide better predictions than first order models. However, it still remains under discussion and only few studies discuss its applicability.

Hence, because they involve shortcomings, steady RANS-based CFD studies require quality assurance and caution in their analysis and post-processing. Although LES is increasingly used, it still involves too much computational resources to be generally performed. They are still mainly used for research purposes on rather simple configurations. New LES approaches based on the lattice Boltzmann method (LBM, see Sec. 3.2.2) are promising as they enable a very cost effective implementation (Obrecht et al., 2013). However, being more detailed, LES approaches bring to light new problems. In particular, the formulation of their boundary conditions is challenging while often being as important as the mass flow model in CFD studies. As a consequence, being relatively efficient, steady RANS methods remain relevant to study urban physics problems as far as their implementation is rigorous and their applicability well specified.

## 3.2 Validation test cases

### 3.2.1 Reference wind-tunnel tests

A compilation of experimental data for the validation of dispersion models (CEDVAL) was developed by the Environmental Wind Tunnel Laboratory of the Meteorological Institute of Hamburg University (CEDVAL, 2013). This database provides extensive and high quality data sets with a detailed documentation for several geometric models. The CEDVAL database is mostly oriented towards the validation of steady RANS models.<sup>2</sup>

---

<sup>2</sup>The CEDVAL-LES database is currently developed for the validation of LES models (CEDVAL-LES, 2014).



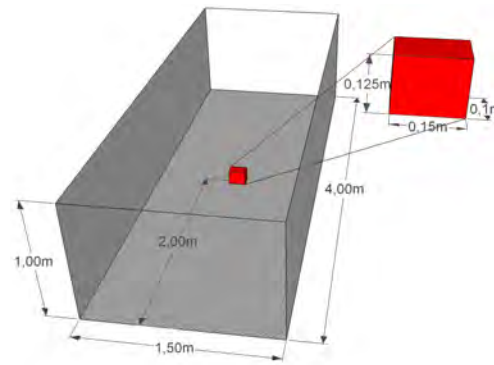


Figure 3.3: Reference wind-tunnel model: the isolated rectangular block (A1-1 case).

Two physical configurations are examined in the current validation study: an isolated rectangular block (A1-1 case of the CEDVAL) and an array of  $3 \times 7$  rectangular blocks (B1-1 case of the CEDVAL). Both models are immersed in a neutrally stratified boundary layer. They present similar test parameters, including the model scale of 1 : 200. Experiments were undertaken in the Blasius wind-tunnel ([Meteorological Institute of Hamburg, 2013](#)). It is a small conventional type boundary layer wind-tunnel whose test section is 4 m long (x-axis), 1.5 m wide (y-axis) and 1 m high (z-axis). Fig. 3.3 and Fig. 3.4 give the two geometric configurations under study and Appendix J provides the sketch of the wind-tunnel.

The experimental boundary layer was modeled using modified Standen spires and uniform LEGO roughness on the floor. According to the experimental documentation, the lower part of the boundary layer profile (approach flow) followed a power law with  $\alpha = 0.21$ . It also corresponds to a log-law profile with  $u^* = 0.377 \text{ m} \cdot \text{s}^{-1}$  and  $z_0 = 7 \times 10^{-4} \text{ m}$ . The elementary obstacle dimensions are 0.15 m (y-axis), 0.1 m (x-axis) and 0.125 m (H, z-axis). As a consequence, the Reynolds number of the tests based on the obstacle height is  $3.725 \times 10^4$ .

The CEDVAL provides high resolution flow measurements for the approach flow and the actual tests with the obstacles. Measurements were taken using a Prandtl tube for the reference velocity and 2D laser Doppler velocimeter for the measured velocities.<sup>3</sup> They are especially detailed for the streamwise middle plane ( $y = 0 \text{ m}$ ) as well as for an horizontal plane ( $z = 0.28 H$  for the A1-1 case and  $z = 0.5 H$  for the B1-1 case). The current validation study mainly focuses on the plane  $y = 0 \text{ m}$ . Next to the obstacles of interest, measurements are reported with a spatial resolution of  $1 \times 10^{-2} \text{ m}$ . Further away, the resolution is coarser ( $1.5$  or  $2 \times 10^{-2} \text{ m}$ ).

Note that for the B1-1 case, the experimental documentation emphasizes the effects of the finite width and length of the array and a very intermittent behavior of the flow with no stable recirculation areas. Because of this unsteady behavior, long averaging times of more than five

---

<sup>3</sup>Experimental errors / precision:

	Probe location <sub>/x,y</sub>	Probe location <sub>/z</sub>	Reference velocity	Measured velocity
A1-1 case	$\leq 10^{-4} \text{ m}$	$\leq 10^{-4} \text{ m}$	$1 \times 10^{-1} \text{ m} \cdot \text{s}^{-1}$	$1 \times 10^{-2} \text{ m} \cdot \text{s}^{-1}$
B1-1 case	$2 \times 10^{-4} \text{ m}$	$5 \times 10^{-5} \text{ m}$	$7 \times 10^{-2} \text{ m} \cdot \text{s}^{-1}$	$2 \times 10^{-2} \text{ m} \cdot \text{s}^{-1}$

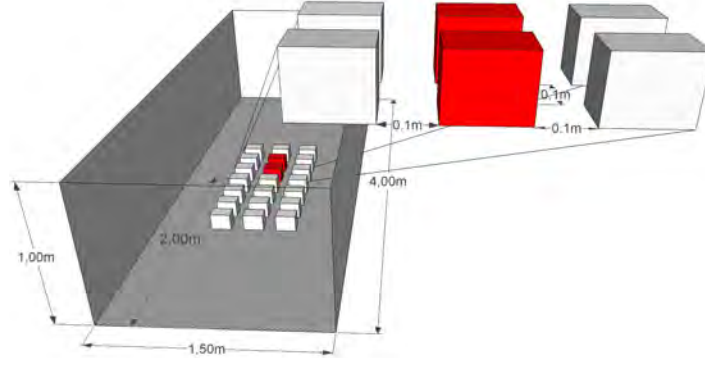


Figure 3.4: Reference wind-tunnel model: the array of rectangular blocks (B1-1 case).

minutes at the model scale were considered in order to get a repeatability of the tests better than 5 % for the flow and concentration fields, and deduce the mean flow field (CEDVAL, 2013).

### 3.2.2 Reference LBM LES simulations

The LBM LES is an innovative CFD approach, which does not directly rely on the resolution of the NS equations. This method is generally interpreted as a discrete version of the Boltzmann transport equation, as follows :

$$\partial_t f + \xi \cdot \nabla_x f + \frac{\mathbf{F}}{m} \cdot \nabla_\xi f = \Omega(f) \quad (3.19)$$

with:  $\begin{cases} f(\mathbf{x}; \xi; t) : \text{the evolution in time of the distribution of one particle in phase space,} \\ \frac{\mathbf{F}}{m} : \text{the external force field per unit of particle mass,} \\ \Omega : \text{the collision operator.} \end{cases}$

Discretization occurs both in phase space and time with a constant time step  $\delta t$ . A regular orthogonal lattice of elementary size  $\delta x$  is used together with a finite set of  $(n + 1)$  particle velocities  $\xi_\alpha$  with  $\xi_0 = \mathbf{0}$ .

Hence, the LBM LES method uses a quite different approach to describe the flow than steady RANS methods and usual NS-based LES approaches. It is based on a mesoscopic viewpoint and computes particles evolution in time and space (propagation and collision processes). Similarly with NS-based LES methods, the LBM LES solves the larger scales of turbulence, which are mostly determined by the geometry of the model, and models the smaller ones. The model used in this study has previously been validated by comparison with wind-tunnel data sets. Because of its formulation, this method is inherently parallel and benefits from a good numerical stability (Obrecht et al., 2014, 2011b).

Simulations were performed in the CETHIL, using a multi-GPU LBM solver, which has been developed in the laboratory (Obrecht, 2012; Obrecht et al., 2011a, 2013). With these computational configuration and numerical implementation, it is possible to run very large scale and high resolution simulations on rather inexpensive hardware.

For current validation purposes, the general settings of the model were specified to correspond to the experimental conditions considering the relative dimensions of the test section and the Reynolds number of  $3.725 \times 10^4$ . Inlet conditions were set so as to reproduce a mean velocity profile that follows the experimental power law. Only smooth walls were modeled because of numerical implementation constraints. The computational domain was discretized into more than  $2.06 \times 10^8$  nodes for the both cases. This corresponds to a physical lattice unit of 3.125 mm. The isolated obstacle in the A1-1 case and the fifth obstacle of the middle row in the B1-1 case were centered 2 m downstream the inlet plane. The latest  $1.28 \times 10^6$  time steps were kept for post-processing. Simulation outputs were summed up every 64 time steps for averaging. This corresponds to  $2 \times 10^4$  samples. Additional simulations were also run considering:

- an empty domain;
- a shorter upstream length for the A1-1 case (fetch = 3 H);
- and a doubled averaging time for the B1-1 case ( $2.56 \times 10^6$  time steps).

A video displaying the evolution in time of the simulated flow was also made for the B1-1 case. The dynamics of the different flow structures developing in the planes  $y = 0$  m and  $z = 0.5$  H can thus be observed.

### 3.2.3 Steady RANS models

Steady RANS simulations were performed using the commercial software ANSYS Fluent 14.5 (Ansys Fluent, 2013b) and a double socket hexacore<sup>4</sup> computation server running Microsoft Windows. Two turbulence models are especially evaluated because of their more detailed formulation than that of the  $Sk-\varepsilon$  and considering previous studies carried out in our laboratory. They are:

- the realizable  $k-\varepsilon$  model ( $Rk-\varepsilon$  model);
- and the Reynolds stress model (RSM).

As the RSM is less used than isotropic eddy viscosity models, less developments and critical studies are available. Its accuracy for external aerodynamics should be investigated further. After some preliminary simulations and to enable straightforward comparisons to be done, the same modeling strategy was implemented for both RANS models.

Meshes were automatically generated using Workbench, the mesher provided together with Fluent, replacing Gambit. The meshing algorithm propagates the linear and surfacic dimensioning specified on the edges and surfaces of interest, especially located at the bottom of the computational domain and on the obstacles. The maximum growth rate of the mesh is 1.1.

For computation, pressure and velocity are coupled using the SIMPLE scheme. Pressure interpolation is of second order. Other discretization schemes were third order MUSCL but additional simulations were run using the second order upwind scheme. For the RSM, the linear pressure strain correlation formulation is used since first tests showed a worse performance of the quadratic

---

<sup>4</sup>CPUs: 2 Intel Xeon X5690 CPU @ 3.47Ghz processors, 6 cores each.

model. Standard wall-functions (Launder and D.B., 1974) were used as first results also showed no significant improvement of the computed flows when using other types of wall-functions.

The ABL (inlet conditions) was designed using preliminary simulations of a long tunnel for both turbulence models. The domain length was taken to be ten times the length of the experimental test section, i.e.  $10 \times 4 = 40$  m, so that the flow can freely develop over a long distance. The computational domain was spatially discretized into more than  $2.1 \times 10^6$  regular control volumes. The mesh was refined near the floor, down to 1.25 cm high. This corresponds to 1/10 of the actual obstacle height, and involves  $z^* \approx 1.44 \times 10^2$  on the floor. The top, side and bottom boundary conditions were set so as to model those of the wind-tunnel test section: the bottom surface was specified as a rough wall, and a no-slip smooth wall condition (zero roughness height) was assigned to the top and side boundaries. A constant velocity inlet was set as inflow and a zero streamwise gradient condition (outflow) was imposed to flow characteristics at the outlet.

Several mean velocity profiles were monitored along the domain center line during the computation. They were post-processed using Matlab.<sup>5</sup> The solution iterative convergence was assumed to be reached when profiles did not vary during at least  $1.5 \times 10^3$  iterations. Profiles were checked each  $5 \times 10^2$  iterations. The boundary layer development along the tunnel was also studied and the mean velocity profiles were compared to CEDVAL data.

After several tests, a combination of inflow properties and roughness features yields a mean profile that matches the experimental approach flow. The equivalent roughness height ( $K_s$ ) is 0.0042 m and  $C_s = 0.625$ .  $K_s$  is lower than two times the height of the first cell but six times the experimental roughness length ( $z_0$ ), which is given equal to  $7 \times 10^{-4}$  m. This is rather small compared to theory as it is expected to be of one order of magnitude higher than  $z_0$  (see Blocken et al. (2007a) and Appendix K.1). However, other computational and numerical factors than the roughness parameterization influence the approach flow profile, which may contribute to make the computational solution different from the theoretical one.

The curve fitting<sup>6</sup> of the RSM-based  $U$ -profile to a logarithmic law for  $z \in [0; 2]H$  gives ( $R^2 = 0.998$ ):

$$U(z) = \frac{0.3808}{0.418} \times [1207 \times z] = \frac{0.3808}{\kappa} \times \left[ \frac{z}{8.28 \times 10^{-4}} \right] \quad (3.20)$$

The identification of the parameters gives thus:

- $u^* = 0.3808 \text{ m} \cdot \text{s}^{-1} \neq 0.377 \text{ m} \cdot \text{s}^{-1}$  ( $\Delta u_{exp-CFD}^* = 1 \%$ );
- $z_0 = 8.28 \times 10^{-4} \text{ m} \neq 7 \times 10^{-4} \text{ m}$  ( $\Delta z_{0;exp-CFD} = 18 \%$ ).

On this basis, the actual relation between  $K_s$  and  $z_0$  is:

$$K_s = \frac{3.17}{C_s} \times z_0 \neq \frac{9.739}{C_s} \times z_0 \quad (3.21)$$

<sup>5</sup><http://fr.mathworks.com/>

<sup>6</sup>The fitting was performed using the curve fitting toolbox of Matlab, which uses the non-linear least square method.

This difference may be explained by the range of height considered in the fitting, and some additional considerations are further discussed in Appendix K.2. However, according to the approach flow profiles shown in Fig. 3.5, the simulated approach flow agrees well with the experimental one. It is thus kept for the actual simulations.

Mean velocity<sup>7</sup> and turbulence<sup>8</sup> profiles for an entire plane were recorded at  $x = 30$  m, which is located in the fully developed region of the mean flow in the lower part of the ABL. Note that the  $k$ -profile was not totally stabilized at this location. Moreover, its value ( $k \approx 0.25 \text{ m}^2 \cdot \text{s}^{-2}$ ) is smaller than the  $k$ -value given by the usual parameterization of an equilibrium ABL ( $k \approx 0.47 \text{ m}^2 \cdot \text{s}^{-2}$ , see Appendix I), and even more than the  $k$ -value that can be deduced from the measurements ( $k \approx 0.8 \text{ m}^2 \cdot \text{s}^{-2}$  according to [Gorlé et al. \(2009\)](#), or  $k \approx 0.55 \text{ m}^2 \cdot \text{s}^{-2}$  according to [Parente et al. \(2011\)](#)). Nevertheless, it is consistent with the turbulence model and computational configuration used. The recorded profile was then specified as inlet condition for the subsequent simulations.

In these actual simulations, the computational domain models the test section of the Blasius wind-tunnel. The rectangular block for the A1-1 case and the fifth block of the central row for the B1-1 case were centered in the middle of the domain ( $2 \text{ m} = 16H$  from the inlet plane). Obstacles were modeled as recesses in the fluid volume with smooth walls. The mesh was still refined near the floor, and even more on the obstacle(s) where high flow gradients occur. The domain was spatially discretized into more than  $2.55 \times 10^6$  tetrahedral cells for the A1-1 case and  $7.47 \times 10^6$  tetrahedral cells for the B1-1 case. With such meshes,  $z^* \approx 5.2 \times 10^1$  on the obstacles windward faces,  $z^* \approx 1.4 \times 10^1$  on the obstacles top faces and  $z^* \approx 3.2 \times 10^1$  (case A1-1) or  $z^* \approx 1.4 \times 10^1$  (case B1-1) on the obstacle rear faces. With the exception of the inflow conditions, numerical settings were kept identical to those described above for the design of the approach flow, including the near wall model (standard wall-functions).

Convergence was assumed to be reached when flow profiles along the domain center line did not vary during at least  $2 \times 10^3$  iterations. More than 15 locations in the plane  $y = 0 \text{ m}$  were checked for both models.

The solution grid independence was verified using a refined grid of more than  $3.90 \times 10^6$  cells for the A1-1 case and more than  $9.09 \times 10^6$  cells for the B1-1 case, which respectively correspond to 1.53 and 1.22 times the basic meshes. This is less than the factor 2 that is often considered but is limited by the first cell height, stretching ratio and available computational resources. Additional simulations for the empty domain and in cases of a rough and smooth floor were also performed for both turbulence models.

As such, the methodology and model settings respect the best practice guidelines given by [COST-Action and 732 \(2007\)](#); [Franke \(2006\)](#); [Tominaga et al. \(2008\)](#) in terms of mesh resolution and discretization schemes. Boundary conditions also respect literature recommendations.

---

<sup>7</sup>Mean velocity components:  $U, V, W$ .

<sup>8</sup>Turbulence characteristics:  $k, \varepsilon$  as well as  $u'u', v'v', w'w', u'v', v'w', u'w'$  for the RSM.

### 3.3 Comparison between numerical results and experimental data

#### 3.3.1 The modeled boundary layer

To study the effects of the modeled ABL and its implications in terms of incident flow, and because the reference LBM LES model accounts for smooth surfaces, the boundary layer development in the actual computational domain was studied thanks to the modeling of empty domains. Two configurations were tested:

- one configuration accounting for the rough bottom boundary condition ( $Ks = 4.2 \times 10^{-3} \text{ m}$ );
- and one configuration accounting for a smooth boundary condition ( $Ks = 0 \text{ m}$ ).

The previously simulated inflow conditions that fit the mean velocity profile of the experimental approach flow were specified as inlet conditions for each case.

Fig. 3.5 gives a comparison between the  $U$ -profiles of the experimental approach flow and the numerical incident flows. The location of the incident flow corresponds to that of the actual model (Blocken et al., 2007a), i.e. 2 m from the inlet plane in the current case. The reduced fetch of the LBM LES models is also reported.

In cases of steady RANS models with a rough floor (solid lines), the inlet and incident profiles match and correspond well to the experimental approach flow profile. This is consistent with the assumption of a fully developed mean flow. Note that the small discrepancy that can be noticed between the  $Rk-\varepsilon$  and RSM mean profiles was already discernible in the preliminary simulation of the inlet profile. As all the other parameters of the simulations are similar, this is due to the differences in the turbulence modeling.

By contrast, when modeling a smooth floor (dashed lines), a clear evolution of the mean velocity profile is observed. The flow adaptation to the floor smooth condition modifies the mean flow profile in the lower part of the domain as an internal boundary layer develops due to the virtual shift of roughness. For the three computational approaches reported, the flow speed is increased by up to  $0.75 \text{ m} \cdot \text{s}^{-1}$  at  $z = H/10$ . This height corresponds to the height of the first cell for RANS models and to four lattice units. At  $z = H/3$ , a wind speed increasing of  $0.23 \text{ m} \cdot \text{s}^{-1}$  is observed. These values correspond respectively to a 30 % and 7 % exceeding of the experimental flow speed. Inlet and incident flows profiles overlap at about  $z = 2H/3$ . The alteration of the mean velocity profile remains relatively weak above the subsequent obstacle height as numerical flow speeds are within 3.5 % of the experimental value up to  $z = 0.25 \text{ m} = 2H$  at least. Note that the particular shape of the LBM LES profile that corresponds to the configuration with the  $3H$  long fetch reflects the development of an internal boundary layer.

Hence, the smaller the considered height, the greater the difference between the experimental approach flow and the numerical incident flows due to the virtual shift of roughness. The concavity of the mean velocity profiles increases and the apex of the curvature moves lower. For both computational methods, the maximum deviation between the inlet and the incident flow profiles is found at  $H/10$ .

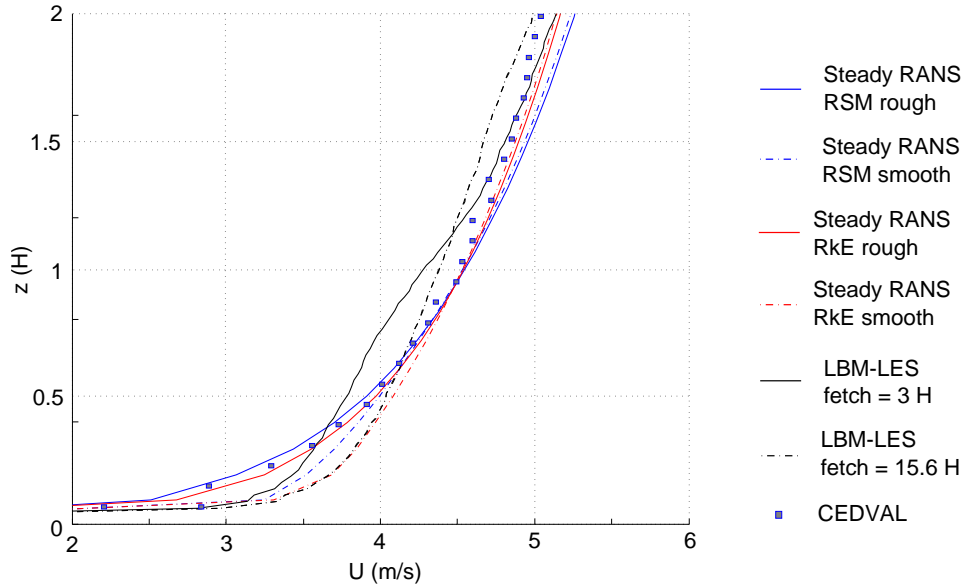


Figure 3.5: Comparison between the experimental approach flow and the numerical incident mean flow profiles depending on the computational approach and bottom boundary condition.

### 3.3.2 The rectangular block

In order to investigate the effects of the incident flow profile as well as roughness on computed flow structures around the obstacle, additional simulations were performed. Smooth floors were modeled in steady RANS configurations and a shorter fetch was considered in LBM LES models. This reduced fetch aims at limiting the alteration of the approach flow due to the virtual shift of roughness, as proposed in [Blocken et al. \(2007a\)](#). However, it is worth mentioning that if this could improve predictions upstream the obstacle, downstream flow features are still fairly influenced by the boundary layer development. Moreover, in the current case, the limited fetch extent also limits the development of turbulence. Seven cases are thus considered for further analysis:

- the steady RANS RSM model with a rough floor (RSM rough);
- the steady RANS RSM model with a smooth floor (RSM smooth);
- the steady RANS  $Rk-\varepsilon$  model with a rough floor ( $Rk-\varepsilon$  rough);
- the steady RANS  $Rk-\varepsilon$  model with a smooth floor ( $Rk-\varepsilon$  smooth);
- the LBM LES model with a limited fetch of  $0.375 \text{ m} = 3 \text{ H}$  (LBM LES short);
- the LBM LES model with the basic fetch of  $1.95 \text{ m} = 15.6 \text{ H}$  (LBM LES);
- the experiment (CEDVAL).

For steady RANS models, simulations were performed using both the third order MUSCL and the second order upwind interpolation schemes. Similar results were observed whatever the order of the numerical resolution scheme, with the exception of the RSM smooth model, for which the numerical convergence was not satisfactory. For this case, profiles in the wake do not stabilize and predictions substantially differ from the predictions obtained with the second order upwind



scheme whose convergence is better. It appears that the RSM model can carry some problems in its formulation when used with a zero roughness boundary condition and a third order resolution scheme. Predictions obtained using the second order upwind scheme are therefore kept for further analysis.

Fig. 3.6 shows the flow field in the plane  $y = 0$  m for each of the above mentioned cases, including the tests performed using the different orders of numerical scheme. All numerical simulations predict the three main flow structures that develop upstream, on the top and downstream the obstacle. Numerical predictions fairly match the experimental data next to the obstacle whereas the cavity zone is always predicted substantially wider than measured in the wind-tunnel. However, a more detailed examination of the 2D flow fields shows that the shapes, extents and locations of the different vortical structures that develop around the obstacle vary depending on the computational method and configuration. In particular, the cavity zone predicted by the  $Rk-\epsilon$  model is always the longest while the standing vortex is predicted too far upstream by the RSM rough model.

To investigate further the deviations observed for the different computational predictions and as made in Meroney et al. (1999), some features of the flow structures are more specifically examined. They correspond to the locations of the upwind vortex center (A), top recirculation center (B), wake vortex center (C), and downstream stagnation region (D). Fig. 3.7 as well as Tab. a.4 in Appendix L.1 compare numerical predictions and experimental data. Data relative to the experimental case are not directly derived from the CEDVAL database but taken from Meroney et al. (1999) because of the measurement grid resolution. Nonetheless, the drawing of 2D mean velocity streamlines based on experimental data shows similar results. Therefore, the related uncertainty is considered to be the resolution of the measurements, i.e.  $1 \times 10^{-2}$  m = 0.08 H near the obstacle and  $1.5 \times 10^{-2}$  m = 0.12 H further away.

All simulation data were post-processed and visualized using the free open-source application Paraview.<sup>9</sup> For LBM LES predictions, values were graphically determined using the mean velocity vectors field. As a regular and high resolution spatial discretization was used for the simulations, no data interpolation was needed. The related uncertainty is two cells, i.e.  $6.25 \times 10^{-3}$  m = 0.05 H. For RANS models, values were graphically determined using 2D streamlines in the plane  $y = 0$  m. Considering the mesh resolution and the complexity of the flow features, the related uncertainties are assumed to be at most two cells, i.e.  $6 \times 10^{-3}$  m  $\approx$  0.05 H, on the obstacle roof and one cell, i.e.  $12.5 \times 10^{-3}$  m = 0.1 H, next to the floor.

Note that despite being straightforward and often used to analyze flow fields, such a graphical 2D post-processing relies on a mathematical interpolation of discrete data and does not take into account the 3D features of the simulated flows. In the current case, the 3D features may be particularly significant in RSM simulations, in which complex 3D recirculation phenomena occur especially above the obstacle. However, the quantitative or detailed analysis of 3D flow properties using e.g. 3D streamlines is very demanding and their interpretation is not obvious. 3D flow

<sup>9</sup><http://www.paraview.org/>



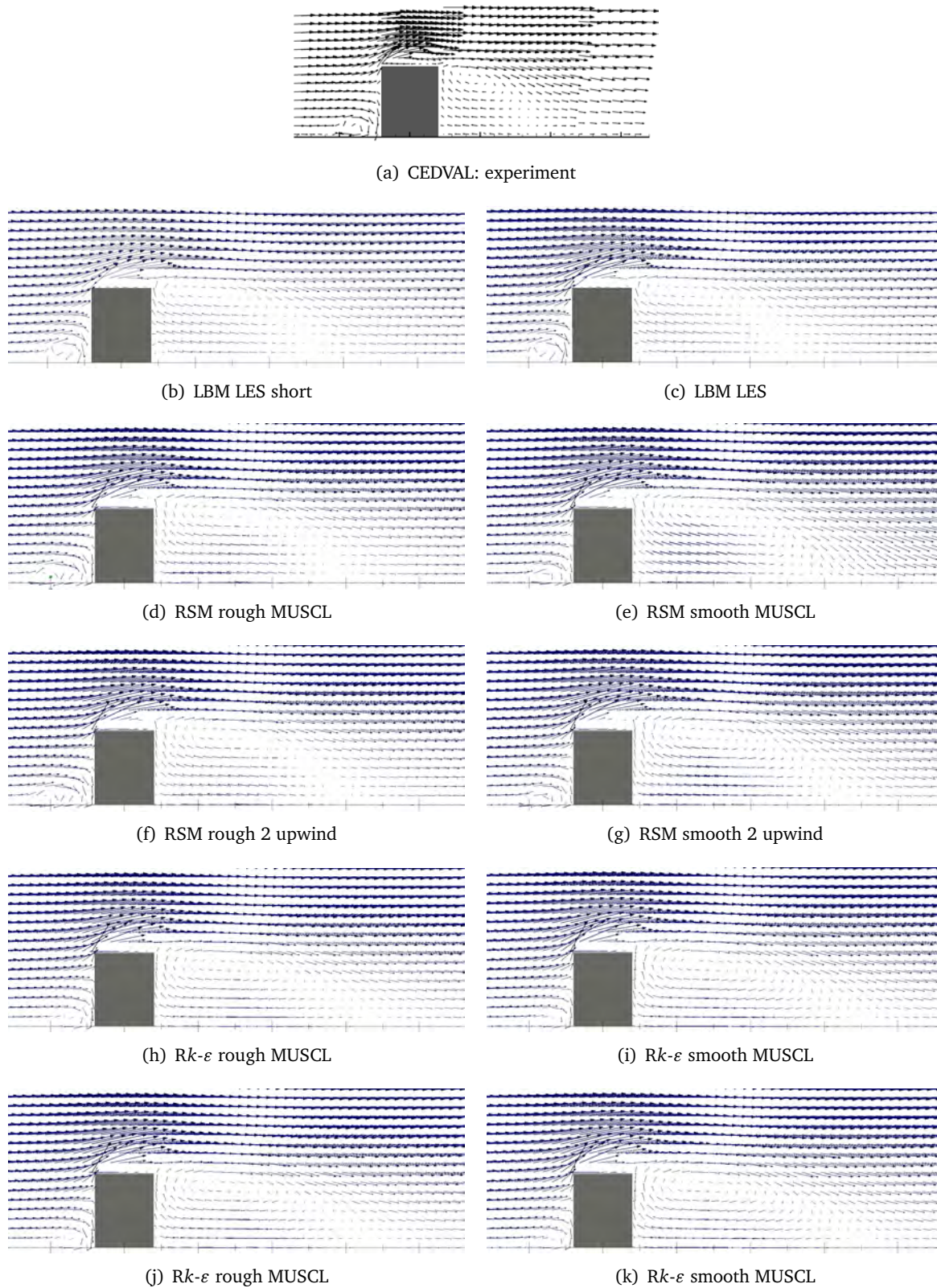


Figure 3.6: Comparison of the mean velocity field for the A1-1 case.

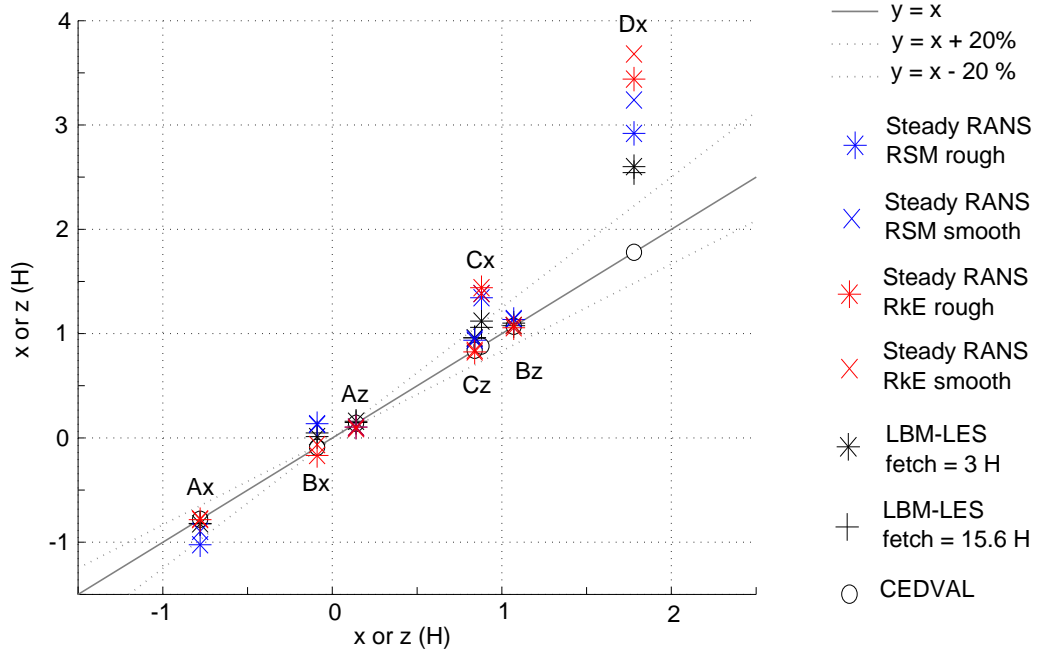


Figure 3.7: Comparison between the numerical and experimental characteristics of the flow structures around the obstacle.

features are therefore important to keep in mind when analyzing flow structures in theoretical symmetry planes.

To complete the analysis, Fig. 3.8 and Fig. 3.9 give a quantitative comparison of the  $U$  and  $W$ -profiles along seven vertical lines in the plane  $y = 0$  m. Those locations almost correspond to the abscissa of:

- the center of the upwind vortex simulated by the steady RANS RSM considering a rough floor:  $x = -1.06H \approx -1.02H$ ;
- the experimental standing vortex center:  $x = -0.82H \approx -0.79H$ ;
- the first third of the obstacle roof:  $x = -0.16H \approx -0.17H$ ;
- the two third of the obstacle roof:  $x = 0.16H \approx 0.17H$ ;
- the experimental downstream vortex center:  $x = 0.96H \approx 0.88H$ ;
- the experimental downstream stagnation point:  $x = 1.80H \approx 1.78H$ ;
- the downstream stagnation point simulated by the steady RANS RSM considering a rough floor:  $x = 2.88H \approx 2.92H$ .

The different analyses highlight the general better agreement between the LBM LES predictions and the experiment than between steady RANS results and the experiment, despite the smooth boundary condition. This is consistent with theory and corroborates the reference choice.

The comparison of the steady RANS models in case of rough floor shows a good prediction of the experimental standing vortex by the  $Rk-\epsilon$  model, while it is simulated upstream by the RSM. Predictions deviate by  $0.22H$ , which exceeds the model uncertainty. However, the first

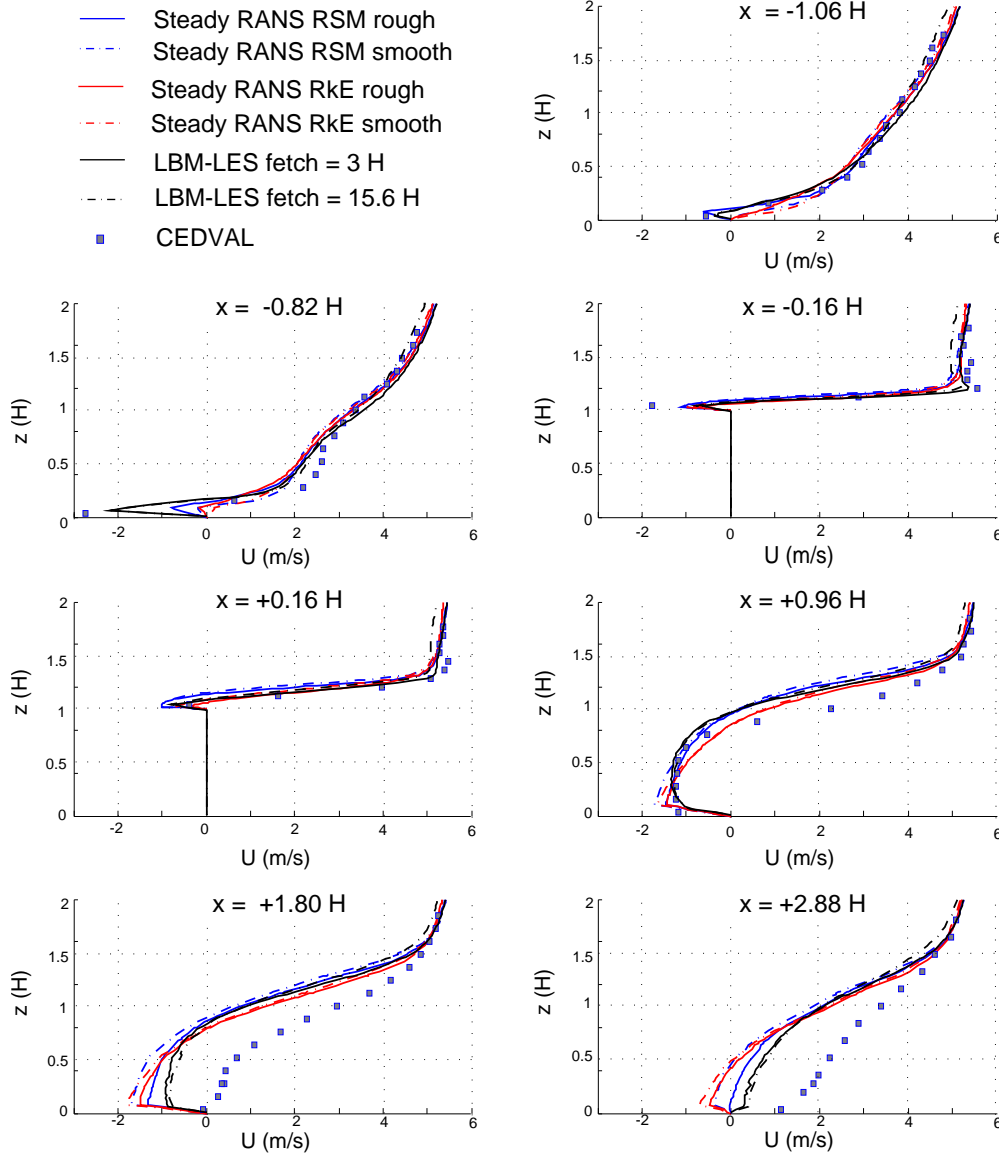


Figure 3.8: Comparison of the  $U$ -profiles around the obstacle.

graphs in Fig. 3.8 and Fig. 3.9 show a good agreement between the experimental and RSM  $U$ - and  $W$ -profiles, with a reversed flow (negative value of  $U$ ) that is not reproduced by the  $Rk-\epsilon$  model. A substantial difference is also observed between the RSM and the experimental top recirculation center, which is simulated  $0.23H$  downstream and  $0.06H$  higher.  $Rk-\epsilon$  predictions better match experimental data, although the center is predicted  $0.1H$  upstream. However, the comparison of the mean velocity profiles at  $x = -0.16H$  and  $x = +0.16H$  almost shows as good a correspondence between the RSM profiles and the experimental points as for the  $Rk-\epsilon$ . In addition, the experimental mean velocity vectors field provided by the CEDVAL suggests a stretched top recirculation. Such an elongated shape is observed in the RSM mean velocity vectors field as well. The examination of its 3D structure shows a strong 3D pattern (see Appendix L.2). The top bubble is rather large and high in the middle of the roof and is flattened and deflected upstream and downwards toward the obstacle edges. Conversely, the  $Rk-\epsilon$  top recirculation is

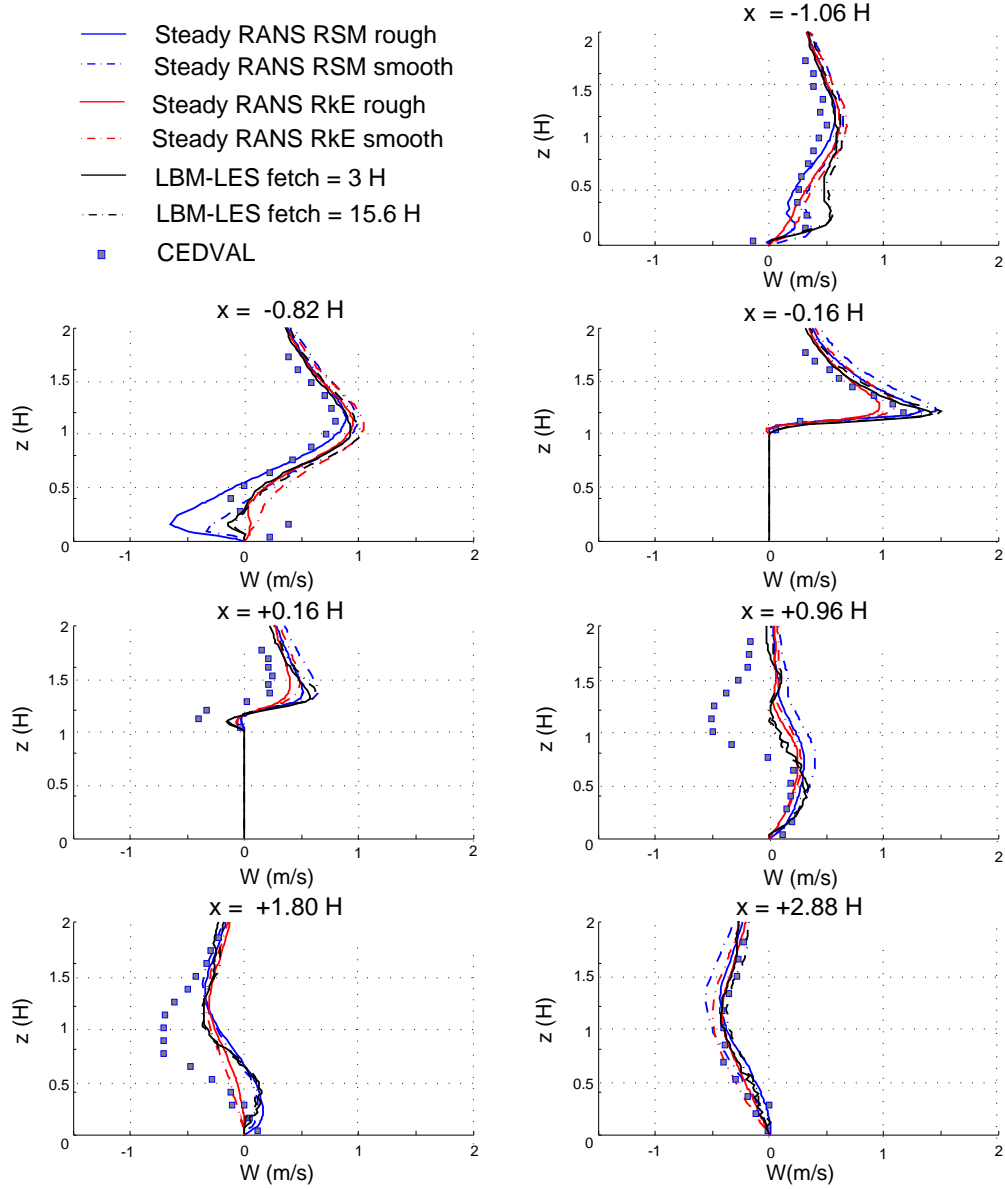


Figure 3.9: Comparison of the  $W$ -profiles around the obstacle.

smaller and more straight over the obstacle width. Regarding the near wake, the  $Rk-\varepsilon$  model predicts a more stretched and flattened recirculation as compared to the RSM and even more to the experiment. The downstream reattachment point is simulated 20 % further away by the  $Rk-\varepsilon$  model than computed by the RSM and is more than twice the length of the experimental one.

In case of smooth floor, RSM results better match LBM LES predictions than those of the  $Rk-\varepsilon$  model. Note that considering LBM LES predictions, no substantial modification of the overall flow is observed when decreasing the fetch. Only small variations of the wake recirculation center and downstream stagnation region are observed. They are slightly closer to the experiment in the configuration with the longer fetch. Next to the obstacle, the different flow structures that are simulated by the RSM fairly match LBM LES predictions. The LBM LES cavity zone is nevertheless over-estimated by the RSM as the downstream stagnation point is simulated 30 % further

downstream. This is however better than simulated by the  $Rk-\varepsilon$ , which predicts this point 51 % further downstream.

As a conclusion, it is difficult to state about a better performance of one of the two steady RANS models tested. In case of rough floor, the experimental flow structures that develop in the vicinity of the obstacle appear better predicted by the  $Rk-\varepsilon$  model, while the cavity zone is better reproduced by the RSM. In case of smooth floor, RSM predictions generally better match LBM LES outputs. However, the near wake is substantially over-predicted in all cases compared to experimental data.

### 3.3.3 The array of rectangular blocks

In order to evaluate the accuracy of the steady RANS methods for more complex configurations than an isolated obstacle and the time dependence of the solution, five cases are considered:

- the steady RANS RSM model (RSM rough);
- the steady RANS  $Rk-\varepsilon$  model ( $Rk-\varepsilon$  rough);
- the LBM LES model with an averaging time of about 30 s ( $1.28 \times 10^6$  lattice time steps);
- the LBM LES model with an averaging time of about 1 min ( $2.56 \times 10^6$  lattice time steps);
- the experiment (CEDVAL).

Note that for each steady RANS models, a second simulation with a finer mesh was run, as well as another using the second order upwind scheme instead of the third order MUSCL scheme.

Fig. 3.10 compares the mean velocity vectors in the canyon formed between the fifth and the sixth block of the central row (plane  $y = 0$  m). For RANS models, 2D velocity streamlines are also lightly sketched to better highlight the flow patterns inside the canyon.

Although the experimental documentation reports a strong flow unsteadiness, a mean flow may exist according to LBM LES results as the time averaged velocity vector field looks similar irrespective of the considered averaged period of time. It is therefore relevant to test steady RANS models on such a case.

Both the experiment and LBM LES predictions show a recirculation between the two obstacles. However, its center is simulated next to the top and rather in the upstream part of the canyon, whereas the experimental one is located near the windward surface. In addition, the LBM LES vortex is rather circular while it presents a larger vertical extent in the experiment. These differences could partly be explained by the bottom boundary condition, which is rough in the experiment but smooth in the LBM LES simulation.

Considering steady RANS models, the simulation post-processing highlights no substantial influence of the numerical scheme. On the contrary, flows predicted by the two turbulence models significantly differ. The  $Rk-\varepsilon$  model does not reproduce the experimental vortical structure, whereas it is simulated by the RSM. Furthermore, the location of the recirculation center that



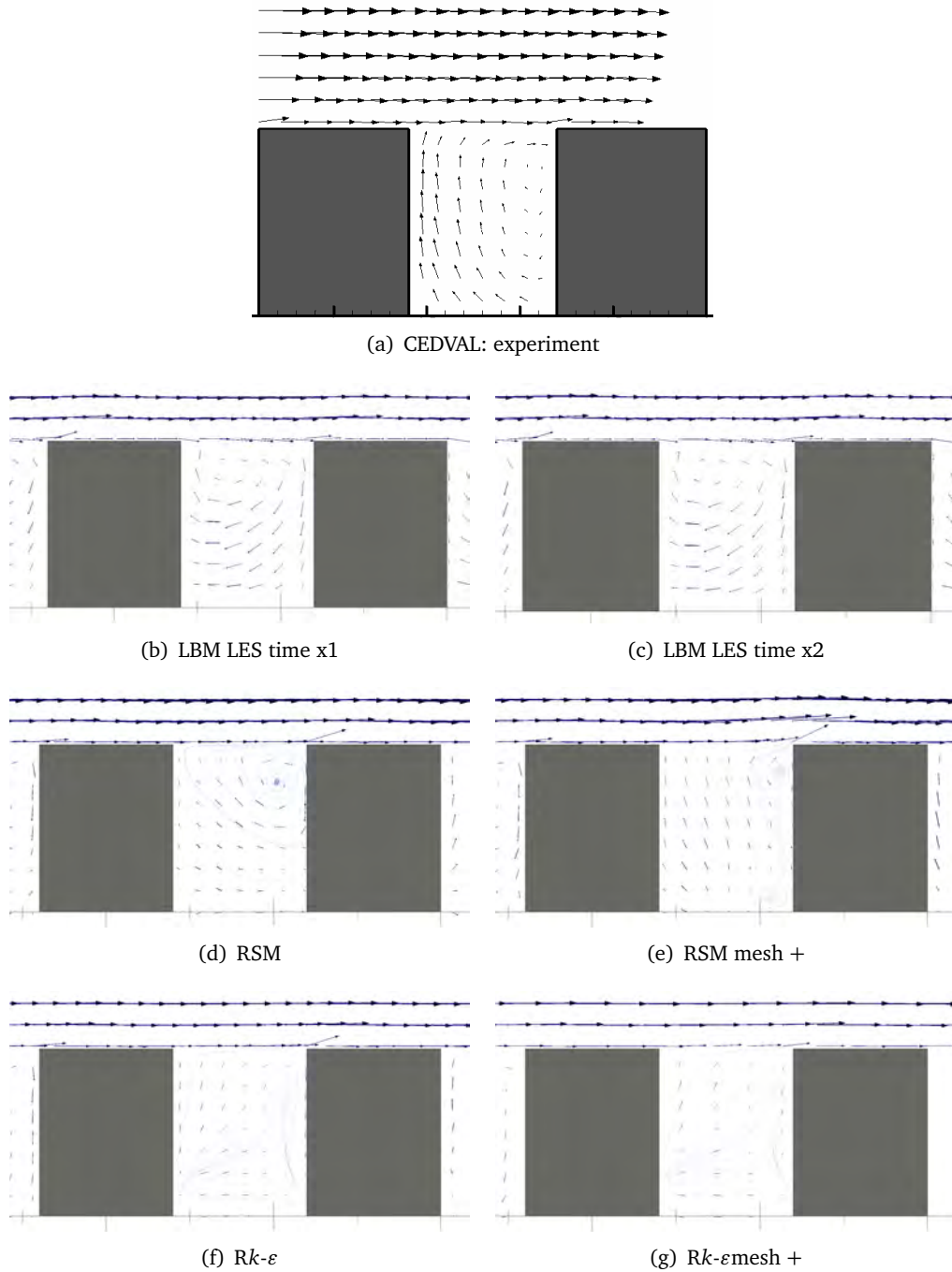


Figure 3.10: Comparison of the mean flow fields and 2D mean velocity streamlines between the fifth and the sixth blocks of the B1-1 case.

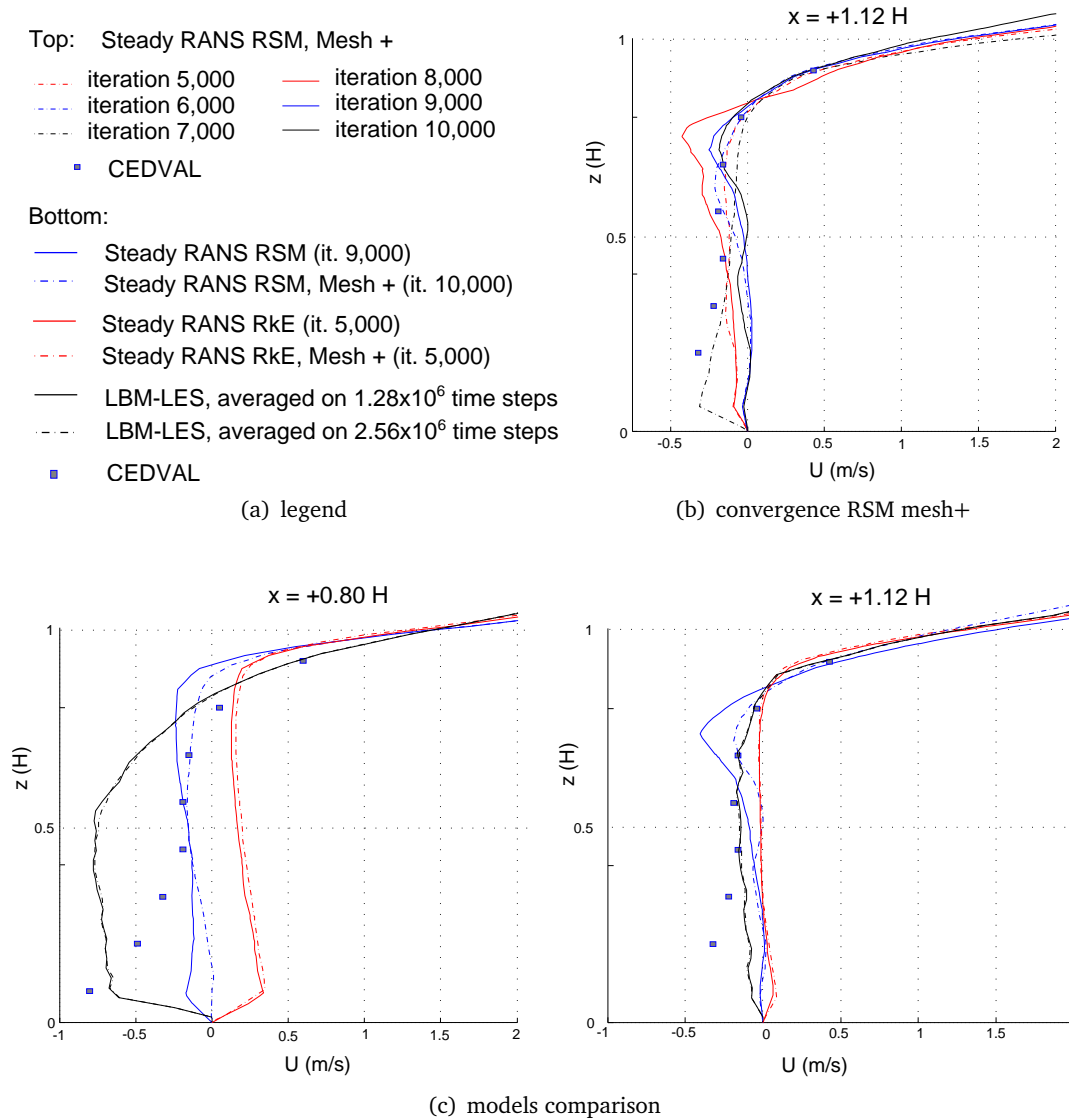


Figure 3.11: Comparison of  $U$ -profiles within the canyon.

is predicted by the RSM fairly corresponds to the experiment. It is found next to the windward surface. Nevertheless, its vertical extent appears less sprawled than in the experiment.

However, although the steady RANS RSM appears capable to reproduce the main physical processes, its convergence is less immediate than for the  $Rk-\epsilon$  model. On the one hand, profiles simulated by the  $Rk-\epsilon$  model well stabilize as functions of the number of iterations, and no difference is observable between the two meshes tested. On the other hand, no clear stabilization of the mean profiles was achieved with the steady RANS RSM whatever the mesh resolution and the numerical scheme. Fig. 3.11(b) gives some monitored  $U$ -profiles next to the windward surface to illustrate this unstable behavior. Profile are taken for the finer mesh each  $10^3$  iterations between  $5 \times 10^3$  and  $10^4$ . A rather periodic behavior of the profiles as a function of the number of iterations can be observed, but the recirculation is always reproduced. Profile variations in the canyon are

contained within a narrow envelope of about  $0.4 \text{ m} \cdot \text{s}^{-1}$  maximum amplitude for the monitored  $U$ -profiles. However, this range also corresponds to the experimental velocity magnitude.

The unstabilized behavior explains the differences that appear between the two RSM models shown in Fig. 3.10. Their respective solutions were intentionally taken at an arbitrary number of iterations for which profiles, and likewise flow patterns, do not match. This unstabilized behavior reflects the complexity of the flow that is highlighted in the experimental documentation. Moreover, the recirculation is even more complex to predict as its center is located very close to the wall, i.e. where wall-functions are influential.

Furthermore, it is worth mentioning that the RSM requires the finer mesh resolution to simulate a symmetric and “smooth” mean flow. For the initial mesh, some non stabilized scroll forms were observed on each side of the array, i.e. on the lateral sides of the shear layer. These structures are nevertheless not inconsistent with physics, as such forms are observed in reality as well as in the dynamic flow behavior simulated by the LBM LES model. The flow field inside the canyon of interest was less affected by the mesh resolution as fairly similar flow features were modeled in both cases shown in Fig. 3.11(c), although the coarser mesh does not produce a perfectly symmetrical 2D horizontal flow pattern. Because of the computational resources needed to perform another mesh sensitivity analysis, no additional simulation was performed.

To further evaluate the accuracy of the computational models, Fig. 3.11(c) compares the experimental and simulated  $U$ -profiles in the middle of the canyon as well as next to the windward surface. This latter location roughly corresponds to the abscissa of the experimental recirculation center. As expected, negative values of  $U$  characterizing the reversed flow can be observed for each configuration tested except for the  $Rk-\epsilon$  model. In the central part of the canyon, LBM LES profiles substantially differ from the experimental profile. The recirculation center is simulated there by the model while it is reported downstream in the experiment. RSM predictions and experimental data substantially deviate in the bottom of the central part of the canyon. This zone corresponds to the two first cells next to the ground. At this location, the non-slipping condition set on the floor and roughness effects constrain the flow. More specifically, these boundary conditions prevent the development of the flow, while experimental measurements show relatively high velocities. Elsewhere and on average, the simulated  $U$ -profiles rather correspond to those of the experiment.

As a conclusion, despite substantially uncertain because of the flow instabilities, the RSM appears to perform better in a multi-obstacle configuration than the  $Rk-\epsilon$  model. Unlike the RSM, this first order model predicts positive or nearly zero  $U$ -velocities in the canyon, and therefore does not reproduce the experimental vortical recirculation.



## 3.4 Model accuracy and reliability

### 3.4.1 Accuracy of the computational methods

In comparison with the free field ABL, for which the flow is mainly determined by the development of turbulence and dissipation due to friction on the floor, flow structures that develop around a sharp-edged obstacle are mainly determined by its geometry. In such separated flows, the mechanically induced turbulence and recirculation phenomena have a directional behavior. They impact on the mean flow field over a large area around and downstream the obstacle. As reminded in Sec. 3.1.2.2, these processes are differently modeled by each computational method and turbulence model addressed in the current validation study. These differences in the mass flow modeling often lead to substantial deviations of numerical predictions. In particular, the over-prediction of the cavity zone is a well known problem of steady RANS methods, especially when used in combination with two-equations closure schemes. Accounting for turbulence anisotropy, second order closure schemes are expected to provide better results than isotropic two-equations models. Furthermore, according to its transient and more detailed formulation, LES should be even more accurate (see Sec. 3.1.3.2).

As expected and considering the A1-1 case, LBM LES predictions generally better match experimental data although a smooth floor was modeled. Steady RANS RSM results are fairly close to the LBM LES ones, whereas  $Rk-\varepsilon$  predictions show substantial deviations. These results suggest that the steady RANS RSM and LBM LES models predict rather similar mass flow behaviors around the sharp-edged obstacle. However,  $Rk-\varepsilon$  predictions better match experimental observations in the obstacle vicinity than the RSM ones do. Note that the reproduction of the top recirculation is improved by the “realizable” formulation of the  $k-\varepsilon$  model. On the contrary, downstream flow structures are better predicted by the RSM.

To enlarge the scope of analysis, other works addressing these case studies were examined. Some studies addressing the A1-1 case and evaluating the accuracy of numerical predictions for the different turbulence models are available in literature. Most of them discuss steady RANS methods used together with a first order model. To the best of our knowledge, only one study addresses RSM computations. A NS-based LES study is also reported.

[Meroney et al. \(1999\)](#) performed several steady RANS simulations using the  $Sk-\varepsilon$ , RNG  $k-\varepsilon$  and the RSM models. Inflow properties were specified to match the mean velocity and turbulence profiles of the experimental approach flow. The flow predicted by the RSM on a refined unstructured grid corresponded well with the experiment next to the obstacle. The cavity zone was however found significantly longer than the experimental one. [Parente et al. \(2011\)](#) proposed and evaluated a modified formulation of the  $Sk-\varepsilon$  model that was consistent with the inflow and rough bottom boundary condition. Predictions were substantially improved as compared to usual modeling approaches as the extents of the top bubble and downstream recirculation were significantly reduced. However, the downstream stagnation region was found 2.2H downstream the obstacle, which is still further away than in the experiment. [Gorlé et al. \(2010\)](#) also evaluated

the performance of an adapted version of the steady RANS  $Sk-\epsilon$  model as well as a NS-based LES model. LES results were found to be more accurate both in terms of mean velocity and concentration fields than the steady RANS predictions. The separation bubble and the cavity zone predicted by the LES method matched well with the experiment. Moreover, the turbulent diffusion coefficients that were computed using some LES results (the time averaged filtered instantaneous velocity and concentration values) showed an anisotropic behavior.

No work addressing the B1-1 case was found. However, our simulation results show the better performance of the LBM LES and steady RANS RSM models in predicting the recirculation in the canyon as compared to the  $Rk-\epsilon$ . Nevertheless, results also stress that the steady RANS RSM, although more accurate, is more demanding as it is less stable, requires finer mesh and involves larger computational resources than the  $Rk-\epsilon$  model.

Hence, this validation study highlights substantial differences in the accuracy of numerical predictions depending on the turbulence modeling and computational strategy, but also on the geometric model considered. The main deviation between numerical and experimental flows and the greatest dispersion of numerical predictions occur for the downstream recirculation phenomena, i.e. the cavity zone in the A1-1 case and the canyon vortex in the B1-1 case. Steady RANS simulations with usual first order closure scheme were found to be less accurate. The implementation of some modifications in the model can improve their performance (Parente et al., 2011) but they generally have a limited scope of applicability (Richards and Norris, 2011). More detailed turbulence models, i.e. steady RANS RSM and above all LES methods, show a better accuracy. This can be explained by their capacity to reproduce turbulence anisotropy as well as transient flow features for LES methods. According to these results and literature, directional effects of turbulence on mass flows as well as fluctuating processes are important to consider when studying complex flows around isolated buildings and in complex configuration involving urban canyons. However, it is still not possible to perform very detailed computations on usual computers such as ours. As a consequence, the steady RANS RSM model is selected for the actual aerodynamic study. Despite having more convergence problems than the  $Rk-\epsilon$  does and being less accurate than the LES, this model appears capable of reproducing the main features of the physics and benefits from an easier access and implementation in usual CFD codes than LES.

### 3.4.2 ABL and roughness modeling effects

Regardless of the computational method and turbulence model, inflow specifications and the homogeneity of the modeled ABL can substantially alter the quality of urban CFD studies. These parameters are especially critical for the prediction of wind conditions at pedestrian level. Properties of the targeted ABL are usually translated in CFD models as inlet boundary conditions. They generally correspond to an equilibrium ABL or a fully developed flow. However, the modeling of the ground roughness can significantly alter the physical accuracy of the computed flows (Blocken et al., 2007a,b). Roughness strengthens friction on surfaces and by this mean affects mean wind profiles. When inflow, ground roughness and computational models are not consistent, unintended streamwise gradients develop and the incident flow profile differs from the inlet one. The

modeled ABL is no more horizontally homogeneous and generally no longer corresponds to the targeted physics.

Considering steady RANS methods and more particularly first order turbulence models, inlet specifications are often based on the recommendations of [Richards and Hoxey \(1993\)](#). The corresponding boundary conditions are part of a more complete set of specifications, which cannot always be simply implemented. Some methods were therefore suggested to improve the consistency and the physical accuracy of numerical models. In particular, [Blocken et al. \(2007b\)](#) detailed different techniques to implement, especially when equivalent sand grain rough wall-functions are used, and [Yang et al. \(2009\)](#) and [Gorlé et al. \(2009\)](#) proposed enhanced boundary conditions to ensure the ABL homogeneity when using steady RANS  $k-\varepsilon$  models.

According to the available literature, at least two studies have examined the influence of the ABL modeling on flow features for the free ABL and the A1-1 case addressed in this study. Steady RANS  $k-\varepsilon$  models were used and the influence of  $k$  on flow features was mainly studied. [Gorlé et al. \(2009\)](#) evaluated two inlet profiles of  $k$  for the simulation of the ABL. Profiles were either based on the recommendations of [Richards and Hoxey \(1993\)](#) or derived from model equations and fitted to the CEDVAL approach flow profiles. The experimental  $k$ -profile was deduced from the measurements of turbulence intensity. The horizontal homogeneity of the ABL was achieved by modifying two constants of the turbulence model. Despite a 40 % difference between both configurations, the  $k$ -profile did not have substantial effects on the mean velocity field. On the contrary, dispersion processes were significantly impacted on. Considering the A1-1 case, [Ai and Mak \(2013\)](#) tested several sets of inflow conditions, which differed by their  $U$ - or  $k$ -profiles. Settings corresponded either to the experimental data, the recommendations of [Richards and Hoxey \(1993\)](#) or the specifications of [Gorlé et al. \(2009\)](#). Results showed that the ABL homogeneity and the value specified for  $k$  substantially affect the predicted mean flow structures around the obstacle. Lower incident values of  $k$  led to longer top and wake recirculation phenomena.

Despite being meaningful for the current validation study, these results cannot be directly extended to other turbulence models such as the RSM, or computational methods such as the LBM LES. For these models, the effects of the turbulence modeling on mean flow patterns should be investigated further as an improvement of the predicted flow structures in the A1-1 case might be expected if higher turbulence levels were modeled. This improvement might be less substantial in the B1-1 case because of the upstream obstacles. However, it is worth mentioning that the  $k$  value that is used in turbulence models is not physical in itself. It is rather a computational parameter, which depends on the model used.<sup>10</sup> Furthermore, roughness models that are implemented in usual CFD codes do not correspond to the physical roughness modeled in wind-tunnels, and even less to real terrain roughness. It is therefore often not possible to fulfill an overall numerical and physical correspondence using usual wall-functions and turbulence models.

---

<sup>10</sup>Note that consecutively to the studies mentioned in the current section, [Richards and Norris \(2011\)](#) proposed an updated set of the specifications that were given in [Richards and Hoxey \(1993\)](#) concerning the mean and turbulent inflow settings. Recommendations for different turbulence models are suggested and the differences between the turbulence levels that are deduced from turbulence models or physical measurements are discussed.

In the current study, the approach flow was modeled using a preliminary simulation of a long and empty tunnel to produce consistent flow features. The adjustment of the approach flow to a virtual shift in roughness and the corresponding modification of the mean flow field around the obstacle according to the computational configuration were then investigated. The modification of the bottom boundary condition from rough to smooth leads to the development of an internal boundary layer with an accelerated flow at the bottom of the computational domain. The related modification of the approach flow profile is substantial up to  $2H/3$  at the actual obstacle location. However, despite the fetches differ by more than a factor of 3 between the two LBM LES configurations tested for the A1-1 case, only a minor displacement of the cavity zone center and downstream stagnation region are observed. They are predicted  $0.06H$  downstream for the configuration with a shorter fetch. Other flow structures are similar. This can be explained by the rather limited deviation that exists between the two incident flow profiles as  $z_0$  is small. A slight decrease in mean velocity occurs above the obstacle height at  $2m$  from the inlet, and the internal boundary layer already develops at  $3H$  from the inlet. However, due to the presence of the obstacle, it is not possible for the flow to progress freely in the influence region of the obstacle as the over-pressure region interacts with the approach flow. The boundary layer development seems thus not to substantially influence mass flow processes and mean flow structures that develop due to the geometry of the obstacle, as long as the incident flow profiles remain roughly comparable and the boundary conditions remain the same. Nonetheless, the effects and properties of turbulence should be investigated further in order to better understand the influence of the ABL and roughness properties on these aerodynamic processes and discuss this conclusion.

On the contrary, according to the steady RANS modeling of the A1-1 case, modeling smooth instead of rough boundary conditions substantially alters predictions. In case of smooth floor, the standing vortex center is simulated closer to the obstacle than in case of rough floor. The length of the cavity zone is also increased. Changes are especially clear in RSM predictions. As compared to the rough case, the standing vortex center is predicted 11 % and 2 % closer to the obstacle, and the downstream stagnation point 12 % and 7 % further downstream by the RSM and  $Rk-\epsilon$  models respectively (case smooth). These results stress the effects of roughness on the flow field around a sharp-edged obstacle. Decreasing roughness reduces the flow resistance on the floor. As a consequence, in case of smooth floor, the wind speed of the incident flow profile is substantially increased in its lower part. In addition, the turbulence development in the approach flow due to friction of the floor is reduced and the development of mean flow structures around obstacles is altered, especially when the flow reverses.

These observations call into question usual ways to physically and numerically model the bottom boundary condition, i.e. the floor roughness and friction on it, as well as its effects on mean flow structures around bluff bodies. LEGO elements or carpets are often used in wind-tunnels, rough wall-functions are often used in CFD models and real terrain roughness is never uniform especially in human-shaped environments. These three roughness types do not correspond to each other. Moreover, it is worth mentioning that the sand grain model that is often included into wall-functions in usual CFD codes requires a minimal cell height near the rough surface. This can greatly constrain the spatial resolution of the simulation or limit its physical accuracy

(Blocken et al., 2007a). Other wall-function formulations based on  $z_0$  exist and overcome some limitations of usual wall-functions (Parente et al., 2011; Richards and Hoxey, 1993), but their implementation is not widespread.

Hence, according to the current validation study, near wall behavior laws cannot be neglected as they substantially contribute to determine the accuracy of CFD studies. Indeed, RANS models highlight substantial modifications of the flow structures depending on the floor roughness. Moreover, LES generally perform well in reproducing the different flow structures around sharp-edged obstacles. The deviation found between the detailed LBM LES results and the experiment regarding the cavity zone length in the A1-1 case and the center of the recirculation in the B1-1 case can certainly be explained by the smooth bottom boundary condition, at least partly. However, the effects of  $k$  should also be studied further to support the current conclusions.

### 3.5 Synthesis of the settings to be used in actual models

The comparison between steady RANS simulation results with detailed experimental and computational data in cases of an isolated obstacle and a multi-obstacle configurations highlighted the ability of the RSM model to reproduce the main aerodynamic processes, yet imperfectly. This model performs on average better than the  $Rk-\epsilon$  model. However, its convergence is less easy to achieve.

According to the current study and literature, other computational parameters than the turbulence model can substantially affect the model accuracy. They especially include the consistency of the ABL, the modeling of roughness, the order of the numerical schemes as well as the mesh resolution. To model the ABL, a preliminary simulation of the approach flow using a long tunnel can be performed to ensure constant mean velocity profiles along the actual domain. Note that in the current study, an even longer tunnel would have been preferably used to model an equilibrium boundary layer both in terms of mean and fluctuating flow features. Standard wall-functions applied with a rough boundary condition at the bottom of the computational domain were found to give satisfactory results when used with third order MUSCL or second order interpolation schemes. However, problems can occur when using the RSM together with a smooth boundary condition with a third order MUSCL numerical scheme. A minimum mesh resolution of 1/10 times the obstacle length at its bottom with a stretching ratio of 1.1 are required to promote the convergence of the mean flow field in complex configurations. Still for complex configurations and to ensure the effective convergence of the solution, it is preferable to monitor some profiles in the symmetry plane and also to check the whole velocity field in a vertical as well as a horizontal plane at least, e.g. in order to verify its overall symmetry when expected. This criterion is a good quality indicator for symmetric models: as the mesh is unstructured, it does not enforce the symmetry and convergence of the solution.

In addition to these conclusions, specific guidelines synthesized in Sec. 3.1.3.1 are to be applied for the modeling of open full scale conditions, especially with respect to the domain size, boundary conditions and mesh resolution at pedestrian level.

## 3.6 Summary

The confrontation of steady RANS  $Rk-\varepsilon$  and RSM predictions with detailed wind-tunnel data and LBM LES results for the three different configurations (1. an empty domain with different roughness conditions; 2. around an isolated rectangular block (A1-1 case); and 3. within an array of identical obstacles (B1-1 case)) brings to light some modeling challenges, especially:

- the modeling of an appropriate ABL;
- the modeling of separated flows around a sharp-edged obstacle and inside canyons;
- the way to analyze the simulation results.

The main conclusion of this validation study is that comparing the steady RANS models, the RSM provides better results for the wake recirculation (A1-1 case) and reproduces the experimental vortex in the canyon (B1-1 case). Its predictions generally fairly match LBM LES results while the  $Rk-\varepsilon$  is closer to the experiment in the vicinity of the A1-1 obstacle. Nevertheless, the numerical convergence is harder to achieve with the RSM, especially when flows experience strong fluctuations, and it carries some problems in its boundary conditions when combining smooth boundary conditions with a third order numerical scheme.

Hence, the better physical accuracy of the steady RANS RSM makes this model the best candidate to be used for the subsequent simulations. However, the limitations highlighted should be kept in mind.



# Chapter 4

## Numerical study of the urban morphology effects on air flow patterns

This chapter presents the modeling and the results of the aerodynamic study carried out on each isolated building and urban block type defined in Sec. 2. The effects of their topology, orientation and relative dimensions on the developing internal and external flow patterns are examined. The resulting pressure distributions on the different surfaces are analyzed for some representative configurations: the cube, the patio, the cube array and the continuous patio array.

### Contents

<b>4.1</b>	<b>General model settings and modeled ABL . . . . .</b>	<b>104</b>
4.1.1	General settings . . . . .	104
4.1.2	The ABL . . . . .	105
<b>4.2</b>	<b>CFD modeling of the isolated building types . . . . .</b>	<b>106</b>
4.2.1	Specific settings of the model . . . . .	106
4.2.2	Simulation results . . . . .	108
<b>4.3</b>	<b>CFD modeling of the urban block types . . . . .</b>	<b>115</b>
4.3.1	Specific settings of the model . . . . .	115
4.3.2	Simulation results . . . . .	116
<b>4.4</b>	<b>Effects of urban morphological features on air flows . . . . .</b>	<b>126</b>
4.4.1	Analysis of the external flows patterns: topology and size effects . . . . .	126
4.4.2	Analysis of the inner flows patterns: effects of topology and orientation . . .	130
<b>4.5</b>	<b>Analysis of the pressure distribution on facades . . . . .</b>	<b>135</b>
4.5.1	Physical background and applications . . . . .	135
4.5.2	Pressure distribution on isolated buildings . . . . .	136
4.5.3	Pressure distribution in arrays . . . . .	139
<b>4.6</b>	<b>Summary . . . . .</b>	<b>142</b>



## 4.1 General model settings and modeled ABL

### 4.1.1 General settings

Computational settings were as much as possible set similar for each case of the two typologies in order to enable more straightforward and relevant comparisons. In particular, the height of the typical buildings is similar, i.e.  $H = H' = 10$  m. This roughly corresponds to three-storey buildings and is often used in CFD studies. For the isolated building typology, the maximum model footprint is  $2H \times 2H = 20 \text{ m} \times 20 \text{ m}$ , and it is  $8H \times 8H = 80 \text{ m} \times 80 \text{ m}$  for the urban block typology.

For the different cases, meshes were automatically generated using Workbench, which propagated the linear and surface dimensioning set on the bottom and top surfaces of the domain as well as on the obstacle. The basic and coarser mesh resolution involves a 1 m mesh dimensioning on the rough floor and 0.3 m cells on the obstacle roofs with a stretching ratio of 1.1. The mesh resolution on the floor corresponds to 1/10 times the obstacle height and involves more than 20 cells along the obstacle characteristic length. Resulting meshes are unstructured and composed of tetrahedral elements, except for the empty tunnel used to simulate the approach flow.

Computational settings deduced from the validation study were kept for the simulations. They especially include:

- the air model: constant density, equal to  $1.225 \text{ kg} \cdot \text{m}^{-3}$  as the model is isothermal;
- the turbulence model: steady RANS RSM, linear pressure strain correlation;
- and the near wall treatment: standard wall-functions, modified for roughness on the floor.

The bottom boundary is modeled as a rough wall as described in Sec. 4.1.2. Obstacle walls as well as the floor of enclosed courtyards are modeled as smooth non-slipping walls. Note that contrary to the previous configurations, the top and lateral boundaries are set symmetric to model open full-scale conditions.

Simulations were run using Ansys Fluent 15. The increase in complexity of the obstacle shape required considering additional convergence criteria with respect to the validation study. Convergence was therefore assessed by monitoring several profiles of mean ( $U, V, W$ ) and fluctuating ( $k, \varepsilon$ ) flow characteristics along the domain center line. The final convergence was verified by symmetry (if relevant) and overall mean flow field in vertical and horizontal planes. For the simplest cases, simulations were generally stopped after  $5 \times 10^3$  or  $6 \times 10^3$  iterations. For more complex configurations, additional simulations and finer meshes were necessary. Appendix M provides the levels of scaled residuals at which simulations were stopped.

According to the validation study, the best practice guidelines (Sec. 3.1.3.1) and the model specificities, Tab. 4.1 summarizes the computational strategy and different model settings generally used for the actual simulations.

All the simulation post-processing was performed using Paraview. Simulation outputs were interpolated when necessary by the software to draw 3D iso-contours of mean velocity and vor-

Model parameter	Adopted settings
Domain size	Inlet, Top, Lateral: $dist \geq 5H$ Outflow: $dist \geq 15H$ $BR_{tot} \leq 5\%$ ; $BR_{H,V} \leq 22\%$
Discretization type	Control volumes
Mesh resolution	Floor: $\leq 1/10H$ , $\geq 2Ks$ Stretching ratio: $\leq 1.1$
Turbulence model	Steady RANS RSM, linear pressure strain
Near-wall treatment	Standard wall functions
Interpolation schemes	Pressure interpolation: SIMPLE Convective variables: MUSCL or 2nd order upwind Turbulence variables: MUSCL or 2nd order upwind
Resolution scheme	Gauss Siedel
Convergence criteria	Monitoring of U, V, W, k, $\varepsilon$ profiles Monitoring of the mean velocity fields in a vertical and a horizontal planes
Boundary conditions	Inflow: preliminary simulated profile Outflow: outflow (zero stream wise gradient) Top and side: symmetry Bottom: rough wall Obstacles: smooth wall

Table 4.1: General model settings to be used in the CFD simulations.

ticity, 3D mean velocity streamlines as well as 2D flow fields (projection of the 3D mean velocity vectors and magnitude) in vertical and horizontal planes. These 3D and 2D drawings together make possible a detailed analysis of the flow field.

#### 4.1.2 The ABL

The approach flows of both the isolated building and the urban block types were simulated using a  $10^4$  m long tunnel as suggested by Blocken et al. (2007a). The bulk velocity is  $5 \text{ m} \cdot \text{s}^{-1}$ . The actual approach flow profile was recorded after  $9 \times 10^3$  m of free flow development. This profile is given in Fig. 4.1 and corresponds to a quasi equilibrium boundary layer in terms of mean and turbulent flow features as variations of both the mean and turbulent profiles were negligible further away. The magnitude of the approach flow velocity equals  $4.3 \text{ m} \cdot \text{s}^{-1}$  at the obstacle height and  $5 \text{ m} \cdot \text{s}^{-1}$  at twice the obstacle height (20 m high). It is a bit more than  $5.5 \text{ m} \cdot \text{s}^{-1}$  at the top of the computational domain. Considering the flow speed at the obstacle height ( $U_H$ ) and the obstacle height ( $H = 10 \text{ m}$ ), the Reynolds number of the simulations is nearly  $3 \times 10^6$ . Hence, the flow is fully turbulent.

The floor roughness parameters, namely  $K_s$  and  $C_s$ , equal  $3 \times 10^{-1} \text{ m}$  and 1 respectively. With such parameters, the approach flow profile would correspond to an open landscape<sup>1</sup> with  $z_0 \approx$

<sup>1</sup>Roughness class number 3 of the Davenport's classification presented in Tab. 1.1, Sec. 1.1.1.

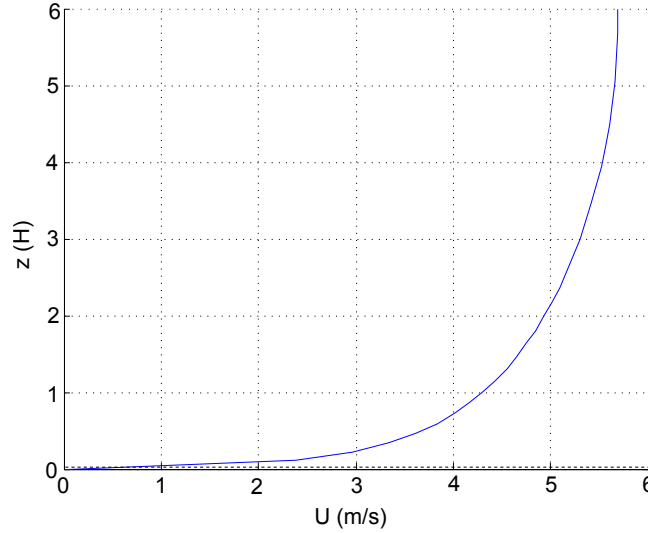


Figure 4.1:  $U$ -profile of the approach flow used for the actual simulations.

$3 \times 10^{-2}$  m according to the formula given by Blocken et al. (2007a) and Appendix K.1. However, although actually being logarithmic, the lower part of the  $U$ -profile (up to  $z = 35$  m) fits the following log-law ( $R^2 = 0.9997$ ):

$$U(z) = \frac{0.3733}{0.418} \times \ln[12.55 \times z] = \frac{0.3733}{\kappa} \times \ln\left[\frac{z}{0.0797}\right] \quad (4.1)$$

The identification of the parameters gives:

- $u^* = 0.373 \text{ m} \cdot \text{s}^{-1}$ ;
- $z_0 = 0.0797 \text{ m}$ .

Eq. 4.2 gives the corresponding relation between  $K_s$  and  $z_0$ :

$$K_s = \frac{3.675}{C_s} \times z_0 \neq \frac{9.739}{C_s} \times z_0 \quad (4.2)$$

As in Sec. 3.2.3, this difference may be explained by the range of height considered in the fitting. Appendix K.3 further discusses this approach flow profile. Note that with  $z_0 = 7.97 \times 10^{-2}$  m, the approach flow profile corresponds to that of an intermediate roughness class between an open and a roughly open landscape (see Tab. 1.1).

## 4.2 CFD modeling of the isolated building types

### 4.2.1 Specific settings of the model

The left hand-side of Fig. 4.2 shows the domain size used to simulate the flow field around the isolated building types. Obstacles are located  $5H$  downstream the inflow plane and  $5H$  from the top and lateral domain boundaries as well. This gives  $BR_{tot} = 3\%$ , with  $BR_H = 18\%$  and

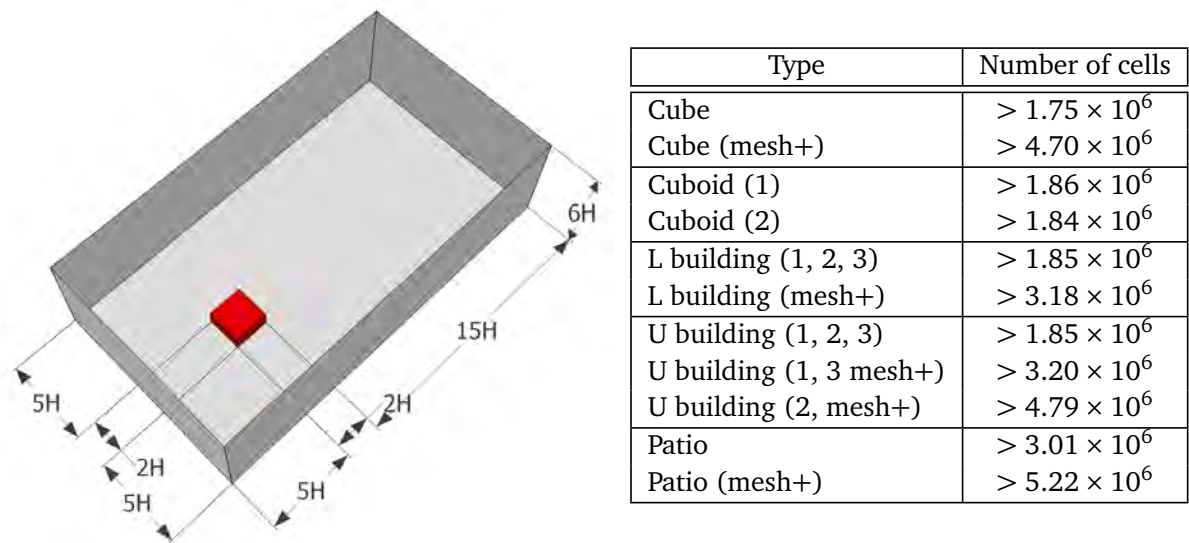


Figure 4.2: Computational domain and number of cells used to model the isolated building types.

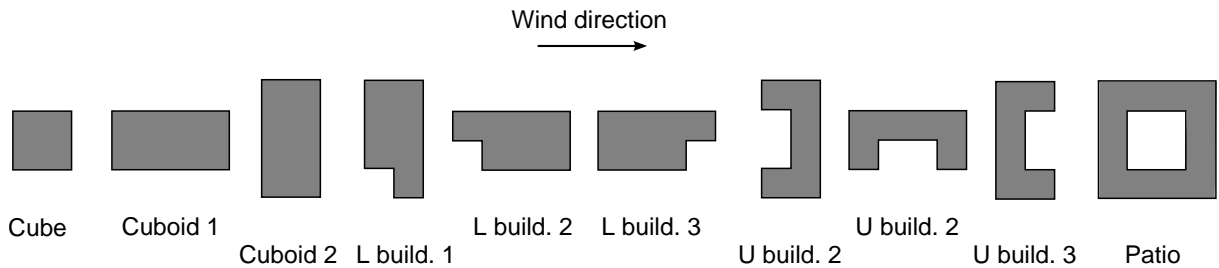


Figure 4.3: Schemes and names of the different configurations tested (isolated types).

$BR_V = 16\%$ . The outflow plane is located  $15H$  or  $16H$  downstream the obstacle. For each asymmetric case, different model orientations in relation to the wind incidence were tested but still with the approach flow direction normal to a facade. Two orientations for the cuboid, three for the L and three for the U-buildings were tested. Fig. 4.3 illustrates the different cases tested and specifies their respective names.

For basic meshes, the number of cells is generally a bit less than  $2 \times 10^6$ . With such a resolution, no clear stabilization of the V-profiles in the wake was achieved for asymmetric cases. Moreover, the patio involved a substantially finer mesh in the courtyard to give stabilized and plausible results, with a mesh resolution down to  $15\text{ cm}$  on the different surfaces. This resulted in a mesh that is composed of more than  $3 \times 10^6$  cells. For basic models, simulations lasted about one working day using the CPU-based computation server. For most of the other cases and in order to reduce the computation time, simulations were run on a 7 GPUs<sup>2</sup> computation server running Linux with 48 Gb of RAM, as it became possible by the latter releases of the CFD software. A reduction of about 10 to 15% of the computation time was estimated. Note that even faster computations were achieved by the parallel use of two machines with 7 GPUs each,<sup>3</sup> but their

<sup>2</sup>GPUs of the first machine: NVIDIA® Tesla™ C1060

<sup>3</sup>GPUs of the second machine : NVIDIA® Tesla™ C2570

simultaneous use was rapidly limited for meshes of about  $4 \times 10^6$  cells. This is certainly due to communication problems between the two machines.

Mesh sensitivity tests were performed for each case (mesh dimensioning  $\times 3/4$ ), with even finer meshes for the cube, the U-building 2 and the patio. The right hand-side of Fig. 4.2 gives the number of cells according to the simulated type. Results of the grid sensitivity tests show a clear improvement of the flow convergence for asymmetric cases as the different profiles yet stabilize. The non-stabilized curved wakes reminding the Von Kármán vortex streets were smoothed out to produce more regular recirculation phenomena. However, though not expected for a RANS mean flow, these instabilities translate realistic phenomena well, as in reality the different flow structures are transient and show such behaviors. A slight improvement of the flow field around the cuboid 1 is also observed with the finer mesh as a small symmetry defect in the wake is also smoothed. Appendix N, which compares the different results for each of the ten simulated cases, shows no substantial differences in the different flow structures for the other cases. The comparison of several flow profiles along the domain symmetry plane confirms this conclusion. Considering these results and the computation time required to run additional simulations with even thinner meshes, no further mesh sensitivity study was performed.

#### 4.2.2 Simulation results

The following presents the post-processed simulation results for each building type. In order to highlight both typical flow structures and the 3D processes yielding such flow structures, flow fields are represented with:

- 3D mean velocity streamlines;
- 3D iso-contours of:
  - mean velocity ( $\|\mathbf{U}\| = 0.5, 1.5 \text{ or } 2.5 \text{ m} \cdot \text{s}^{-1}$ );<sup>4</sup>
  - and vorticity ( $\|\boldsymbol{\omega}\| = 0.5, 1.5 \text{ or } 5.5 \text{ rad} \cdot \text{s}^{-1}$ );<sup>5</sup>
- 2D mean velocity fields (vectors and magnitude) in:
  - the vertical plane  $y = 0 \text{ m}$  or  $y = -7.5 \text{ m}$ ;<sup>6</sup>
  - and the horizontal plane  $z = 2 \text{ m}$ .<sup>7</sup>

The explanation of the different color codes and schemes illustrating the section planes and coordinates system are also given for each case. For asymmetric cases, the 3D mean velocity streamlines and the 3D iso-contours of mean velocity are also given for another orientation in relation to the wind incidence. All figures are based on the refined meshes to avoid misinterpretation due

---

<sup>4</sup>The selected flow speeds respectively correspond to calm conditions, intermediate conditions between calm and light air, and almost light breeze conditions of the Beaufort scale. Therefore, they inform on the relative wind comfort.

<sup>5</sup>The selected vorticity levels highlight the main vortices and recirculation regions developing around constructions.

<sup>6</sup>The selected plane generally cuts in the middle of the court if it exists

<sup>7</sup>This plane corresponds to a pedestrian level height and is located higher than two cells from the ground.

to the different data representation as some of them are based on the cell values. In particular, slight differences in the 3D iso-contours of vorticity can appear even if no substantial differences in the predicted flow fields effectively exist. To complete and make the analysis of the different flow fields easier, Appendix N provides comprehensive results for each of the ten different case studies and the different tested meshes. Larger figures and additional 2D velocity fields are also provided.

The different flow structures identified in Fig. 1.9, Sec. 1.2.3 usually develop upstream, on the top and sides as well as downstream the obstacles. They correspond to the standing / horseshoe vortex, separation bubbles formed at the leading edges of the obstacles and wake recirculation phenomena. Note that the two horizontal parts of the arch vortex appear stronger than its middle vertical part. This vertical structure is particularly expected in the symmetry plane of symmetric configurations but it often appears badly defined.

Recirculation phenomena present lower velocities in their core and show higher intensities of vorticity at their boundaries. High vorticity zones correspond to regions of high shear stress and the local development of eddies because of friction between two layers of different velocities. The maximum level of vorticity is always observed at the top leading edge of the obstacle. Flow separates at this location. It substantially accelerates and the most important change in flow direction occurs, which leads to such important vorticity levels.

The stagnation regions upstream the obstacle and often on the windward surface of the obstacle also appear quite distinctly on the different figures. They are characterized by low velocity regions and local changes in the streamlines directions. A higher velocity (and vorticity) zone is often observed upstream the obstacles at pedestrian level, which corresponds to the upwind standing vortex. High velocity zones developing on each side of the obstacle at the same height correspond to the corner streams. Downstream the obstacle, elongated and swirled flow structures of lower velocity develop bordering the extension of the corner streams.

The extent of the cavity zone varies with the relative dimensions of the obstacles. It is especially clear in cases of rectangular-shaped obstacles. Smaller or longer near wake recirculation phenomena develop depending on the obstacle width and length.

The observed trends as well as some modified flow structures observed for non-rectangular-shaped building types are in accordance with the indications given in [Brown and DeKay \(2000\)](#) and reproduced in Fig. 1.10, Sec. 1.2.3. In addition, specific phenomena develop inside courtyards. Their properties depend on the openness and orientation of the court with respect to the wind incidence. These recirculation phenomena generally interact with the surrounding flows and distort the basic flow structures around the obstacle compared to those developing around compact rectangular-shaped buildings. The alteration of the basic flow structures are especially clear when the court has one lateral side open at least.

These different effects of the building topology, orientation and relative dimensions on the internal and external flow patterns are discussed in detail in Sec. 4.4.2 and Sec. 4.4.1.

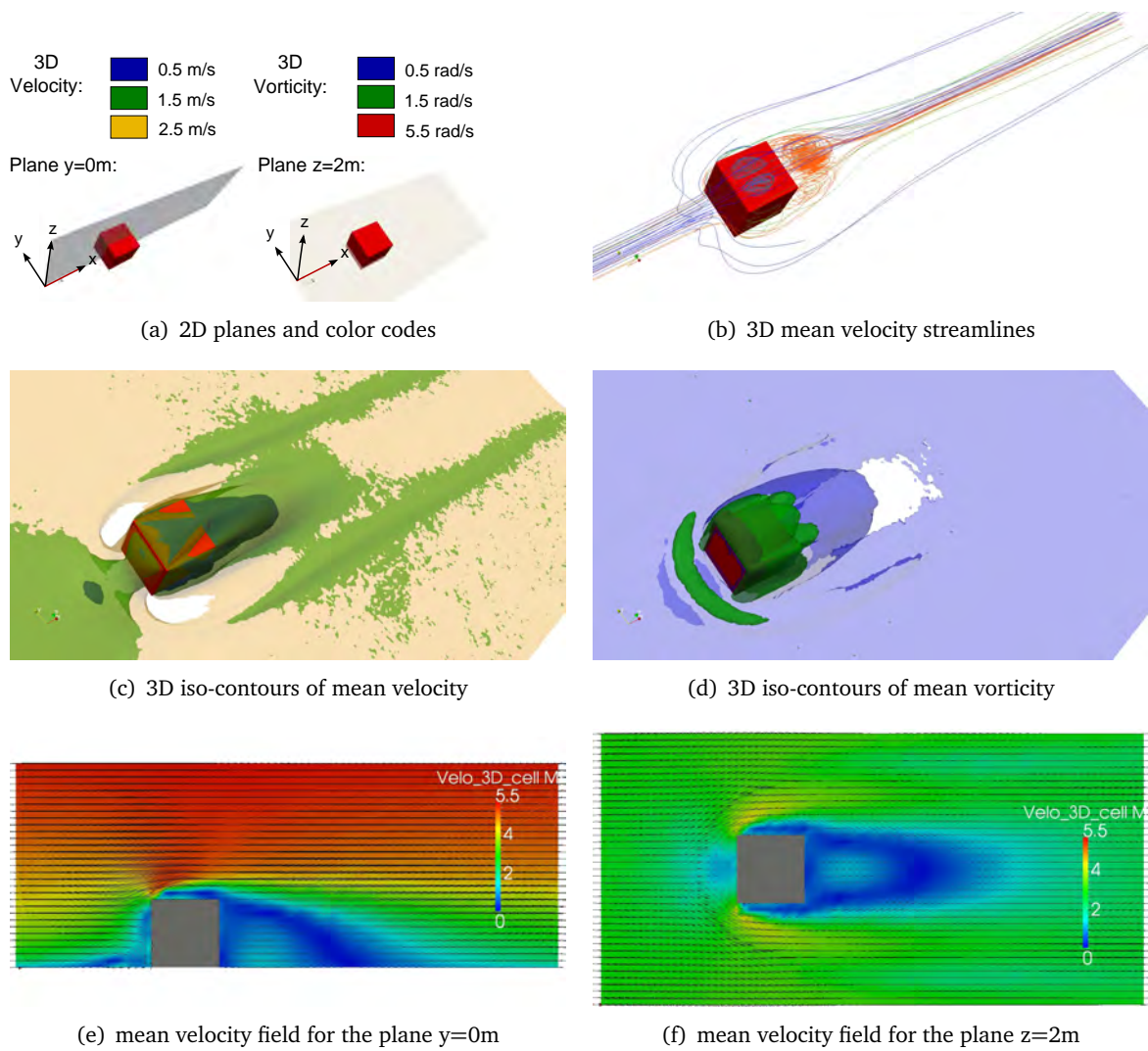


Figure 4.4: Aerodynamic results for the cube.



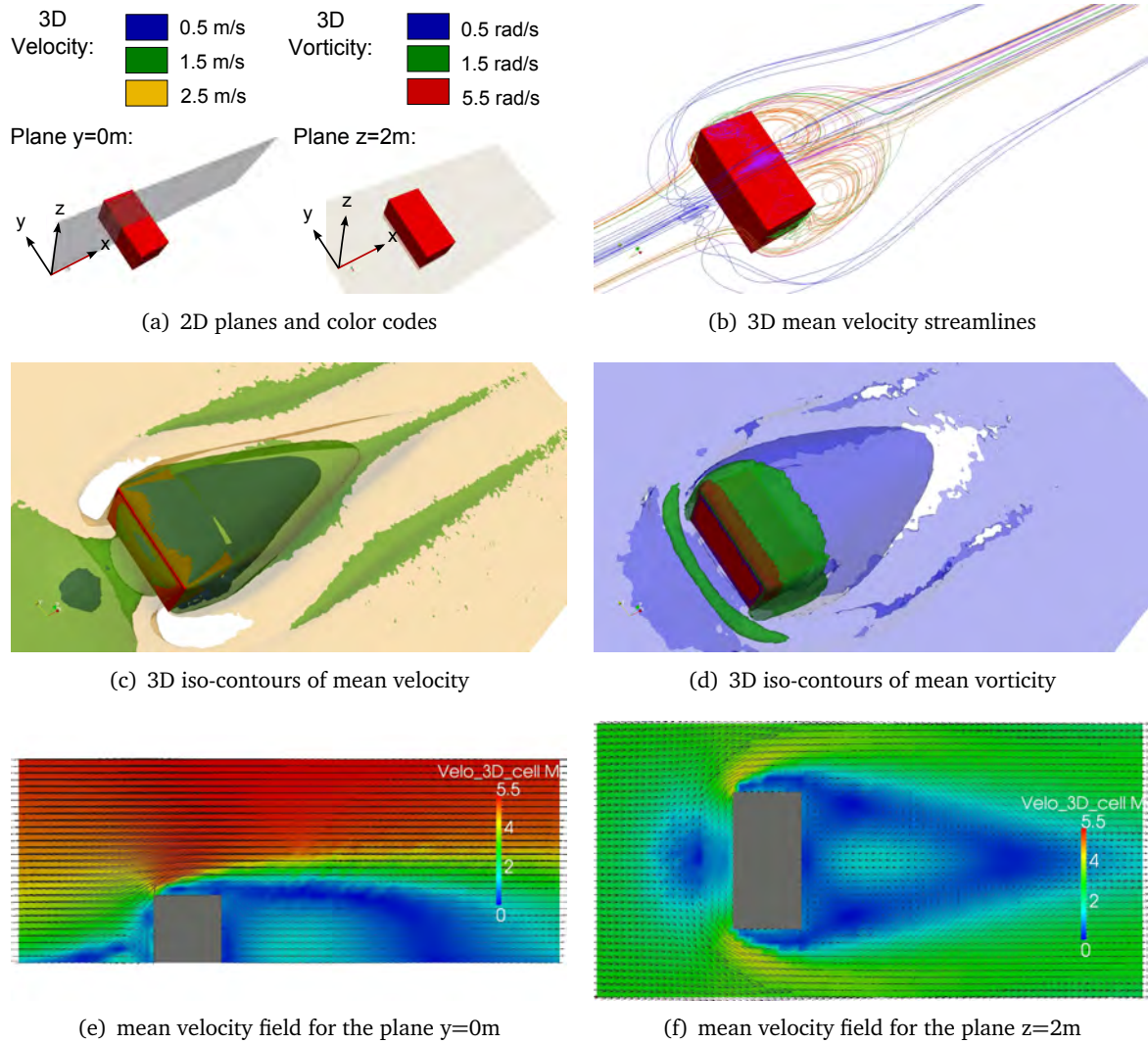


Figure 4.5: Aerodynamic results for the cuboid.

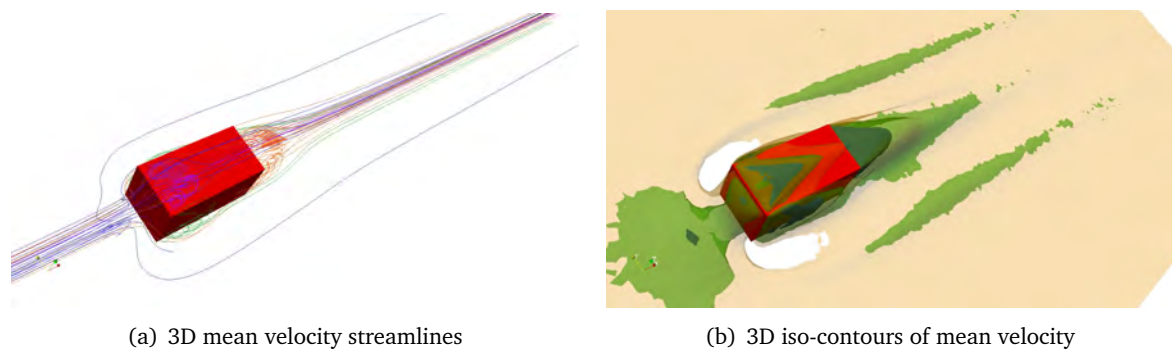


Figure 4.6: Aerodynamic results for the cuboid: orientation effects.



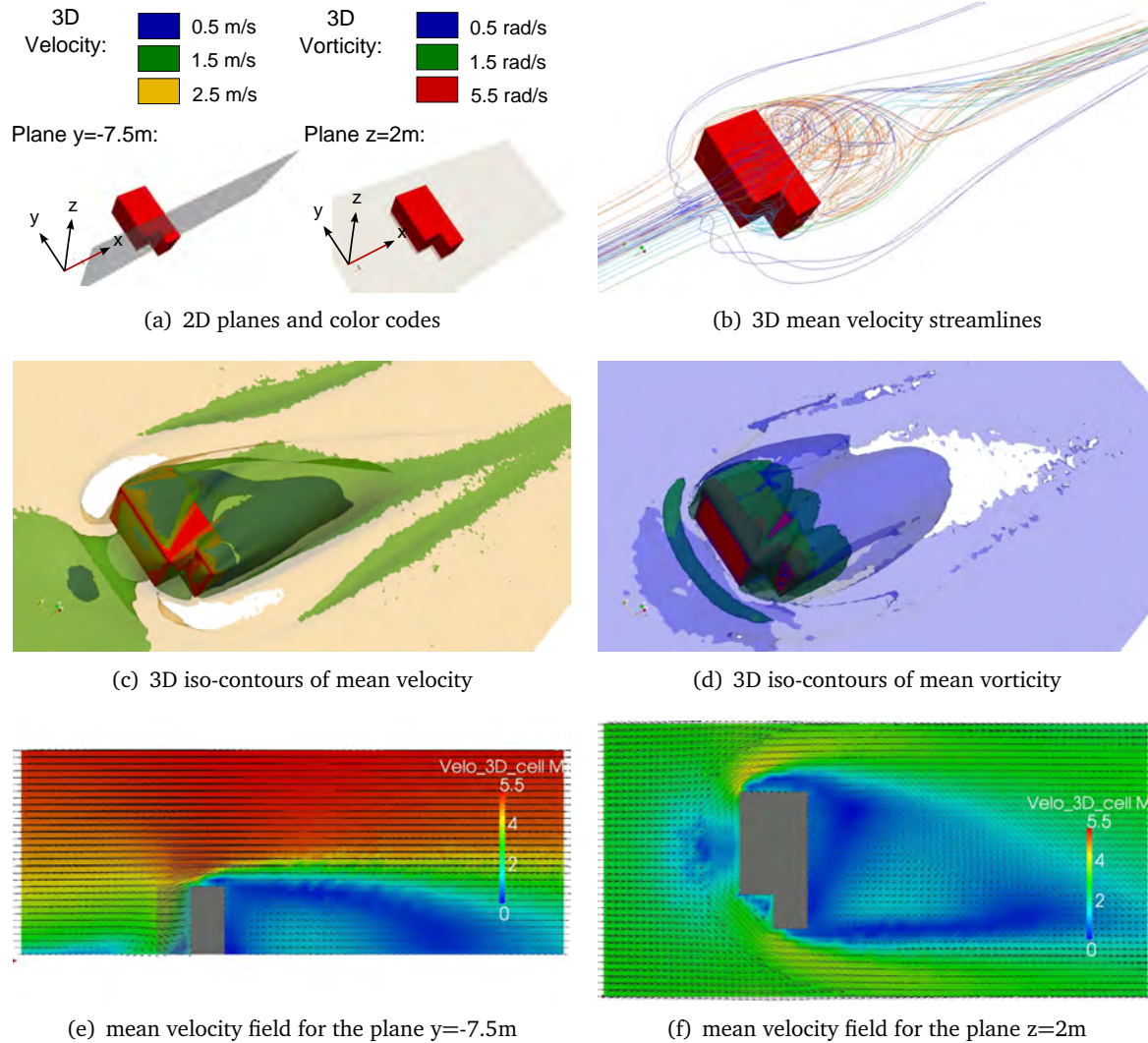


Figure 4.7: Aerodynamic results for the L building.

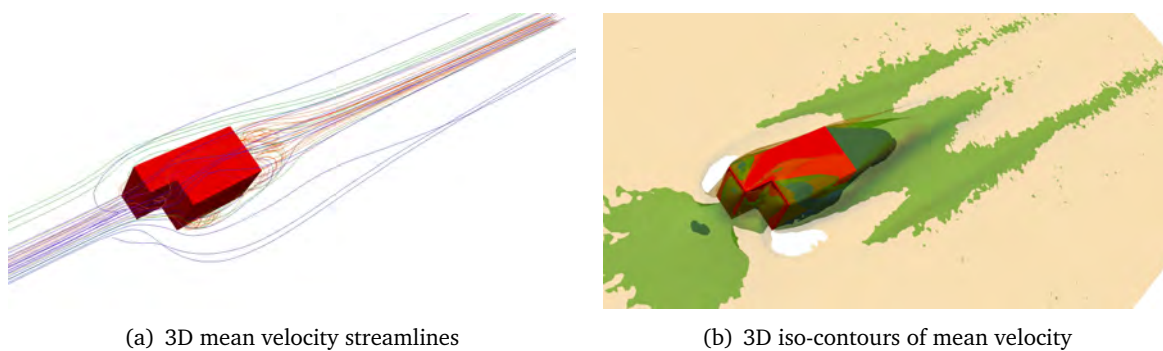


Figure 4.8: Aerodynamic results for the L building: orientation effects.

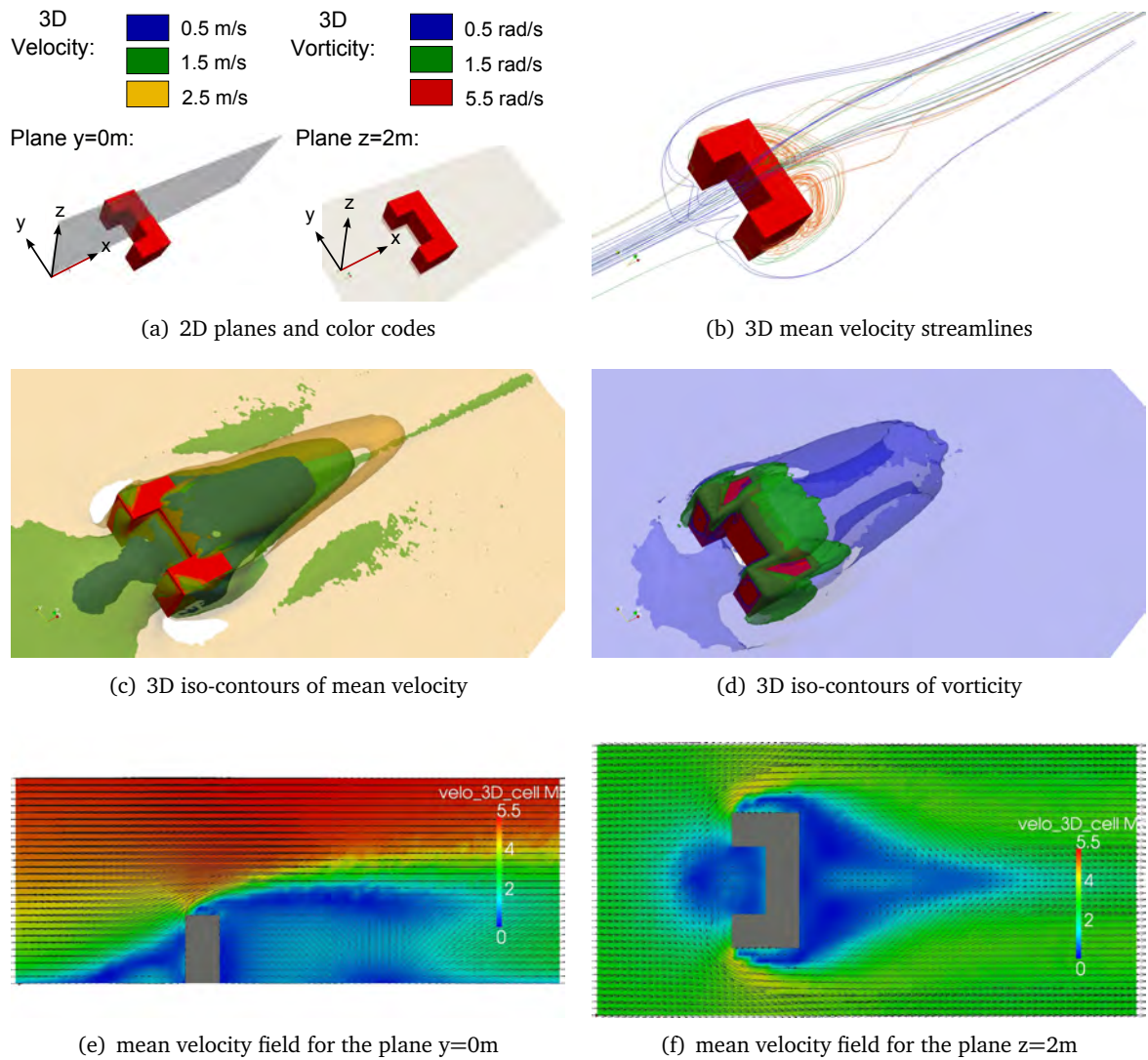


Figure 4.9: Aerodynamic results for the U building.

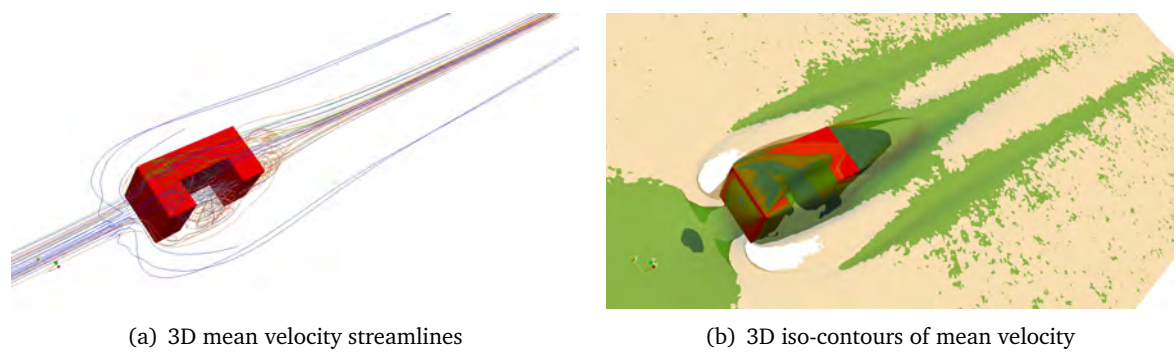


Figure 4.10: Aerodynamic results for the U building: orientation effects.

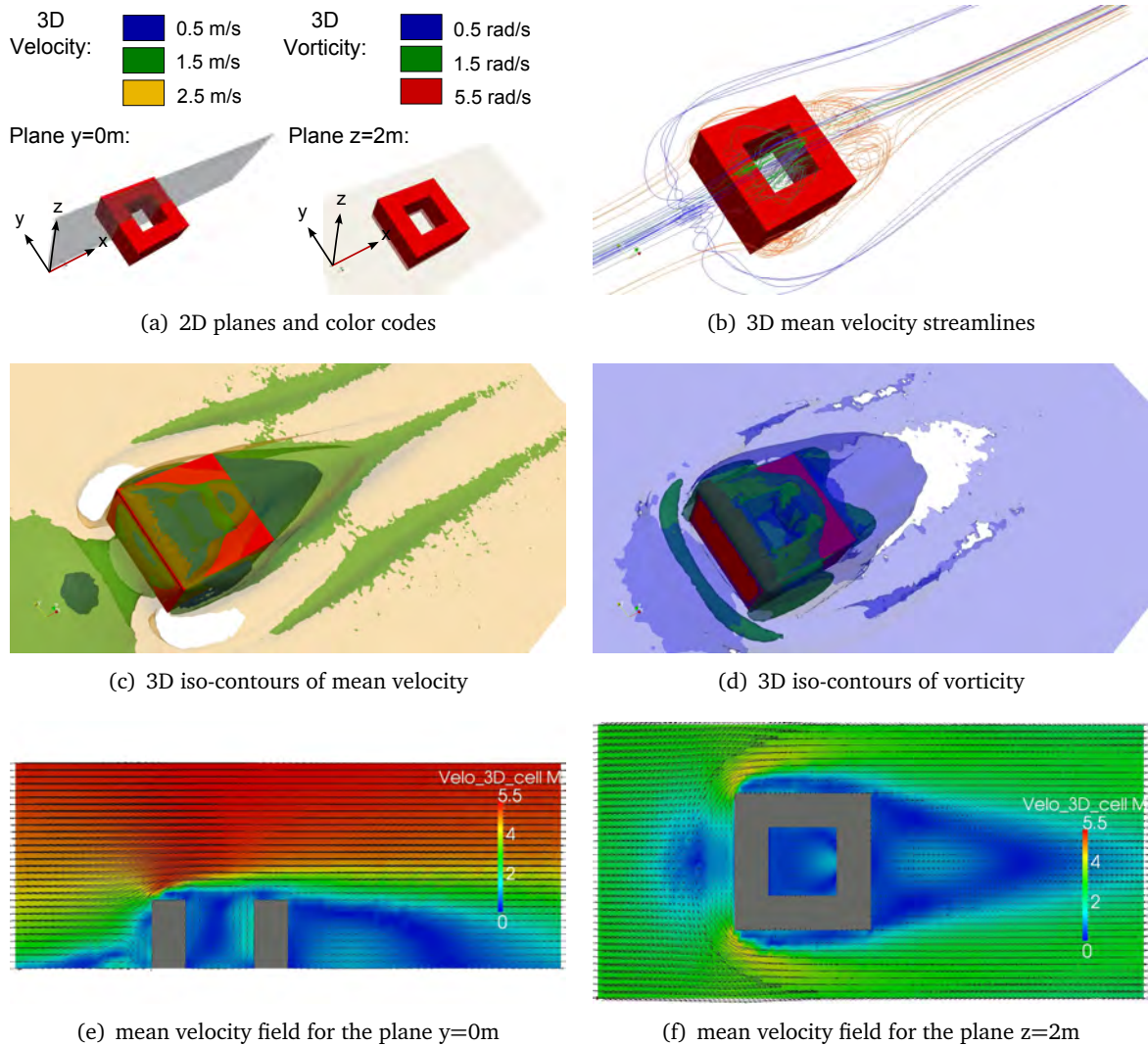


Figure 4.11: Aerodynamic results for the patio.

## 4.3 CFD modeling of the urban block types

### 4.3.1 Specific settings of the model

The left hand-side of Fig. 4.12 shows the domain size used to simulate the different urban block types. Obstacles are located  $5H$  downstream the inlet plane as well as  $5H$  from the top boundary of the domain. The distance between the obstacles and the lateral boundaries of the domain is at least  $13H$  because of the increased width of the obstacles. As such,  $BR_V = 16.7\%$  and  $BR_H = 23.5\%$ .  $BR_H$  is slightly higher than recommended for the horizontal direction ( $BR_H = 22\%$ ), but  $BR_{tot} = 3.9\%$ , which is in accordance with the recommended  $BR_{tot} \leq 5\%$ . Note that the increased domain width was also taken into account when modeling the approach flow used in the subsequent simulations. The outflow is located  $20H$  downstream the model, which is further than for the isolated types because of the increased length of the models.

In addition to the domain size, the only substantial difference of the current computational configuration as compared with that of the isolated types is the reduced order of the numerical schemes. They were specified as second order upwind because stability problems occur when using the third order MUSCL scheme especially in cases of non crossing forms.

For the row and the U blocks, two model orientations are tested with respect to the mean wind incidence. Flow patterns that develop inside a street canyon undergoing a wind parallel or normal to the street axis, as well as the potential sheltering effect of a U block as it is sometimes considered in urban planning<sup>8</sup> can thus be examined. Fig. 4.13 illustrates the different cases tested and presents their respective names.

Considering these urban block types, the basic mesh resolution ( $1\text{ m}$  on the ground and  $0.3\text{ m}$  on the obstacle roofs) was often not sufficient to obtain converged and symmetric solutions. Significantly finer mesh resolutions were needed to simulate the cube array, row block 2, U block 2 and the continuous patio array. Simulations were generally stopped after  $6 \times 10^3$  iterations for simpler cases and after  $1 \times 10^4$  iterations for more complex cases. For the most finely discretized models, simulations last between one week and more than two weeks. Note that no stabilized, smooth and symmetric wake could have been achieved for the U block 2 even after  $1 \times 10^4$  iterations and a great number of cells ( $\approx 13$  days of computation). As a consequence, results presented hereafter might only be approximates of the flow solution, assuming the effective existence of a stable and symmetric mean flow. In addition, only a local convergence was achieved for the continuous patio array. Numerical instabilities occurred periodically during the computation. They disturbed the flow especially in the wake. The solution was taken for further analysis after  $6 \times 10^3$  iterations as no instabilities occurred during more than  $2 \times 10^3$  iterations before. However, an instability yet emerges in one of the lateral downstream patio, which led to a numerical discontinuity some iterations later.

---

<sup>8</sup>For example, U blocks oriented South and facing the sun but blocking the wind coming from the North are often observed in the Northern hemisphere.



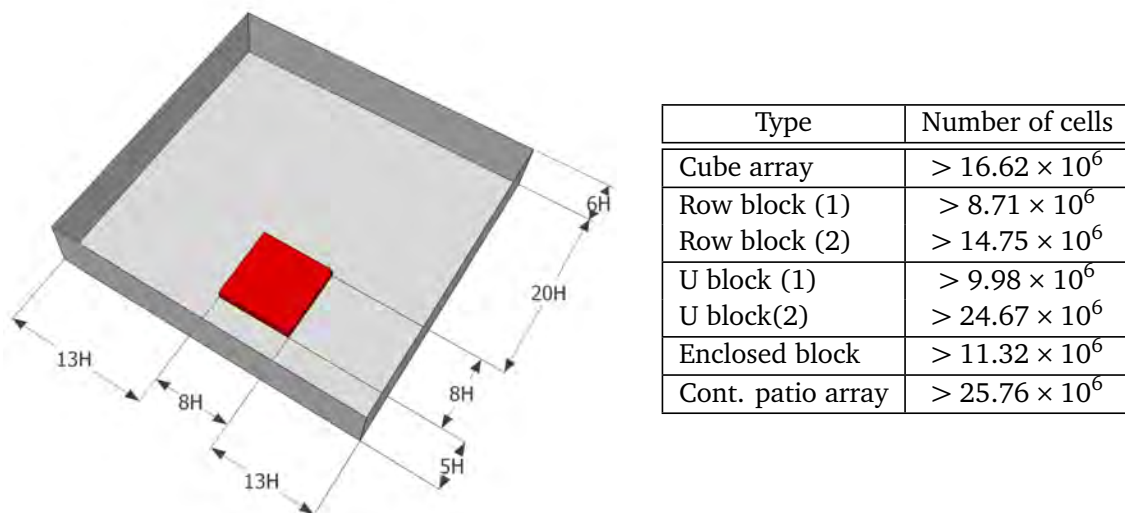


Figure 4.12: Computational domain and number of cells used to model the urban block types.

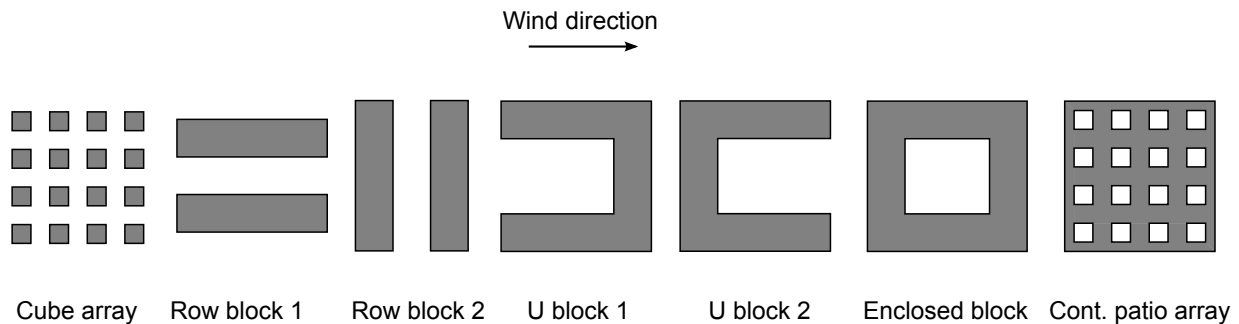


Figure 4.13: Schemes and names of the different configurations tested (urban block types).

The right-hand side of Fig. 4.12 shows the number of cells used to appropriately simulate the flow for each type. Values vary between  $8.7 \times 10^6$  and  $2.5 \times 10^7$  elements, which is five times more than required for the isolated types and involved quite long computation times. Because of the big meshes required, simulations were preferably run on only one of the computation servers running Linux with 7 GPUs. However, for the finest meshes (cube array, row block 2, U block 2 and continuous patio array), simulations were run on the CPU-based computation server because the RAM of the GPU-based server was not sufficient. As a consequence and considering these computation time and hardware limitations, no mesh sensitivity study could be performed.

### 4.3.2 Simulation results

First of all, in order to verify the relevance of our simulation outputs in such complex configurations, some simulated flow regimes are compared to existing studies. For that purpose, morphometric indicators are estimated, including the aspect and length to height ratios ( $H/W$  and  $L/H$  (Oke, 1988)) of the canyons formed within the cube array and the row block 2. Simulation results are in accordance with literature indications:

- with  $H/W = 1$  and  $L/H = 1$ , a dominant skimming flow regime is observed between the different cubes of the cube array as recirculation phenomena develop in canyons;
- with  $H/W = 2$  and  $L/H = 8$ , a complex flow pattern that does neither correspond to a skimming nor to an isolated flow regime is observed between the two rows of the row block 2. Note that however, no clear 2D recirculation is observed in the theoretical symmetry plane. The computed flow is clearly dominated by the convergence of the two lateral streams, which springs upwards around the symmetry plane. This flow behavior corresponds to the indications given in [Beranek \(1984a\)](#), which reports the development of (uncomfortable) transverse flows between parallel and long buildings that stand perpendicular to the wind incidence.

Then, extending the application of the  $W/S$  ratio of passage between buildings ([Blocken et al., 2007a](#)), this indicator was calculated for the first line of the cube array, the row block 1 and the U block 1. The simulated flow regimes in the upstream part of these configurations verify literature statements:

- with  $W/S = 1$ , a faster flow than the external corner streams is observed between the cubes of the first line as corner streams interact with each other;
- with  $W/S = 1.58$  and  $3.17$  a transition towards the isolated flow regime is observed between the two rows of the row block 1 and the isolated flow regime is observed between the two arms of the U block. Flows developing around the parallel constructions weakly interact for the row block 1 and do not interact for the U block 1. These results are also in accordance with indications given in [Beranek \(1984a\)](#).

According to these first results, predictions correspond to literature statements, at least with respect to the internal flow patterns. Recirculation phenomena as well as forced flows appear reproduced by the computational model.

The following presents the flow fields for each of the seven case studies in terms of:

- 3D mean velocity streamlines:
  - one drawing mostly illustrating the internal flows;
  - one drawing mostly illustrating the external flows, i.e. the group effect;
- 3D iso-contours of:
  - mean velocity  $\|U\| = 0.5, 1.5$  or  $2.5 \text{ m} \cdot \text{s}^{-1}$ ;
  - vorticity  $\|\omega\| = 0.5, 1.5$  or  $5.5 \text{ rad} \cdot \text{s}^{-1}$ ;
- 2D mean velocity fields (vectors and magnitude) in:
  - the vertical plane  $y = 0 \text{ m}$  as well as another plane specific to the type, which generally cuts in the middle of courtyards or through continuous parts of the blocks;
  - the horizontal plane  $z = 2 \text{ m}$ .

Again, the explanation of the different color codes and schemes illustrating the section planes and coordinates system are given for each case. To complete the analysis, Appendix O provides

comprehensive results with larger figures for each of the seven case studies, including other 3D mean velocity streamlines and 2D velocity fields. In particular, Appendix O provides comparative sections highlighting the different recirculation phenomena that develop in the central or external rows of cubes or patios, as well as sections illustrating mean flow conditions in the lateral parts of the wider internal open spaces.

At the first glance, Fig. 4.14 - 4.20 highlight both a general effect of the blocks as well as specific inner flow structures.

On the one hand and with the exception of the row block 1, a general group effect appears. Widespread single or merged singular flow regions develop upstream (over pressure region, horseshoe vortex) and downstream (cavity zones) the blocks. A second reattachment is often observed at the aft corners of the types. This produces two accelerated flows on the lateral sides of the wake. This phenomenon may be related to the increased length of the blocks in comparison with the isolated building types as it does not clearly develop for these latter cases.

On the other hand, flow speeds inside blocks appear on average weaker than outside especially in recirculation regions. Rather high velocities can be however observed especially in the row block 1 where the flow velocity almost corresponds to the external one, at the very upstream part of the cube array, where the flow is accelerated as previously mentioned ( $W/S = 1$ ) as well as in the lateral parts of the street formed in the row block 2.

In comparison with the isolated building types, differences due to the size of the courts for types of the same topology are stressed. On the one hand, similar flow structures develop in the patio and the enclosed block. On the other hand, a relatively self-contained but unbounded vortical recirculation that does not correspond to what happens in the U building 3 develops in the court of the U block 2.

Aerodynamic interactions between detached obstacles appear as well. They are particularly visible in the row block 2 and the cube array, which shows the two flow regimes identified in [Coceal et al. \(2014\)](#), i.e. flow paths in alleys and recirculation phenomena between the cubes. For the most fractal types, i.e. the arrays, a streamwise evolution of the inner flow patterns is also observed from the upwind edge of the blocks to their core, illustrating border effects and the relative flow adaptation to the built structure. However, because of the limited number of elements, no clear self-similar flow could be observed (see [Kastner-Klein et al. \(2004\)](#), Sec.1.2.3).

These different internal and external flow structures and their links with the morphological features of the blocks are further discussed in Sec. 4.4.1 and Sec. 4.4.2.

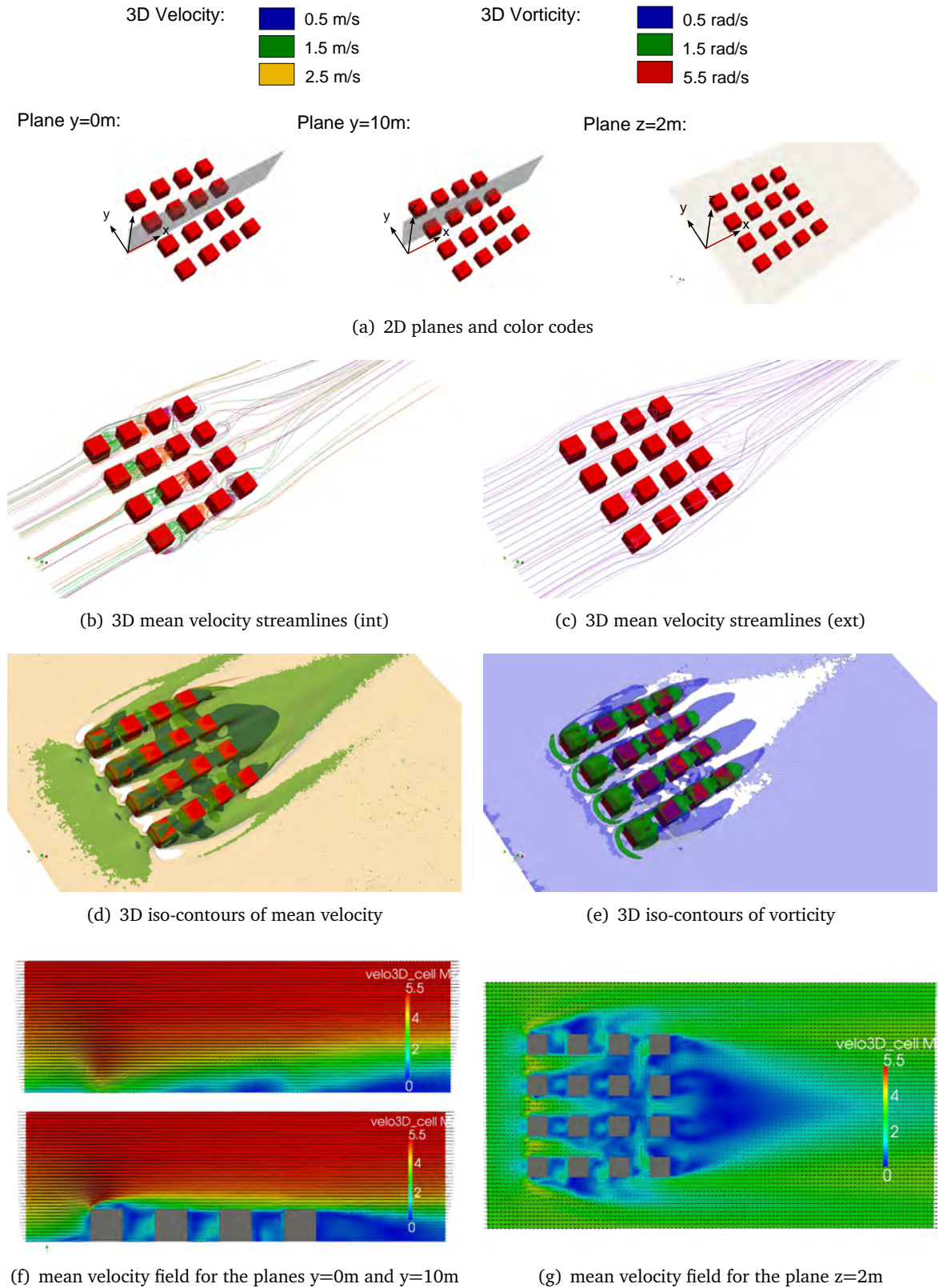


Figure 4.14: Aerodynamic results for the cube array.



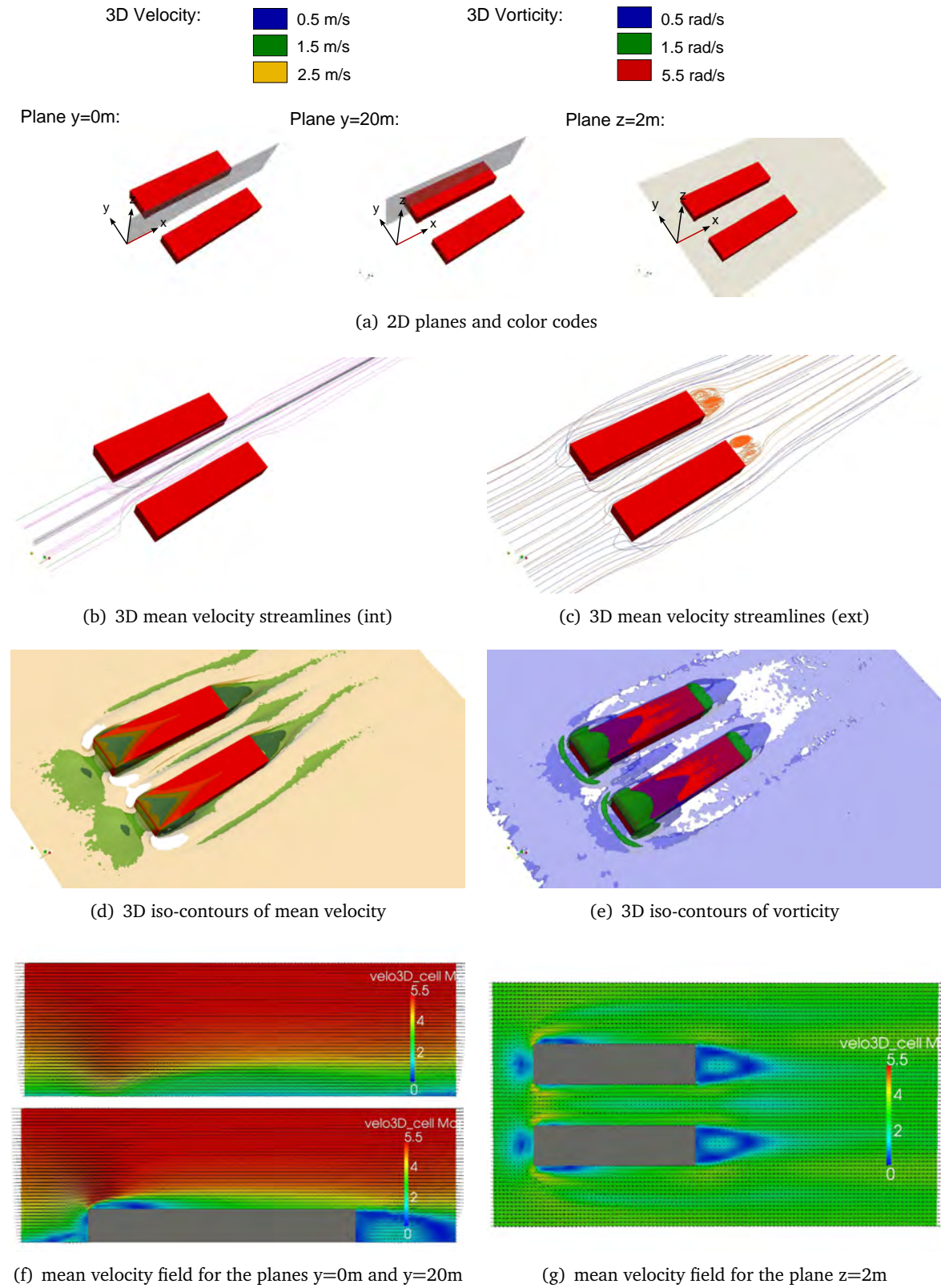


Figure 4.15: Aerodynamic results for the row block 1.

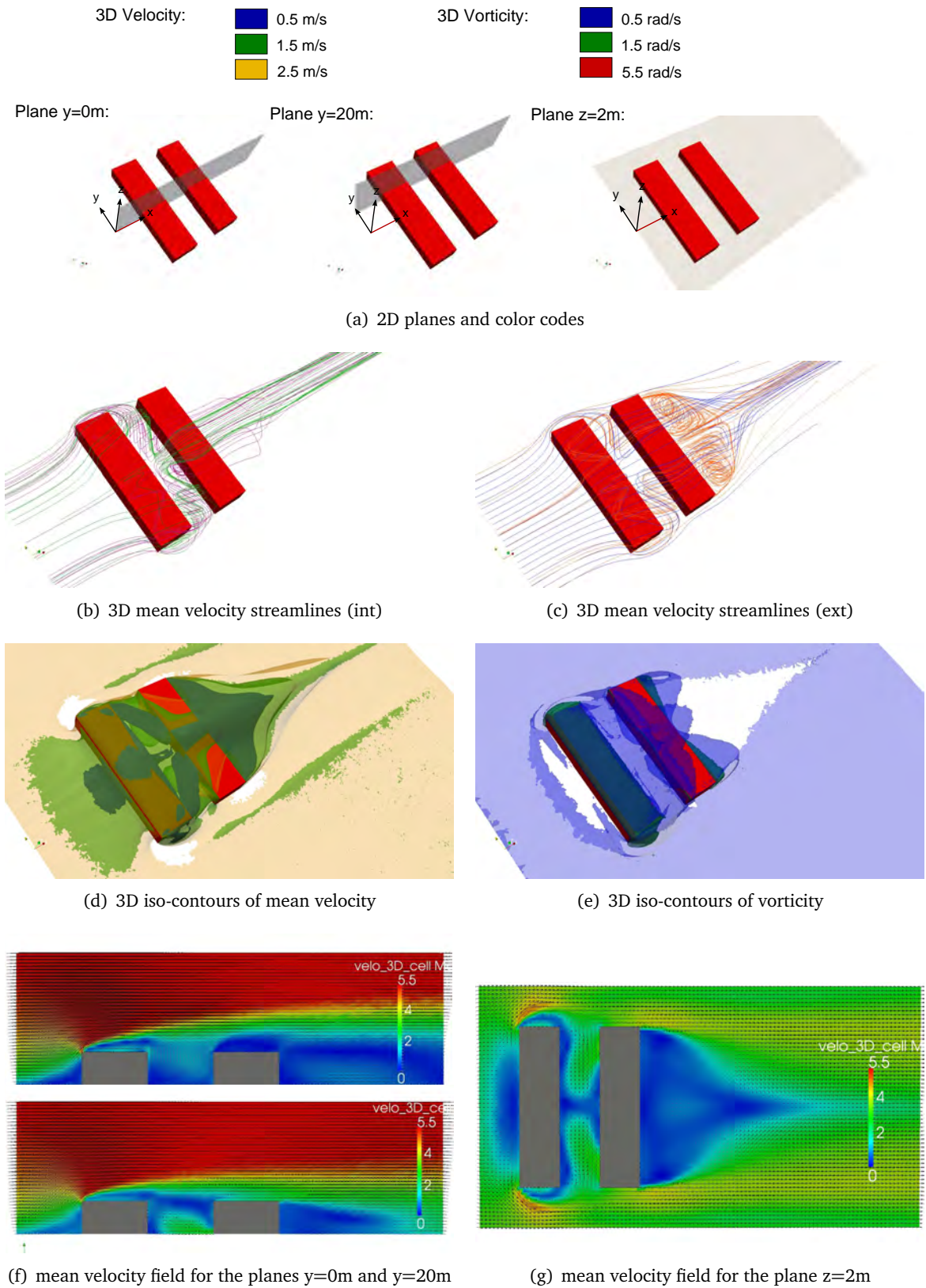


Figure 4.16: Aerodynamic results for the row block 2.



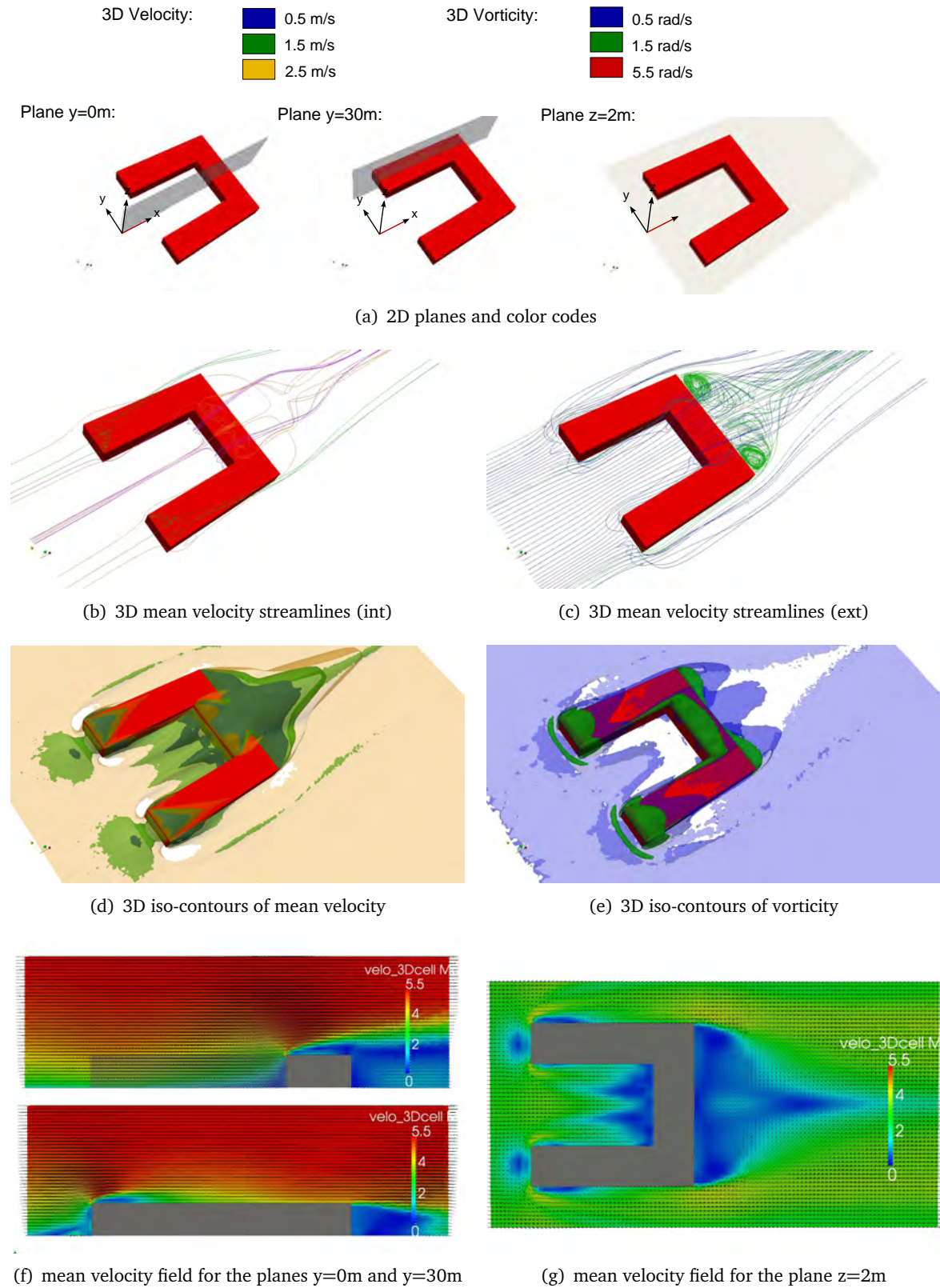


Figure 4.17: Aerodynamic results for the U block 1.

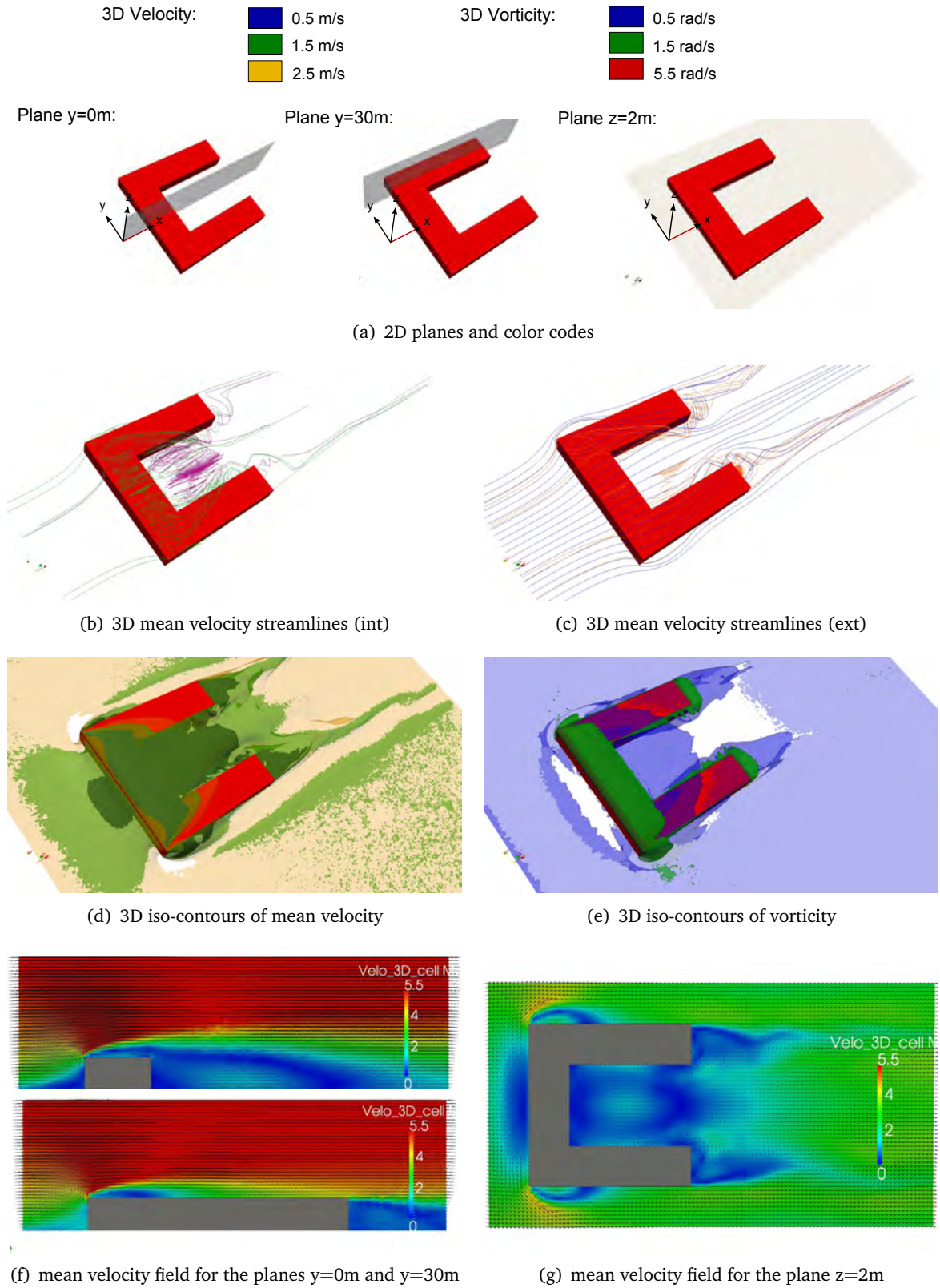


Figure 4.18: Aerodynamic results for the U block 2.



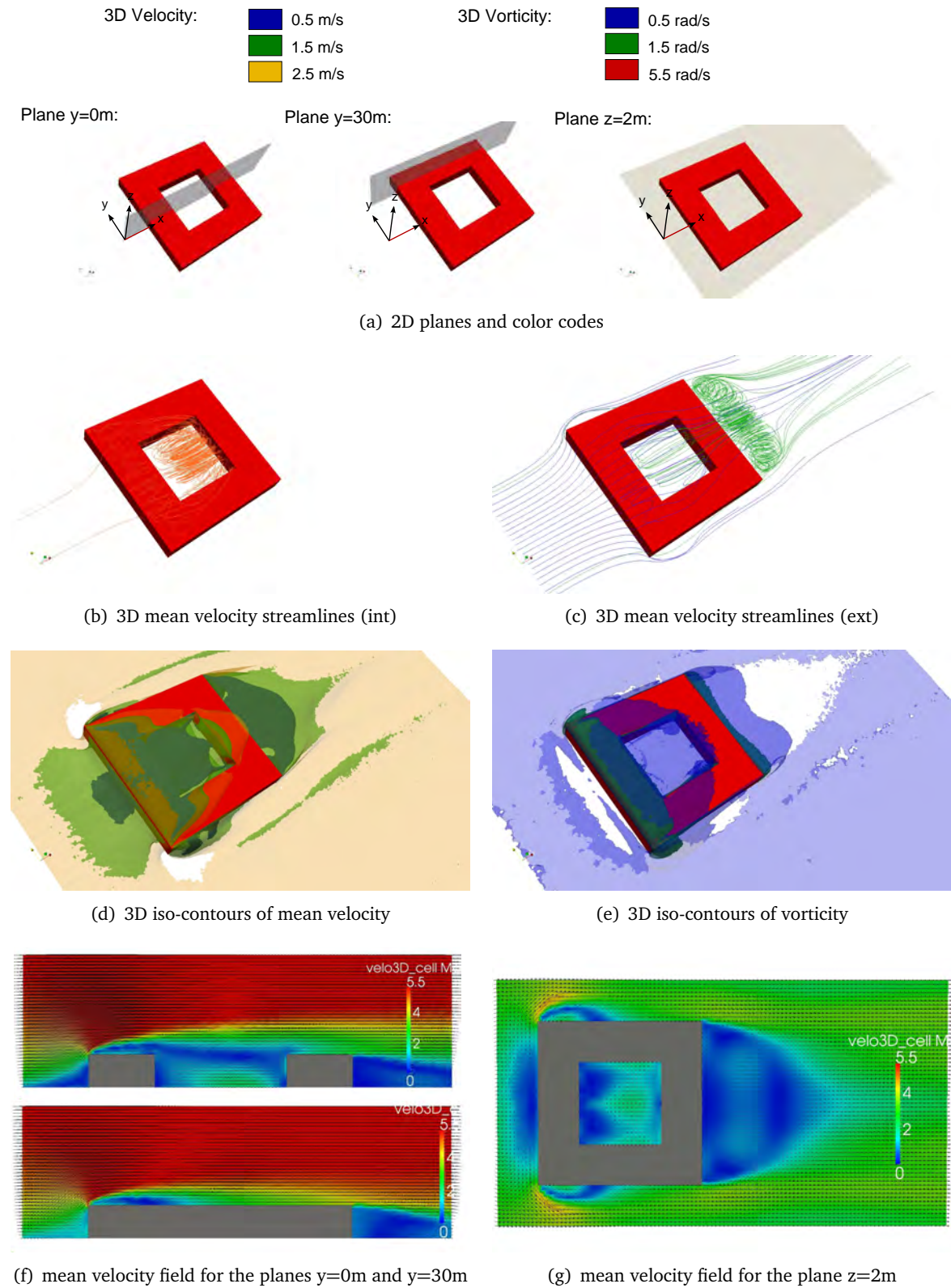


Figure 4.19: Aerodynamic results for the enclosed block.

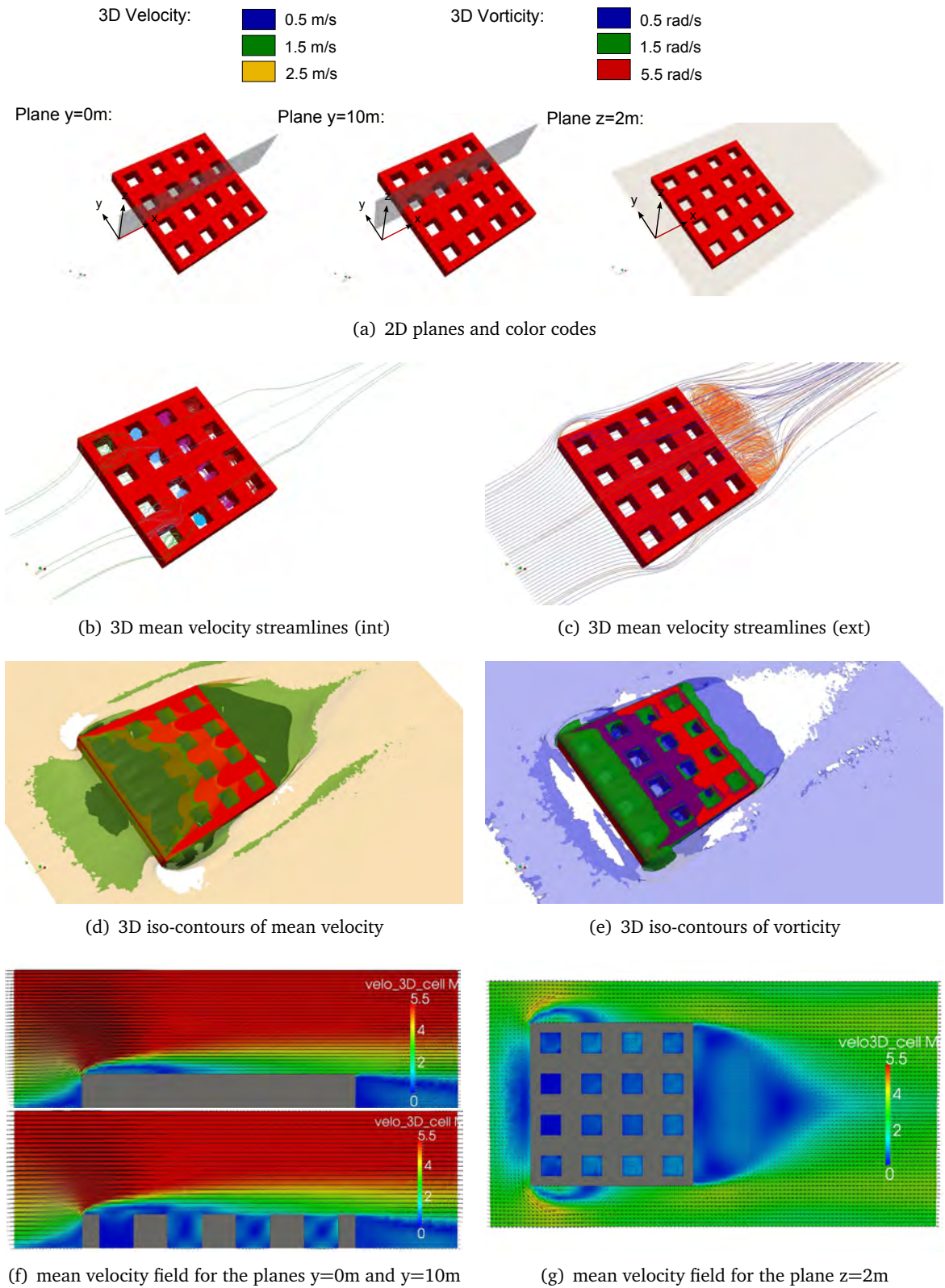


Figure 4.20: Aerodynamic results for the continuous patio array.

## 4.4 Effects of urban morphological features on air flows

### 4.4.1 Analysis of the external flows patterns: topology and size effects

The basic upwind, top, side and downstream flow structures highlighted in Sec. 1.2.3 generally develop around each obstacle or group of obstacles. However, they can be distorted, retrained or even inhibited depending on the morphological configuration.

Firstly focusing on types having a rectangular external perimeter and because all types have the same height, direct effects of the obstacles relative dimensions emerge. In complement to the 3D views, Tab. 4.2 recapitulates the main characteristics of flow structures around these rectangular-based types in the plane  $y = 0$  m. Values were graphically determined using 2D streamlines. As a consequence, some differences can occur in comparison with the 3D analysis, especially with respect to the top bubble, which might not be captured by the 2D flow post-processing.

According to these 2D features and the one hand, the upwind vortex center is located about  $0.5H$  upstream the isolated building types and  $0.35H$  upstream the urban blocks. Moreover, considering the isolated building types, the wider the obstacle, the higher its center: it is located at  $z = 0.1H$  and  $z = 0.2H$  for the thinner and wider obstacles respectively. However, it is located at  $z = 0.175H$  for the urban block types, thus a bit lower than for the  $2H$  wide building types. These 2D features confirm the differences in the location of the upstream stagnation zones depending on the obstacle width that can be observed on the 3D iso-contours of mean velocity. They also highlight differences in the structure of the upwind part of the horseshoe vortex, which can also be deduced from the 3D iso-contours of mean vorticity. Hence, counter-intuitively, the wider the obstacle is, the closer is the upwind vortex. Moreover, the wider the obstacle is, the more intense are the corner streams. Higher flow speeds are observed in the plane  $z = 2$  m for the urban block types that have a continuous windward facade. The relation linking the vortex height to the relative dimensions of the built structure is more complex as contrasting trends occur. The vortex center does not necessarily move upwards when the obstacle width increases. Such a rising behavior occurs for high  $H/W$  ( $0.5 \leq H/W \leq 1$ ) but a slightly descending one occurs for low  $H/W$  obstacles ( $H/W \leq 0.25$ ). Note that the obstacle length seems not to affect the upwind vortex, at least in the symmetry plane.

Still according to the 2D flow features and on the other hand, the downstream reattachment point is located significantly closer to the obstacle for the cuboid 2 than for the cube or the patio. However, that of the cuboid 1 is located significantly further away. The downstream reattachment points of the enclosed block and the continuous patio array are located even further away.<sup>9</sup> Thus, the wider the obstacle, the longer and wider the cavity zone, but the longer the obstacle, the shorter the cavity zone. The obstacle length moderates the effects of its width.

---

<sup>9</sup>The relative distances of the downstream reattachment point from the downstream surface of the obstacles are 65 % for the parallelepiped 2, 100 % for the cube, 115 % for the patio, 155 % for the cuboid 1, 187 % for the enclosed block and 225 % for the continuous patio array.

Case	Upwind vortex		Top vortex		Wake recirculation		Downstream stagnation	
	X/H	Z/H	X/H	Z/H	X/H	Z/H	X/H	Z/H
Cube	0.52	0.10	-	-	0.65	0.80	2.0	0.0
Cuboid 1	0.50	0.20	0.56	1.15	-	-	3.1	0.0
Cuboid 2	0.55	0.10	-	-	0.70	0.82	1.3	0.0
Patio	0.55	0.20	0.30	1.1	0.9	0.80	2.3	0.0
Encl. block	0.37	0.17	1.1	1.22	1.70	0.60	3.7	0.0
Patio array	0.35	0.17	0.87	1.17	1.9	0.67	4.5	0.0

Table 4.2: Location of flow structures around the rectangular-shaped types in the plane  $y=0m$ . For the centers of the upwind and top vortices, abscissa are given with respect to the upwind surface of the obstacles. For the wake recirculation center and downstream stagnation region, they are given with respect to the downwind surfaces of the obstacles.

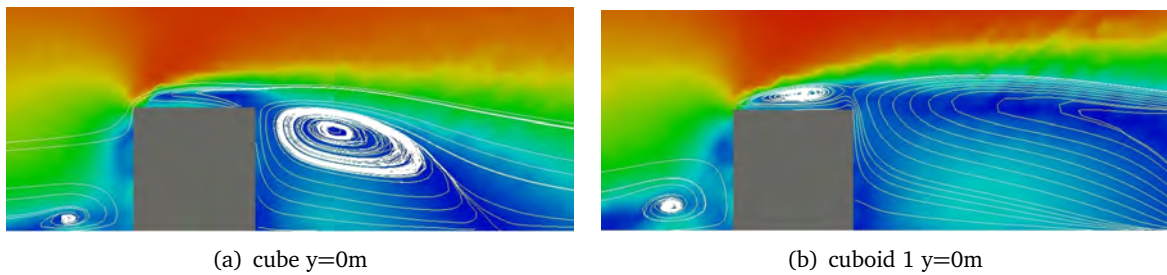


Figure 4.21: 2D mean velocity streamlines around the cube and the cuboid 1.

Further than the extent of the wake recirculation, its shape appears conditioned by the interactions between the lateral aft vortices and the top separated flow. These lateral aft vortices develop next to the downwind corners of obstacles. Their location and more precisely their spacing is therefore determined by the obstacle width. However, depending on the obstacle relative dimensions, they can produce either rather linear cavity zones for relatively narrow buildings, e.g. the cube, or more curved and widespread zones for larger obstacles, e.g. the enclosed block. The central part of the near wake appears for its part to be dependent on the shear layer separation at the central top leading edge.

The internal structure of the block also influences the flow around it, but apparently to a lesser extent than its overall width. Indeed, quite similar flow structures are observed around the enclosed block and the continuous patio array. The cavity zone is nonetheless longer downstream the continuous patio array than downstream the enclosed block.

Regarding the cavity zone in more details, Fig. 4.21 compares the 2D flow structures around the cube and the cuboid 1 in the theoretical symmetry plane. No clear closed vortical and vertical flow appears in the wake of the cuboid 1. This observation is supported by the behavior of the corresponding 3D streamlines downstream this obstacle shown in Fig. 4.6. The two lateral counter-rotative vortices appear well developed and stretched streamwise whereas no vertical one appears. Moreover, a secondary upwards flow occurs downstream the reattachment. Such an unclosed arch vortex was also experimentally observed by [Meinders and Hanjalic \(1999\)](#) in a



cube array. On the contrary, the vertical vortical flow appears well defined downstream the cube and the other rectangular-shaped types. Furthermore, 3D streamlines and the mean velocity field in the plane  $z = 2\text{ m}$  highlight a rather 2D behavior in the central part of the downstream recirculation of the enclosed block and the continuous patio array (see Fig. 4.20 and Fig. 4.19). This results are supported by [Matinuzzi and Tropea \(1993\)](#), who stressed a 2D flow development in the wake of sharp-edged obstacles with  $W/H \geq 6$ . These different regimes might be related to the development of the aft corner vortices and above separated flow, which develops over a longer area when increasing the obstacle width, up to a critical point for which the major part of the incoming flow passes over the obstacle with a rather 2D behavior.

In a first stage, the obstacle width appears to be the most determining factor in shaping the main flow structures around rectangular-shaped obstacles, i.e. the upwind standing vortex and the downstream cavity zone. The length and inner composition of obstacles can however substantially modulate its effects, especially with respect to the near wake recirculation. As the height of obstacle is constant, these results verify statements given in [Beranek \(1984a\)](#). However, all the above-mentioned basic flow structures, i.e. the upwind vortex, cavity zone and other top and side recirculation phenomena, are substantially altered when increasing the complexity of the obstacle shape. In particular, the basic flow structures are generally distorted, weakened, amplified or even prevented when obstacles can be crossed by the flow, present high  $W/L$  and a particular upwind flow state, or are no more symmetric with respect to the wind direction.

Merged, aggregated or isolated effects occur depending on the porosity of the structure. Fig. 4.15 shows that each row of the row block 1 creates its own recirculation phenomena as rows are widely spaced. Flow structures around each row almost correspond to those that develop around an isolated obstacle. On the contrary, a general group effect emerges around the cube array. Although the effect of each row of cubes can be observed in its vicinity, more general flow structures are created due to their interactions (Fig. 4.14). A wide low velocity zone appears upstream the array and an aggregated near wake is produced downstream. Because the incoming flow can cross the array, the near wake is stretched as compared to that of continuous constructions. The downstream low velocity region extends roughly  $10H$  downstream the array, which is about 50 % further than for the continuous patio array, although its external dimensions are larger. However, the region of very low velocity corresponding to the near wake recirculation is located a bit closer to the central cubes than it is for the continuous patio array. This is certainly due to the smaller dimensions of the cubes. Hence, at the upper scale of the urban block, the overall upwind disturbed region is reduced when obstacles are sufficiently close to each other to interact but sufficiently distant to let the incoming flow pass through compared to a continuous configuration. The wake is also stretched. Conversely, for widely spaced obstacles, flows do not interact and an almost isolated flow regime occurs. For closer obstacles, the external flows are expected to behave like around a continuous obstacle.

Further examining the particular flow structures around the U building 1 highlights differences between the induced flow structures and those of the cuboid 1. Both types have the same external footprint but the U building 1 presents an upstream court bounded on its lateral and

downstream sides as well as a thin obstacle core. The cavity zone appears smaller and spade-shaped. Conversely, the near wakes of the U building 3 and cuboid 1, as well as those of the U building 2 and the cuboid 2 respectively resemble to each other. Such a spade-shaped cavity zone also develops downstream the U block 1 and the row block 2, which also have an upstream semi-open space and present continuous rear faces but rather thin building cores. In these configurations, the tip of the spade is very narrow and long. It progresses substantially further than the remainder of the cavity region, even further than the cavity zone of the square-shaped types. The relative low depth of structures together with the particular upstream flow state may thus affect the detachment of the above shear layer, which is maintained further higher in such configurations as compared to what happens for longer built structures. This may also affect the shape of the top bubble and in particular its reattachment. Indeed, the very low velocity zone at the top exceeds the roof. An elongated region of higher vorticity also extends at the obstacle height downstream the central part of the thin roof, translating a shear flow at this location. This corresponds to the extension of the roof low velocity zone. This higher vorticity region comes in addition to the distinct vorticity zones characterizing the lateral aft vortices, which generally develop downwind built structures. Hence, the particular detachment of the above shear layer induced by thinner buildings, which is potentially strengthened by the upwind flow conditions that force the flow upwards, appears as a decisive factor in shaping the near wake.

Regarding asymmetric configurations, distortions of the basic flow structures appear clearly around the L building 1, U building 2 and L building 3. Because of the asymmetric flow blockage and the non reattachment of the flow on its smaller side, the near wake of the L building 1 shows a main and wider aft corner vortex. The size of the second aft vortex is significantly reduced. As a result, the cavity zone is curved on one side and rather leaf-shaped in the horizontal plane. The length of the near wake is maximum on the court side and not in the plane  $y = 0$  m. Its horizontal extent is nonetheless similar to that of the cuboid 1. This particular shape can be compared to the curved flow structures that were observed in the non-stabilized results of the asymmetric configurations mentioned in Sec. 4.2.1. They were characterized by some kinds of whirls in the wakes. Such distorted forms also appear in the wake of the stabilized mean flows around the other asymmetric configurations. However, in these configurations, the distortion of the wake is weaker than it is for the L building 1. The flow has more room to reattach on the sides of the obstacles. Moreover, as compared to the L building 1 configuration, the stronger aft vortex seems to develop on the opposite side, i.e. on the court side.

The upwind location of the court in the L building 2 as well as the correspondence between the shape of the semi-open court and the path of the corner stream decrease the blocking effect as compared to that of the cuboid 2. Consequently, the upstream vorticity is reduced and likewise the upwind standing vortex. On the contrary, the resulting corner streams appear a bit accelerated in comparison with those of the cuboid 2. Same sort of effects can be observed for symmetric configurations. Especially, the court of the U building 1 affects the development of the upwind standing vortex. The latter is amplified because the lateral paths of the flow that generally continue to form the horseshoe vortex are partially blocked. Similarly, the downstream court of the U building 3 is integrated into the cavity zone. As a consequence, the basic shape of the near wake

recirculation is altered. A complex 3D flow structure develops with two main horizontal swirls, which correspond to the modification of the usual aft corner vortices.

When the dimensions and in particular the length of semi-enclosed courts increase, as it is the case for the U blocks 1 and 2, differentiated flow structures develop. An internal recirculation is created, which is further discussed in Sec. 4.4.2. As the upstream flow blockage of the U block 1 is completely modified in comparison with that of a rectangular-shaped obstacle, the horseshoe vortex does not form. Only small and local recirculation phenomena can be observed upstream the two arms of the block and in the corner between the court floor and its upwind facade. Reciprocally, the downstream cavity region of the U block 2 is also altered as the cavity zone forms in the court creating the development of an internal vortical flow that is totally contained in the court. Only minor recirculation phenomena develop downstream the arms of the U block 2. Note that in the symmetry plane, the downstream reattachment region occurs at the same distance from the model core in the U block 1 and row block 2.

As a conclusion, the total external footprint of the types mostly determine the shape and extent of the flow structures that develop around them. For building groups, the porosity of the built structure is also essential. Considering rectangular-shaped built structures of constant height, increased width yields wider and longer downstream recirculation phenomena. However, the length and internal composition of the built structures moderate the development of the cavity zone and other recirculation phenomena. In particular, semi-open courts modify the different external flow structures whatever their location in relation to the wind incidence. They can amplify, distort, reduce or even inhibit the different external recirculation phenomena and reciprocally involve particular inner flows.

#### **4.4.2 Analysis of the inner flows patterns: effects of topology and orientation**

As they can more or less interfere with the external flow structures, inner flows that develop in courts significantly differ from one configuration to another. Their shapes and velocities vary, depending on the formal features of the court. In particular, the horizontal openness, relative dimensions and orientation of the courts in relation to the approach flow incidence are determining factors in shaping these inner flows.

The most obvious recirculation phenomena develop inside enclosed courts, i.e. in the patio, enclosed block and continuous patio array. Inside, flows are mostly 2D and the vortical structures develop vertically as they are driven by the above flow. Nevertheless, separated bubbles above courts can substantially increase the complexity of these inner flows.

According to Fig. 4.11 and Fig. 4.19 as well as the 2D mean velocity streamlines in the theoretical symmetry plane of the court given in Fig. 4.22(a) and Fig. 4.22(b), flow structures inside the patio and the enclosed block are fairly similar. A single 2D vortex linked with the upwind top separated bubble develops. However, the vortex developing in the enclosed block is horizontally stretched due to the increased dimensions of the court, and shows quite high velocities at pedestrian level. On the contrary, according to Fig. 4.20, Fig. 4.23(f) and Fig. 4.23(h), only weak flow

structures develop in the first line of patios of the continuous patio array. They strongly interact with the top bubble that is superimposed to them on their entire surface. In particular, recirculation phenomena that develop in the central patios substantially differ from that of the isolated patio. Two structures are formed, the upper one being merged with the general top recirculation. On the contrary, the recirculation developing in the external rows is like that developing inside the isolated patio. A single vortex develops, whose center is located just above the top of the patio. This vortex is horizontally asymmetric as its center and upper boundary are quite close to each other. It almost forms a cover over the patio. Note that according to the 3D streamlines, all the single recirculation phenomena above-mentioned, which correspond to enclosed courts undergoing an undisturbed incident flow, experience a flow supply from above, mainly through their lateral downstream parts. These additional flows come from the rollers that develop on the upstream part of the roof.

Semi-enclosed courts may also experience well defined and independent recirculation phenomena as in the U block 2 (see Fig. 4.18 and Fig. 4.22(d)). Such flow structures develop because of the court dimensions and the long arms. These properties prevent the formation of the lateral aft vortices and forbid any lateral flow supply downwind the spanwise part of the block. In such a configuration, a rather 2D vortical structure develops as well, showing velocities lower than in the enclosed block. As there is no downstream flow blockage, the detached flow can reattach on the downstream part of the court and continue its path downstream. Hence, as can be seen by comparing Fig. 4.22(b) and Fig. 4.22(d), the recirculation center is located about  $0.5H$  further in the U block 2 than in the enclosed block, but at a similar height. On the contrary, only a very small recirculation appears at the corner between the floor and the upwind wall of the U block 1. No general upstream flow blockage occurs but corner streams develop around the upwind face of the U block arms. As a consequence, quite high velocities are observed over a large part of the court, especially in its upstream part, and the horseshoe vortex does not develop as the flow entering the court cannot exit on the sides. The over-pressure zone that is created in the court induces an upward flow, which might intensify the shear layer detachment as compared to the U block 2.

When the court has one lateral side open, 3D internal flow structures develop. The upper flow induces a vertical flow recirculation while the lateral flow drives it horizontally. The flow around the U building 2 illustrates well such complex 3D flow structures. Inside its court, the velocity is slightly higher than in the patio. However, both configurations show quite similar velocity distributions. Higher flow speeds occur in the downstream part of the court in the plane  $y = 0\text{ m}$ . Note that the shape of the recirculation developing in the U building 2 resembles to a half arch vortex that can generally be observed downstream regular cuboid buildings. This can be explained by the fact that the semi-open court forms an under-pressure region, has both a side and the top open, and is entirely located in the wake of the windward surface. However, because of the downstream wall, the recirculation is constrained and the downstream part on the flow is forced downwards, similarly to what occurs for upstream and downstream bounded recirculation phenomena such as those developing in patios or between cubes in the cube array.

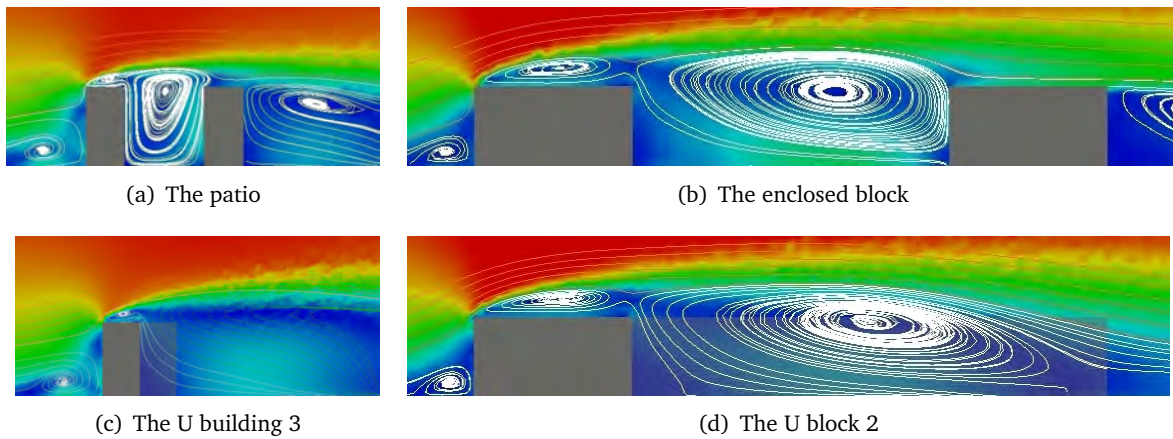


Figure 4.22: 2D comparison between the flow structures in the theoretical symmetry plane of the courts of the patio, enclosed block, U building 3 and U block 2.

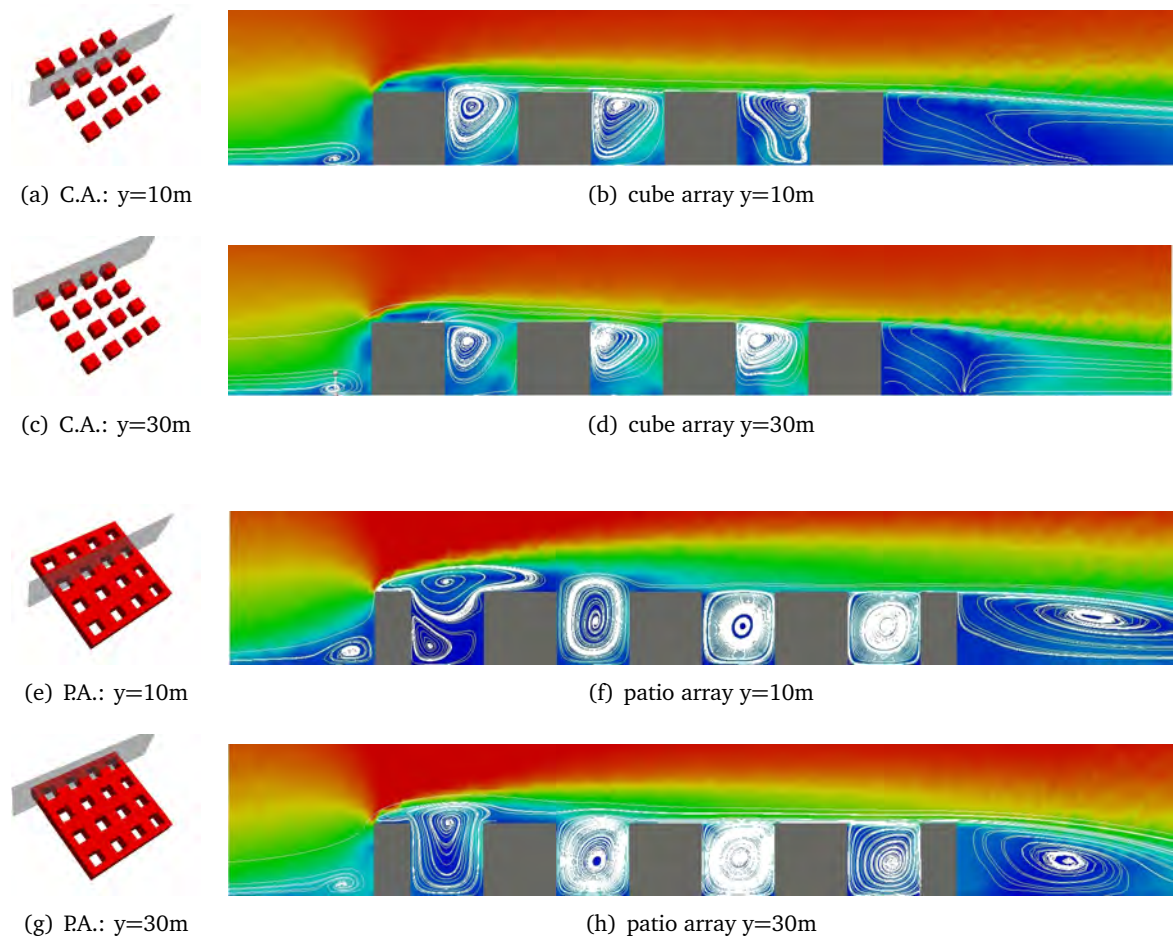


Figure 4.23: 2D streamwise evolution of the internal recirculation phenomena through the cube and continuous patio arrays.

For configurations with courts horizontally open on two consecutive sides, typically for L buildings, vertical tubes of flow can develop in the corners of the court. Such structures clearly develop in upwind courts of the L buildings 1 and 2. The roller is however larger in the first configuration than in the second due to the increased building width. In these courts, rather high velocities occur because corner streams drive the flow fast. Conversely, the flow speed is nearly zero in the downwind court of the L building 3 because it is integrated into the cavity zone.

In case of crossing outdoor spaces, i.e. in the cube array and the row blocks, clear flow paths appear in alleys as the flow is channeled inside. High velocities occur at pedestrian level in the upstream part of the cube array and the row block 1 because of the corner streams. High flow velocities also occur in the street of the row block 2. The flow that enters on the sides is then forced to the center by the aft corner vortices of the leading row. Transverse flows are enforced inwards by the downwind obstacle. Hence, for the three tested configurations, crossing alleys involve privileged flow paths. However, this is possible because of the relative dimensions of the (un)built structures under study. For alleys parallel to the incoming flow direction, narrower streets would produce another internal flow regime. The flow would mainly be blocked by the combined effects of the windward surfaces. For a normal wind incidence, the flow might also be blocked because the separated bubble could fill the extremities of the streets.

In addition to the topology, dimensional effects also explain the structures that develop between cubes of the cube array. With  $H/W = 1$ , distorted arch vortices develop between the cubes. However, it is worth mentioning that the lateral closure of open space appears predominant over its dimensions. As a matter of fact, even if the court of the enclosed block is longer ( $H/W = 4$ ) than the street width of the row block 2 ( $H/W = 2$ ), a 2D vortical recirculation develops in the court though not in the street.

Besides the effects of the outdoor space closure and dimensions, the effects of another parameter are highlighted by the analysis of the flow structures inside arrays. The distance of the considered location from the windward facade or more generally the external edges of the built structure appears determining in shaping the inner flow structures. In the cube and the continuous patio arrays, vortical flow structures develop inside the canyons and patios. They generally present higher velocities near the windward facades but present substantial structural differences depending on the location considered. Flow structures evolve from the edges of the blocks to their core. Nevertheless, as seen in Sec. 4.3, these evolutions induced by border effects may be visible through all the arrays because a limited number of elements is considered.

To better understand these evolutions and complete the 3D flow analysis given in Sec. 4.3.2, Fig. 4.23(b), Fig. 4.23(d), Fig. 4.23(f) and Fig. 4.23(h) show the 2D main flow structures and velocities in the central and external rows of the cube array and the continuous patio array respectively. Appendix P gives comprehensive results for all the rows of these two types.

Lower velocity vortices are generally observed in the central rows than in the lateral rows. For the cube array, this may be because of momentum exchanges with the lateral flows that converge toward the array especially downstream the second line (see Fig. 4.14). For the continuous patio

array, this can be explained by the fact that the top separated bubble has a triangular shape. It is longer in the central part (see Fig. 4.20). Moving from the center to the sides, flow recovery is faster. The above flow driving force is thus improved.

Velocity magnitudes in arrays also vary streamwise. On the one hand, for the same reason as above, flow speeds are very low in the upstream patios of the continuous patio array. They increase then in the central rows, while the flow speed in the downstream patio of the external row decreases. Strong interactions occur between the flows inside the upstream patios and the top bubble. In central patios, the top bubble extends downwards inside, thus creating a low velocity structure. This structure is superimposed over a second vortical structure, which develops in the bottom leeward part of the patio. In the two upwind lateral patios and the two central patios of the second line, inner flows still experience the effects of the top separated flow. Single recirculation phenomena develop over a height exceeding that of the patio. Further downstream, the top separated bubble vanishes and the flow reattaches on the roof. As a consequence, single above driven inner flows develop. They are contained and centered in the volume of the patios. With the exception of the upstream split vortices, all these recirculation phenomena show a rather 2D (vertical) behavior.

On the other hand, aerodynamic processes occurring in the cube array differ from those of the continuous patio array as the cube array is composed of detached and relatively small elements. Because of its porosity, there is no general top bubble over the group and 3D flows develop between cubes. Intensified corner streams penetrate the built structure in its central upstream part and lateral flows enter in its downstream lateral parts. Therefore, higher velocities occur in the upstream part of the cube array than further in the central rows. Conversely, the velocity magnitude tends to increase streamwise for the external rows. In the upstream canyons, relatively well defined recirculation phenomena develop. Considering the symmetry planes of canyons, they appear centered in the upstream upper part of the canyon. Conversely, relatively messy structures develop in the downstream canyons. They are centered like the upstream ones in the central rows whereas they are moved downstream next to the windward face of canyons in the lateral rows. This particular behavior may be related to the complex 3D flows that develop around the third line of cubes. Horizontal vortices take place upstream the lateral cubes, driving the flow outwards the array. On the contrary, the horizontal vortices that take place downstream drive the flow inwards. Top flows enter the array downstream this third line of cubes as well, and low velocity regions occur between them. These combined effects may form an aerodynamic bound to the streamwise flow progression and consequently contribute to create such particular flow patterns downstream.

Hence, according to these case studies, the relative openness of the external spaces appears to be the most decisive morphological factor in shaping the internal flow structures. In cases of enclosed courts, rather independent vortical recirculation phenomena usually develop, driven by the above shear flow. However, their covering by a separated top bubble can substantially increase the complexity of the recirculation phenomena. When openness emerges on the court sides, the aerodynamic structures that develop more or less interact with the surrounding flows,



depending on the court depth. For thin courts, flows can merge with the nearby recirculation phenomena while rather self-contained structures usually develop in deep courts. In crossing forms, dimensional effects, which actually define the streamwise or spanwise porosity of built structures, are also determining in shaping flow paths (or blockage). Different flow regimes can occur depending on the streets width. Fractal built structures highlight flow adaptation and border effects on the developing inner recirculation phenomena. Interactions with the above separated top bubble or momentum exchanges with lateral flows can substantially affect inner flow structures, creating very complex recirculation phenomena.

## 4.5 Analysis of the pressure distribution on facades

### 4.5.1 Physical background and applications

As different flow phenomena develop around buildings (flow impingement, separation, reattachment), pressure distribution over the different faces of building envelopes differs. Pressure distribution on each surface is also often uneven. Moreover, as aerodynamic processes are transient, pressure fluctuates as well. However, it is their time averaged intensity, i.e. the mean pressure, that is used to study building ventilation and infiltration issues. Steady RANS models can thus provide useful mean pressure values that correspond to the computed flow fields next to buildings.

Mean pressures on building facades are proportional to the dynamic pressure of the approach flow ( $P_{dyn}$ ) that is given by the Bernoulli principle. This principle basically applies for inviscid and incompressible fluids, and a steady - non separated - flow. In this case and assuming that gravity is the only external force, the Bernoulli principle states that the quantity  $P + \rho gh + 1/2 \rho u^2$  is constant along a streamline. Neglecting gravity,  $P + 1/2 \rho u^2$  is constant along a streamline. Eq. 4.3 gives the expression of  $P_{dyn}$ :

$$P_{dyn} = 0.5 \times \rho_{air} \times U_H^2 \quad (4.3)$$

with:  $\begin{cases} P_{dyn} : \text{the dynamic pressure [Pa]}, \\ U_H : \text{the reference wind speed at the upwind wall height H [m} \cdot \text{s}^{-1}\text{]}, \\ \rho_{air} : \text{the local outdoor ambient air density [kg} \cdot \text{m}^{-3}\text{]}. \end{cases}$

Eq. 4.4 gives the formula that relates the difference between the atmospheric pressure ( $P_{ref}$ ) and the mean pressure on the building surface ( $P_w$ ) to the dynamic pressure (ASHRAE, 2005):

$$\Delta P = P_w - P_{ref} = C_p \times P_{dyn} \quad (4.4)$$

with:  $\begin{cases} C_p : \text{the dimensionless pressure coefficient}, \\ P_w : \text{the surface mean pressure [Pa]}, \\ P_{ref} : \text{the reference atmospheric pressure [Pa]}, \\ P_{dyn} : \text{the dynamic pressure [Pa]}. \end{cases}$



When dealing with building ventilation and infiltration problems, the objective is to determine  $C_p$ , which depends on the very local aerodynamic conditions next to the walls.<sup>10</sup> More precisely, what actually mostly matters is the difference between  $C_p$  at different locations ( $\Delta C_p$ ). For example, assuming the effects of the building interior negligible,  $\Delta C_p$  informs on the building ventilation and infiltration potential induced due to pressure gradients.

Hence, to evaluate pressure conditions on the building envelope and further discuss their implications in terms of building thermo-aeraulic behavior,  $C_p$  was calculated for the different surfaces of the cube, patio, cube array and continuous patio array, as follows:

$$C_p = \frac{P - P_{ref}}{0.5 \times \rho \times U_H^2} \quad (4.5)$$

with:  $\left\{ \begin{array}{l} P : \text{the local static pressure in [Pa],} \\ P_{ref} : \text{the reference pressure taken equal to } 1.01325 \times 10^5 \text{ Pa,} \\ \text{(note that } P - P_{ref} \text{ it is directly given as a simulation output by Fluent),} \\ \rho : \text{the fluid density taken equal to } 1.225 \text{ kg} \cdot \text{m}^{-3}, \\ U_H : \text{the reference wind speed, taken equal to } 4.3 \text{ m} \cdot \text{s}^{-1}, \text{ which is the approach flow} \\ \text{velocity at the obstacle height, i.e. } H = 10 \text{ m high.} \end{array} \right.$

The selected case studies would highlight the effects of the building topology as well as the built environment on different physical exchanges occurring at building outer walls.

$C_p$  distribution as well as the surface averaged  $C_p$  for each face of the different types considered were determined using Paraview. The following gives 3D views of the  $C_p$  distribution on each type supplemented by the surface averaged values of  $C_p$ . In addition, Appendix Q.1 provides the detailed pressure distributions as well as unfolded 2D views of the different surfaces for each of the four built structures examined. Wind-tunnel data from TPU (2003) relative to rather comparable configurations are also reported to support the analysis. The related case studies and  $C_p$  values are given in Appendix Q.3. Tests were undertaken at the scale 1 : 100 and the approach flow profile followed a 0.22 power law. The velocity was  $7.4 \text{ m} \cdot \text{s}^{-1}$  at  $10^{-2} \text{ m}$  high in the wind-tunnel, which corresponds to  $22 \text{ m} \cdot \text{s}^{-1}$  at 11 m high on full-scale. The wind speed should not affect  $C_p$  as far as the flow is Reynolds number independent. However, we nonetheless remind the reader that in our simulations  $U_{ref} = 4.3 \text{ m} \cdot \text{s}^{-1}$  at the obstacle height and the approach flow profile fits a 0.204 power law (see Appendix K.3).

#### 4.5.2 Pressure distribution on isolated buildings

Fig. 4.24 and Fig. 4.25 give a general 3D view of the  $C_p$  distribution on the surfaces of the cube and patio. The color scale is limited to the range  $[-1.6; +0.8]$ . Some lower values were never-

---

<sup>10</sup>Note that literature often considers  $-1 < C_p < +1$ .

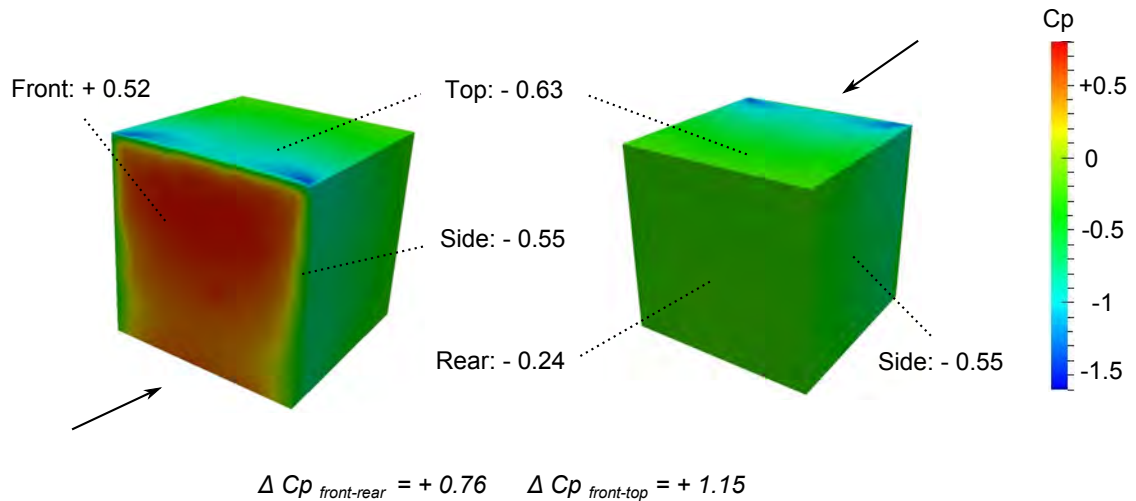


Figure 4.24: Distribution and surface averaged value of  $C_p$  for each face of the cube envelope.

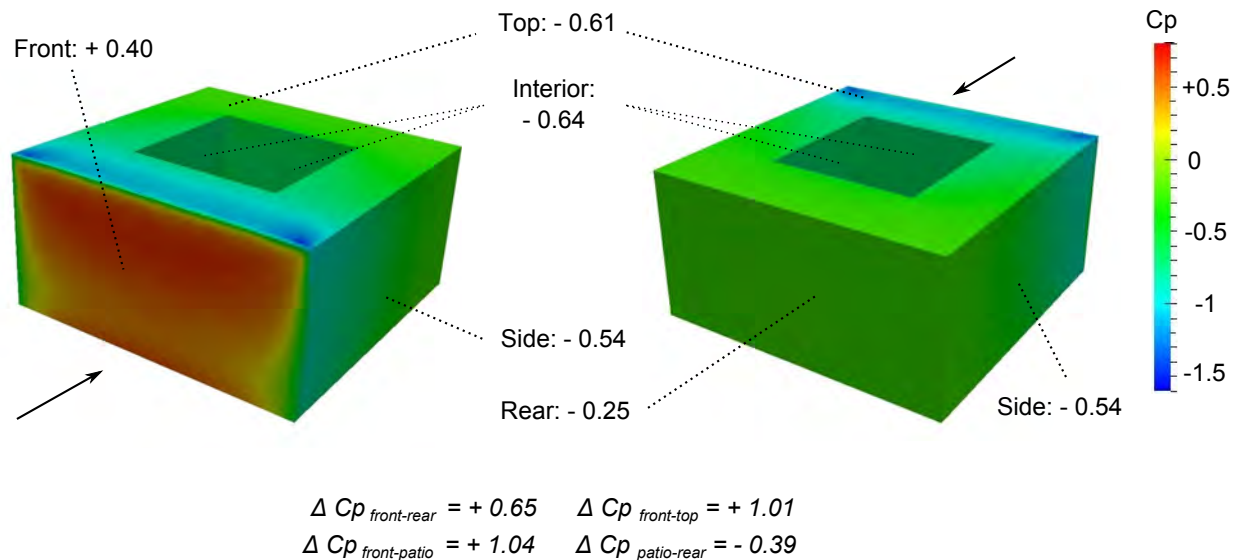


Figure 4.25: Distribution and surface averaged value of  $C_p$  for each face of the patio envelope.

theless computed especially on the upwind upper corners, where lower pressures are generally physically observed and where CFD simulations generally have problems as well. Despite being not distinguishable on the views, the total range of  $C_p$  is integrated in the computation of the surface averaged values.

The front faces of both the cube and patio experience over-pressure. The maximum occurs on their symmetry axis, at a height of about  $2H/3$ . This location corresponds to the stagnation point of windward surface. The external lateral, top and rear faces are under-pressure surfaces and experience suction. This is consistent with the different recirculation phenomena that develop at these locations. Especially, the lowest  $C_p$  are observed downstream flow separation, i.e. directly downstream the leading edges of the obstacles. Because of the top bubble, the top face exhibits lower pressure than side faces. The rear face exhibits even higher pressure, though still negative.

As separated bubbles of finite length or wider recirculation phenomena develop in the vicinity of the obstacles, the range of  $C_p$  on each individual surface varies. The rear face shows a rather homogeneous  $C_p$  distribution, whereas the top and side faces exhibit high  $C_p$  gradients. This is due to the flow separation at the upwind edge and its subsequent reattachment on the obstacle faces. Note that though high velocity gradients are computed at the top leading edges of the obstacles, the  $C_p$  distribution is effectively continuous between the different surfaces.

These simulated  $C_p$  distributions match well experimental results. However, the absolute values of the surface averaged  $C_p$  differ. They are greater in the experiment than simulated for all the cube surfaces as well as for the front face of the patio / cuboid model. Experimental  $\Delta C_p$  are higher as well. These differences can be explained, at least in part, by the differences in the configurations studied, assumptions done when performing steady RANS CFD simulations as well as the resolution of the experimental measures, which might not be sufficient to capture border effects.

The quantitative comparison of the surface averaged  $C_p$  on the cube and the patio highlights similar values on the top, side and rear faces of the two types, which both have a square external footprint. On the contrary, the surface averaged  $C_p$  differ for the front face. That of the patio is 23 % lower than that of the cube. This may be due to the increased width of the patio windward surface, which modifies the upwind standing vortex. This difference implies a difference in  $\Delta C_{p_{F-R}}$  as well. It equals 0.76 for the cube while it is 0.65 for the patio. Wider obstacle seems thus to yield lower streamwise surface averaged pressure difference. This conclusion is confirmed by the wind-tunnel results. Experimental results show similar surface averaged  $C_p$  for the front faces of the two case studies, but the surface averaged  $C_p$  on the top and rear faces are lower in the relatively larger configuration. As a consequence,  $\Delta C_{p_{F-R}}$  is found 0.2 lower in the cuboid case than in the cube case both numerically and experimentally. Although not equal, same trends are also observed for  $\Delta C_{p_{F-S}}$ .

As the interior of the patio is sheltered by the upstream part of the building, it is an under-pressure zone. Inside,  $C_p$  distribution is quite homogeneous. This behavior resembles to that of the rear face. This can be explained by the fact that both walls interact with wide recirculation phenomena and are totally located in the “wake” of the windward surface. Slightly higher  $C_p$  are noticeable on the windward surface of the patio but the difference is not significant. The surface averaged  $C_p$  is  $-0.64$ . This value does not correspond to the value observed on lateral sides of the roof at the same abscissa where  $C_p$  equals  $0.56$ . It rather corresponds to the averaged  $C_p$  over the entire obstacle roof. This can be related to the fact that the court is located right in the middle of the obstacle and undergoes the effects of the top separated flow, which does not well reattach upstream. As a consequence, the surface averaged  $C_p$  inside the patio are always lower than those of the outer walls.<sup>11</sup> Hence, particular and very low pressure conditions occur inside an isolated patio. Inner pressure conditions directly depend on the flow state above, and are strongly affected by separation processes.

---

<sup>11</sup>  $\Delta C_{p_{F-patio}} = 1.04$ ,  $\Delta C_{p_{S-patio}} = 0.10$  and  $\Delta C_{p_{R-patio}} = 0.39$ .

### 4.5.3 Pressure distribution in arrays

To evaluate the effects of the surrounding built environment and verify the hypothesis drawn previously, the  $C_p$  distribution was evaluated on the different surfaces of the cube and continuous patio array. Fig. 4.26 and Fig. 4.27 give a general view of these  $C_p$  distributions and specify the surface averaged  $C_p$ . As for the isolated building cases, the color scale is limited to the range  $[-1.6; +0.8]$ , while the computation of the different surface averaged  $C_p$  accounts for the total  $C_p$  range. For more details, Appendix 4.5.3 gives the surface averaged  $C_p$  for each individual face of each array and the pressure coefficient differences ( $\Delta C_p$ ) between spanwise surfaces.  $C_p$  distributions over the surfaces of four cubes and patios located in the different lines of the arrays are also developed.

Similar to the isolated building types, the only surfaces that experience over-pressure are the front ones, with a maximum located at about  $2H/3$ . Nevertheless, the windward surface averaged  $C_p$  are lower on the windward faces of arrays than on the corresponding isolated configurations ( $-0.15$ ). All the other surfaces show negative values of  $C_p$ . On the outer walls of arrays, surface averaged  $C_p$  values are also lower than on the isolated building types. Deviation between the surface averaged  $C_p$  computed on the rear faces are  $-0.14$  for the cubes and  $-0.3$  for the patios. Hence, the overall  $\Delta C_{p_{F-R}}$  is the same for the cube and the cube array, while it is higher for the continuous patio array than for the isolated patio. The lowest  $C_p$  occur on the roof, right after the leading edges of the obstacles, where the flow separates. On the upstream parts of the arrays,  $C_p$  appear also lower than on the roof of the isolated types.

The windward surface averaged  $C_p$  of the continuous patio array is lower than that of the cube array. The same applies for the rear and side faces. The surface averaged  $C_p$  on the external surfaces of the continuous patio array are in general about  $0.2$  lower than those of the cube array. As a consequence and despite their obvious morphological differences, both configurations produce almost similar aerodynamic drags:  $\Delta C_{p_{F-R}} = 0.74$  for the cube array and  $\Delta C_{p_{F-R}} = 0.80$  for the continuous patio array. On the contrary, pressure conditions inside the two types significantly differ in intensity and distribution.

In the cube array, the range of surface averaged  $C_p$  is rather limited. It varies from  $-0.42$  on the rear face of the upstream cubes to  $-0.21$  on the front face of the downstream cubes, i.e. over a  $0.21$  range. Within all the array, each downwind face is in relative under-pressure with respect to the windward face of the corresponding cube as well as the facing windward face of the corresponding canyon. Not considering  $\Delta C_{p_{F-R}}$  for the first line of cubes, pressure differences between the streamwise opposite walls of cubes or canyons vary between  $0.2$  and  $0.03$ . On the contrary, very different surface averaged  $C_p$  are observed in the patios of the continuous patio array. They vary over a  $0.66$  range. However, inside each patio, differences in  $C_p$  are negligible.

Because of their exposition to the incoming flow, particular pressure conditions are observed in the upstream part of each array. As the first line of cubes experiences flow impingement and separation, high  $C_p$  gradients occur on the windward, top and side faces of these cubes. Moreover, the distribution of  $C_p$  on each cube is asymmetric, the internal sides of cubes showing lower

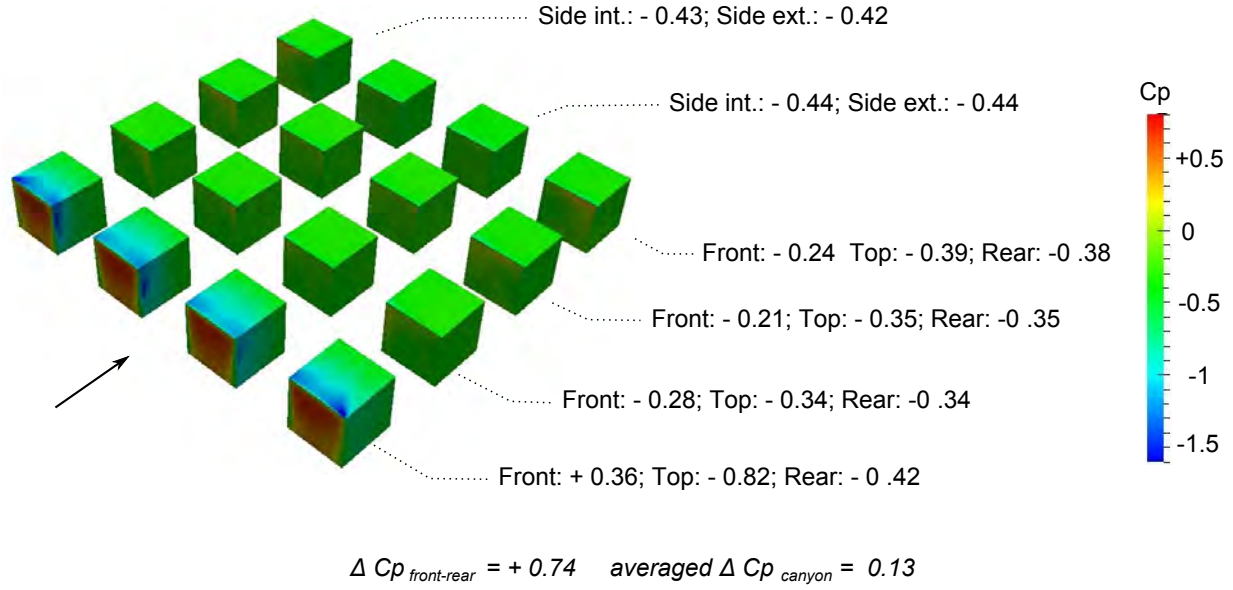


Figure 4.26: Distribution and surface averaged of  $Cp$  for the cube array.

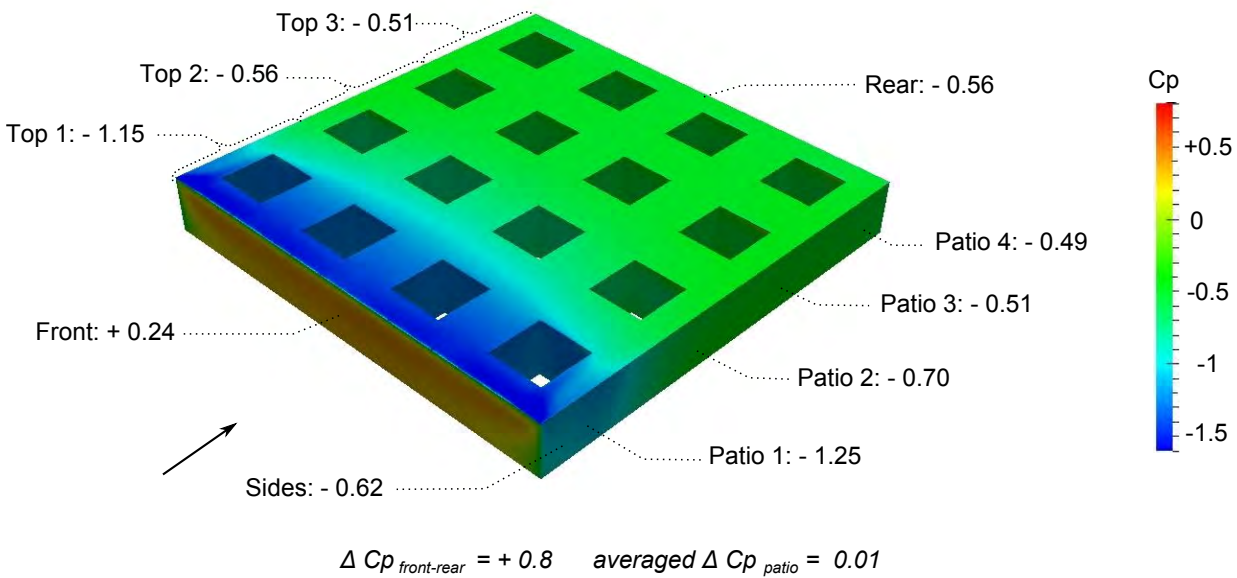


Figure 4.27: Distribution and surface averaged of  $Cp$  for the continuous patio array.

pressures. Similarly, lower surface averaged  $Cp$  occur on the sides of the inner cubes than on the exterior cubes. This is because corner streams are intensified between the cubes and the upwind blocking effect is lower on the sides. The lowest surface averaged  $Cp$  are therefore computed on the central cubes. The upwind over-pressure yields high surface averaged  $\Delta C p_{F-R}$  through the cubes belonging to the first line.  $\Delta C p_{F-R} = 0.78$  on average. Although the windward surface averaged  $Cp$  of the continuous patio array is lower than that of the cube array, built volumes located between the front face and the first line of patios experience even higher pressure difference.  $\Delta C p_{F-R} = 1.5$  on average. Such an important  $Cp$  difference is due to the very low pressure conditions characterizing the first line of patios. Inside,  $Cp = -1.25$ , which is substantially lower than the value observed in the court of the isolated patio type. Nonetheless, this

value still roughly corresponds to the surface averaged  $C_p$  characterizing the upstream third of the roof, which is very affected by the flow separation and the development of the top bubble. As a consequence, important pressure differences also occur between the first and the second line of patios ( $\Delta C_p = 0.57$  on average).

Further in the arrays, pressure conditions still evolve. Different behaviors are observed depending on the distance of the considered location from the upstream edge of the structure and lateral sides. Because border effects and interactions with the surrounding flows induce different flow structures in the arrays (see Sec. 4.4.2), pressure distributions on the different surfaces also vary. Nevertheless, differences are less important than when involving the front surfaces because of the mask effect (see Sec. 1.2.3). In particular, pressure gradients are smaller and pressure distributions are generally relatively homogeneous over each individual surface. Note that however, the windward faces of the external cubes experience non-negligible pressure gradients as top and lateral secondary flows impinge on them.

All along the cube array, the external canyons undergo quite similar and higher surface averaged pressure gradients ( $|\Delta C_p| = 0.19$  on average) than the central canyons. Higher surface averaged  $\Delta C_p$  also occur between the front and rear faces of the external cubes than for the central ones, but their streamwise evolution is not monotonic. A particular behavior is observed for the second line of cubes as  $\Delta C_{p_{F-R}}$  is substantially weaker than it is in the downstream lines. Moreover, similarly to what happens in the first line, only small differences of  $C_p$  occur between the external and the internal cubes, while substantial differences appear in the third and fourth lines. The second line shows the lowest drag force, with  $\Delta C_p = 0.09$  for the lateral cubes and 0.03 for the central cube, while  $\Delta C_p = 0.20$  and 0.08 for the lateral and central cubes of the third and fourth lines respectively. This particular evolution of the surface averaged  $C_p$  can be put in relation with the particular flow phenomena that occur around the third line of cubes as discussed in Sec. 4.4.2.

Unlike for the cube array, the pressure distribution is quite homogeneous inside a patio, as a rather isolated recirculation develops in each patio (or sometimes two, including the top separated bubble).  $C_p$  values are also almost similar linewise in the third and fourth lines, while differences appear in the second line because the central patios are still affected by the top separated flow. A small pressure increase occurs between the second and the third lines ( $\Delta C_p = 0.17$  on average). There is no significant variation of  $C_p$  between the third and the fourth lines of patios ( $\Delta C_p = 0.01$  on average). This might be explained by the relatively similar flow conditions above. The flow has reattached and is rather adapted to the structure, as can be seen on the 3D iso-velocity and iso-vorticity contours in Fig. 4.20. Note that  $\Delta C_p$  equals  $-0.08$  between the downstream patio and the rear face of the block. This means that the downstream patios are in relative under-pressure with respect to the rear face of the urban block.

According to these observations and results of Sec. 4.4, downstream the first line of cubes, pressure conditions inside the cube array are mostly determined by momentum exchanges with the lateral flows. Conversely, pressure conditions in the continuous patio array are mostly determined by the flow separation and reattachment on its roof.

Hence, switching from an isolated building to a group configuration completely modifies the pressure distributions on the building surfaces, especially when obstacles are located far from the block edges. Indeed, over-pressure and separation occur on the windward edges as for isolated buildings, and lateral momentum exchanges can potentially take place through the lateral boundaries. Inside groups, pressure differences for a given construction are generally lower than in the case of isolated obstacles and pressure gradients on surfaces are significantly reduced. These conclusions are confirmed by the wind-tunnel data as similar surrounding effects are observed in the experimental results. For central built structures, a significant reduction of the windward  $C_p$  as well as of the  $\Delta C_{p_{F-R}}$  are reported. The experimental data can nevertheless not be directly compared to the current numerical results as quite different configurations are considered.

## 4.6 Summary

This chapter stresses substantial effects of the building topology, relative dimensions and surrounding built environment on the development of recirculation phenomena within the canopy layer. Usual main flow structures highlighted in Sec. 1.2.3 generally develop around buildings and groups of buildings. However, they can be significantly, even quasi totally, altered by semi-open courtyards or the porosity of built structures. When courtyards are almost or totally enclosed, relatively isolated recirculation phenomena develop inside, driven by the above flow. When sufficiently large alleys cross built structures, clear flow paths develop inside, although showing different behaviors depending on the orientation of the alley with respect to the wind incidence.

The highlighted flow structures involve very different flow speeds and directions. This induces heterogeneous pressure conditions on buildings facades, especially considering exposed or sheltered walls. High  $C_p$  gradients or relatively homogeneous  $C_p$  distributions occur depending on the morphological properties of the built structure and the location studied.

However, it is worth reminding that although the CFD model was showed capable of reproducing the main physical processes developing in complex configurations, its validation showed an imperfect reproduction of the different flow structures around buildings. As a consequence, these different results provide indications on the flow features and  $C_p$  distribution next to buildings, but a more detailed approach is required to guarantee very accurate predictions.

— *Main contribution of this chapter:* —

- *Highlight typical 3D flow structures that develop according to the morphological properties of constructions.*
- *Provide the  $C_p$  distribution on the building facades of typical isolated and urban constructions; relate this distribution to the main surrounding flow structures.*

## **Part III**

# **Effects of urban air flows on the building energy balance**





# Chapter 5

## Numerical study of the urban morphology effects on the building external convective heat transfer

This chapter presents how CFD can improve the estimates of  $h_{c,w}$  used in building physics. The accuracy of the turbulence model and near wall treatment in predicting convective heat transfers is evaluated against experimental and detailed numerical data and an improved temperature wall-function designed for  $k-\varepsilon$  models is adapted to the RSM. The convective heat transfers developing at the facades of the cube, the patio, the cube array and continuous patio array are analyzed.

### Contents

---

<b>5.1 Theoretical background . . . . .</b>	<b>146</b>
5.1.1 Physical basis . . . . .	146
5.1.2 Usual convective heat transfer correlations for building physics . . . . .	147
5.1.3 Improving of the estimations of building external convective heat transfer using CFD . . . . .	149
5.1.3.1 Modeling convective heat transfers with CFD . . . . .	149
5.1.3.2 CFD-based $h_{c,w}-U_{10}$ correlations . . . . .	151
5.1.3.3 CFD-based modified wall-functions for temperature . . . . .	153
<b>5.2 Validation study . . . . .</b>	<b>155</b>
5.2.1 Evaluation of the accuracy of CFD in modeling convective heat transfers . . .	155
5.2.1.1 Validation test case - 1 . . . . .	155
5.2.1.2 Model comparison with the experiment . . . . .	158
5.2.2 Performance of wall-functions in modeling convective heat transfer . . . . .	162
5.2.2.1 Validation test case - 2 . . . . .	162
5.2.2.2 Sensitivity analysis of $h_{c,w}$ to the turbulence model and near wall treatment . . . . .	164
5.2.2.3 Adaptation of the customized temperature wall-function of Defraeye et al. (2011a) to the RSM . . . . .	166
5.2.2.4 Applicability of the revised customized temperature wall-function for the RSM for high $z^*$ . . . . .	168
<b>5.3 Analysis of <math>h_{c,w}</math> distribution on building facades . . . . .</b>	<b>174</b>
5.3.1 Settings of the coupled thermal and aerodynamic model . . . . .	174
5.3.2 Distribution of the convective heat transfers on isolated buildings . . . . .	176
5.3.3 Distribution of the convective heat transfers in arrays . . . . .	177
<b>5.4 Summary . . . . .</b>	<b>180</b>

---

## 5.1 Theoretical background

### 5.1.1 Physical basis

In addition to ventilation and infiltration processes, three types of heat transfer affect the building energy balance. They are:

- radiative exchanges between surfaces of different temperatures;
- conduction through continuous masses undergoing temperature gradients;
- and convection, which involves heat transport due to the motion of fluids.

On surfaces, both radiative and convective heat exchanges occur. The total relative heat flux that leaves a surface is thus a function of these two phenomena.

The knowledge of surface heat fluxes is especially required for the assessment of the building relative heat gains through the envelope. Surface heat exchanges particularly impact on the building energy balance in cases of highly glazed and low insulated buildings. Such buildings do not satisfactorily prevent heat losses between the indoor ambiance and the surrounding environment. Examples of other applications for which surface heat exchanges are important are the convective cooling of solar panels and the turbulent thermal transfers in cities, which influence the urban heat island.

Bouyer et al. (2011), among others, shows the preponderant contribution of radiative heat exchanges in determining the building energy demand, and especially of the short-wave radiative transfers. These transfers are strongly dependent on urban morphology as solar masks prevent their occurrence. Because of these masks, the convective contribution is often preponderant over the radiative contribution in determining the building external surface heat exchanges (see Sec. 6.2.1) in an urban context. This is especially the case when surface temperature differences are low and wind speeds are high. Convective heat transfers depend on different parameters related to the properties of the fluid, flow and surface. Considering building outer walls, factors that mostly determine these heat exchanges between the building and the surrounding air are:

- the approach and incident flows properties, which depend on the wind direction and speed, the type of the upstream terrain as well as the potential effects of the surrounding constructions and urban objects (see Fig. 1.13, Sec. 1.2.3);
- the features of the surface, including its orientation, size and roughness;
- and the difference between the air and wall temperatures as well as the nature of convection, which is related to the Richardson number ( $Ri$ ).

Focusing on the effects of the surrounding flow field, convective heat transfers on building facades are very dependent on the general as well as very local aerodynamic conditions next to the surface. On the one hand and considering flat plates, increasing the flow speed and turbulence level enhances convective heat exchanges by improving the relative heat removal. On the

other hand, the momentum energy analogy does not apply for heat transfer around sharp-edged bluff bodies (Defraeye et al., 2010). Local flow separation, stagnation or recirculation lead to different intensities of convective heat transfer. In recirculation zones, convective heat exchanges are low although these zones are characterized by high levels of turbulent kinetic energy. This is due to heat entrapment into the recirculation phenomena, which maintains the near flow at a temperature close to that of the wall. On the contrary, heat transfers are high in flow impinging regions. Turbulent kinetic energy levels are low in these regions but wind speeds are high and temperature differences between the fluid and the wall are maximized. Similarly, the intermittent flow reattachment on building facades improves convective heat transfers (Meinders et al., 1999).

As stressed in the previous chapters, the different processes determining the convective heat transfers are strongly conditioned by the local built morphology. Therefore, very different distributions and intensities of convective heat transfers can occur on a surface depending on the local aerodynamic conditions. For basic boundary layer configurations over flat plate, convective heat transfers directly depend on the flow velocity and turbulence as well as on the surface roughness. For complex separated flows, convective heat transfers are mostly determined by the different flow structures that develop next to the heated surface. They can completely differ from the heat transfers that develop over flat plates.

### 5.1.2 Usual convective heat transfer correlations for building physics

Convective heat transfer at building external facade is generally expressed using a coefficient  $h_{c,w}$ . This coefficient is not physical in itself but expresses the relation between the density of convective heat flux normal to a surface and the difference between the surface temperature and a reference temperature, as follows:

$$h_{c,w} = \frac{q_{c,w}}{T_w - T_{ref}} \quad (5.1)$$

$$\text{with: } \begin{cases} h_{c,w} : \text{the convective heat transfer coefficient } [\text{W} \cdot \text{m}^{-2} \cdot \text{K}^{-1}], \\ q_{c,w} : \text{the convective heat transfer per surface unit } [\text{W} \cdot \text{m}^{-2}], \\ T_w : \text{the wall surface temperature } [\text{K}], \\ T_{ref} : \text{the reference temperature, generally the free stream temperature } [\text{K}]. \end{cases}$$

Existing correlations linking external  $h_{c,w}$  with a reference wind speed and that are applicable for building outer walls are reviewed in Defraeye et al. (2011b). These correlations are either based on reduced-scale experiments undertaken for bluff bodies located in a turbulent boundary layer, full-scale measurements taken on building facades, or, more recently, CFD modeling (see Sec. 5.1.3.3). Correlations are generally linear functions of the reference wind speed in case of natural convection or power law functions of the wind speed in case of forced convection. Focusing on building energy simulation programs, Mirsadeghi et al. (2013) reviewed different models used to compute the external convective heat transfers. These models are generally derived from

reduced-scale or full-scale experimental studies, but numerous and diverse models are reported. Note that some building energy simulation programs such as Trnsys account for fixed values that are defined by the program or user-defined profiles of  $h_{c,w}$ .

Numerous building energy simulation programs use models that are derived from the correlations of Jürges, which rely on an experiment undertaken for a flat vertical square copper plate mounted parallel to the flow (Defraeye et al., 2010). Two correlations were suggested depending on the wind speed. The first takes into account the effects of buoyancy, and the second applies for forced convection:

$$\begin{aligned} h_{c,w} &= 4U + 5.6 \text{ for } U_{\infty} < 5 \text{ m} \cdot \text{s}^{-1} \\ h_{c,w} &= 7.1 U^{0.78} \text{ for } U_{\infty} > 5 \text{ m} \cdot \text{s}^{-1} \end{aligned} \quad (5.2)$$

On this basis, a widely implemented  $h_{c,w}$  model in BES programs is the model of Mc Adams. This model suggests a power law formulation for  $h_{c,w}$  as a function of the free stream wind speed:

$$h_{c,w} = 5.678 \left[ m + n \left( \frac{U_{\infty}}{0.3048} \right)^p \right] \quad (5.3)$$

with:  $\begin{cases} h_{c,w} : \text{the external convective heat transfer coefficient } [\text{W} \cdot \text{m}^{-2} \cdot \text{K}^{-1}], \\ U_{free} : \text{the free stream wind velocity } [\text{m} \cdot \text{s}^{-1}], \\ m, n, p : \text{model parameters depending on the surface roughness and wind speed.} \end{cases}$

In particular for  $V_f < 4.88 \text{ m} \cdot \text{s}^{-1}$ ,  $p = 1$ , which forms a linear correlation resembling to the one provided by Jürges, which accounts for buoyancy effects, whereas for  $V_f > 4.88 \text{ m} \cdot \text{s}^{-1}$ ,  $p = 0.78$ , which is similar to the power law correlation proposed by Jürges for forced convection. This model is implemented in ESP-r, IES and IDA. However, its implementation in building energy models is sometimes simplified into a linear correlation. The CIBS model is also derived from the same experimental work but proposes a linear function of the local wind speed:

$$h_{c,w} = 4.1 U_{loc} + 5.8 \quad (5.4)$$

with  $U_{loc}$ : the local wind velocity. This model is implemented in ESP-r and TAS.

The fact that these models are based on reduced-scale tests that involved flat planes casts doubts on their applicability for more complex geometries such as buildings. Correlations derived from full-scale measurements on buildings are more suitable. Their scope for applicability is however often limited as they correspond to specific configurations and experimental conditions. Moreover, the reliability of some experimental correlations lack completeness about their experimental setup. It is therefore difficult to guarantee their relevancy (Mirsadeghi et al., 2013). In addition, there is no consensus about the definition of the reference wind speed to be used ( $U_{\infty}$ ,  $U_{10}$  or  $U_{loc}$ )<sup>1</sup> to estimate  $h_{c,w}$ . This ambiguity may affect the usability of models especially because local wind data are generally not available.

---

<sup>1</sup> $U_{\infty}$  is the free stream wind velocity, which is also sometimes called  $U_{free}$ .  $U_{10}$  is the approach flow velocity at 10m high.  $U_{loc}$  is the local wind speed, taken relatively close to the surface of interest.  $U_{loc}$  can substantially differ from the wind speed of the approach flow.

Hence, because of these various assumptions, the use of one or another model can lead to substantial deviation in the predictions of the building cooling and heating demand. For example, the estimates of the annual cooling energy demand of an isolated and well insulated building deviate respectively by  $\pm 30\%$  and  $\pm 6\%$  from the averaged values when using the different models available in ESP-r (Mirsadeghi et al., 2013). Furthermore, these averaged values do not necessarily correspond to the effective value of  $h_{c,w}$ . Such uncertainty on  $h_{c,w}$  may have substantial consequences on the assessment of building thermal behavior, especially in cases of thermally inefficient buildings, which represent a large part of the current building stock. Moreover, these uncertainties significantly affect the estimate of the cooling demand while the convective cooling of sun-heated surfaces is important and the artificial cooling has a worse environmental footprint than heating. Therefore, further detailed experimental and computational studies are necessary to improve current building thermal engineering practices.

### 5.1.3 Improving of the estimations of building external convective heat transfer using CFD

#### 5.1.3.1 Modeling convective heat transfers with CFD

For the reasons outlined in Sec. 5.1.2, CFD-based  $h_{c,w}$  correlations that specifically address building physics problems emerge. Similarly to aerodynamic problems, generic building configurations such as cubes, cube arrays or cuboids are generally considered. Such numerical approaches can take into account most of the factors that influence  $h_{c,w}$  outlined in Sec. 5.1.1. These factors include the different features of the approach flow as well as the geometry and thermal properties of the built environment. Studies dealing with natural, mixed or forced convection can also be carried out. Compared to usual experimental techniques, CFD studies also benefit from the other advantages stressed in Sec. 1.2.2, including the high spatial resolution of the computed solution.  $h_{c,w}$  correlations that have quite a large scope of applicability can thus be deduced. However, such CFD approaches keep also their drawbacks and involve additional modeling challenges.

Heat transport in the laminar boundary layer plays a decisive role in determining the heat exchanges between the surface and the surrounding air as the largest temperature gradients occur there. As a consequence, convective heat transfers do not only depend on the macroscopic flow features and the turbulence modeling. They also depend to a large degree on the flow properties very close to walls and therefore, on the near wall treatment. Modeling accurately building external convective heat transfers is therefore even more complicated than it is for building aerodynamics only.

The behavior of the thermal boundary layer can generally not be accurately captured by usual logarithmic models because information about the thermal behavior of the viscous and buffer layers is needed (Blocken et al., 2009). Solving the thermal boundary layer in terms of flow and related physical variables using the low Reynolds number modeling (LRNM) approach requires a very fine mesh next to the wall. However, despite being more accurate than usual approaches that rely on wall-functions, the LRNM can barely be used when dealing with urban problems

because of the size of the elements studied (Sec. 3.1.2.3). Building usually have a length scale of  $10^1$  m or more, while the typical thickness of the thermal boundary layer is often of about  $10^{-4}$  m. Wall-functions are therefore commonly used.

In Fluent, an internal coupling makes it possible to model convective heat transfers at outer walls.<sup>2</sup> Anisothermal problems can be solved provided that the energy equation is enabled and appropriate boundary conditions for the inlet and the surfaces of interest are specified. Convective heat transfer coefficients can then be assessed for every elementary surface according to the local aerodynamic and thermal conditions.

When dealing with  $z^* \approx 1$  and smooth walls, it is possible to perform LRNM-based simulations by using to the so called “enhanced wall treatment”. This model can evolve between a LRNM approach for small  $z^*$  and a wall-function formulation for higher  $z^*$ . Thus, the enhanced wall treatment can take care of both occurrences of low and high  $z^*$  values in a model.

Similarly to the models implemented to compute near wall velocities, standard temperature wall-functions are based on a law-of-the wall for temperature. This model involves a dimensionless temperature  $T^*$ :

$$T^* = \frac{(T_w - T_p) \rho C C_\mu^{1/4} k_p^{1/2}}{q_w} \quad (5.5)$$

with:  $\left\{ \begin{array}{l} T^* : \text{the dimensionless temperature,} \\ T_w : \text{the wall temperature [K],} \\ T_p : \text{the temperature in the first cell [K],} \\ \rho : \text{the fluid density [kg} \cdot \text{m}^{-3}\text{],} \\ C : \text{the specific heat of the fluid [J} \cdot \text{kg}^{-1} \cdot \text{K}^{-1}\text{],} \\ C_\mu : \text{the model constant,} \\ k_p : \text{the turbulent kinetic energy in the first cell [m}^2 \cdot \text{s}^{-2}\text{],} \\ q_w : \text{the wall heat flux per surface unit [W} \cdot \text{m}^{-2}\text{].} \end{array} \right.$

Considering incompressible flows and smooth walls, standard temperature wall-functions compute  $T^*$  as a linear or logarithmic function of  $z^*$  (see Sec. 3.1.2.3) depending on the thermal sub-layer thickness  $z_T^*$ , as follows (Ansys Fluent, 2013a):

◦ if  $z^* < z_T^*$ :  $T^* = Pr z^*$  (5.6)

◦ if  $z^* > z_T^*$ :  $T^* = Pr_t \left( \frac{1}{\kappa} \times \ln(E z^*) + P \right)$  (5.7)

with<sup>3</sup>: 
$$P = 9.24 \left[ \left( \frac{Pr}{Pr_w} \right)^{3/4} - 1 \right] \left[ 1 + 0.28 e^{-0.007 \frac{Pr}{Pr_{t,w}}} \right] \quad (5.8)$$

---

<sup>2</sup>Radiative heat transfers can also be modeled but they are not addressed in this thesis.

<sup>3</sup>For rough walls and given  $E' = E/fr$ , the expression is:  $P_{rough} = 3.15 \times Pr^{0.695} \left[ \frac{1}{E'} - \frac{1}{E} \right] + \left[ \frac{E'}{E} \right]^{0.6} P$ .

$$\text{and: } \begin{cases} z^* : \text{the dimensionless wall unit,} \\ Pr : \text{the molecular Prandtl number,} \\ Pr_{t,w} = 0.85 \text{ at the wall by default in Fluent: the wall turbulent Prandtl number.} \end{cases}$$

Given  $T^*$ , either  $T_w$  or  $q_w$  can be computed according to Eq. 5.5 depending on the specified wall boundary condition.  $h_w$  can then be deduced according to Eq. 5.1. Hence,  $h_w$  is computed by wall-functions as a function of the local thermal and aerodynamic conditions, assuming an universal law-of-the-wall for both the flow and the related variables. Neglecting the radiative contribution,  $h_w = h_{c,w}$ .

### 5.1.3.2 CFD-based $h_{c,w}-U_{10}$ correlations

Because of the huge uncertainties related to usual  $h_{c,w}$  correlations used in building physics (Sec. 5.1.2) and the inaccuracy of standard wall-functions in predicting surface heat transfers (Sec. 5.1.3.1 and Sec. 5.2.2), CFD-based  $h_{c,w}-U_{10}$  correlations were recently derived from LRNM studies. In particular, [Blocken et al. \(2009\)](#) and [Defraeye et al. \(2011b\)](#) proposed  $h_{c,w}-U_{10}$  correlations to be used for isolated buildings standing perpendicular to the wind incidence. These correlations were only suggested for the front and rear faces of the obstacle because the validation study highlighted the inability of the turbulence model (steady RANS  $Rk-\varepsilon$ ) to reproduce satisfactorily the thermal field next to the top and side faces of sharp-edged obstacles, where flow separation and reattachment occur (see Sec. 5.2.1.2).

Spatially differentiated  $h_{c,w}-U_{10}$  correlations distribution were deduced by the two studies. These correlations have a general power law form, as usual for forced convection problems:

$$h_{c,w} = A \times U_{10}^B \quad (5.9)$$

$$\text{with: } \begin{cases} A : \text{the proportionality coefficient,} \\ B : \text{the power law exponent.} \end{cases}$$

Fig. 5.1 shows the spatial distributions of the correlations derived by [Defraeye et al. \(2011b\)](#). The coefficient  $A$  increases from the bottom to the top of the windward face while it shows a local maximum in the middle of the rear face, at  $z = 0.3H$ . Conversely, the power law exponent  $B$  is almost constant over the front face with the exception of its bottom part, and increases from the bottom to the top on the rear face. Note that [Blocken et al. \(2009\)](#) found a better correspondence between the windward  $h_{c,w}$  distribution and  $k^{1/2}$  than between  $h_{c,w}$  and  $U_{10}$ .

As surface averaged values are often used, surface averaged correlations were also proposed (still for forced convection cases):

$$\text{for the front face (Blocken et al., 2009): } h_{c,w} = 4.6 \times U_{10}^{0.89} \quad (5.10)$$

$$\text{for the front face (Defraeye et al., 2011b): } h_{c,w} = 5.01 \times U_{10}^{0.85} \quad (5.11)$$



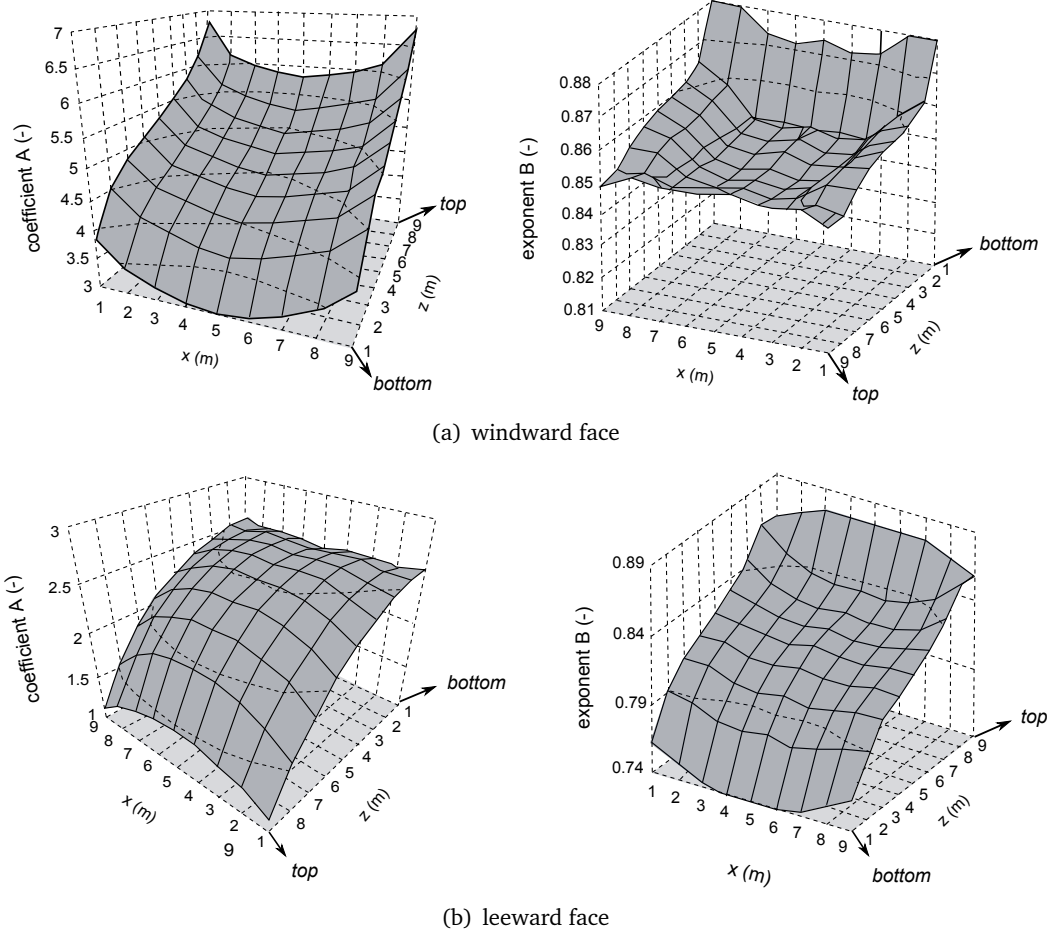


Figure 5.1: Distribution of the coefficient A and exponent B characterizing the  $h_{c,w} - U_{10}$  correlation derived by Defraeye et al. (2011b).

$$\text{for the rear face (Defraeye et al., 2011b): } h_{c,w} = 2.27 \times U_{10}^{0.83} \quad (5.12)$$

Note that Eq. 5.10 is valid for  $1 \leq U_{10} \leq 4 \text{ m} \cdot \text{s}^{-1}$  and Eq. 5.11 and Eq. 5.12 apply for  $0.15 \leq U_{10} \leq 7.5 \text{ m} \cdot \text{s}^{-1}$  as the flow field is Reynolds number independent in this range.

Correlations giving  $h_{c,w}$  as a function of  $U_{10}$  as well as the temperature difference between the wall and the free stream and the plan areal fraction ( $\lambda_p$ ) were also proposed by Liu et al. (2015) for buildings located in built environment. These correlations are based on LES simulations of cube arrays, are suitable for configurations for which  $1.8 \times 10^5 < Re < 5 \times 10^6$  and address both the effects of forced and natural convection processes. For the windward, leeward and roof faces, the correlations are expressed as follows:

$$h_{c,w} = \sqrt{[(a + b\lambda_p)U_{10}^c]^2 + (d\Delta T^e)^2} \quad (5.13)$$

Tab. 5.1 synthesizes the values of  $a$ ,  $b$ ,  $c$ ,  $d$  and  $e$  for the different faces.

Tab. 5.2 compares the surface averaged  $h_{c,w}$  estimated using either the correlation of Jürges,

	a	b	c	d	e
windward	2.94	-4.34	0.94	1.52	0.36
leeward	0.99	0.72	0.94	1.52	0.36
roof	3.13	1.50	0.84	1.55	0.36

Table 5.1: Coefficients related to the  $h_{c,w} - U_{10}$  correlations of [Liu et al. \(2015\)](#).

	$U_{10} = 1 \text{ m} \cdot \text{s}^{-1}$	$U_{10} = 4 \text{ m} \cdot \text{s}^{-1}$	$U_{10} = 7 \text{ m} \cdot \text{s}^{-1}$
Jürges (exp.)	9.6	21.6	32.39
Deviation (%)	91	33	24
Model of Mc Adams	4.47	21.06	32.38
Deviation (%)	-11	29	24
Model of CIBS	9.9	22.2	34.5
Deviation (%)	98	37	32
<a href="#">Defraeye et al. (2011b)</a>	5.01	16.28	26.19
Deviation - reference (%)	0	0	0

Table 5.2: Comparison of the surface averaged  $h_{c,w}$  [ $\text{W} \cdot \text{m}^{-2} \cdot \text{K}^{-1}$ ] values for the front face of a building estimated using different models available in literature.

the models of Mc Adams and the CIBS, or the surface averaged correlation of [Defraeye et al. \(2011b\)](#) for wind velocities ( $U_{10}$ ) equal to 1, 4 and  $7 \text{ m} \cdot \text{s}^{-1}$ . Note that despite the differentiation of the reference wind speeds in the original formulae, all the reference wind speeds are currently taken equal to  $U_{10}$  for the sake of simplicity and due to the lack of other information, especially with respect to  $U_{loc}$ .

The original experimental correlation and the derived literature models give rather similar results for relatively high wind speeds. Conversely, substantial differences occur for low wind speeds. The model of Mc Adams gives substantially lower results, which actually better corresponds to the  $h_{c,w}$  value computed using the correlation of [Defraeye et al. \(2011b\)](#). With the exception of this particular  $h_{c,w}$  value, all the estimates of  $h_{c,w}$  derived from the experiment of Jürges, undertaken for a flat plate, over-estimate the CFD-based  $h_{c,w}$  estimates, derived for a theoretical cubical building. Results are nearly doubled for low wind speeds and are over-estimated from 25 % to more than 33 % for higher wind speeds. These results stress the important uncertainty that characterizes the assessment of the building external convective heat transfers and support the need of more accurate  $h_{c,w}$  estimates to improve usual building engineering practices.

### 5.1.3.3 CFD-based modified wall-functions for temperature

[Defraeye et al. \(2011a\)](#) and [Blocken et al. \(2009\)](#) evaluated the accuracy of standard wall-functions in predicting convective heat transfers. A substantial over-prediction of  $h_{c,w}$  was found as differences up to 60 % compared to LRNM predictions were highlighted. As stressed in Sec. 5.1.3, the fact that temperature fields are inaccurately reproduced by the usual logarithmic formulation of wall-functions is due to the high temperature gradients that occur in the thermal boundary layer. As a consequence, modifications to usual temperature wall-functions were recently pro-

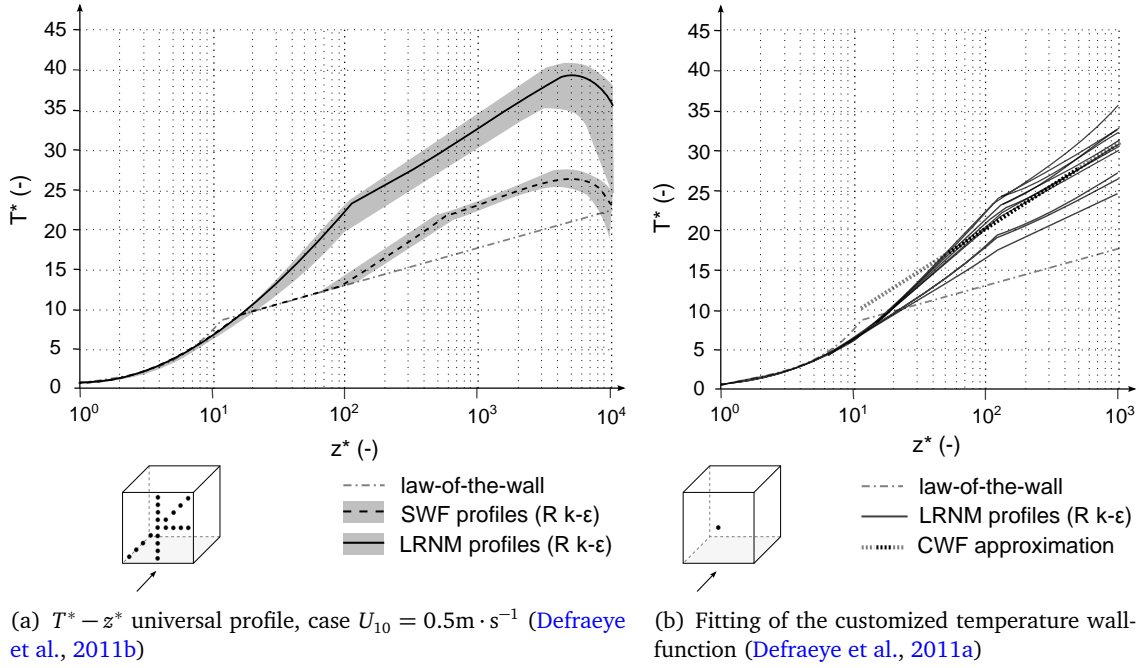


Figure 5.2: Bases of the customized temperature wall-function. (Based on (Defraeye et al., 2011a,b))

posed to improve their accuracy. In particular, Defraeye et al. (2011a) proposed an improved temperature wall-function to be used with the steady RANS  $Rk-\epsilon$  model in case of turbulent forced convection. This temperature wall-function is based on the analysis of the  $T^* - z^*$  profiles, which were computed using the LRNM. Fig. 5.2(a) shows that these profiles follow an universal behavior characterized by logarithmic correlations. The first logarithmic correlation applies for  $3 \times 10^1 \leq z^* \leq 10^2$  and the second correlation applies for  $10^2 < z^* \leq 4 \times 10^3$  at least for  $U_{10} \geq 0.5 \text{ m} \cdot \text{s}^{-1}$ . Fitting this latter relationship using standard temperature wall-functions is possible in Fluent by modifying the turbulent Prandtl number value ( $Pr_{t,w}$ ) at the wall from 0.85 to 1.95 (see Fig. 5.2(b)). This modified formulation of the standard temperature wall-function is called the customized temperature wall-function. Its use substantially improves the accuracy of predictions as results showed a 10% maximum deviation of the surface averaged  $h_{c,w}$  compared to LRNM predictions in case of an isolated cube. Deviation reached 40% with the standard temperature wall-function. The performance of this customized temperature wall-function is also verified for cuboids of different relative dimensions representing buildings.

Still using the steady RANS  $Rk-\epsilon$  model, Defraeye et al. (2012) evaluated then the performance of the customized temperature wall-function in case of mixed convection. The case study was a cube immersed in a turbulent boundary layer. Different Richardson numbers between 0 and 52 were tested. The customized temperature wall-function was found to be a bit less accurate compared to LRNM predictions than it was in case of forced convection and Richardson number dependent. Its performance was nevertheless still substantially better than that of the usual wall-functions: the maximum deviation was 16% (instead of 10%) while the deviation observed with standard wall-functions was 47%.

[Allegrini et al. \(2012c\)](#) also studied the accuracy of this customized temperature wall-function and that of standard temperature wall-function in case of convective mixed flows in a street canyon, still using the steady RANS  $Rk-\varepsilon$  model. Buoyancy effects were modeled using the Boussinesq approximation. The Richardson number range was  $[0.14; 13.7]$ . The customized temperature wall-function was found to perform well when applied to mixed convective flows, whereas the standard temperature wall-function was more accurate when applied to forced convective flows. This counter intuitive behavior may be explained by differences in turbulence intensities simulated around the bluff-body or inside the canyon. As a result, an adaptive temperature wall-function was designed to account for both occurrences of flow regimes in the street canyon, by fitting one or the other temperature wall-function depending on the local Richardson number. The accuracy of the computed  $h_{c,w}$  was thus improved: a deviation less than 10% compared to LRNM predictions was generally found over the range of Richardson numbers tested.

The methodologies implemented in these three reference studies resulted in modified temperature wall-functions, which substantially improve the accuracy of the heat transfers modeling in CFD simulations when using temperature wall-functions. However, it is worth reminding that their use does not improve the accuracy of the flow fields computed by the turbulence models. Errors in the assessment of heat transfers due to inaccurate predictions of the flow remain. In addition, the applicability of these improved temperature wall-functions is constrained due to the methodology implemented to determine them as discussed in [Defraeye et al. \(2010\)](#). In particular, focusing on forced convection problems, Fig. 5.2(b) shows that the customized temperature wall-function preferentially applies for a  $z^*$  range of 50 to 500 as the fitting was performed for this range of values. This corresponds to the theoretical range for applicability of wall-functions. However, Fig. 5.2(a) shows that the logarithmic correlation extends for higher  $z^*$ , up to at least  $10^3$  for  $U_{10} \geq 0.5 \text{ m} \cdot \text{s}^{-1}$ . In addition, the customized temperature wall-function was designed using steady RANS  $Rk-\varepsilon$ -based CFD simulations.  $T^*$  being a function of  $k$ , it may differ depending upon the turbulence model used. As a consequence, if the customized temperature wall-function is expected to perform satisfactorily when used together with other  $k-\varepsilon$  turbulence models, its reliability when used together with other turbulence models deserves further research.

## 5.2 Validation study

### 5.2.1 Evaluation of the accuracy of CFD in modeling convective heat transfers

#### 5.2.1.1 Validation test case - 1

##### Experimental configuration

To evaluate the accuracy of our aerodynamic and thermal coupled model, numerical results were compared to experimental data-sets taken from [Meinders et al. \(1999\)](#). This study reports different profiles of  $h_{c,w}$  and wall surface temperature ( $T_w$ ) in case of a small heated cube that is located in a turbulent boundary layer. The wind tunnel section is  $6 \times 10^{-1} \text{ m}$  wide and  $5 \times 10^{-2} \text{ m}$

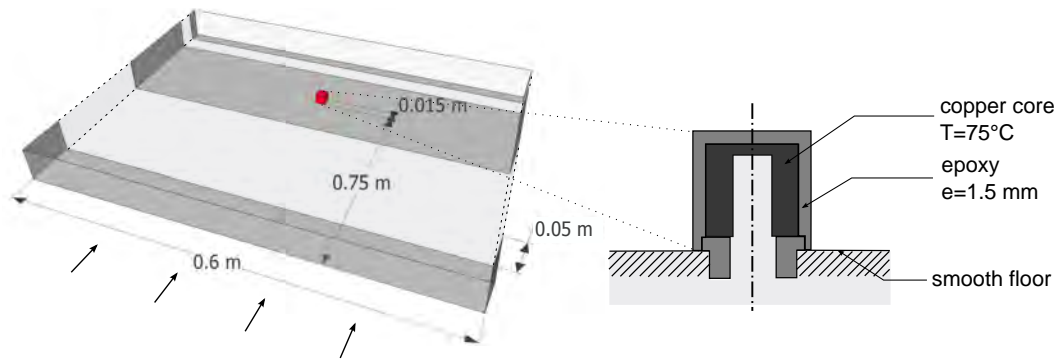


Figure 5.3: Reference experimental configuration. (Based on (Meinders et al., 1999))

high. The temperature of the approach flow was 21 °C. The obstacle is composed of an internal copper core heated at a temperature of 75 °C covered by a  $1.5 \times 10^{-3}$  m thick layer of epoxy. The external edges of the cube are  $1.5 \times 10^{-2}$  m long. Its leading face was located  $7.5 \times 10^{-2}$  m downwind a trip. Fig. 5.3 illustrates the experimental model.

Measurements of the external surface temperature were taken using infrared thermography.  $h_{c,w}$  was derived from the local heat transfers. The radiative flux was approximated using the Stephan Boltzmann relationship and the 3D temperature distribution in the epoxy was deduced by solving the conduction problem knowing the temperature of the copper core. The accuracy of the heat transfer coefficients is 5% to 10%, lowest accuracy occurring on the cube edges. According to Defraeye et al. (2010), uncertainties respective to  $h_{c,w}$  at the cube edges are higher because of the methodology used to compute these coefficients. The finite volume method was used, but the resolution of the measurements was lower near the obstacle edges, which increased the uncertainties on the computed values.

Several Reynolds numbers were tested, but the case  $Re = 4.4 \times 10^3$  is selected for further analysis as most of information is available for this case. The corresponding bulk velocity is  $U_{bulk} = 4.47 \text{ m} \cdot \text{s}^{-1}$ . In such a configuration,  $Ri = 1.36 \times 10^{-3}$ . This is a case of predominant forced convection and buoyancy effects can be neglected.

This reference experimental study differs from those usually considered in building physics. It basically addresses more electronical problems. However, anisotherm reference experimental data are not widespread. Moreover, this reference experiment was also used to validate the LBM LES aerodynamic model addressed in Sec. 3.2.2 by Obrecht et al. (2011b) as well as the LRNM approach used to compute the convective heat fluxes addressed in Sec. 5.1.3.3 and Sec. 5.2.2.1 by Defraeye et al. (2010). As a consequence, computational data for heat transfers relative to this case study are also available for further comparisons.

### Coupled aerodynamic and thermal model

The same methodology as in Defraeye et al. (2010) was implemented for the computational modeling due to the lack of information about the experimental setup. The approach flow profile was firstly designed by modeling an empty domain whose dimensions were taken as follows:<sup>4</sup>

<sup>4</sup> $99 \times 10^{-2}$  m corresponds to  $75 + 1.5 + 15 \times 1.5 \text{ cm} = 50 + 1 + 15 H$

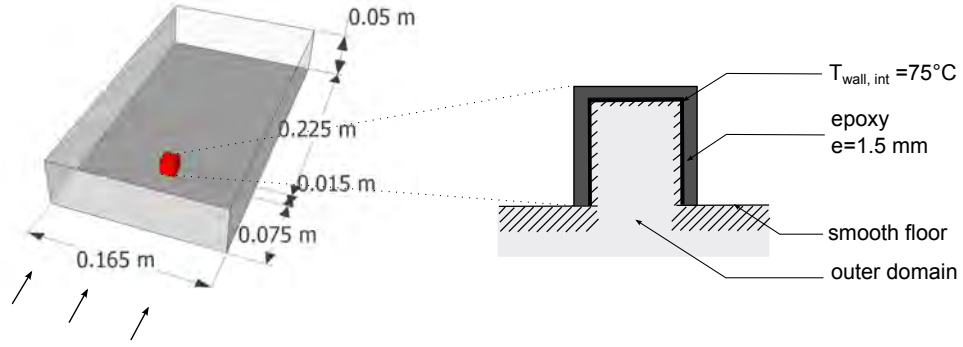


Figure 5.4: Computational model used for the first part of the thermal model validation study.

	epoxy	air	others
$\rho$ [kg · m <sup>-3</sup> ]	1191	1.225	adiabatic
$C_p$ [J · kg <sup>-1</sup> · K <sup>-1</sup> ]	1650	1006.43	
$\lambda$ [W · m <sup>-1</sup> · K <sup>-1</sup> ]	0.237	0.0242	
$T$ [K]	$T_{w,int} = 348$	$T_{inlet} = 294$	

Table 5.3: Thermal properties of the model used.

- length =  $99 \times 10^{-2} \text{ m} = 66 \text{ H}$ ;
- width =  $16.5 \times 10^{-2} \text{ m} = 11 \text{ H}$ ;
- height =  $5 \times 10^{-2} \text{ m} = 3.3 \text{ H}$ , as in the experiment.

The approach flow profile was recorded  $6.75 \times 10^{-1} \text{ m} = 45 \text{ H}$  from the inlet plane, i.e. 5 H upstream the actual location of the cube front face. This profile was set as inlet conditions for the actual simulations, for which only a 5 H long fetch was kept as recommended in [Franke \(2006\)](#); [Tominaga et al. \(2008\)](#). The epoxy layer was explicitly modeled as done in [Defraeye et al. \(2010\)](#). Tab. 5.3 details the thermal properties of this material as well as the other thermal features of the model. Unlike the epoxy layer, the copper core was only modeled by an internal wall temperature boundary condition set at 75 °C. This temperature was uniformly set in the experiment with a very low uncertainty. Note that the layer of epoxy that apparently lied between the floor and the copper core in the experiment is not modeled. However, no experimental data are reported for the bottom part of the cube. The inflow temperature was set to 21 °C as in the experiment. The top boundary condition was specified adiabatic. Fig. 5.4 synthesizes the computational configuration.

All the surfaces of the domain and the cube were modeled as zero roughness height (smooth) walls. The mesh was refined near the floor and even more next to the fluid/solid interface and within the epoxy layer, down to  $3 \cdot 10^{-4} \text{ m}$ . The resulting mesh is composed of more than  $4.42 \times 10^6$  cells, including more than  $4.85 \times 10^5$  cells in the volume of epoxy and  $3.93 \times 10^6$  tetrahedral cells in the fluid. With this mesh resolution,  $z^* \approx 1$  on the cube surface, which makes the use of wall-functions not very relevant. Nevertheless, it is not unreasonable because of the linear formulation of the wall-function for low  $z^*$ . Additional simulations were therefore performed using the enhanced wall treatment that is implemented in Fluent.

and  $16.5 \times 10^{-2} \text{ m}$  corresponds to  $5 \times 1.5 + 1.5 + 5 \times 1.5 \text{ cm} = 5 + 1 + 5 \text{ H}$ .



To evaluate the effects of the turbulence model and better compare our simulation outputs to those of Defraeye et al. (2010), both steady RANS  $Rk-\epsilon$  and RSM simulations were performed. Second order numerical schemes were used because the aerodynamic validation study highlighted problems when using the RSM with a smooth bottom boundary condition and the third order MUSCL numerical scheme. No substantial loss of accuracy was observed when using the second order scheme for the isolated obstacle case. Simulations were initialized with  $2 \times 10^3$  iterations accounting for standard wall-functions instead of the enhanced wall treatment because numerical stability problems occurred otherwise. Other computational settings were kept similar to those used in the aerodynamic study.

Simulations were performed using Ansys Fluent 15 using the GPU-based calculation server running Linux. The solution iterative convergence was studied by monitoring  $T_w$  and  $h_{c,w}$  on the vertical and horizontal mid lines of the windward and leeward faces of the cube as well as on the mid lines of the top and lateral faces. These profiles were then confronted to the experimental data and the simulations results of Defraeye et al. (2010). The computational configuration of the latter study mainly differs from the current one by the structured mesh that was used and the lateral boundary conditions set. They were specified periodic. However, the difference in these specifications is assumed to be negligible as the lateral boundaries are located sufficiently far from the obstacle. In addition to the  $Rk-\epsilon$  model, the results obtained by Defraeye et al. (2010) using the SST  $k-\omega$  model are considered. This model generally provides better results than  $k-\epsilon$  models in low Reynolds number regions of the flow. Such a region currently represents a large part of the domain given the small dimensions involved. However, the SST  $k-\omega$  model was found to give less accurate predictions of the flow field on the top of the cube than the  $Rk-\epsilon$  does, as no flow reattachment was predicted.

In the following, only heat transfers are addressed as the aerodynamic model has already been validated and discussed in Sec. 3.3.

#### 5.2.1.2 Model comparison with the experiment

Fig. 5.5 compares the experimental and numerical profiles of  $h_{c,w}$  for two lines circling the cube. Line A-B-C-D belongs to the vertical mid-plane of the cube and line A'-B'-C'-D' belongs to the horizontal one. The reported  $h_{c,w}$  profiles differ either by the turbulence model used, the number of iterations considered or the near wall treatment. Appendix R gives the corresponding graphs for  $T_w$ . Experimental data are taken from Meinders et al. (1999) and numerical results of Defraeye et al. (2010) are also reported. The corresponding data were extracted from the published graphs using the open source software Engauge Digitizer.<sup>5</sup> Slight grey strips represent regions of higher experimental uncertainties due to the low resolution of measurements next to the cube edges as precised in Defraeye et al. (2010).

A first quality assurance analysis supports the relevancy of the LRNM-based predictions as profiles show symmetric behaviors where expected. The order of magnitude of  $h_{c,w}$  and  $T_w$  also

---

<sup>5</sup><http://digitizer.sourceforge.net/>

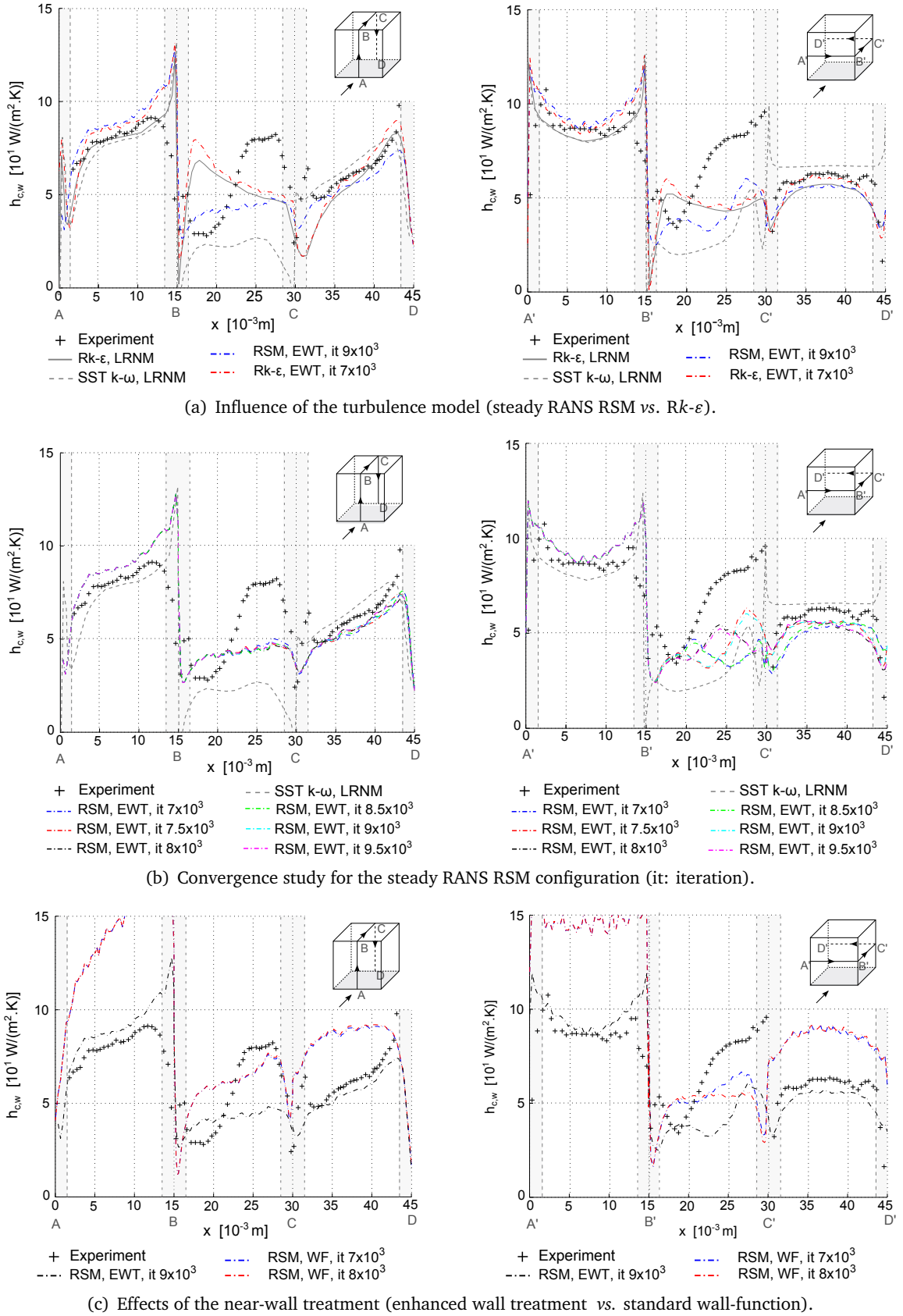


Figure 5.5: Comparison of the numerical and experimental  $h_{c,w}$  profiles around the small cube: effects of the turbulence model.

Exp.: data from [Meinders et al. \(1999\)](#); LRNM ( $Rk-\epsilon$ ): data from [Defraeye et al. \(2010\)](#).



corresponds to the experimental one. However, profiles do not stabilize as functions of the number of iterations when using the RSM, especially on the sides of the cube. On the contrary, profiles simulated by the  $Rk-\epsilon$  show satisfactory iterative convergence. Fig. 5.5(b) illustrates the rather periodic behavior that was observed during the RSM computation. According to the different profiles recorded, profiles evolve with a period of  $1.5 \times 10^3$  iterations. Current instabilities of  $h_{c,w}$  profiles translate instabilities in the modeled flow field as no stabilized mean velocity field could have been achieved. The wake fluctuates from one side of the theoretical symmetry plane to the other even after a great number of iterations. According to Fig. 5.5(b), the amplitude of variation seems to slightly decrease when increasing the number of iterations. This suggests that a further stabilization of the profiles might occur. Nevertheless, simulation was stopped after  $9.5 \times 10^3$  iterations because of time constraints. Similarly to what happened in the aerodynamic validation study, this unstabilized behavior occurs where the experimental study stresses strong flow unsteadiness and strong vortex shedding effects, which can call into question the existence of an effective mean flow as assumed in steady RANS approaches.

Fig. 5.5(c) shows that  $h_{c,w}$  profiles on the cube side do not stabilize when using standard wall-function instead of the enhanced wall treatment together with the RSM either. The variation range is nevertheless reduced and the accuracy of numerical predictions on the side and top faces of the cube appears improved. However, unrealistic values of  $h_{c,w}$  are computed on the other faces. Predictions are almost twice the experimental value on the cube front face. Hence, standard wall-functions do not perform well for very low  $z^*$ . The use of the enhanced wall treatment gives more realistic results. As expected, they correspond to those obtained using a LRNM approach.

Beyond the fluctuations that occur during RSM computations, Fig. 5.5(a) shows a satisfactory match between all the simulated  $h_{c,w}$  profiles and the experimental measures for the windward face of the cube (line segments A-B and A'-B') in terms of distribution and averaged value. A slight over-estimation of  $h_{c,w}$  by both steady RANS models is however observed. Larger discrepancies arise next to the top edge. Uncertainties on experimental data are also higher there (see Sec. 5.2.1.1). Appendix R shows a better correspondence between the simulated  $T_w$  profiles and experimental data at this location. Note that results of Defraeye et al. (2010) match well experimental points with respect to  $h_{c,w}$  whereas  $T_w$  were a bit overestimated. Current results behave conversely. The different results are nevertheless almost in the range of experimental uncertainty.

The accuracy of numerical predictions is also satisfactory for the leeward face of the cube despite a slight under-estimation of  $h_{c,w}$  (or over-estimation of  $T_w$ ). However, discrepancies between the predictions obtained using the different turbulence models are no more negligible for this face, although being still relatively small. RSM predictions match the  $Rk-\epsilon$  predictions of Defraeye et al. (2010) along the line C'-D'. These estimates of  $h_{c,w}$  are lower than those we obtained using the  $Rk-\epsilon$  model, which yields predictions that better correspond to experimental data except near the edges of the face. Differences between the RSM and  $Rk-\epsilon$  predictions are about  $4 \text{ W} \cdot \text{m}^{-2} \cdot \text{K}^{-1}$  or less, which is less than 10% of the  $h_{c,w}$  value. Same trends are logically observed for  $T_w$  although both models over-estimate experimental data from 1.5 to 2.6 °C. However, this belongs to the experimental uncertainty (2.85 °C). Focusing on the vertical profile (line

segment C-D), the slope of the RSM profile corresponds well to the experimental one, but the intensity of  $h_{c,w}$  is under-estimated by about  $5 \text{ W} \cdot \text{m}^{-2} \cdot \text{K}^{-1}$ . This represents a deviation of 8% and slightly exceeds the experimental uncertainty. Conversely, the averaged value of  $h_{c,w}$  appears well reproduced by the  $Rk-\epsilon$  model. However, the slope of the profile is steeper than reported by the experiment, involving lower  $h_{c,w}$  intensities at the bottom of the face and higher intensities at the top.

Contrary to the front and rear faces, numerical predictions substantially deviate from experimental data on the top and side faces. Predictions also differ depending on the turbulence model. As observed on the other faces of the cube,  $Rk-\epsilon$ -based predictions are very close to those of Defraeye et al. (2010), which supports a good implementation of the model. These predictions completely differ from experimental data in distribution on the top and side faces of the cube, although Defraeye et al. (2010) reports a good prediction of the flow at the top of the cube. The experimental profile shows increasing  $h_{c,w}$  streamwise on the top of the cube (line segment B-C), with a minimum at the location of the vortex center and a maximum in the reattachment region. A decreasing profile is simulated by the  $Rk-\epsilon$  model. Nonetheless, line averaged values correspond well. Similarly, an increasing  $h_{c,w}$  profile is reported for the experiment streamwise on the cube side (line segment B'-C') whereas a relatively constant  $h_{c,w}$  profile is predicted by the  $Rk-\epsilon$  model.  $h_{c,w}$  distributions simulated using the RSM better match experimental data. The simulated  $h_{c,w}$  profile increases streamwise on the top face of the cube and a relatively good, but unstabilized, distribution is even predicted by this model on the cube side face. However, the model significantly under-estimates the intensity of  $h_{c,w}$  and shows low  $h_{c,w}$  gradients compared to experimental data.

Furthermore, Fig. 5.5(a) highlights an interesting resemblance between the profile distributions simulated by the RSM and those simulated using the SST  $k-\omega$  model by Defraeye et al. (2010). The RSM gives however better estimates of  $h_{c,w}$  and  $T_w$  intensities, especially on the top and side faces. Appendix R also stresses relatively similar trends respective to  $T_w$  for the line A'-B'-C'-D'<sup>6</sup> between the RSM predictions and the results obtained using some enhanced turbulence models reported in Seeta Ratnam and Vengadesan (2008). RSM distributions are especially in good agreement with the  $T_w$  profiles computed using the improved SST  $k-\omega$  model, which was found to be the most accurate model as compared to DNS results.

As a conclusion, both turbulence models predict rather similar and accurate  $h_{c,w}$  and  $T_w$  profiles on the front and rear faces of the cube when used with the LRNM. However, large deviations occur on the other faces between the experimental and numerical profiles, as well as between the different turbulence models. Nonetheless, the RSM appears to predict  $h_{c,w}$  distribution better than the  $Rk-\epsilon$  does on the top and lateral faces of the cube, but substantially under-estimates  $h_{c,w}$  intensities. In addition, the simulated  $h_{c,w}$  profiles fluctuate where the flow experiences a strong unsteady behavior.

<sup>6</sup>Results for the line A-B-C-D seem to have problems in the paper, so that they are not considered in this thesis.

## 5.2.2 Performance of wall-functions in modeling convective heat transfer

### 5.2.2.1 Validation test case - 2

#### Reference LRNM study

To further analyze the accuracy of our numerical model in conditions closer to an urban configuration, this section considers the case study addressed in Defraeye et al. (2010, 2011a). The combined effects of the turbulence model and wall-functions are examined.

The case study is a cube with a characteristic length of 10m that is located in a turbulent boundary layer. Wall-functions are generally required for such a configuration because of the model dimensions, but Defraeye et al. (2010, 2011a) reported and compared results obtained using a LRNM approach and standard wall-functions. Given the validation of the LRNM approach presented in Sec. 5.2.1.2, the accuracy of wall-functions was evaluated for this case study by comparison with LRNM predictions and the improved temperature wall-function discussed in Sec. 5.1.3.3 was deduced.

The velocity of the approach flow taken at 10m high is  $U_{10} = 0.5 \text{ m} \cdot \text{s}^{-1}$ . Its temperature is  $10^\circ\text{C}$  and that of the cube surfaces is  $20^\circ\text{C}$ .<sup>7</sup> As recommended in Tominaga et al. (2008), the cube is located 5H from the inlet, lateral and top boundaries and 15H from the outlet plane. Lateral boundary conditions were set periodic and the top boundary condition symmetric. As the LRNM can only account for smooth surfaces, a smooth wall boundary condition was specified for the bottom of the domain. An equilibrium ABL profile that corresponds to that of a low roughness terrain with  $z_0 = 0.03 \text{ m}$  was specified as inlet conditions<sup>8</sup> according to the guideline given in Tominaga et al. (2008):

$$U(z) = \frac{u^*}{\kappa} \times \ln \left[ \frac{z - z_0}{z_0} \right] \quad (5.14)$$

$$k(z) = 3.3 \times (u^*)^2 \quad (5.15)$$

$$\varepsilon(z) = \frac{(u^*)^3}{\kappa \times (z + z_0)} \quad (5.16)$$

Note that although  $z_0$  is small and because of the smooth bottom boundary condition, stream-wise gradients necessarily develop along the domain. Nevertheless, the corresponding modification of the incident flow profile happens for both simulations, i.e. the simulation performed using

---

<sup>7</sup>Note that  $Ri \approx 13$  with such a low velocity and physical configuration. This means that buoyancy would effectively influence the flow in reality. However, using CFD models, it is possible not to consider these thermal effects but only forced convection processes. Considering such a configuration allows to save computational resources and to keep a reasonable size for near wall cells, yet carrying out a LRNM study. In addition, Defraeye et al. (2010) showed the relevancy of such an approach to deduce  $h_{c,w} - U_{10}$  correlations that are relevant for higher wind speeds.

<sup>8</sup>The friction velocity  $u^*$  can be deduced from Eq. 5.14 given  $U_{10} = 0.5 \text{ m} \cdot \text{s}^{-1}$  and  $z_0 = 0.03 \text{ m}$  as follows:

$$U_{10} = \frac{u^*}{\kappa} \times \ln \left[ \frac{10 - z_0}{z_0} \right] \iff u^* = \frac{U_{10} \times \kappa}{\ln \left[ \frac{10 - z_0}{z_0} \right]} = 3.6 \times 10^{-2} \text{ m} \cdot \text{s}^{-1}$$

the LRNM and the simulation using wall-functions. As a result, both predictions can be compared under similar conditions.

As Defraeye et al. (2010) found that the steady RANS  $Rk-\varepsilon$  model predicts better the flow around the cube than the other first order turbulence models tested compared to the experimental results of Meinders et al. (1999), this model was used in the actual simulations. Two different mesh resolutions that only differ next to walls were used. On the one hand,  $2.6 \times 10^6$  cells composed the mesh used to perform the LRNM-based simulation. This involved the highest  $z^*$  on the cube edges to be smaller than 3. On the other hand,  $1.1 \times 10^6$  cells composed the mesh used to perform the wall-function-based simulation. This involved  $10 \leq z^* \leq 280$  on the cube surface, which belongs to the recommended range for applicability of usual wall-functions.

### Computational model

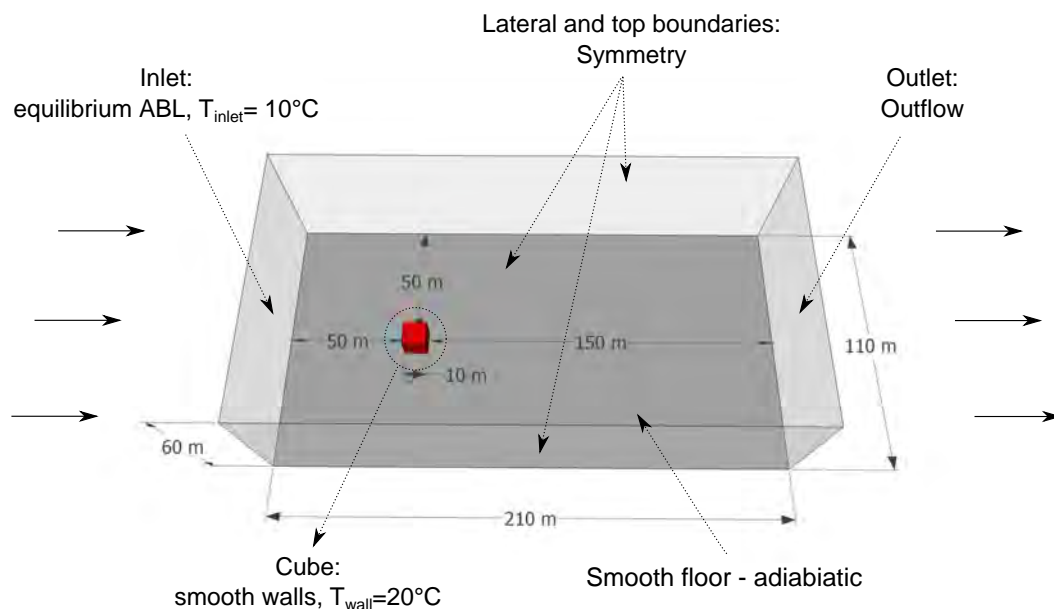


Figure 5.6: Computational model used for the second part of the thermal model validation study.

The modeling strategy implemented in the current study is similar to that described in Defraeye et al. (2010). It includes the domain size and most of the model settings. However, contrary to the reference study, an unstructured mesh of  $2.01 \times 10^6$  cells was used. This mesh involves 1 m cells on the floor and 0.3 m cells on the cube roof. It is built according to the mesh parameterization used in the aerodynamic study (Sec. 4.2.1). Inflow conditions were specified by assigning a user-defined function at the inlet plane of the computational domain. Unlike the reference study, the top and lateral boundary conditions were set symmetric. Other parameters that are not specified in the reference paper were kept similar to those used in the previous models, including the constant density gas model (forced convection) and its properties. Fig. 5.6 illustrates the computational model used.

Simulations were performed using either the steady RANS  $Rk-\varepsilon$  model as done in the reference study or the RSM. Usual standard wall-functions and customized wall-functions for temperature

(see Sec. 5.1.3.3) were tested for both turbulence models. The enhanced wall treatment was also tested with the RSM. Note that  $z^* \gg 1$  in this case. This means that the enhanced wall treatment does not involve the LRNM but behaves as a wall-function on the cube surfaces.

Height cases are firstly compared in terms of  $h_{c,w}$  profiles:

- the three reference predictions from Defraeye et al. (2010, 2011a), which were obtained using the steady RANS  $Rk-\epsilon$  model together with either the LRNM approach, the standard temperature wall-function or the customized temperature wall-function;
- predictions we obtained using the steady RANS  $Rk-\epsilon$  model together with either standard wall-functions or the customized temperature wall-function, in order to directly compare our simulation outputs to those of the reference study;
- and predictions we obtained using the steady RANS RSM together with standard wall-functions, the customized temperature wall-function or the enhanced wall treatment, in order to evaluate the effects of the turbulence modeling and the accuracy of the different wall-functions for a turbulence model else than the  $Rk-\epsilon$ .

Convergence was verified by monitoring  $h_{c,w}$  profiles on the mid-lines of the different faces of the cube as well as the overall contours of  $h_{c,w}$  on these faces.

#### 5.2.2.2 Sensitivity analysis of $h_{c,w}$ to the turbulence model and near wall treatment

Fig. 5.7 compares the  $h_{c,w}$  profiles we simulated using either the steady RANS  $Rk-\epsilon$  or the RSM turbulence models together with standard wall-functions to those taken from Defraeye et al. (2010) for the lines A-B-C-D and A'-B'-C'-D'. Reference results obtained using the LRNM approach or standard wall-functions are reported. The respective influences of the near wall treatment and the turbulence model can thus be distinguished.  $h_{c,w}$  profiles simulated using the steady RANS RSM and the enhanced wall treatment are also reported as this model was used in the first part of the current validation study (Sec. 5.2.1).

All the different profiles simulated using wall-functions follow the same trends. The variations of  $h_{c,w}$  as functions of the location on the lines A-B-C-D or A'-B'-C'-D' are fairly similar for all the models. However,  $h_{c,w}$  intensities differ depending on the turbulence model and the near wall treatment. As expected, predictions obtained using the  $Rk-\epsilon$  model together with standard wall-functions correspond to the reference  $h_{c,w}$  profiles taken under the similar computational configuration. A slight and constant positive difference between the corresponding profiles nevertheless appears except on the rear face where they match well.

$h_{c,w}$  intensities predicted by the RSM together with the standard temperature wall-function are generally lower than those predicted using the  $Rk-\epsilon$  model except on the rear face of the cube. There, the RSM-based profile are more symmetric along the vertical mid line than those simulated using the  $Rk-\epsilon$  model. However, intensities are comparable. RSM-based  $h_{c,w}$  profiles also generally vary over a wider range of values and show more distinguishable inflection points. Differences in the predicted  $h_{c,w}$  between the two models are about  $0.5 \text{ W} \cdot \text{m}^{-2} \cdot \text{K}^{-1}$  on the front

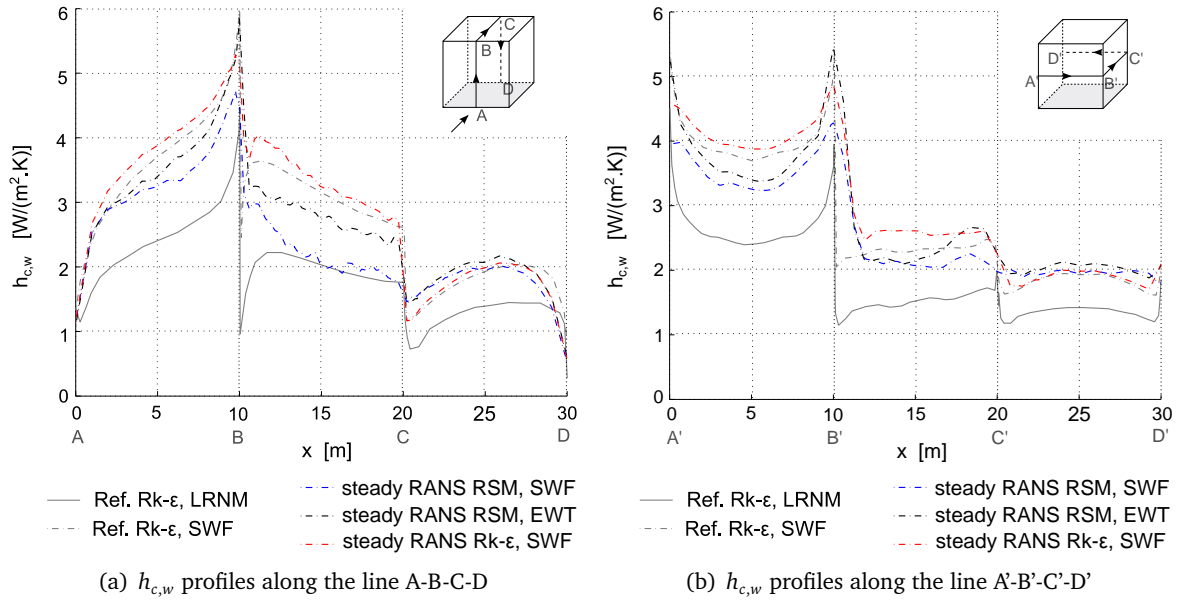


Figure 5.7: Comparison of the  $h_{c,w}$  profiles around the cube: effects of the turbulence model and near-wall treatment.

face (with a maximum occurring around the center) as well as on the side face. A larger difference of between  $0.9$  and  $1.3 \text{ W} \cdot \text{m}^{-2} \cdot \text{K}^{-1}$  occurs on the top face.

Comparing the predictions obtained with the RSM together with either standard wall-function or the enhanced wall treatment highlights rather similar behaviors of the  $h_{c,w}$  profiles on the front, rear and lateral faces of the cube.  $h_{c,w}$  intensities simulated using the enhanced wall treatment are nevertheless slightly higher (about  $+0.2 \text{ W} \cdot \text{m}^{-2} \cdot \text{K}^{-1}$ ) than those based on the standard wall-function. This comparable behavior confirms the theory, i.e. the enhanced wall treatment resembles to usual wall-functions for high  $z^*$  (see Sec. 5.1.3.1). However, a greater difference occurs on the top face, where the averaged difference is of  $+0.5 \text{ W} \cdot \text{m}^{-2} \cdot \text{K}^{-1}$  with maximum reaching  $+0.75 \text{ W} \cdot \text{m}^{-2} \cdot \text{K}^{-1}$  in the middle of the face, which represents a 37 % deviation.

Contrary to the previous case (Sec. 5.2.1.2), for which the RSM gives quite similar predictions as the  $Rk-\epsilon$  on the front face, slightly lower  $h_{c,w}$  intensity on the rear face and completely different trends on the top and side faces of the cube, RSM predictions currently differ in intensity from those of the  $Rk-\epsilon$  for all faces but the rear one. Distributions are however relatively comparable on the different faces of the cube.

Further comparing the wall-function-based  $h_{c,w}$  profiles to the reference profiles simulated using the LRNM reveals a significant over-estimation of  $h_{c,w}$  by standard wall-functions. This observation is supported by literature studies, as discussed in Sec. 5.1.3. A better match is however achieved when using the RSM. Deviation is of 37 % compared to LRNM predictions while deviation is of 61 % when using the  $Rk-\epsilon$  model. Heat transfers appear to be more accurately estimated when computed using this turbulence model together with standard wall-functions than when using the  $Rk-\epsilon$  model. This may be due to a better estimate of  $k$  by the RSM. Furthermore,  $h_{c,w}$  distributions simulated using the enhanced wall treatment are closer to those of the reference



LRNM profiles than those simulated using the standard wall-functions. However,  $h_{c,w}$  intensities are higher, and therefore less close to the LRNM predictions. In addition, this near wall model cannot account for roughness.

As a conclusion, the current study verifies that standard wall-functions do not perform well in predicting convective heat transfers at walls. They cannot be considered sufficiently accurate to be generally used for building physics problems. Errors appear nevertheless reduced when using the RSM instead of the  $Rk-\epsilon$  model, especially on the front face of isolated sharp-edged obstacles.

### 5.2.2.3 Adaptation of the customized temperature wall-function of Defraeye et al. (2011a) to the RSM

To improve the accuracy of standard wall-functions in predicting heat transfers when performing steady RANS RSM simulations, the applicability of the customized temperature wall-function proposed by Defraeye et al. (2011a) was tested.

Previous results show rather comparable distributions of  $h_{c,w}$  on the faces of the cube when using the  $k-\epsilon$  and RSM turbulence models. In addition, the expression of standard wall-functions is the same for both models. Therefore, it is assumed that a modification of the  $Pr_{t,w}$  value would also decrease the deviation between the RSM wall-function-based  $h_{c,w}$  predictions and those derived from a LRNM approach. Indeed, Sec. 5.2.1.2 shows that LRNM results give accurate predictions of the heat transfers irrespective of the turbulence model used on the windward and leeward faces of the cube. As a consequence, additional simulations were performed accounting for the modification of the  $Pr_{t,w}$  value from 0.85 to 1.95.

Appendix S provides the  $h_{c,w}$  profiles we obtained accounting for the modified value of  $Pr_{t,w}$  together with either the steady RANS RSM or the  $Rk-\epsilon$  model. These profiles are compared to the reference profiles from Defraeye et al. (2011a), still for the lines A-B-C-D and A'-B'-C'-D'. Both reference profiles obtained using either a LRNM approach or the customized temperature wall-function are reported.

Results show a good match between our steady RANS  $Rk-\epsilon$  results and those of Defraeye et al. (2011a). These profiles are also in good correspondence with the LRNM predictions. However in this configuration, the  $h_{c,w}$  profiles simulated by the RSM under-estimate LRNM results, especially on the front and top faces of the cube. An averaged difference of  $0.5 \text{ W} \cdot \text{m}^{-2} \cdot \text{K}^{-1}$  is observed. This represents a 20 % and 25 % difference on these faces respectively. An averaged under-estimation of  $h_{c,w}$  also occurs on the lateral face, and the distribution is more constant than for the LRNM. As this behavior also occurs when using the  $Rk-\epsilon$  model, it may be explained by wall-function effects rather than turbulence model effects.

This general under-estimation of  $h_{c,w}$  observed when using the customized temperature wall-function designed for  $k-\epsilon$  models together with the RSM was expected as the RSM was shown to provide lower  $h_{c,w}$  when used with standard wall-functions than the  $Rk-\epsilon$  does in Sec. 5.2.1.2. As a consequence and in order to improve the accuracy of the heat transfer predictions by the RSM

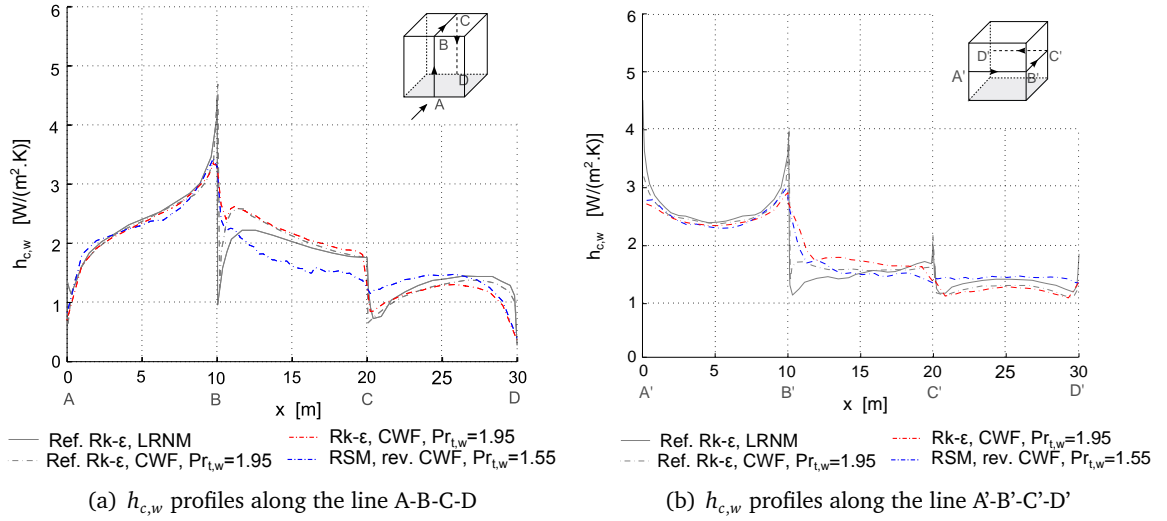


Figure 5.8: Comparison of the  $h_{c,w}$  profiles obtained using the optimized  $Pr_{t,w}$  value together with the appropriate turbulence model.

together with wall-functions, the  $Pr_{t,w}$  value was modified to fit the reference LRNM profiles. The case study characterized by a 10 m high cube and a reference wind velocity  $U_{10} = 0.5 \text{ m} \cdot \text{s}^{-1}$  is still considered.

According to Eq. 5.5 and Eq. 5.7,  $q_{w,c}$ , and likewise  $h_{c,w}$ , is a decreasing function of  $Pr_{t,w}$ . Therefore, different  $Pr_{t,w}$  values lower than 1.95 stepping down by 0.2 were tested to fit the LRNM results. Appendix S provides the different profiles obtained using the modified  $Pr_{t,w}$  tested. A good match between simulations outputs and the reference LRNM- $h_{c,w}$  profiles along the lines A-B-C-D and A'-B'-C'-D' is obtained for  $Pr_{t,w} = 1.55$ . Fig. 5.8 shows that the accuracy of the resulting profiles is similar to that of the reference customized temperature wall-function designed for the Rk- $\epsilon$  model by Defraeye et al. (2011a).

To further verify the accuracy of this new modified temperature wall-function all over the windward and leeward faces, several simulated  $h_{c,w}$  profiles were compared to LRNM predictions for different vertical lines on the cube faces (Defraeye, 2009).<sup>9</sup> Fig. 5.9 reports the results for two vertical profiles located 1 m and 3 m from the edge of the front and rear faces of the cube. Appendix T.1 provides the comprehensive results for six vertical profiles taken each one meter away from the lateral edges to the middle of the faces. As the problem is symmetric, only the left hand side of faces is shown. Profiles simulated using the Rk- $\epsilon$  model together with the original customized temperature wall-function ( $Pr_{t,w} = 1.95$ ) are also reported on the graphs for completeness.

Not considering border locations, results show a good agreement between the different profiles reported. Profiles simulated using both the Rk- $\epsilon$  or the RSM models together with their respective customized temperature wall-function match very well with each other and with LRNM

<sup>9</sup>These LRNM-based  $h_{c,w}$  profiles were kindly provided to us by T. Defraeye, who used them to deduce the  $h_{c,w}-U_{10}$  correlations addressed in Sec. 5.1.3.2.



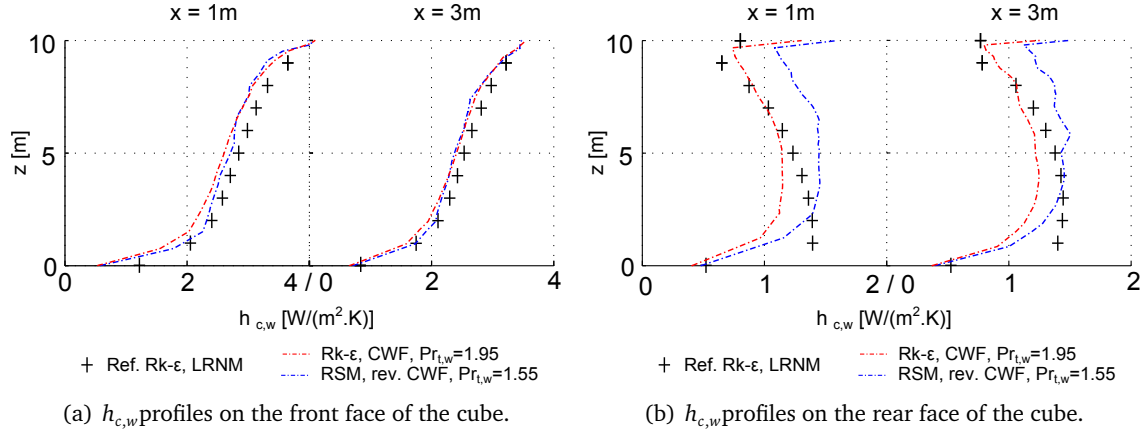


Figure 5.9: Comparison between vertical  $h_{c,w}$  profiles simulated using the original or the revised customized temperature wall-function together with the appropriate turbulence model and the LRNM results of Defraeye (2009) for  $U_{10} = 0.5 \text{ m} \cdot \text{s}^{-1}$ .

results on the front face of the cube, both in terms of distribution and intensity. Some deviation is however observed on the rear face of the cube. Our simulated  $h_{c,w}$  profiles differ from LRNM results for both turbulence models in the bottom quarter part of the face. A deviation of about  $0.25 \text{ W} \cdot \text{m}^{-2} \cdot \text{K}^{-1}$  is observed higher between our two simulated  $h_{c,w}$  profiles. The RSM predictions are closer to LRNM results at the bottom part of the face, whereas the  $Rk-\epsilon$  predictions are closer to LRNM results at the top part of the face. However, compared to the error induced by the use of the standard temperature wall-function, the accuracy of predictions is much improved.

As a consequence, this revised form of the customized temperature wall-function is proposed as the revised customized temperature wall-function for the RSM ( $Pr_{t,w}(RSM) = 1.55$  instead of  $Pr_{t,w}(Rk-\epsilon) = 1.95$ ). As such, it keeps the limitations and scope for applicability of the original customized temperature wall-function, especially with respect to  $z^*$ .

#### 5.2.2.4 Applicability of the revised customized temperature wall-function for the RSM for high $z^*$

Customized temperature wall-functions were originally derived for  $50 \leq z^* \leq 500$  (see Fig. 5.2, Sec. 5.1.3.3). As a consequence, assuming cell sizes of about 0.5 m, they relevantly apply for relatively low wind speeds. In such a configuration, considering a theoretical 10 m high cubical building and  $U_{10} = 0.5 \text{ m} \cdot \text{s}^{-1}$ , Fig. 5.10 shows that  $z^* \approx 4.5 \times 10^2$  on average on the cube front face. Some higher  $z^*$  are noticed on the bottom lateral part of the face, but maximum  $z^*$  are lower than  $10^3$ . Therefore, the simulated  $z^*$  values are mainly in the original range of applicability of the customized temperature wall-function, i.e. the range for which the customized temperature wall-function has been fitted to LRNM results by Defraeye et al. (2011a).

Fig. 5.10 shows that increasing the reference wind speed from e.g.  $U_{10} = 0.5 \text{ m} \cdot \text{s}^{-1}$  to  $U_{10} = 5 \text{ m} \cdot \text{s}^{-1}$  does not change the distribution of  $z^*$  on the cube front and rear faces. However, it involves  $z^*$  values higher than  $5 \times 10^2$ .  $z^*$  values are even often higher than  $4 \times 10^3$  on the cube

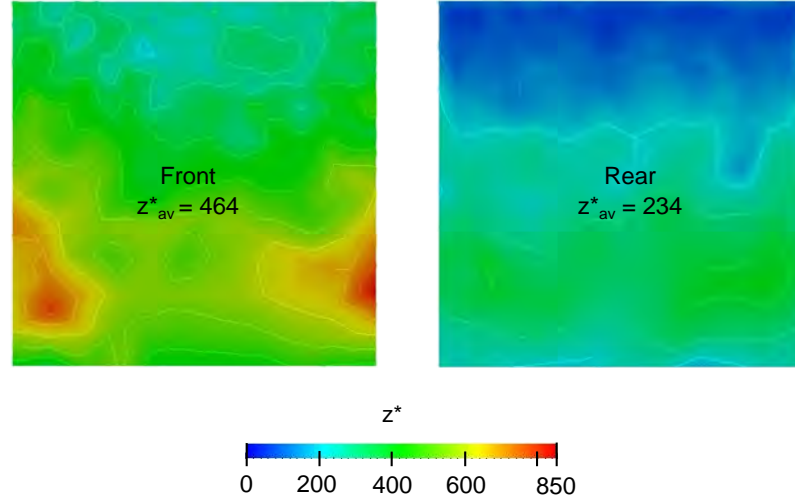
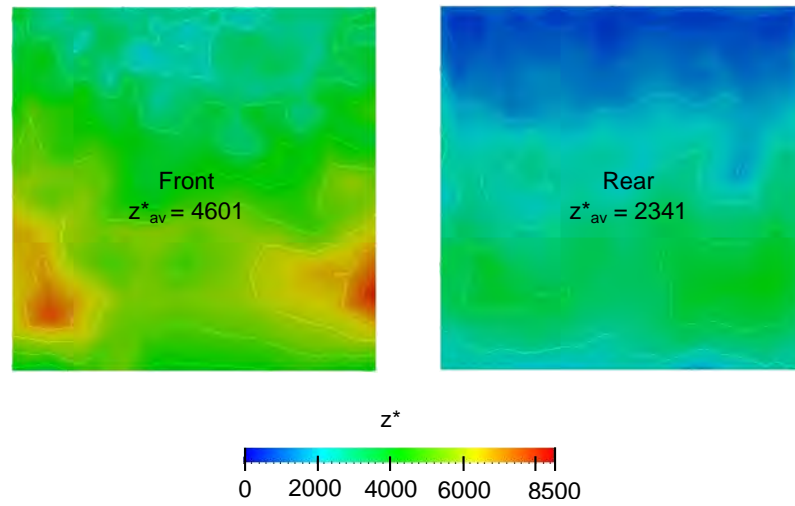
(a)  $z^*$  on the front (left) and rear (right) faces of the cube for  $U_{10} = 0.5 \text{ m} \cdot \text{s}^{-1}$ (b)  $z^*$  on the front (left) and rear (right) faces of the cube for  $U_{10} = 5 \text{ m} \cdot \text{s}^{-1}$ 

Figure 5.10: Comparison of the distributions of  $z^*$  on the front and rear faces of the cube in cases of  $U_{10} = 0.5$  or  $5 \text{ m} \cdot \text{s}^{-1}$ .

front face, where the surface averaged  $z^*$  equals  $4.6 \times 10^3$ . These  $z^*$  values exceed the original scope for applicability of the customized temperature wall-function. As a consequence, if cell size has to be kept around  $0.5 \text{ m}$  in CFD models, the applicability of both the original and the revised customized temperature wall-functions should be evaluated for high  $z^*$ .

For this purpose, additional simulations were performed and analyzed. The case study is the same as in the previous section but  $U_{10}$  is taken equal to  $5 \text{ m} \cdot \text{s}^{-1}$ . Settings kept similar to the previous case study especially include the mesh ( $2.01 \times 10^6$  cells), the turbulence model (RSM) and the near-wall treatment (revised customized temperature wall-function for the RSM). Increasing the approach flow speed from  $U_{10} = 0.5 \text{ m} \cdot \text{s}^{-1}$  to  $U_{10} = 5 \text{ m} \cdot \text{s}^{-1}$  can simply be achieved by modifying the  $u^*$  value of the approach flow from  $0.036 \text{ m} \cdot \text{s}^{-1}$  to  $0.36 \text{ m} \cdot \text{s}^{-1}$  in the user-defined function set as inlet conditions of the model. This modification also applies for the other inflow parameters, namely  $k$  and  $\varepsilon$ .

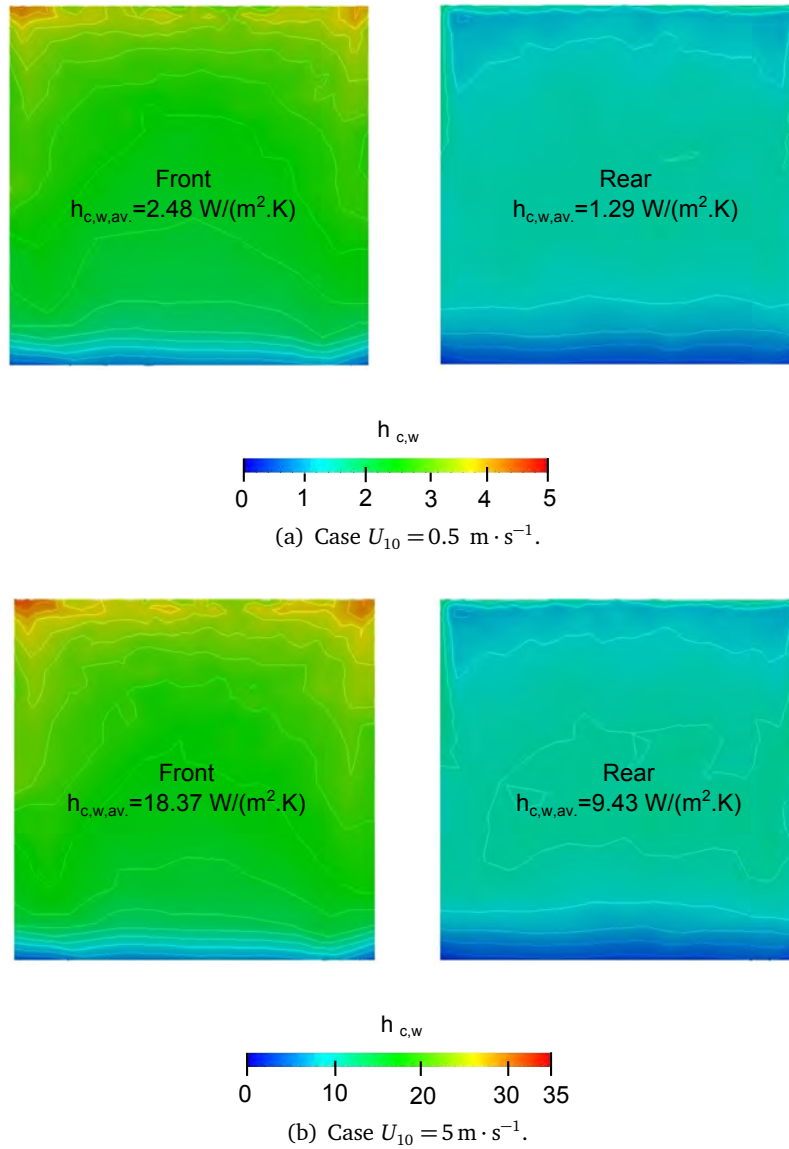


Figure 5.11: Comparison between the distributions of  $h_{c,w}$  simulated using the revised customized temperature wall-function for the RSM on the front and rear faces of the cube in cases of  $U_{10} = 0.5$  or  $5 \text{ m} \cdot \text{s}^{-1}$ .

Fig. 5.11 compares the distributions and intensities of  $h_{c,w}$  that were computed either in case of  $U_{10} = 0.5 \text{ m} \cdot \text{s}^{-1}$  or  $U_{10} = 5 \text{ m} \cdot \text{s}^{-1}$ . Only the front and rear faces of the cube are examined as the thermal model was validated for these faces. Similar  $h_{c,w}$  distributions are observed on these faces for both wind speeds.  $h_{c,w}$  intensities are nevertheless substantially increased when considering  $U_{10} = 5 \text{ m} \cdot \text{s}^{-1}$ . Surface averaged  $h_{c,w}$  values are multiplied by a factor 7.3 on the examined faces of the cube.

Both spatially differentiated and surface averaged  $h_{c,w} - U_{10}$  correlations were derived from LRNM studies by Defraeye et al. (2010) for wind speeds up to  $7.5 \text{ m} \cdot \text{s}^{-1}$  for the windward and leeward faces of the cube (see Fig. 5.1 and Sec. 5.1.3.2). Therefore, it is possible to evaluate the accuracy of the model by comparing our simulation outputs to reference data derived from

LRNM studies in case of  $U_{10} = 5 \text{ m} \cdot \text{s}^{-1}$ . To evaluate the performance of the revised customized temperature wall-function for the RSM, five models, which differ by the turbulence model, the temperature wall-function or mesh resolution used, were tested:

- 1. the steady RANS  $Rk-\varepsilon$  / standard temperature wall-function;
- 2. the steady RANS  $Rk-\varepsilon$  / customized temperature wall-function;
- 3. the steady RANS RSM / temperature wall-function;
- 4. the steady RANS RSM / revised customized temperature wall-function for the RSM;
- and 5. the same as for the case 4 but considering a refined mesh of  $4.8 \times 10^6$  cells.

The solution iterative convergence was verified by monitoring some  $h_{c,w}$  profiles and overall contours on the cube surfaces. Data post-processing including the computation of the surface averaged values was performed using Paraview.

Tab. 5.4 compares the surface averaged  $h_{c,w}$  simulated using these different models on the front and rear faces of the cube with the corresponding values estimated using the  $h_{c,w}-U_{10}$  correlation (Eq. 5.11 and 5.12). Results for  $U_{10} = 0.5$  and  $5 \text{ m} \cdot \text{s}^{-1}$  are compared. Note that the tests 1 and 5 were only performed for  $U_{10} = 0.5 \text{ m} \cdot \text{s}^{-1}$  or  $U_{10} = 5 \text{ m} \cdot \text{s}^{-1}$  respectively.

Accordingly to literature results and the observation reported in Sec. 5.2.2.2, the use of standard temperature wall-functions significantly over-estimates of the reference  $h_{c,w}$  values. Considering the RSM simulations, the relative deviation is greater in case of  $U_{10} = 5 \text{ m} \cdot \text{s}^{-1}$  than in case of  $U_{10} = 0.5 \text{ m} \cdot \text{s}^{-1}$ . The relative difference is multiplied by more than a factor 1.5 on both the front and rear faces of the cube, and reaches nearly 60% on the rear face. On the contrary, the accuracy of the original and the revised customized temperature wall-functions used together with the appropriate turbulence model appears generally improved in case of  $U_{10} = 5 \text{ m} \cdot \text{s}^{-1}$ . The accuracy of predictions is only reduced on the rear face of the cube when using the RSM. However, the deviation is smaller than 10% in comparison with the reference data, which remains acceptable considering the accuracy of steady RANS approaches and usual building physics models. Still considering  $U_{10} = 5 \text{ m} \cdot \text{s}^{-1}$ , refining the mesh improves the accuracy of the revised customized temperature wall-function predictions on the front face of the cube, but reduces it on the rear face. Nevertheless, the loss of accuracy is of  $0.38 \text{ W} \cdot \text{m}^{-2} \cdot \text{K}^{-1}$  (4.5 points), which is almost negligible for building physics applications.

Hence, the comparison of the surface averaged values of  $h_{c,w}$  confirms that the use of standard temperature wall-function yields too large deviations compared to LRNM-based values to be relevantly used to study building physics problems. On the contrary, the original and the revised versions of the customized temperature wall-function predict surface averaged  $h_{c,w}$  with a satisfactory accuracy for the basic and high  $z^*$  values tested.

To further verify the accuracy of the revised customized temperature wall-function for the RSM in case of high  $z^*$ , the spatial distribution of the simulated  $h_{c,w}$  was also confronted to the detailed  $h_{c,w}$  data of Defraeye (2009). These data were obtained using the LRNM for  $U_{10} = 5 \text{ m} \cdot \text{s}^{-1}$ . Fig. 5.12 compares the corresponding  $h_{c,w}$  profiles for three vertical profiles located 1 m and 3 m

Reference velocity: $U_{10}$		Front face		Rear face	
		$0.5 \text{ m} \cdot \text{s}^{-1}$	$5 \text{ m} \cdot \text{s}^{-1}$	$0.5 \text{ m} \cdot \text{s}^{-1}$	$5 \text{ m} \cdot \text{s}^{-1}$
$h_{c,w} - U_{10}$	$[\text{W} \cdot \text{m}^{-2} \cdot \text{K}^{-1}]$	2.78	19.68	1.28	8.63
Rk- $\epsilon$ , SWF	$[\text{W} \cdot \text{m}^{-2} \cdot \text{K}^{-1}]$	4.0	—	1.63	—
Relative deviation	%	43.9	—	27.3	—
Rk- $\epsilon$ , ori. CWF	$[\text{W} \cdot \text{m}^{-2} \cdot \text{K}^{-1}]$	2.44	17.78	1.07	7.54
Relative deviation	%	12.2	9.7	16.4	12.6
RSM, SWF	$[\text{W} \cdot \text{m}^{-2} \cdot \text{K}^{-1}]$	3.47	27.32	1.74	13.68
Relative deviation	%	24.8	38.8	35.9	58.5
RSM, rev. CWF	$[\text{W} \cdot \text{m}^{-2} \cdot \text{K}^{-1}]$	2.48	18.37	1.29	9.43
Relative deviation	%	11	6.7	1	9.2
RSM, rev. CWF Mesh +	$[\text{W} \cdot \text{m}^{-2} \cdot \text{K}^{-1}]$	—	18.59	—	9.81
Relative deviation	%	—	5.5	—	13.7

Table 5.4: Comparison of the surface averaged  $h_{c,w}$  computed using the reference  $h_{c,w} - U_{10}$  correlation of Defraeye et al. (2010) or estimated using CFD simulations for the cube in cases of  $U_{10} = 0.5 \text{ m} \cdot \text{s}^{-1}$  and  $U_{10} = 5 \text{ m} \cdot \text{s}^{-1}$ .

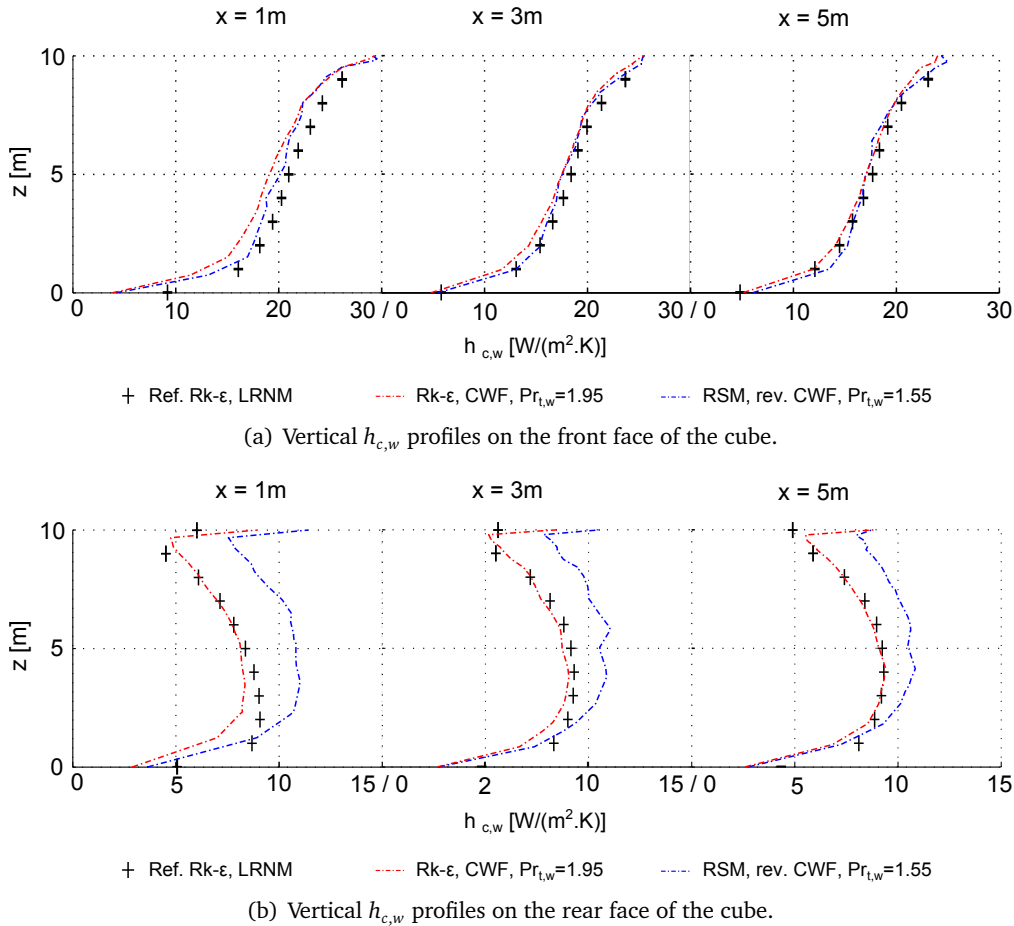


Figure 5.12: Comparison between the simulated  $h_{c,w}$  profiles using the original and revised customized temperature wall-function together with the appropriate turbulence model with reference LRNM data of Defraeye (2009) for  $U_{10} = 5 \text{ m} \cdot \text{s}^{-1}$ .

from the lateral edges of the cube front and rear faces as well as on the symmetry axis. As the problem is symmetric, results are only reported for a half of each face. Fig. 5.12 reports the profiles we obtained using the  $Rk-\varepsilon$  model together with the original customized temperature wall-function of Defraeye et al. (2010) as well, in order to compare the relative performance of the two wall-function-based improved models. Appendix T.2 provides more complete results and compares the different  $h_{c,w}$  profiles along six vertical lines located every meter of the cube faces. Appendix T.1 provides the corresponding profiles in case of  $U_{10} = 0.5 \text{ m} \cdot \text{s}^{-1}$  for comparison.

The different profiles reported show similar trends.<sup>10</sup> In particular, a very good match is observed between the LRNM and wall-function-based  $h_{c,w}$  profiles on the front face. Deviations are nevertheless observed on the rear face. On the one hand, profiles obtained using the  $Rk-\varepsilon$  model together with the original customized temperature wall-function correspond well to LRNM results despite a small deviation at the bottom of the face. This behavior was already observed in Sec. 5.2.2.3. On the other hand,  $h_{c,w}$  profiles simulated using the RSM together with the revised customized temperature wall-function show higher  $h_{c,w}$  intensities. As expected from Tab. 5.4, a loss of accuracy of these predictions occurs compared to the configuration with  $U_{10} = 0.5 \text{ m} \cdot \text{s}^{-1}$ . This behavior is unexpected as  $z^*$  values are relatively low on this face. In addition, Tab. 5.4 shows a similar accuracy of the surface averaged  $h_{c,w}$  values derived from the  $Rk-\varepsilon$  and RSM models performed using the appropriate version of the customized temperature wall-function on the rear face of the cube and in case of  $U_{10} = 5 \text{ m} \cdot \text{s}^{-1}$ . The deviation of the simulated profiles compared to LRNM results increases with height, similarly to what was already observed in case of  $U_{10} = 0.5 \text{ m} \cdot \text{s}^{-1}$ . Deviation also varies with the distance to the lateral edge of the cube face as differences are reduced closer to the symmetry axis. Typical deviations of  $2.5$  and  $1.5 \text{ W} \cdot \text{m}^{-2} \cdot \text{K}^{-1}$  are observed  $1 \text{ m}$  from the lateral edge of the face and on the symmetry axis respectively. This represents a difference of  $30\%$  and  $15\%$  respectively. However, Sec. 5.2.1 shows that the RSM predicts more constant horizontal profiles of  $h_{c,w}$  on the rear face of the obstacles than the  $Rk-\varepsilon$  does, which yields variations that better correspond to experimental data. As a consequence, the deviation observed between the RSM-based profiles and the reference  $Rk-\varepsilon$  LRNM data may not be due to the temperature wall-function used, but to the turbulence model.

Hence, the revised customized temperature wall-function for the RSM appears to be accurate both in terms of distribution and intensity on the front face of the cube for high  $z^*$  values. Its accuracy is however reduced on the rear face. Nevertheless, the predicted surface averaged  $h_{c,w}$  values are satisfactory, and its performance is significantly improved compared to that of the standard temperature wall-function. As a consequence the revised customized temperature wall-function is kept for the actual studies.

---

<sup>10</sup>Substantial deviations however occur between the wall-function and LRNM based  $h_{c,w}$  profiles on the edges of the faces. This may be due to border effects. They are therefore not further discussed in the current analysis.

## 5.3 Analysis of $h_{c,w}$ distribution on building facades

### 5.3.1 Settings of the coupled thermal and aerodynamic model

Coupled thermal and aerodynamic simulations are performed in order to examine the relations between the different flow structures examined in Sec. 4.4 and the convective heat exchanges that develop on building facade. Results provide further information on the effects of the building topology and urban surroundings on the convective heat transfers at buildings outer walls. The case studies considered to examine these processes are the cube, patio, cube array and continuous patio array, as done in Sec. 4.5 to examine the  $C_p$  distribution on building facades.

Simulations were generally performed using the same computational configurations as in the aerodynamic study, i.e. the overall geometry and the mesh were kept. Computations were initialized using the simulation results of the aerodynamic study. This way, simulations started with realistic flow fields and some numerical stability problems are avoided. Nevertheless, because of the numerical stability problems occurring for the continuous patio array type, simulations were initialized with the aerodynamic field computed after  $4 \times 10^3$  iterations. For the aerodynamic part of the model, simulation settings were kept similar to those used in the aerodynamic study (see Sec. 4.1.1). The only difference is that all simulations were performed using second order upwind numerical schemes as it was done in the validation study (Sec. 5.2.1 and Sec. 5.2.2). The revised customized temperature wall-function for the RSM is used as Sec. 5.2.2.3 and Sec. 5.2.2.4 highlight the substantial improvement provided by this wall-function compared to standard temperature wall-functions. No radiative heat transfers are accounted for. Although Sec. 5.2.2.4 shows the good performance of the revised customized temperature wall-function for  $z^* > 4 \times 10^3$ , the finest meshes addressed in Sec. 4.3 are used when possible to remain as long as possible close to the range of  $z^*$  for which the customized temperature wall-function was originally derived.

The inflow temperature was set at  $T_{ext} = 288 \text{ K}$ , i.e.  $T_{ext} = 15^\circ \text{C}$ . To study the external convective heat fluxes that develop at building envelope, the building model is simplified assuming:

- an interior homogeneous temperature of  $T_{int} = 293 \text{ K}$ , i.e.  $T_{int} = 20^\circ \text{C}$ ;
- zero thickness outer walls ( $e_w = 0.00 \text{ m}$ );
- and an equivalent interior  $h_{c,w}$  equal to  $1 \text{ W} \cdot \text{m}^{-2} \cdot \text{K}^{-1}$ , standing for the cumulative effects of the interior surface heat transfers and the thermal conduction of the wall.

Fig. 5.13 summarizes the main settings of the thermal model. Neglecting the contribution of the external convective heat transfers, this thermal configuration models a building envelope of  $1 \text{ W} \cdot \text{m}^{-2} \cdot \text{K}^{-1}$  total thermal transmittivity, i.e. a total thermal resistance<sup>11</sup> of  $1 \text{ m}^2 \cdot \text{K} \cdot \text{W}^{-1}$ . This corresponds to a relatively thermally inefficient envelope made of walls composed of e.g. 15 cm of concrete ( $\lambda_{conc.} = 1.5 \text{ W} \cdot \text{m}^{-1} \cdot \text{K}^{-1}$ ) and about 4 cm of insulation ( $\lambda_{insul.} = 0.05 \text{ W} \cdot \text{m}^{-1} \cdot \text{K}^{-1}$ )

---

<sup>11</sup>As it does not consider the 3D distribution of the heat flux inside walls, this model is not very realistic. As simulations are steady state, the effects of the thermal mass are also overlooked, although important for the building thermal comfort and energy management. Nevertheless, the aim of this study is to evaluate and examine the distribution and intensity of  $h_{c,w}$  at outer building walls. This can be achieved using this simple model.



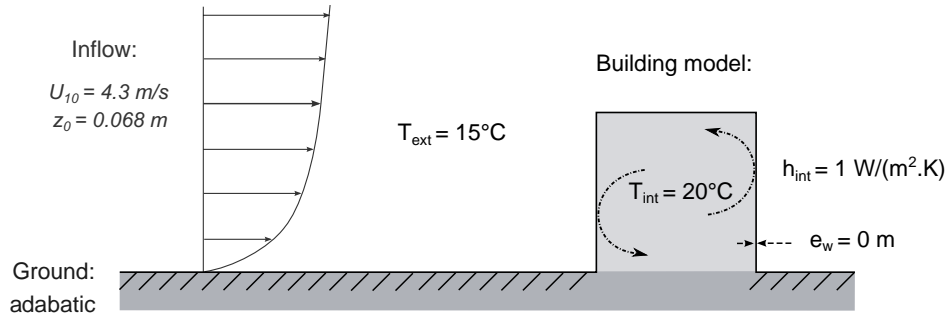


Figure 5.13: Settings of the actual thermal model.

with an interior surface heat transfer coefficient  $h_{int} = 8 \text{ W} \cdot \text{m}^{-2} \cdot \text{K}^{-1}$ . Such a wall is about three times less efficient than required by the French RT 2012,<sup>12</sup> but twice more efficient than traditional Haussmannian walls oriented towards the courtyard (APUR, 2011). In such cases, the convective contribution to the total building heat exchanges is important.

Given  $\Delta T_{int-ext} = 5^\circ\text{C}$ ,  $U_{10} = 4.3 \text{ m} \cdot \text{s}^{-1}$  and  $H = 10 \text{ m}$ ,  $Ri = 9.42 \times 10^{-2} \ll 1$ . This means that this is a case of predominant forced convection and buoyancy effects can be neglected. Therefore, the use of the constant density air model is theoretically relevant. However, considering the low wind speeds that occur in recirculation zones, especially in building wakes and inside enclosed courtyards, buoyancy effects might affect the flow field in these regions in reality.<sup>13</sup> These effects are nevertheless assumed negligible as the temperature difference is small and a reference wind speed of  $1.5 \text{ m} \cdot \text{s}^{-1}$ , i.e. 2.5 times less than the current reference wind velocity, would be necessary to reach  $Ri = 1$ .

Convergence was verified by monitoring the contours of  $h_{c,w}$  on different faces of the model and monitoring some vertical and horizontal profiles of  $h_{c,w}$  on the obstacle faces. Recordings were done every  $5 \times 10^2$  iterations. The simulation was assumed converged when the variation of the different  $h_{c,w}$  contours and profiles was negligible during  $2 \times 10^3$  iterations at least. Note that because of the numerical stability problems already stressed in Sec. 4.3, only  $2 \times 10^3$  iterations were run for the continuous patio array.

<sup>12</sup>For building outer walls, the threshold U-values given in the two last French thermal regulations are:

- RT 2005:  $U = 0.45 \text{ W} \cdot \text{m}^{-2} \cdot \text{K}^{-1}$  for walls and  $U = 0.28 \text{ W} \cdot \text{m}^{-2} \cdot \text{K}^{-1}$  for roofs;
- RT 2012:  $U = 0.36 \text{ W} \cdot \text{m}^{-2} \cdot \text{K}^{-1}$  on average for the building envelope.

<sup>13</sup>Buoyancy might increase turbulence and convective heat transfers especially when wind speeds are low and temperature differences are high. Based on numerical results, Defraeye et al. (2012) mention increased  $h_{c,w}$  intensity on the different faces of an isolated sharp edged obstacle when increasing the Richardson number from 0.1 to 52 ( $Re > 3 \times 10^5$ ). In addition, strong buoyancy alters  $h_{c,w}$  distributions at the bottom of the front face and the top of the rear face. Based on wind-tunnel tests on a street canyon ( $0.65 \leq Fr \leq 17.3$ ;  $9 \times 10^3 \leq Re \leq 3 \times 10^4$ ), Allegrini et al. (2012a) report a strengthening of the main vortex developing in the street canyon when the two vertical walls and the ground are heated up. However, for high Reynolds number, the center of the vortex is located at the same place as it is in an isothermal configuration and the air change rate is not changed by increasing wall temperature. When only the windward wall is heated up, the flow structures in the canyon are completely modified for low  $Re$ , and a second vortex develop. For high  $Re$ , the flow structure is similar to the isothermal case. Hence, on the one hand, in case of mixed convection, buoyancy increases heat transfers and may even modify the flow field. Neglecting these processes can induce an under-estimation of  $h_{c,w}$  and a wrong evaluation of its distribution. On the other hand, for high  $Re$  and low  $Ri$ , buoyancy effects do not significantly impact on the flow patterns developing around building as convection is forced.



### 5.3.2 Distribution of the convective heat transfers on isolated buildings

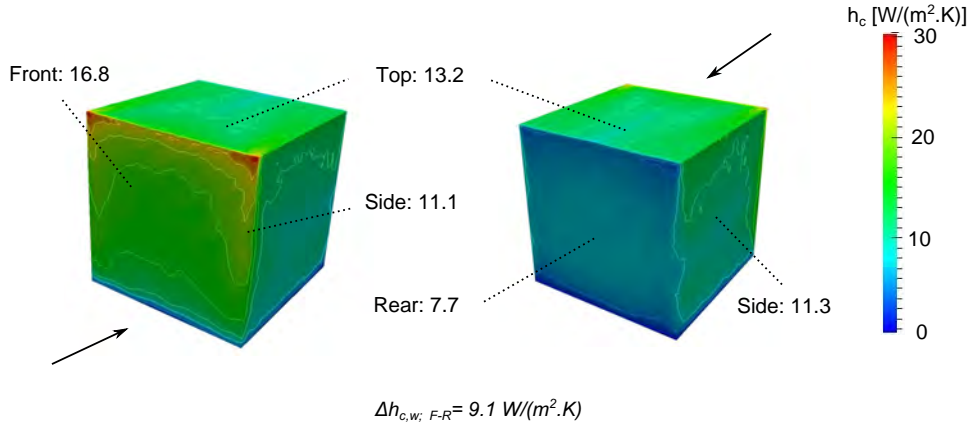


Figure 5.14: Distribution and surface averaged values of  $h_{c,w}$  for each face of the cube.

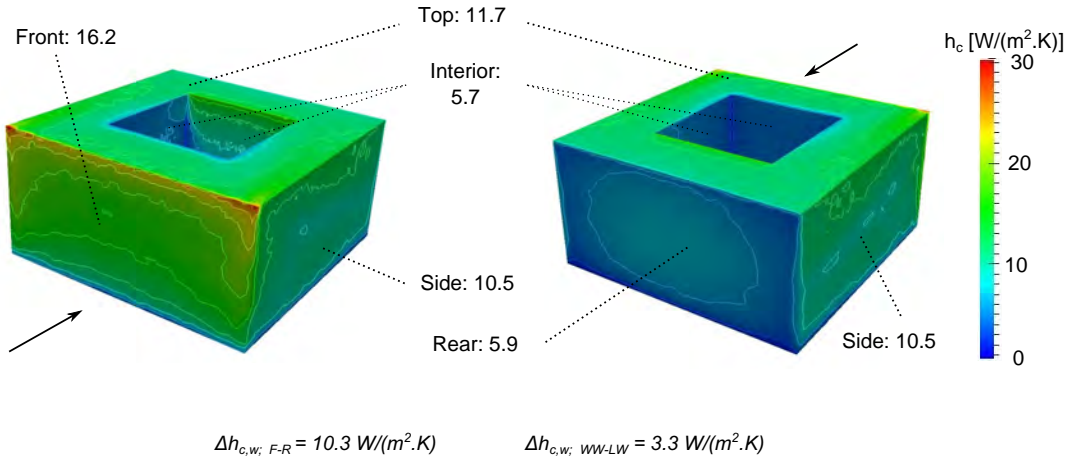


Figure 5.15: Distribution and surface averaged values of  $h_{c,w}$  for each face of the patio.

Fig. 5.14 and Fig. 5.15 show the distribution of  $h_{c,w}$  on the different faces of the cube and the patio respectively. Surface averaged values are also specified. Simulation results were post-processed using Paraview, based on the  $h_{c,w}$  values directly exported from Fluent. Appendix U.1 develops the detailed  $h_{c,w}$  distributions for the different faces of the cube and the patio as well as the corresponding surface averaged values.

As expected, the distributions and intensities of  $h_{c,w}$  on the front and rear faces of the cube resemble to those reported in Sec. 5.2.2.4.  $h_{c,w}$  intensities are however reduced because of the lower incident wind speed. The decrease is of 19% and 8% in the current case compared to the case addressed in Sec. 5.2.2.4, on the front and rear faces of the cube respectively.

As in Sec. 4.5 relatively to the  $C_p$  distribution, extreme  $h_{c,w}$  values ( $> 30 \text{ W} \cdot \text{m}^{-2} \cdot \text{K}^{-1}$ ) are simulated on the upwind top corners of the obstacles, which may be due to numerical problems, and high gradients occur on the obstacle front face. However, there is logically no other clear resemblance between the distribution of  $C_p$  and  $h_{c,w}$ , because of the differences in the physical processes they are related to.

Relatively similar  $h_{c,w}$  distribution occur on the cube and the external faces of the patio. The highest  $h_{c,w}$  intensity occurs on the top of the obstacle front faces, where high flow velocities develop without flow separation nor recirculation. This behavior is consistent with the observations reviewed in Sec. 5.1. The lowest  $h_{c,w}$  reciprocally occurs in sheltered zones, and especially on the leeward faces of the obstacles. The lateral and top faces of the theoretical buildings show clear recirculation effects, which are characterized by low  $h_{c,w}$  values.

Slightly lower  $h_{c,w}$  intensities are observed on the external faces of the patio than on the cube. About 5 % lower surface averaged values are found on the front and sides faces of the patio than on the cube. The decrease is of 10 to 23 % for the rear and top faces. However, the surface averaged  $h_{c,w}$  difference between the front and rear faces of the two types is almost similar as it equals  $9 \text{ W} \cdot \text{m}^{-2} \cdot \text{K}^{-1}$  and  $10 \text{ W} \cdot \text{m}^{-2} \cdot \text{K}^{-1}$  for the cube and the patio respectively.

$h_{c,w}$  intensities on walls surrounding the court are relatively low. They are comparable to those occurring on the rear face of the building. On average, convective heat transfers developing there are more than two times weaker than those occurring on the roof of the building. Convective heat transfers are however not homogeneous inside the patio. The specific  $h_{c,w}$  distribution is well correlated to the recirculation that develops inside the patio. Maximum  $h_{c,w}$  occur on the upper part of the windward face, leading to a higher surface averaged  $h_{c,w}$  value on this face than on the others. It is however half time lower than on the front face of the building. Relatively high  $h_{c,w}$  values are also observed on the downstream part of the lateral faces. These relatively higher  $h_{c,w}$  values can be explained by the fact that new fresh air enters the courtyard from above at the top downstream part of the patio. This air supply comes with a higher velocity and lower temperature than in the court, thus intensifying convective heat exchanges at this location.

Hence,  $h_{c,w}$  distributions on the building outer walls as well as in the courtyard are strongly correlated to the flow structures that develop around the building and inside courtyards. In particular, it is verified that flow impingement on surface leads to high  $h_{c,w}$  intensities and recirculation phenomena yield lower  $h_{c,w}$  intensities. As a consequence, according to these results, the building topology is crucial in defining the distribution of convective heat transfers on its envelope in case of buildings located in an open terrain.

### 5.3.3 Distribution of the convective heat transfers in arrays

Fig. 5.16 and Fig. 5.17 show the distribution of  $h_{c,w}$  on the different faces of the cube and continuous patio arrays respectively. Some aggregated surface averaged values are also specified. Again, simulation results are post-processed using Paraview based on the  $h_{c,w}$  values directly exported from Fluent. Appendix U.2 provides the  $h_{c,w}$  distribution and surface averaged values for the different faces of four cubes and patios (the same as addressed in Appendix Q.2) and summarizes the surface averaged  $h_{c,w}$  for every faces of the two blocks.

The relative sheltering provided by the surrounding buildings substantially affects the development of convective heat transfers at building facades. As mean wind speeds are generally reduced and recirculation phenomena develop,  $h_{c,w}$  intensities are smaller inside the arrays than

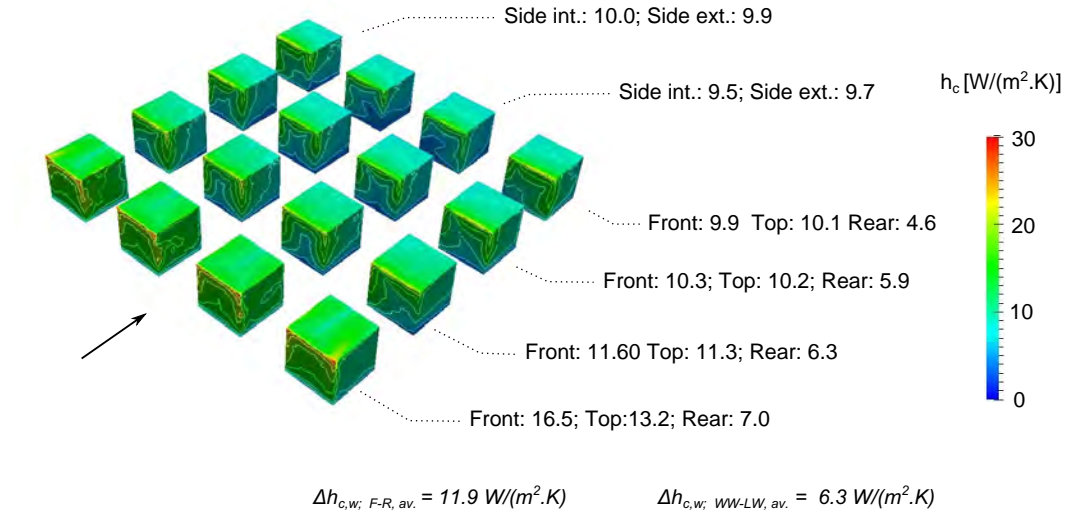


Figure 5.16: Distribution and surface averaged  $h_{c,w}$  values for the cube array.

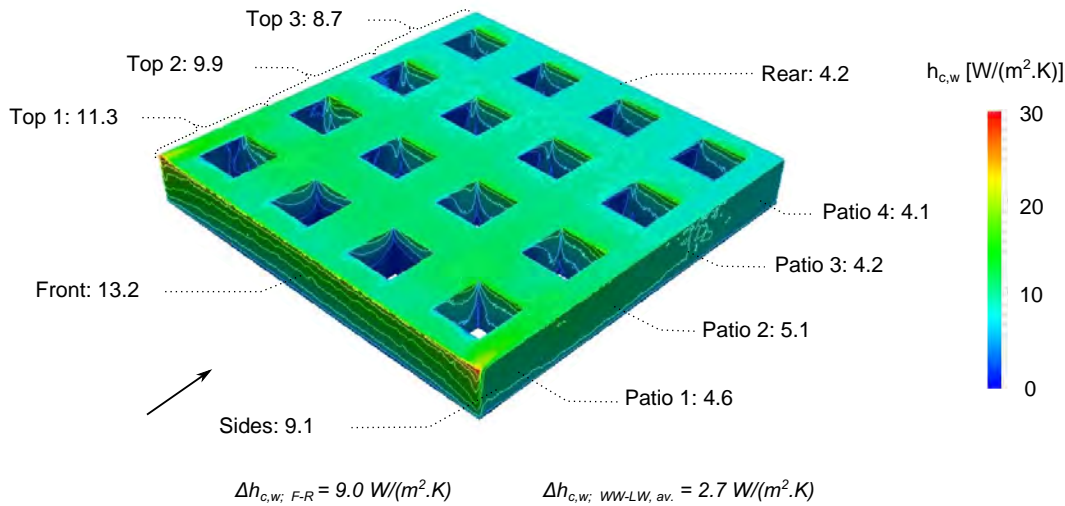


Figure 5.17: Distribution and surface averaged  $h_{c,w}$  values for the continuous patio array.

for isolated building configurations. External walls of arrays show  $h_{c,w}$  distributions and intensities that are comparable to those of isolated buildings. They are although slightly smaller, which is certainly explained by the increased size of arrays compared to isolated building types.

On average, the convective heat transfers that develop on the central cubes of the first line of the cube array are similar to those that develop in the isolated cube case. Slightly lower  $h_{c,w}$  intensities are observed on the front and rear faces of the cubes, but higher surface averaged  $h_{c,w}$  intensities occur in the top and especially on the sides of the cube. This may be related to the intensification of the corner streams in alleys. This behavior characterizes the first line of the array, for which there are substantial differences between the surface averaged  $h_{c,w}$  intensities on the different faces of each cube because of the incident flow impingement on the front faces, and for which corner streams intensify the convective heat exchanges on their internal faces.

$h_{c,w}$  intensity decreases downstream in the cube array. Convective heat transfers occurring on the external faces of cubes are higher than on their internal faces because of the lower blocking

effect.  $h_{c,w} = 11.6 \text{ W} \cdot \text{m}^{-2} \cdot \text{K}^{-1}$  on average on the cubes located in the first line on the array, whereas  $h_{c,w} = 7.3 \text{ W} \cdot \text{m}^{-2} \cdot \text{K}^{-1}$  in the fourth line.  $h_{c,w}$  intensities are also more homogeneous over the building as all faces are sheltered from winds by the surrounding obstacles and recirculation phenomena develop. The air may be heated up by surrounding obstacles as well, so that wind and thermal conditions are more homogeneous inside the array. However, windward faces still undergo higher convective heat transfers. Surface averaged  $h_{c,w}$  intensities occurring on these faces are similar to those occurring on the roof, where no clear separated bubble develops. The rear face of obstacles generally show the lowest  $h_{c,w}$  intensities.

The surface averaged  $h_{c,w}$  difference between the windward and leeward faces of cubes is increased for the fourth line of cubes compared to the third line although a gradual decrease of these values is observed upstream. Three main factors contribute to produce this behavior: the development of a wider aggregated flow behavior downstream the cube array, the absence of buildings downstream the fourth line of cubes and the specific aerodynamic structures that develop around the third line of cubes. In addition, flow convergence between the third and fourth lines of cubes leads to relatively high  $h_{c,w}$  intensities on the windward faces of the fourth line of cubes while their leeward faces are characterized by  $h_{c,w}$  intensities similar to those of the third line. However, the differences involved are small ( $< 1 \text{ W} \cdot \text{m}^{-2} \cdot \text{K}^{-1}$ ), even on the windward faces of the cubes. Therefore, they are more interesting because of their relations with specific flow structures than for further energy applications. In addition, it is worth mentioning that for all buildings and especially the lateral ones, the  $h_{c,w}$  distribution is not symmetric on each cube. This is due to border effects and the limited spatial extent of the array. The flow behavior at the border of the array induces some of the flow structures observed in the cube array. It would not have such an influence in wider configurations.

Streamwise progression of  $h_{c,w}$  as well as the effects of the external flows on  $h_{c,w}$  distribution and intensities also characterize the convective heat transfers that develop in the continuous patio array. The influence of the top separated bubble is clear. In particular, homogeneous surface averaged  $h_{c,w}$  intensities are observed in the two central patios in the first line of patios. On the contrary, increased  $h_{c,w}$  intensities are observed on the windward faces and downstream parts of the internal sides of the external patios of the first line as well as on the patios of the second line. In the lateral and downstream patios of the array, the importance of the entrapped flow recirculation phenomena as drivers of the convective heat transfers is clearly highlighted by the  $h_{c,w}$  distribution. The development of vortices inside canyons yields circular  $h_{c,w}$  distribution on the side faces and higher  $h_{c,w}$  intensities on the upper part of windward faces.

On average,  $h_{c,w}$  intensity inside a patio equals  $3.8$  to  $5.3 \text{ W} \cdot \text{m}^{-2} \cdot \text{K}^{-1}$ . As noticed for the isolated patio case, these values roughly correspond to the surface averaged  $h_{c,w}$  occurring on the rear face of the array. Because of the top flow structures that develop either over the isolated patio or over the array, patios for which  $h_{c,w}$  distribution resembles to that of the isolated patio configuration are the external patios of the second line. These patios are located at the end of the top recirculation. They undergo momentum exchanges with the above flow, which are relatively close to those developing over the isolated patio. These patios are characterized by the highest

$h_{c,w}$  intensity on their windward faces, which is nearly equal to that found on the windward face of the isolated patio. On the contrary, the lowest  $h_{c,w}$  intensities of the array are found on the leeward faces of the third and fourth lines of patios.

Comparing  $h_{c,w}$  distributions and intensities between the cube array and the continuous patio array stresses the effects of the block porosity and the development of recirculation phenomena at the entire urban block scale. In particular, the facts that the porosity of the cube array forbids the development of a unique upstream standing vortex, and that no wide recirculation develops over the array, involve higher  $h_{c,w}$  intensities on the front and top faces of the cube array than for the continuous patio array. On the contrary, because of the development of resembling flow behaviors and structures on the side and downstream faces of the two arrays, these faces show  $h_{c,w}$  intensities that are on average comparable.

## 5.4 Summary

Usual standard wall-function generally fails to predict satisfactorily the convective heat transfer at building outer walls. LRNM approaches give more accurate predictions but involve too fine cells to be generally used to study building and urban physics problems. As a consequence, customized temperature wall-functions were developed for steady RANS  $k-\varepsilon$  models, to fit LRNM results for  $50 \leq z^* \leq 500$  on the front and rear faces of isolated sharp-edged obstacles (Defraeye et al., 2010). By re-adjusting the formulation of the temperature wall-function to fit LRNM predictions, this chapter introduces the revised customized temperature wall-function for the RSM. Its performance is verified for high  $z^*$  values, allowing the study of urban problems in case of forced convection.

The convective heat exchanges on a isolated and non-isolated cubical and patio buildings are strongly correlated to the flow field around them, which depends on the building shape and surroundings. Substantial differences of  $h_{c,w}$  in terms of distribution and intensity occur depending on the wall orientation in relation to the wind incidence and its relative sheltering. The development of recirculation phenomena are also essential in shaping the building convective heat transfers. Sheltered walls generally show the lowest and most homogeneous  $h_{c,w}$  intensity and distributions. The obstacle dimensions also influence  $h_{c,w}$  intensities, although to a lesser extent. On average, the wider the obstacle is, the lower are the  $h_{c,w}$  intensities.

### *Main contribution of this chapter:*

- Adapt the existing customized temperature wall-function of Defraeye et al. (2011a) to make it applicable with the RSM and high  $z^*$ .
- Provide the distribution of  $h_{c,w}$  on the facades of typical isolated and urban constructions; relate this distribution to the main surrounding flow structures.

# Chapter 6

## Urban morphology, air flows and building energy loads - Synthesis and discussion

This last chapter synthesizes and discusses the results of the thesis from an applicative perspective. It evaluates the effects of the built morphology on the building energy demand. Nonetheless, the aim is not to provide results that are directly operational but rather to discuss the relevancy of current building physics engineering approaches, especially with respect to infiltration and convective heat transfer problems. Therefore, the related building energy needs estimated using either the standard or simulated values of  $Cp$  and  $h_{c,w}$  are compared. Hence, this chapter develops the contributions of the work toward a more integrated urban design process and a better assessment of the building energy performance.

### Contents

---

<b>6.1</b>	<b>Effects of urban morphology on air infiltration through the building envelope .</b>	<b>182</b>
6.1.1	Discussion . . . . .	182
6.1.2	Case studies . . . . .	185
6.1.2.1	Assessment of the heat losses due to infiltration . . . . .	185
6.1.2.2	Results and analysis . . . . .	189
6.1.2.3	Synthesis . . . . .	193
<b>6.2</b>	<b>Effects of urban morphology on the building external convective heat losses . .</b>	<b>194</b>
6.2.1	Discussion . . . . .	194
6.2.2	Case studies . . . . .	199
6.2.2.1	Assessment of the heat losses due to convection . . . . .	199
6.2.2.2	Results and analysis . . . . .	201
6.2.2.3	Synthesis . . . . .	205
<b>6.3</b>	<b>Effects of urban air flows on building energy loads due to air infiltration and heat transmission . . . . .</b>	<b>206</b>
6.3.1	Relative contribution of air infiltration and heat transmission to the building energy loads . . . . .	206
6.3.2	Analysis of the effects of the building topology and urban context on the building energy loads induced by external air flows . . . . .	211
<b>6.4</b>	<b>Summary . . . . .</b>	<b>214</b>

---

## 6.1 Effects of urban morphology on air infiltration through the building envelope

### 6.1.1 Discussion

Air flows mechanically develop between zones of different pressures. When building outer walls undergo different pressure conditions or when the indoor air is thermally stratified, such air flows effectively develop across buildings if there is no significant pressure losses in between, i.e. depending on the interior design. This property is used for the natural ventilation of buildings, either benefiting from natural or forced convection effects. Pressure differences also impact on infiltration processes, which are particularly challenging for well-insulated buildings.

Unlike air intakes and HVAC systems, infiltrations are often due to defects in the construction work. Their location is generally not predictable. They can take place almost everywhere in the building envelope and take different shapes and dimensions. Infiltrations may also be due to the porosity of construction materials. Therefore, a permeability level of building outer walls is usually considered to represent the effects of infiltration on the building energy loads. This permeability is understood as an intrinsic property of walls, and mass exchange involved are related to surface averaged pressure values.<sup>1</sup>

The permeability of a zone provides information about the flow rate that develops through walls depending on the pressure difference ( $\Delta P$ ). For a component, this flow rate can be expressed by a power law, as follows (CSTB, 2012a):

$$Q_{\Delta P} = K \times (\Delta P)^n \quad (6.1)$$

with:  $\left\{ \begin{array}{l} Q_{\Delta P} : \text{the air flow rate through } 1 \text{ m}^2 \text{ of wall undergoing } \Delta P \text{ [m}^3 \cdot \text{h}^{-1} \cdot \text{m}^{-2}\text{]}, \\ \Delta P = P_{ext} - P_{int} : \text{the pressure difference between outdoors and indoors [Pa]}, \\ P_{ext} : \text{the pressure acting on the external faces of the envelope [Pa]}, \\ P_{int} : \text{the indoor pressure [Pa]}, \\ K : \text{the coefficient of permeability [m}^{5/3} \cdot \text{s}^{1/3} \cdot \text{kg}^{-2/3}\text{]}, \\ n : \text{the power law exponent, usually taken equal to } 2/3. \end{array} \right.$

Pressure acting on the external face of the wall ( $P_{ext}$ ) can be estimated using Eq. 4.5, which involves the knowledge of both  $U_{ref}$  and  $C_p$  on the building outer walls.

In France, the Th-BCE rules (CSTB, 2012a) develop the methodology to be implemented to study the building energy performance from the RT 2012 point of view. The Th-BCE rules also provide some standard values relative to building and environmental characteristics. These values should be implemented into building energy simulation tools to assess the building energy consumption.

---

<sup>1</sup>The pressure values considered for a wall may differ depending on the height of the envelope component.



Considered height	Screening	$C_p$ windward	$C_p$ leeward	$C_p$ roof Pitch / vertical		
				30 – 60°	60 – 80°	> 80°
$h < 15$ m	Open	+0.50	−0.70	−0.20	−0.60	−0.70
	Normal	+0.25	−0.50	−0.20	−0.50	−0.60
	Screened	+0.05	−0.30	−0.20	−0.40	−0.50
15 m < $h$ < 50 m	Open	+0.65	−0.70	−0.20	−0.60	−0.70
	Normal	+0.45	−0.50	−0.20	−0.50	−0.60
	Screened	+0.25	−0.30	−0.20	−0.40	−0.50
$h > 50$ m	Open	+0.80	−0.70	−0.20	−0.60	−0.70

Table 6.1:  $C_p$  values given by the Th-BCE appendix for crossing building zones (CSTB, 2012a). Windward and leeward faces are conventionally distributed.

In particular, the Th-BCE rules develop the methodology to implement in order to assess infiltration flow rates. Tab. 6.1 synthesizes the generic  $C_p$  values provided for this purpose. These values depend on the height considered, the wall orientation with respect to the wind incidence and its relative sheltering. It is worth mentioning that no specific wind direction is considered: only windward and leeward faces are distinguished. According to the Th-BCE rules, to compute the infiltration flow rate in case of an isolated cuboidal building, windward and leeward faces are distributed conventionally: half of the vertical outer walls are assumed windward and the remaining vertical outer walls are assumed leeward.

In all cases, windward faces are specified with a positive  $C_p$  value. Leeward and roof faces are specified with negative  $C_p$ . According to these standard values and considering buildings smaller than 15 m high, the relative sheltering of buildings influences more pressure conditions on the windward faces than on the others. On windward faces, surface averaged  $C_p$  varies from +0.5 to +0.05. Nevertheless, the absolute values of  $C_p$  are also substantially reduced in cases of sheltered walls for the other faces. The more exposed the building is to winds, the more intense are the surface averaged  $C_p$  and the pressure differences between the windward and the leeward faces. In case of an isolated building, the  $C_p$  difference between the windward and the leeward faces ( $\Delta C_{p_{W-Lw}}$ ) is  $\Delta C_{p_{W-Lw}} = 1.2$ . It is  $\Delta C_{p_{W-Lw}} = 0.75$  in the “normal” case.

Sec. 4.5.2 provides the simulated  $C_p$  values in cases of an isolated and a non-isolated cubical buildings. Unlike the standard values, the simulated  $C_p$  values strongly depend on the wind direction. Results highlight substantial differences between the surface averaged  $C_p$  depending on the face orientation with respect to the wind direction. Surface averaged  $C_p$  can vary by more than 100 % between two consecutive walls. Significant effects of the surroundings on  $C_p$  intensities and distributions are also stressed. Considering cubical buildings, the maximum  $C_p$  difference between building outer walls occurs when the building is isolated. In such a configuration, the surface averaged  $C_p$  difference between the front and rear face reaches  $\Delta C_{p_{F-R}} = 0.76$ . It is  $\Delta C_{p_{F-T}} = 1.15$  between the front and top faces. Similarly to standard values, the intensity of the simulated surface averaged  $C_p$  is significantly reduced when surrounding obstacles are present, especially on the front faces of obstacles. However, in this case and considering a



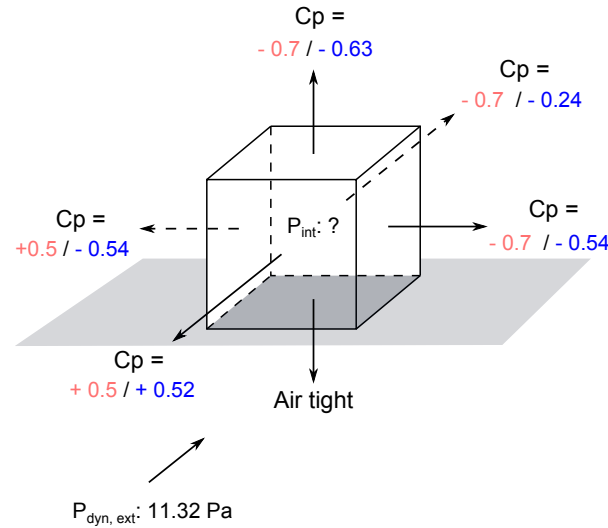


Figure 6.1: Comparison between the generic surface averaged  $C_p$  values provided by the Th-BCE rules (CSTB, 2012a) and the simulated surface averaged  $C_p$  values for an isolated 10m high cubical building.

Red: standard values; Blue: simulated surface averaged values (see Sec. 4.5).

cubical building that belongs to a network, the surface averaged  $C_p$  is simulated negative and  $\Delta C_{p_{F-R}} = 0.08$ .

Fig. 6.1 highlights the differences between the simulated surface averaged  $C_p$  values and those provided by the Th-BCE rules in case of an isolated 10 m high cubical building, whose front face is perpendicular to the wind incidence. In order to respect the conventional distribution of  $C_p$  on the building outer walls, its front and one of its side faces are assumed windward for the specification of the standard values. The other side and rear faces are assumed leeward. Note that any side face of the building is windward according to simulation because the wind incidence considered is perpendicular to the front face of the building. This explains the substantial difference observed between the surface averaged  $C_p$  values compared on the left side on the cube in Fig. 6.1. With the exception of this left side face, only the rear face shows a significant deviation between the standard and the simulated surface averaged  $C_p$ . A rather good concordance is observed on the other faces.

In order to further compare the standard and simulated surface averaged  $C_p$ , Tab. 6.2 (a) synthesizes these  $C_p$  values as well as the related  $P_{ext}$  for each face of an isolated and a non-isolated 10m high cubical buildings.  $P_{ext}$  is computed using Eq. 4.5 considering  $U_{10} = 4.3 \text{ m} \cdot \text{s}^{-1}$ . For the non-isolated configuration, the standard values considered are those related to the “normal” configuration. The corresponding selected numerical results are those of the cube 3.2 of the cube array (see Appendix Q.2 for the index). This cube is considered the most representative of a building located in an urban environment because it is located the most downstream possible with respect to the leading edge of the array, without being at the border of the array.<sup>2</sup> Similarly,

---

<sup>2</sup>Although particular aerodynamic conditions were observed around the third line of cubes, and because it is located in the middle of the array,  $C_p$  values characterizing this cube appear representative of those of a sheltered buildings.

Tab. 6.2 (b) compares the different surface averaged  $C_p$  values for the same configurations but addresses patios. As the patio array is continuous, the non-isolated patio type only involves the roof and vertical walls surrounding the court as outer walls. As a consequence, only these five faces are considered hereafter to study this configuration, both when addressing standard and simulated values of  $C_p$ . The numerical results selected to characterize this non-isolated patio configuration are those of the patio 3.2 of the continuous patio array (see Appendix Q.2) for the same reason as above. Note that in both cases of an isolated and a non-isolated patios, the standard values of  $C_p$  taken for the walls that surround the court are those of the “normal” configuration.

The standard and simulated  $C_p$  values differ by 4% on the front face of an isolated cubical building. They deviate by nearly 200% on the front face of the non-isolated building. Only considering the front and rear faces of the building, the corresponding  $\Delta C_{p_{F-R}}$  differ by 40% and 90% in cases of an isolated and a non-isolated configurations respectively. Substantial differences are also observed between the standard and simulated  $C_p$  values for the patio, especially with respect to the walls surrounding the court. On the one hand, quasi homogeneous surface averaged  $C_p$  values of about  $-0.63$  are deduced from simulations on each of the four walls surrounding the court. On the other hand, standard values still distinguish windward and leeward faces, which involves substantially different  $C_p$  around the court. Because of the change of sign between the standard and the simulated  $C_p$  value on the windward face of the patio, the deviation is of 300%. Such differences may lead to substantial deviation in the estimate of the air flow rate through constructions, especially with respect to the prediction of unintended air flow rates due to infiltration.

## 6.1.2 Case studies

### 6.1.2.1 Assessment of the heat losses due to infiltration

According to the article 17 of the French RT 2012 (MEEDDM, 2010), the infiltrated flow rate  $Q_{4Pa}$  through a building envelope that experiences a pressure difference of 4 Pa should not exceed:

- $Q_{4Pa,surf} = 0.6 \text{ m}^3 \cdot \text{h}^{-1} \cdot \text{m}_{\text{env}}^{-2}$  for houses;<sup>3</sup>
- $Q_{4Pa,surf} = 1 \text{ m}^3 \cdot \text{h}^{-1} \cdot \text{m}_{\text{env}}^{-2}$  for apartment buildings.<sup>4</sup>

For each part of the building envelope,  $K$  can be estimated according to Eq. 6.1 as follows:

$$K_{def,facade}^{zone} = \sum_i \frac{A_{facade}^i \times Q_{4Pa,surf}^i}{4^{2/3}} \quad (6.2)$$

The same formula applies for the roof, considering  $K_{def,facade}^{roof}$  and  $A_{roof}^i$ .

<sup>3</sup>This corresponds to  $Q_{4Pa,surf} = 1.67 \times 10^{-4} \text{ m}^3 \cdot \text{s}^{-1} \cdot \text{m}^{-2}$ .

<sup>4</sup>This corresponds to  $Q_{4Pa,surf} = 2.78 \times 10^{-4} \text{ m}^3 \cdot \text{s}^{-1} \cdot \text{m}^{-2}$

		front	rear	top	sides	$\Delta_{F-R}$
Isolated						
$C_p$	Th-BCE	+0.5	-0.70	-0.70	+0.5/-0.7	+1.2
	Simu.	+0.52	-0.24	-0.63	-0.54	+0.76
$P_{ext}$	Th-BCE	+5.66	-7.93	-7.93	+5.66/-7.93	+13.59
	Simu.	+5.89	-2.72	-7.13	-6.12	+8.61
Deviation (%)		+4	-66	-10	-	-37
Non-isolated						
$C_p$	Th-BCE	+0.25	-0.50	-0.60	+0.25/-0.5	+0.75
	Simu.	-0.23	-0.31	-0.34	-0.30	+0.08
$P_{ext}$	Th-BCE	2.83	-5.66	-6.80	+2.83/-5.66	+8.43
	Simu.	-2.60	-3.51	-3.85	-3.40	+0.91
Deviation (%)		-192	-38	-43	-	-89

a) The cube

		Exterior				Court		
		front	rear	top	sides	Lw	Ww	sides
Isolated								
$C_p$	Th-BCE	+0.50	-0.70	-0.70	+0.5/-0.7	-0.50	+0.25	+0.25/-0.5
	Simu.	+0.40	-0.25	-0.61	-0.54	-0.64	-0.63	-0.65
$P_{ext}$	Th-BCE	+5.66	-7.93	-7.93	+5.66/-7.93	-5.66	+2.83	+2.83/-5.66
	Simu.	+4.53	-2.83	-6.91	-6.12	-7.25	-7.13	-7.36
Deviation(%)		-20	-64	-13	-	28	-352	-
Non-isolated								
$C_p$	Th-BCE	+	-	-0.60	-	-0.50	+0.25	-0.50
	Simu.	-	-	-0.51	-	-0.52	-0.50	-0.53
$P_{ext}$	Th-BCE	-	-	-6.80	-	-5.66	+2.83	-5.66
	Simu.	-	-	-5.78	-	-5.89	-5.66	-6.00
Deviation(%)		-	-	-13	-	4	-300	6

b) The patio

Table 6.2: Comparison by face of the generic surface averaged  $C_p$  values (and the corresponding  $P_{ext}$  [Pa]) provided by the Th-BCE rules (CSTB, 2012a) or simulated (Sec. 4.5) in cases of 10m high isolated and non-isolated buildings (cubes or patios).

$C_p$  values taken for the non-isolated building as well as the interior of the patios correspond to the case “normal” of the Th-BCE rules. The cube patio 3.2 (resp. patio 3.2) of the cube array (resp. continuous patio array, see Appendix Q.2) is considered for the non-isolated building case.

As a consequence:

- $K_{surf} = 6.61 \times 10^{-5} \text{ m}^{5/3} \cdot \text{s}^{1/3} \cdot \text{kg}^{-2/3}$  for houses;
- and  $K_{surf} = 1.10 \times 10^{-4} \text{ m}^{5/3} \cdot \text{s}^{1/3} \cdot \text{kg}^{-2/3}$  for apartment buildings.

Hence, knowing  $P_{ext}$  and  $K_{surf}$ , and only considering mass transfers due to infiltration and not to HVAC systems, it is possible to determine the interior pressure of a zone ( $P_{int}$ ) by resolving the mass balance of the considered zone. Note that  $P_{int}$  is assumed constant in the whole zone, including on the interior side of the building envelope. Neglecting buoyancy effects, the aeraulic balance for the zone is given by:

$$\sum_i \text{sign}_{\Delta P_i} A_i K |\Delta P_i|^n = 0 \quad (6.3)$$

with:

$$\Delta P_i = P_{ext,i} - P_{int} = \left( \frac{Cp_{ext,i} \times \rho \times U_{10}^2}{2} \right) - P_{int} \quad (6.4)$$

and:  $\left\{ \begin{array}{l} A_i : \text{the area of the face } i, \\ K : \text{the permeability coefficient } [\text{m}^{5/3} \cdot \text{s}^{1/3} \cdot \text{kg}^{-2/3}], \\ \text{sign}_{\Delta P_i} : \text{the sign of } \Delta P_i \text{ [Pa]}, \\ P_{ext,i} : \text{the pressure acting on the external side of the wall } i \text{ [Pa]}, \\ P_{int} : \text{the interior pressure assumed constant and homogeneous [Pa]}, \\ n = 2/3 : \text{the power law exponent,} \\ Cp_{ext,i} : \text{the external pressure coefficient of the wall } i, \\ \rho : \text{the air density } [\text{kg} \cdot \text{m}^{-3}], \\ U_{10} : \text{the reference velocity at 10 m high } [\text{m} \cdot \text{s}^{-1}]. \end{array} \right.$

It is worth mentioning that the power law exponent of 2/3 necessitates to consider the absolute value of  $\Delta P$ . Consequently, the sign of  $\Delta P$  to be included into Eq. 6.3 has to be guessed *a priori*, i.e. before the numerical resolution of the equation. Furthermore, Eq. 6.3 does not necessarily imply a unique solution. In complex cases, there can be several stable mass balances, and likewise values of  $P_{int}$ . However, in the following, only one solution is considered and assumed unique. It corresponds to the first realistic value computed for  $P_{int}$ , which verifies (see Appendix W):

$$P_{ext,i} / (P_{ext,i} < P_{int}) \leq P_{int} < P_{ext,j} / (P_{ext,j} > P_{int}) \quad (6.5)$$

Considering a 10 m high cubical zone that has its five external walls (including the roof) in contact with the outdoors and an air permeability in accordance with the French RT 2012, the numerical resolution<sup>5</sup> of Eq. 6.3 gives:

- $P_{int} = -3.14 \text{ Pa}$  according to the  $Cp$  values of the Th-BCE rules. In this case, two vertical walls are considered windward according to the conventional distribution of  $Cp$ .

<sup>5</sup>The numerical resolution of Eq. 6.3 was performed using the free application Wolfram: <http://www.wolframalpha.com/>

- $P_{int} = -3.86 \text{ Pa}$  according to the simulated  $C_p$  values presented in Sec. 4.5. In this case, the front and rear faces are in relative over-pressure compared to indoors. Indeed, no realistic  $P_{int}$  was computed when assuming  $\Delta P > 0$  on the front face of the cube only (Appendix W.1).

Currently and further in this thesis, buildings are considered composed of a single zone.

The air flow rate due to infiltration ( $Q_{inf}$ ) through the envelope can be deduced from the previous results by summing up all the air flows entering the zone, i.e. the air flow rates through walls for which  $\Delta P = P_{ext} - P_{int} > 0$ . According to the standard  $C_p$  values, the air flow rate due to infiltration is  $Q_{inf,tot} = 0.06 \text{ m}^3 \cdot \text{s}^{-1}$ , whereas it is  $Q_{inf,tot} = 0.04 \text{ m}^3 \cdot \text{s}^{-1}$  according to the simulated  $C_p$  values. These air flow rates correspond to  $Q_{inf,m^2} = 0.41 \text{ m}^3 \cdot \text{h}^{-1} \cdot \text{m}_{env}^{-2}$  and  $Q_{inf,m^2} = 0.27 \text{ m}^3 \cdot \text{h}^{-1} \cdot \text{m}_{env}^{-2}$  respectively, when reduced to the surface unit of envelope and considering 1 h long period of time. Hence, the two predictions  $Q_{inf,tot}$ , and likewise  $Q_{inf,m^2}$ , differ by 34%. The use of standard values leads to the highest estimate of  $Q_{inf}$ .

These infiltrated air flow rates induce heat losses from the indoor environment. These heat losses ( $E_{inf}$ ) can be evaluated as follows:

$$E_{inf} = \rho_{air} Q_{inf} C_{air} \Delta T \quad (6.6)$$

with: 
$$\begin{cases} \rho_{air} : \text{the air density } [\text{m}^3 \cdot \text{s}^{-1}], \\ Q_{inf} : \text{the volumic air flow rate } [\text{kg} \cdot \text{m}^{-3}], \\ C_{air} : \text{the thermal capacity of the air } [\text{J} \cdot \text{kg}^{-1} \cdot \text{K}^{-1}], \\ \Delta T = T_{int} - T_{ext} : \text{the temperature difference between indoors and outdoors } [\text{K}]. \end{cases}$$

Considering  $\rho_{air} = 1.225 \text{ kg} \cdot \text{m}^{-3}$ ,  $C_{air} = 1.004 \times 10^3 \text{ J} \cdot \text{kg}^{-1} \cdot \text{K}^{-1}$  and  $\Delta T = 10^\circ \text{C}$ , the total heat losses due to infiltration through the envelope are:

- $E_{inf,tot} = 693 \text{ W}$  according to the standard  $C_p$  values;
- and  $E_{inf,tot} = 460 \text{ W}$  according to the simulated  $C_p$  values.

Assuming a three-storey building whose floors are  $10^2 \text{ m}^2$  wide, these heat losses reduced to the surface unit of floor are:

- $E_{inf,m^2} = 2.03 \text{ W} \cdot \text{m}_{floor}^{-2}$  according to the standard  $C_p$  values;
- and  $E_{inf,m^2} = 1.35 \text{ W} \cdot \text{m}_{floor}^{-2}$  according to the simulated  $C_p$  values.

As any other parameter than  $Q_{inf}$  varies in Eq. 6.6, the relative deviation between the estimates  $E_{inf,tot}$  and  $E_{inf,m^2}$  based on the standard or simulated  $C_p$  values is still equal to 34%.

In order to evaluate the effects of the building topology and urban environment on the infiltrated air flow rates and related energy needs, the same methodology was implemented to determine  $P_{int}$ ,  $Q_{inf,tot}$ ,  $Q_{inf,m^2_{env}}$ ,  $E_{inf,tot}$  and  $E_{inf,m^2_{floor}}$  in cases of:

Physical parameter		Properties	
Ref. wind speed	$[\text{m} \cdot \text{s}^{-1}]$	$U_{10}$ (approach flow)	4.3
Air density	$[\text{kg} \cdot \text{m}^{-3}]$	constant	1.225
$P_{ext}$	$[\text{Pa}]$	constant by face	$C_p \times 0.5 \rho U_{10}^2$
$P_{int}$	$[\text{Pa}]$	constant in the building	?
$K_{Q_{4Pa}+}$	$[\text{m}^{5/3} \cdot \text{s}^{1/3} \cdot \text{kg}^{-2/3}]$	uniform	$6.614 \times 10^{-5}$
$K_{Q_{4Pa}-}$	$[\text{m}^{5/3} \cdot \text{s}^{1/3} \cdot \text{kg}^{-2/3}]$	uniform	$3.31 \times 10^{-4}$

Table 6.3: Synthesis of the physical parameters used in the computations of  $Q_{inf}$  and  $E_{inf}$ .

- an isolated patio;
- a cubical building that belongs to a network;
- a patio building that belongs to a network.

All the different configurations are studied assuming an envelope that respects the RT 2012 requirements as well as an inefficient envelope, whose permeability is five times higher than required by the French RT 2012. These two variants are further named “ $Q_{4Pa}+$ ” and “ $Q_{4Pa}-$ ” respectively. Tab. 6.3 summarizes the different physical parameters used in computations. Configurations for which only the windward and leeward faces are active are also studied to evaluate the consequences of the simplification involved by the conventional distribution of  $C_p$ . The two configurations are further named “All” and “Ww+Lw” respectively. Appendix V.1 illustrates them. Appendix V.2 synthesizes the corresponding areas of active envelope and floor used to reduce  $Q_{inf,tot}$  and  $E_{inf,tot}$  to the surface unit of envelope or floor ( $Q_{inf,m_{env}^2}$  and  $E_{inf,m_{floor}^2}$ ). In particular, it is worth mentioning that although the patio has a surface of envelope 3 or 1.4 times larger than that of the isolated or non-isolated cube respectively, it also presents a floor area 3 times larger than that of the cubical building.

### 6.1.2.2 Results and analysis

Tab. 6.4 (a) synthesizes the different results in terms of  $P_{int}$ ,  $Q_{inf,m_{env}^2}$  and  $E_{inf,m_{floor}^2}$  for a 10 m high cubical building located either in an open terrain or in a theoretical urban environment. Results obtained both using the standard and simulated  $C_p$  values are reported. Tab. 6.4 (b) synthesizes the corresponding results but addresses patios. Appendix X.1 provides the corresponding total infiltrated air flow rates ( $Q_{inf,tot}$ ) and energy needs ( $E_{inf,tot}$ ) for the cubes and patios.

Because of the assumption on the performance of the envelopes, the estimates of  $E_{inf}$  deviate by a factor of 5 between the case  $Q_{4Pa}+$  and  $Q_{4Pa}-$ . Tab. 6.4 and Appendix X.1 also highlight substantial differences between the estimates of  $Q_{inf}$  and  $E_{inf}$  based on the standard or simulated  $C_p$  values. Predictions based on simulation are generally lower than those based on the standard  $C_p$  values. Results deviate the most for non-isolated configurations, with an averaged difference of about 82 and 92% for the cube and patio respectively. This can be explained by the fact that the Th-BCE rules still consider windward faces with positive  $C_p$  values and leeward faces with negative  $C_p$  values, whereas simulations indicate rather homogeneous surface averaged  $C_p$  in such configurations.

Faces in contact with outdoor		Isolated		Non-isolated	
		All	Ww+Lw	All	Ww+Lw
$P_{int}$	Th-BCE	-3.14	-1.14	-2.90	-1.42
	Simu.	-3.86	1.59	-3.41	-3.06
Deviation (%)		-23	+240	-17	-116
$Q_{4Pa} : +$					
$Q_{inf}$	Th-BCE	0.41	0.43	0.31	0.31
	Simu.	0.27	0.32	0.04	0.07
$E_{inf}$	Th-BCE	2.31	0.97	1.74	0.71
	Simu.	1.53	0.71	0.23	0.16
$Q_{4Pa} : -$					
$Q_{inf}$	Th-BCE	2.03	2.14	1.53	1.56
	Simu.	1.35	1.58	0.21	0.35
$E_{inf}$	Th-BCE	11.56	4.87	8.69	3.56
	Simu.	7.66	3.59	1.17	0.80
Deviation (%)		-34	-26	-87	-78

a) The cube

Faces in contact with outdoor		Isolated		Non isolated	
		All	Ww+Lw	All	Ww+Lw
$P_{int}$	Th-BCE	-3.13	-1.24	-4.46	-1.42
	Simu.	-5.43	-2.26	-5.89	-5.78
Deviation (%)		-73	-82	-32	-308
$Q_{4Pa} : +$					
$Q_{inf}$	Th-BCE	0.37	0.39	0.26	0.31
	Simu.	0.21	0.14	0.02	0.03
$E_{inf}$	Th-BCE	2.14	0.89	0.68	0.71
	Simu.	1.18	0.32	0.04	0.06
$Q_{4Pa} : -$					
$Q_{inf}$	Th-BCE	1.87	1.94	1.28	1.56
	Simu.	1.03	0.71	0.08	0.14
$E_{inf}$	Th-BCE	10.68	4.43	3.40	1.19
	Simu.	5.89	1.62	0.21	0.11
Deviation (%)		-45	-63	-93	-91

b) The patio

Table 6.4: Comparison of  $P_{int}$  [Pa],  $Q_{inf,m^2}$  [ $m^3 \cdot h^{-1} \cdot m_{env}^{-2}$ ] and  $E_{inf,m^2}$  [ $W \cdot m_{floor}^{-2}$ ] calculated using the Th-BCE or the simulated  $C_p$  values for buildings located in different urban configurations.

Ww+Lw: only the windward and leeward faces;

abs: absolute difference; rel.: relative difference;

$Q_{4Pa}+$ : the air permeability of the building envelope respects the RT 2012 requirements;

$Q_{4Pa}-$ : the air permeability of the envelope is five times higher than required by the RT 2012.

$Q_{inf}$  estimated using the simulated  $Cp$  values is nearly zero for the non-isolated cube and patio. This is also explained by the rather homogeneous  $Cp$  distribution predicted on their different faces. More generally, because of the sheltered conditions induced by the surrounding constructions, the estimates of  $Q_{inf,tot}$ ,  $E_{inf,tot}$ ,  $Q_{inf,m^2}$ ,  $E_{inf,m^2}$  are lower for non-isolated configurations than for isolated buildings. Not considering the whole envelope area active but only the windward and leeward faces of the building instead also highlights lower estimates of  $Q_{inf,t}$  and  $E_{inf}$ .

Regarding the effect of the building shape, the estimated  $Q_{inf,tot}$ , and likewise  $E_{inf,tot}$ , are higher for the patio than for the cube. This is mainly explained by the larger envelope area of the patio. Note that although different morphologies are addressed, the estimates of  $Q_{inf,tot}$  and  $E_{inf,tot}$  based on the standard  $Cp$  values are the same for the non-isolated cube and patio that can exchange only through their windward and leeward faces. This is explained by the fact that the considered surface of exchanges as well as the involved  $Cp$  values are the same for both cases. More generally, the estimates of  $Q_{inf,tot}$  and  $E_{inf,tot}$  based on the standard  $Cp$  values are significantly higher than when computed using the simulated surface averaged  $Cp$ . According to the latter results,  $Q_{inf,tot}$  and  $E_{inf,tot}$  are higher for the non-isolated cube than the non-isolated patio.

Although  $Q_{inf,tot}$  is generally computed higher for the patio than for the cube,  $Q_{inf,m^2}$  and  $E_{inf,m^2}$  are predicted lower for the patio than for the cube when assuming the whole envelope active. This trend is observed for both the isolated and the non-isolated configurations, and both according to the standard or the simulated values of  $Cp$ . This is due to the larger floor area of the patio and the lower proportion of front face as well as the particular pressure conditions inside the court. These results highlight the effects of the building topology on the contribution of infiltration to the building energy balance.

In order to further discuss the effects of the building typology and the built environment on the building energy balance, Tab. 6.5 summarizes the absolute and relative changes of  $E_{inf,m^2}$  between:

- the isolated cube and patio;
- the isolated cube and the non-isolated cube;
- the isolated patio and the non-isolated patio;
- the non-isolated cube and patio.

Appendix X.1 synthesizes the corresponding values, but addresses the changes of  $E_{inf,tot}$ . Note that the fact that the relative deviations are the same for each case irrespective of the envelope permeability is due to the fact that the factor 5 assumed between the considered permeability levels ( $Q_{4Pa+}$  and  $Q_{4Pa-}$ ) is simplified in the division.

Although the strong assumption involved by the use of the conventional distribution of  $Cp$ , the relative changes of  $E_{inf,m^2}$  induced by a modification of the built configuration and estimated considering the whole envelope or only the windward and leeward faces active are rather comparable. According to simulation, significant deviations only occur when there is a change of building type, i.e. between the isolated cube and patio.



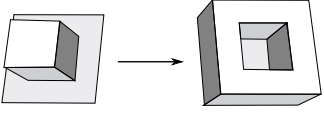
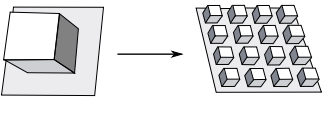
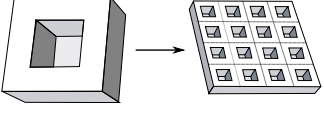
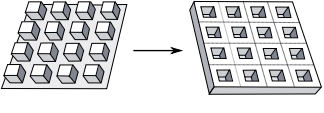
Faces in contact with outdoor			$Q_{4Pa} : +$		$Q_{4Pa} : -$	
			All	Ww+Lw	All	Ww+Lw
	Th-BCE	abs.	-0.18	-0.09	-0.88	-0.44
		rel. (%)	-7.6	-9.0	-7.6	-9.0
	Simu.	abs.	-0.35	-0.39	-1.77	-1.97
		rel. (%)	-23.1	-54.8	-23.1	-54.8
	Th-BCE	abs.	-0.57	-0.26	-2.87	-1.31
		rel. (%)	-24.8	-26.9	-24.8	-26.9
	Simu.	abs.	-1.30	-0.56	-6.50	-2.79
		rel. (%)	-84.7	-77.8	-84.7	-77.8
	Th-BCE	abs.	-1.45	-0.65	-7.27	-3.24
		rel. (%)	-68.1	-73.2	-68.1	-73.2
	Simu.	abs.	-1.14	-0.30	-5.68	-1.52
		rel. (%)	-96.4	-93.5	-96.4	-93.5
	Th-BCE	abs.	-1.06	-0.47	-5.29	-2.37
		rel. (%)	-60.9	-66.7	-60.9	-66.7
	Simu.	abs.	-0.19	-0.14	-0.96	-0.69
		rel. (%)	-82.0	-86.8	-82.0	-86.8

Table 6.5: Evaluation of the effects of the building topology and urban morphology on  $E_{inf,m^2}$  [ $W \cdot m_{floor}^{-2}$ ] according to the Th-BCE rules or simulation results.

Results provided by Appendix X.1 verify the higher level of  $E_{inf,tot}$  involved by the isolated patio than by the isolated cube. The highest differences of  $E_{inf,tot}$  are observed between these isolated building configurations, when the estimates are based on the standard  $C_p$  values. More precisely, an evolution of 177% is assessed when considering the whole envelope active. The estimates of  $E_{inf,tot}$  based on the standard  $C_p$  values follow the same trend for the non-isolated configurations. However, changes in  $E_{inf,tot}$  are much lower and are zero when only the windward and leeward faces are addressed. On the contrary, simulation-based results indicate a non-negligible decrease of  $E_{inf,tot}$  between the non-isolated cube and patio, although the surface of envelope is either increased (case “All”) or kept constant (case “Lw+Ww”) between these two configurations. This is due to the lower  $C_p$  differences simulated in the patio configuration.

As previously noticed, switching from an isolated to a non-isolated configuration significantly reduces the energy needs. In particular, according to the simulated  $C_p$  values,  $E_{inf,tot}$  decreases by nearly 100% for the patio. The decrease is of 80% for the cube. Because the floor area is preserved between the isolated and non-isolated configurations, the relative variation of  $E_{inf,m^2}$  are the same for these cases. According to simulation, the relative decrease of  $E_{inf,tot}$ , and likewise  $E_{inf,m^2}$ , is slightly lower when considering the windward and leeward faces only. The trend is opposite according to the standard  $C_p$  values. Higher relative differences occur when considering the windward and leeward faces active and not the whole envelope. In addition, the decrease of  $E_{inf}$  is estimated substantially smaller than according to the simulation results. Assuming the whole envelope or only the windward and leeward faces active, an averaged decrease of 25% and 70% are predicted for the cube and the patio respectively according to the standard values

of  $C_p$ . The corresponding decreases are of 81 % and 95 % according to the simulated surface averaged  $C_p$  values.

The relative changes of  $E_{inf,tot}$  and  $E_{inf,m^2}$  are the same between the isolated and the non-isolated cubes and patios because the floor area does not change. However, this is not the case when comparing the isolated or the non-isolated cubes and patios. As a consequence, opposite trends are generally observed between  $E_{inf,tot}$  and  $E_{inf,m^2}$ .<sup>6</sup> On the one hand,  $E_{inf,tot}$  increases when switching from the cube to the patio as the surface of envelope is higher for patios. Difference of  $E_{inf,tot}$  are maximum ( $> 100\%$ ) for isolated configurations. On the other hand,  $E_{inf,m^2}$  decreases when switching from the cube to the patio. The decrease is estimated higher when based on the simulated  $C_p$  values than on the standard values, and is intensified in the non-isolated configuration. Regarding the non-isolated configuration for which  $E_{inf,tot}$  is predicted lower for the patio than the cube according to simulation ( $\approx -50\%$ ), the relative decrease of  $E_{inf,m^2}$  is predicted even higher ( $\approx -85\%$ ).

### 6.1.2.3 Synthesis

The different results presented in this section highlight a clear effect of the building shape in terms of compactness and topology on the energy needs induced by air infiltration. In particular, patio cases mostly involve higher total energy needs mainly because of their larger envelope areas compared to the cube. However, they involve lower energy needs when reduced to the surface unit of floor. Considering non-isolated configurations, the related  $E_{inf,tot}$  is even predicted lower for the patio than the for cube when estimated using the simulated  $C_p$  values.

This behavior illustrates the lower infiltration levels induced in cases of relatively homogeneous pressure conditions, as they occur inside the patio or in sheltered zones. Similarly, the effects of the built environment on the energy needs are clear. Because of the sheltering induced by surrounding constructions, the built environment substantially decreases the building energy needs of constructions due to infiltration.

In addition, results highlight substantial differences between the estimates of  $E_{inf}$  based on the standard or the simulated  $C_p$  values. Both the absolute energy needs estimated for each case as well as their change between one morphological configuration to another substantially deviate. In particular, the estimates of  $E_{inf,m^2}$  are more than 90 % lower when computed using the simulated  $C_p$  values than when estimated using the standard  $C_p$  values for the non-isolated patio configuration. Similarly, the relative decrease of  $E_{inf,m^2}$  between the isolated and the non-isolated cubes is predicted 50 to 60 points more important according to simulation than with respect to the Th-BCE rules. More generally,  $E_{inf}$  is generally estimated lower when based on the simulated surface averaged  $C_p$  values than when based on the standard values, and the effects of the built morphology are predicted greater.

---

<sup>6</sup>The only case for which trends are similar is the non-isolated building, according to the simulated  $C_p$  values.

Nevertheless, it is worth reminding that these observations involve substantial assumptions. Especially, only one wind direction is considered in simulation, while a conventional distribution of windward and leeward faces is assumed for the standard approach. In addition, the uniform distribution of  $K$  is convenient to use during the design process of buildings, but it is not realistic. During the building operative phase, infiltration flow rates would differ from those addressed in this study as air tightness defects are generally local. Infiltration flow rates are therefore dependent on the local  $C_p$  value, which is itself dependent on the wind direction and speed. As highlighted in [Costola et al. \(2010\)](#), these local  $C_p$  values may induce effective air flow rates that substantially deviate with respect to the estimates based on surface averaged  $C_p$  values. Moreover, it is worth mentioning that the absolute energy needs involved by air tight buildings are low. As a consequence, in such cases, the effective impact of the built morphology on the energy needs due to infiltration is almost negligible even if their relative effects appear significant. Such consideration is nonetheless important when addressing building aging issues.

## 6.2 Effects of urban morphology on the building external convective heat losses

### 6.2.1 Discussion

Thermal exchanges that develop on a surface involve radiative and convective heat transfers. The corresponding heat transfer coefficients are often called  $h_{r,w}$  and  $h_{c,w}$ . In France, usual engineering studies addressing the thermal performance of the building envelope (thermal transmittivity) are based on the Th-U rules ([CSTB, 2012b](#)) of the French thermal regulation (RT 2012 ([MEED-DEM, 2010](#))). These rules develop the methodology to be implemented to estimate the thermal resistance of a wall. In particular, the Th-U rules provide correlations to compute the external surface heat transfer coefficients as functions of some environmental parameters.

To determine the radiative contribution to the total surface heat exchange,  $h_{r,w}$  is assumed to be a cubic function of the mean radiant temperature:

$$h_{r,w} = \varepsilon \times h_{r,o} = \varepsilon \times 4 \sigma_0 T_m^3 \quad (6.7)$$

$$\text{with: } \begin{cases} \varepsilon : \text{ the surface hemispheric emissivity,} \\ h_{r,o} : \text{ the radiative coefficient of a black body } [\text{W} \cdot \text{m}^2 \cdot \text{K}^{-1}], \\ \sigma_0 = 5.67 \times 10^{-8} \text{ W} \cdot \text{m}^{-2} \cdot \text{K}^{-4} : \text{ the Stefan Boltzmann constant,} \\ T_m : \text{ the mean surface temperature (actual and surrounding surfaces) } [\text{K}]. \end{cases}$$

To determine the convective contribution to the total surface heat exchanges,  $h_{c,w}$  is assumed to be a linear function of the wind speed:

$$h_{c,w} = 4 + 4 \times U_{loc} \quad (6.8)$$

with:  $U_{loc}$  : the wind velocity next to the surface  $[\text{m} \cdot \text{s}^{-1}]$ .

However, there is a lack of knowledge and information about the flow field around buildings, especially in cities. Therefore,  $U_{10}$  taken at the meteorological station is usually considered to determine  $h_{c,w}$  instead of  $U_{loc}$ , although Sec. 1 and Sec. 4 show that  $U_{10}$  generally significantly differs from  $U_{loc}$ . This assumption involves a constant and homogeneous  $h_{c,w}$  value on all the different faces of a building, and irrespective of the properties of the surrounding terrain. For example, considering  $U_{10} = 4.3 \text{ m} \cdot \text{s}^{-1}$ , the surface averaged  $h_{c,w}$  is assumed equal to  $21.2 \text{ W} \cdot \text{m}^{-2} \cdot \text{K}^{-1}$  on all building surfaces.<sup>7</sup>

Based on the results of the coupled CFD and thermal simulations, Sec. 5.3 reports different distributions and intensities of  $h_{c,w}$  on the different faces of buildings. According to these results,  $h_{c,w}$  strongly depends on the local wind speed and the development of recirculation phenomena next to walls. Sec. 5.3 also stresses the substantial influence of the surrounding environment on  $h_{c,w}$  intensities. For example, still considering  $U_{10} = 4.3 \text{ m} \cdot \text{s}^{-1}$ , the averaged  $h_{c,w}$  intensity of a 10 m high cubical building is reduced by 34 % when switched from an isolated configuration to a theoretical urban environment.

Still considering the theoretical isolated 10 m high cubical building, Fig. 6.2 compares the simulated surface averaged  $h_{c,w}$  values with that derived from the Th-U rules. Rather comparable surface averaged  $h_{c,w}$  values are observed on the cube front face but substantial deviations occur on the other faces. Maximum differences are observed on the lateral and rear faces, where the standard value over-estimates the simulated surface averaged  $h_{c,w}$  by a factor 2 and 3 respectively. Although the computational model used to determine  $h_{c,w}$  on the different faces of a building is not validated for its top and lateral faces, experimental results addressed in Sec. 5.2.1 show lower averaged  $h_{c,w}$  intensities on these faces than on the front face. This behavior is certainly not accurately reproduced by the computational model, but trends are verified. The predicted surface averaged  $h_{c,w}$  values are lower on the side and top faces than on the front face of the cube. As a consequence, although certainly being coarse estimates, the simulated  $h_{c,w}$  values on these faces should be more realistic than the standard values, which assume a homogeneous and high  $h_{c,w}$  value on all the building envelope.

Convective heat transfers take part in the total building heat exchanges by heat transmission through the envelope. As a consequence, the differences in the estimates of the surface averaged  $h_{c,w}$  values highlighted in Fig. 6.2 on all but the front faces may lead to substantial deviations in the actual assessment of the building energy demand. This would be especially the case for non- or low insulated buildings, for which the convective contribution to the total heat losses of the building is important.

According to Fig. 6.3, the thermal resistance of a wall ( $R_{th}$ ) that is composed of concrete and insulation material can be estimated using the electrical analogy. Only considering 1D heat

---

<sup>7</sup>Note that without specific information about the wind speed or temperature, a unique value of  $h_{ext}$  is considered by the Th-U and Th-BCE rules. This value equals  $25 \text{ W} \cdot \text{m}^{-2} \cdot \text{K}^{-1}$ . Assuming  $h_{rad} \approx 5 \text{ W} \cdot \text{m}^{-2} \cdot \text{K}^{-1}$ , this standard constant value differs by about 5 % from the one currently considered.

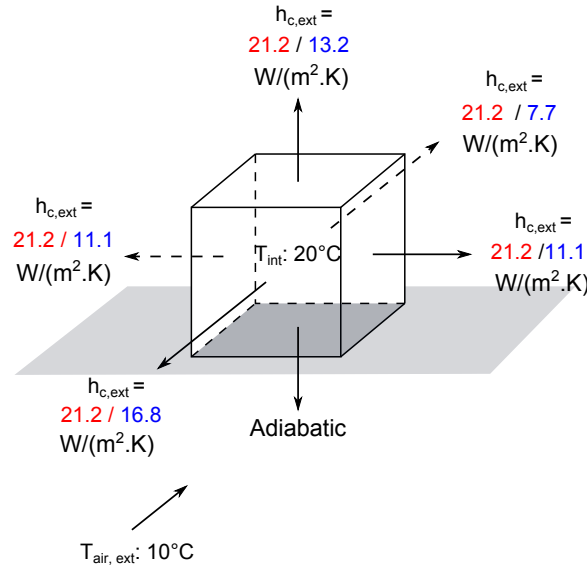


Figure 6.2: Comparison between the generic surface averaged  $h_{c,w}$  values provided by the Th-U rules (CSTB, 2012b) and the simulated surface averaged  $h_{c,w}$  values for an isolated 10m high cubical building.

Red: standard values; Blue: simulated surface averaged values (see Sec. 5.3.2 and Sec. 5.3.3).

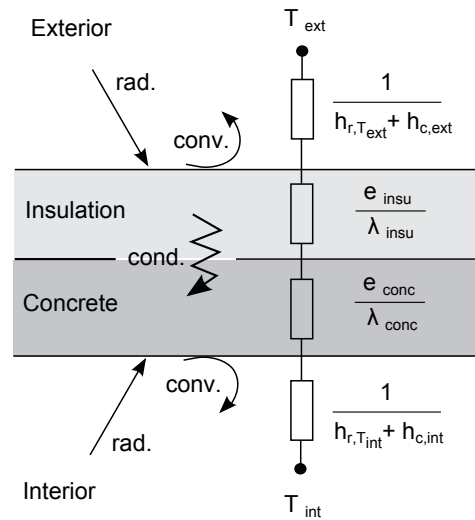


Figure 6.3: Electrical analogy for 1D heat transfers through a wall.

Convective heat transfer		
flow direction	upwards	horizontal
$h_{c,int} [W \cdot m^{-2} \cdot K^{-1}]$	5.0	2.5

Table 6.6: Standard  $h_{c,int}$  values used in the computations.

Radiative heat transfer		
temperature	$T = 10^\circ C$	$T = 20^\circ C$
$h_{r,T} [W \cdot m^{-2} \cdot K^{-1}]$	5.1	5.7

Table 6.7: Standard  $h_{rad}$  values used in the computations.

transfers and steady state conditions,  $R_{th}$  is given by:

$$R_{th} = \frac{1}{h_{int}} + \frac{e_{conc}}{\lambda_{conc}} + \frac{e_{insu}}{\lambda_{insu}} + \frac{1}{h_{ext}} \quad (6.9)$$

with:  $\left\{ \begin{array}{l} R_{th} : \text{the total thermal resistance of the wall } [K \cdot m^2 \cdot W^{-1}], \\ h_{int} : \text{the internal heat transfer coefficient } [W \cdot m^{-2} \cdot K^{-1}], \\ h_{ext} : \text{the external heat transfer coefficient } [W \cdot m^{-2} \cdot K^{-1}], \\ e_{conc} : \text{the concrete layer thickness } [m], \\ \lambda_{conc} : \text{the thermal conductivity of the concrete } [W \cdot m^{-1} \cdot K^{-1}], \\ e_{insu} : \text{the insulation layer thickness } [m], \\ \lambda_{insu} : \text{the thermal conductivity of the insulation } [W \cdot m^{-1} \cdot K^{-1}]. \end{array} \right.$

In order to highlight the differences between the standard and simulated values of  $h_{c,w}$  and  $R_{th}$  for different built configurations, Tab. 6.8 (a) and Tab. 6.8 (b) synthesize the corresponding values on the different faces of a cubical and a patio buildings that are either isolated or located in a theoretical urban environment. The estimates of  $R_{th}$  assume walls composed of one concrete and one insulation layers, and the following parameters:

- $h_{int} = 10.7$  and  $8.2 W \cdot m^{-2} \cdot K^{-1}$  for the roof<sup>8</sup> and walls<sup>9</sup>
- $h_{ext} = 5.1 + h_{c,w} W \cdot m^{-2} \cdot K^{-1}$  for all parts of the envelope;<sup>10</sup>
- $e_{conc} = 1.5 \times 10^{-1} m$  and  $\lambda_{conc} = 1.5 W \cdot m^{-1} \cdot K^{-1}$  for the concrete layer,
- and  $e_{insu} = 1.25 \times 10^{-1} m$  and  $\lambda_{insu} = 0.05 W \cdot m^{-1} \cdot K^{-1}$  for the insulation layer.

Similarly to Sec. 6.1.1, the surface averaged  $h_{c,w}$  values considered for the non-isolated cube (respectively patio) are those of the cube 3.2 (respectively patio 3.2) of the cube array (respectively continuous patio array, see Appendix U.2 for the index). To further examine the sensitivity of the energy needs to  $h_{c,w}$  depending on the thermal performance of the envelope, Tab. 6.8 also reports the values of  $R_{th}$  in case of non-insulated walls ( $e_{insu} = 0$ ). The addressed high and low insulation levels are further named “Insul.+” and “Insul.—” respectively.

As previously noticed, standard  $h_{c,w}$  are generally higher than the simulated surface averaged  $h_{c,w}$ . Deviations are especially significant in non-isolated configurations and courtyards. Relatively sheltered aerodynamic conditions develop in such configurations, which reduce convective heat transfers. Maximum differences occur for the walls surrounding the enclosed courtyard of the patio as a very specific recirculation develops there (Sec. 4.4.2). However, in cases of well-insulated walls,  $h_{c,w}$  does not significantly affect the total thermal resistance of walls. A maximum  $R_{th}$  deviation of 3 % occurs for the wall for which the standard and simulated values of  $h_{c,w}$  deviate

<sup>8</sup> $h_{int} = h_{rad,20^\circ} + h_{c,top} = 5.7 + 5.0 W \cdot m^{-2} \cdot K^{-1}$  (see Tab. 6.6 and Tab. 6.7)

<sup>9</sup> $h_{int} = h_{rad,20^\circ} + h_{c,horiz.} = 5.7 + 2.5 W \cdot m^{-2} \cdot K^{-1}$  (see Tab. 6.6 and Tab. 6.7 respectively)

<sup>10</sup> $h_{ext} = h_{rad,10^\circ} + h_{c,w} = 5.1 + h_{c,w} W \cdot m^{-2} \cdot K^{-1}$  (see Fig. 6.3, Tab. 6.6 and Tab. 6.7)

		Isolated				Non-isolated			
		front	rear	top	side	front	rear	top	side
$h_{c,w}$	Th-U	21.2	21.2	21.2	21.2	21.2	21.2	21.2	21.2
	Simu.	16.8	7.7	13.1	11.2	9.7	4.7	9.9	7.6
Deviation (%)		-21	-64	-38	-47	-54	-78	-53	-64
Insul. : +									
$R_{th}$	Th-U	2.76	2.76	2.73	2.76	2.76	2.76	2.73	2.76
	Simu.	2.77	2.80	2.75	2.78	2.79	2.82	2.76	2.80
Deviation (%)		0.2	1.5	0.6	0.9	1.1	2.3	1.1	1.5
Insul. : -									
$R_{th}$	Th-U	0.26	0.26	0.23	0.26	0.26	0.26	0.23	0.26
	Simu.	0.27	0.30	0.25	0.28	0.29	0.32	0.26	0.30
Deviation (%)		2.9	15.4	7.3	9.0	11.7	24.6	12.4	15.7

a) The cube

		Isolated							Non-isolated			
		front	rear	top	side	LW	WW	sides	LW	WW	sides	top
$h_{c,w}$	Th-U	21.2	21.2	21.2	21.2	21.2	21.2	21.2	21.2	21.2	21.2	21.2
	Simu.	16.2	5.9	11.7	10.5	4.5	7.8	5.2	2.9	6.4	3.6	9.5
Deviation (%)		-24	-72	-45	-50	-79	-63	-76	-86	-70	-83	-53
Insul. : +												
$R_{th}$	Th-U	2.76	2.76	2.73	2.76	2.76	2.76	2.76	2.76	2.76	2.76	2.73
	Simu.	2.77	2.81	2.75	2.79	2.83	2.80	2.82	2.85	2.81	2.84	2.76
Deviation (%)		0.3	1.9	0.8	0.9	2.4	1.4	2.1	3.1	1.8	2.9	1.1
Insul. : -												
$R_{th}$	Th-U	0.26	0.26	0.23	0.26	0.26	0.26	0.26	0.26	0.26	0.26	0.23
	Simu.	0.27	0.31	0.25	0.29	0.33	0.30	0.32	0.35	0.31	0.34	0.26
Deviation (%)		3.4	20.3	9.3	10.0	25.4	15.2	22.7	33.3	18.7	30.6	13.1

b) The patio

Table 6.8: Comparison by face of the generic surface averaged  $h_{c,w}$  values [ $\text{W} \cdot \text{m}^{-2} \cdot \text{K}^{-1}$ ] (and the corresponding  $R_{th}$  [ $\text{m}^2 \cdot \text{K} \cdot \text{W}^{-1}$ ]) provided by the Th-U rules (CSTB, 2012b) or simulated (Sec. 5.3) in cases of 10 m high isolated and non-isolated buildings (cubes or patios).

The cube / patio 3.2 of the cube / continuous patio array (see Appendix U.2) is considered for the non-isolated building case.

the most. The deviation is of 1.4 % on average, which is negligible considering the uncertainties related to the estimate of  $h_{c,w}$ . However, this averaged deviation reaches 14.5 % for non-insulated walls. Regarding the non-isolated and non-insulated patio configuration, the estimates of  $R_{th}$  differ by 23 % on average. These values are still almost in the range of uncertainties characterizing the estimate of  $h_{c,w}$ , yet improved by the development of the revised customized temperature wall-function for the RSM. They are nonetheless not negligible as they reflect the effects of the local wind environment on the convective heat transfers.

Hence, these results verify that the less insulated the wall is, the more deviate the estimated  $R_{th}$  based on the Th-U rules or simulation. Similarly, the less exposed the wall is to winds, the greater is the deviation between the two estimates.

## 6.2.2 Case studies

### 6.2.2.1 Assessment of the heat losses due to convection

The French RT 2012 requires the thermal transmittivity of a building envelope to be less than  $U_{env} = 0.36 \text{ m}^2 \cdot \text{K} \cdot \text{W}^{-1}$ . Neglecting thermal bridges and considering only opaque walls, it can correspond to an envelope that is made of a  $1.5 \times 10^{-1} \text{ m}$  thick layer of concrete and a  $1.25 \times 10^{-1} \text{ m}$  thick layer of insulation<sup>11</sup> (case “Insul.+” of Sec. 6.2.1).

Considering a building envelope composed of several walls  $i$  of area  $A_i$  undergoing 1D heat transfers and under steady state conditions, the energy needs ( $E_{conv}$ ) required to balance the relative heat losses due to heat transmission through the envelope can be estimated according to the thermal balance of the building:

$$\sum_i [U_i \times A_i] \times (T_{int} - T_{ext}) + E_{conv} = 0 \quad (6.10)$$

with: 
$$U_i = \frac{1}{R_{th,i}} \quad (6.11)$$

and: 
$$\left\{ \begin{array}{l} T_{int} : \text{the indoor temperature [K]}, \\ T_{ext} : \text{the outdoor temperature [K]}, \\ U_i : \text{the thermal transmissivity coefficient of the wall } i [\text{W} \cdot \text{m}^{-2} \cdot \text{K}^{-1}], \\ R_{th,i} : \text{the thermal resistance of the wall } i [\text{m}^2 \cdot \text{K} \cdot \text{W}^{-1}], \\ A_i : \text{the area of the wall } i [\text{m}^2], \\ E_{inf} : \text{the instantaneous energy need [W]}. \end{array} \right.$$

Note that being a function of the geometry and surrounding thermal conditions,  $h = h_{rad} + h_c$  varies from one side of the wall to the other, and from one wall to the others. Tab. 6.6 and Tab. 6.7 provide some reference values of  $h_{rad}$  and  $h_{c,int}$  depending on the mean radiant temperature or the direction of the heat flux respectively (CSTB, 2012b).

<sup>11</sup>This correspondence considers  $\lambda_{conc} = 1.5 \text{ W} \cdot \text{m}^{-1} \cdot \text{K}^{-1}$  and  $\lambda_{insu} = 0.05 \text{ W} \cdot \text{m}^{-1} \cdot \text{K}^{-1}$ .



Physical parameter		Properties	
$T_{ext}$	[°C]	$T_{freestream}$	10
$T_{int}$	[°C]	constant in the building	20
$e_{insul+}$	[m]	homogeneous	$12.5 \times 10^{-2}$
$e_{insul-}$	[m]	homogeneous	0
$\lambda_{insul}$	[W · m <sup>-1</sup> · K <sup>-1</sup> ]	1D	0.05
$e_{concrete}$	[m]	homogeneous	$15 \times 10^{-2}$
$\lambda_{concrete}$	[W · m <sup>-1</sup> · K <sup>-1</sup> ]	1D	1.5
$h_{c,int}$	[W · m <sup>-2</sup> · K <sup>-1</sup> ]	upward	5.0
		horizontal	2.5
$h_{rad}$	[W · m <sup>-2</sup> · K <sup>-1</sup> ]	$T = 10^\circ\text{C}$	5.1
		$T = 20^\circ\text{C}$	5.7

Table 6.9: Synthesis of the physical parameters used in the computations of  $U_{env}$  and  $E_{conv}$ .

In order to study the sensitivity of the building energy balance to the considered  $h_{c,w}$  value on the building outer wall,  $E_{conv}$  was evaluated for the isolated 10 m high cubical building. Walls are assumed composed of one  $1.5 \times 10^{-1}$  m thick concrete layer and one  $1.25 \times 10^{-1}$  m thick insulation layer as in Sec. 6.2.1. The  $h_{c,w}$  values used to compute  $h_{ext}$  are either deduced from the Th-U rules or taken equal to the simulated surface averaged  $h_{c,w}$  values given in Sec. 5.3.2.

According to the standard  $h_{c,w}$  values,  $E_{conv} = 6.05 \text{ W} \cdot \text{m}_{\text{floor}}^{-2}$ . It is  $E_{conv} = 6.00 \text{ W} \cdot \text{m}_{\text{floor}}^{-2}$  according to the simulated  $h_{c,w}$  values. As expected, the difference between the two estimates of  $E_{conv}$  is almost negligible because of the high thermal performance of the considered envelope. Without insulation,  $E_{conv} = 65.7 \text{ W} \cdot \text{m}_{\text{floor}}^{-2}$  and  $E_{conv} = 60.5 \text{ W} \cdot \text{m}_{\text{floor}}^{-2}$  according to the standard and simulated  $h_{c,w}$  values respectively. This represents a 8 % difference. Deviation increases, but remains relatively low although no more negligible. This low difference is explained by the fact that the considered building is still exposed to the incident wind. According to Sec. 6.2.1, this deviation should be even higher in case of a non-isolated configuration.

As a consequence, and to further examine the effects of the building topology and urban context on the building heat losses due to heat transmission through its envelope, the same exercise was carried out to determine  $U_{env}$  and  $E_{conv}$  in cases of:

- an isolated patio;
- a cubical building that belongs to a network;
- a patio building that belongs to a network.

As in Sec. 6.1.2.1 and because of the limited scope of the thermal model validation, all these different configurations are also studied considering only the windward and leeward faces active. Tab. 6.9 summarizes the different physical parameters used in the computations.

### 6.2.2.2 Results and analysis

Tab. 6.10 (a) synthesizes the different results in terms of  $U_{env}$  and  $E_{conv}$  reduced to the surface unit of floor ( $E_{conv,m^2}$ ) for the 10m high cubical building located either in an open terrain or in a theoretical urban environment. Results obtained in cases of an insulated (Insul. +) and a non-insulated (Insul. -) building, and using both the standard or the simulated  $h_{c,w}$  values are reported for comparison. Tab. 6.10 (b) synthesizes the corresponding results but addresses patios. Appendix X.2 provides the corresponding total energy needs ( $E_{conv,tot}$ ) due to heat transmission through the building envelope.

Results confirm the highest sensitivity of  $U_{env}$  and  $E_{conv}$ , which are proportional, to the  $h_{c,w}$  value for non-isolated and non-insulated buildings. As expected from Tab. 6.8, the estimates of  $U_{env}$  and  $E_{conv}$  based on simulation results are generally lower than those based on the Th-U rules. On the one hand, deviations between the estimates of  $E_{inf}$  based on the standard or simulated values of  $h_{c,w}$  are negligible in cases of well-insulated buildings. On the other hand and with the exception of the non-isolated cubical building that has its five outer walls active, all non-insulated buildings show deviations about ten times higher than in the corresponding insulated cases. The lowest deviation (8%) between the regulation and the simulation-based estimates occurs for the buildings, which are the most exposed to the incident winds. The highest deviation (20%) occurs for the buildings that are the most sheltered. Note that for each configuration, the deviation observed between the  $U_{env}$  and  $E_{conv}$  calculated using either the standard or the simulated values of  $h_{c,w}$  are almost the same when considering that the whole envelope of the building or only its windward and leeward faces active.

The cubical building has the same surface of exchanges irrespective of the urban configuration. As a consequence, the use of standard values of  $h_{c,w}$  yields similar estimates of  $E_{conv}$  for the isolated and non-isolated configurations. On the contrary, the use of the simulated  $h_{c,w}$  values induces a lower estimate of  $E_{conv}$  in the non-isolated case than in the isolated case. However, this decrease is almost negligible in case of a well-insulated building, and appears relatively small for the non-insulated cubical buildings. Still according to prediction based on simulation,  $E_{conv,tot}$  is the lowest for the non-isolated cube, and the highest for the isolated patio. The change of  $E_{conv,tot}$  between the isolated and the non-isolated cubes is smaller than the change occurring between the isolated and the non-isolated patios, which is mainly explained by dimensional effects. The envelope area of the patio decreases when switched from an isolated to a non-isolated configuration, whereas that of the cube remains the same.

Similarly to Sec. 6.1.2.2, trends are opposite when examining  $E_{conv,m^2}$ . Considering non-insulated buildings,  $E_{conv,m^2}$  estimated according to simulation results for the non-isolated patio equals 26 and  $7 \text{ W} \cdot \text{m}_{\text{floor}}^{-2}$  for the cases “All” and “Lw+Ww” respectively. These values place this configuration as the most efficient of the different configurations tested. This efficiency is explained by the low surface of envelope to floor ratio as well as the low  $h_{c,w}$  intensities characterizing the walls surrounding the court. Conversely, the isolated cube appears as the less efficient. In this case,  $E_{conv,m^2}$  equals 60 and  $24 \text{ W} \cdot \text{m}_{\text{floor}}^{-2}$  according to the simulated  $h_{c,w}$  for the cases “All”

Faces in contact with outdoor		Isolated		Non-isolated	
		All	Ww+Lw	All	Ww+Lw
Insul. : +					
$U_{env}$	Th-U	0.36	0.36	0.36	0.36
	Simu.	0.36	0.36	0.36	0.36
$E_{conv}$	Th-U	6.05	2.42	6.05	2.42
	Simu.	6.00	2.39	5.96	2.38
Deviation (%)		-0.8	-0.9	-0.9	-1.7
Insul. : -					
$U_{env}$	Th-U	3.94	3.85	3.94	3.85
	Simu.	3.63	3.53	3.41	3.27
$E_{conv}$	Th-U	65.7	25.6	65.7	25.7
	Simu.	60.5	23.6	56.8	21.8
Deviation (%)		-7.9	-8.1	-15.6	-15.0

a) The cube

Faces in contact with outdoor		Isolated		Non-isolated	
		All	Ww+Lw	All	Ww+Lw
Insul. : +					
$U_{env}$	Th-U	0.36	0.36	0.36	0.36
	Simu.	0.36	0.36	0.36	0.35
$E_{conv}$	Th-U	6.05	2.41	2.83	0.81
	Simu.	5.98	2.38	2.78	0.79
Deviation (%)		-1.2	-1.5	-1.9	-2.4
Insul. : -					
$U_{env}$	Th-U	3.94	3.85	4.05	3.85
	Simu.	3.49	3.37	3.35	3.06
$E_{conv}$	Th-U	65.7	25.6	31.5	8.6
	Simu.	58.1	22.5	26.1	6.8
Deviation (%)		-11.5	-12.3	-17.2	-20.4

b) The patio

Table 6.10: Comparison of  $U_{env}$  [ $W \cdot m^{-2} \cdot K^{-1}$ ] and  $E_{conv}$  [ $W \cdot m_{floor}^{-2}$ ] calculated using the Th-BCE or the simulated  $h_{c,w}$  values for buildings located in different urban configurations.

Ww+Lw: only the windward and leeward faces;

abs: absolute difference; rel.: relative difference;

Insul. +: the building carries a  $1.25 \times 10^{-2}$  m layer of insulation material;

Insul. -: the building is not insulated.

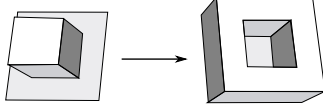
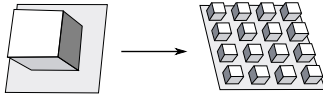
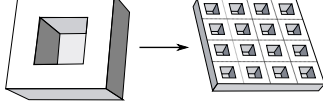
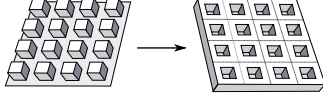
Faces in contact with outdoors			Insul. : +		Insul. : -	
			All	Ww+Lw	All	Ww+Lw
	Th-U	abs.	0.00	0.00	0.00	0.00
		rel. (%)	0.0	0.0	0.0	0.0
	Simu.	abs.	-0.03	-0.01	-2.37	-1.08
		rel. (%)	-0.4	-0.5	-3.9	-4.6
	Th-U	abs.	0.00	0.00	0.00	0.00
		rel. (%)	0.0	0.0	0.0	0.0
	Simu.	abs.	-0.04	-0.02	-3.73	-1.76
		rel. (%)	-0.7	-0.8	-6.2	-7.5
	Th-U	abs.	-3.22	-1.61	-34.9	-17.1
		rel. (%)	-53.2	-66.7	-52.1	-66.7
	Simu.	abs.	-3.20	-1.60	-32.06	-15.68
		rel. (%)	-53.6	-67.0	-55.1	-69.7
	Th-U	abs.	-3.22	-1.61	-34.19	-17.10
		rel. (%)	-53.2	-66.7	-52.1	-66.7
	Simu.	abs.	-3.19	-1.59	-30.70	-14.99
		rel. (%)	-53.5	-66.9	-54.1	-68.8

Table 6.11: Comparison between  $E_{conv}$  [ $W \cdot m_{floor}^{-2}$ ] for different urban configurations: effects of the building topology and urban morphology.

and “Lw+Ww” respectively. Moreover, contrary to  $E_{conv,tot}$ , the change of  $E_{conv,m^2}$  between the isolated and the non-isolated cube is higher than the change occurring between the isolated and the non-isolated patios.

In order to further discuss the effects of the building typology and built environment, and similarly to Sec. 6.1.2.2, Tab. 6.11 summarizes the changes of  $E_{conv,m^2}$  between:

- the isolated cube and patio;
- the isolated cube and the non-isolated cube;
- the isolated patio and the non-isolated patio;
- the non-isolated cube and patio.

Appendix X.2 synthesizes the corresponding values, but addresses the differences of  $E_{conv,tot}$ .

As above-mentioned, the Th-U rules often involve a constant  $h_{c,w}$  value on the different faces of buildings and the surface of envelope is similar in cases of the isolated and the non-isolated cubes. On the one hand, no change of  $E_{conv,tot}$  between these two configurations is assessed according to the standard  $h_{c,w}$  values. Similarly, no change of  $E_{conv,tot}$  is assessed either between the non-isolated cube and patio when considering only their windward and leeward faces active. On the other hand, the corresponding estimates of  $E_{conv,tot}$  decrease a little according to simulation because of differences in  $h_{c,w}$  distributions and intensities. Conversely, both the regulation- and simulation-based predictions indicate that a  $E_{conv,tot}$  decreases by 50 to 70 % between the isolated and the non-isolated patio; increases by about 40 % between the non-isolated cube and patio (case “All”); and increases by 200 % between the isolated cube and patio. Nevertheless, these

relative changes appear weakly induced by a modification of the heat transfers intensities through the envelope. No changes of heat transfer intensity is even involved when considering standard  $h_{c,w}$  values. In fact, changes of  $E_{conv,tot}$  are almost proportional to the change of the surface of envelope between the buildings compared. Hence, the changes of  $E_{conv,tot}$  between the different types are completely explained by dimensional effects according to the standard approach; and much more explained by dimensional effects than by a modification of heat transfers intensity through the envelope according to simulation.

As opposed to  $E_{conv,tot}$ , the evolution of  $E_{conv,m^2}$  estimated using the standard values of  $h_{c,w}$  is zero between the isolated cube and patio. This is explained by the facts that both the envelope and the floor area are increased by a factor of 3 between these types and that the thermal resistance of walls is similar. Because of dimensional reasons as well, a decrease of  $E_{conv,m^2}$  is assessed between the isolated and the non-isolated patio (same floor area and smaller envelope area) as well as between the non-isolated cube and patio (larger envelope area but even larger floor area). Hence, changes of  $E_{conv,m^2}$  based on the standard values of  $h_{c,w}$  are solely due to dimensional effects as well. They do not include any influence of specific flow structures around buildings as  $h_{c,w}$  is assumed equal on all surfaces.

On the contrary, changes of  $E_{conv,m^2}$  estimated using the simulated  $h_{c,w}$  values clearly highlight the different contributions of the surrounding flows to the buildings convective heat exchanges. These contributions are directly addressed when comparing the isolated cube and patio as well as the isolated and non-isolated cubes. Similarly, differences in the changes of  $E_{conv,m^2}$  between, on the one hand the isolated and non-isolated patios, and on the other hand the non-isolated cube and patio, can also be attributed to different contributions of the surrounding thermal and aerodynamic conditions. Indeed, the ratio between the increase of the envelope area by the increase of the floor area equals 7/15 (case "All") and 1/3 (case "Lw+Ww") for both cases. These correspondences also explain the similar relative differences of  $E_{conv,m^2}$  induced by the use of the standard  $h_{c,w}$  values.

According to simulation, the relative changes of  $E_{conv,m^2}$  occurring between the isolated cube and patio as well as between the isolated and non-isolated cubes are higher in case of non-insulated buildings. In such cases, surroundings appear more influential in determining  $E_{conv,m^2}$  than the shape of the building. Assuming all walls active, a decrease of  $E_{conv,m^2}$  by 3.9% is predicted between the isolated cube and patio, whereas it is 6.2% between the isolated and non-isolated cubes. These trends are mainly explained by two factors. First, low  $h_{c,w}$  characterize the court of the patio and this type presents a smaller front to floor area ratio than the cube. This is mainly why  $E_{conv,m^2}$  is lower for the patio than for the cube. However, the isolated patio still presents a windward wall that faces the undisturbed incident flow, which is not the case for the non-isolated building. This second factor appears more influential and explains the weaker influence of the building topology than of the surroundings in determining  $E_{conv,m^2}$ . Nevertheless, the differences of  $E_{conv,m^2}$  currently discussed are minor. They might not be very significant considering the uncertainties related to  $h_{c,w}$ .

Still according to simulation, quite similar  $E_{conv,m^2}$  are estimated for the isolated patio and the non-isolated cube. As a consequence, their comparison with  $E_{conv,m^2}$  of the non-isolated patio configuration stresses similar trends. The relative changes of  $E_{conv,m^2}$  differ by 0.1 point when addressing well-insulated buildings and by 1 point when addressing non-insulated buildings. For both cases, switching from the initial configuration to the non-isolated patio decreases  $E_{conv,m^2}$  by about 54 % (case “All”) and 68 % (case “Lw+Ww”).

### 6.2.2.3 Synthesis

First of all, the results outlined in this section confirm that  $h_{c,w}$  weakly influences the estimate of  $E_{conv}$  for well-insulated buildings. In such cases, the energy needs involved are very low. However, results show the importance of the  $h_{c,w}$  value used when addressing the energy demand of non-insulated buildings. Comparing estimates of  $E_{conv,m^2}$  based either on the standard or the simulated  $h_{c,w}$  values stresses differences up to 20 % in cases of non-insulated sheltered buildings. These differences are explained by the uniform distribution and high value of  $h_{c,w}$  is often assumed when using the Th-U rules. Such an uncertainty corresponds to the usual contribution of thermal bridges to the heat balance of houses (ADEME, 2015).<sup>12</sup>

The presence of surrounding constructions decreases the external convective heat transfers of a building. According to simulation, the built environment induces an averaged decrease of  $h_{c,w}$  of  $4 \text{ W} \cdot \text{m}^{-2} \cdot \text{K}^{-1}$  between the isolated and the non-isolated cube. This represents a 33 % relative deviation, which is substantial. However, the corresponding energy needs decrease by less than 1 % and by about 7 % in cases of an insulated and a non-insulated building, which is relatively low. Hence, although  $h_{c,w}$  intensities are significantly impacted by the surrounding environment, the energy needs appear relatively weakly sensitive to a modification of  $h_{c,w}$  intensities due to the built environment. Similar trends were also highlighted by Liu et al. (2015). According the case studies reported, although  $h_{c,w}$  decreases by 38 % when switching a cubical building from an almost isolated configuration to a built environment, its energy consumption varies by 1.3 % for heating and 4 % for cooling at most. According to the case studies addressed in this thesis, dimensional effects appear much more influential than  $h_{c,w}$  in determining  $E_{conv,m^2}$ . Nonetheless, it is worth reminding that the current study addressed forced convection only. Thermal effects might modulate the current conclusions, although generally leading to relatively weak convective heat transfers.

---

<sup>12</sup>Heat losses due to thermal bridges represent on average 5 to 10 % of the total heat losses of traditional French houses that were built before 1974 (ADEME, 2015), which is the year of the first French thermal regulation.

## 6.3 Effects of urban air flows on building energy loads due to air infiltration and heat transmission

### 6.3.1 Relative contribution of air infiltration and heat transmission to the building energy loads

To evaluate the relative contribution of air infiltration and heat transmission through the building envelope on the building energy demand, Tab. 6.12 (a) and 6.12 (b) synthesize the corresponding combined energy demand reduced to the surface unit of floor ( $E_{i+c,m^2} = E_{inf,m^2} + E_{conv,m^2}$ ) for the cube and patio respectively. These values are assessed using either the standard or the simulated values of  $Cp$  and  $h_{c,w}$  for comparison. The different cases studied in Sec. 6.1.2.1 and Sec. 6.2.2.1 in terms of built configuration as well as envelope performance (air permeability and thermal insulation) are reported. Appendix Y.3.1 provides the corresponding values of  $E_{i+c,tot}$ .

As expected from previous results, the estimates of  $E_{i+c}$  based on the simulated values of  $Cp$  and  $h_{c,w}$  are lower than those based on the corresponding standard values. Results show higher relative deviation in cases of well-insulated buildings that are highly permeable to air. For non-isolated buildings, deviation reaches 51 % on average. It is 20 % for the isolated cube and 30 to 41 % for the isolated patio, depending on the number of faces assumed active. These results confirm the relatively low sensitivity of the regulation-based estimates of  $E_{i+c}$  to the sheltering provided by surrounding constructions. Nevertheless, cases of well-insulated buildings that are highly permeable to air are not very realistic, and involve rather low energy needs. Regarding buildings that are totally efficient or non-efficient in terms of thermal insulation and air tightness, predictions based on the standard or simulated  $Cp$  and  $h_{c,w}$  values deviate by 10 % to 30 % depending on the configuration addressed. Although being smaller than the 50 % addressed above, this remains substantial as the less efficient the building is, the higher is the deviation, and the higher are the involved energy needs.

Tab. 6.12 also highlights the greater impact of the building insulation than of its air tightness on the energy demand, at least for the configurations currently examined. With respect to the most efficient cubical building, increasing the air permeability of the envelope by a factor of 5 multiplies  $E_{i+c}$  by a factor of 2 for isolated buildings and by less when surrounding buildings are present. Removing the thermal insulation multiplies  $E_{i+c}$  by a factor of more than 8 considering both the isolated and non-isolated configurations. These trends are comparable for the patio and do not substantially differ if based on the standard or simulated values of  $Cp$  and  $h_{c,w}$ . However, insulation and air tightness are properties of buildings and not uncertain parameters that are affected by the surrounding aerodynamic conditions. Therefore, their effects are no further discussed in this thesis. These wall properties only serve to fix archetypal building envelopes in order to further discuss the relative effects of  $Cp$  and  $h_{c,w}$  on the building energy loads.

To further examine the relative effects of air infiltration and heat transmission through the envelope, diagrams provided in Fig. 6.4 show the relative contribution of  $E_{inf,m^2}$  and  $E_{conv,m^2}$  to  $E_{i+c,m^2}$  for the different configurations involving the 10 m high cubical building. Values estimated

		Isolated			Non-isolated		
Insul.	$Q_{4Pa}$	$E_{reg}$	$E_{sim}$	Dev (%)	$E_{reg}$	$E_{sim}$	Dev (%)
All faces in contact with outdoors							
+	+	8.4	7.5	−9.9	7.8	6.2	−20.4
+	−	17.6	13.7	−22.4	14.7	7.13	−51.6
−	+	68.0	62.1	−8.8	67.4	57.0	−15.4
−	−	77.2	68.2	−11.7	74.4	58.0	−22.1
Windward and leeward faces in contact with outdoors							
+	+	3.4	3.1	−8.2	3.1	2.5	−18.9
+	−	7.3	6.0	−17.8	6.7	3.2	−46.9
−	+	26.6	24.3	−8.8	26.3	22.0	−16.7
−	−	30.5	27.1	−11.0	29.2	22.6	−22.6

a) The cube

		Isolated			Non-isolated		
Insul.	$Q_{4Pa}$	$E_{reg}$	$E_{sim}$	Dev (%)	$E_{reg}$	$E_{sim}$	Dev (%)
All faces in contact with outdoors							
+	+	8.2	7.2	−12.6	3.5	2.8	−19.7
+	−	16.7	11.9	−29.0	6.2	3.0	−52.1
−	+	67.8	59.3	−12.5	32.2	26.1	−18.8
−	−	76.4	64.0	−16.1	34.9	26.3	−24.7
Windward and leeward faces in contact with outdoors							
+	+	3.3	2.7	−18.0	1.0	0.8	−22.6
+	−	6.8	4.0	−41.5	2.0	0.7	−55.2
−	+	26.5	22.8	−14.0	8.8	6.8	−22.3
−	−	30.1	24.1	−19.8	9.7	6.9	−29.0

b) The patio

Table 6.12: Comparison between the  $E_{i+c,m^2} [W \cdot m_{\text{floor}}^{-2}]$  estimated using the standard or simulated values of  $C_p$  and  $h_{c,w}$  in cases of an isolated and a non-isolated buildings that are insulated and air-tight or not.

Insul. +: insulated building; −: non-insulated building;

$Q_{4Pa}$  +: air tight building;  $Q_{4Pa}$  −: air permeable building;

Reg. (resp. Sim.): estimates based on the standard (respectively simulated)  $C_p$  and  $h_{c,w}$ .

Dev: deviation between the estimates of  $E_{tot}$  based on the standard or simulated values of  $C_p$  and  $h_{c,w}$ .



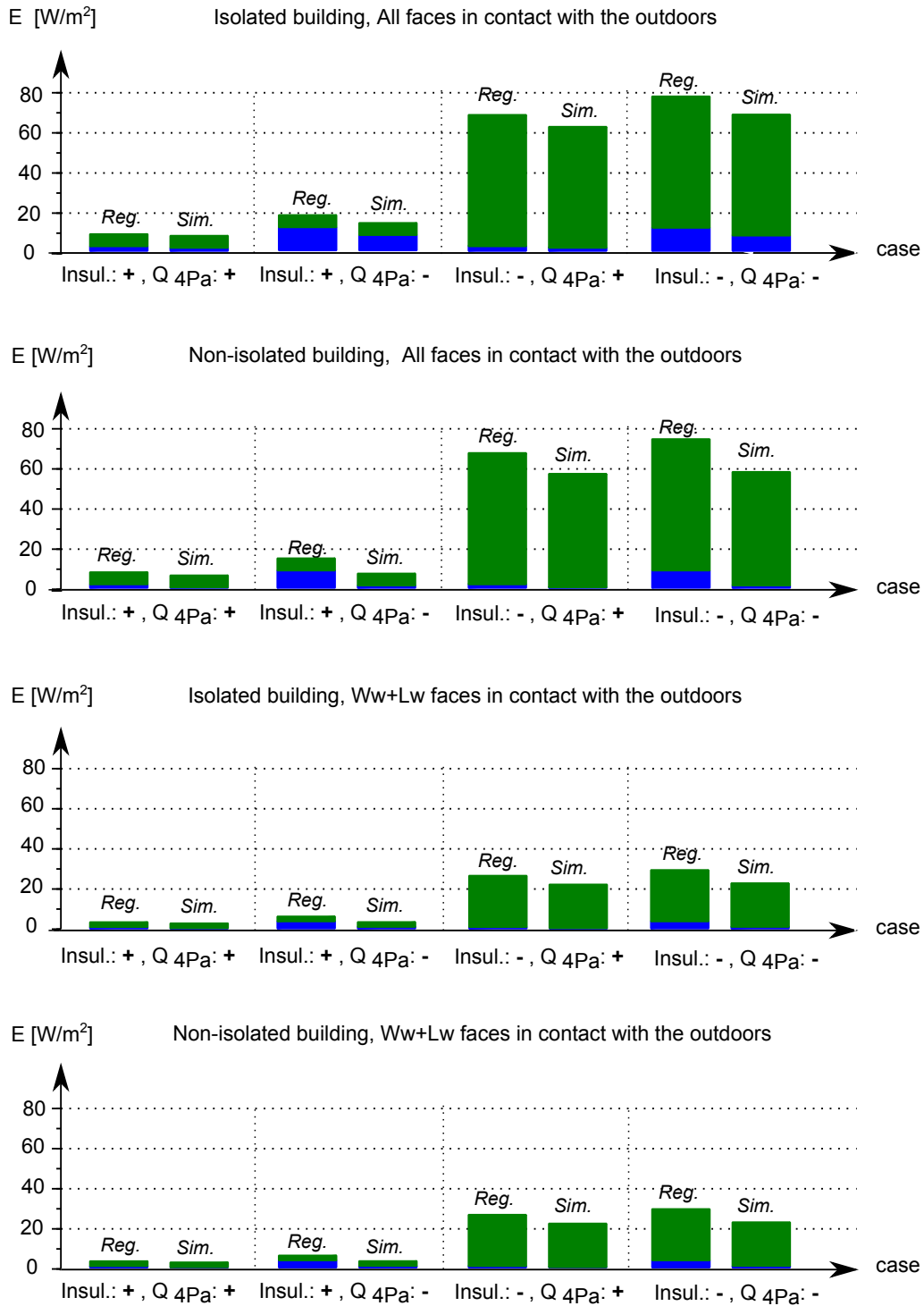


Figure 6.4: Comparison of the energy needs per  $m^2$  of floor area ( $E_{i+c,m^2}$ ) differentiated depending on  $E_{inf,m^2}$  or  $E_{conv,m^2}$  for the cubical building located either in an open terrain or in a theoretical urban environment.

Blue: contribution of air infiltration ( $E_{inf,m^2}$ ); Green: contribution of heat transmission ( $E_{conv,m^2}$ );  
 Insul. +: insulated building; -: non-insulated building;  
 Q<sub>4Pa</sub>+: air tight building; Q<sub>4Pa</sub> -: air permeable building;  
 Reg. (resp. Sim.): estimates based on the standard (respectively simulated)  $C_p$  and  $h_{c,w}$ .

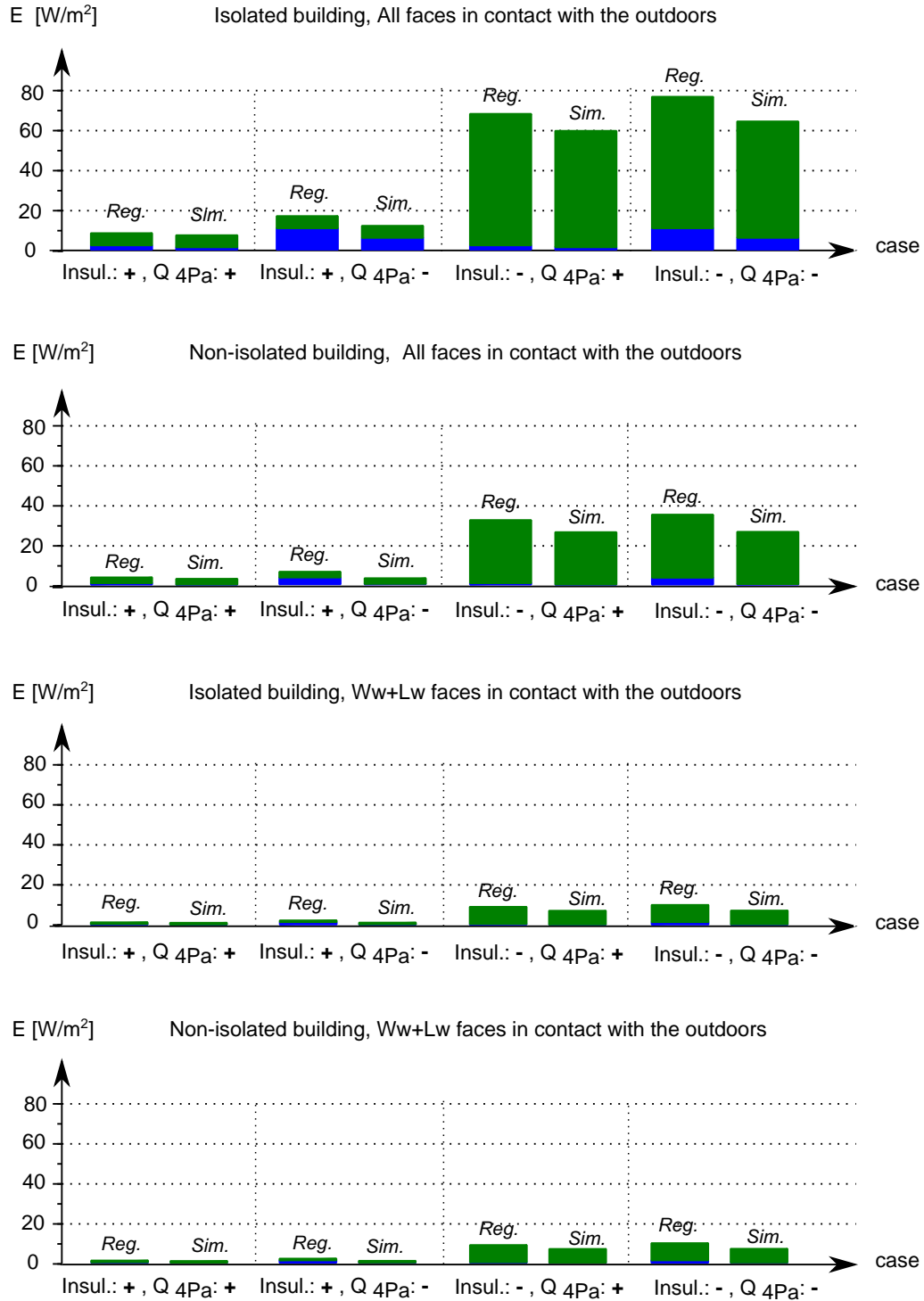


Figure 6.5: Comparison of the energy needs per m<sup>2</sup> of floor area ( $E_{i+c,m^2}$ ) differentiated depending on  $E_{inf,m^2}$  or  $E_{conv,m^2}$  for the patio building located either in an open terrain or in a theoretical urban environment.

Blue: contribution of air infiltration ( $E_{inf,m^2}$ ); Green: contribution of heat transmission ( $E_{conv,m^2}$ );  
 Insul.+: insulated building; -: non-insulated building;  
 Q<sub>4Pa</sub>+: air tight building; Q<sub>4Pa</sub> -: air permeable building;  
 Reg. (resp. Sim.): estimates based on the standard (respectively simulated)  $C_p$  and  $h_{c,w}$ .

using the standard or simulated  $C_p$  and  $h_{c,w}$  values are differentiated. Fig. 6.5 focuses on the same results but addresses the patio case. Appendix Y.3.1 gives the corresponding diagrams, but reports the total energy needs, i.e.  $E_{inf,tot}$ ,  $E_{conv,tot}$  and  $E_{i+c,tot}$  for the different cases.

In accordance with the analysis of Tab. 6.12, infiltration plays a higher relative role in defining  $E_{i+c}$  in cases of well-insulated buildings than in cases of non-insulated buildings. This is especially the case when buildings can exchange heat and air through their whole envelope. According to the estimates of  $E_{i+c,m^2}$  based on the standard values of  $C_p$  and  $h_{c,w}$ ,  $E_{inf,m^2}$  represents 27% and 21% of  $E_{i+c,m^2}$  in cases of an insulated and lowly permeable (Insul. + and  $Q_{4Pa+}$ ) isolated and non-isolated buildings respectively. These ratios reach 65% and 67% when buildings are well-insulated but highly permeable (Insul. + and  $Q_{4Pa-}$ ). Considering the simulated  $C_p$  and  $h_{c,w}$  values, these ratios are 18, 2, 53 and 12% respectively. Note that the latter values are characterized by a higher variability between the patio and cube cases. According to these simulation-based results, the presence of surrounding constructions significantly reduces the relative contribution of air infiltration on the combined energy needs. These effects are estimated much weaker when based on the standard  $C_p$  values.

Considering non-insulated buildings, the relative effects of infiltration are weaker. They are even almost negligible for lowly permeable buildings. On average, heat losses due to infiltration only represent 2 and 10% of  $E_{i+c,m^2}$  in cases of non-insulated buildings that are lowly and highly permeable respectively.

Hence, these results show a relatively weaker contribution of infiltration to  $E_{i+c}$  compared to that of heat transmission through the envelope for the configurations currently studied. However, heat losses due to infiltration are relatively more important in cases of well-insulated buildings. They can even become preponderant for extreme cases, i.e. when buildings are insulated but highly permeable to air. Nevertheless, the estimate of the relative contributions of  $E_{inf}$  and  $E_{conv}$  to  $E_{i+c}$  substantially deviates depending on the  $C_p$  and  $h_{c,w}$  values used in the computation. For example,  $E_{inf}$  is estimated substantially higher than  $E_{conv}$  in the case of a well-insulated building that is highly permeable to air according to the standard values of  $C_p$  and  $h_{c,w}$  irrespective of its environment. In such a case, simulation predicts a rather equivalent contribution of  $E_{inf}$  and  $E_{conv}$  for isolated buildings. The contribution of  $E_{inf}$  to  $E_{i+c}$  is estimated significantly reduced when surrounding buildings are present.

More generally, the estimates of  $E_{i+c}$  based on the simulated  $C_p$  and  $h_{c,w}$  values show a lower contribution of infiltration ( $E_{inf}$ ), and inversely a higher contribution of heat transmission ( $E_{conv}$ ) through the envelope than the estimates of  $E_{i+c}$  based on the standard values do. It is especially the case when considering sheltered built contexts. This behavior may be explained by the strong assumptions involved by the standard approach. Indeed, the conventional distribution of  $C_p$  on the building outer walls does not take into account the wind direction and the Th-BCE rules only differentiate three categories of built configurations (screening). This allows a wide scope for application, but involves substantial uncertainties, which generally yield high estimates of the infiltration flow rates. These strong assumptions can even sometimes yield counter-intuitive physical configurations, which do not correspond to realistic effects of the built context. In partic-

ular, Sec. 6.1.2.2 and Appendix X show that the use of standard  $C_p$  values may predict a building energy behavior that is opposite to what is predicted by simulation and physically expected. It is especially the case when considering the changes of  $E_{inf,tot}$  between the non-isolated cube and patio (case “All”). Similarly, the assumption generally made when using the Th-U rules about  $h_{c,w}$  leads to a general overestimation of the building convective heat losses, and does not represent physics. According to the standard  $h_{c,w}$  values, no change of  $E_{conv,m^2}$  is predicted between the non-isolated cube and patio (case “All”) as well as between the isolated and the non-isolated cubes<sup>13</sup> (see Sec. 6.2.2.2). Although relatively small in absolute values these differences are important as they involve different physics.

### 6.3.2 Analysis of the effects of the building topology and urban context on the building energy loads induced by external air flows

To finally examine the effects of the building topology and urban context on the combined building energy needs due to air infiltration and convective heat transfers, and as done in Sec. 6.1.2.1 and Sec. 6.2.2.2, Tab. 6.13 summarizes the changes of  $E_{i+c,m^2}$  between:

- the isolated cube and patio;
- the isolated cube and the non-isolated cube;
- the isolated patio and the non-isolated patio;
- the non-isolated cube and patio.

Each building configuration addressed in Sec. 6.3.1 is reported. Appendix Y.3.2 synthesizes the corresponding values, but addresses the changes of  $E_{i+c,tot}$ .

A modification of the built structure mostly induces a change of  $E_{i+c,tot}$  in cases of non-insulated and highly permeable buildings. However, the relative effect of the built structure on  $E_{i+c,tot}$  is estimated the highest in cases of insulated and highly permeable buildings.

On the one hand, because  $E_{conv,tot}$  is almost proportional to the active area of envelope and  $E_{inf,tot}$  is related to the active area of envelope, although not straightforwardly, changes of  $E_{i+c,tot}$  are generally strongly related to changes in the surface of envelope. For example,  $E_{i+c,tot}$  increases from the isolated cube to the patio as well as from the non-isolated cube to patio when considering the whole envelope active. On the contrary, decreasing the surface of envelope from one configuration to another leads to a decrease of  $E_{i+c,tot}$ . Such a trend occurs between the isolated and non-isolated patio. In such cases, distinguishing the effects of the flow field modification on the change of  $E_{i+c,tot}$  from those induced by dimensionality of constructions is complex.

On the other hand, when comparing buildings that have the same active surface of envelope, changes in  $E_{i+c,tot}$  directly reflects the effects of the flow field modification induced by differences in the built structure. Such a change is observed between the isolated and non-isolated cubes, as

---

<sup>13</sup>These cases have in common that the surface of envelope to floor ratio remains the same between the different configuration addressed.

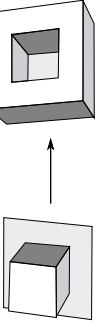

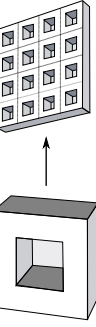
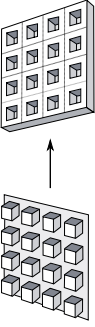
Faces / outdoors		Insul : + $Q_{4Pa} : +$		Insul : + $Q_{4Pa} : -$		Insul : - $Q_{4Pa} : +$		Insul : - $Q_{4Pa} : -$	
		All	Ww+Lw	All	Ww+Lw	All	Ww+Lw	All	Ww+Lw
	Reg.	abs.	-0.18	-0.09	-0.88	-0.44	-0.18	-0.09	-0.88
		rel. (%)	-2.8	-2.6	-5.0	-6.0	-0.3	-0.3	-1.1
	Simu.	abs.	-0.38	-0.41	-1.80	-1.98	-2.72	-1.47	-4.14
		rel. (%)	-5.0	-13.0	-13.2	-33.1	-4.4	-6.1	-6.1
	Reg.	abs.	-0.57	-0.26	-2.87	-1.31	-0.57	-0.26	-2.87
		rel. (%)	-6.9	-7.7	-16.3	-18.0	-0.8	-1.0	-3.7
	Simu.	abs.	-1.34	-0.58	-6.54	-2.81	-5.03	-2.32	-10.22
		rel. (%)	-17.8	-18.6	-47.8	-47.0	-8.1	-9.6	-15.0
	Reg.	abs.	-4.68	-2.26	-10.50	-4.85	-35.65	-17.74	-41.47
		rel. (%)	-57.1	-68.4	-62.7	-70.9	-52.6	-66.9	-54.3
	Simu.	abs.	-4.34	-1.90	-8.88	-3.11	-3.32	-15.98	-37.74
		rel. (%)	-60.6	-70.2	-74.8	-77.7	-56.0	-70.1	-58.9
	Reg.	abs.	-4.28	-2.08	-8.51	-3.98	-35.25	-15.57	-39.48
		rel. (%)	-54.9	-66.7	-57.7	-66.7	-52.3	-66.7	-53.1
	Simu.	abs.	-3.38	-1.73	-4.15	-2.28	-30.90	-15.13	-31.66
		rel. (%)	-54.5	-68.2	-58.1	-71.9	-54.2	-68.9	-54.6

Table 6.13: Evaluation of the effects of the building topology and urban morphology on the energy needs due to thermal transmission through the envelope ( $E_{conv}$  [ $W \cdot m_{floor}^{-2}$ ]) according to the Th-BCE rules or simulation results.

well as the non-isolated cube and patio (case Ww+Lw). Changes of  $E_{i+c,tot}$  are estimated differently depending on the  $Cp$  and  $h_{c,w}$  values used. As expected from Sec. 6.1.2.2 and Sec. 6.2.2.2, standard values under-estimate the effects of the built morphology with respect to simulation. According to the standard values, there is even no change of  $E_{i+c,tot}$  between the non-isolated cube and patio, and a relative low change of  $E_{i+c,tot}$  between the isolated and non-isolated cubes ( $\Delta E_{i+c,tot} = 4$  to 18%). Because the  $h_{c,w}$  value is assumed constant on the different faces of buildings, these effects are only due to infiltration. Conversely, the simulated surface averaged values of  $Cp$  and  $h_{c,w}$  differ from one face of a building to the other and are case specific. According to them, changes of  $E_{i+c,tot}$  are of 4 to 16% between the non-isolated cube and patio, and  $\Delta E_{i+c,tot}$  are of 16 to 48% between the isolated and non-isolated cubes. Hence, the effects of the built environment on the relative decrease of  $E_{i+c,tot}$  appear more important than the effects of the building topology in case of non-isolated buildings (case Ww+Lw).

Reducing  $E_{i+c,tot}$  to the surface unit of floor highlights the highest sensitivity of the isolated cube to the effects of winds in terms of infiltration and convective heat losses. Reciprocally, the non-isolated patio shows the lowest sensitivity to these effects. This is mainly explained by the lower surface of envelope to floor ratio of the non-isolated patio than of the cube. Nonetheless, lower  $h_{c,w}$  intensities and  $Cp$  differences occur inside the court of patio than around the cube, which reinforces these trends.

Switching from a cubical building to a patio, or from an isolated building to a non-isolated building generally leads to a decrease of  $E_{i+c,m^2}$ . As for  $E_{i+c,tot}$ , the highest absolute decrease of  $E_{i+c,m^2}$  is observed for non-insulated and permeable buildings (Insul. – and  $Q_{4Pa}$ –). In contrast, the highest relative decrease of  $E_{i+c,m^2}$  is observed for buildings that are insulated but highly permeable to air (Insul. + and  $Q_{4Pa}$ –). Changes of  $E_{i+c,tot}$  due to a modification of the built structure are generally predicted higher according to simulation than when based on the standard values. These results were expected from Sec. 6.1.2.2 and Sec. 6.2.2.2 and are in accordance with Appendix Y.3.2. Larger deviations occur between the isolated cube and patio as well as between the isolated and non-isolated cubes. In these cases, the change of  $E_{i+c,m^2}$  is predicted 2 to 10 times higher when using the simulated values of  $Cp$  and  $h_{c,w}$  instead of the standard values. For these cases, the relative changes of  $E_{i+c,m^2}$  are often lower than 8% according to the standard values. They are generally estimated to be of 5 to 20% according to simulation, but can reach more than 45%. These estimated decreases of  $E_{i+c,m^2}$  are relatively lower than for the two other cases addressed, which also involve dimensional effects.

Switching from the isolated to the non-isolated patios or between the non-isolated cube and patio involves a relative decrease of  $E_{i+c,m^2}$  of more than 50%. This decrease can even reach more than 75% according to simulation. Nevertheless, assuming that 53% and 67% of the  $E_{i+c,m^2}$  decrease is due to dimensional effects for the cases “All” and “Ww+Lw” respectively, the contribution of changes in the infiltrated air flow rates and convective heat transfers are estimated to be:

- considering insulated buildings: 5 and 8% between the isolated and non-isolated patios and 1.5 and 3% between the non-isolated cube and patio, according to the standard and simulated  $Cp$  and  $h_{c,w}$  values respectively;

- considering non-insulated buildings: 0 and 3.5 % between the isolated and non-isolated patios and 0 and 2 % between the non-isolated cube and patio, according to the standard and simulated  $C_p$  and  $h_{c,w}$  values respectively.

Hence, although involving a short-coming about the dimensional effects, these results also highlight the higher relative effect of the built morphology, and especially of the urban context, on  $E_{i+c,m^2}$  in cases of well-insulated buildings. Changes of  $E_{i+c,m^2}$  are nevertheless less important when they initially involve a patio or a non-isolated cube than an isolated cube, which is explained by the sheltered wind conditions that already characterize in the initial configurations. However, it is worth reminding that if the relative contribution of the built structure on the building energy needs due to infiltration and convective heat transfers are higher in case of well-insulated buildings, the absolute energy needs involved in such cases are much lower than in case of non-insulated buildings.

## 6.4 Summary

The evaluation of the impact of infiltration and transmission through building envelope on its energy balance highlights significant relative effects of the built morphology on the energy demand, especially for well-insulated buildings. Considering the surface of envelope to floor ratio constant, modifying the building topology and urban context does not much alter heat transmission through the envelope, nor likewise  $E_{conv,m^2}$ . The morphology of the built structure has a higher relative impact on infiltration processes, whose relative contribution is not negligible for well-insulated buildings. In particular, switching from exposed to sheltered conditions, e.g. inside an almost enclosed courtyard or behind a built mask, induces a substantial decrease of the energy demand due to infiltration.

In addition, results show the improvement brought by the consideration of realistic values of  $C_p$  and  $h_{c,w}$  to better estimate the building energy performance. Substantial deviation can occur between predictions of the building energy demand that are based on the standard or simulated values. This is especially the case when constructions involve sheltered walls. The effects of the built structure are substantially under-estimated when assessed implementing a standard approach. According to the case studies developed in this chapter, the standard approach appears not to properly integrate the effects of built masks on the building energy demand due to air infiltration and heat transmission.

### *Main contribution of this chapter:*

- *Estimate the uncertainty related to the use of standard  $C_p$  and  $h_{c,w}$  values to evaluate the building energy demand due to air infiltration and heat transmission through the envelope.*
- *Estimate the effects of the built structure on the building energy loads induced by the surrounding flows in terms of air infiltration and heat convection.*

# Conclusions and perspectives

## General summary of the work

The fast growth of urban population involves a significant increase of the energy needs, natural resources consumption, heat releases, waste production and GHG emissions. Buildings represent 32 % of the total final energy consumption in the world and have an impact on urban micro-climates. Those micro-climates reciprocally condition the building energy demand and citizens' health and comfort. The bio-climatic design of buildings and urban areas is a key strategy toward a sustainable urban development. Within this context, this thesis brings new knowledge to the two following issues:

- *What are the flow patterns that develop next to buildings according to the local urban morphology?*
- *How do these specific flow structures affect the building energy loads due to infiltration flows and convective heat fluxes?*

To answer these questions, this thesis was organized into three main parts.

The first part synthesizes the properties of urban aerodynamics and urban physics, and analyzes existing urban fabrics from a morphological point of view. In particular, Ch. 1 reviews and synthesizes the different physical processes and spatial scales involved in the development of urban aerodynamic processes. These processes are related to anthropic parameters, such as human thermal and wind comfort and building energy loads. On this basis, the thesis formulates the scientific issues and objectives of the research with respect to the state of the art in urban physics. The proposed methodology is described and the scope of the study is outlined. More specifically, this study focuses on the relations between the morphology of built structures and the aerodynamic phenomena and convective heat transfers developing on the urban block scale. Ch. 2 reviews the main existing approaches that relate urban morphological properties with typical bio-climatic and energy behaviors. It also reviews the different urban morphometric indicators addressing urban physical phenomena. The synthesis of these indicators highlights the critical urban morphological factors that determine the aerodynamic processes developing next to buildings. Lastly, the analysis and abstraction of traditional urban patterns lead to the design of generic typologies of built structures for small scale aerodynamic studies.

The second part of the thesis validates the CFD model with respect to detailed experimental and numerical data, and presents the numerical experiments performed on the different mor-



phological types. The simulations of the approach flow and configurations with obstacles are performed using steady RANS models. Ch. 3 compares  $Rk-\varepsilon$  and RSM-based flow predictions with the reference data and examines their accuracy in reproducing air flows around sharp edged obstacles. The modeling issues faced are discussed with respect to literature, especially regarding the modeling of a consistent ABL and the accuracy of steady RANS approaches. On this basis, the thesis details the different case studies from an aerodynamic point of view. More particularly, Ch. 4 develops the post-processing strategy defined to perform an extensive 3D analysis of the mean aerodynamic processes that develop according to the construction shape and built environment. The effects of the shape of built structures on the development of external and internal flow structures are especially examined. The resulting distribution of pressure coefficient ( $C_p$ ) on facades is finally analyzed and related to the main flow structures and morphological properties of the case studies.

The last part of the proposed methodology couples heat and air fluxes to evaluate the contribution of urban air flows to the building energy loads in terms of air infiltration and convective heat transfers. Ch. 5 evaluates the accuracy of the RSM in reproducing the convective heat transfers by comparing the simulation results with detailed experimental data in case of an isolated small cube. It also evaluates the accuracy of wall-functions in predicting these heat transfers for usual and high  $z^*$  values by comparing predictions with detailed LRNM data in case of a theoretical cubical building. On this basis, the distribution of convective heat transfer coefficient ( $h_{c,w}$ ) on building facades is analyzed and related to the main flow structures and morphological properties of the case studies. In this order of ideas, Ch. 6 compares the estimates of the building energy loads due to air infiltration and heat transmission for representative case studies that are well insulated and air tight or not. The estimates are either based on the simulated or standard  $C_p$  and  $h_{c,w}$  values in order to discuss the improvement brought by CFD to the assessment of building energy loads. Finally, the effects of urban morphology on the combined building energy needs due to air infiltration and heat convection at the envelope of constructions are discussed.

To conclude, the sequencing of this three-stage work gradually increases the model complexity, but also the number of assumptions, to provide answers to the initial questions. It progresses from rather large scope considerations to detailed computational studies. It returns lastly to more general engineering issues, thus opening the perspectives of this work.

## Synthesis of the main results

As detailed above, this thesis is an exploratory study that lays the scientific and methodological foundations of a transverse approach for studying urban energy and bio-climatic issues. This approach involves concepts and tools of building and urban physics, as well as urban planning and architecture. It especially studies the relations between urban morphology, aerodynamic processes and the building energy loads due to air infiltration and external convective heat transfers. Each part of the study provides intermediate results that can nonetheless be used as such in further applicative or research studies and projects.

At first, although not being an original scientific result, the state of the art synthesized in Part I draws attention to the necessity of - and provide valuable material to - reflecting on sustainable cities from a bio-climatic and transverse point of view. Indeed, city and construction's shapes directly impact on the outdoor thermal and wind comfort and building energy loads, which are critical sustainable development issues. As a consequence, this overview of the different urban physical phenomena and the related means and tools for study can be helpful to several construction and city actors.

Focusing on the scientific contribution of the work, the review of urban morphometric indicators highlights urban porosity and rugosity as key factors in determining the urban aerodynamic processes developing in the UCL. These morphological factors are related to the topological, geometrical and dimensional criteria that more generally characterize urban morphology. From an urban and building physics perspective, these relations are especially relevant to be studied on the urban block scale. Hence, two generic typologies of five urban morphological types are designed mainly based on topological criteria: one of isolated buildings and one of urban blocks. The cube, the cuboid, the L the U and the patio compose the isolated building typology. The cube array, the row block, the U block, the enclosed block and the continuous patio array compose the urban block typology. These typologies are composed of regular and orthogonal forms to keep their genericity. They allow a wide scope of use, a high level of representativeness and detailed studies. The complexity of each type could be further increased in terms of relative dimensions, obstacles height, arrangement of building groups and overall geometrical complexity.

Numerical (CFD) experiments are performed to study the mean flow structures that develop according to the morphological properties of the different types. Considering an isolated obstacle configuration, the validation study stresses that the use of the steady RANS RSM yields better prediction of the wake recirculation than the  $Rk-\epsilon$  does, while flows predicted by the latter model are closer to the experiment in the obstacle vicinity (A1-1 case). Considering a multi-obstacle configuration, the RSM reproduces the experimental vortex in the canyon, yet imperfectly, which is not achieved when using the  $Rk-\epsilon$  model (B1-1 case). Moreover, RSM-based predictions fairly match LBM LES results. Therefore, accounting for turbulence anisotropy appears beneficial when aiming to study the recirculation phenomena in complex configurations using a steady RANS approach, although simulation converges hardlier with the RSM especially when flows experience strong fluctuations.

The 3D post-processing of the actual CFD simulations stresses substantial effects of the building topology, relative dimensions and surrounding built environment on the development of recirculation phenomena within the UCL. Well-known main flow structures generally develop around buildings and groups of buildings, but semi-open courtyards and the porosity of built structures significantly alter them. In addition, relatively isolated recirculation phenomena develop within almost enclosed courtyards and clear flow paths develop in sufficiently large alleys crossing built structures. These flows show different behaviors depending on the orientation of the alley with respect to the wind incidence. Border effects are also important especially in arrays. 3D momentum exchanges with external flows, such as, e.g., reattaching corner streams or the upwind top

separated bubble, substantially affect the development of internal flow structures. This prevents self-similar flow structures to develop in cases on insufficiently wide (and homogeneous) built environments and induces complex 3D flows.

The different flow structures that develop around constructions involve heterogeneous pressure conditions on buildings facades. Faces directly exposed to the undisturbed incident flow experience high  $C_p$  intensities while separated zones are characterized by very low (negative)  $C_p$  intensities. High  $C_p$  gradients occur on the faces where flow separates and reattaches, especially on the roof of buildings. Large recirculation phenomena yield a relatively homogeneous distribution of low intensity  $C_p$ , especially in the wake of buildings. Pressure conditions in enclosed courtyards appear directly related to the pressure conditions above. Therefore, very low  $C_p$  characterizes courts that are located directly under a top separated bubble.

These particular pressure conditions impact on air infiltration through the building envelope. Their relative effect is particularly important for insulated buildings. According to simulation, switching from open to sheltered conditions, e.g. inside an almost enclosed courtyard or behind a built mask, substantially decreases the energy demand due to infiltration. In particular, switching from an exposed to a sheltered building may decrease its energy needs per surface unit of floor due to air infiltration through walls by 78 % up to 85 %. Non considering specific pressure conditions but standard values instead, these relative effects are estimated to be of about 25 %.

Local aerodynamic conditions also impact on the building energy balance because of the convective heat transfers they induce at outer walls, which can be estimated more accurately than usual using CFD. With respect to experimental data, the RSM gives accurate predictions of  $h_{c,w}$  on the front and rear faces of isolated obstacles. However, usual standard wall-function generally fails to predict  $h_{c,w}$  satisfactorily at building outer walls. As a consequence, the customized temperature wall-function designed by Defraeye et al. (2011a) for steady RANS  $k-\varepsilon$  model and forced convection was adapted to the RSM. Modifying the  $Pr_{t,w}$  from 0.85 (standard temperature wall-function) or 1.95 (customized temperature wall-function) to 1.55 (revised customized temperature wall-function for the RSM) induces satisfactory  $h_{c,w}$  predictions compared to LRNM data, including for high  $z^*$  values.

Building external convective heat exchanges are strongly correlated to the flow field around them, which depends itself on the building shape and surroundings. On the one hand, high  $h_{c,w}$  occur in flow impinging zones and high flow speed regions. On the other hand, low  $h_{c,w}$  characterize large recirculation areas, especially within enclosed courtyards and the wake of obstacles. As a consequence high  $h_{c,w}$  gradients occur on the windward faces of buildings that are located in an array. Their bottom part is characterized with low  $h_{c,w}$  because of recirculation phenomena, while their top part is characterized with high  $h_{c,w}$  because of the above impinging flow.

The effects of the external convective heat transfers on the building energy balance are almost negligible for well-insulated buildings. However, the effects of external convection on the building energy needs are not negligible for non-insulated buildings. Considering the surface of envelope constant, the relative contribution of heat transmission to the building energy needs is

less sensitive to a modification of the built structure than is the relative contribution of infiltration. Switching from an exposed to a sheltered non-insulated building may decrease the energy needs per surface unit of floor due to heat transmission through walls by 7 %. This decrease is not foreseen when using standard  $h_{c,w}$  values, as constant and high  $h_{c,w}$  values are generally assumed disregarding the building surrounding aerodynamic conditions.

Hence, the evaluation of the impact of air infiltration and heat transmission through the envelope on the building energy balance highlights significant relative effects of the built morphology on the energy demand, especially for well-insulated buildings. Note that the building energy demand is strongly correlated to the surface of envelope to floor ratio. Considering this ratio constant, the morphology of the built structure has a higher relative impact on infiltration processes than on convective exchanges. The relative contribution of infiltration is not negligible for well-insulated buildings. Furthermore, results show the improvement brought by the use of specific values of  $C_p$  and  $h_{c,w}$  to estimate the building energy performance. Substantial deviation can occur between such predictions when based on the standard or simulated values, especially when addressing sheltered building configurations.

### **Perspectives and open problems**

The results of this thesis highlight the relevance of implementing an integrated and detailed approach of urban physics to better understand the building energy behavior. They could advantageously be extended to humidity transfer problems, natural ventilation and indoor air quality issues and even to the convective cooling of active systems integrated to building facades such as solar panels.

However, the methodology implemented in this exploratory study involves strong assumptions. In particular, this thesis only addresses generic case studies with smooth and homogeneous walls. It also considers one typical wind that is characterized by one direction, one profile speed and one low turbulence level; uses a steady RANS approach; and addresses forced convection. Increasing the complexity of the environmental parameters, geometric model and the modeled physics to come closer to reality would provide results that would be more directly applicable. Nonetheless, the generalization of such an approach using usual CFD tools requires substantial computational resources. In addition, the turbulence modeling remains problematic. To study accurately building physics problems, more detailed computational methods are necessary. However, they require even more computational resources.

To tackle these challenges, recently developed models and computational techniques as well as dedicated full-scale experiments appear promising. On the one hand, the development and use of cost effective and more detailed computational approaches would allow for a large development of such an approach, and would provide a better understanding of the urban air and heat fluxes. On the other hand, dedicated full-scale experiments would provide the necessary and fundamental knowledge to further study urban outdoor thermal and aerodynamic conditions as well as the building energy behavior.

Furthermore, this thesis calls into question usual trends of building engineering and urban planning, especially with respect to the relation between buildings and their environment and more generally the bio-climatic design. Indeed, urban forms yield particular aerodynamic and thermal conditions that are more or less adapted to specific climates and usages. One morphological type would therefore not be optimal in every context, even if it represents economical achievement. Additionally, the more insulated and air tight the building is, the less energy it needs due to infiltration and heat transmission, which is generally considered as an objective. However, the more efficient the building envelope is (as usually understood), the less the building can benefit from its environment to naturally maintain comfortable and healthy indoor conditions, which is cost free and the very basis of the bio-climatic approach...

# Bibliography

- Acero, J. A., Arrizabalaga, J., Kupski, S., Katzschner, L., Jul. 2013. Deriving an urban climate map in coastal areas with complex terrain in the basque country (spain). *Urban Climate* 4, 35–60.
- ADEME, 2013a. Chiffres clés climat, air et énergie, 2013th Edition.
- ADEME, 2013b. Chiffres clés du bâtiment, énergie environnement.
- ADEME, 2015. La transition énergétique pour la croissance verte: isoler son logement (guide pratique).
- Adolphe, L., 2001a. Modeling the link between built environment and urban climate: towards simplified indicators of the city environment. In: *Actes IBPSA. Rio de Janeiro, Brazil*, pp. 679–684.
- Adolphe, L., 2001b. A simplified model of urban morphology: application to an analysis of the environmental performance of cities. *Environment and Planning B: Planning and Design* 28 (2), 183–200.
- Ai, Z., Mak, C., Oct. 2013. CFD simulation of flow and dispersion around an isolated building: Effect of inhomogeneous ABL and near-wall treatment. *Atmospheric Environment* 77, 568–578.
- Allegrini, J., Dorer, V., Carmeliet, J., 2012a. Analysis of convective heat transfer at building facades in street canyons and its influence on the predictions of space cooling demand in buildings. *Journal of Wind Engineering and Industrial Aerodynamics* 104-106, 464–473.
- Allegrini, J., Dorer, V., Carmeliet, J., 2012b. Influence of the urban microclimate in street canyons on the energy demand for space cooling and heating of buildings. *Energy and Buildings* 55, 823–832.
- Allegrini, J., Dorer, V., Carmeliet, J., 2013. Wind tunnel measurements of buoyant flows in street canyons. *Building and environment* 59, 315–326.
- Allegrini, J., Dorer, V., Carmeliet, J., 2015. Influence of morphologies on the microclimate in urban neighbourhoods (under review). *Journal of Wind Engineering and Industrial Aerodynamics*.
- Allegrini, J., Dorer, V., Defraeye, T., Carmeliet, J., 2012c. An adaptive temperature wall function for mixed convective flows at exterior surfaces of buildings in street canyons. *Building and Environment* 49, 55–66.
- Ansys Fluent, 2013a. Fluent release 14.5 theory guide.

- Ansys Fluent, 2013b. Fluent release 14.5 user guide.
- APUR, 2011. Analyse de la performance thermique des logements parisiens construits entre 1851 et 1914. Tech. rep.  
URL [http://www.apur.org/sites/default/files/documents/APAPU240\\_03.pdf](http://www.apur.org/sites/default/files/documents/APAPU240_03.pdf)
- APUR, 2012. Les ilots de chaleur a Paris. Tech. Rep. cahier 1, Atelier parisien d'urbanisme.
- ASHRAE, 2005. American Society of Heating, Refrigerating and Air-Conditioning Engineers (ASHRAE) Handbook: Fundamentals. American Society of Heating, Refrigerating, and Air-Conditioning Engineers.
- Athamena, K., 2012. Modélisation et simulation des microclimats urbains: étude de l'impact de la morphologie urbaine sur le confort dans les espaces extérieurs. cas des éco-quartiers. Ph.D. thesis, Ecole Centrale Nantes, Nantes, France.
- Barlow, J. F., Coceal, O., 2009. A review of urban roughness sublayer turbulence. Met Office Research and Development-Technical Report (527).
- Beranek, W., 1984a. Wind environment around building configurations. *Heron* 29, 33–70.
- Beranek, W., 1984b. Wind environment around single buildings of rectangular shape. *Heron* 29, 1–31.
- Blocken, B., 2012. Urban physics inaugural lecture.  
URL <http://alexandria.tue.nl/extra2/redes/blocken2012.pdf>
- Blocken, B., Oct. 2013. CFD in urban physics and urban wind energy - Urban Physics Autumn School (UPAS13).
- Blocken, B., 2014a. 50 years of computational wind engineering: Past, present and future. *Journal of Wind Engineering and Industrial Aerodynamics* 129, 69–102.
- Blocken, B., Jun. 2014b. Sports and buildings aerodynamics (MOOC).  
URL [Coursera.org](http://Coursera.org)
- Blocken, B., Carmeliet, J., 2004. Pedestrian wind environment around buildings: Literature review and practical examples. *Journal of Thermal Envelope and Building Science* 28 (2), 107–159.
- Blocken, B., Carmeliet, J., 2008. Pedestrian wind conditions at outdoor platforms in a high-rise apartment building: generic sub-configuration validation, wind comfort assessment and uncertainty issues. *Wind and Structures* 11 (1), 51–70.
- Blocken, B., Carmeliet, J., Stathopoulos, T., 2007a. CFD evaluation of wind speed conditions in passages between parallel buildings-effect of wall-function roughness modifications for the atmospheric boundary layer flow. *Journal of Wind Engineering and Industrial Aerodynamics* 95 (9-11), 941–962.

- Blocken, B., Defraeye, T., Derome, D., Carmeliet, J., 2009. High-resolution CFD simulations for forced convective heat transfer coefficients at the facade of a low-rise building. *Building and Environment* 44 (12), 2396–2412.
- Blocken, B., Gualtieri, C., 2012. Ten iterative steps for model development and evaluation applied to computational fluid dynamics for environmental fluid mechanics. *Environmental Modelling & Software* 33, 1–22.
- Blocken, B., Moonen, P., Stathopoulos, T., Carmeliet, J., 2008. Numerical study on the existence of the venturi effect in passages between perpendicular buildings. *Journal of engineering mechanics* 134 (12), 1021–1028.
- Blocken, B., Roels, S., Carmeliet, J., 2004. Modification of pedestrian wind comfort in the silvertop tower passages by an automatic control system. *Journal of Wind Engineering and Industrial Aerodynamics* 92 (10), 849–873.
- Blocken, B., Stathopoulos, T., 2013. CFD simulation of pedestrian-level wind conditions around buildings: Past achievements and prospects. *Journal of Wind Engineering and Industrial Aerodynamics* 121, 138–145.
- Blocken, B., Stathopoulos, T., Carmeliet, J., 2007b. CFD simulation of the atmospheric boundary layer: wall function problems. *Atmospheric Environment* 41 (2), 238–252.
- Bottema, M., 1999. Towards rules of thumb for wind comfort and air quality. *Atmospheric Environment* 33, 4009–4017.
- Bouyer, J., 2009. Modélisation et simulation des microclimats urbains: Etude de l'impact de l'aménagement urbain sur les consommations énergétiques des bâtiments. Ph.D. thesis, Université de Nantes, Nantes, France.
- Bouyer, J., Inard, C., Musy, M., 2011. Microclimatic coupling as a solution to improve building energy simulation in an urban context. *Energy and Buildings* 43 (7), 1549–1559.
- Bozonnet, E., 2006. Les microclimats urbains et la demande énergétique du bâti. XXIVe Rencontres Universitaires de Génie Civil.
- Britter, R. E., Hanna, S. R., 2003. Flow and dispersion in urban areas. *Annual revue of fluid mechanics* (35), 469–496.
- Brown, G., DeKay, M., 2000. Sun wind and light: architectural design strategies, 2nd Edition. John Wiley & Sons Inc.
- Burdet, E., 2011. Vers un modèle morphologique des tissus urbains. Tech. rep., Université de Marne la Vallée Paris Est, France.
- Carmeliet, J., 2015. Urban Physics Winter School (UPWS15).  
URL <http://www.carmeliet.arch.ethz.ch/Events/UP2015>



- Carpentieri, M., Robins, A. G., Jul. 2009. Wind tunnel experiments of flow and dispersion in a real urban area. In: The 7th international conference on urban climate. Yokohama, Japan.
- Carpentieri, M., Robins, A. G., Baldi, S., 2009. Three dimensional mapping of air flow at an urban canyon intersection. *Boundary layer meteorology* 133, 277–296.
- CEDVAL, 2013. Compilation of experimental data for validation of microscale dispersion models. URL [http://www.mi.uni-hamburg.de/CEDVAL\\_Validation\\_Data.427.0.html](http://www.mi.uni-hamburg.de/CEDVAL_Validation_Data.427.0.html)
- CEDVAL-LES, 2014. Compilation of experimental data for validation of LES-based numerical flow and dispersion models. URL <http://www.mi.uni-hamburg.de/CEDVAL-LES-V6332.0.html>
- CEREN, 2014. Données statistiques du centre d'études et de recherches économiques sur l'énergie. Tech. rep. URL <http://www.ceren.fr/publications/>
- Cheng, H., Castro, I. P., 2002. Near wall flow over urban-like roughness. *Boundary-Layer Meteorology* 104 (2), 229–259.
- Coccal, O., Goulart, E. V., Branford, S., Glyn Thomas, T., Belcher, S. E., 2014. Flow structure and near-field dispersion in arrays of building-like obstacles. *Journal of Wind Engineering and Industrial Aerodynamics* 125, 52–68.
- COST-Action, 732, 2007. Best practice guidelines for the CFD simulation of flows in the urban environment. In: Quality assurance and improvement of microscale meteorological models, COST office Edition. Jorg Franke, Antti Hellsten, Heinke Schlunzen, Bertrand Carissimo.
- Costola, D., Blocken, B., Ohba, M., Hensen, J., 2010. Uncertainty in airflow rate calculations due to the use of surface-averaged pressure coefficients. *Energy and Buildings* 42 (6), 881–888.
- CSTB, 2012a. Annexe à l'arrêté portant approbation de la méthode de calcul Th-BCE 2012: Méthode de calcul Th-BCE 2012. Tech. rep.
- CSTB, 2012b. RT2012: Règles Th-U, fascicule 4 parois opaques. Tech. rep.
- DAPPLE, 2002-2010. Dispersion of air pollution and its penetration into the local environment. URL <http://www.dapple.org.uk/index.html>
- Defraeye, T., 2009. LRNM-based convective heat transfer coefficients on the windward and leeward faces of a 10 m cubical building.
- Defraeye, T., Blocken, B., Carmeliet, J., 2010. CFD analysis of convective heat transfer at the surfaces of a cube immersed in a turbulent boundary layer. *International Journal of Heat and Mass Transfer* 53 (1-3), 297–308.
- Defraeye, T., Blocken, B., Carmeliet, J., 2011a. An adjusted temperature wall function for turbulent forced convective heat transfer for bluff bodies in the atmospheric boundary layer. *Building and Environment* 46 (11), 2130–2141.

- Defraeye, T., Blocken, B., Carmeliet, J., 2011b. Convective heat transfer coefficients for exterior building surfaces: Existing correlations and CFD modelling. *Energy Conversion and Management* 52 (1), 512–522.
- Defraeye, T., Blocken, B., Carmeliet, J., May 2012. CFD simulation of heat transfer at surfaces of bluff bodies in turbulent boundary layers: Evaluation of a forced-convective temperature wall function for mixed convection. *Journal of Wind Engineering and Industrial Aerodynamics* 104-106, 439–446.
- European-Comission, 2014. The 2020 climate and energy package.  
URL [http://ec.europa.eu/clima/policies/package/index\\_en.htm](http://ec.europa.eu/clima/policies/package/index_en.htm)
- European Union, 2011. Energy efficiency plan 2011.  
URL [http://europa.eu/legislation\\_summaries/energy/energy\\_efficiency/en0029\\_en.htm](http://europa.eu/legislation_summaries/energy/energy_efficiency/en0029_en.htm)
- Firley, E., Stahl, C., 2010. The urban housing handbook. John Wiley & Sons.
- Franke, J., 2006. Recommendations of the COST action C14 on the use of CFD in predicting pedestrian wind environment. In: The fourth international symposium on computational wind engineering. Yokohama, Japan, pp. 529–532.
- Gandemer, J., 1975. Inconfort du au vent aux abords des batiments: étude aerodynamique du champ de vitesse dans les ensembles batis, étude complementaire. CSTB.
- Gandemer, J., 1976. Intégration du phénomène vent dans la conception du milieu bâti: guide méthodologique et conseils pratiques. Ministère de l'équipement, Direction de l'aménagement foncier et de l'urbanisme : diffusion, La documentation française.
- GIEC, 2013. Changements climatiques 2013: les éléments scientifiques, résumé a l'intention des décideurs. Tech. rep., OMM, PNUE.
- Givoni, B., 1998. Climate considerations in building and urban design. John Wiley & Sons Inc.
- Golany, G. S., 1996. Urban design morphology and thermal performance. *Atmospheric Environment* 30 (3), 455–465.
- Gorlé, C., Rambaud, P., van Beeck, J., 2010. Large eddy simulation of flow and dispersion in the wake of a rectangular building. In: CWE 2010. USA.
- Gorlé, C., van Beeck, J., Rambaud, P., Van Tendeloo, G., 2009. CFD modelling of small particle dispersion: The influence of the turbulence kinetic energy in the atmospheric boundary layer. *Atmospheric Environment* 43 (3), 673–681.
- Gousseau, P., Blocken, B., Stathopoulos, T., Van Heijst, G. J. F., 2011. CFD simulation of near-field pollutant dispersion on a high-resolution grid: a case study by LES and RANS for a building group in downtown montreal. *Atmospheric Environment* 45 (2), 428–438.
- Grimmond, C., Oke, T. R., 1999. Aerodynamic properties of urban areas derived from analysis of surface form. *Journal of applied meteorology* 38, 1262–1292.

- Groleau, D., Marenne, C., 1995. Environmental specificities of the urban built forms. In: Rebuild–Rebuilding the European city - Integration of Renewable energies in established urban structures European conference. Corfu, Greece.
- Hermosilla, T., Palomar-Vazquez, J., Balaguer-Beser, A., Balsa-Barreiro, J., Ruiz, L. A., 2014. Using street based metrics to characterize urban typologies. *Computers, Environment and Urban Systems* 44, 68–79.
- Hooff, T. v., Blocken, B., 2010. On the effect of wind direction and urban surroundings on natural ventilation of a large semi-enclosed stadium. *Computers & Fluids* 39 (7), 1146–1155.
- Hu, T., Yoshie, R., Jan. 2013. Indices to evaluate ventilation efficiency in newly-built urban area at pedestrian level. *Journal of Wind Engineering and Industrial Aerodynamics* 112, 39–51.
- Huang, Y., 2010. Methodology of climatic design of urban district for buildings energy efficiency. Ph.D. thesis, Université de Nantes, école centrale Nantes, Nantes, France.
- Huang, Y., Musy, M., Hégron, G., Chen, H., Li, B., 2008. Factors of urban forms that impact building energy consumption. In: *Proceedings of the World Renewable Energy Congress WREC*.
- IEA, 2010. Final energy consumption by sector, 2010.  
URL [www.iea.org](http://www.iea.org)
- INSEE, 2012. Evolution de la population dans le monde jusqu'en 2013.  
URL [http://www.insee.fr/fr/themes/tableau.asp?reg\\_id=98&ref\\_id=CMPTEF02153](http://www.insee.fr/fr/themes/tableau.asp?reg_id=98&ref_id=CMPTEF02153)
- IPCC, 2007. Bilan 2007 des changements climatiques - rapport de synthèse, contribution des groupes de travail I, II et III au quatrième rapport d'évaluation du groupe d'experts intergouvernemental sur l'évolution du climat. Tech. rep., Groupe d'experts intergouvernemental sur l'évolution du climat.
- JU2003, 2003. Joint urban 2003.  
URL <http://www.noaa.inel.gov/projects/ju03/ju03.htm>
- Kastner-Klein, P., Berkowicz, R., Britter, R., 2004. The influence of street architecture on flow and dispersion in street canyons. *Meteorology and Atmospheric Physics* 87 (1-3).
- Kastner Klein, P., Rotach, M. W., Fedorovich, E., Aug. 2000. Experimental study on mean flow and turbulence characteristics in an urban roughness sublayer. In: *Proceedings 14th Symp. on boundary layer and turbulence*. Colorado, USA, pp. 306–309.
- Khanduri, A., Stathopoulos, T., Bédard, C., 1998. Wind induced interference effects on buildings - a review of the state-of-the-art. *Engineering structures* 20 (7), 617–630.
- Kovar-Panskus, A., Moulinneuf, L., Savory, E., Abdelqari, A., Sini, J.-F., Rosant, J.-M., Robins, A., Toy, N., 2002. A wind tunnel investigation of the influence of solar-induced wall-heating on the flow regime within a simulated urban street canyon. *Water, Air and Soil Pollution: Focus* 2 (5-6), 555–571.

Larousse, 2014. Bioclimatique - definition.

URL <http://www.larousse.fr/dictionnaires/francais/bioclimatique/9396?q=bioclimatique#9301>

Lateb, M., Masson, C., Stathopoulos, T., Bédard, C., Aug. 2010. Numerical simulation of pollutant dispersion around a building complex. *Building and Environment* 45 (8), 1788–1798.

Launder, B., D.B., S., 1974. The numerical computation of turbulent flows. *Computer Methods in Applied Mechanics and Engineering* 3, 269–289.

Leitl, B., 2000. Validation data for microscale dispersion modeling. *EUROTRAC Newsletter* (22), 28–32.

Leitl, B., Schatzmann, M., 2005. Generation of wind tunnel data sets in support of the Joint Urban 2003: final report phase II. Tech. rep., Meteorological Institute of Hamburg.

Lesieur, M., 1994. La turbulence. Collection Grenoble sciences. EDP Sciences.

Lévy, A., 2005. Formes urbaines et significations: revisiter la morphologie urbaine. *Espaces et sociétés* (4), 25–48.

Liu, J., Heidarinejad, M., Gracik, S., Srebric, J., 2015. The impact of exterior surface convective heat transfer coefficients on the building energy consumption in urban neighborhoods with different plan area densities. *Energy and Buildings*.

Maizia, M., Feb. 2010. Quand la ville se met au vert - interview: “il faut passer du quartier exceptionnel à toute la collectivité”. *Sciences et avenir - hors série* 161.

Matinuzzi, R., Tropea, C., 1993. The flow around surface-mounted, prismatic obstacles placed in fully developed channel flow. *Journal of fluids engineering* 115, 85–92.

MEEDDEM, Oct. 2010. Arrêté du 26 octobre 2010 relatif aux caractéristiques thermiques et aux exigences de performance énergétique des bâtiments nouveaux et des parties nouvelles de bâtiments.

MEEDDM, 2010. Réglementation thermique “ Grenelle Environnement 2012 ”.

URL [http://www.rt-batiment.fr/fileadmin/documents/RT2012/06\\_07\\_2010\\_-\\_generalisation\\_des\\_batiments\\_a\\_basse\\_consommation.pdf](http://www.rt-batiment.fr/fileadmin/documents/RT2012/06_07_2010_-_generalisation_des_batiments_a_basse_consommation.pdf)

Meinders, E., Hanjalic, K., 1999. Vortex structure and heat transfer in turbulent flow over a wall mounted matrix of cubes. *International journal of heat and fluid flow* (20), 255–267.

Meinders, E., Hanjalic, K., Martinuzzi, R., 1999. Experimental study of the local convection heat transfer from a wall mounted cube in turbulent channel flow. *Journal of heat transfer* 121, 564–573.

Memon, R. A., Leung, D. Y., Liu, C.-H., 2009. An investigation of urban heat island intensity (UHII) as an indicator of urban heating. *Atmospheric Research* 94 (3), 491–500.

- Meroney, R., Leitl, B. M., Rafailidis, S., Schatzmann, M., 1999. Wind-tunnel and numerical modeling of flow and dispersion about several building shapes. *Journal of Wind Engineering and Industrial Aerodynamics* 81 (1), 333–345.
- Meteorological Institute of Hamburg, 2013. Environmental wind tunnel laboratory, BLASIUS wind tunnel.  
URL <http://www.mi.uni-hamburg.de/BLASIUS-wind.425.0.html>
- Mirsadeghi, M., Costola, D., Blocken, B., Hensen, J., 2013. Review of external convective heat transfer coefficient models in building energy simulation programs: Implementation and uncertainty. *Applied Thermal Engineering* 56 (1-2), 134–151.
- Moonen, P., Oct. 2013. Wind tunnel research - Urban Physics Autumn School (UPAS13).
- Moonen, P., Defraeye, T., Dorer, V., Blocken, B., Carmeliet, J., 2012a. Urban physics: Effect of the micro-climate on comfort, health and energy demand. *Frontiers of Architectural Research* 1 (3), 197–228.
- Moonen, P., Dorer, V., Carmeliet, J., 2011. Evaluation of the ventilation potential of courtyards and urban street canyons using RANS and LES. *Journal of Wind Engineering and Industrial Aerodynamics* 99 (4), 414–423.
- Moonen, P., Dorer, V., Carmeliet, J., 2012b. Effect of flow unsteadiness on the mean wind flow pattern in an idealized urban environment. *Journal of Wind Engineering and Industrial Aerodynamics* 104-106, 389–396.
- Neophytou, M., Jan. 2015. Urban micro-climate and breathability - Urban Physics Winter School (UPWS15).
- Obrecht, C., 2012. High performance lattice boltzmann solvers on massively parallel architectures with applications to building aerodynamics. Ph.D. thesis, INSA de Lyon, Lyon, France.
- Obrecht, C., Kuznik, F., Merlier, L., Roux, J.-J., Tourancheau, B., 2014. Towards aerodynamic simulations at urban scale using the lattice boltzmann method. *Environmental Fluid Mechanics*.
- Obrecht, C., Kuznik, F., Tourancheau, B., Roux, J.-J., 2011a. A new approach to the lattice boltzmann method for graphics processing units. *Computers & Mathematics with Applications* 61 (12), 3628–3638.
- Obrecht, C., Kuznik, F., Tourancheau, B., Roux, J.-J., 2013. Multi-GPU implementation of the lattice boltzmann method. *Computers & Mathematics with Applications* 65 (2), 252–261.
- Obrecht, C., Kuznik, F., Tourancheau, B., Roux, J.-J., others, 2011b. Towards urban-scale flow simulations using the lattice boltzmann method. In: *Journal of Building Performance Simulation*. pp. 933–940.
- Oke, T., 1987. *Boundary layer climates*, 2nd Edition. Routledge.
- Oke, T., 1988. Street design and urban canopy layer climate. *Energy and Buildings* (11), 103–113.

- Oke, T. R., 2006a. Initial guidance to obtain representative meteorological observations at urban sites. Tech. Rep. 81, World meteorological organization.
- Oke, T. R., 2006b. Towards better scientific communication in urban climate. *Theoretical and Applied Climatology* 84 (1-3), 179–190.
- Panagiotou, I., Neophytou, M. K.-A., Hamlyn, D., Britter, R. E., 2013. City breathability as quantified by the exchange velocity and its spatial variation in real inhomogeneous urban geometries: An example from central London urban area. *Science of the Total Environment* 442, 466–477.
- Panerai, P., Castex, J., Depaule, J. C., 2006. *Formes urbaines: de l'ilot a la barre, parentheses Edition*. Eupalinos.
- Parente, A., Gorié, C., Beeck, J., Benocci, C., 2011. A comprehensive modelling approach for the neutral atmospheric boundary layer: Consistent inflow conditions, wall function and turbulence model. *Boundary-Layer Meteorology* 140 (3), 411–428.
- Peterka, J., Meroney, R., Kothari, K., 1985. Win flow patterns about buildings. *Journal of wind engineering and industrial aerodynamics* 21, 21–38.
- Ramponi, R., Oct. 2013. Thermal comfort in the urban environment - Urban Physics Autumn School (UPAS13).
- Ramponi, R., Blocken, B., 2012. A computational study on the influence of urban morphology on wind-induced outdoor ventilation. In: *iEMSs International congress on Environmental Modeling and Software*. R. Seppelt, A.A. Voinov, S. Lange, D. Bankamp, Germany.
- Rasheed, A., 2009. Multiscale modeling of urban climate. Ph.D. thesis, EPFL, Lausanne, Switzerland.
- Ratti, C., Baker, N., Steemers, K., 2005. Energy consumption and urban texture. *Energy and Buildings* 37 (7), 762–776.
- Ratti, C., Di Sabatino, S., Britter, R., 2006. Urban texture analysis with image processing techniques: winds and dispersion. *Theoretical and Applied Climatology* 84 (1-3), 77–90.
- Ratti, C., Raydan, D., Steemers, K., 2003. Building form and environmental performance archetypes, analysis and an arid climate. *Energy and Buildings* (35), 46–59.
- Richards, P., Hoxey, R. P., 1993. Appropriate boundary conditions for computational wind engineering models using the  $k-\epsilon$  turbulence model. *Journal of Wind Engineering and Industrial Aerodynamics* (46-47), 145–153.
- Richards, P., Norris, S., 2011. Appropriate boundary conditions for computational wind engineering models revisited. *Journal of Wind Engineering and Industrial Aerodynamics* 99 (4), 257–266.
- Robinson, D., 2006. Urban morphology and indicators of radiation availability. *Solar Energy* 80 (12), 1643–1648.

- Robinson, D., 2011. Computer modelling for sustainable urban design: physical principles, methods and applications. Earthscan Ltd.
- Rogers, R., 2000. Villes durables pour une petite planète. Le moniteur editions.
- Sagaut, P., Deck, S., Terracol, M., 2013. Multiscale and Multiresolution Approaches in Turbulence, second edition. Imperial College Press.
- Salat, S., 2011. Cities and Forms: On sustainable Urbanism, Hermann Edition. CSTB.
- Santamouris, M., 2014. On the energy impact of urban heat island and global warming on buildings. *Energy and Buildings* 82, 100–113.
- Schatzmann, M., Leidl, B., 2011. Issues with validation of urban flow and dispersion CFD models. *Journal of Wind Engineering and Industrial Aerodynamics* 99 (4), 169–186.
- Scherer, D., Fehrenbach, U., Beha, H., Parlow, E., 1999. Improved concepts and methods in analysis and evaluation of the urban climate for optimizing urban planning processes. *Atmospheric Environment* 33 (24), 4185–4193.
- Schlünzen, K. H., Grawe, D., Bohnenstengel, S. I., Schlüter, I., Koppmann, R., 2011. Joint modelling of obstacle induced and mesoscale changes: Current limits and challenges. *Journal of Wind Engineering and Industrial Aerodynamics* 99 (4), 217 – 225, the Fifth International Symposium on Computational Wind Engineering.
- Seeta Ratnam, G., Vengadesan, S., 2008. Performance of two equation turbulence models for prediction of flow and heat transfer over a wall mounted cube. *International Journal of Heat and Mass Transfer* 51 (11-12), 2834–2846.
- Stathopoulos, T., 2006. Pedestrian level winds and outdoor human comfort. *Journal of Wind Engineering and Industrial Aerodynamics* 94 (11), 769–780.
- Steemers, K., Baker, N., Crowther, D., Dubiel, J., Nikolopoulou, M.-H., Ratti, C., 1997. City texture and microclimate. *Urban Design Studies* 3, 25–50.
- Steemers, K., Ramos, M., Sinou, M., 2004. Concevoir des espaces extérieurs en environnement urbain: une approche bioclimatique - Morphologie urbaine, RUROS project - rediscovering the urban realm and open spaces Edition. Energy environemnt and sustainable development porgramme, key action 4: City of tomorrow and cultural heritage.
- Stewart, I. D., Oke, T. R., 2012. Local climate zones for urban temperature studies. *Bulletin of the American Meteorological Society* 93 (12), 1879–1900.
- Theurer, W., 1999. Typical building arrangements for urban air pollution modelling. *Atmospheric Environment* (33), 4057–4066.
- Tominaga, Y., Mochida, A., Yoshie, R., Kataoka, H., Nozu, T., Yoshikawa, M., Shirasawa, T., 2008. AIJ guidelines for practical applications of CFD to pedestrian wind environment around buildings. *Journal of Wind Engineering and Industrial Aerodynamics* 96 (10-11), 1749–1761.

- Tominaga, Y., Stathopoulos, T., 2010. Numerical simulation of dispersion around an isolated cubic building: Model evaluation of RANS and LES. *Building and Environment* 45 (10), 2231–2239.
- Tominaga, Y., Stathopoulos, T., 2011. CFD modeling of pollution dispersion in a street canyon: Comparison between LES and RANS. *Journal of Wind Engineering and Industrial Aerodynamics* 99 (4), 340–348.
- TPU, 2003. Wind tunnel database based on wind tunnel experiment (tokyo polytechnic university). URL <http://wind.arch.t-kougei.ac.jp/system/eng/contents/code/tpu>
- WHO, GHO, 2013. Urban population growth.  
URL [http://www.who.int/gho/urban\\_health/situation\\_trends/urban\\_population\\_growth\\_text/en/](http://www.who.int/gho/urban_health/situation_trends/urban_population_growth_text/en/)
- Wieringa, J., Davenport, A. G., Grimmond, C., Oke, T. R., 2001. New revision of davenport roughness classification. In: 3rd European and African Conference on Wind Engineering. Eindhoven, Netherlands.
- Yang, Y., Gu, M., Chen, S., Jin, X., 2009. New inflow boundary conditions for modelling the neutral equilibrium atmospheric boundary layer in computational wind engineering. *Journal of Wind Engineering and Industrial Aerodynamics* 97 (2), 88–95.
- Yoshie, R., Mochida, A., Tominaga, Y., Kataoka, H., Harimoto, K., Nozu, T., Shirasawa, T., 2007. Cooperative project for CFD prediction of pedestrian wind environment in the architectural institute of japan. *Journal of Wind Engineering and Industrial Aerodynamics* 95 (9-11), 1551–1578.





# Appendices



# Appendices of Part 1

## Contents

---

<b>A</b>	<b>Classification of the terrain categories - power law profile . . . . .</b>	<b>A. 2</b>
<b>B</b>	<b>Urban morphological properties and urban flow regimes . . . . .</b>	<b>A. 3</b>
<b>C</b>	<b>Properties of the scales related to urban physics . . . . .</b>	<b>A. 4</b>
<b>D</b>	<b>Overview of the archetypes used in urban physics . . . . .</b>	<b>A. 5</b>
D.1	Archetypes of street canyons . . . . .	A. 5
D.2	Urban archetypes based on pavilions, terraces and courts . . . . .	A. 5
D.3	Typical building arrangements for the study of street level dispersion processes	A. 6
<b>E</b>	<b>Local climate zones . . . . .</b>	<b>A. 7</b>
<b>F</b>	<b>Formulae of the urban morpho-metric indicators . . . . .</b>	<b>A. 8</b>
F.1	UMMIs principally related to the openness of urban structures toward the sun, the sky and the atmosphere . . . . .	A. 8
F.2	UMMIs mostly related to unbuilt volumes and urban roughness, addressing aerodynamic issues . . . . .	A. 9
F.3	UMMIs mainly related to the architectural properties of buildings and their interface with the outdoors . . . . .	A. 11

---

## A Classification of the terrain categories - power law profile

Similarly to the Davenport's classification, a classification of terrains with the corresponding power law exponent  $\alpha$  exists. Only four types of terrain are distinguished here and the order of the different categories goes from the roughest to the smoothest landscapes.

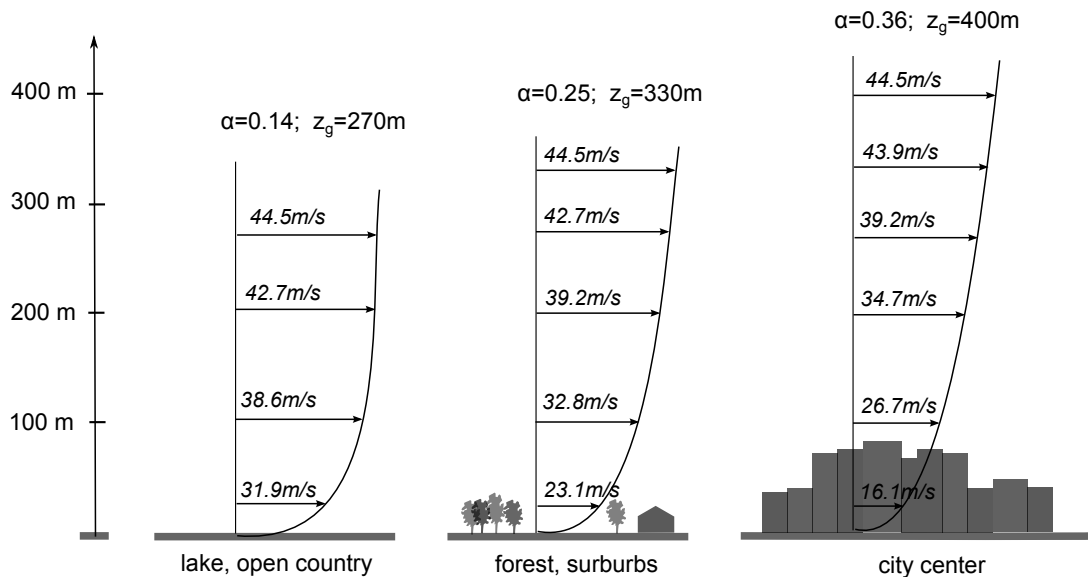


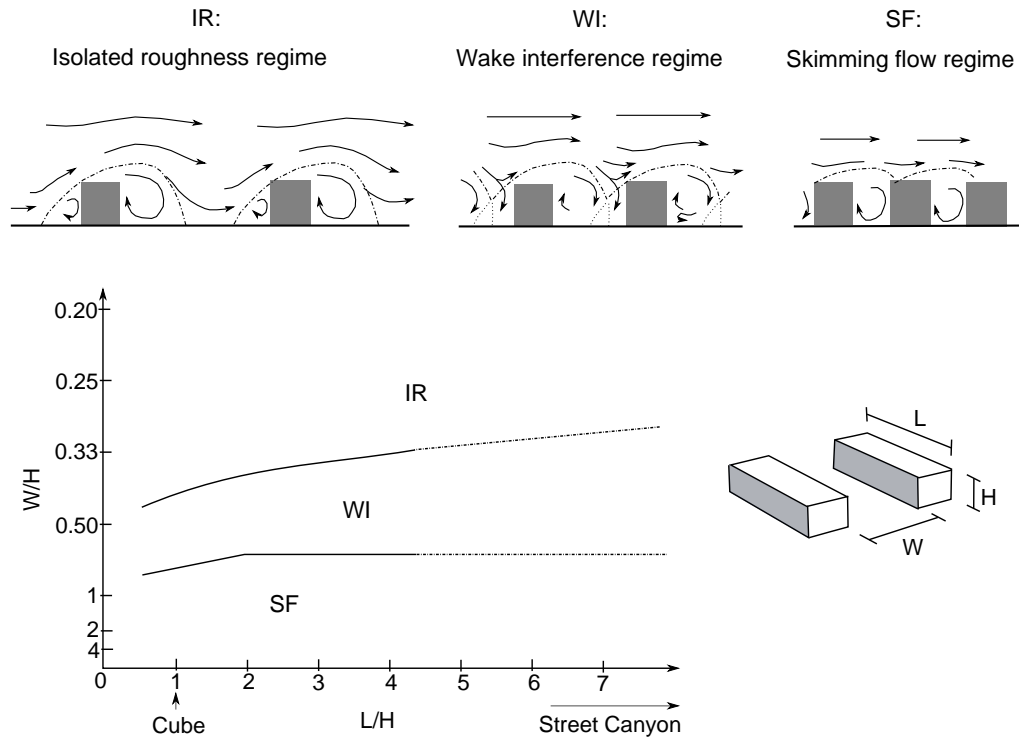
Figure a.1: Wind profiles depending on the landscape. (Based on (Gandemer, 1976).)

Category	$\alpha$ (-)	$\delta$ (m)	Landscape description
1.	0.33	460	Large city centers, in which at least 50% of buildings are higher than 25 m, over a distance of at least 0.8 km or ten times the height of the structure upwind, whichever is greater.
2.	0.22	370	Urban and suburban areas, wooded areas, or other terrain with numerous closely spaced obstructions having the size of single family dwellings or larger, over a distance of at least 460 m or ten times the height of the structure upwind, whichever is greater.
3.	0.14	270	Open terrain with scattered obstructions having heights generally less than 9 m, including flat open country typical of meteorological station surroundings.
4.	0.10	210	Flat, unobstructed areas exposed to wind flowing over water for at least 1.6 km, over a distance of 460 m or ten times the height of the structure inland, whichever is greater.

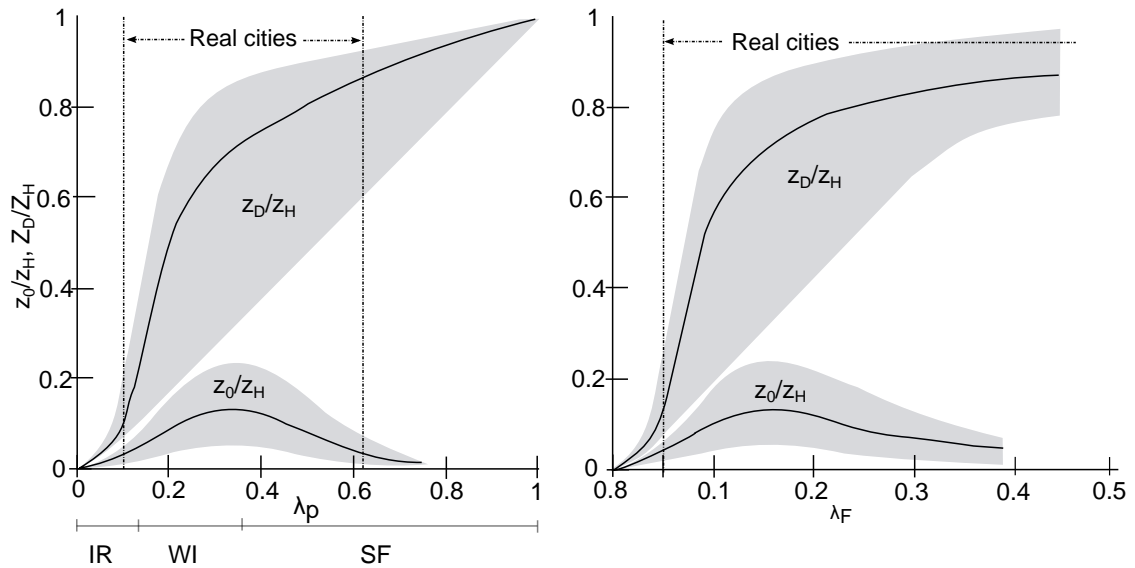
Table a.1: Atmospheric boundary layer parameters and power law. (Adapted from (ASHRAE, 2005))

$\alpha$ : power law exponent corresponding to the terrain category,  $\delta$ : layer thickness.

## B Urban morphological properties and urban flow regimes



(a) Urban flow regimes in canyons. (Based on (Oke, 1988))



(b) Urban surface parameters depending on the plot and front area ratios. (Based on (Grimmond and Oke, 1999))

Figure a.2: Urban morphological properties and urban flow regimes. (Based on (Grimmond and Oke, 1999; Oke, 1988))

## C Properties of the scales related to urban physics

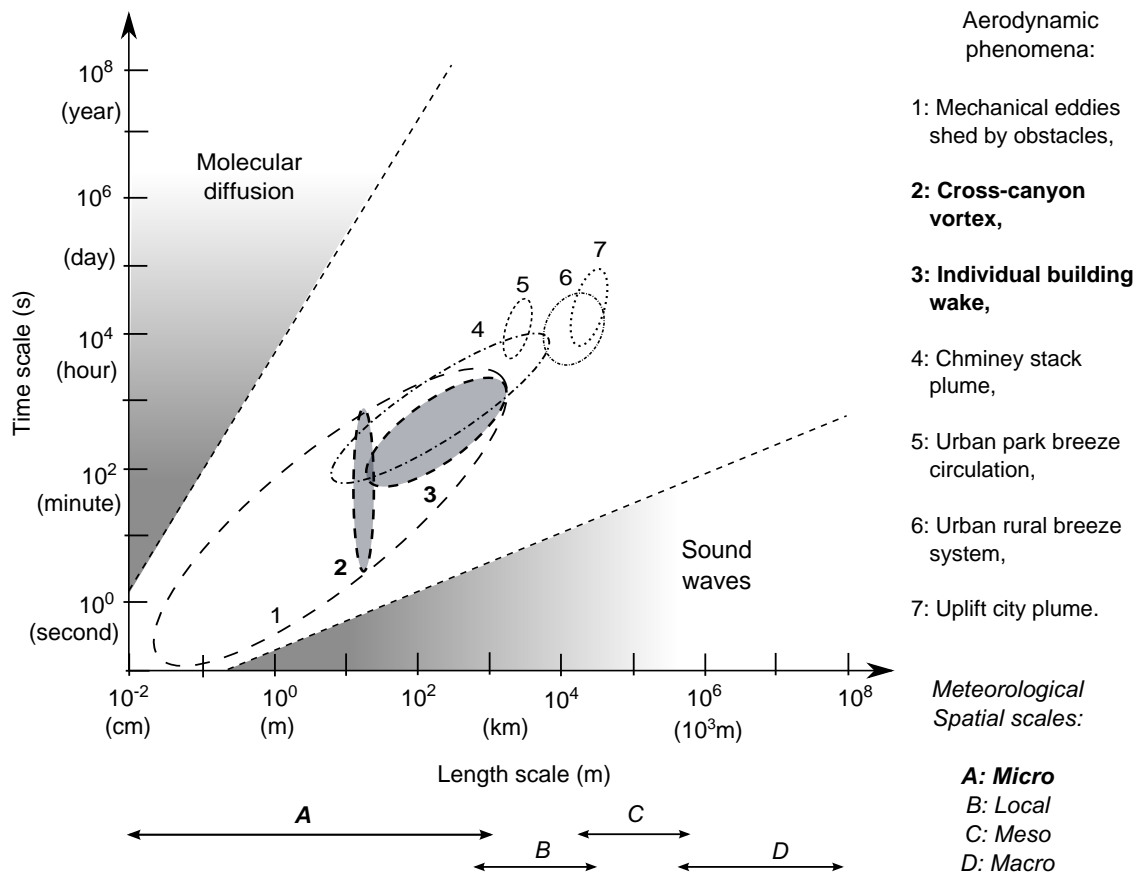


Figure a.3: Spatial and temporal scales of the different aerodynamic phenomena related to urban physics. (From (Oke, 2006b))

Name of layer	Typical dimension	Scaling parameter	Spatial scale
UBL-UCL	$\sim 10^1$ m	$z_H, D, L$	Micro
UBL-RSL	$\sim 10^1$ m	$z_H, D, L$	Micro
UBL-ISL	$\sim 10^2$ m	$z, D, u^*, \theta^*$	Local
Outer UBL	$\sim 10^3$ m	$z, D, W^*, T^*$	Meso
UCL unit	Typical length (horiz.)	Built features	Climatic scale
Building	$\sim 10 \times 10$ m <sup>2</sup>	Building	Micro $\gamma$
Canyon	$\sim 30 \times 40$ m <sup>2</sup>	Street, canyon	Micro $\beta$
Block	$\sim 500 \times 500$ m <sup>2</sup>	Block, factory	Micro $\alpha$
UTZ, UCL, LCZ (App. E)	$\sim 5 \times 5$ km <sup>2</sup>	City center, residential or industrial zone	Meso $\gamma$ (local)
City	$\sim 25 \times 25$ km <sup>2</sup>	Urban area	Meso $\beta$
Urban environment	$\sim 100 \times 100$ km <sup>2</sup>	City + surroundings	Meso $\alpha$

Table a.2: Detailed spatial scales of the UCL. (From (Oke, 2006b))

## D Overview of the archetypes used in urban physics

### D.1 Archetypes of street canyons

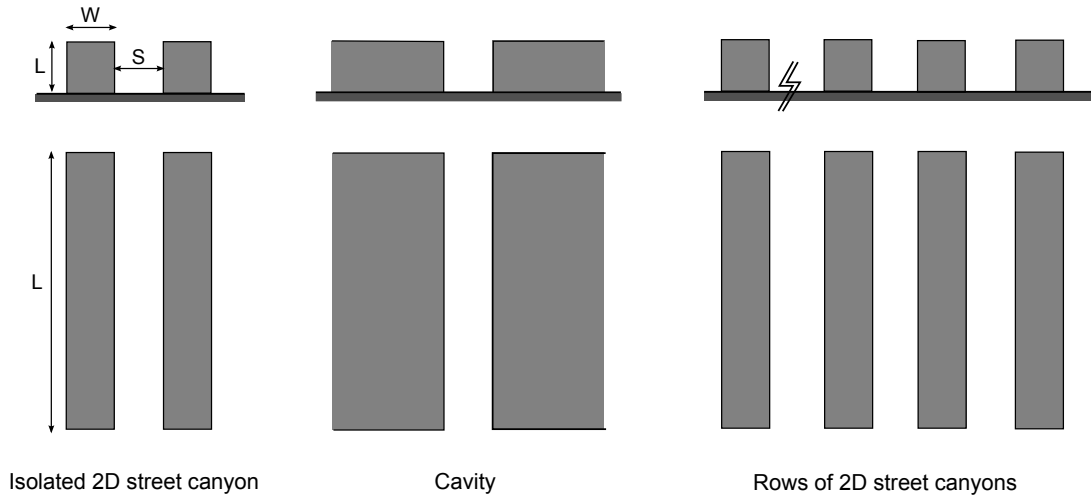


Figure a.4: Different types street canyons. (From ([Kastner-Klein et al., 2004](#)))

### D.2 Urban archetypes based on pavilions, terraces and courts

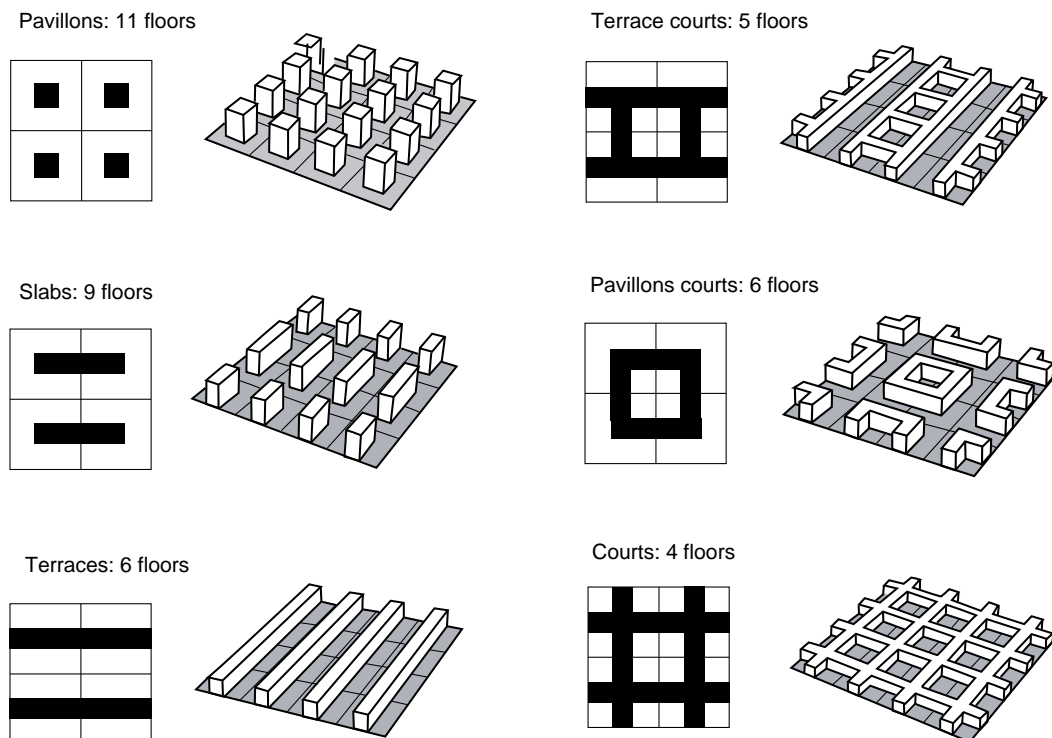


Figure a.5: Urban archetypes based on pavilions, terraces and courts. (From ([Steemers et al., 1997](#)))



### D.3 Typical building arrangements for the study of street level dispersion processes










	Illustration	Description
1		Single or double family buildings; 1 to 2 stories
2		Dense urban development, Residential and commercial; 1 to 3 stories
3		Building rows, building blocks; 2 to 4 stories
4		Block edge buildings; 2 to 4 stories
5		City centers
6		Commercial areas
7		Industrial areas
8		Green areas with few trees
9		Parks with trees, forest areas

Table a.3: Typical building arrangements for the study of street level dispersion processes. (From (Theurer, 1999))

## E Local climate zones

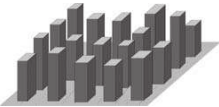
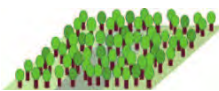


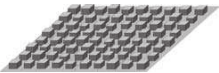
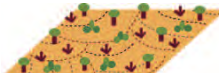
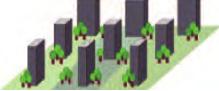



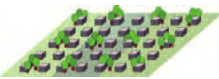
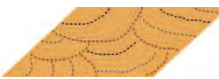
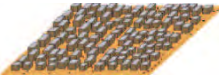




Built types	Definition	Land cover types	Definition
1. Compact high-rise 	Dense mix of tall buildings to tens of stories. Few or no trees. Land cover mostly paved. Concrete, steel, stone, and glass construction materials.	A. Dense trees 	Heavily wooded landscape of deciduous and/or evergreen trees. Land cover mostly pervious (low plants). Zone function is natural forest, tree cultivation, or urban park.
2. Compact midrise 	Dense mix of midrise buildings (3–9 stories). Few or no trees. Land cover mostly paved. Stone, brick, tile, and concrete construction materials.	B. Scattered trees 	Lightly wooded landscape of deciduous and/or evergreen trees. Land cover mostly pervious (low plants). Zone function is natural forest, tree cultivation, or urban park.
3. Compact low-rise 	Dense mix of low-rise buildings (1–3 stories). Few or no trees. Land cover mostly paved. Stone, brick, tile, and concrete construction materials.	C. Bush, scrub 	Open arrangement of bushes, shrubs, and short, woody trees. Land cover mostly pervious (bare soil or sand). Zone function is natural scrubland or agriculture.
4. Open high-rise 	Open arrangement of tall buildings to tens of stories. Abundance of pervious land cover (low plants, scattered trees). Concrete, steel, stone, and glass construction materials.	D. Low plants 	Featureless landscape of grass or herbaceous plants/crops. Few or no trees. Zone function is natural grassland, agriculture, or urban park.
5. Open midrise 	Open arrangement of midrise buildings (3–9 stories). Abundance of pervious land cover (low plants, scattered trees). Concrete, steel, stone, and glass construction materials.	E. Bare rock or paved 	Featureless landscape of rock or paved cover. Few or no trees or plants. Zone function is natural desert (rock) or urban transportation.
6. Open low-rise 	Open arrangement of low-rise buildings (1–3 stories). Abundance of pervious land cover (low plants, scattered trees). Wood, brick, stone, tile, and concrete construction materials.	F. Bare soil or sand 	Featureless landscape of soil or sand cover. Few or no trees or plants. Zone function is natural desert or agriculture.
7. Lightweight low-rise 	Dense mix of single-story buildings. Few or no trees. Land cover mostly hard-packed. Lightweight construction materials (e.g., wood, thatch, corrugated metal).	G. Water 	Large, open water bodies such as seas and lakes, or small bodies such as rivers, reservoirs, and lagoons.
8. Large low-rise 	Open arrangement of large low-rise buildings (1–3 stories). Few or no trees. Land cover mostly paved. Steel, concrete, metal, and stone construction materials.	VARIABLE LAND COVER PROPERTIES	
9. Sparsely built 	Sparse arrangement of small or medium-sized buildings in a natural setting. Abundance of pervious land cover (low plants, scattered trees).	b. bare trees	Leafless deciduous trees (e.g., winter). Increased sky view factor. Reduced albedo.
10. Heavy industry 	Low-rise and midrise industrial structures (towers, tanks, stacks). Few or no trees. Land cover mostly paved or hard-packed. Metal, steel, and concrete construction materials.	s. snow cover	Snow cover >10 cm in depth. Low admittance. High albedo.
		d. dry ground	Parched soil. Low admittance. Large Bowen ratio. Increased albedo.
		w. wet ground	Waterlogged soil. High admittance. Small Bowen ratio. Reduced albedo.

Figure a.6: Local climate zones (LCZs). (From (Stewart and Oke, 2012))

## F Formulae of the urban morpho-metric indicators

### F.1 UMMIs principally related to the openness of urban structures toward the sun, the sky and the atmosphere

Aspect ratio for symmetric configurations [–]:

$$\frac{H}{W} \quad (.12)$$

with:  $\begin{cases} H : \text{height of the bordering facades;} \\ W : \text{canyon width.} \end{cases}$

Aspect ratio for irregular configuration and any direction (at the point  $P_i$ ) [–]:

$$\left( \frac{H}{W} \right)_{P_i} = \frac{h_{i1} + h_{i2}}{2(w_{i1} + w_{i2})} \quad (.13)$$

with:  $\begin{cases} h_{i1}, h_{i2} : \text{height of bordering facade 1 and 2 respectively;} \\ w_{i1}, w_{i2} : \text{horizontal distance between } P_i \text{ and each obstructing facade.} \end{cases}$

Occlusivity factor [–]:

$$O_{c,pr} = \frac{1}{N_{horiz.sections}} \times \sum_{N_{horiz.sections}} \frac{P_{i,n}}{P_{j,n}} \quad (.14)$$

with:  $\begin{cases} N_{horiz.sections} : \text{total number of horizontal sections;} \\ P_{i,n} : \text{built perimeter of the section } n; \\ P_{j,n} : \text{unbuilt perimeter of the section } n. \end{cases}$

For this indicator a variant can be calculated:

$$O_{c,area} = \frac{1}{N_{horiz.sections}} \times \sum_{N_{horiz.sections}} \frac{A_{i,n}}{A_{j,n}} \quad (.15)$$

with:  $\begin{cases} N_{horiz.sections} : \text{total number of horizontal sections;} \\ A_{i,n} : \text{built area of the section } n; \\ A_{j,n} : \text{unbuilt area of the section } n. \end{cases}$

## F.2 UMMIs mostly related to unbuilt volumes and urban roughness, addressing aerodynamic issues

Passage width ratio between building [–]:

$$R_b = \frac{W}{S} \text{ with } S = (B_l \times B_s^2)^{1/3} \quad (.16)$$

$$\text{with: } \begin{cases} W : \text{width of the passage;} \\ S : \text{building influence scale;} \\ B_l : \text{larger dimension of the windward facade;} \\ B_s : \text{smaller dimension of the windward facade.} \end{cases}$$

Blockage ratio [–]:

$$R_b = \frac{B_w \times B_h}{(B_w + W)^2} \quad (.17)$$

$$\text{with: } \begin{cases} B_w : \text{buildings width;} \\ B_h : \text{buildings height;} \\ W : \text{street width.} \end{cases}$$

Total blockage ratio used in wind-tunnel tests and CFD models [–]:

$$BR_{tot} = \frac{A_{model}}{A_{domain}} = \frac{W_{model} \times H_{model}}{W_{domain} \times H_{domain}} \quad (.18)$$

$$\text{with: } \begin{cases} A_{model} : \text{frontal area of the model;} \\ A_{domain} : \text{area of the domain cross section;} \\ W_{model} : \text{width of the model;} \\ H_{model} : \text{height of the model;} \\ W_{domain} : \text{width of the domain;} \\ H_{domain} : \text{height of the domain.} \end{cases}$$

Directional blockage ratio in the vertical direction [–]:

$$BR_V = \frac{H_{model}}{H_{domain}} \quad (.19)$$

$$\text{with: } \begin{cases} H_{model} : \text{height of the model;} \\ H_{domain} : \text{height of the domain.} \end{cases}$$

Directional blockage ratio in the horizontal direction [–]:

$$BR_H = \frac{W_{model}}{W_{domain}} \quad (.20)$$

with:  $\begin{cases} W_{model} : \text{width of the model;} \\ W_{domain} : \text{width of the domain.} \end{cases}$

Passage ratio [–]:

$$P_R = \left( \frac{W}{B_w} \right) \times \left( 1 + \frac{W_1}{W_1 + W_2} \right) \quad (.21)$$

with:  $\begin{cases} W : \text{passage width perpendicular to the wind direction;} \\ B_w : \text{width of the windward facade perpendicular to the wind direction;} \\ 1 + \frac{W_1}{W_1 + W_2} : \text{adjustment factor, see (Hu and Yoshie, 2013).} \end{cases}$

Frontal areal fraction [–]:

$$R_b = \frac{A_F}{A_T} \quad (.22)$$

with:  $\{A_F : \text{the surface on the windward faces;}$

Plan area ratio [–]:

$$R_b = \frac{A_P}{A_T} \quad (.23)$$

with:  $\begin{cases} A_P : \text{the footprint of built structures;} \\ A_T : \text{the total ground surface.} \end{cases}$

Mean Porosity [–]:

$$P_i = \frac{\sum_{\text{open volumes}} \Pi \times r_{hi}^2 \times l_i}{\sum_{\text{open volumes}} V_i + \sum_{\text{built volumes}} V_j} \quad (.24)$$

with:  $\begin{cases} r_{hi} : \text{equivalent hydraulic radius of the open volume;} \\ l_i : \text{length of the open volume;} \\ V_i : \text{mean canopy volume above the open space i;} \\ V_j : \text{mean volume of the built volume j.} \end{cases}$

Sinuosity [–]:

$$S_i = \frac{\sum_{\text{streets segments}} \cos^2(\theta_i) \times l_i}{\sum_{\text{streets segments}} l_i} \quad (.25)$$

with:  $\begin{cases} \theta_i : \text{angle between axis of the street segment i and the wind direction;} \\ l_i : \text{length of the street segment i.} \end{cases}$

**Absolute rugosity [m]:**

$$R_a = \frac{\sum_{\text{built}} A_i \times h_i}{\sum_{\text{built}} A_i + \sum_{\text{unbuilt}} A_j} \quad (.26)$$

with:  $\begin{cases} A_i : \text{area of the building i;} \\ h_i : \text{height of the building i;} \\ A_j : \text{area of the unbuilt space j.} \end{cases}$

**Relative rugosity following the direction  $\alpha$  [m]:**

$$R_\alpha = \frac{\sqrt{\sum_i (h_i - R_\alpha)^2 \times l_i^2}}{\sum_i l_i} \quad (.27)$$

$$\text{Variance} = R_\alpha^2 \quad (.28)$$

with:  $\begin{cases} R_\alpha : \text{mean canopy height in the } \alpha \text{ direction;} \\ h_i : \text{height of built or unbuilt element i;} \\ l_i : \text{width of the built or unbuilt element i in the } \alpha \text{ direction;} \\ \sum_i l_i : \text{diameter of the area considered.} \end{cases}$

### F.3 UMMIs mainly related to the architectural properties of buildings and their interface with the outdoors

**Volumetric compactness factor [m<sup>-1</sup>]:**

$$C = \frac{A}{V} = C_f \times C_s \quad (.29)$$

◦ Form Factor [—]:

$$C_f = \frac{A}{V^{2/3}} \quad (.30)$$

◦ Size Factor [ $\text{m}^{-1}$ ]:

$$C_s = \frac{1}{V^{1/3}} \quad (.31)$$

with:  $\begin{cases} A : \text{area of the building envelope;} \\ V : \text{building volume.} \end{cases}$

**Passive Volume Ratio** [–]:

$$PVR = \frac{\sum_{<2h} A_i \times h_i}{V} \quad (.32)$$

with:  $\begin{cases} h_i : \text{height of the room;} \\ A_i : \text{floor area located less than two times the room height;} \\ V : \text{total volume.} \end{cases}$

**Contiguity** [–]:

$$Cont. = \frac{\sum_{buildings} \frac{A_{cont.} \times A_{floor}}{A_{vert.}}}{\sum_{buildings} A_{floor}} \quad (.33)$$

with:  $\begin{cases} A_{cont.} : \text{area of the adjacent walls;} \\ A_{vert.} : \text{area of the building facade;} \\ A_{floor} : \text{area of the building floor.} \end{cases}$

# Appendices of Part 2

## Contents

---

<b>G</b>	<b>RANS transport equations for the momentum . . . . .</b>	<b>A. 15</b>
G.1	Equations for the momentum . . . . .	A. 15
G.1.1	Standard $k-\varepsilon$ model . . . . .	A. 15
G.1.2	Realizable $k-\varepsilon$ model . . . . .	A. 15
G.1.3	Reynolds stress model . . . . .	A. 16
G.2	Modeling the turbulent viscosity . . . . .	A. 18
G.3	Equation for energy - Convective heat transfer modeling . . . . .	A. 19
G.3.1	Standard and Realizable $k-\varepsilon$ models . . . . .	A. 19
G.3.2	Reynolds stress model . . . . .	A. 19
<b>H</b>	<b>Wall-functions . . . . .</b>	<b>A. 20</b>
H.1	Law-of -the wall . . . . .	A. 20
H.2	Modified wall-functions for roughness . . . . .	A. 20
H.2.1	Effects on the momentum: . . . . .	A. 20
H.2.2	Effects on heat transfers: . . . . .	A. 21
<b>I</b>	<b>Usual inlet conditions for steady RANS methods . . . . .</b>	<b>A. 22</b>
I.1	Usual inlet conditions for steady RANS $k-\varepsilon$ models . . . . .	A. 22
I.2	Usual inlet conditions for steady RANS RSM models . . . . .	A. 22
<b>J</b>	<b>Blasius wind-tunnel . . . . .</b>	<b>A. 23</b>
<b>K</b>	<b>Discussion of the approach flow profiles . . . . .</b>	<b>A. 24</b>
K.1	Theoretical relationship between $z_0$ and $K_s$ . . . . .	A. 24
K.2	Approach flow profiles used in the validation study . . . . .	A. 25
K.3	Approach flow profile in the actual tests . . . . .	A. 27
<b>L</b>	<b>Complements to the case study A1-1 . . . . .</b>	<b>A. 28</b>
L.1	Comparison of the 2D flow features . . . . .	A. 28
L.2	Comparison of the top bubbles predicted by the steady RANS models . . . . .	A. 28
<b>M</b>	<b>Levels of the scaled residuals reached at the end of simulations . . . . .</b>	<b>A. 29</b>

---



<b>N</b>	<b>Aerodynamic results for the isolated building types . . . . .</b>	<b>A. 30</b>
N.1	The cube . . . . .	A. 30
N.2	The cuboid 1 . . . . .	A. 34
N.3	The cuboid 2 . . . . .	A. 38
N.4	The L-building 1 . . . . .	A. 42
N.5	The L-building 2 . . . . .	A. 46
N.6	The L-building 3 . . . . .	A. 50
N.7	The U-building 1 . . . . .	A. 54
N.8	The U-building 2 . . . . .	A. 58
N.9	The U-building 3 . . . . .	A. 62
N.10	The Patio . . . . .	A. 66
<b>O</b>	<b>Aerodynamic results for the urban block types . . . . .</b>	<b>A. 70</b>
O.1	The cube array . . . . .	A. 70
O.2	The row block 1 . . . . .	A. 72
O.3	The row block 2 . . . . .	A. 74
O.4	The U-block 1 . . . . .	A. 76
O.5	The U-block 2 . . . . .	A. 78
O.6	The enclosed block . . . . .	A. 80
O.7	The continuous patio array . . . . .	A. 82
<b>P</b>	<b>2D internal recirculation phenomena for the cube and the continuous patio arrays</b>	<b>A. 84</b>
<b>Q</b>	<b>Distribution of <math>C_p</math> on the building surfaces . . . . .</b>	<b>A. 86</b>
Q.1	Simulation results: $C_p$ for the cube and the patio . . . . .	A. 86
Q.2	Simulation results: $C_p$ for the cube array and the continuous patio array . . .	A. 87
Q.3	Wind tunnel data of $C_p$ . . . . .	A. 91

---

## G RANS transport equations for the momentum

### G.1 Equations for the momentum

#### G.1.1 Standard $k$ - $\varepsilon$ model

As a  $k$ - $\varepsilon$  model, the  $Sk$ - $\varepsilon$  addresses fully turbulent flows. The different empirical constants that are involved by the models were found to give accurate predictions for a wide range of wall-bounded and free shear flows.

Transport equation for  $k$ :

$$\frac{\partial}{\partial t}(\rho k) + \frac{\partial}{\partial x_i}(\rho k u_i) = \frac{\partial}{\partial x_j} \left[ \left( \mu + \frac{\mu_t}{\sigma_k} \right) \frac{\partial k}{\partial x_j} \right] + G_k + G_b - \rho \varepsilon - Y_M + S_k \quad (.34)$$

Transport equation for  $\varepsilon$ :

$$\frac{\partial}{\partial t}(\rho \varepsilon) + \frac{\partial}{\partial x_i}(\rho \varepsilon u_i) = \frac{\partial}{\partial x_j} \left[ \left( \mu + \frac{\mu_t}{\sigma_k} \right) \frac{\partial \varepsilon}{\partial x_j} \right] + C_{1\varepsilon} \frac{\varepsilon}{k} (G_k + C_{3\varepsilon} G_b) - C_{2\varepsilon} \rho \frac{\varepsilon^2}{k} + S_\varepsilon \quad (.35)$$

with:  $\left\{ \begin{array}{l} G_k : \text{generation of turbulence kinetic energy due to mean velocity gradients,} \\ G_b : \text{generation of turbulence kinetic energy due to buoyancy,} \\ Y_M : \text{contribution of the fluctuating dilatation in compressible turbulence,} \\ C_{1\varepsilon} = 1.44, C_{2\varepsilon} = 1.92, C_{3\varepsilon} = 0.09 : \text{model constants,} \\ \sigma_k = 1.0, \sigma_\varepsilon = 1.3 : \text{turbulent Prandtl numbers for } k \text{ and } \varepsilon, \\ S_k, S_\varepsilon : \text{user defined source terms.} \end{array} \right.$

#### G.1.2 Realizable $k$ - $\varepsilon$ model

This model was shown to improve the  $Sk$ - $\varepsilon$  predictions, especially when the flows include vortices. According to [Ansys Fluent \(2013a\)](#), initial studies highlighted its best performance as compared to the other  $k$ - $\varepsilon$  models when modeling separated flows and complex secondary flow features.

Transport equation for  $k$ :

$$\frac{\partial}{\partial t}(\rho k) + \frac{\partial}{\partial x_i}(\rho k u_i) = \frac{\partial}{\partial x_j} \left[ \left( \mu + \frac{\mu_t}{\sigma_k} \right) \frac{\partial k}{\partial x_j} \right] + G_k + G_b - \rho \varepsilon - Y_M + S_k \quad (.36)$$

Transport equation for  $\varepsilon$ :

$$\frac{\partial}{\partial t}(\rho \varepsilon) + \frac{\partial}{\partial x_i}(\rho \varepsilon u_i) = \frac{\partial}{\partial x_j} \left[ \left( \mu + \frac{\mu_t}{\sigma_\varepsilon} \right) \frac{\partial \varepsilon}{\partial x_j} \right] + \rho C_1 S_\varepsilon - \rho C_2 \frac{\varepsilon^2}{k + \sqrt{\nu \varepsilon}} + C_{1\varepsilon} \frac{\varepsilon}{k} C_{3\varepsilon} G_b + S_\varepsilon \quad (.37)$$

$$\text{with: } \begin{cases} G_k : \text{generation of turbulence kinetic energy due to mean velocity gradients,} \\ G_b : \text{generation of turbulence kinetic energy due to buoyancy,} \\ Y_M : \text{contribution of the fluctuating dilatation in compressible turbulence,} \\ C_1 = \max \left[ 0.43, \frac{\eta}{\eta + 5} \right], \quad \eta = S \frac{k}{\varepsilon}, \quad S = \sqrt{2S_{ij}S_{ij}} \\ C_2 = 1.9 : \text{model constant,} \\ C_{1\varepsilon} = 1.44 : \text{model constant,} \\ \sigma_k = 1.0, \sigma_\varepsilon = 1.2 : \text{turbulent Prandtl numbers for } k \text{ and } \varepsilon, \\ S_k, S_\varepsilon : \text{user defined source terms.} \end{cases}$$

The equation for  $k$  is the same as in the  $Sk-\varepsilon$  model, with the exception of the model constants. On the contrary, the equation for  $\varepsilon$  differs as  $G_k$  does not appear and the destruction term  $(\rho C_2 \frac{\varepsilon^2}{k + \sqrt{\nu\varepsilon}})$  does not have any singularity contrary to the term  $C_{2\varepsilon} \rho \frac{\varepsilon^2}{k}$  of the  $Sk-\varepsilon$  model.

### G.1.3 Reynolds stress model

**Transport equation for the Reynolds stress ( $\overline{u'_i u'_j}$ ):**

$$\frac{\partial \overline{u'_i u'_j}}{\partial t} + \underbrace{\frac{\partial \overline{u_k u'_i u'_j}}{\partial x_k}}_{C_{ij}} = P_{ij} + T_{ij} + \psi_{ij} + \phi_{ij} + D'_{ij} + G_{ij} + \varepsilon'_{ij} \quad (.38)$$

$$\text{With: } \begin{cases} \frac{\partial \overline{u'_i u'_j}}{\partial t} : \text{the local time derivative,} \\ C_{ij} = \frac{\partial \overline{u_k u'_i u'_j}}{\partial x_k} : \text{the convective term,} \\ P_{ij} = - \left( \overline{u'_k u'_j} \frac{\partial \overline{u_i}}{\partial x_k} + \overline{u'_k u'_i} \frac{\partial \overline{u_j}}{\partial x_k} \right) : \text{the stress production tensor,} \\ T_{ij} = - \frac{\partial \overline{u'_i u'_j u'_k}}{\partial x_k} : \text{the diffusion due to velocity fluctuations,} \\ \psi_{ij} = - \frac{1}{\rho} \left( \frac{\partial \overline{p' u'_i}}{\partial x_j} + \frac{\partial \overline{p' u'_j}}{\partial x_i} \right) : \text{the diffusion due to pressure fluctuations,} \\ \phi_{ij} = \frac{p'}{\rho} \left( \frac{\partial u'_i}{\partial x_j} + \frac{\partial u'_j}{\partial x_i} \right) : \text{the pressure strain tensor,} \\ D'_{ij} = \nu \frac{\partial^2 \overline{u'_i u'_j}}{\partial x_k \partial x_k} : \text{the molecular diffusion tensor,} \\ G_{ij} = -\beta (g_i \overline{u'_j T} + g_j \overline{u'_i T}) : \text{the buoyancy induced production term,} \\ \varepsilon'_{ij} = -2\nu \frac{\partial u'_i}{\partial x_k} \frac{\partial u'_j}{\partial x_k} : \text{the viscous dissipation tensor.} \end{cases}$$

Note that the sum of  $T_{ij}$  and  $\psi_{ij}$  is often considered as the turbulent diffusion term.

The terms  $C_{ij}$ ,  $D_{L,ij}$ ,  $P_{ij}$  and  $F_{ij}$  do not require any modeling whereas the terms  $D_{T,ij}$ ,  $G_{ij}$ ,  $\phi_{ij}$ ,  $\varepsilon_{ij}$  need to be modeled to close the system of equations. Following equations gives their respective modeling in Fluent:

**The turbulent diffusive transport:**

$$D_{T,ij} = \frac{\partial}{\partial x_k} \left( \frac{\mu_t}{\sigma_k} \frac{\partial \overline{u'_i u'_j}}{\partial x_k} \right) \quad (.39)$$

with  $\sigma_k = 0.82 \neq 1.0$  that is used in  $k-\varepsilon$  models.

**The linear pressure strain model:**

It is usually decomposed into the sum of the slow pressure strain term ( $\phi_{ij,1}$ , the return to isotropy term) plus the rapid pressure-strain term ( $\phi_{ij,2}$ ) and the wall reflection term ( $\phi_{ij,w}$ ) that is responsible for the redistribution of the normal stress near the wall by damping the normal stress perpendicular to the wall and enhancing those parallel to the wall.

$$\phi_{ij,1} \equiv -C_1 \rho \frac{\varepsilon}{k} \left( \overline{u'_i u'_j} - \frac{2}{3} \delta_{ij} k \right) \quad (.40)$$

with:  $C_1 = 1.8$ .

$$\phi_{ij,2} \equiv -C_2 \left[ (P_{ij} + F_{ij} + \frac{5}{6} G_{ij} - C_{ij}) - \frac{2}{3} \delta - ij(P + \frac{5}{6} G - C) \right] \quad (.41)$$

with:  $C_2 = 0.6$ ,  $P = 0.5 P_{kk}$ ,  $G = 0.5 G_{kk}$  and  $C = 0.5 C_{kk}$ .

$$\begin{aligned} \phi_{ij,w} \equiv & C'_1 \frac{\varepsilon}{k} \left( \overline{u'_k u'_m} n_k n_m \delta_{ij} - \frac{3}{2} \overline{u'_i u'_k} n_j n_k - \frac{3}{2} \overline{u'_j u'_k} n_i n_k \right) \frac{C_l k^{3/2}}{\varepsilon d} \\ & + C'_2 \left( \phi_{km,2} n_k n_m \delta_{ij} - \frac{3}{2} \phi_{ik,2} n_j n_k - \frac{3}{2} \phi_{jk,2} n_i n_k \right) \frac{C_l k^{3/2}}{\varepsilon d} \end{aligned} \quad (.42)$$

$$\text{with: } \begin{cases} C'_1 = 0.5, C'_2 = 0.3 : \text{model constants,} \\ n_k : \text{the } x_k \text{ component of the unit normal to the wall,} \\ d : \text{the normal, distance to the wall,} \\ C_l = \frac{1}{\kappa} C_\mu^{3/4} \text{ where: } C_\mu = 0.09 \text{ and } \kappa \text{ is the van Karman constant.} \end{cases}$$

**The effects of buoyancy on turbulence:**

$$\begin{aligned} G_{ij} &= -\rho \beta (g_i \overline{u'_j \theta} + g_j \overline{u'_i \theta}); \quad \overline{U_i \theta} = \frac{\mu_t}{Pr_t} \left( \frac{\partial T}{\partial x_i} \right) \\ \iff G_{ij} &= -\frac{\mu_t}{\rho Pr_t} \left( g_i \frac{\partial \rho}{\partial x_j} + g_j \frac{\partial \rho}{\partial x_i} \right) \end{aligned} \quad (.43)$$

with  $Pr_t = 0.85$ : the turbulent Prandtl number for energy.

**The dissipation tensor:**

$$\varepsilon_{ij} = \frac{2}{3} \delta_{ij} (\rho \varepsilon + Y_M) \quad (.44)$$

where:  $\begin{cases} Y_M = 2\rho \varepsilon M_t^2 : \text{additional dilatation dissipation term,} \\ M_t = \sqrt{\frac{k}{a^2}} : \text{the turbulent } Ma \text{ number,} \\ a \equiv \sqrt{\gamma RT} : \text{the speed of the sound.} \end{cases}$

*Modeling of  $k$ :*

- in the bulk flow region:

$$k = \frac{1}{2} \overline{u'_i u'_i} \quad (.45)$$

- to obtain the boundary conditions for the Reynolds stresses:

$$\frac{\partial}{\partial t}(\rho k) + \frac{\partial}{\partial x_i}(\rho k u_i) = \frac{\partial}{\partial x_j} \left[ \left( \mu + \frac{\mu_t}{\sigma_k} \right) \frac{\partial k}{\partial x_j} \right] + \frac{1}{2}(P_{ii} + G_{ii}) - \rho \varepsilon (1 + 2M_t^2) + S_k \quad (.46)$$

with:  $\sigma_k = 0.82$ . This equation resembles to that used in the  $Sk$ - $\varepsilon$  model.

*Modeling of the scalar  $\varepsilon$ :*

$$\frac{\partial}{\partial t}(\rho \varepsilon) + \frac{\partial}{\partial x_i}(\rho \varepsilon u_i) = \frac{\partial}{\partial x_j} \left[ \left( \mu + \frac{\mu_t}{\sigma_\varepsilon} \right) \frac{\partial \varepsilon}{\partial x_j} \right] + C_{1\varepsilon} \frac{1}{2}(P_{ii} + C_{3\varepsilon} G_{ii}) \frac{\varepsilon}{k} - C_{2\varepsilon} \rho \frac{\varepsilon^2}{k} + S_\varepsilon \quad (.47)$$

with:  $\sigma_\varepsilon = 1.0$ ,  $C_{1\varepsilon} = 1.44$ ,  $C_{2\varepsilon} = 1.92$  and  $C_{3\varepsilon}$  a function of the local flow direction in relation to the gravitational vector.

*Near wall treatment when using the standard wall functions:*

$$\frac{\overline{u_\tau'^2}}{k} = 1.098, \quad \frac{\overline{u_\eta'^2}}{k} = 0.247, \quad \frac{\overline{u_\lambda'^2}}{k} = 0.655, \quad \frac{\overline{-u'_\tau u'_\eta}}{k} = 0.255 \quad (.48)$$

with:  $\begin{cases} \tau : \text{the tangential coordinate,} \\ \eta : \text{the normal coordinate,} \\ \lambda : \text{the binormal coordinate,} \\ k : \text{the turbulent kinetic energy that is computed according to Eq. .46..} \end{cases}$

## G.2 Modeling the turbulent viscosity

Both the  $Sk$ - $\varepsilon$ ,  $Rk$ - $\varepsilon$  and RSM models use the same formulation to compute the turbulent viscosity  $\mu_t$ :

$$\mu_t = \rho C_\mu \frac{k^2}{\varepsilon} \quad (.49)$$

In the  $Sk-\varepsilon$  and the RSM model,  $C_\mu = 0.09$  and is *constant*. In the  $Rk-\varepsilon$  model,  $C_\mu$  is a *variable* model parameter, which depends of the mean strain and rotation rates, the angular velocity of the system rotation,  $k$  and  $\varepsilon$ . It recovers the standard value of 0.09 for an inertial sub layer in an equilibrium boundary layer.

### G.3 Equation for energy - Convective heat transfer modeling

#### G.3.1 Standard and Realizable $k-\varepsilon$ models

$$\frac{\partial}{\partial t}(\rho E) + \frac{\partial}{\partial x_i}[u_i(\rho E + p)] = \frac{\partial}{\partial x_j} \left( \lambda_{eff} \frac{\partial T}{\partial x_j} + u_i(\tau_{ij})_{eff} \right) + S_h \quad (.50)$$

$$\text{with: } \begin{cases} E : \text{ the total energy,} \\ \lambda_{eff} = \lambda + \frac{C_p \mu_t}{Pr_t} \text{ the effective thermal conductivity,} \\ \tau_{ij} : \text{ the deviatoric stress tensor, which is not computed in pressure based solver.} \end{cases}$$

#### G.3.2 Reynolds stress model

$$\frac{\partial}{\partial t}(\rho E) + \frac{\partial}{\partial x_i}[u_i(\rho E + p)] = \frac{\partial}{\partial x_j} \left( \left( \lambda + \frac{C_p \mu_t}{Pr_t} \right) \frac{\partial T}{\partial x_j} + u_i(\tau_{ij})_{eff} \right) + S_h \quad (.51)$$

$$\text{with: } \begin{cases} E : \text{ the total energy,} \\ \tau_{ij} : \text{ the deviatoric stress tensor, which is not computed in pressure based solver.} \end{cases}$$

The equation is the same as the one used in the  $Sk-\varepsilon$  and  $Rk-\varepsilon$  turbulence models.

## H Wall-functions

### H.1 Law-of -the wall

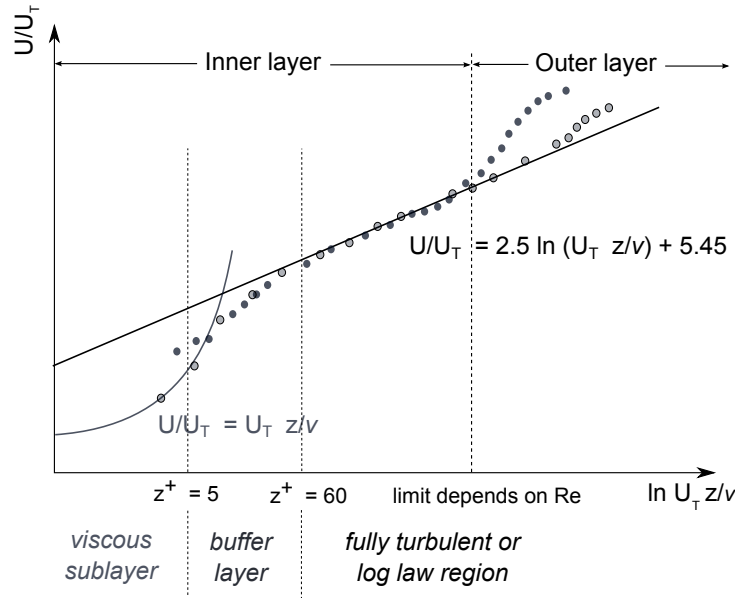


Figure a.7: Law-of-the-wall giving the mean velocity profile as a function of the distance to the wall, plotted in a semi-log scale. (Adapted from (Ansys Fluent, 2013a).)

The boundary layer velocity profile evolves as a function of the dimensionless wall unit  $z^+$  as follows. For:

- $z^+ < 4$ , the flow is laminar and the velocity is a linear function of the distance to the wall,
- $4 < z^+ < 50$ , the transition occurs between the laminar and the turbulent flow, both the effects of the molecular viscosity and turbulence are important,
- $z^+ > 50$ , the flow is turbulent and the velocity is a logarithmic function of the distance to the wall (log law).

## H.2 Modified wall-functions for roughness

### H.2.1 Effects on the momentum:

$\Delta B = \frac{1}{\kappa} \ln(fr)$  depends on the dimensionless roughness height ( $K_s^+$ ) that is given in Eq. .52 and the roughness constant ( $C_s$ ) that depends on the type of roughness:

$$K_s^+ = \frac{K_s u^*}{\nu} \quad (.52)$$

- for  $K^+ \leq 2.25$ , the hydro-dynamically smooth regime occurs. The roughness function is:

$$\Delta B = 0 \quad (.53)$$

- for  $2.25 < K^+ \leq 90$ , the transitional regime occurs. The roughness function is:

$$\Delta B = \frac{1}{\kappa} \times \ln \left[ \frac{K_s^+ - 2.25}{87.75} + C_s K_s^+ \right] \times \sin[0.4258 \times (\ln K_s^+ - 0.811)] \quad (.54)$$

- for  $K^+ > 90$ , the fully rough regime occurs. The roughness function is:

$$\Delta B = \frac{1}{\kappa} \times \ln(1 + C_s K_s^+) \quad (.55)$$

Hence, for  $z^* > 11.25$  and a fully rough regime, the wall function is given by Eq. .56:

$$U^* = \frac{1}{\kappa} \times \ln \left[ \frac{E z^*}{1 + C_s K_s^+} \right] = \frac{1}{\kappa} \times \ln \left[ \frac{E u^* y_p}{\nu (1 + C_s \frac{K_s u^*}{\nu})} \right] \quad (.56)$$

### H.2.2 Effects on heat transfers:

P is modified for rough wall as follows:

$$P_{rough} = 3.15 Pr^{0.695} \left( \frac{1}{E'} - \frac{1}{E} \right)^{0.359} + \left( \frac{E'}{E} \right)^{0.6} P \quad (.57)$$

with:  $E' = \frac{E}{f r}$  the wall function constant modified for roughness.



## I Usual inlet conditions for steady RANS methods

### I.1 Usual inlet conditions for steady RANS $k$ - $\varepsilon$ models

According to [Richards and Hoxey \(1993\)](#); [Richards and Norris \(2011\)](#):

$$U(z) = \frac{u^*}{\kappa_{k-\varepsilon}} \ln \left( \frac{z}{z_0} \right) \quad (.58)$$

$$k(z) = \frac{u^{*2}}{\sqrt{C_\mu}} = 3.333 u^{*2} \quad (.59)$$

$$\varepsilon(z) = \frac{u^{*3}}{\kappa_{k-\varepsilon} z} \quad (.60)$$

with:  $\kappa_{k-\varepsilon} = \sqrt{(C_{\varepsilon 2} - C_{\varepsilon 1} \sigma_\varepsilon \sqrt{C_\mu})} = 0.433$

According to [Tominaga et al. \(2008\)](#):

$$U(z) = U_r \exp \left( \frac{z}{z_{ref}} \right)^\alpha \quad (.61)$$

$$k(z) = (I(z)U(z))^2 \quad \text{with} \quad I(z) = 0.1 \left( \frac{z}{z_{ref}} \right)^{(-\alpha-0.05)} \quad (.62)$$

$$\varepsilon(z) = C_\mu^{1/2} k(z) \frac{U_{ref}}{z_{ref}} \alpha \left( \frac{z}{z_{ref}} \right)^{(\alpha-1)} \quad (.63)$$

### I.2 Usual inlet conditions for steady RANS RSM models

According to [Richards and Norris \(2011\)](#) for the quasi isotropic LRR Reynolds stress transport model:

$$U(z) = \frac{u^*}{\kappa_{RS}} \ln \left( \frac{z}{z_0} \right) \quad (.64)$$

$$k(z) = 2.975 u^{*2} \quad (.65)$$

$$\frac{\overline{u_\tau'^2}}{k} = 0.882, \quad \frac{\overline{\rho u_\eta'^2}}{k} = 0.498, \quad \frac{\overline{u_\lambda'^2}}{k} = 0.620, \quad \frac{\overline{u_\tau' u_\eta'}}{\rho k} = \frac{1}{2.975} \approx 0.336 \quad (.66)$$

$$\varepsilon(z) = \frac{u^{*3}}{\kappa_{RS} z} \quad (.67)$$

with:  $\kappa_{RS} = \sqrt{\frac{(C_{\varepsilon 2,RS} - C_{\varepsilon 1,RS} \sigma_{\varepsilon,RS})}{2.975^3 C_{\mu,RS}}} = 0.404$

## J Blasius wind-tunnel

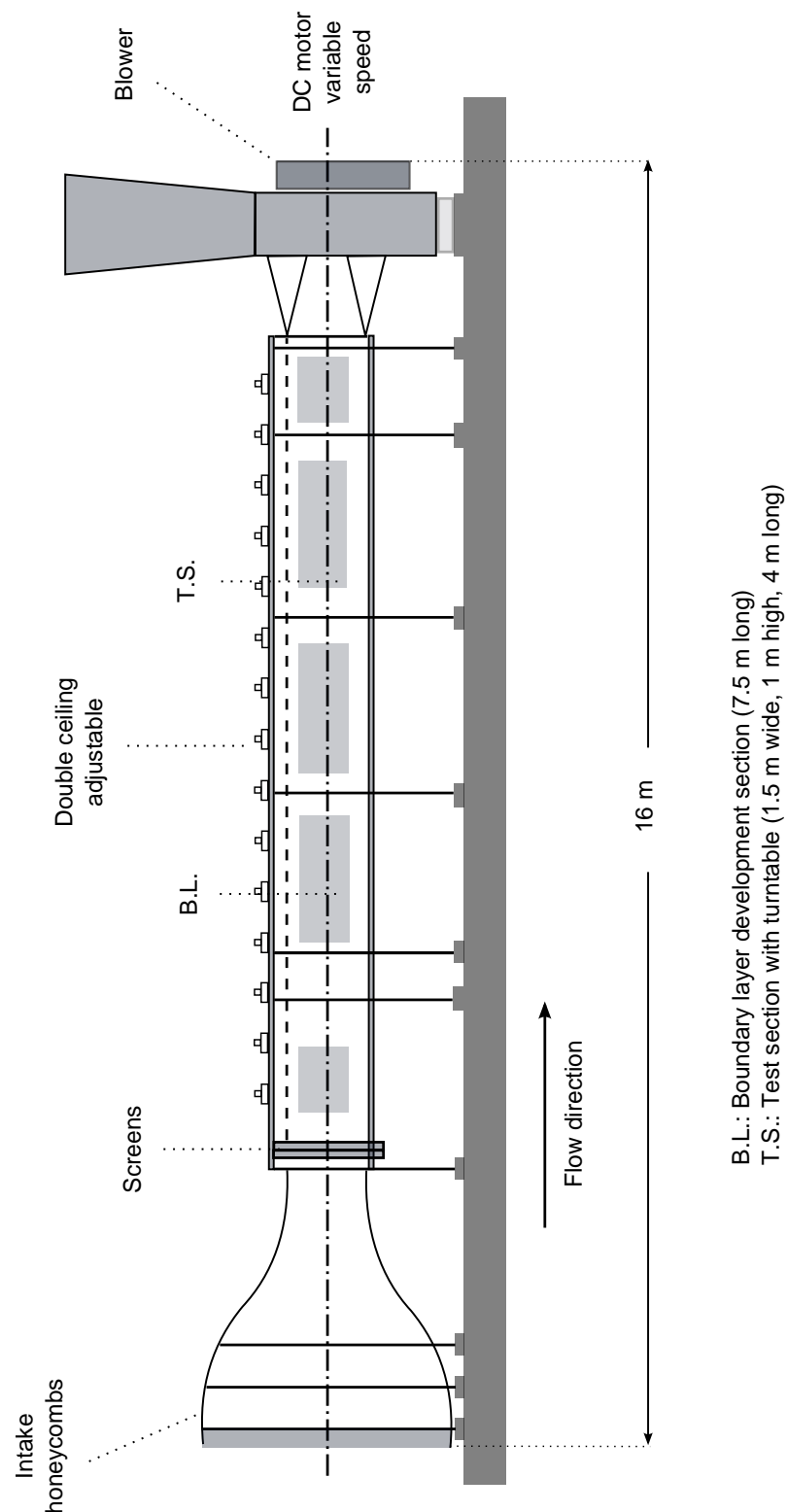


Figure a.8: Sketch of the Blasius wind-tunnel. (Adapted from ([Meteorological Institute of Hamburg, 2013](#)).)

## K Discussion of the approach flow profiles

### K.1 Theoretical relationship between $z_0$ and $K_s$

The  $U$ -profile for an equilibrium atmospheric boundary layer is given by:

$$\frac{U_{ABL}(z)}{u^*} = \frac{1}{\kappa} \times \ln \left[ \frac{z}{z_0} \right]$$

For  $z^+ > 11.25$  and a fully turbulent regime, and considering:

$$u_t = \frac{\tau_w}{\rho}; \quad u^* = C_\mu^{1/4} \times k^{1/2}; \quad K_s^+ = \frac{\rho K_s u^*}{\mu}$$

the law-of-the-wall for the mean velocity modified for roughness at the first cell height ( $z_p$ ) is:

$$\begin{aligned} \frac{U_{wall} u^*}{u_t^2} &= \frac{1}{\kappa} \times \ln \left[ E \frac{\rho u^* z}{\mu} \right] - \frac{1}{\kappa} \times \ln(1 + C_s K_s^+) \\ &= \frac{1}{\kappa} \times \ln \left[ E \frac{\rho u^* z_p}{\mu \times (1 + C_s K_s^+)} \right] \end{aligned}$$

For an equilibrium boundary layer:

$$y^+ \approx y^* \Leftrightarrow u^* \approx u_t$$

Considering:

- $C_s K_s^+ \sim 1 \frac{1 \times 10^1 \times 10^{-1}}{10^{-5}} = 10^3 \gg \gg 1 \Rightarrow 1 + C_s K_s^+ = C_s K_s^+$
- $u^* = u_t \Rightarrow \frac{U_{wall} u^*}{u_t^2} = \frac{U_{wall}}{u^*}$
- $U_{ABL}(z_p) = U_{wall,p} \Rightarrow \frac{1}{\kappa} \times \ln \left[ \frac{z}{z_0} \right] = \frac{1}{\kappa} \times \ln \left[ E \frac{\rho u^* z_p}{\mu \times (1 + C_s K_s^+)} \right]$

gives:

$$\begin{aligned} \frac{1}{\kappa} \times \ln \left[ \frac{z_p}{z_0} \right] &= \frac{1}{\kappa} \times \ln \left[ E \frac{\rho u^* z_p}{\mu C_s \frac{\rho K_s u^*}{\mu}} \right] = \frac{1}{\kappa} \times \ln \left[ E \frac{z_p}{C_s K_s} \right] \\ &\Leftrightarrow z_0 = \frac{C_s K_s}{E} \\ &\Leftrightarrow K_s = \frac{E}{C_s} \times z_0 = \frac{9.739}{C_s} \times z_0 \end{aligned}$$

## K.2 Approach flow profiles used in the validation study

Only considering the experimental points used as reference to model the approach flow and for  $z \in [0; 0.45] \text{ m} \Leftrightarrow [0; 3.6] \text{ H}$ , the fitted logarithmic law is:

$$U(z) = \frac{0.3718}{0.418} \times \ln[1312 \times z] = \frac{0.3718}{\kappa} \times \ln\left[\frac{z}{4.76 \times 10^{-4}}\right] \quad (.68)$$

This gives:

- $u_{fit}^* = 0.3718 \text{ m}$  (the experimental documentation gives:  $u_{exp}^* = 0.3777 \text{ m}$ ),
- $z_{0,fit} = 7.62 \times 10^{-4} \text{ m}$  (the experimental documentation gives:  $z_{0,exp} = 7 \times 10^{-4} \text{ m}$ ).

Approach flow: RSM,  $z \in [0 ; 2] \text{ H}$

-  $u^* = 0.3808 \text{ m/s}$       -  $R^2 = 0.998$   
 -  $z_0 = 8.2850 \times 10^{-4} \text{ m}$       -  $RMSE = 0.0362$

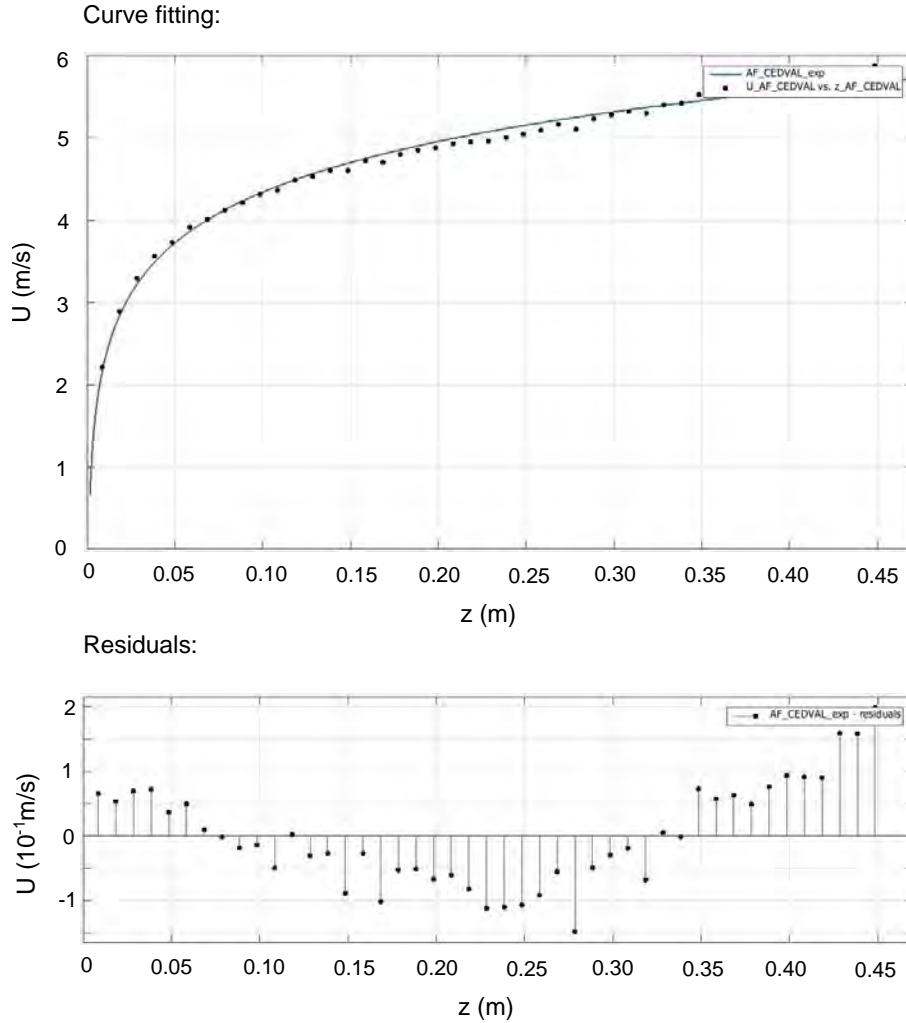


Figure a.9: Fitting of the experimental approach flow.

Considering the steady RANS  $Rk-\epsilon$  configuration and for  $z \in [0; 0.25] \text{ m} \Leftrightarrow [0; 2] \text{ H}$ , the fitted

logarithmic law is:

$$U(z) = \frac{0.317}{0.418} \times \ln[2101 \times z] = \frac{0.317}{\kappa} \times \ln\left[\frac{z}{4.76 \times 10^{-4}}\right] \quad (.69)$$

With  $C_s = 0.625$ , the resulting relationship between  $z_{0,Rk-\epsilon}$  and  $K_s$  is:

$$K_s = \frac{5.51}{C_s} \times z_{0,Rk-\epsilon}$$

Considering the steady RANS RSM configuration and for  $z \in [0; 0.25]\text{m} \Leftrightarrow [0; 2]\text{H}$ , the fitted logarithmic law is:

$$U(z) = \frac{0.381}{0.418} \times \ln[1207 \times z] = \frac{0.381}{\kappa} \times \ln\left[\frac{z}{8.29 \times 10^{-4}}\right] \quad (.70)$$

With  $C_s = 0.625$ , the resulting relationship between  $z_{0,RSM}$  and  $K_s$  is:

$$K_s = \frac{3.17}{C_s} \times z_{0,RSM}$$

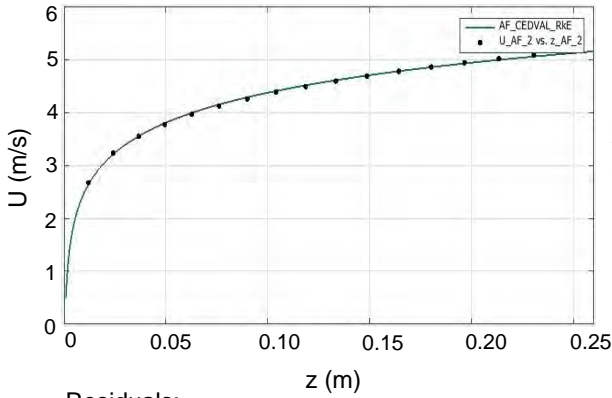
Approach flow: Rk- $\epsilon$ ,  $z \in [0 ; 2] \text{ H}$

-  $u^*=0.317 \text{ m/s}$       -  $R^2=0.9997$   
-  $z_0=4.7596 \times 10^{-4} \text{ m}$       -  $RMSE=0.0138$

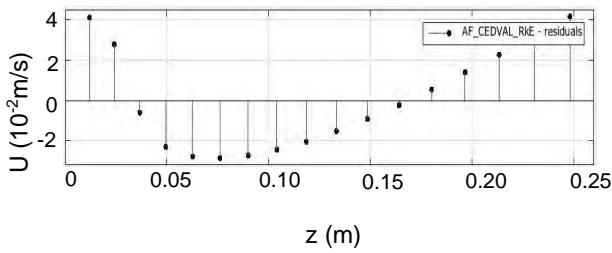
Approach flow: RSM,  $z \in [0 ; 2] \text{ H}$

-  $u^*=0.3808 \text{ m/s}$       -  $R^2=0.998$   
-  $z_0=8.2850 \times 10^{-4} \text{ m}$       -  $RMSE=0.0362$

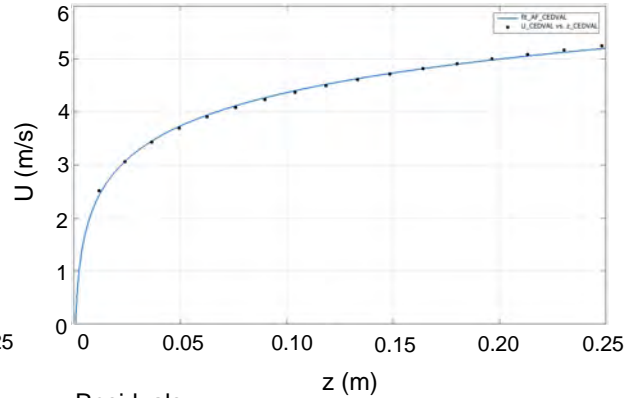
Curve fitting:



Residuals:



Curve fitting:



Residuals:

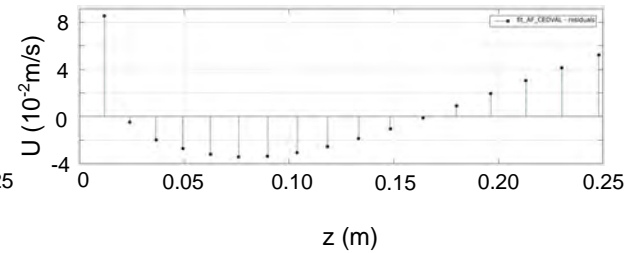


Figure a.10: Fitting of the steady RANS approach flow.

### K.3 Approach flow profile in the actual tests

For  $z \in [0; 60]$ m, the fitted logarithmic law is:

$$U(z) = \frac{0.3605}{0.418} \times \ln[14.72 \times z] = \frac{0.3605}{\kappa} \times \ln\left[\frac{z}{0.06793}\right] \quad (.71)$$

With  $C_s = 1$ , the resulting relationship between  $z_0$  and  $K_s$  is:

$$K_s = \frac{4.42}{C_s} \times z_0$$

For  $z \in [0; 35]$ m, the fitted logarithmic law is:

$$U(z) = \frac{0.3733}{0.418} \times \ln[12.55 \times z] = \frac{0.3733}{\kappa} \times \ln\left[\frac{z}{0.07968}\right] \quad (.72)$$

With  $C_s = 1$ , the resulting relationship between  $z_0$  and  $K_s$  is:

$$K_s = \frac{3.77}{C_s} \times z_0$$

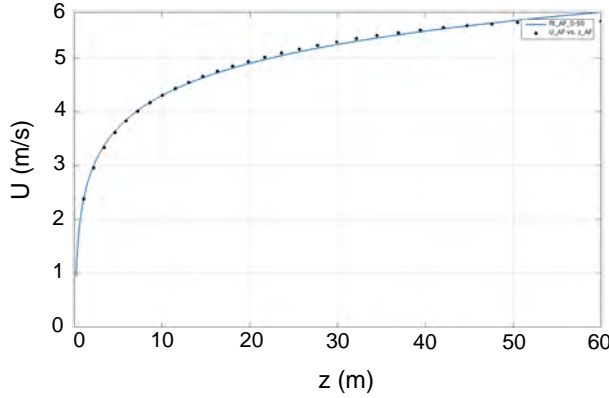
Approach flow:  $z \in [0 ; 60]$  m

-  $u^*=0.3605$  m/s      -  $R^2=0.9965$   
-  $z_0=0.067934$  m      -  $RMSE=0.0529$

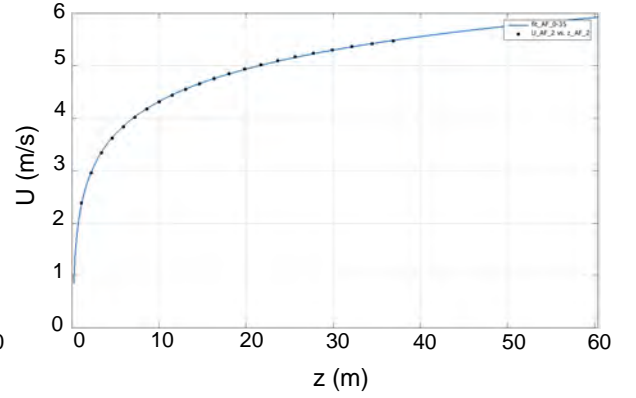
Approach flow:  $z \in [0 ; 35]$  m

-  $u^*=0.3733$  m/s      -  $R^2=0.9997$   
-  $z_0=0.067968$  m      -  $RMSE=0.0138$

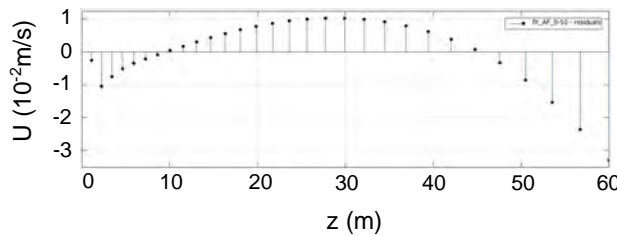
Curve fitting:



Curve fitting:



Residuals:



Residuals:

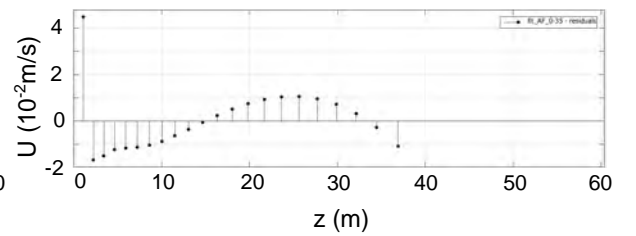


Figure a.11: Fitting of the approach flow for the actual simulations.

## L Complements to the case study A1-1

### L.1 Comparison of the 2D flow features

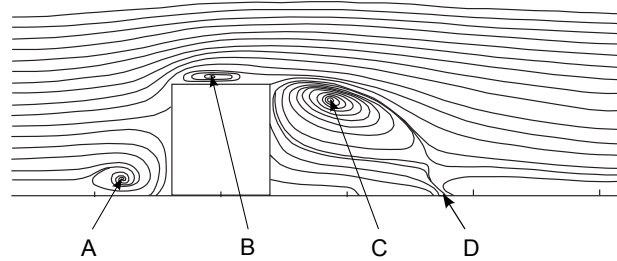


Figure a.12: Identification of the flow structures (Adapted from [Meroney et al. \(1999\)](#)).

	A		B		C		D	
Case	X/H	Z/H	X/H	Z/H	X/H	Z/H	X/H	Z/H
Exp. CEDVAL	-0.78	0.14	-0.09	1.07	0.88	0.84	1.78	0.00
LBM LES fetch= 3 H	-0.82	0.17	0.01	1.08	1.12	0.95	2.60	0.00
LBM LES fetch= 15.6 H	-0.82	0.15	0.05	1.10	1.06	0.96	2.54	0.00
RANS RSM rough	-1.02	0.10	0.14	1.14	1.34	0.94	2.92	0.00
RANS RSM smooth	-0.89	0.10	0.13	1.14	1.38	0.95	3.24	0.00
RANS Rk- $\epsilon$ rough	-0.800	0.10	-0.17	1.06	1.44	0.82	3.44	0.00
RANS Rk- $\epsilon$ smooth	-0.78	0.09	-0.06	1.08	1.36	0.85	3.68	0.00

Table a.4: Main characteristics of the flow structures around the obstacle for the case A1-1.

### L.2 Comparison of the top bubbles predicted by the steady RANS models

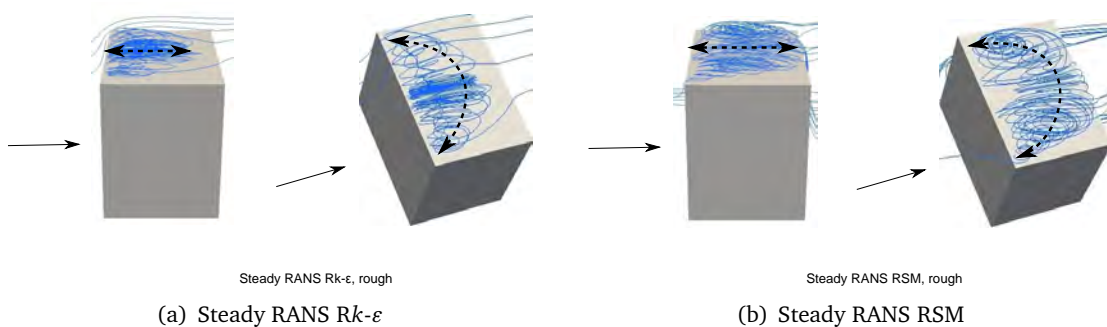


Figure a.13: Top bubbles simulated by the steady RANS Rk- $\epsilon$  and RSM turbulence models for the case A1-1.

## M Levels of the scaled residuals reached at the end of simulations

The threshold levels of scaled residuals were set very small ( $10^{-6}$  for the continuity,  $10^{-8}$  for the mean velocity components and  $10^{-7}$  for the Reynolds stresses,  $k$  and  $\varepsilon$ ), so that they will generally not be the stop criterion of the simulation. Convergence was preferably assessed by monitoring of several profiles in the computational domain.

Tab. a.5 provides an upper bound of the scaled residuals at which the simulations were stopped for each case study:

	Continuity	U, V, W	k, $\varepsilon$
Cube	$< 7.5 \times 10^{-4}$	$< 2.5 \times 10^{-6}$	$< 7.5 \times 10^{-6}$
Cube mesh +	$< 2.5 \times 10^{-4}$	$< 1 \times 10^{-6}$	$< 2.5 \times 10^{-6}$
Cuboid 1	$< 5 \times 10^{-3}$	$< 2.5 \times 10^{-8}$	$< 2.5 \times 10^{-4}$
Cuboid 1 mesh +	$< 1 \times 10^{-5}$	$< 2.5 \times 10^{-9}$	$< 2.5 \times 10^{-7}$
Cuboid 2	$< 1 \times 10^{-5}$	$< 2.5 \times 10^{-9}$	$< 5 \times 10^{-8}$
Cuboid 2 mesh +	$< 2.5 \times 10^{-5}$	$< 2.5 \times 10^{-8}$	$< 7.5 \times 10^{-7}$
L building 1	$< 2.5 \times 10^{-3}$	$< 2.5 \times 10^{-5}$	$< 5 \times 10^{-5}$
L building 1 mesh +	$< 2.5 \times 10^{-5}$	$< 5 \times 10^{-8}$	$< 1 \times 10^{-6}$
L building 2	$< 2.5 \times 10^{-3}$	$< 7.5 \times 10^{-6}$	$< 5 \times 10^{-4}$
L building 2 mesh +	$< 2.5 \times 10^{-5}$	$< 2.5 \times 10^{-8}$	$< 2.5 \times 10^{-6}$
L building 3	$< 5 \times 10^{-3}$	$< 1 \times 10^{-5}$	$< 2.5 \times 10^{-4}$
L building 3 mesh +	$< 5 \times 10^{-6}$	$< 5 \times 10^{-9}$	$< 7.5 \times 10^{-8}$
U building 1	$< 2.5 \times 10^{-3}$	$< 7.5 \times 10^{-6}$	$< 2.5 \times 10^{-4}$
U building 1 mesh +	$< 2.5 \times 10^{-5}$	$< 1 \times 10^{-8}$	$< 1 \times 10^{-6}$
U building 2	$< 2.5 \times 10^{-3}$	$< 1 \times 10^{-5}$	$< 2.5 \times 10^{-4}$
U building 2 mesh +	$< 1 \times 10^{-5}$	$< 2.5 \times 10^{-9}$	$< 2.5 \times 10^{-7}$
U building 3	$< 1 \times 10^{-3}$	$< 5 \times 10^{-6}$	$< 1 \times 10^{-4}$
U building 3 mesh +	$< 2.5 \times 10^{-4}$	$< 7.5 \times 10^{-7}$	$< 2.5 \times 10^{-5}$
Patio	$< 1 \times 10^{-4}$	$< 2.5 \times 10^{-7}$	$< 7.5 \times 10^{-6}$
Patio mesh +	$< 2.5 \times 10^{-5}$	$< 5 \times 10^{-8}$	$< 1 \times 10^{-5}$
Cube array	$< 2.5 \times 10^{-3}$	$< 2.5 \times 10^{-6}$	$< 2.5 \times 10^{-4}$
Row block 1	$< 2.5 \times 10^{-4}$	$< 2.5 \times 10^{-6}$	$< 2.5 \times 10^{-6}$
Row block 2	$< 1 \times 10^{-4}$	$< 2.5 \times 10^{-7}$	$< 1 \times 10^{-5}$
U block 1	$< 5 \times 10^{-5}$	$< 2.5 \times 10^{-7}$	$< 2.5 \times 10^{-6}$
U block 2	$< 2.5 \times 10^{-3}$	$< 1 \times 10^{-5}$	$< 1 \times 10^{-4}$
Enclosed block	$< 2.5 \times 10^{-4}$	$5 \times 10^{-7}$	$< 2.5 \times 10^{-5}$
Cont. Patio array	$< 2.5 \times 10^{-4}$	$< 2.5 \times 10^{-7}$	$< 5 \times 10^{-6}$

Table a.5: Levels of the scaled residuals reached at the end of simulations.

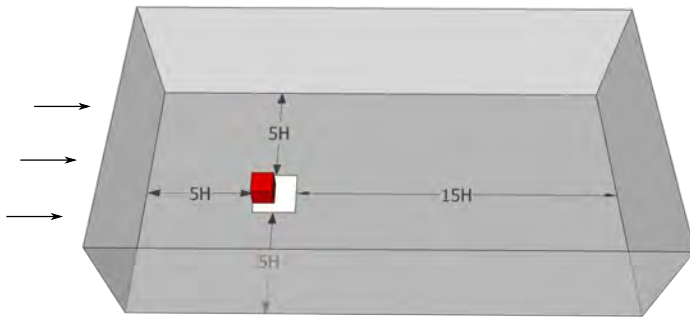


## N Aerodynamic results for the isolated building types







### N.1 The cube

*Basic*

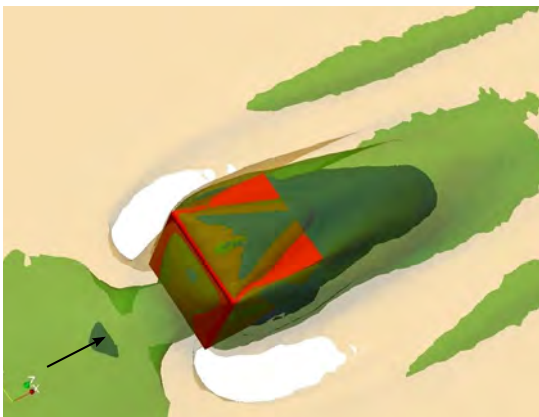
Computational configuration:



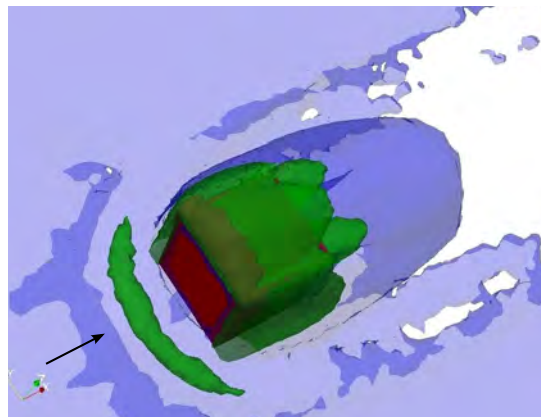
Legend

3D Velocity:		0.5 m/s
		1.5 m/s
		2.5 m/s
3D Vorticity:		0.5 rad/s
		1.5 rad/s
		5.5 rad/s

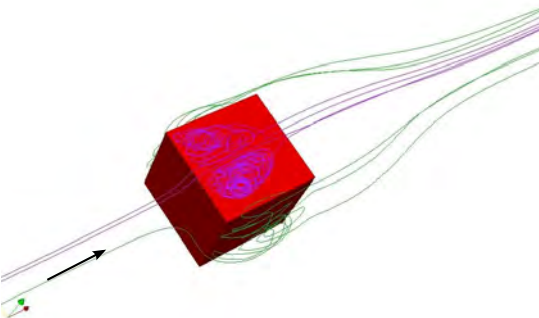
3D mean velocity:



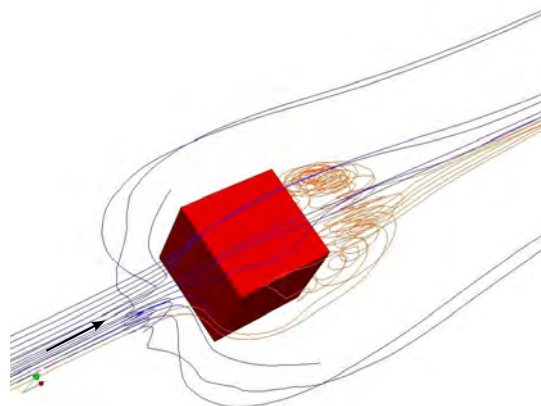
3D vorticity:



Streamlines (int):

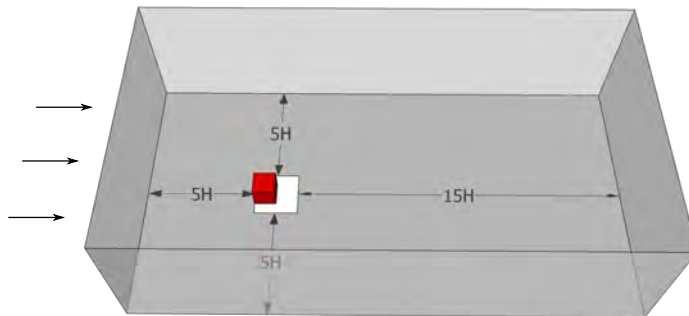


Streamlines (ext):



*Mesh +*

Computational configuration:



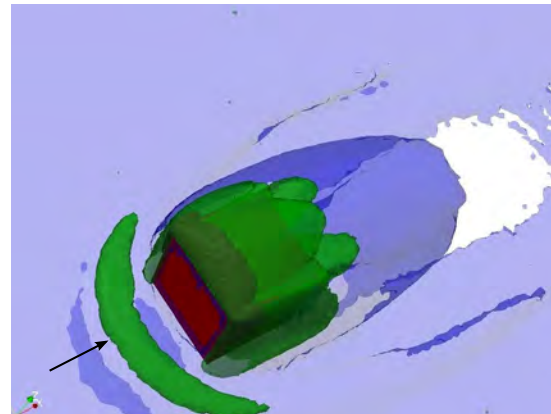
Legend

3D Velocity:	<span style="display: inline-block; width: 15px; height: 15px; background-color: blue; margin-right: 5px;"></span>	0.5 m/s
	<span style="display: inline-block; width: 15px; height: 15px; background-color: green; margin-right: 5px;"></span>	1.5 m/s
	<span style="display: inline-block; width: 15px; height: 15px; background-color: yellow; margin-right: 5px;"></span>	2.5 m/s
3D Vorticity:	<span style="display: inline-block; width: 15px; height: 15px; background-color: blue; margin-right: 5px;"></span>	0.5 rad/s
	<span style="display: inline-block; width: 15px; height: 15px; background-color: green; margin-right: 5px;"></span>	1.5 rad/s
	<span style="display: inline-block; width: 15px; height: 15px; background-color: red; margin-right: 5px;"></span>	5.5 rad/s

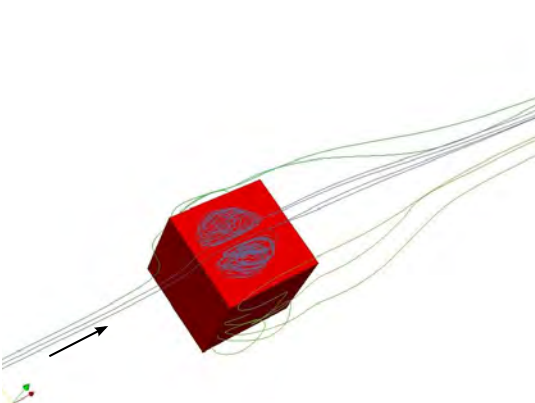
3D mean velocity:



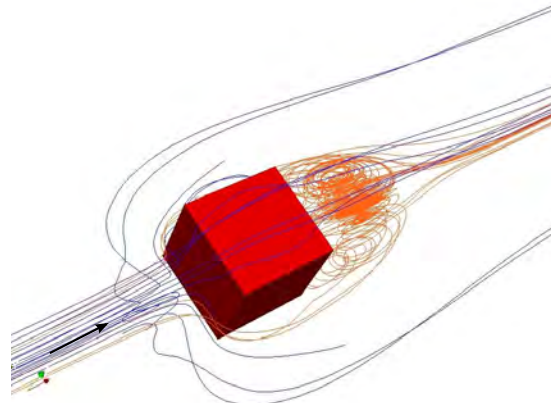
3D vorticity:



Streamlines (int):

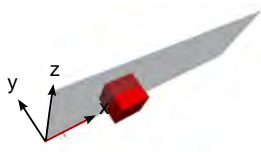


Streamlines (ext):

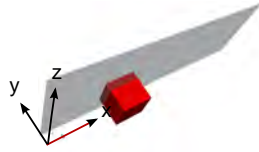


*Basic*

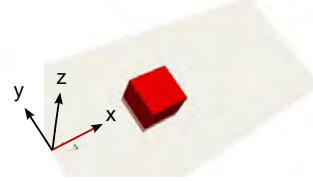
Plane  $y=0\text{m}$ :



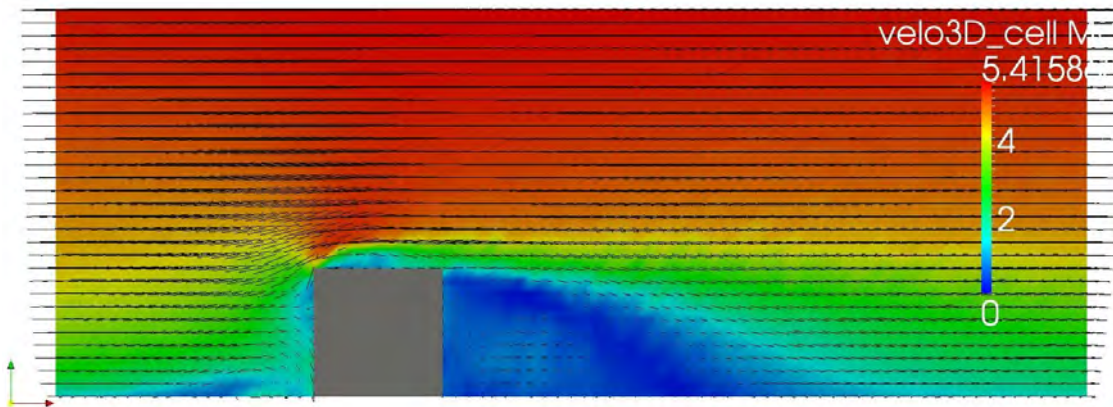
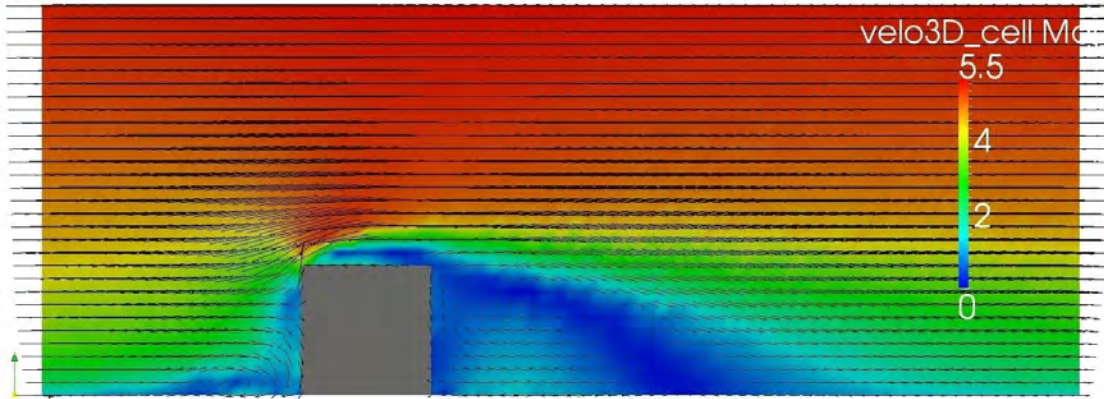
Plane  $y=2.5\text{m}$ :



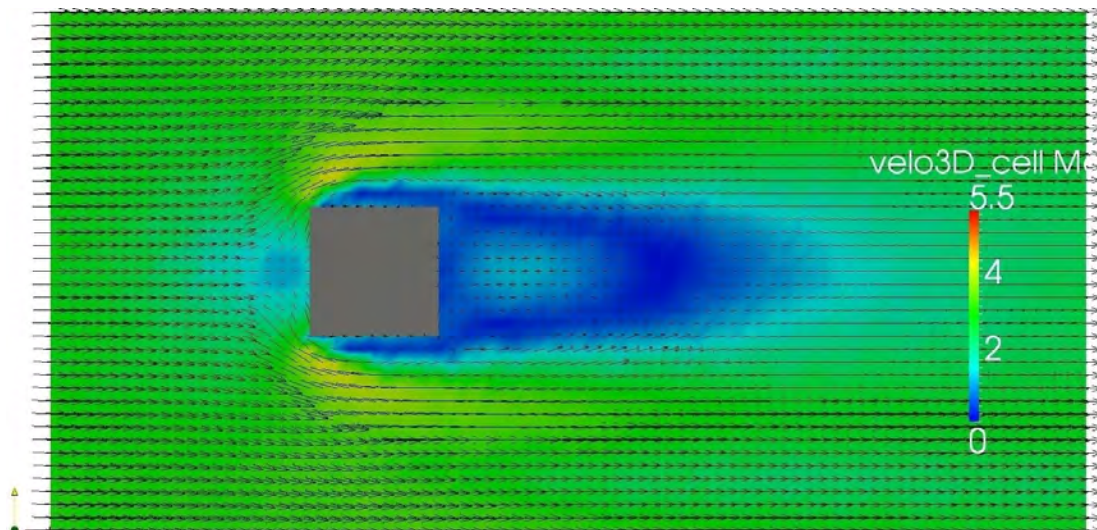
Plane  $z=2\text{m}$ :



Mean velocity field, planes  $y=0\text{m}$  and  $2.5\text{m}$ :



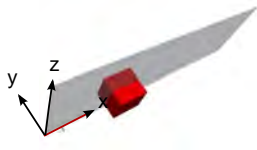
Mean velocity field, plane  $z=2\text{m}$ :



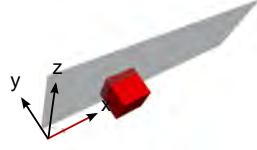


*Mesh +*

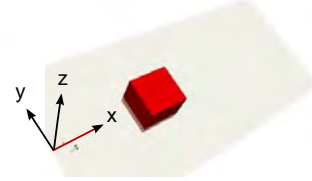
Plane  $y=0\text{m}$ :



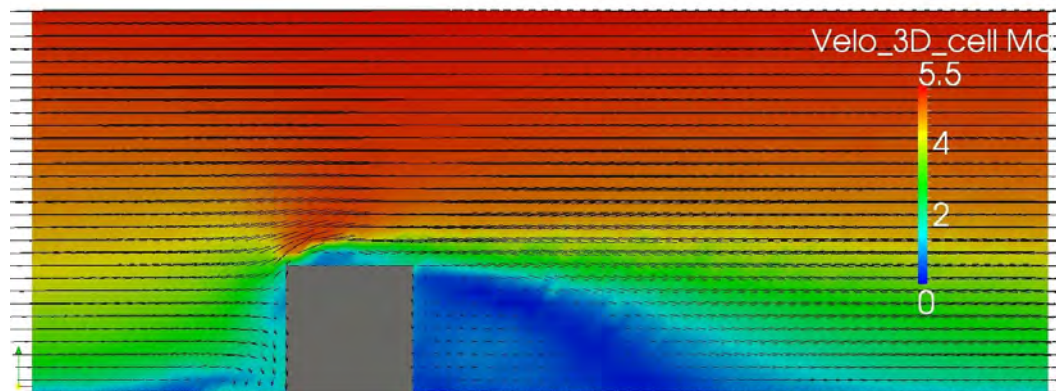
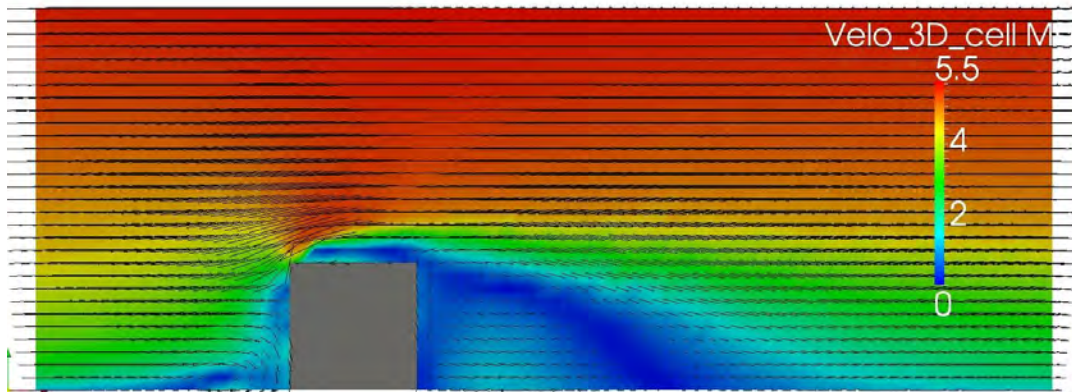
Plane  $y=2.5\text{m}$ :



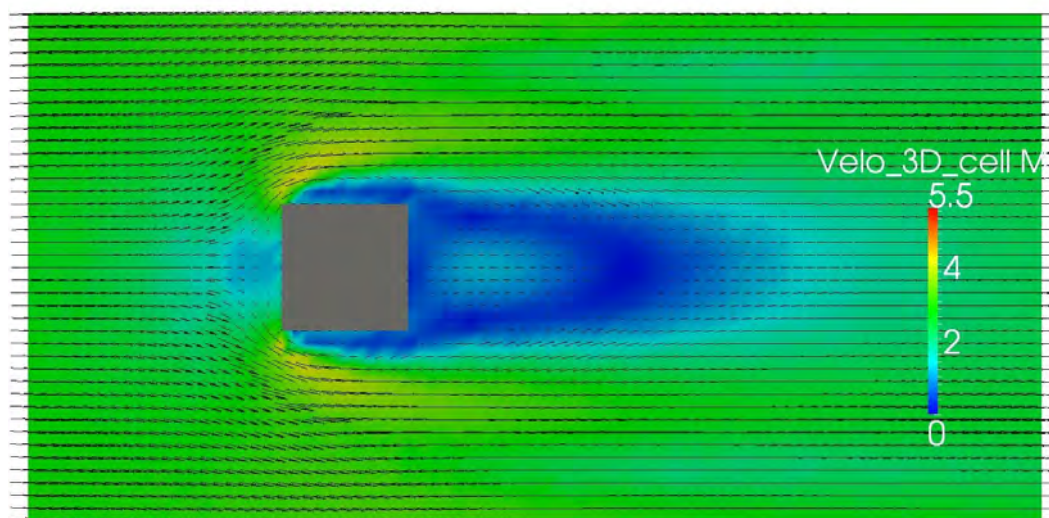
Plane  $z=2\text{m}$ :



Mean velocity field, planes  $y=0\text{m}$  and  $2.5\text{m}$ :



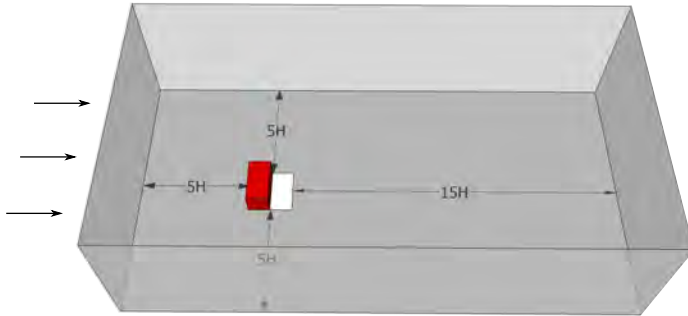
Mean velocity field, plane  $z=2\text{m}$ :









## N.2 The cuboid 1

*Basic*

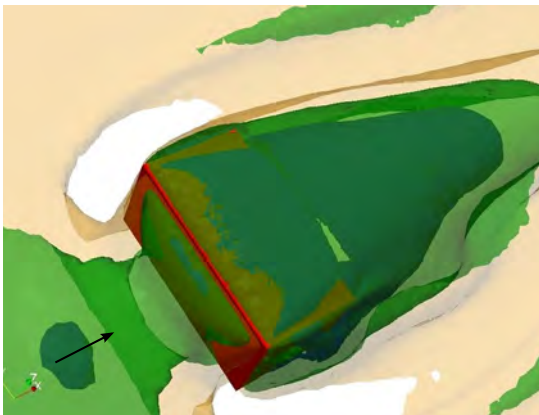
Computational configuration:



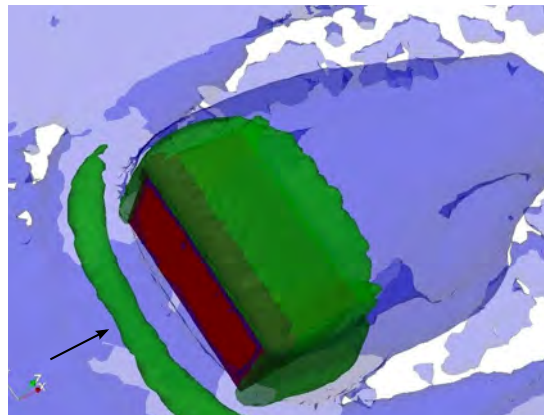
Legend

3D Velocity:		0.5 m/s
		1.5 m/s
		2.5 m/s
3D Vorticity:		0.5 rad/s
		1.5 rad/s
		5.5 rad/s

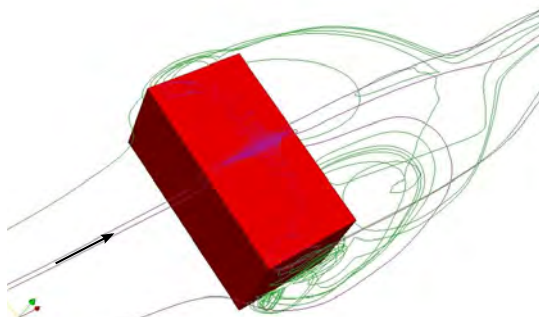
3D mean velocity:



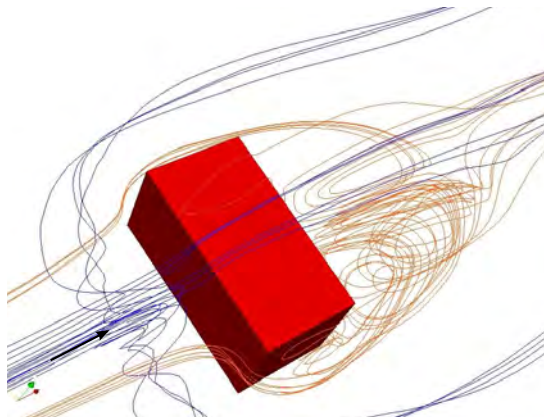
3D vorticity:



Streamlines (int):

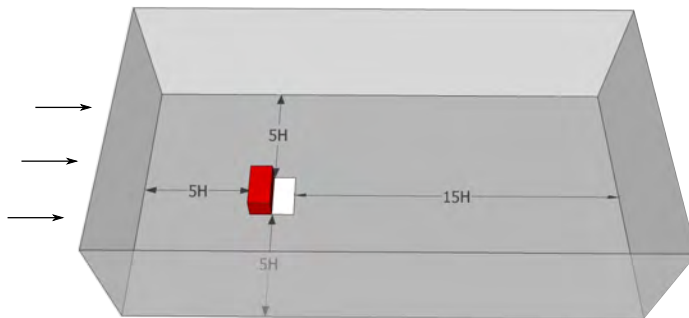


Streamlines (ext):



*Mesh +*

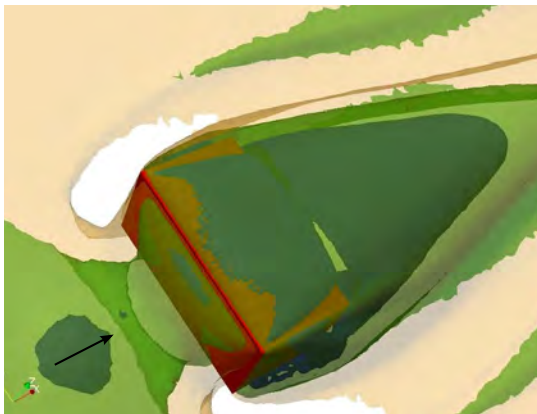
Computational configuration:



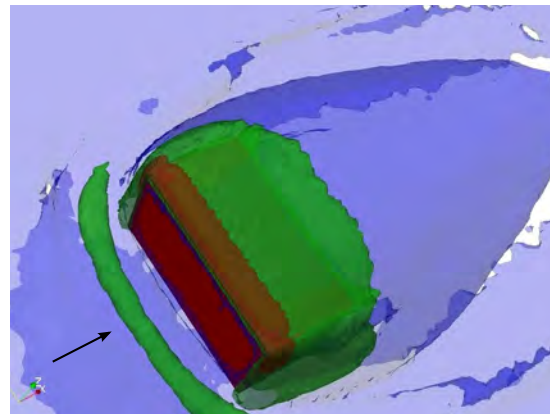
Legend

3D Velocity:	<span style="display: inline-block; width: 15px; height: 15px; background-color: blue; margin-right: 5px;"></span>	0.5 m/s
	<span style="display: inline-block; width: 15px; height: 15px; background-color: green; margin-right: 5px;"></span>	1.5 m/s
	<span style="display: inline-block; width: 15px; height: 15px; background-color: yellow; margin-right: 5px;"></span>	2.5 m/s
3D Vorticity:	<span style="display: inline-block; width: 15px; height: 15px; background-color: blue; margin-right: 5px;"></span>	0.5 rad/s
	<span style="display: inline-block; width: 15px; height: 15px; background-color: green; margin-right: 5px;"></span>	1.5 rad/s
	<span style="display: inline-block; width: 15px; height: 15px; background-color: red; margin-right: 5px;"></span>	5.5 rad/s

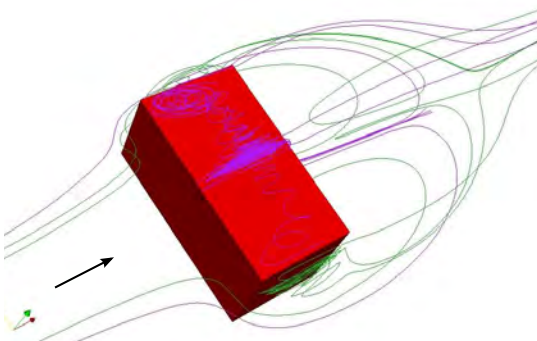
3D mean velocity:



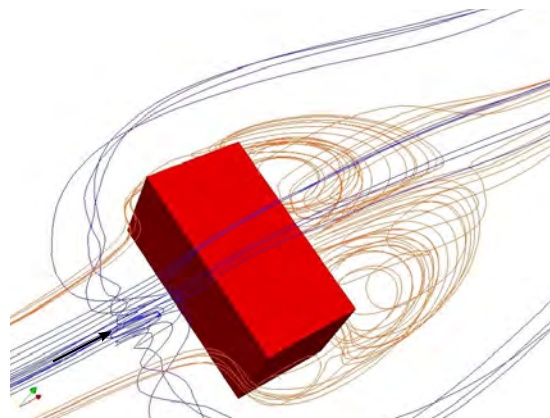
3D vorticity:



Streamlines (int):



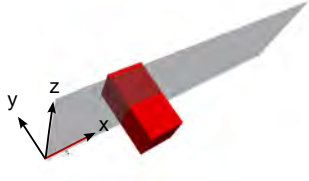
Streamlines (ext):



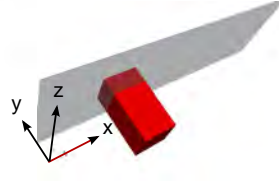


*Basic*

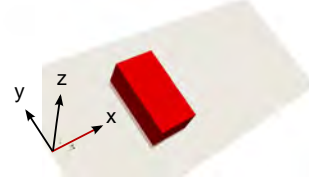
Plane  $y=0\text{m}$ :



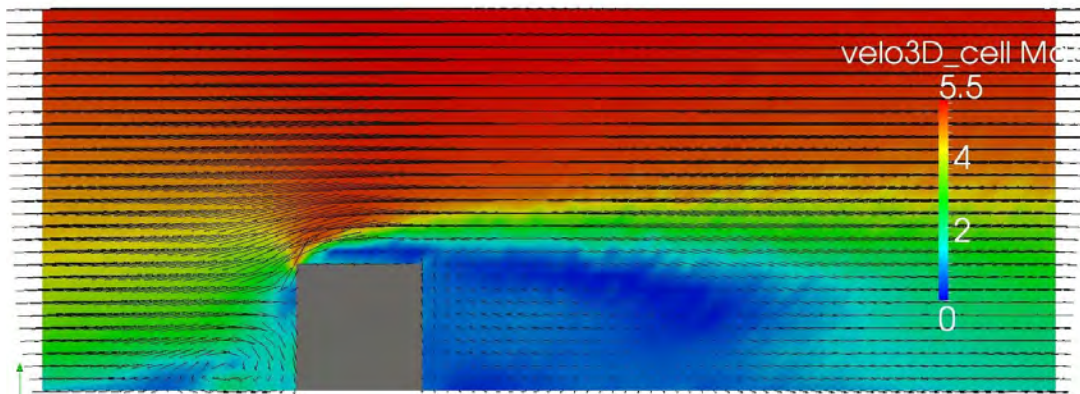
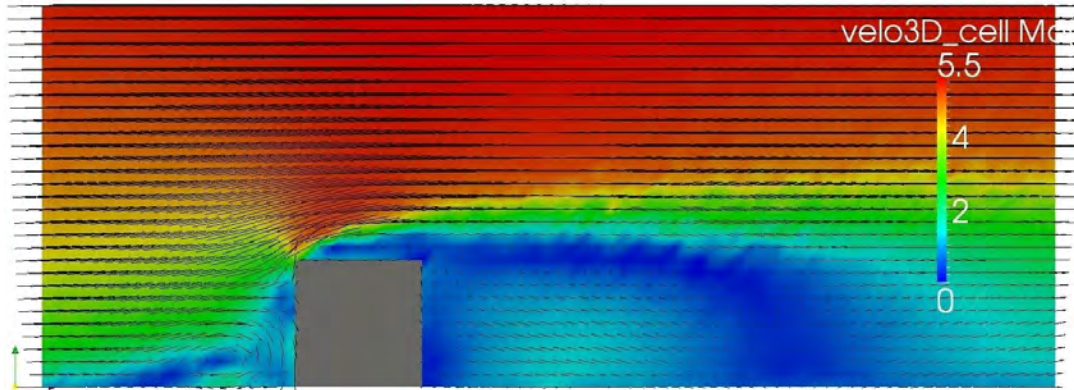
Plane  $y=5\text{m}$ :



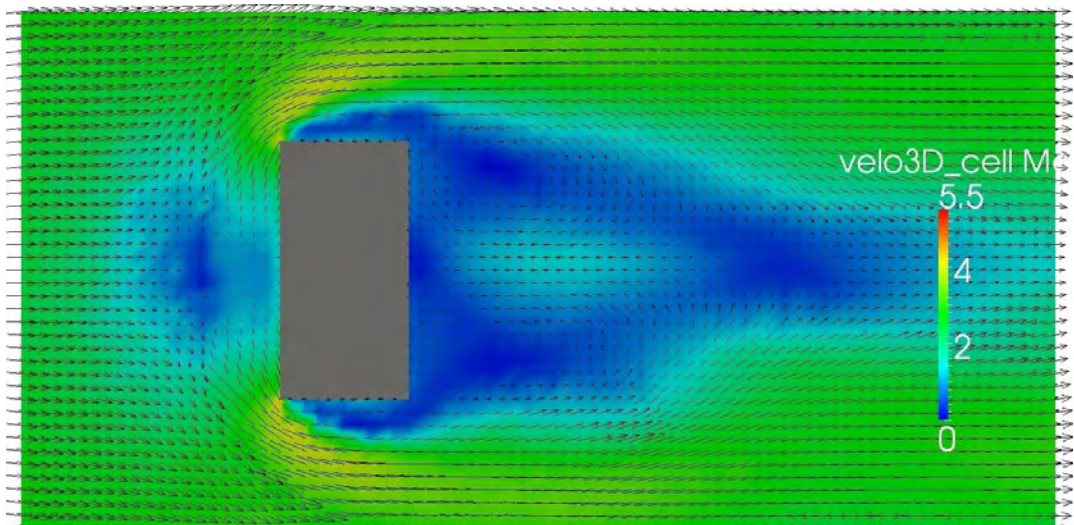
Plane  $z=2\text{m}$ :



Mean velocity field, planes  $y=0\text{m}$  and  $5\text{m}$ :



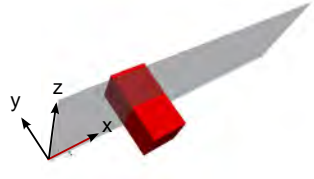
Mean velocity field, plane  $z=2\text{m}$ :



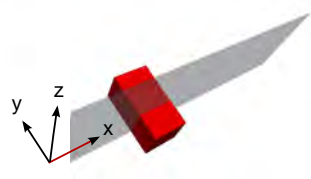


*Mesh +*

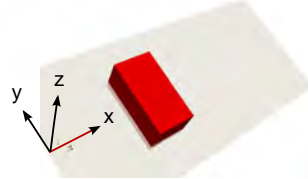
Plane y=0m:



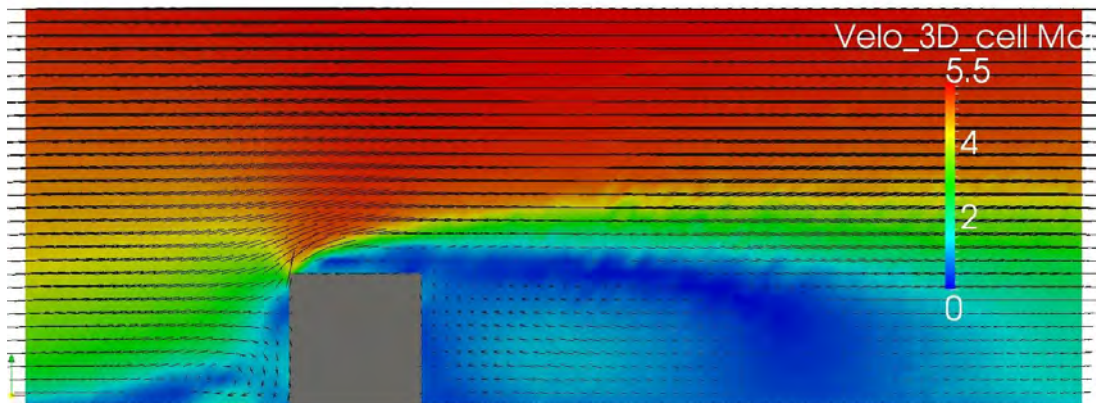
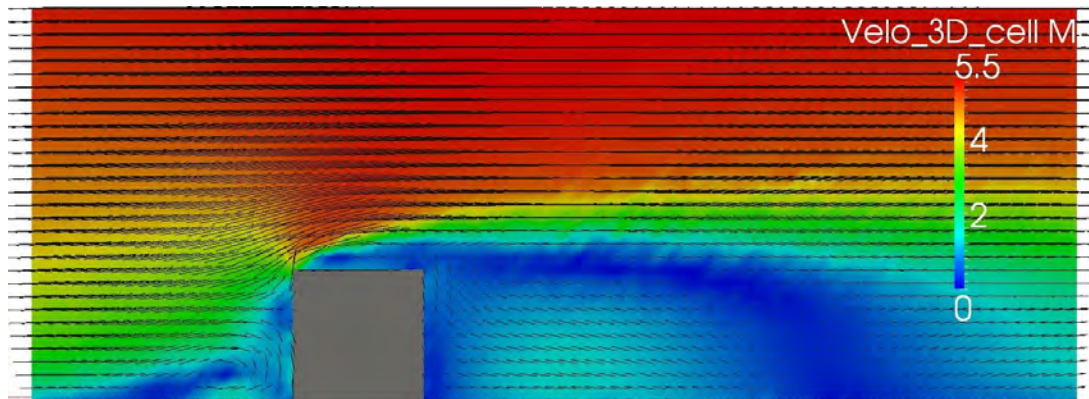
Plane y=-2.5m:



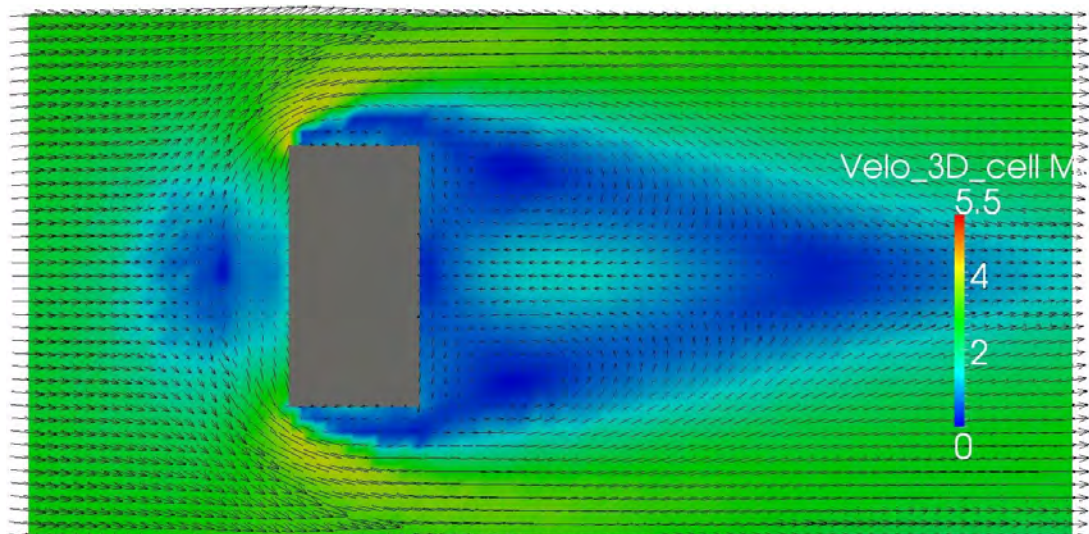
Plane z=2m:



Mean velocity field, planes y=0m and -2.5m:



Mean velocity field, plane z=2m:

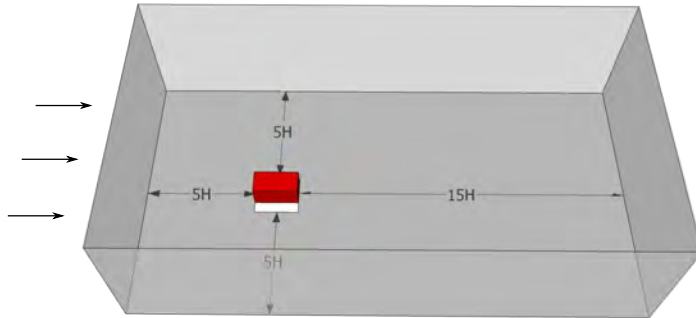










### N.3 The cuboid 2

*Basic*

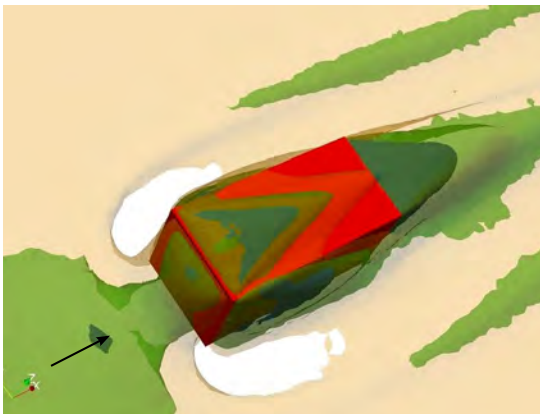
Computational configuration:



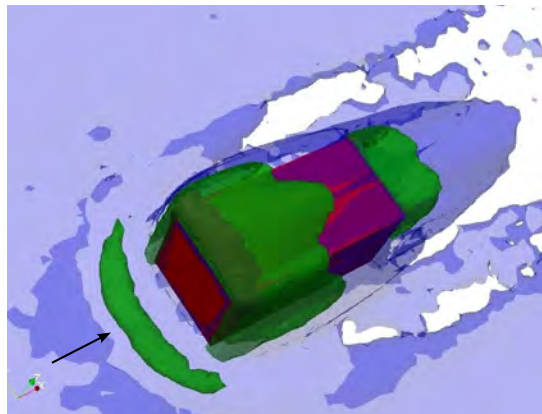
Legend

3D Velocity:		0.5 m/s
		1.5 m/s
		2.5 m/s
3D Vorticity:		0.5 rad/s
		1.5 rad/s
		5.5 rad/s

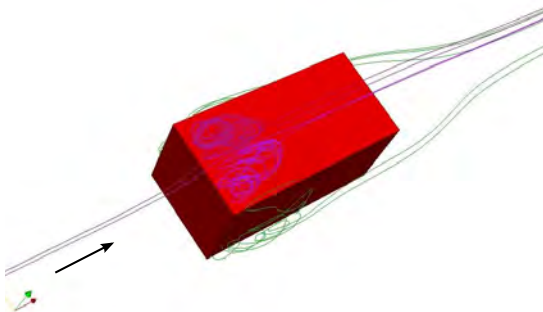
3D mean velocity:



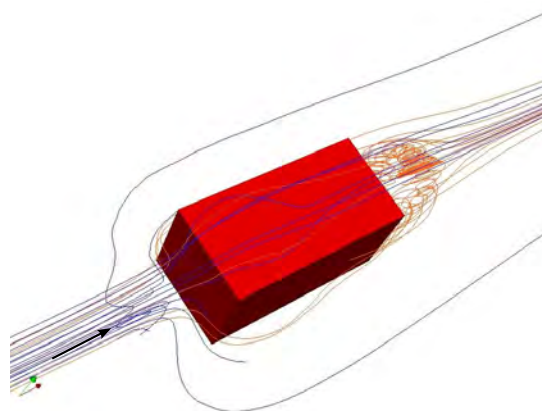
3D vorticity:



Streamlines (int):

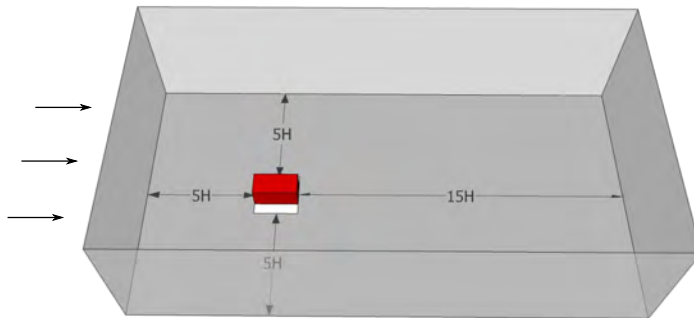


Streamlines (ext):



*Mesh +*

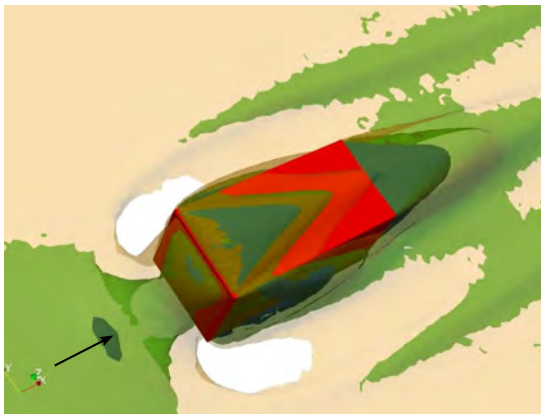
Computational configuration:



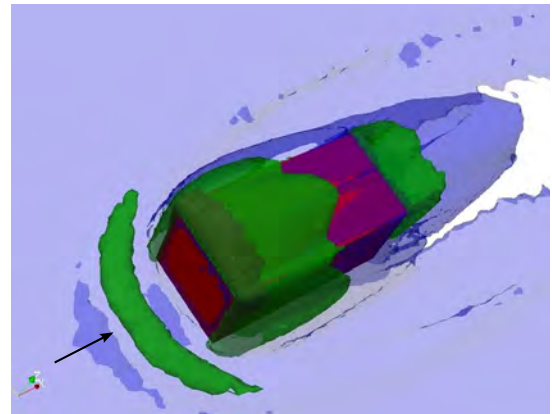
Legend

3D Velocity:	<span style="display: inline-block; width: 15px; height: 15px; background-color: blue; margin-right: 5px;"></span>	0.5 m/s
	<span style="display: inline-block; width: 15px; height: 15px; background-color: green; margin-right: 5px;"></span>	1.5 m/s
	<span style="display: inline-block; width: 15px; height: 15px; background-color: yellow; margin-right: 5px;"></span>	2.5 m/s
3D Vorticity:	<span style="display: inline-block; width: 15px; height: 15px; background-color: blue; margin-right: 5px;"></span>	0.5 rad/s
	<span style="display: inline-block; width: 15px; height: 15px; background-color: green; margin-right: 5px;"></span>	1.5 rad/s
	<span style="display: inline-block; width: 15px; height: 15px; background-color: red; margin-right: 5px;"></span>	5.5 rad/s

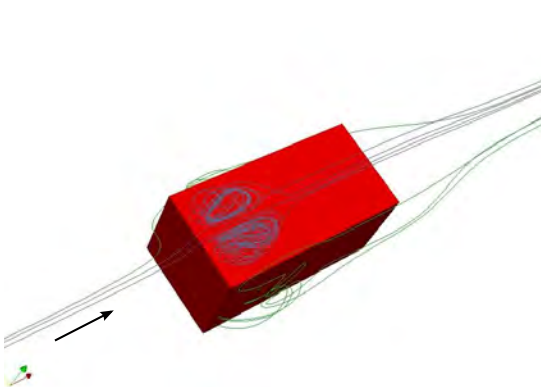
3D mean velocity:



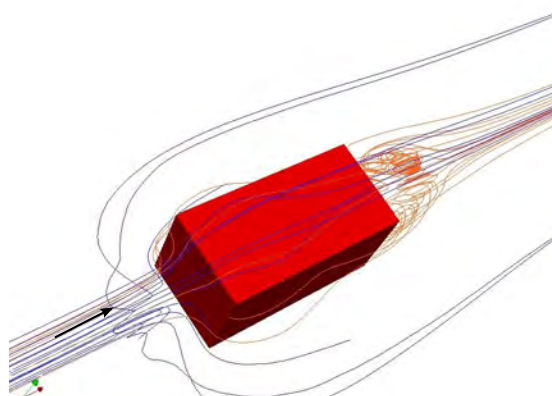
3D vorticity:



Streamlines (int):

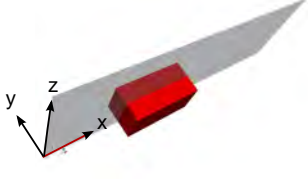


Streamlines (ext):

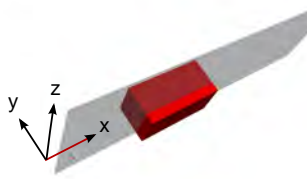


*Basic*

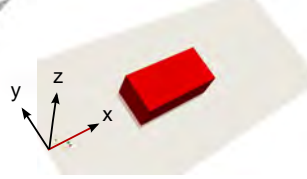
Plane  $y=0\text{m}$ :



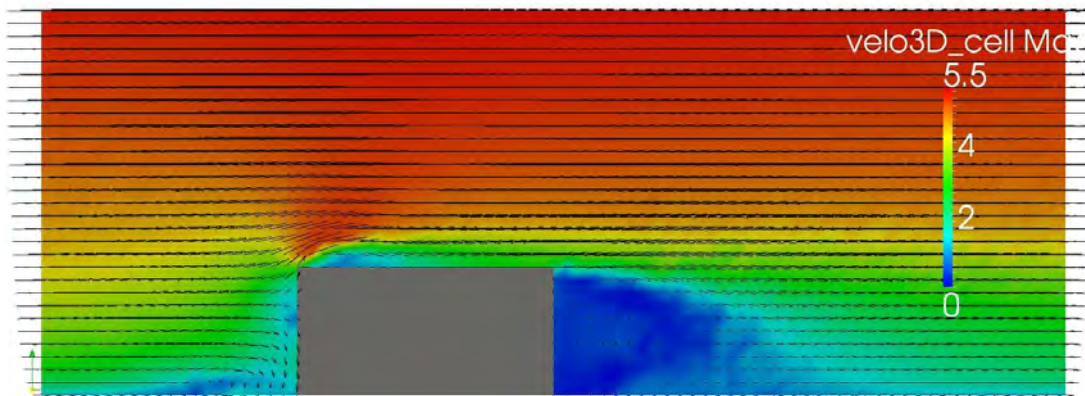
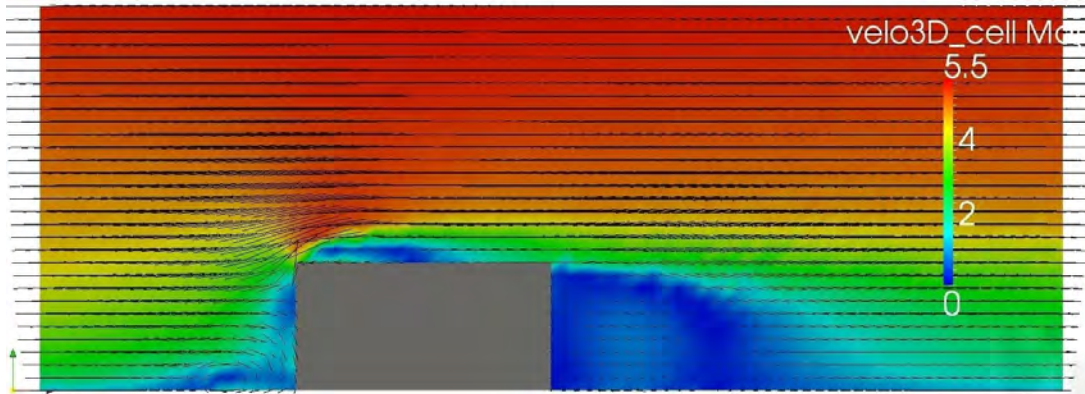
Plane  $y=-2.5\text{m}$ :



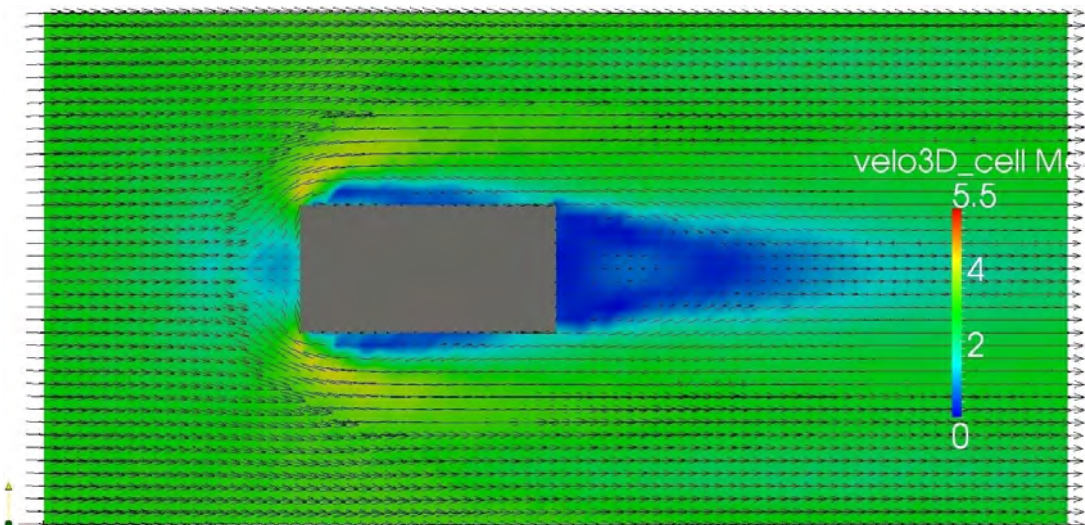
Plane  $z=2\text{m}$ :



Mean velocity field, planes  $y=0\text{m}$  and  $-2.5\text{m}$ :



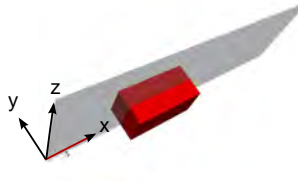
Mean velocity field, plane  $z=2\text{m}$ :



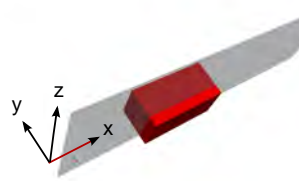


*Mesh +*

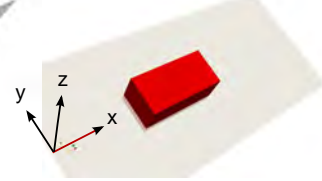
Plane  $y=0\text{m}$ :



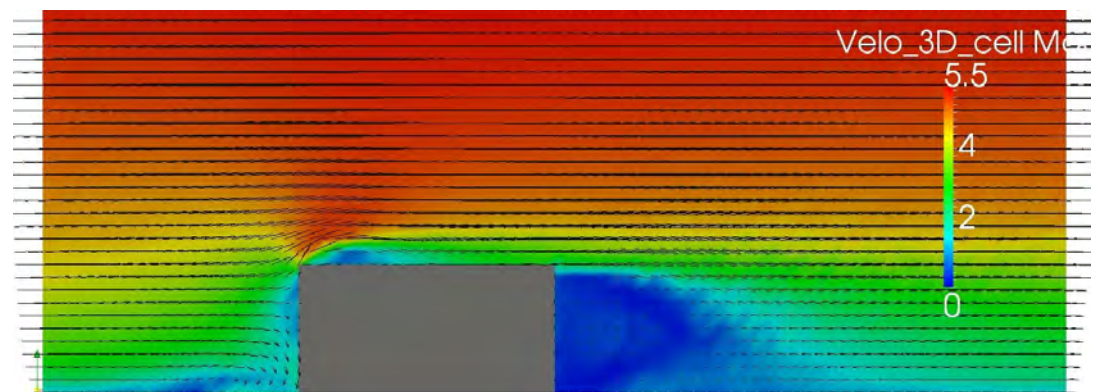
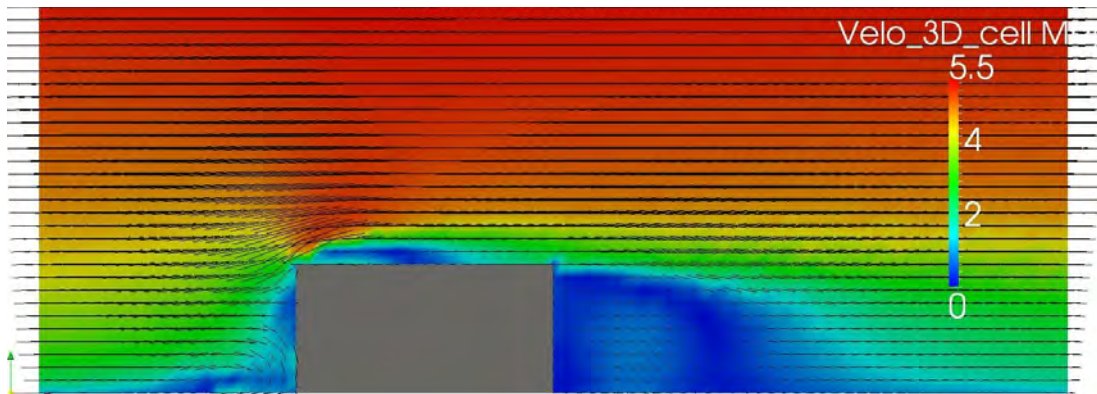
Plane  $y=-2.5\text{m}$ :



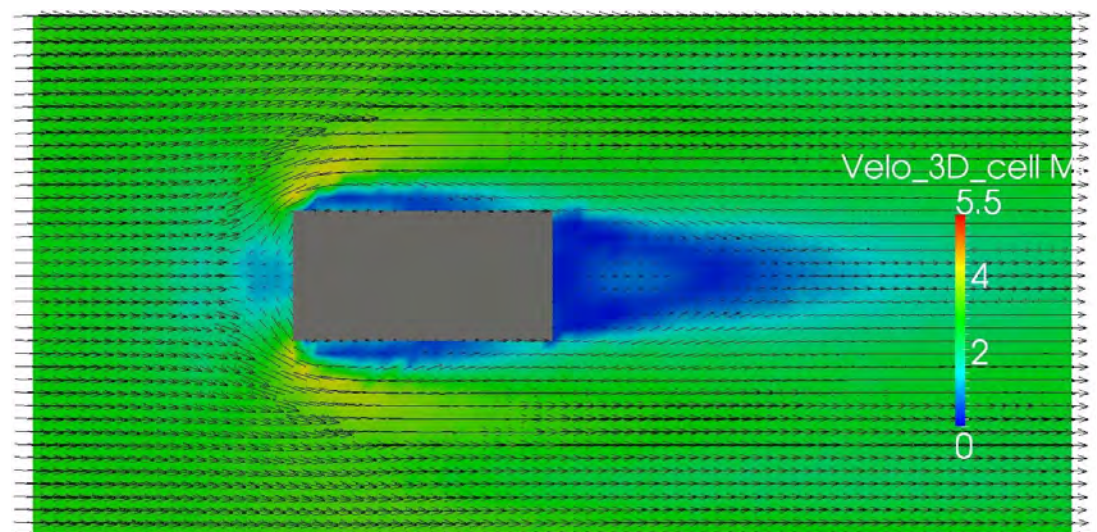
Plane  $z=2\text{m}$ :



Mean velocity field, planes  $y=0\text{m}$  and  $-2.5\text{m}$ :



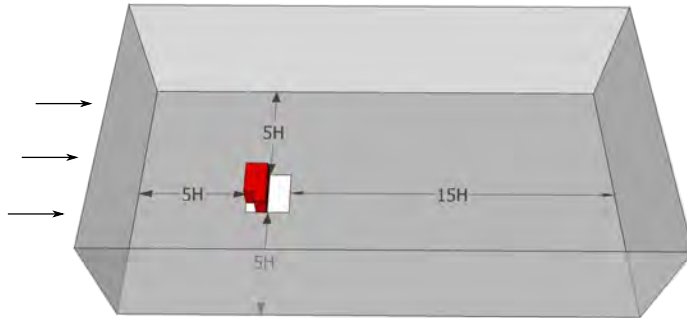
Mean velocity field, plane  $z=2\text{m}$ :









## N.4 The L-building 1

*Basic*

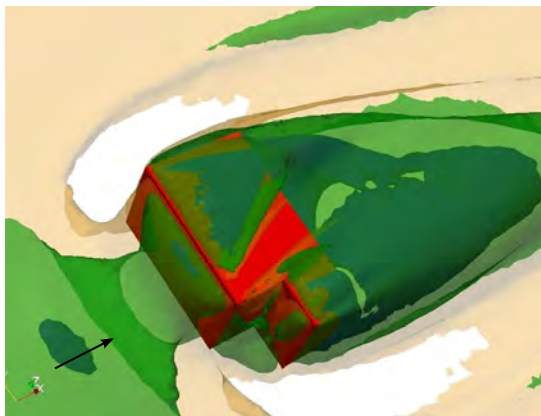
Computational configuration:



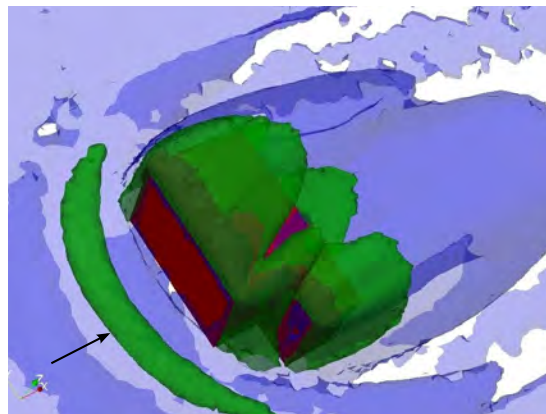
Legend

3D Velocity:		0.5 m/s
		1.5 m/s
		2.5 m/s
3D Vorticity:		0.5 rad/s
		1.5 rad/s
		5.5 rad/s

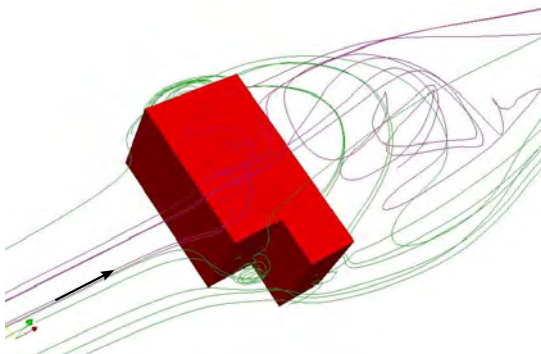
3D mean velocity:



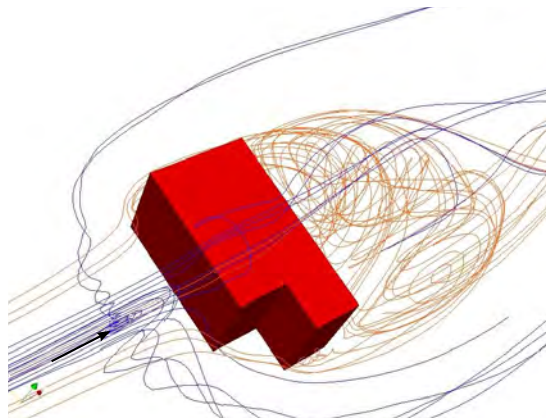
3D vorticity:



Streamlines (int):



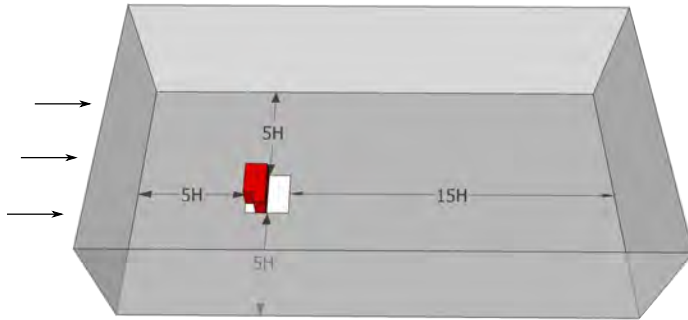
Streamlines (ext):





*Mesh+*

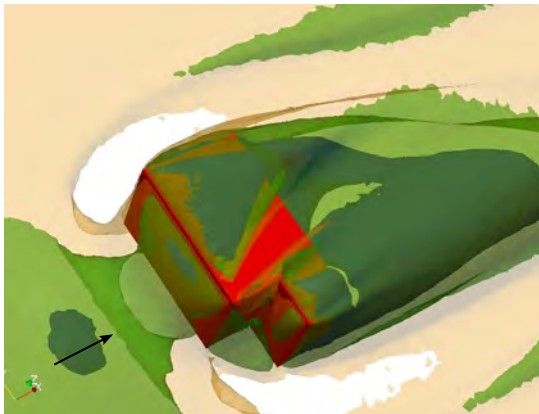
Computational configuration:



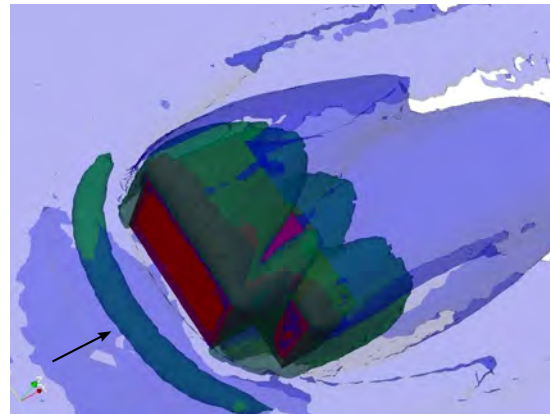
Legend

3D Velocity:	<span style="display:inline-block; width:15px; height:15px; background-color:blue;"></span>	0.5 m/s
	<span style="display:inline-block; width:15px; height:15px; background-color:green;"></span>	1.5 m/s
	<span style="display:inline-block; width:15px; height:15px; background-color:yellow;"></span>	2.5 m/s
3D Vorticity:	<span style="display:inline-block; width:15px; height:15px; background-color:blue;"></span>	0.5 rad/s
	<span style="display:inline-block; width:15px; height:15px; background-color:green;"></span>	1.5 rad/s
	<span style="display:inline-block; width:15px; height:15px; background-color:red;"></span>	5.5 rad/s

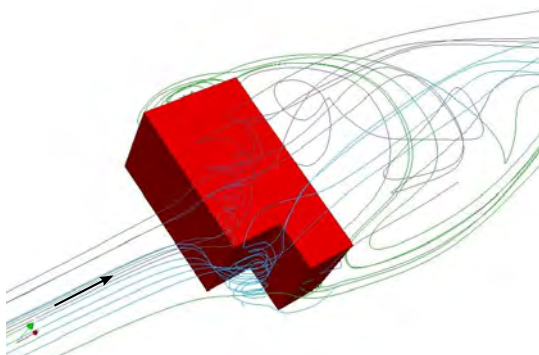
3D mean velocity:



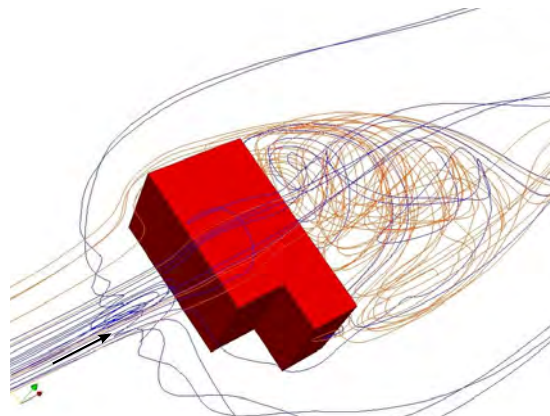
3D vorticity:



Streamlines (int):

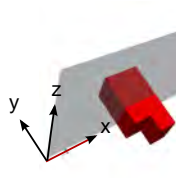


Streamlines (ext):

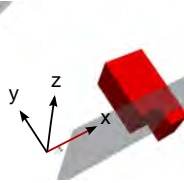


*Basic*

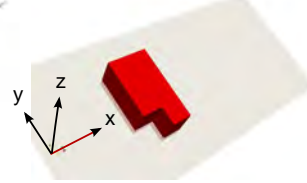
Plane  $y=0\text{m}$ :



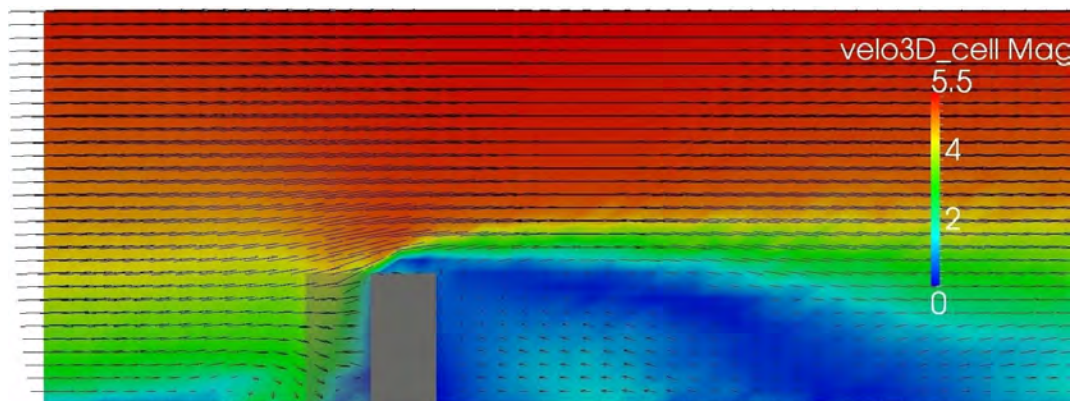
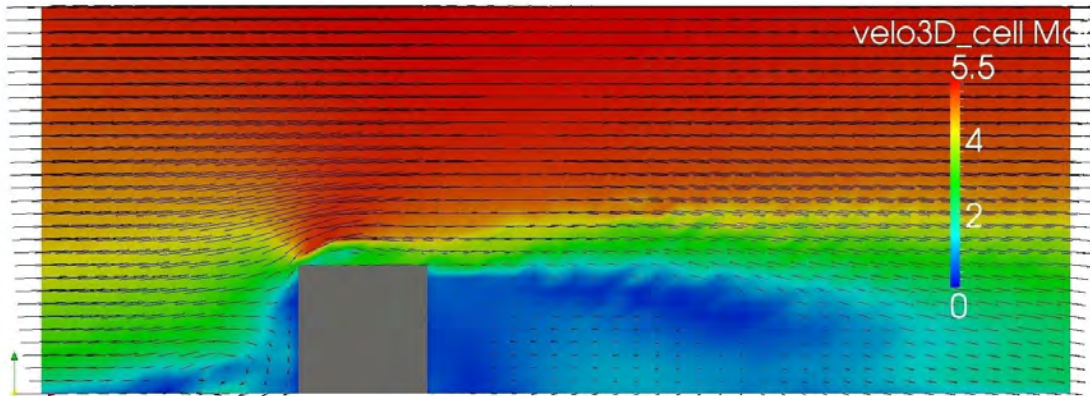
Plane  $y=-7.5\text{m}$ :



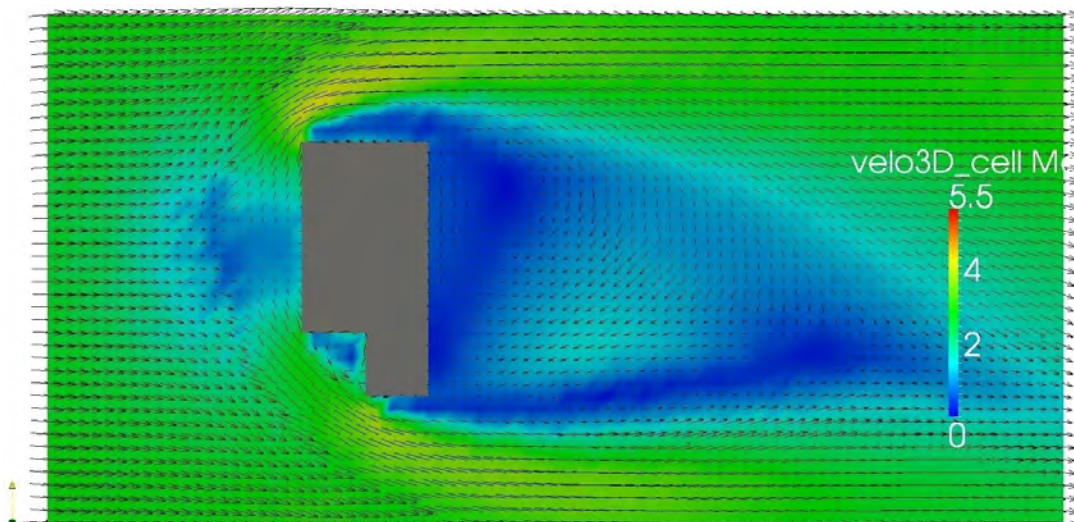
Plane  $z=2\text{m}$ :



Mean velocity field, planes  $y=0\text{m}$  and  $-7.5\text{m}$ :



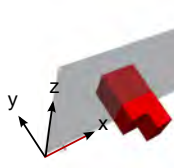
Mean velocity field, plane  $z=2\text{m}$ :



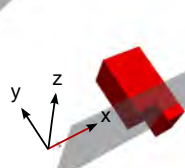


*Mesh +*

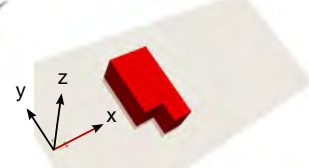
Plane y=0m:



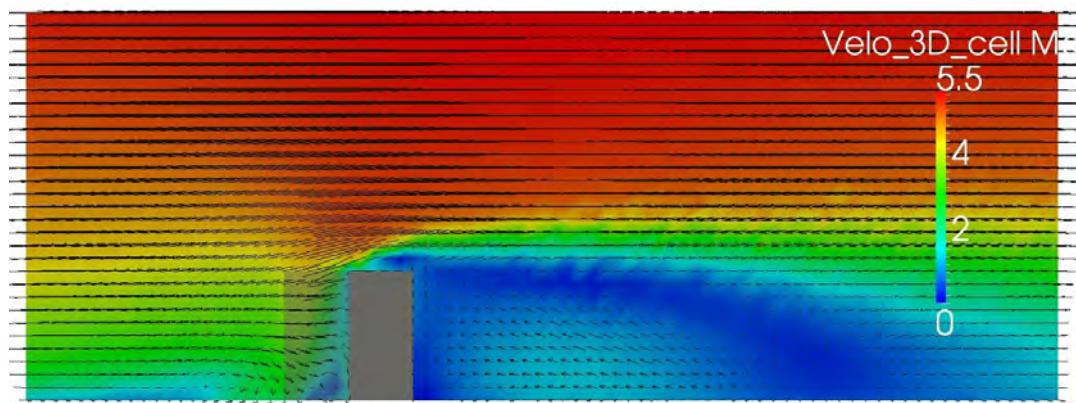
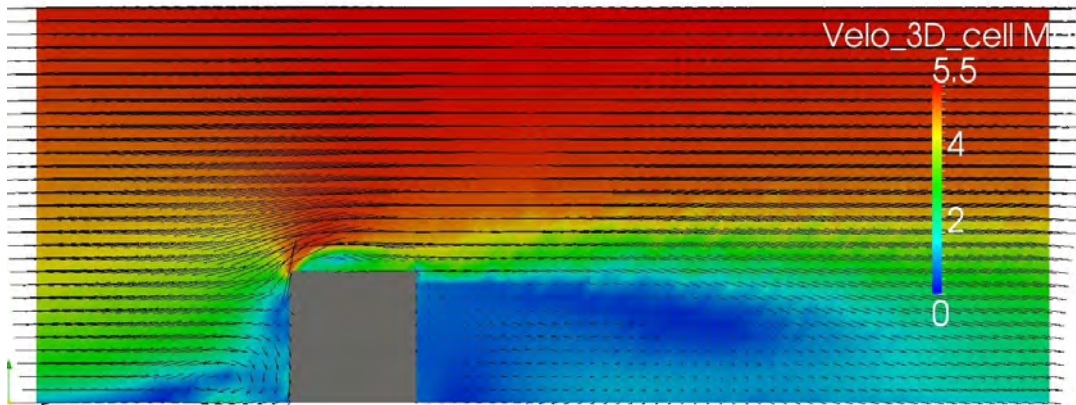
Plane y=-7.5m:



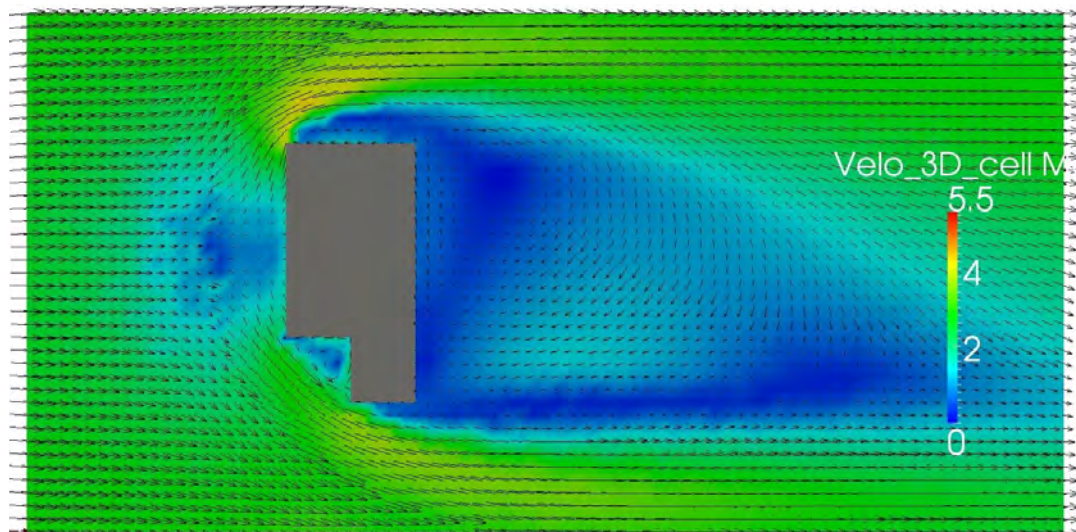
Plane z=2m:



Mean velocity field, planes y=0m and -7.5m:



Mean velocity field, plane z=2m:

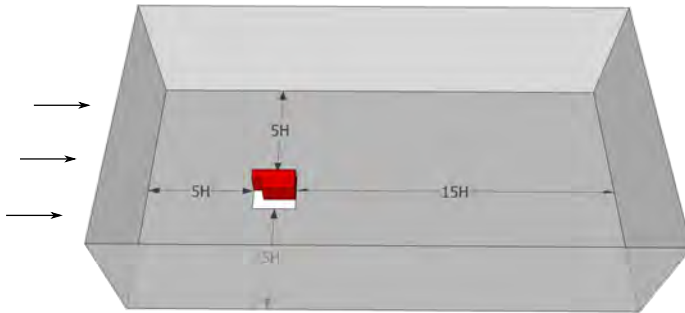










## N.5 The L-building 2

*Basic*

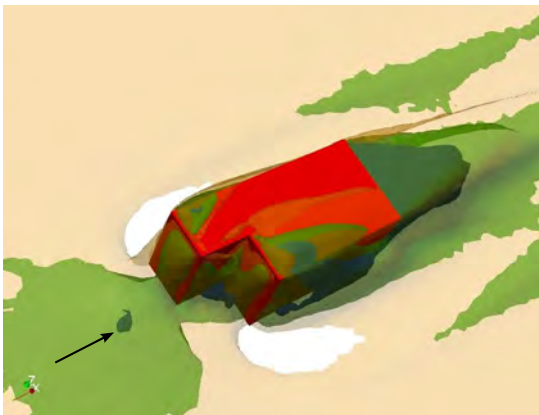
Computational configuration:



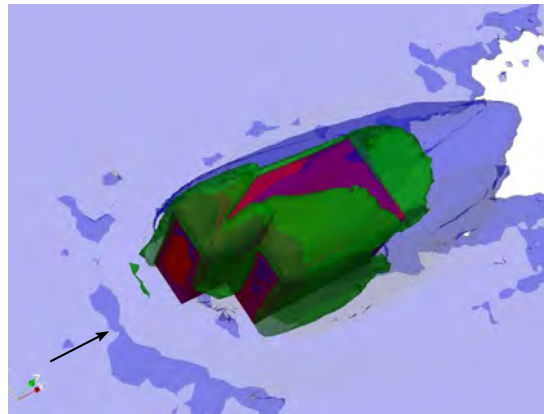
Legend

3D Velocity:		0.5 m/s
		1.5 m/s
		2.5 m/s
3D Vorticity:		0.5 rad/s
		1.5 rad/s
		5.5 rad/s

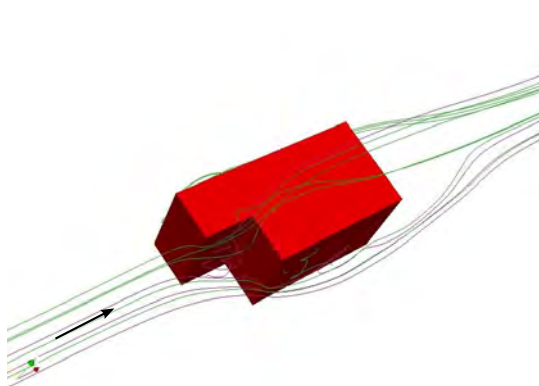
3D mean velocity:



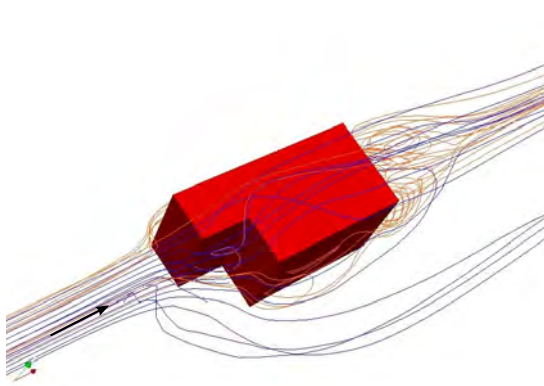
3D vorticity:



Streamlines (int):

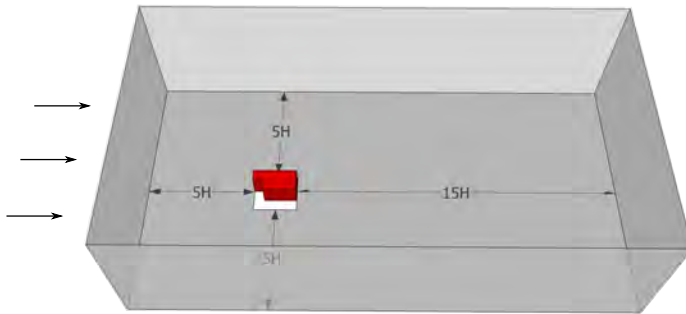


Streamlines (ext):



*Mesh +*

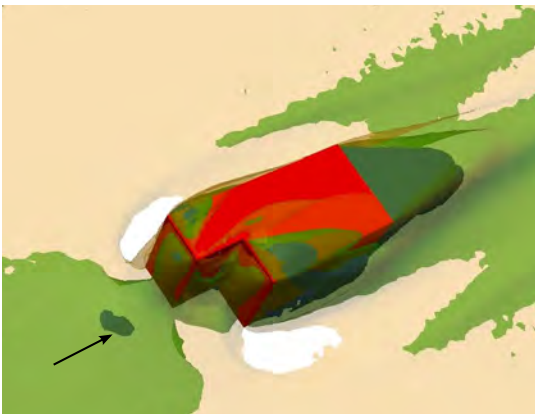
Computational configuration:



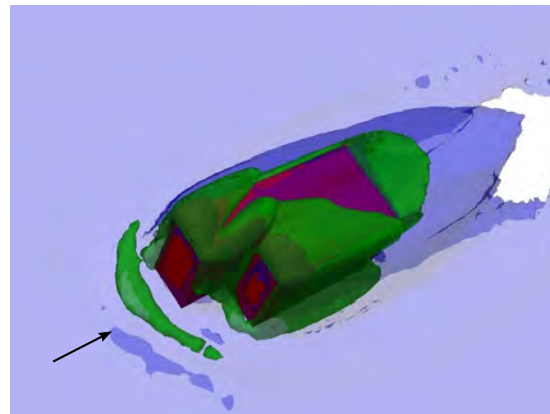
Legend

3D Velocity:	<span style="display:inline-block; width:15px; height:15px; background-color:blue;"></span>	0.5 m/s
	<span style="display:inline-block; width:15px; height:15px; background-color:green;"></span>	1.5 m/s
	<span style="display:inline-block; width:15px; height:15px; background-color:yellow;"></span>	2.5 m/s
3D Vorticity:	<span style="display:inline-block; width:15px; height:15px; background-color:blue;"></span>	0.5 rad/s
	<span style="display:inline-block; width:15px; height:15px; background-color:green;"></span>	1.5 rad/s
	<span style="display:inline-block; width:15px; height:15px; background-color:red;"></span>	5.5 rad/s

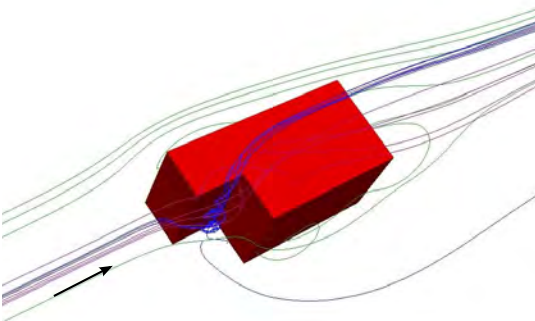
3D mean velocity:



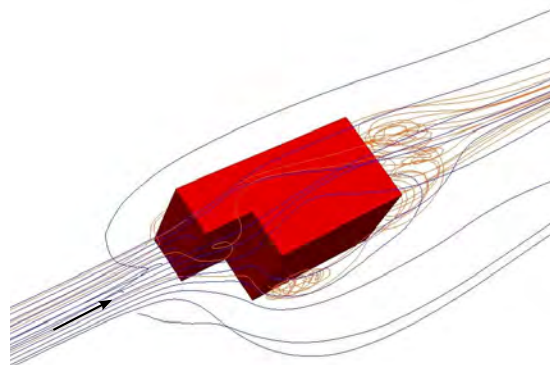
3D vorticity:



Streamlines (int):

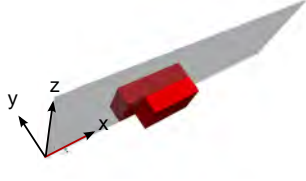


Streamlines (ext):

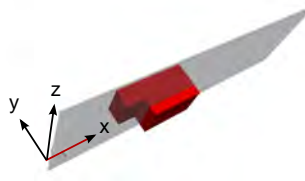


*Basic*

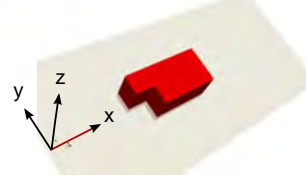
Plane  $y=0\text{m}$ :



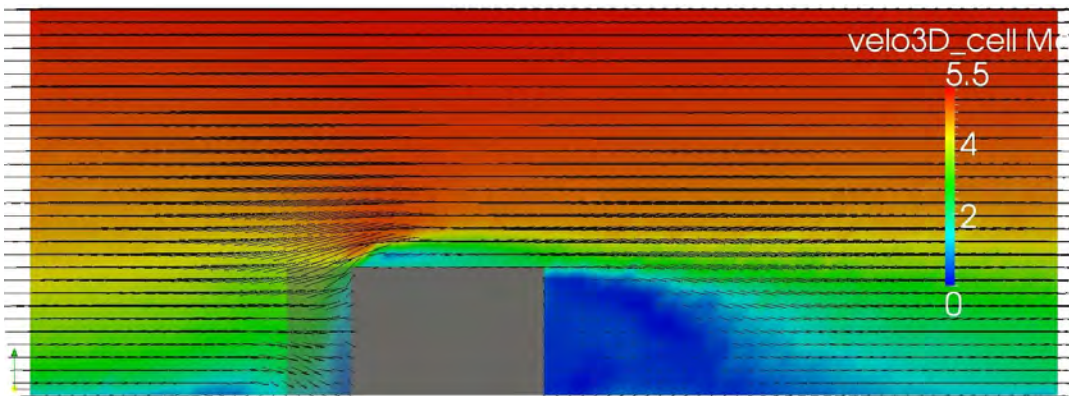
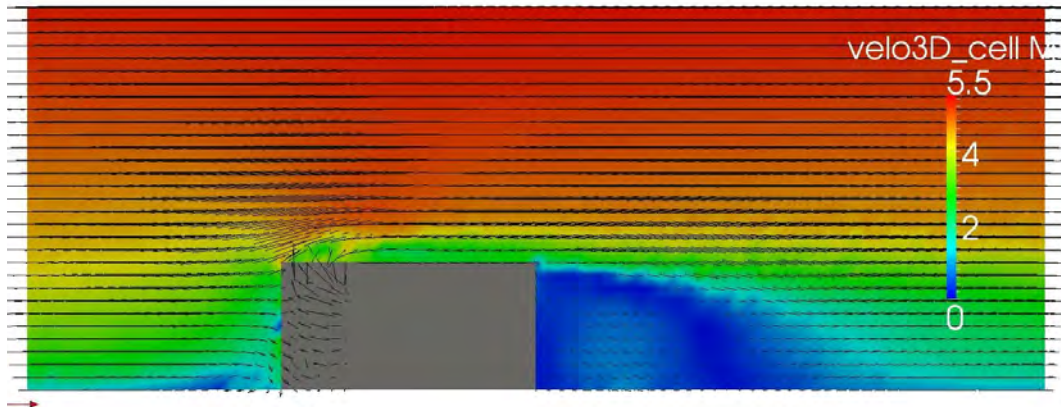
Plane  $y=-2.5\text{m}$ :



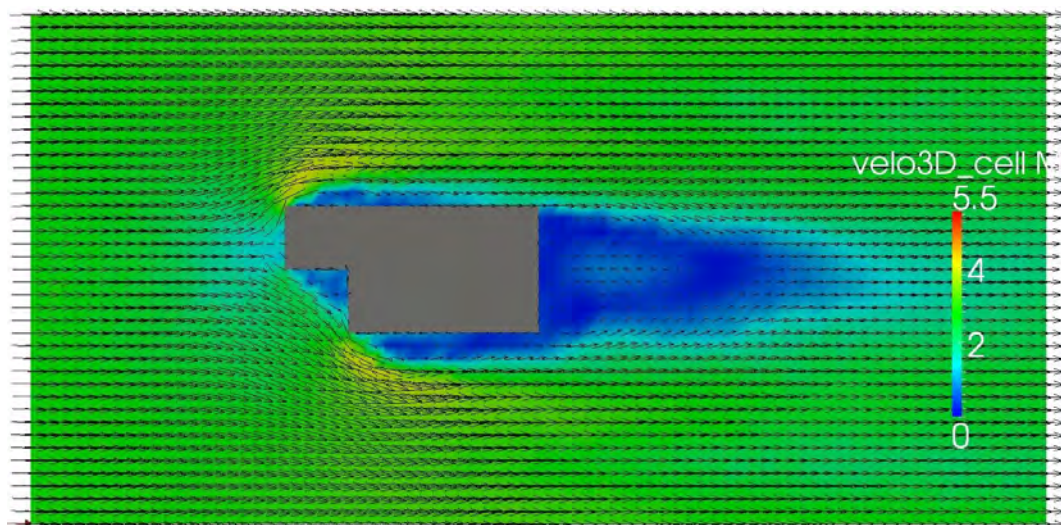
Plane  $z=2\text{m}$ :



Mean velocity field, planes  $y=0\text{m}$  and  $-2.5\text{m}$ :



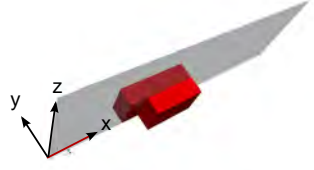
Mean velocity field, plane  $z=2\text{m}$ :



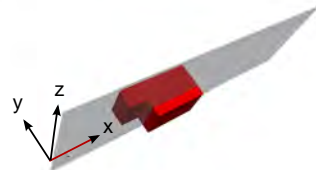


*Mesh +*

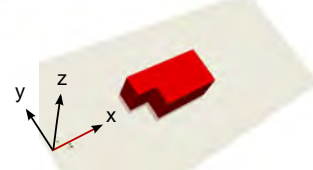
Plane y=0m:



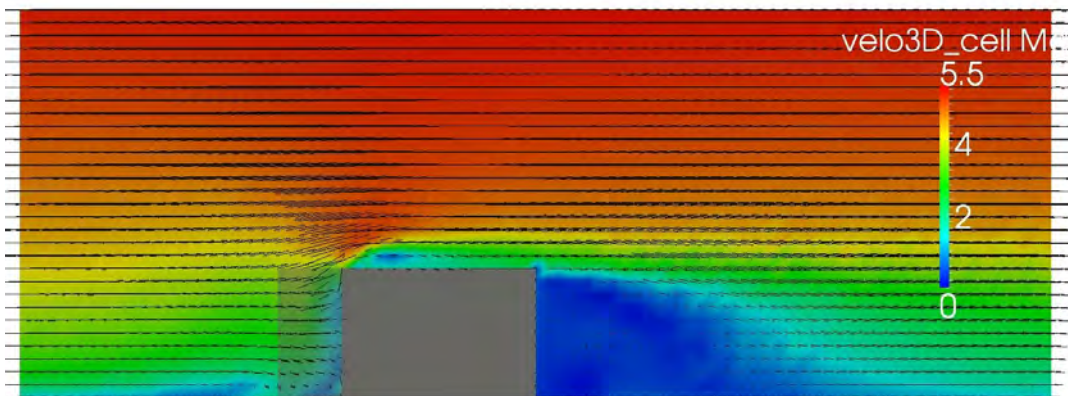
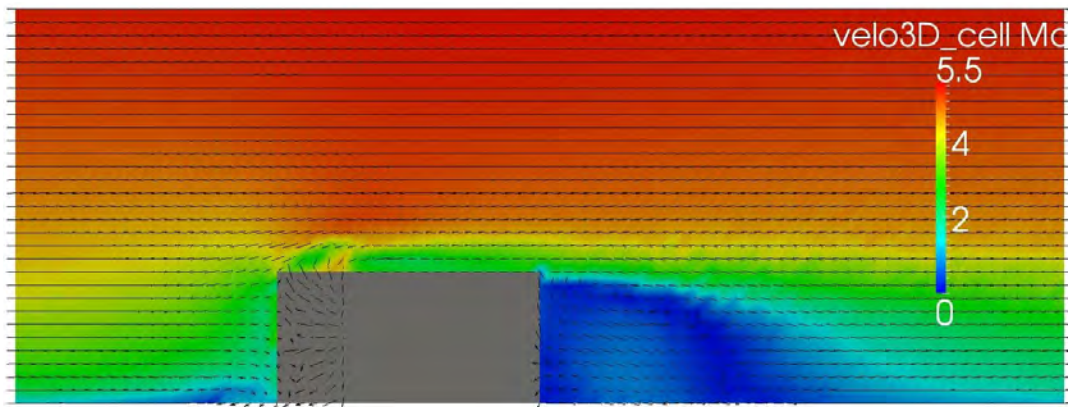
Plane y=-2.5m:



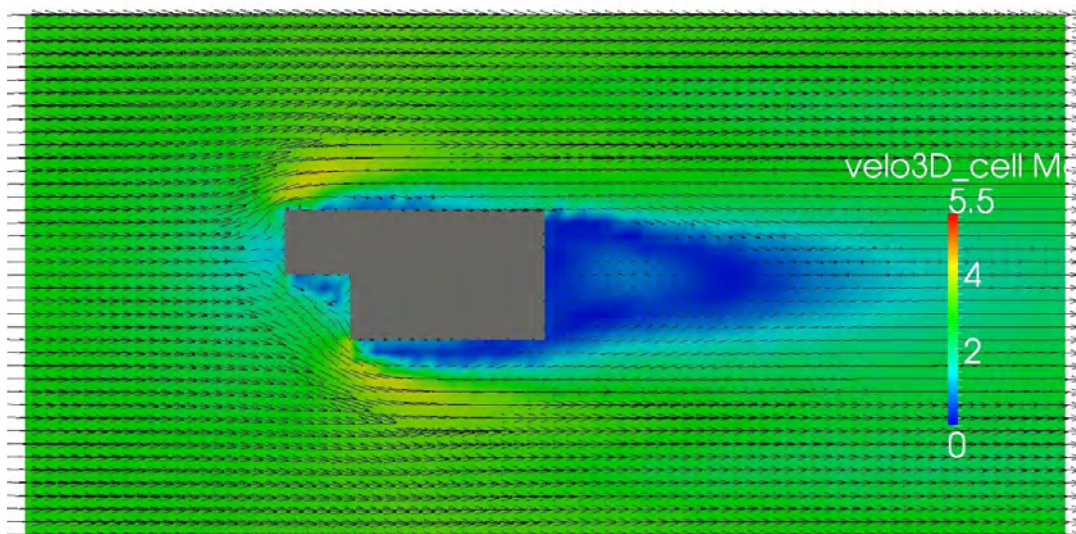
Plane z=2m:



Mean velocity field, planes y=0m and -2.5m:



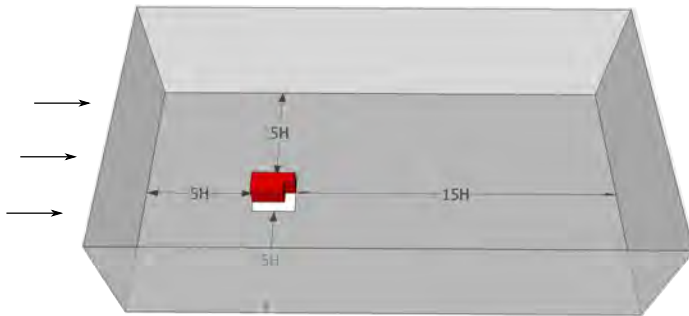
Mean velocity field, plane z=2m:









## N.6 The L-building 3

*Basic*

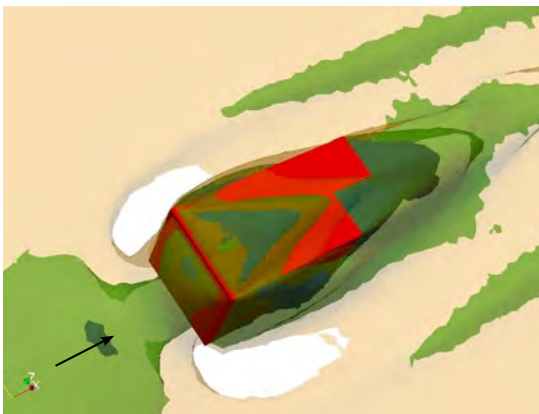
Computational configuration:



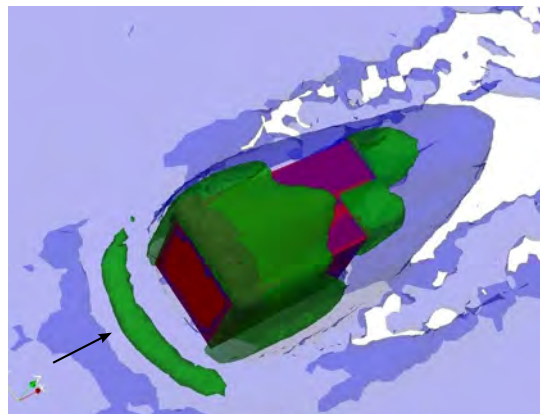
Legend

3D Velocity:		0.5 m/s
		1.5 m/s
		2.5 m/s
3D Vorticity:		0.5 rad/s
		1.5 rad/s
		5.5 rad/s

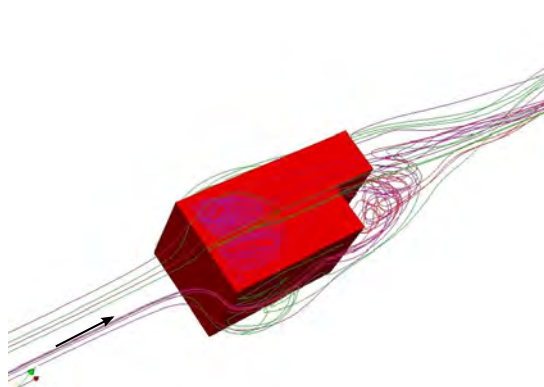
3D mean velocity:



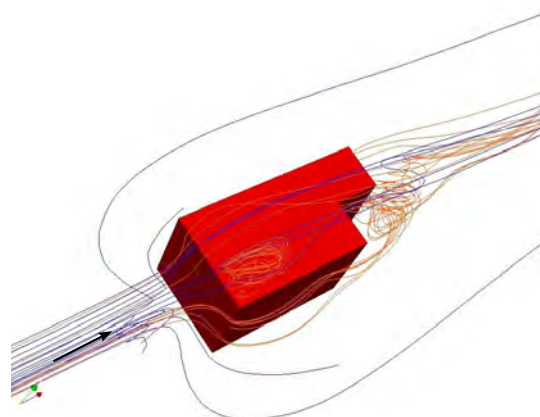
3D vorticity:



Streamlines (int):

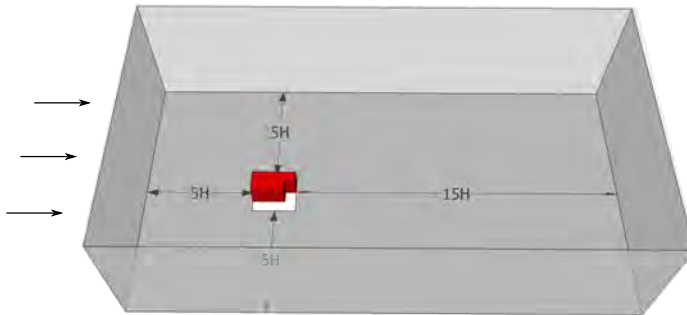


Streamlines (ext):



*Mesh +*

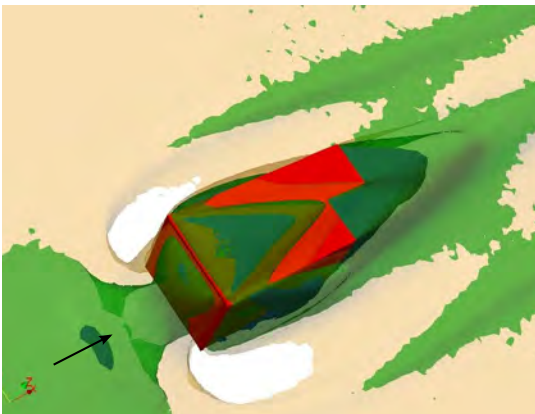
Computational configuration:



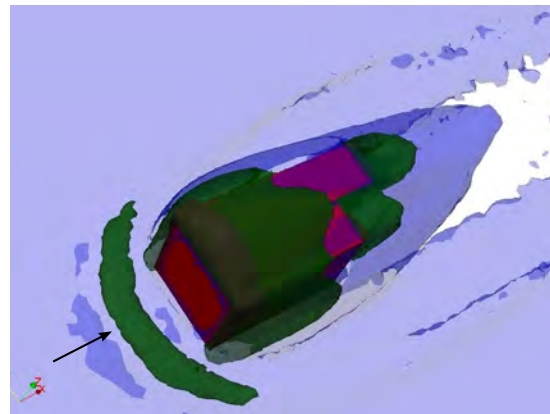
Legend

3D Velocity:	<span style="display:inline-block; width:15px; height:15px; background-color:blue;"></span>	0.5 m/s
	<span style="display:inline-block; width:15px; height:15px; background-color:green;"></span>	1.5 m/s
	<span style="display:inline-block; width:15px; height:15px; background-color:yellow;"></span>	2.5 m/s
3D Vorticity:	<span style="display:inline-block; width:15px; height:15px; background-color:blue;"></span>	0.5 rad/s
	<span style="display:inline-block; width:15px; height:15px; background-color:green;"></span>	1.5 rad/s
	<span style="display:inline-block; width:15px; height:15px; background-color:red;"></span>	5.5 rad/s

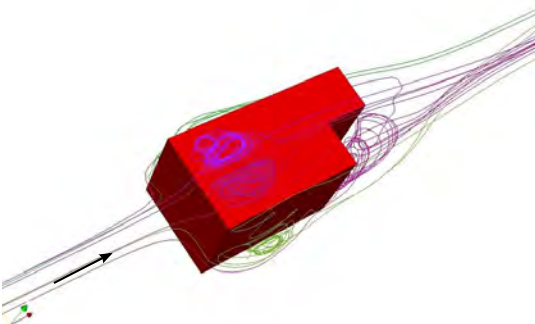
3D mean velocity:



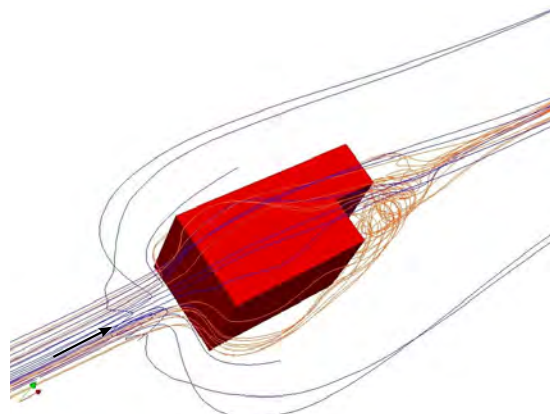
3D vorticity:



Streamlines (int):



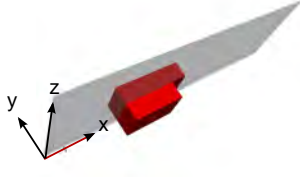
Streamlines (ext):



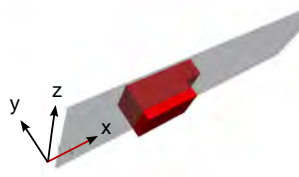


*Basic*

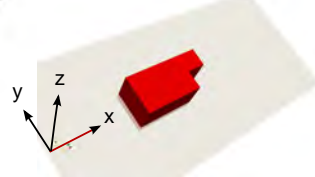
Plane  $y=0\text{m}$ :



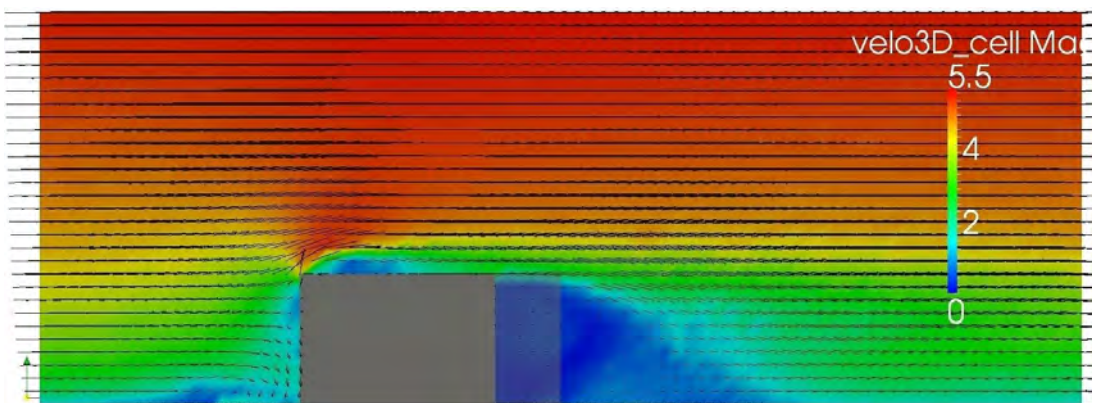
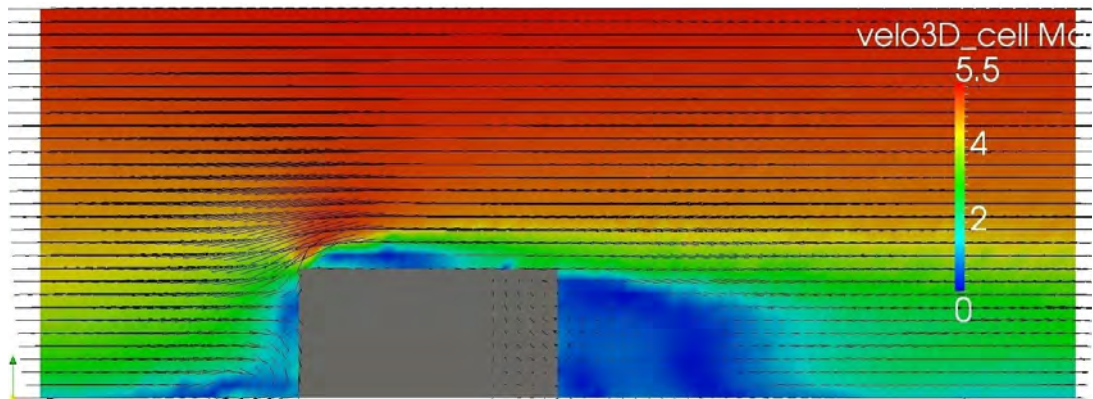
Plane  $y=-2.5\text{m}$ :



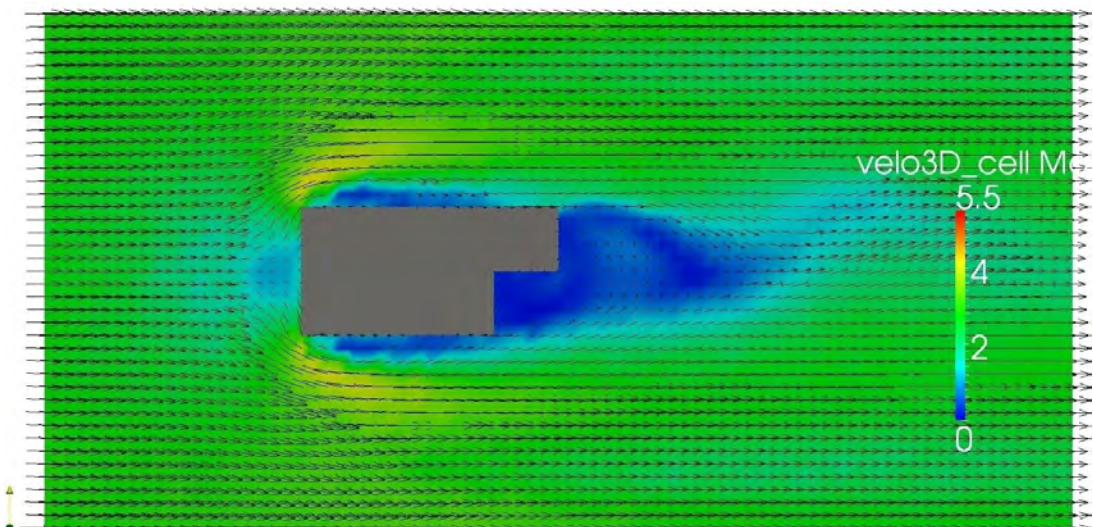
Plane  $z=2\text{m}$ :



Mean velocity field, planes  $y=0\text{m}$  and  $-2.5\text{m}$ :



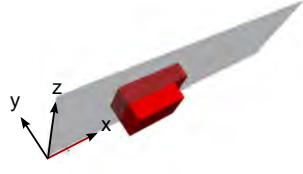
Mean velocity field, plane  $z=2\text{m}$ :



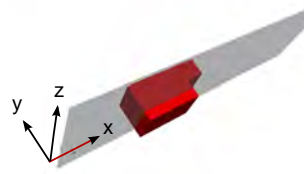


*Mesh+*

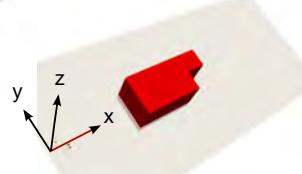
Plane  $y=0\text{m}$ :



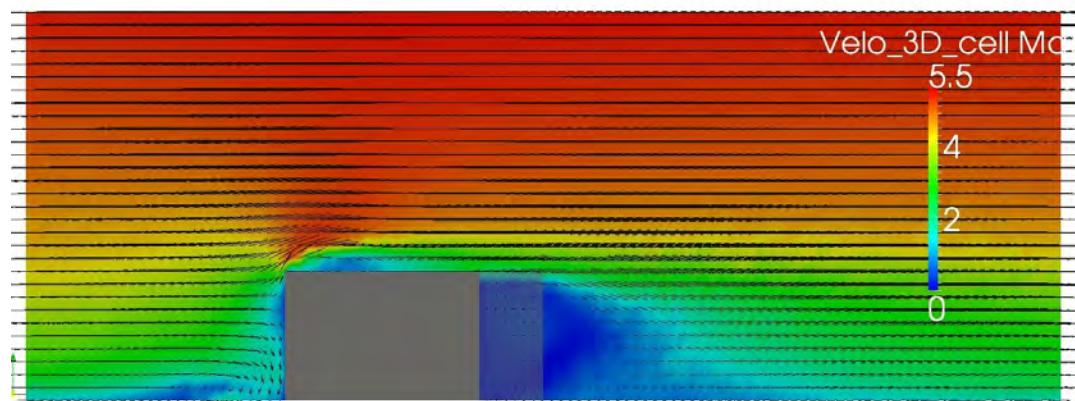
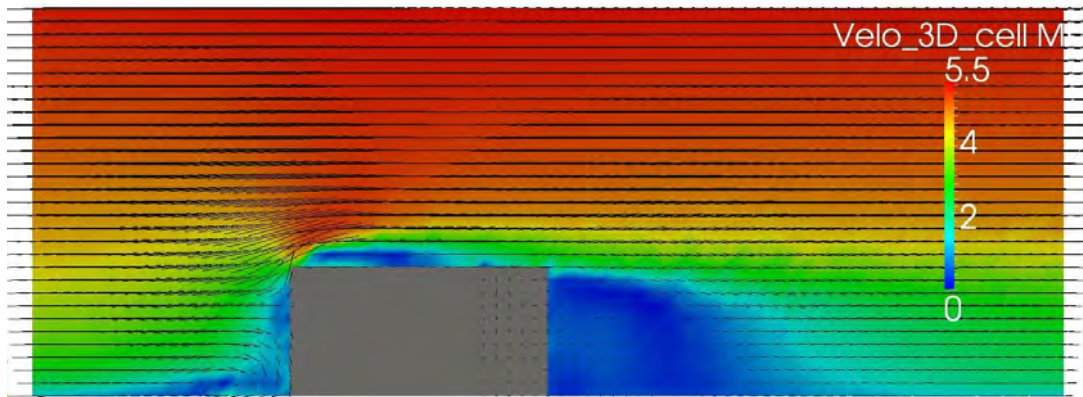
Plane  $y=-2.5\text{m}$ :



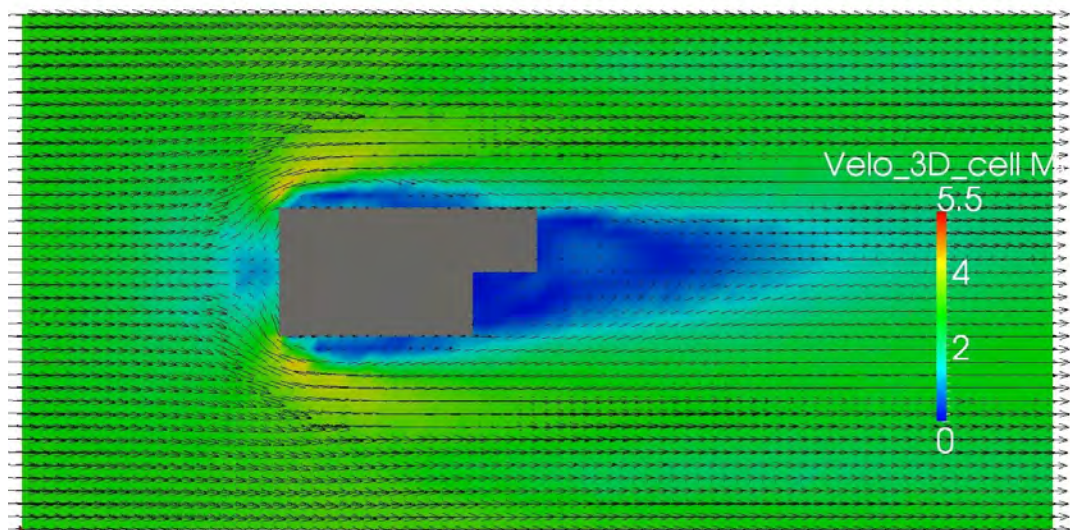
Plane  $z=2\text{m}$ :



Mean velocity field, planes  $y=0\text{m}$  and  $-2.5\text{m}$ :



Mean velocity field, plane  $z=2\text{m}$ :

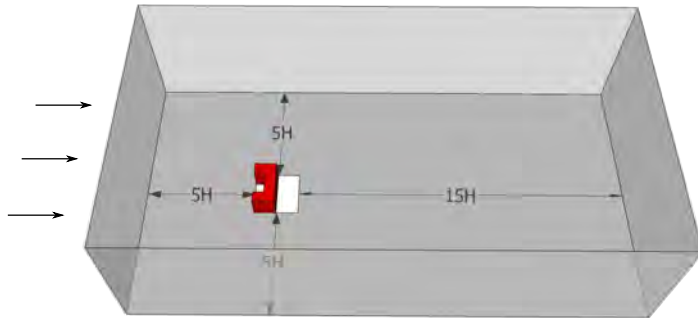










## N.7 The U-building 1

*Basic*

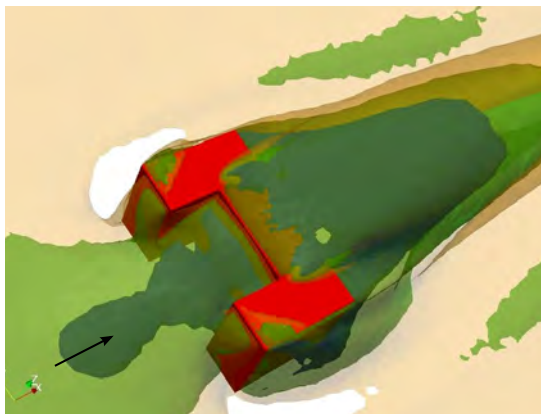
Computational configuration:



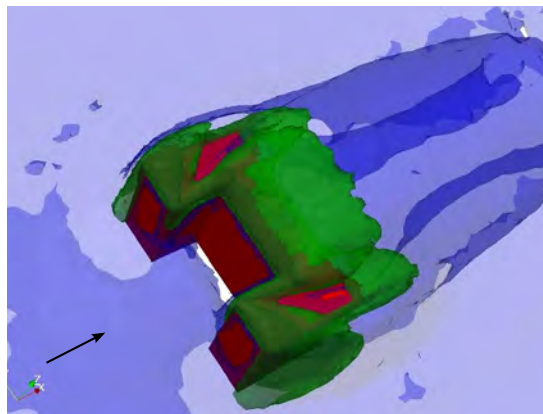
Legend

3D Velocity:		0.5 m/s
		1.5 m/s
		2.5 m/s
3D Vorticity:		0.5 rad/s
		1.5 rad/s
		5.5 rad/s

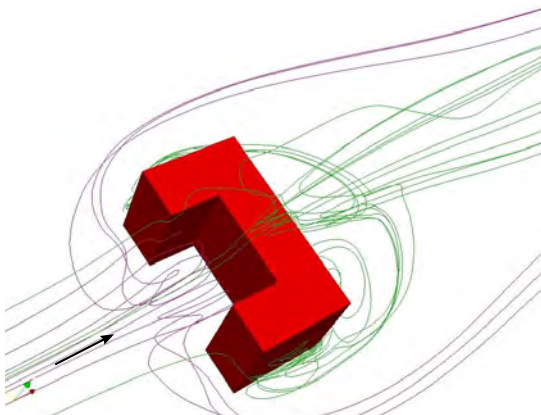
3D mean velocity:



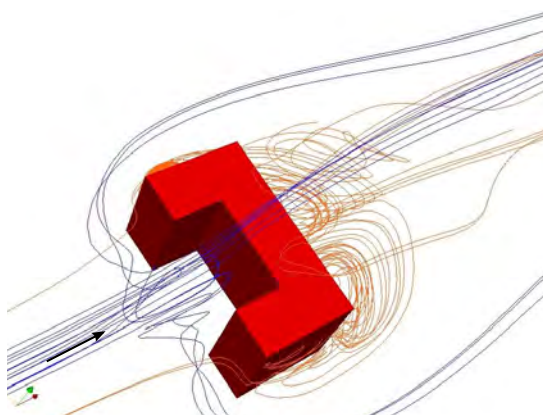
3D vorticity:



Streamlines (int):

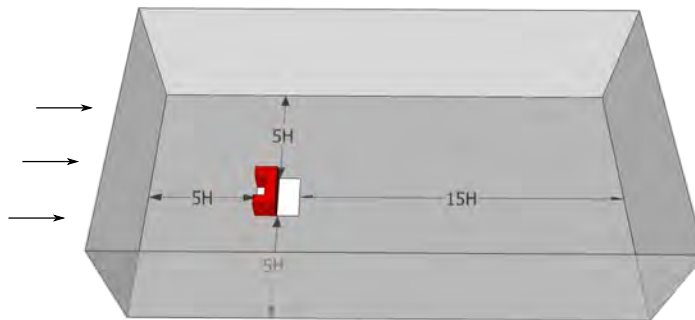


Streamlines (ext):



*Mesh +*

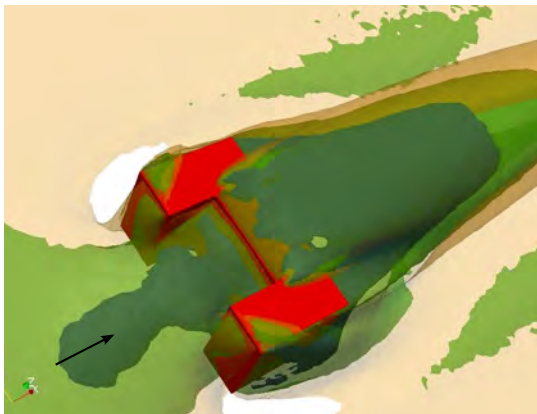
Computational configuration:



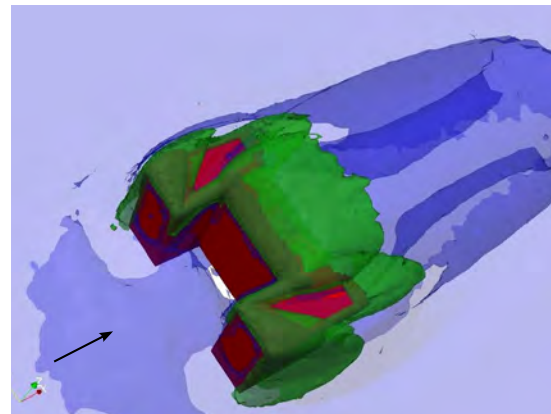
Legend

3D Velocity:	<span style="display:inline-block; width:15px; height:15px; background-color:blue;"></span>	0.5 m/s
	<span style="display:inline-block; width:15px; height:15px; background-color:green;"></span>	1.5 m/s
	<span style="display:inline-block; width:15px; height:15px; background-color:yellow;"></span>	2.5 m/s
3D Vorticity:	<span style="display:inline-block; width:15px; height:15px; background-color:blue;"></span>	0.5 rad/s
	<span style="display:inline-block; width:15px; height:15px; background-color:green;"></span>	1.5 rad/s
	<span style="display:inline-block; width:15px; height:15px; background-color:red;"></span>	5.5 rad/s

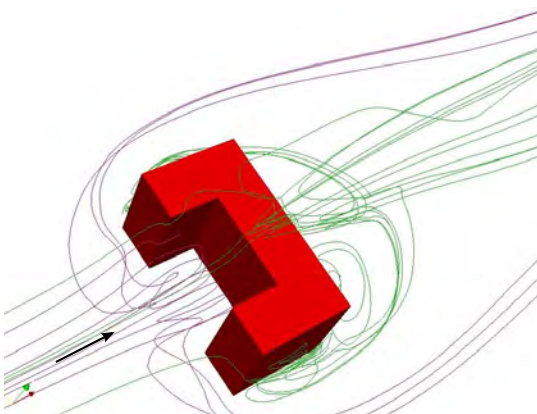
3D mean velocity:



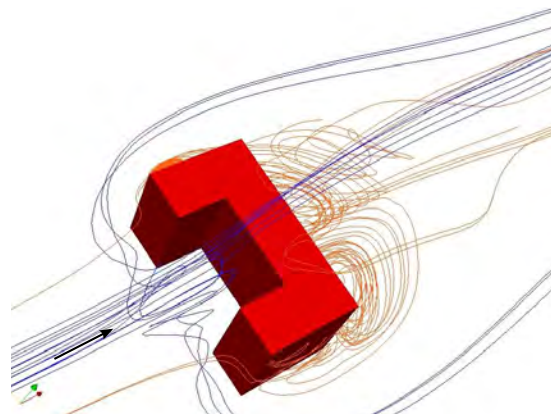
3D vorticity:



Streamlines (int):



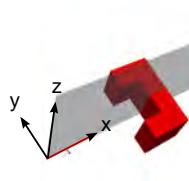
Streamlines (ext):



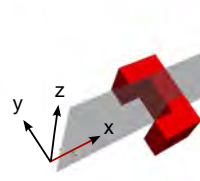


*Basic*

Plane  $y=0\text{m}$ :



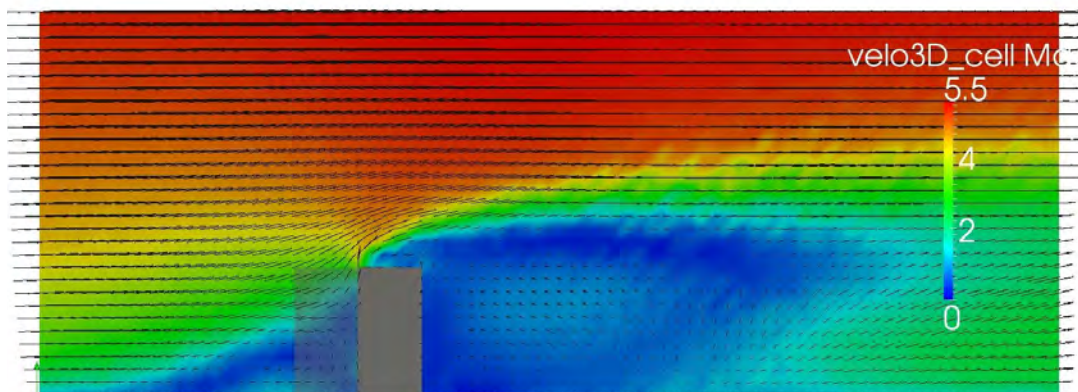
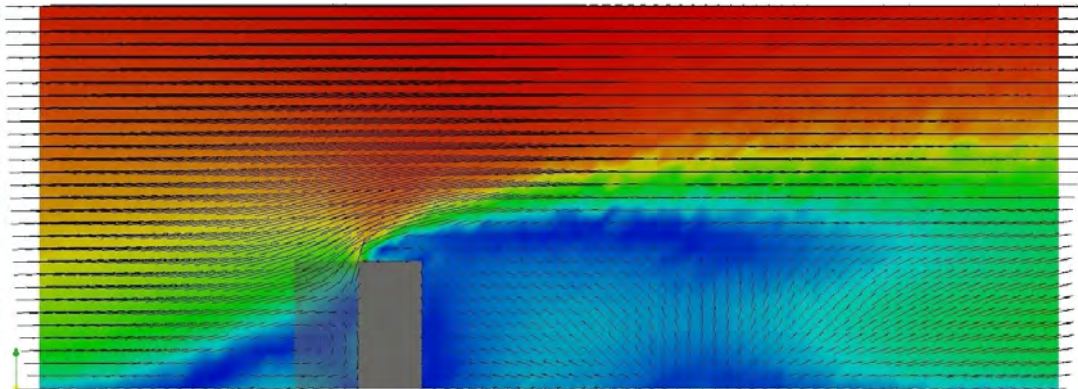
Plane  $y=-2.5\text{m}$ :



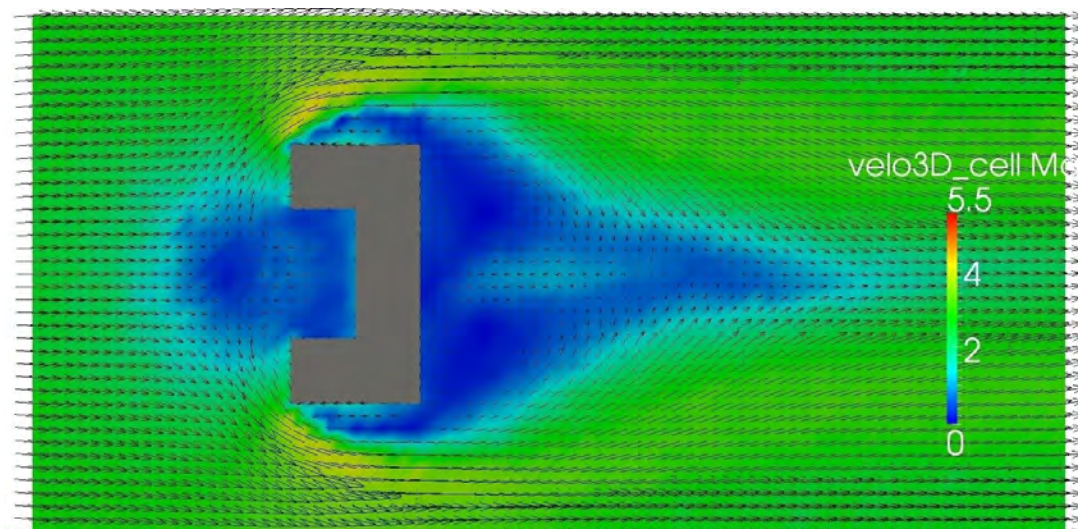
Plane  $z=2\text{m}$ :



Mean velocity field, planes  $y=0\text{m}$  and  $-2.5\text{m}$ :



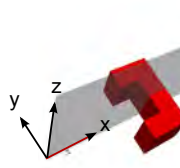
Mean velocity field, plane  $z=2\text{m}$ :



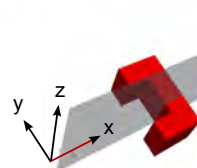


*Mesh +*

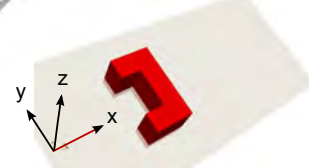
Plane  $y=0\text{m}$ :



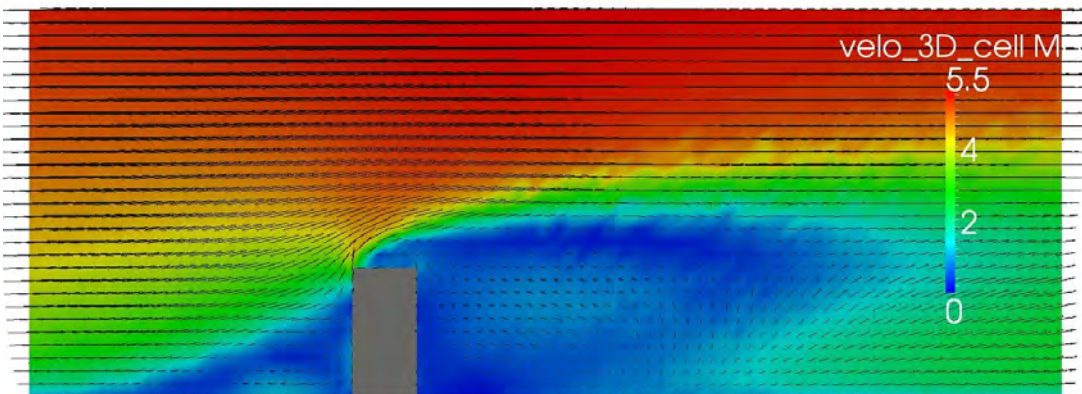
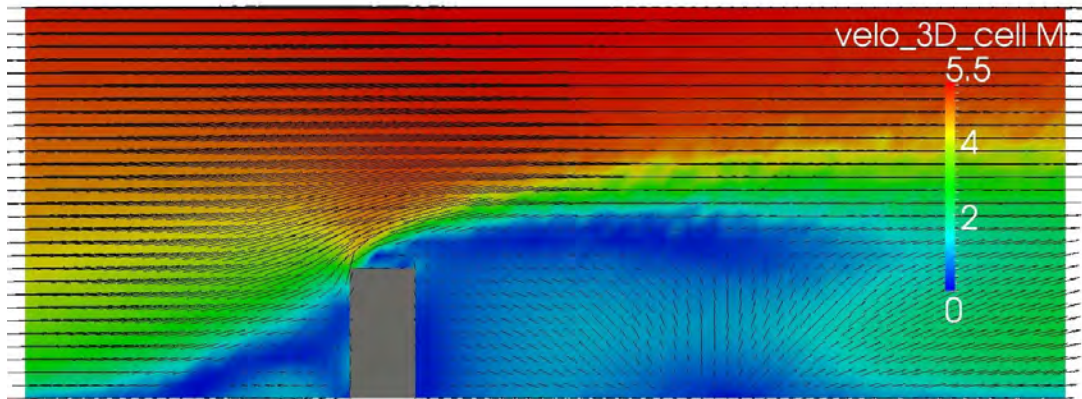
Plane  $y=-2.5\text{m}$ :



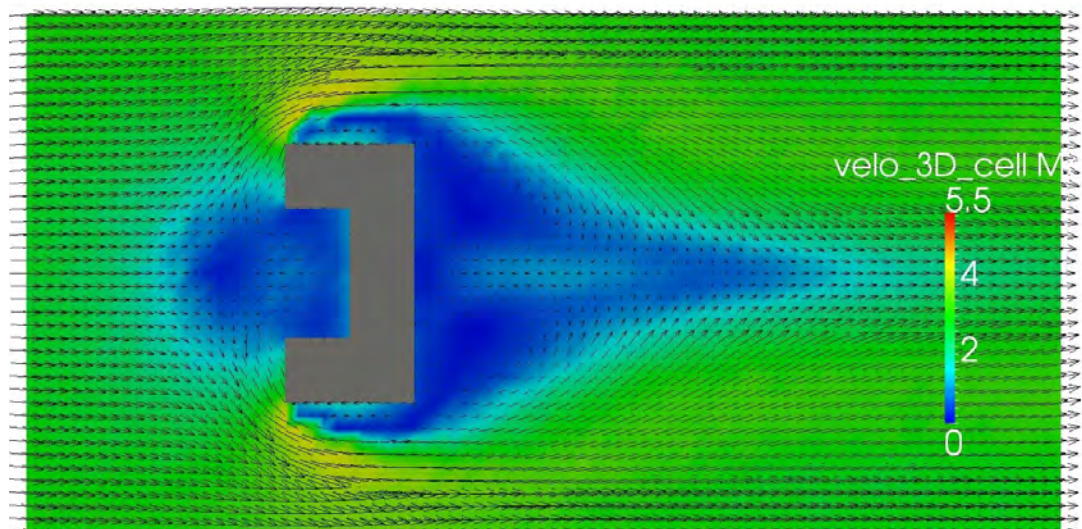
Plane  $z=2\text{m}$ :



Mean velocity field, planes  $y=0\text{m}$  and  $-2.5\text{m}$ :



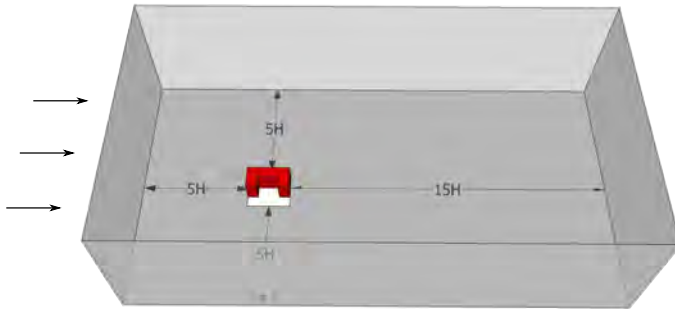
Mean velocity field, plane  $z=2\text{m}$ :









## N.8 The U-building 2

### Basic

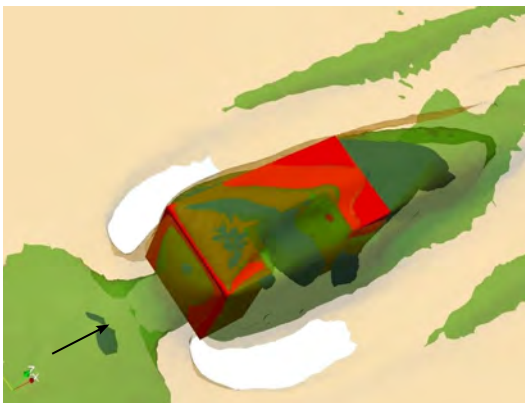
Computational configuration:



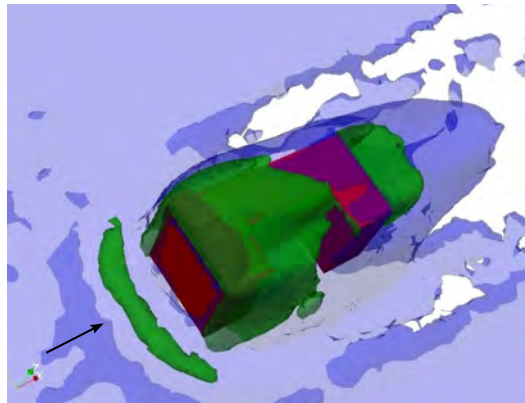
Legend

3D Velocity:		0.5 m/s
		1.5 m/s
		2.5 m/s
3D Vorticity:		0.5 rad/s
		1.5 rad/s
		5.5 rad/s

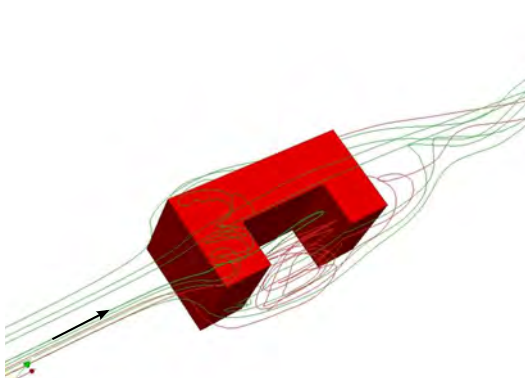
3D mean velocity:



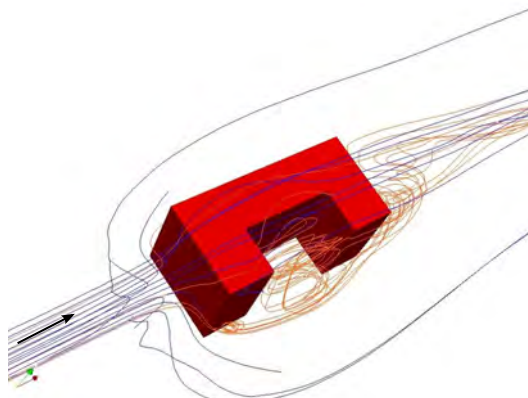
3D vorticity:



Streamlines (int):

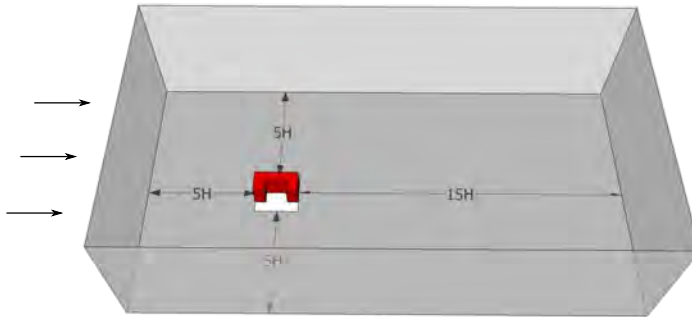


Streamlines (ext):



*Mesh +*

Computational configuration:



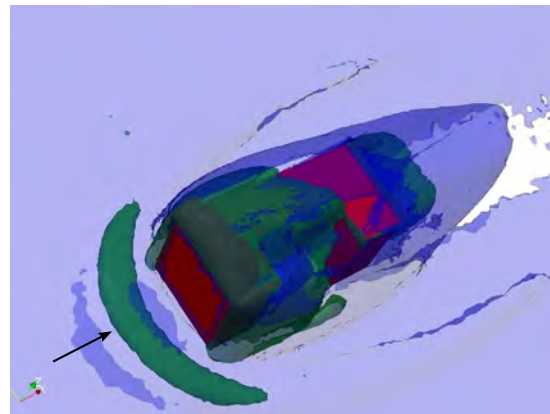
Legend

3D Velocity:	<span style="display:inline-block; width:15px; height:15px; background-color:blue;"></span>	0.5 m/s
	<span style="display:inline-block; width:15px; height:15px; background-color:green;"></span>	1.5 m/s
	<span style="display:inline-block; width:15px; height:15px; background-color:yellow;"></span>	2.5 m/s
3D Vorticity:	<span style="display:inline-block; width:15px; height:15px; background-color:blue;"></span>	0.5 rad/s
	<span style="display:inline-block; width:15px; height:15px; background-color:green;"></span>	1.5 rad/s
	<span style="display:inline-block; width:15px; height:15px; background-color:red;"></span>	5.5 rad/s

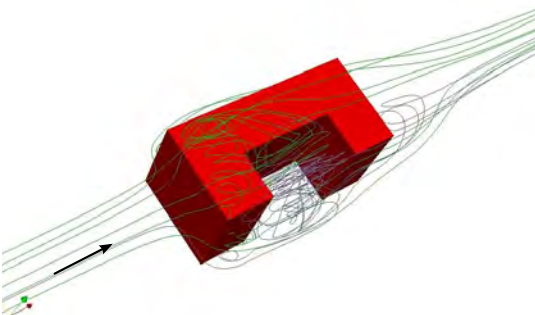
3D mean velocity:



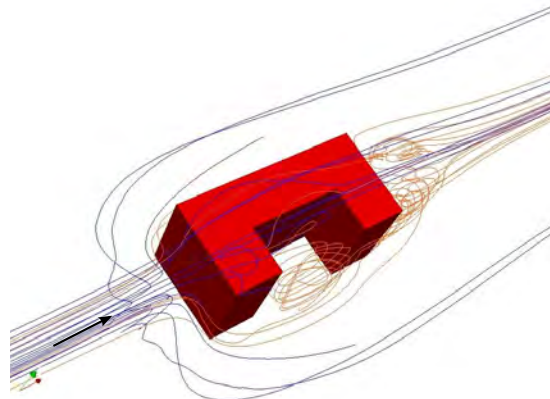
3D vorticity:



Streamlines (int):



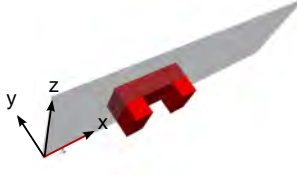
Streamlines (ext):



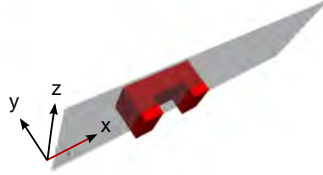


*Basic*

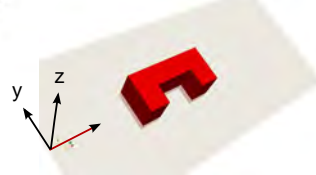
Plane  $y=0\text{m}$ :



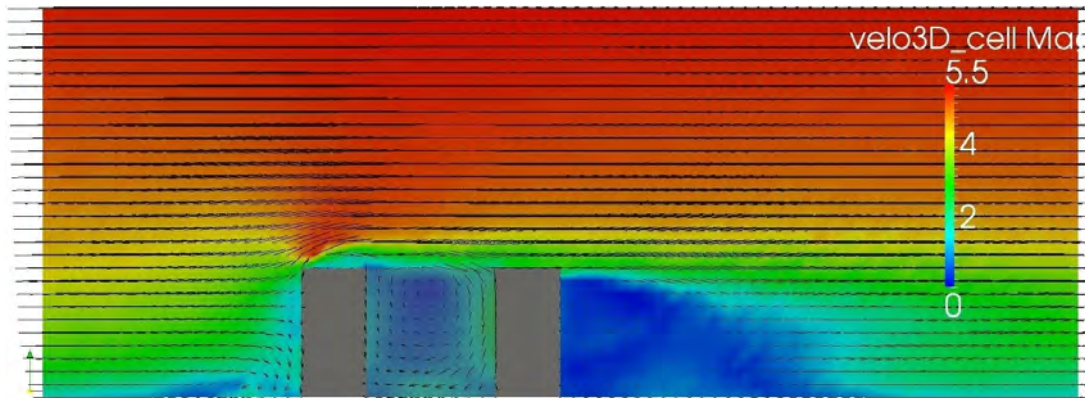
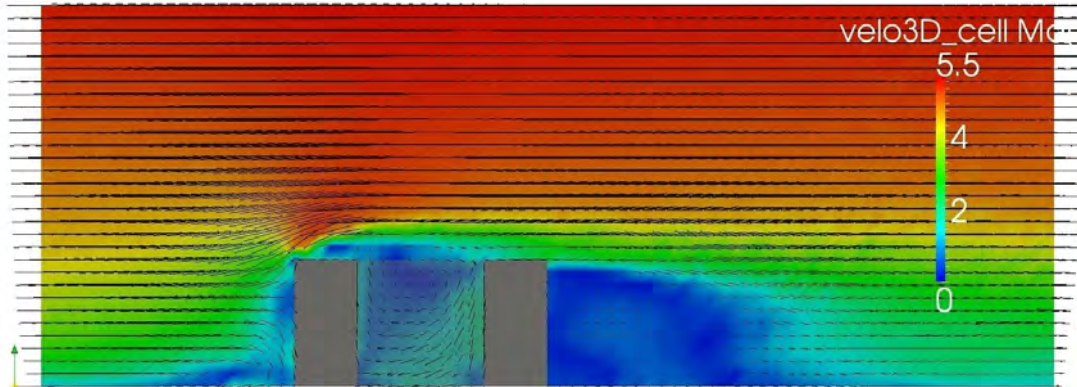
Plane  $y=-2.5\text{m}$ :



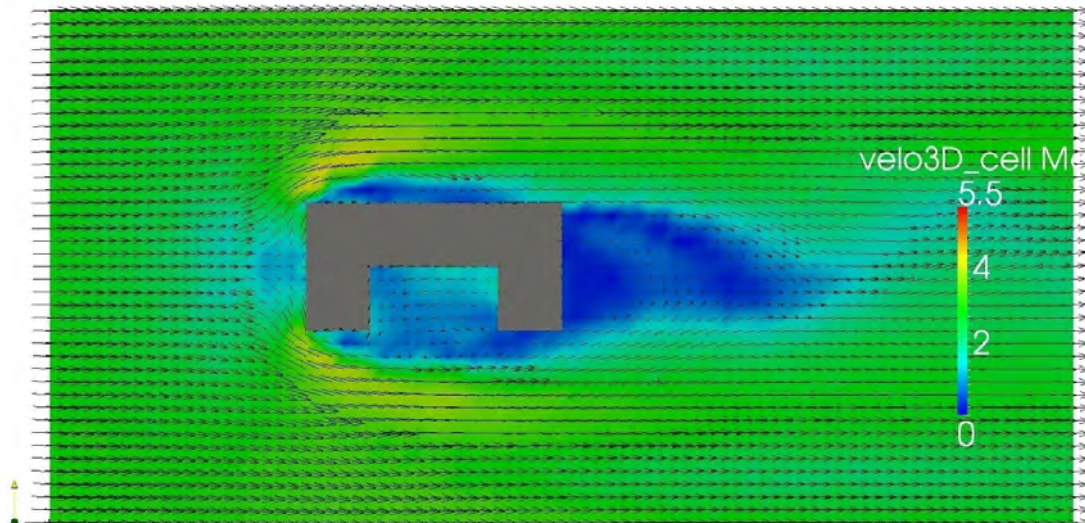
Plane  $z=2\text{m}$ :



Mean velocity field, planes  $y=0\text{m}$  and  $-2.5\text{m}$ :



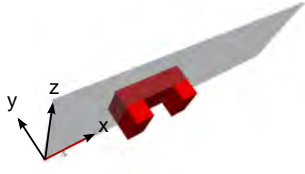
Mean velocity field, plane  $z=2\text{m}$ :



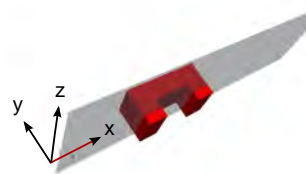


*Mesh +*

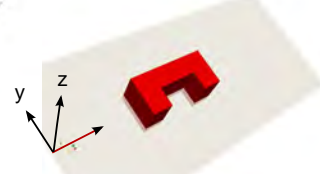
Plane y=0m:



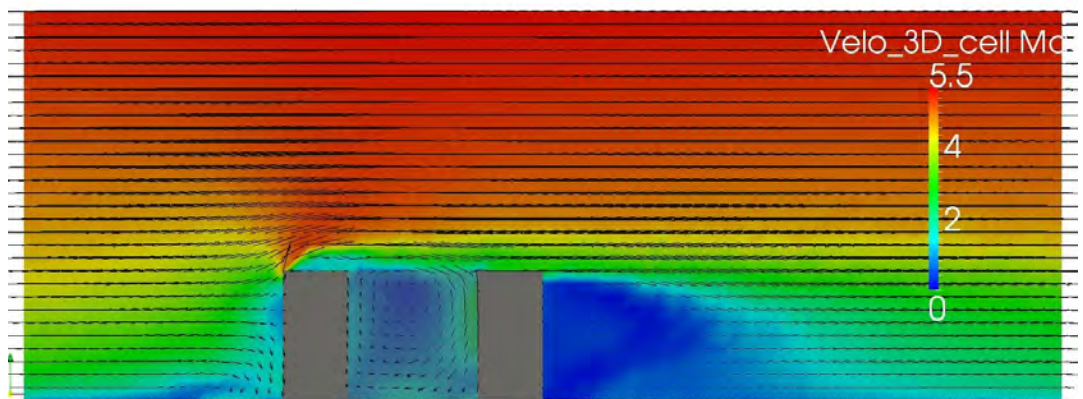
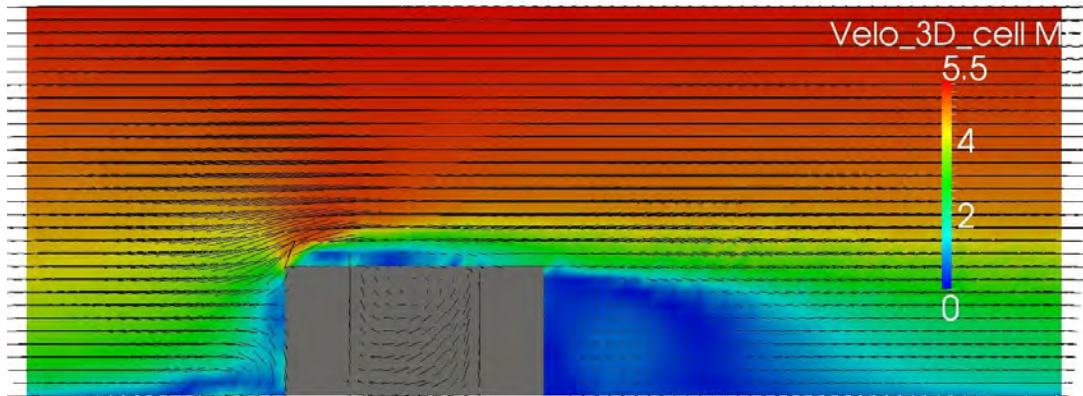
Plane y=-2.5m:



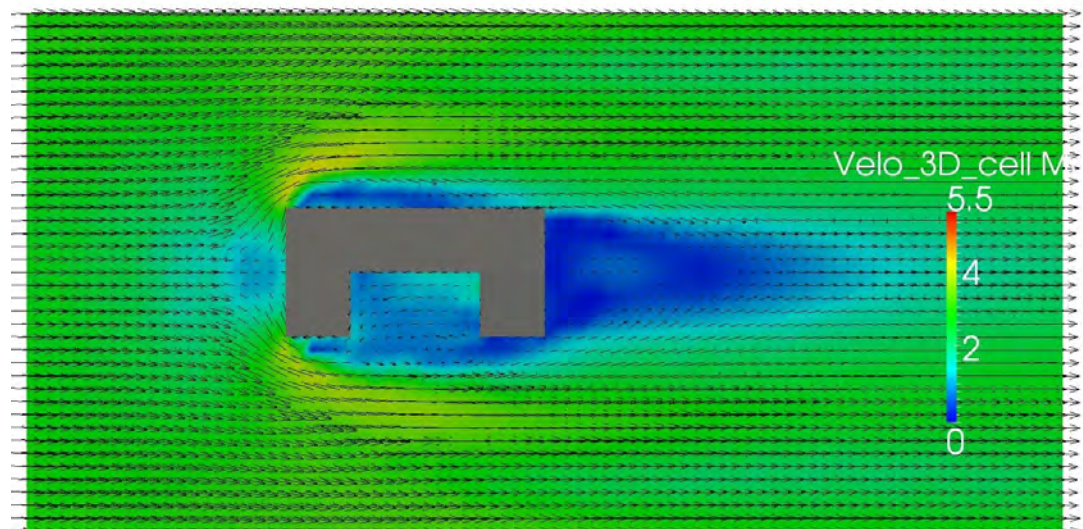
Plane z=2m:



Mean velocity field, planes y=0m and -2.5m:



Mean velocity field, plane z=2m:

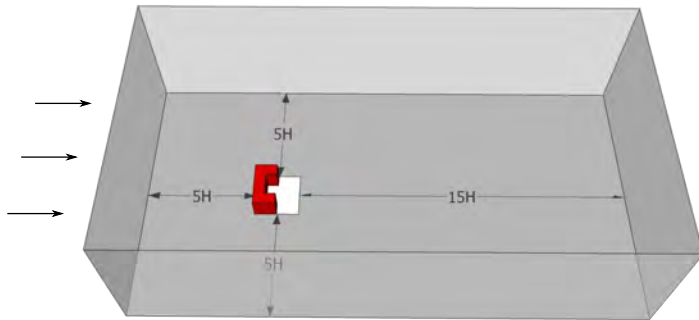










## N.9 The U-building 3

*Basic*

Computational configuration:



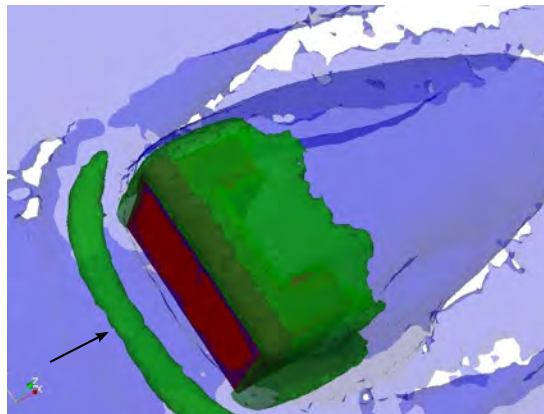
Legend

3D Velocity:		0.5 m/s
		1.5 m/s
		2.5 m/s
3D Vorticity:		0.5 rad/s
		1.5 rad/s
		5.5 rad/s

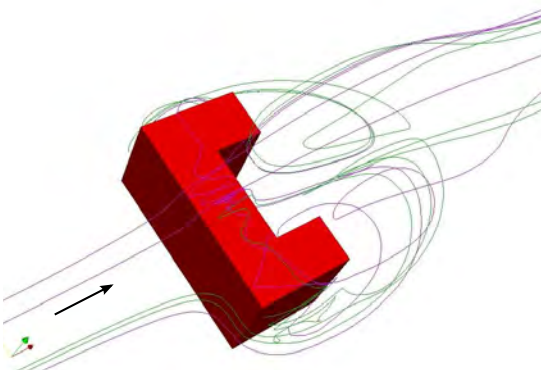
3D mean velocity:



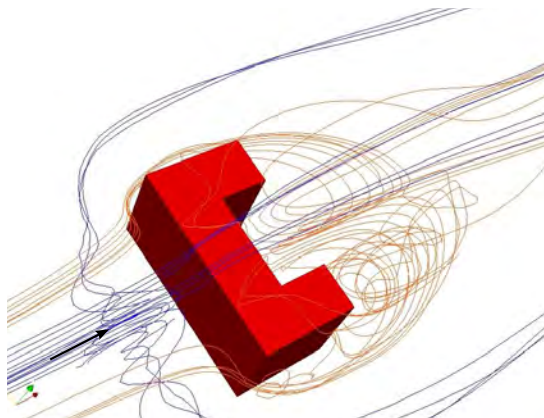
3D vorticity:



Streamlines (int):

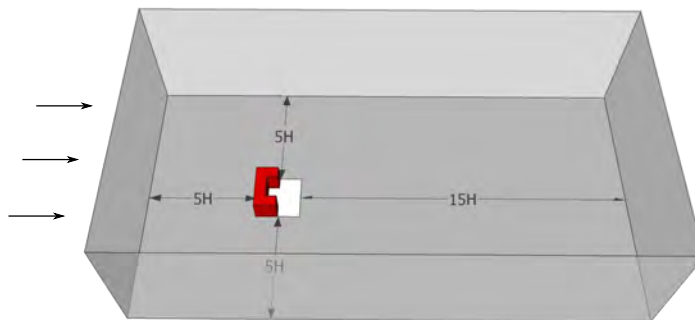


Streamlines (ext):



*Mesh +*

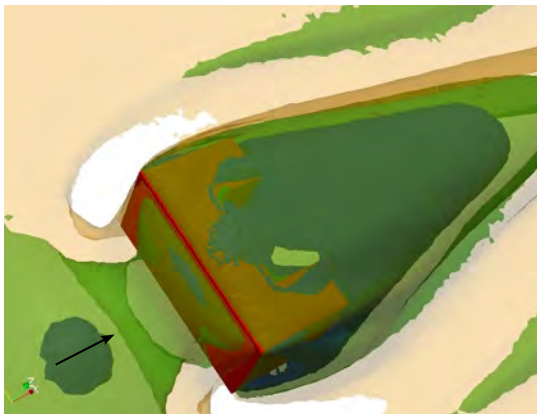
Computational configuration:



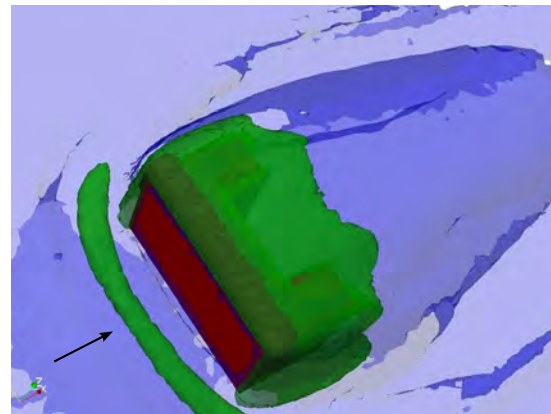
Legend

3D Velocity:	<span style="display:inline-block; width:15px; height:15px; background-color:blue;"></span>	0.5 m/s
	<span style="display:inline-block; width:15px; height:15px; background-color:green;"></span>	1.5 m/s
	<span style="display:inline-block; width:15px; height:15px; background-color:yellow;"></span>	2.5 m/s
3D Vorticity:	<span style="display:inline-block; width:15px; height:15px; background-color:blue;"></span>	0.5 rad/s
	<span style="display:inline-block; width:15px; height:15px; background-color:green;"></span>	1.5 rad/s
	<span style="display:inline-block; width:15px; height:15px; background-color:red;"></span>	5.5 rad/s

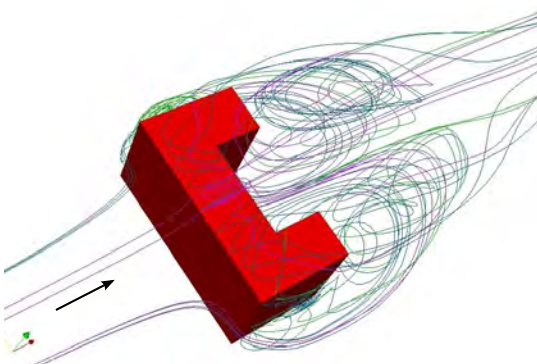
3D mean velocity:



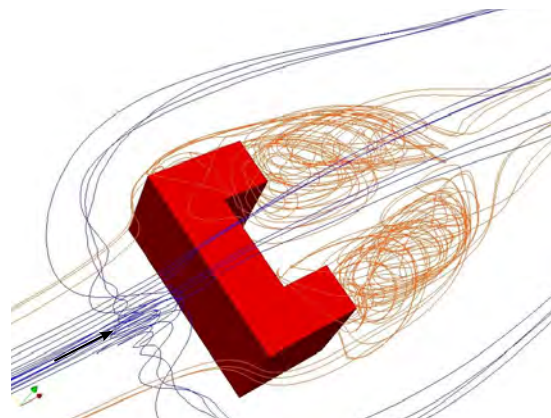
3D vorticity:



Streamlines (int):



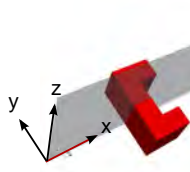
Streamlines (ext):



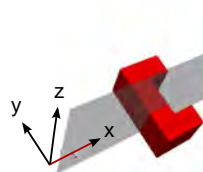


*Basic*

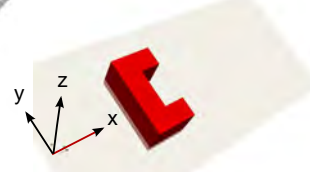
Plane  $y=0\text{m}$ :



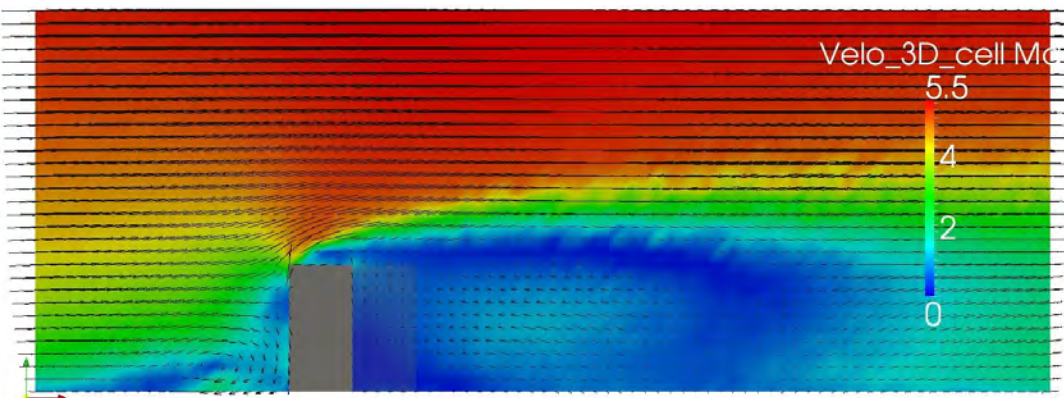
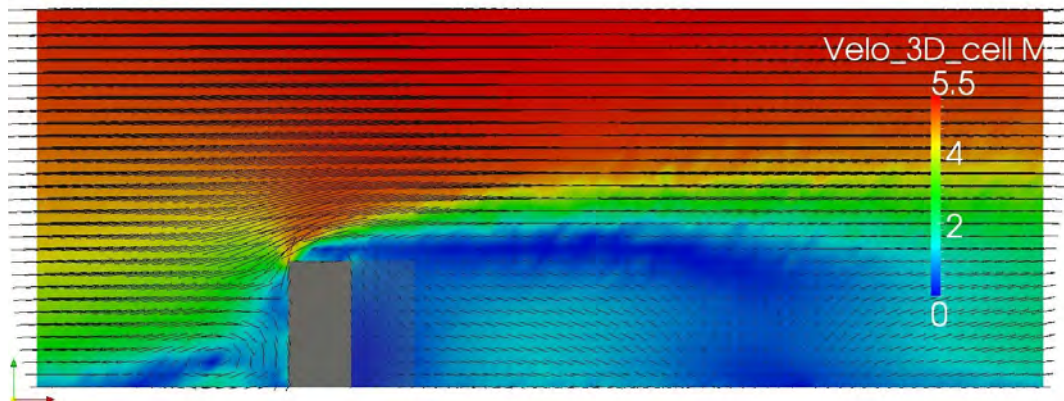
Plane  $y=-2.5\text{m}$ :



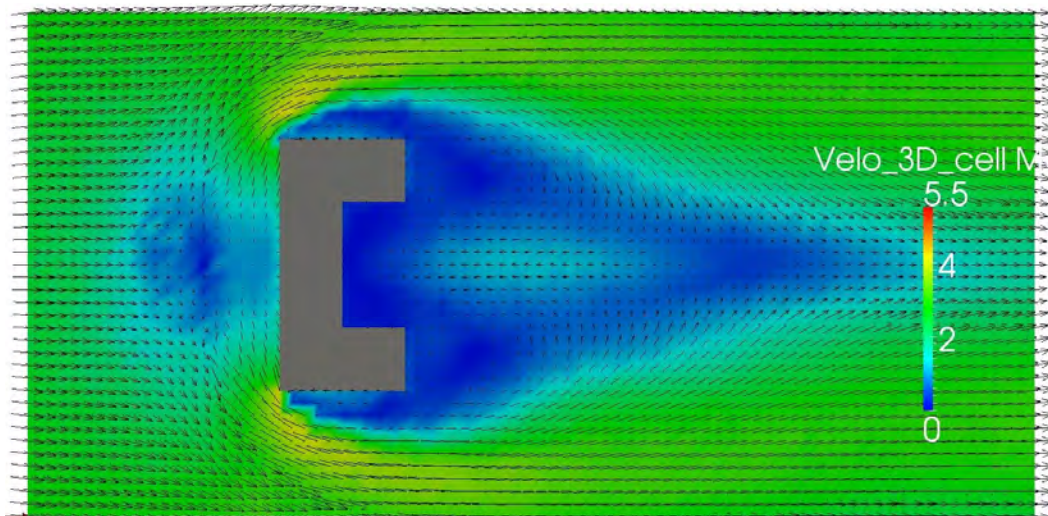
Plane  $z=2\text{m}$ :



Mean velocity field, planes  $y=0\text{m}$  and  $-2.5\text{m}$ :



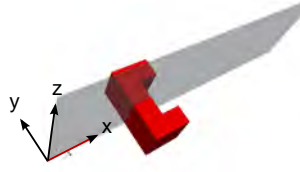
Mean velocity field, plane  $z=2\text{m}$ :



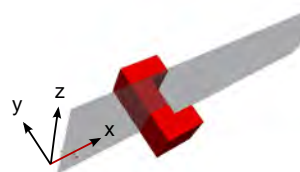


*Mesh+*

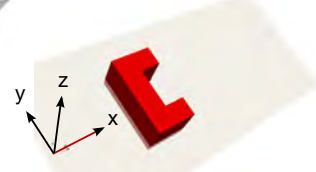
Plane  $y=0\text{m}$ :



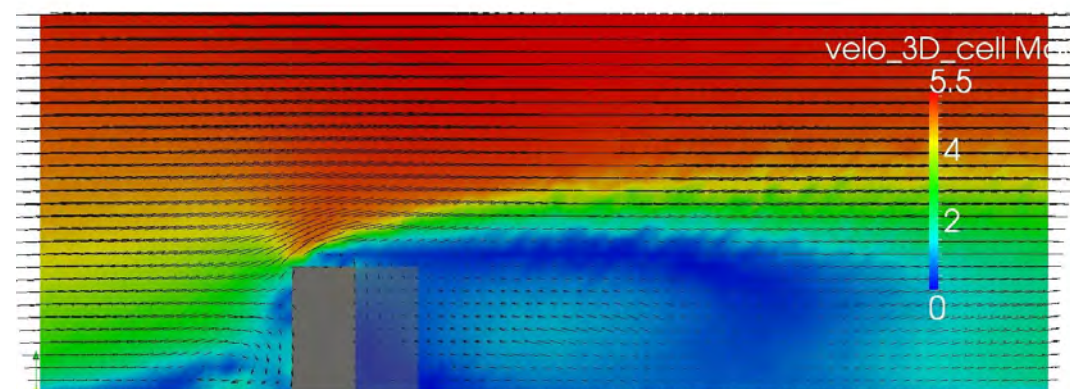
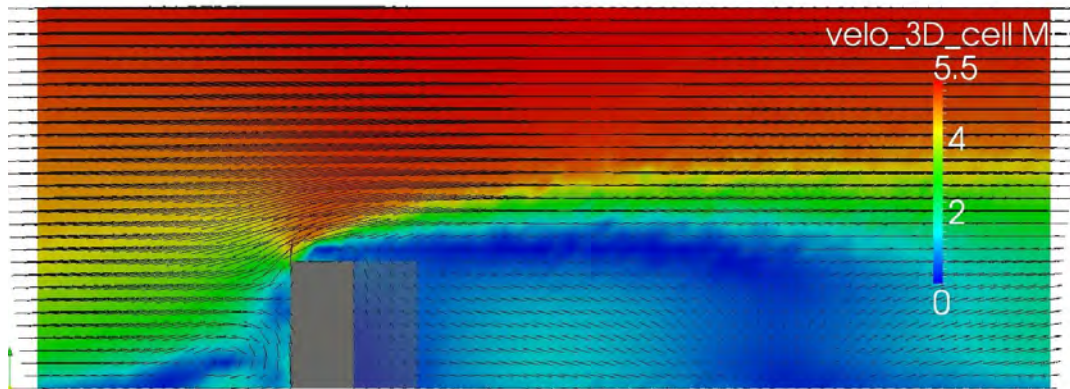
Plane  $y=-2.5\text{m}$ :



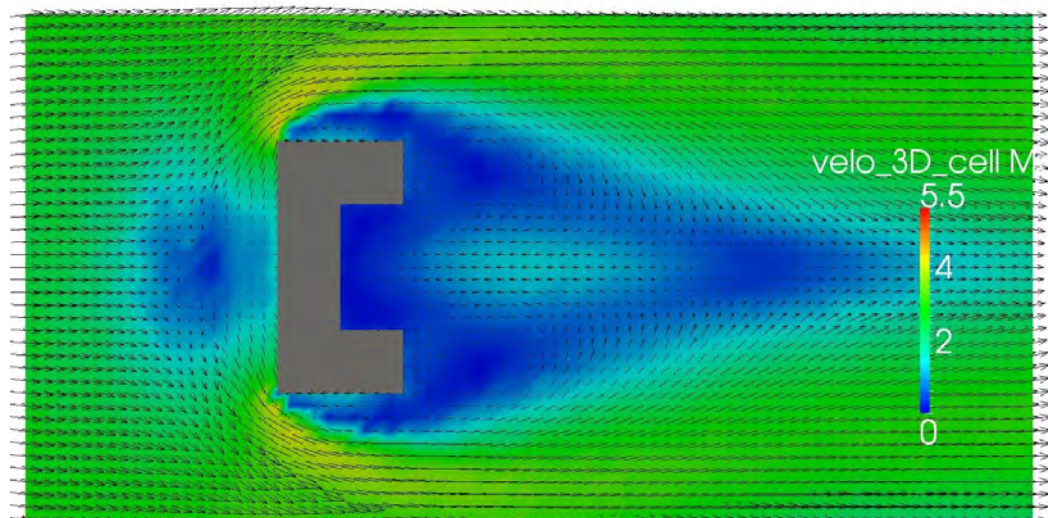
Plane  $z=2\text{m}$ :



Mean velocity field, planes  $y=0\text{m}$  and  $-2.5\text{m}$ :



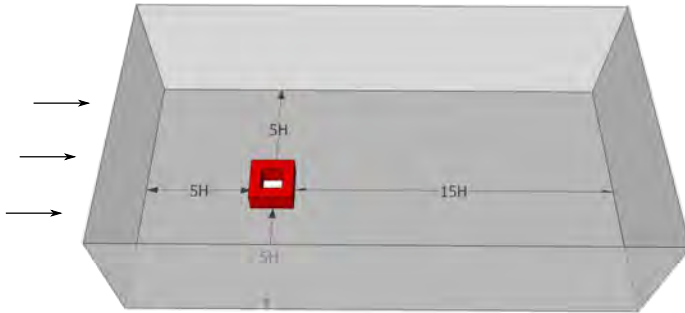
Mean velocity field, plane  $z=2\text{m}$ :









## N.10 The Patio

### Basic

Computational configuration:



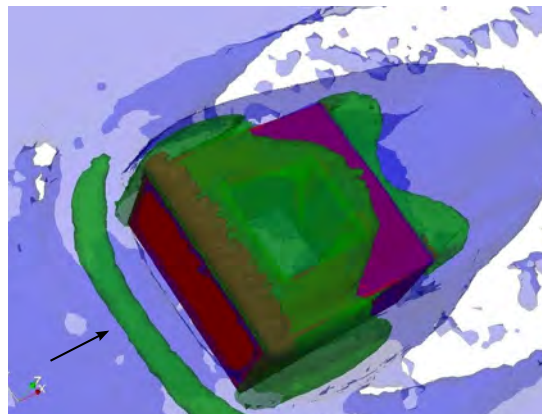
Legend

3D Velocity:		0.5 m/s
		1.5 m/s
		2.5 m/s
3D Vorticity:		0.5 rad/s
		1.5 rad/s
		5.5 rad/s

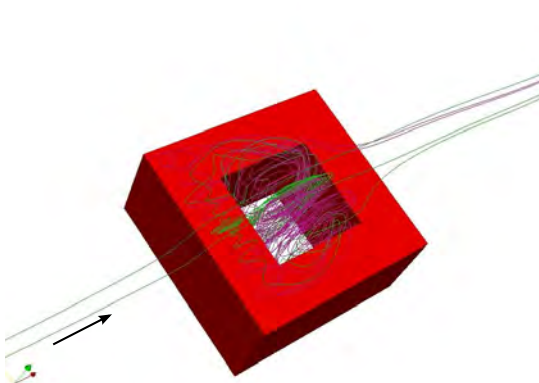
3D mean velocity:



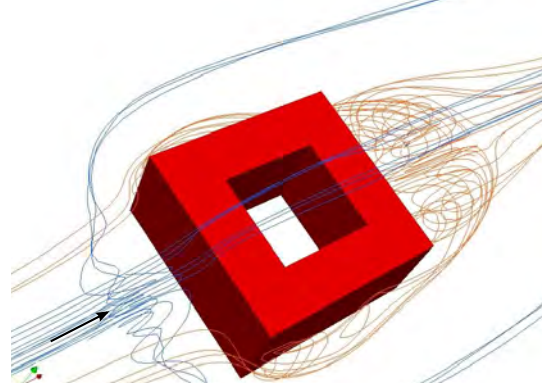
3D vorticity:



Streamlines (int):



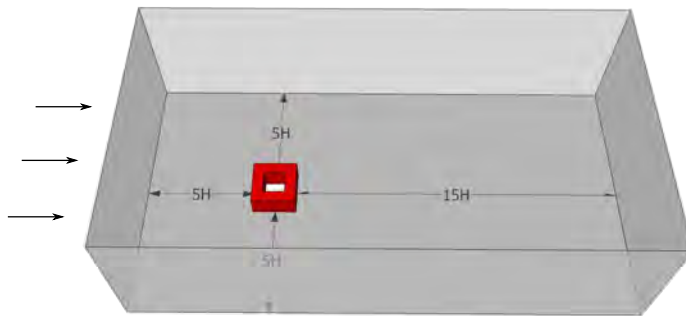
Streamlines (ext):





*Mesh +*

Computational configuration:



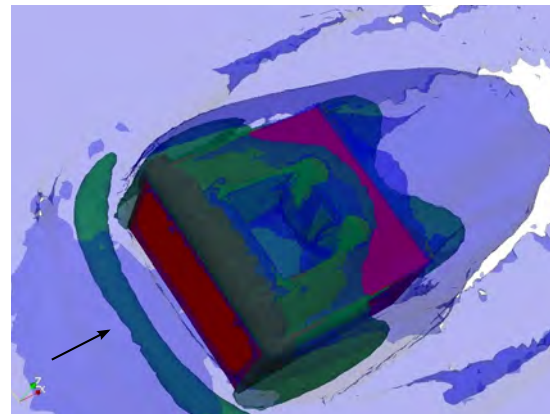
Legend

3D Velocity:	<span style="display:inline-block; width:15px; height:15px; background-color:blue;"></span>	0.5 m/s
	<span style="display:inline-block; width:15px; height:15px; background-color:green;"></span>	1.5 m/s
	<span style="display:inline-block; width:15px; height:15px; background-color:yellow;"></span>	2.5 m/s
3D Vorticity:	<span style="display:inline-block; width:15px; height:15px; background-color:blue;"></span>	0.5 rad/s
	<span style="display:inline-block; width:15px; height:15px; background-color:green;"></span>	1.5 rad/s
	<span style="display:inline-block; width:15px; height:15px; background-color:red;"></span>	5.5 rad/s

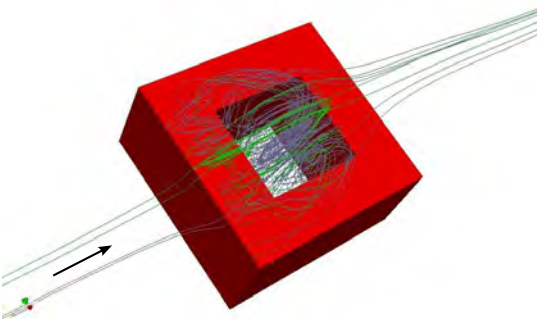
3D mean velocity:



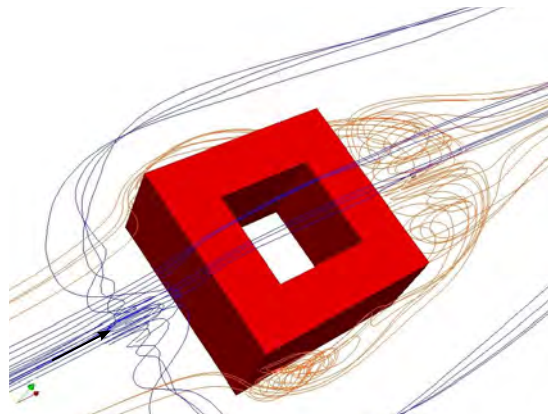
3D vorticity:



Streamlines (int):

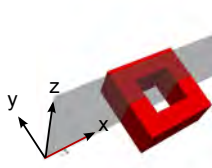


Streamlines (ext):

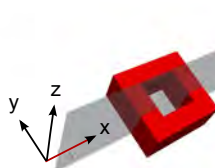


*Basic*

Plane  $y=0\text{m}$ :



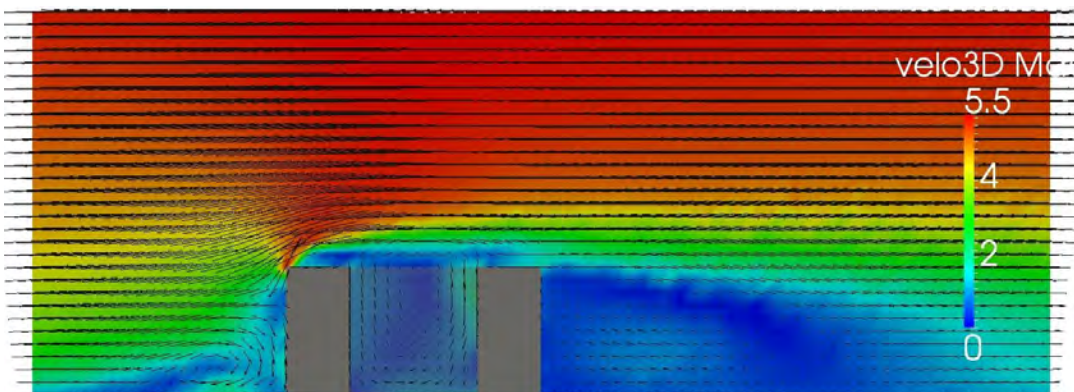
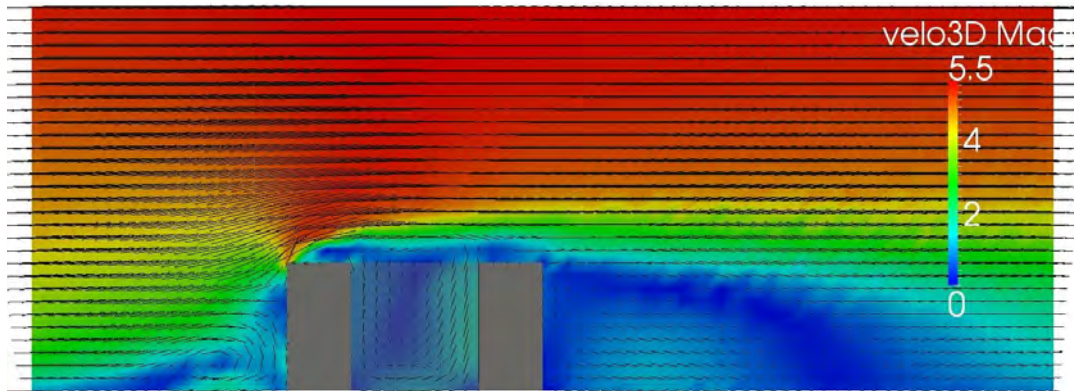
Plane  $y=-2.5\text{m}$ :



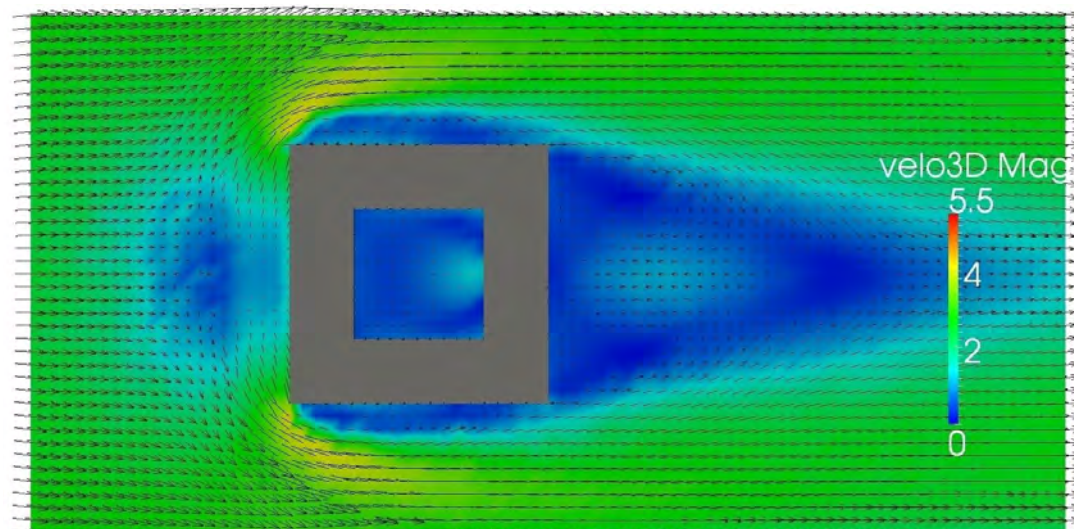
Plane  $z=2\text{m}$ :



Mean velocity field, planes  $y=0\text{m}$  and  $-2.5\text{m}$ :



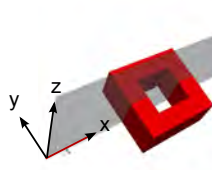
Mean velocity field, plane  $z=2\text{m}$ :



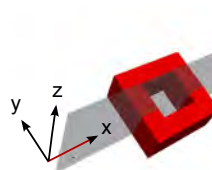


*Mesh +*

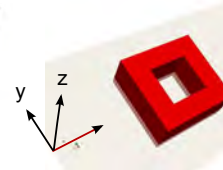
Plane  $y=0\text{m}$ :



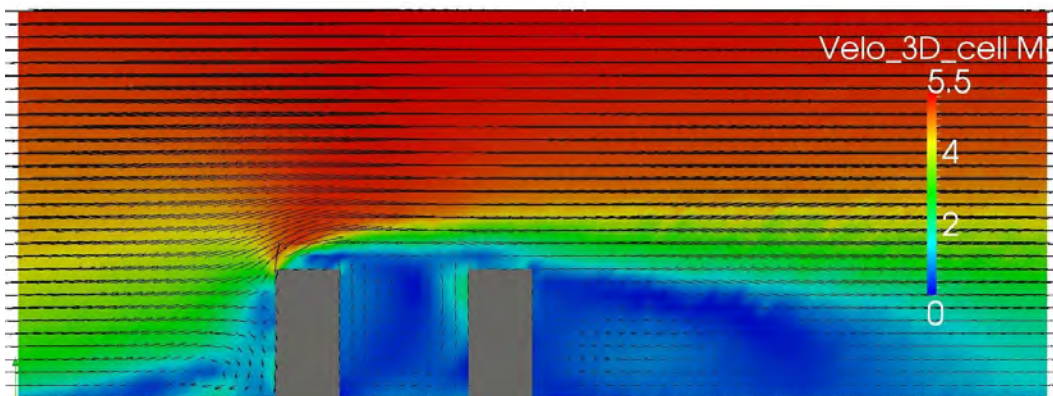
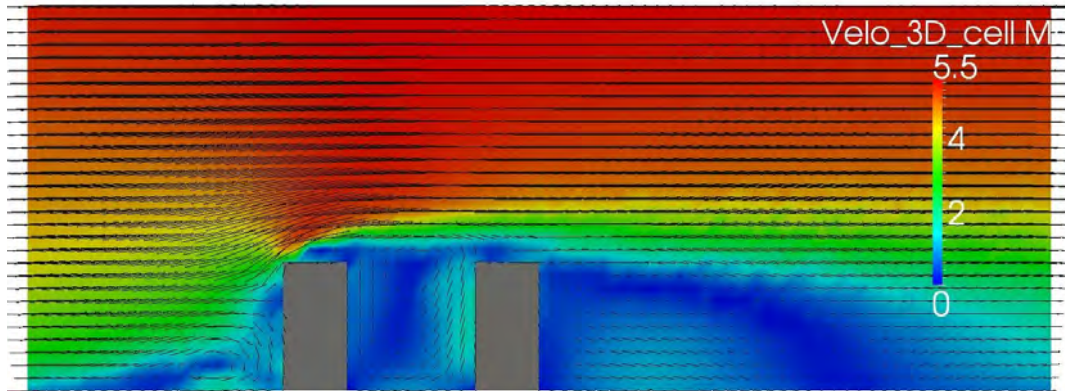
Plane  $y=-2.5\text{m}$ :



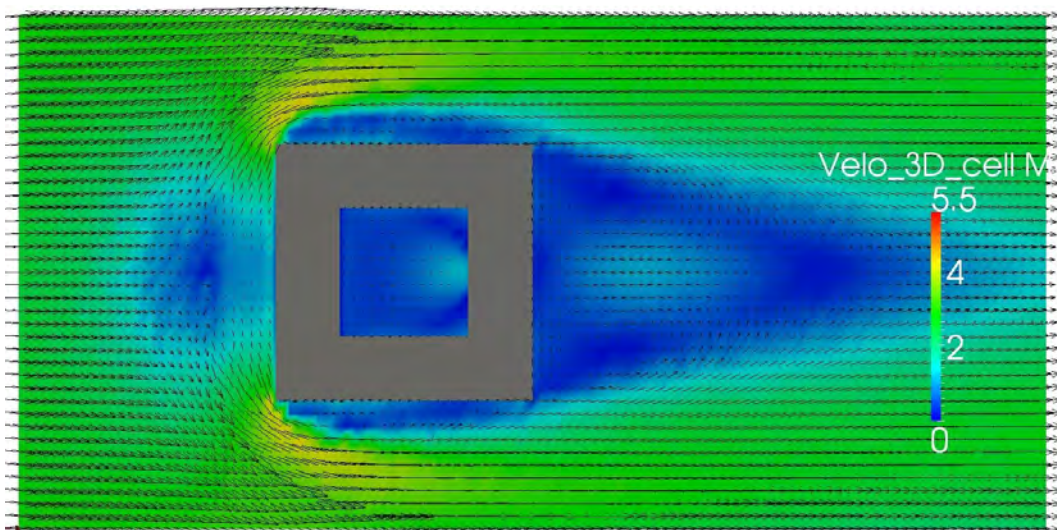
Plane  $z=2\text{m}$ :



Mean velocity field, planes  $y=0\text{m}$  and  $-2.5\text{m}$ :



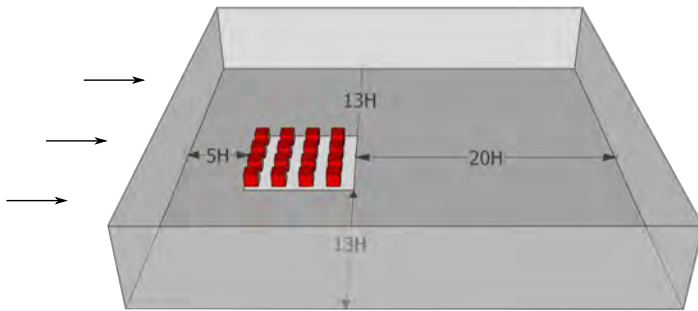
Mean velocity field, plane  $z=2\text{m}$ :









## O Aerodynamic results for the urban block types

### O.1 The cube array

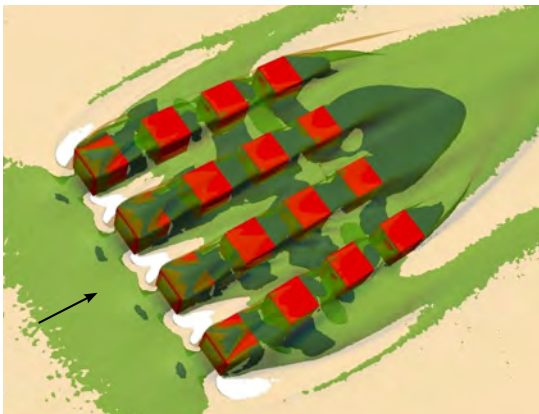
Computational configuration:



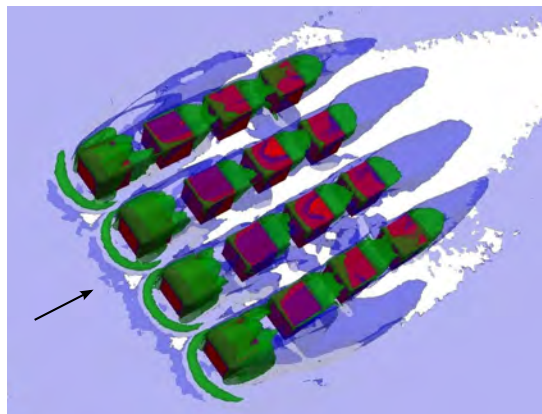
Legend

3D Velocity:		0.5 m/s
		1.5 m/s
		2.5 m/s
3D Vorticity:		0.5 rad/s
		1.5 rad/s
		5.5 rad/s

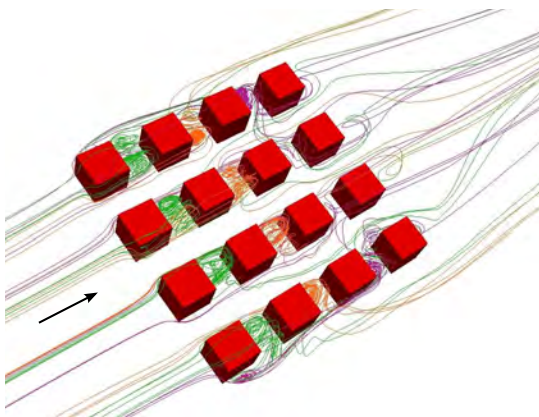
3D mean velocity:



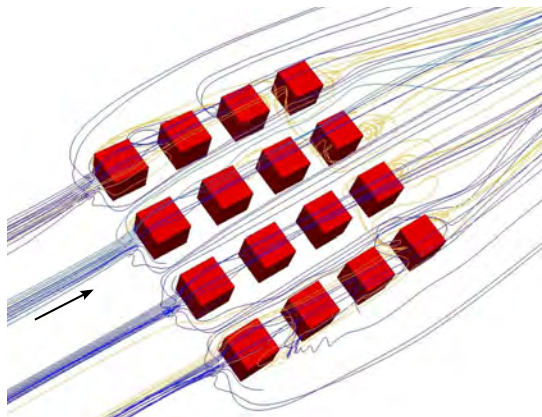
3D vorticity:



Streamlines (int):

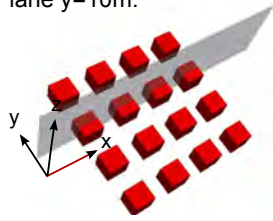


Streamlines (ext):

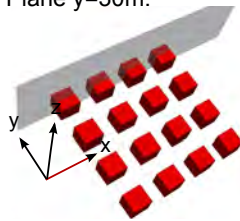




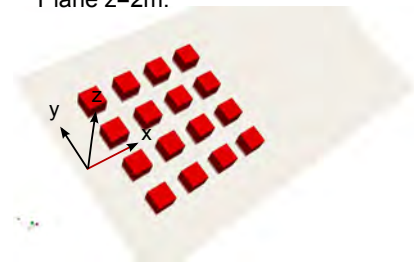
Plane y=10m:



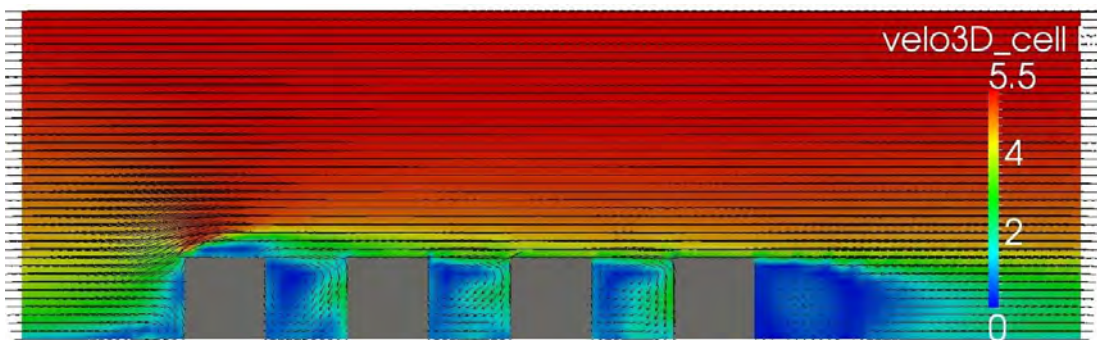
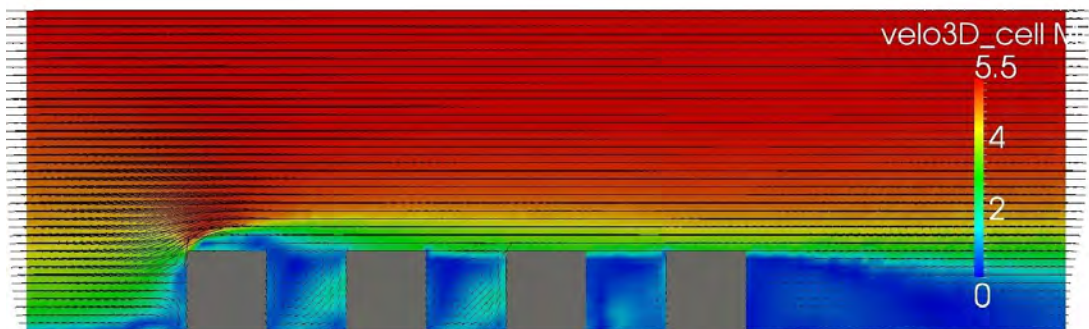
Plane y=30m:



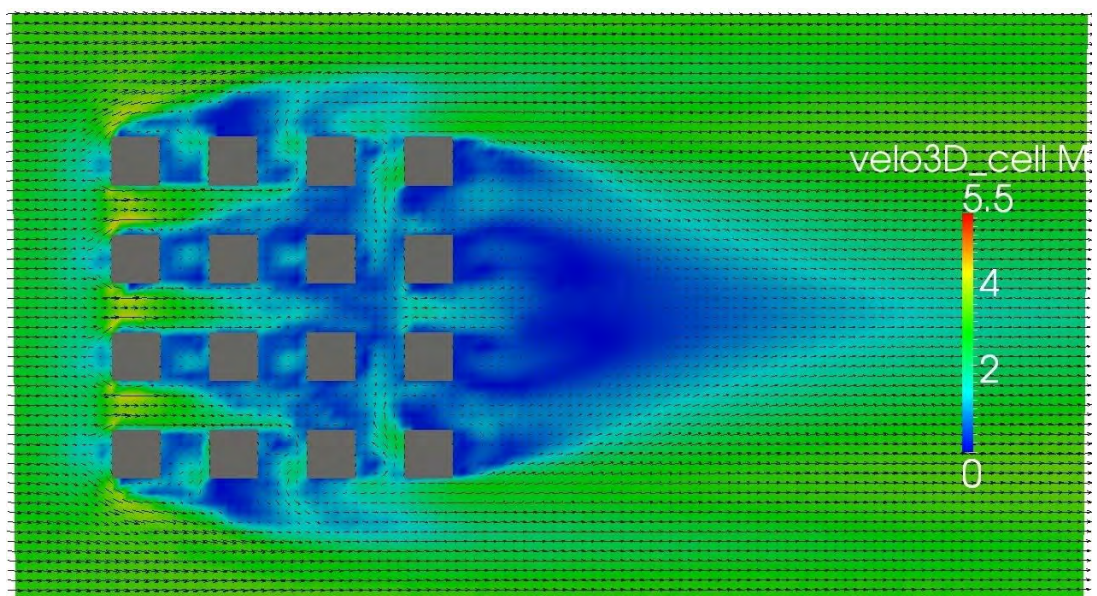
Plane z=2m:



Mean velocity field, planes y=10m and 30m:

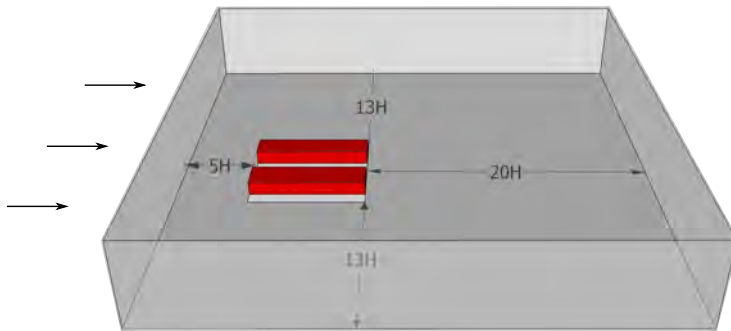


Mean velocity field, plane z=2m:









## O.2 The row block 1

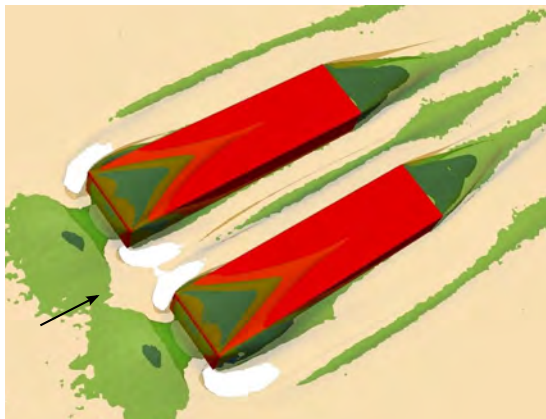
Computational configuration:



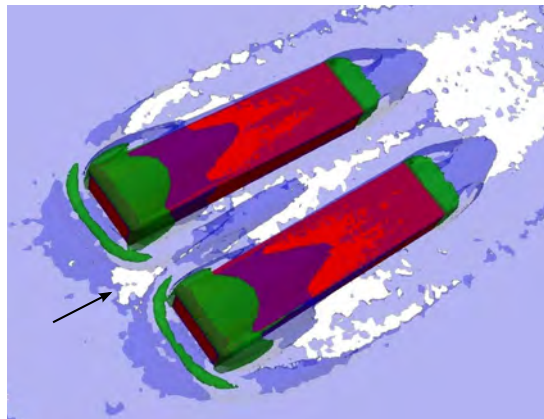
Legend

3D Velocity:		0.5 m/s
		1.5 m/s
		2.5 m/s
3D Vorticity:		0.5 rad/s
		1.5 rad/s
		5.5 rad/s

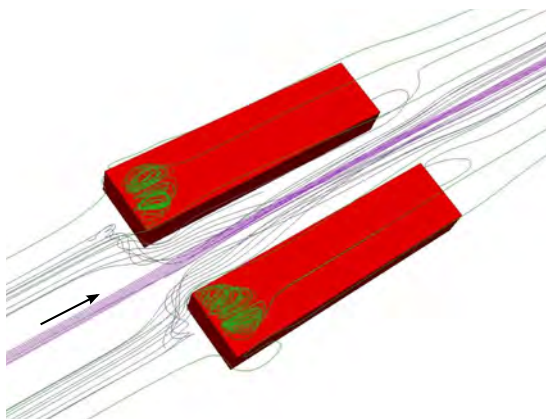
3D mean velocity:



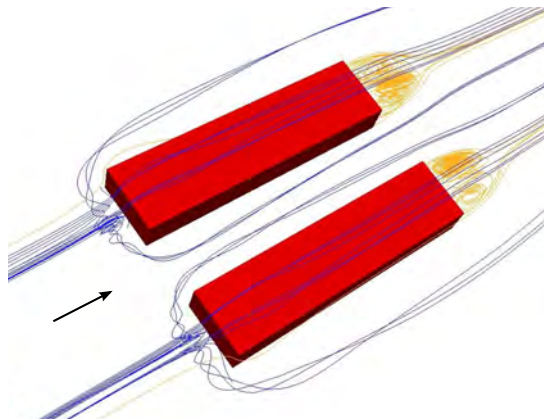
3D vorticity:



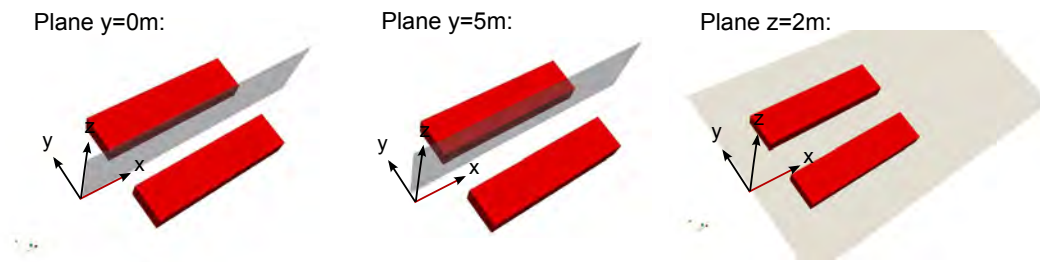
Streamlines (int):



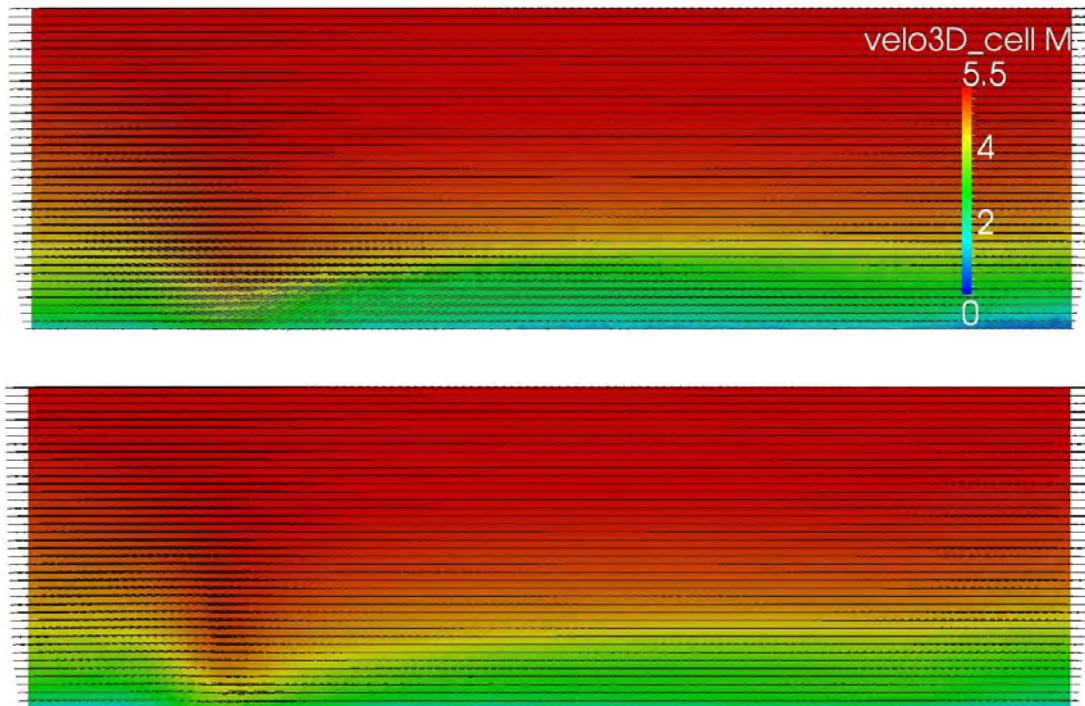
Streamlines (ext):



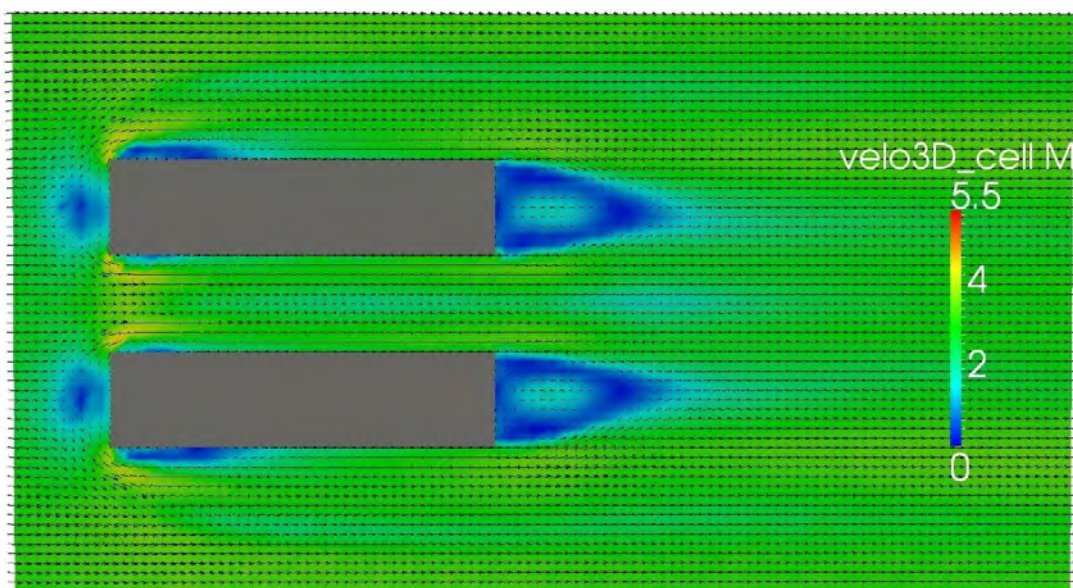




Mean velocity field, planes y=0m and 5m:

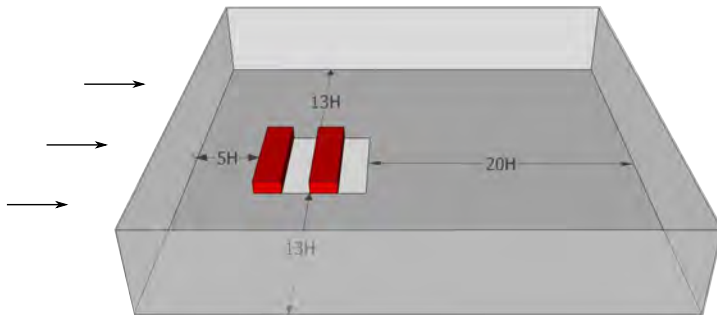


Mean velocity field, plane z=2m:









### O.3 The row block 2

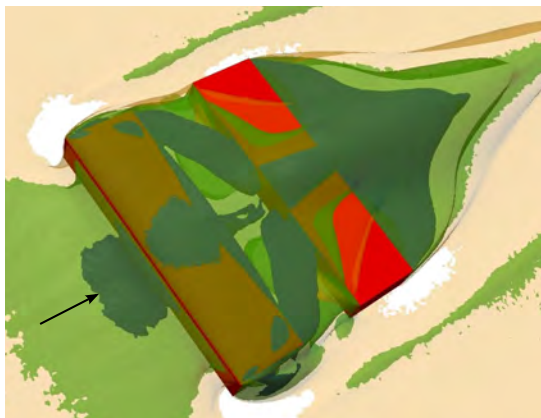
Computational configuration:



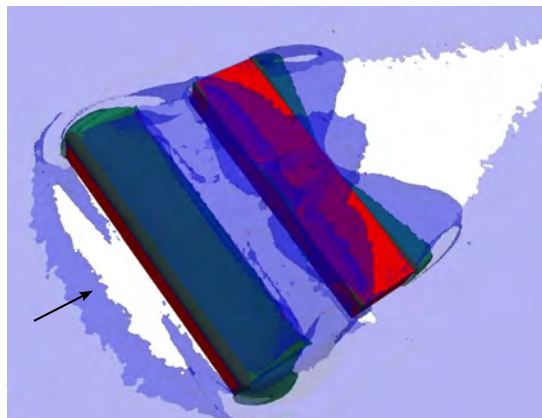
Legend

3D Velocity:		0.5 m/s
		1.5 m/s
		2.5 m/s
3D Vorticity:		0.5 rad/s
		1.5 rad/s
		5.5 rad/s

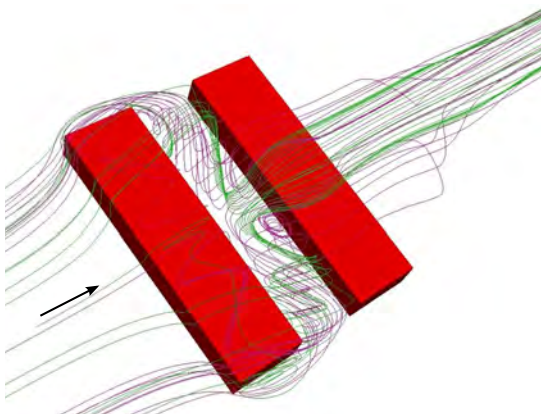
3D mean velocity:



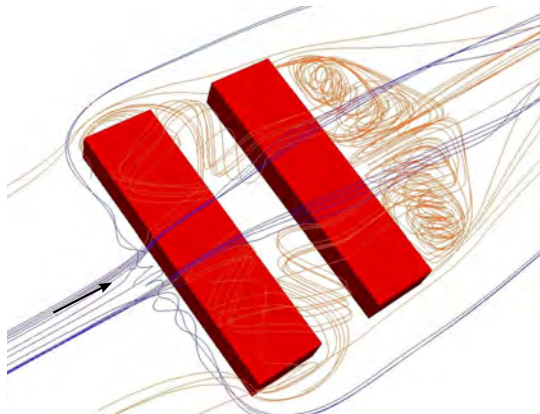
3D vorticity:



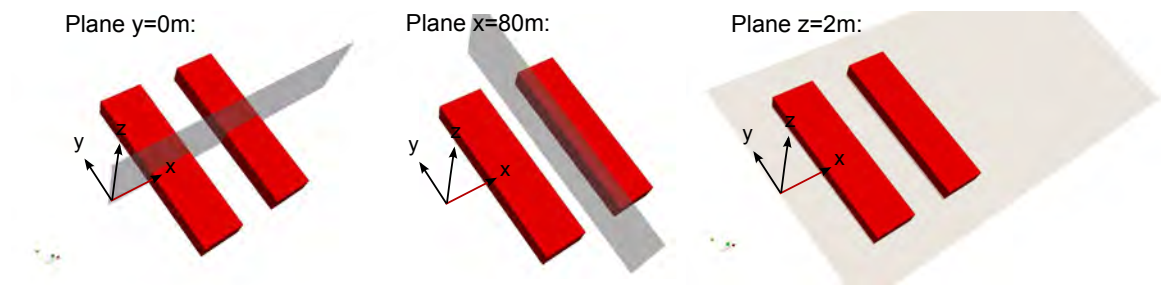
Streamlines (int):



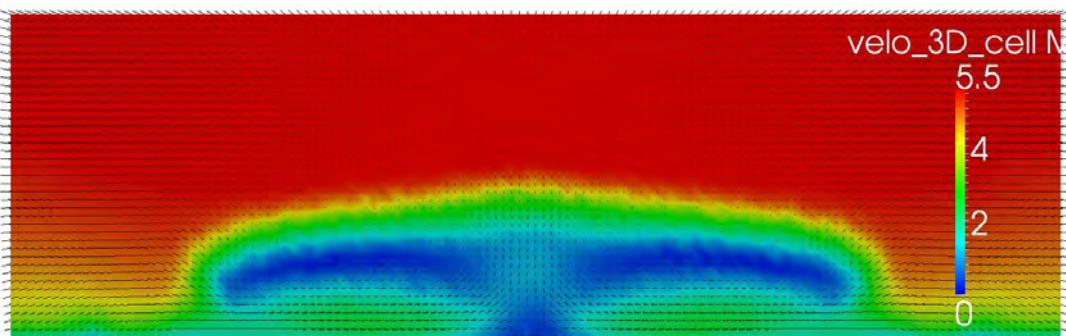
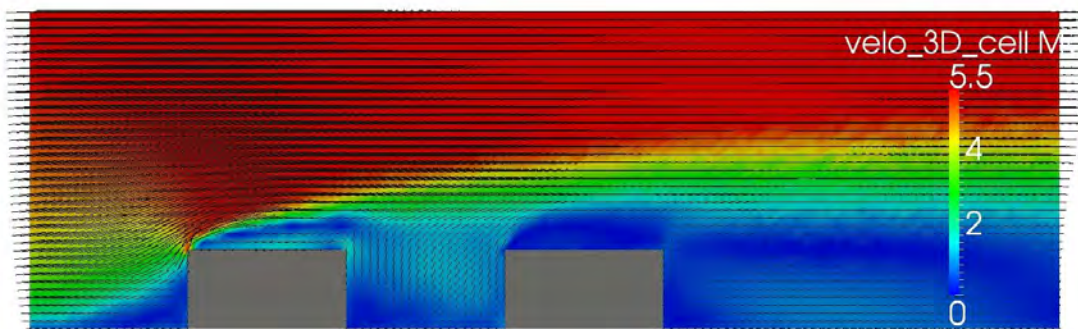
Streamlines (ext):



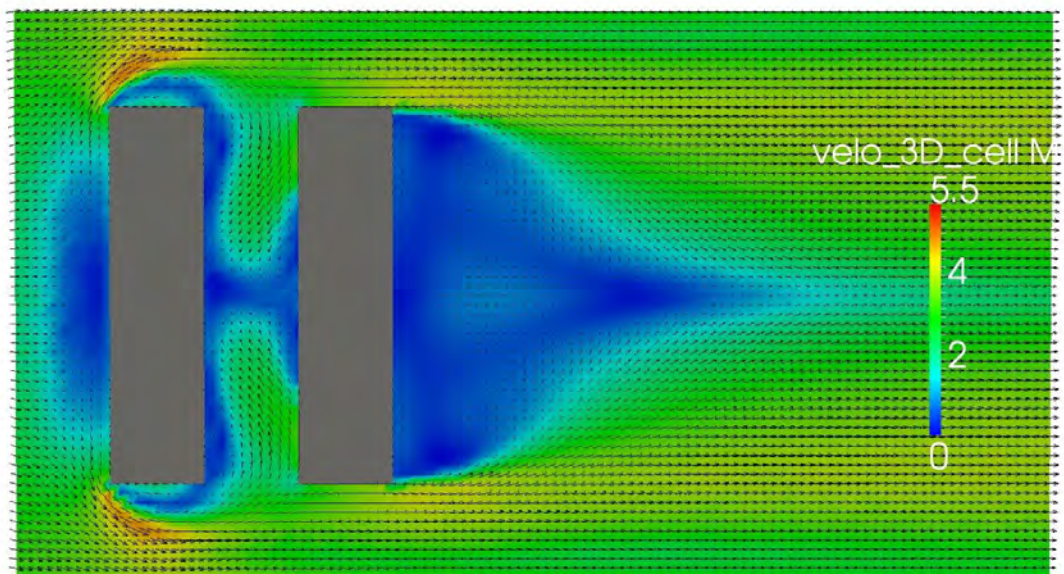




Mean velocity field, planes  $y=0\text{m}$  and  $x=80\text{m}$ :



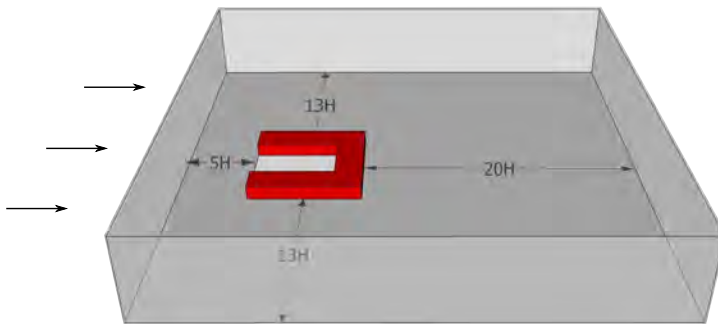
Mean velocity field, plane  $z=2\text{m}$ :











#### O.4 The U-block 1

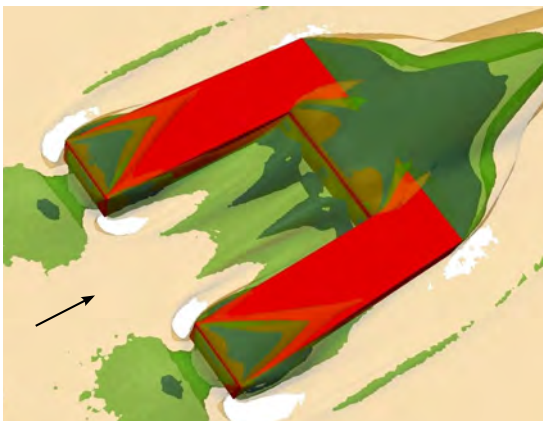
Computational configuration:



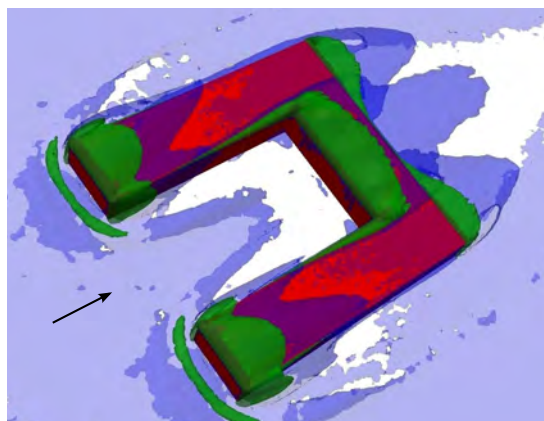
Legend

3D Velocity:		0.5 m/s
		1.5 m/s
		2.5 m/s
3D Vorticity:		0.5 rad/s
		1.5 rad/s
		5.5 rad/s

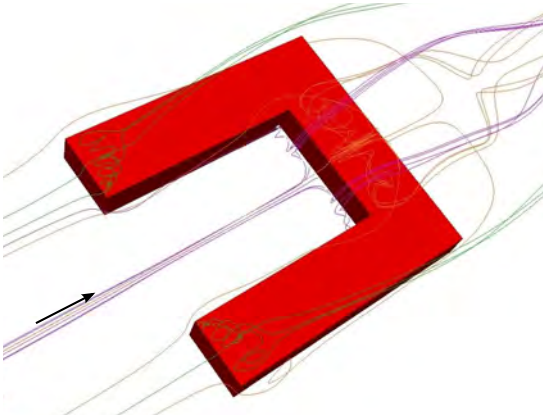
3D mean velocity:



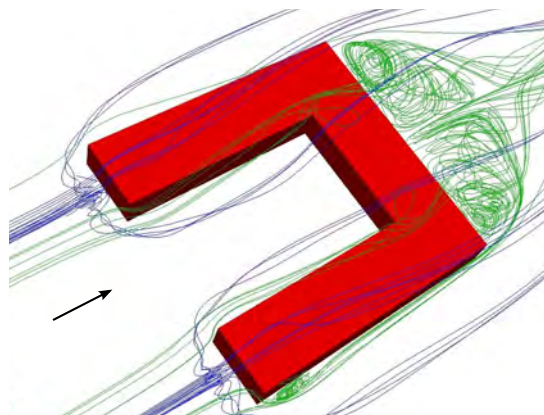
3D vorticity:

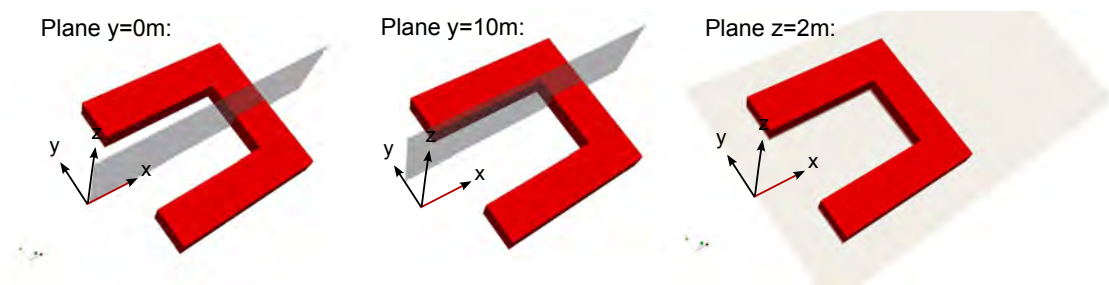


Streamlines (int):

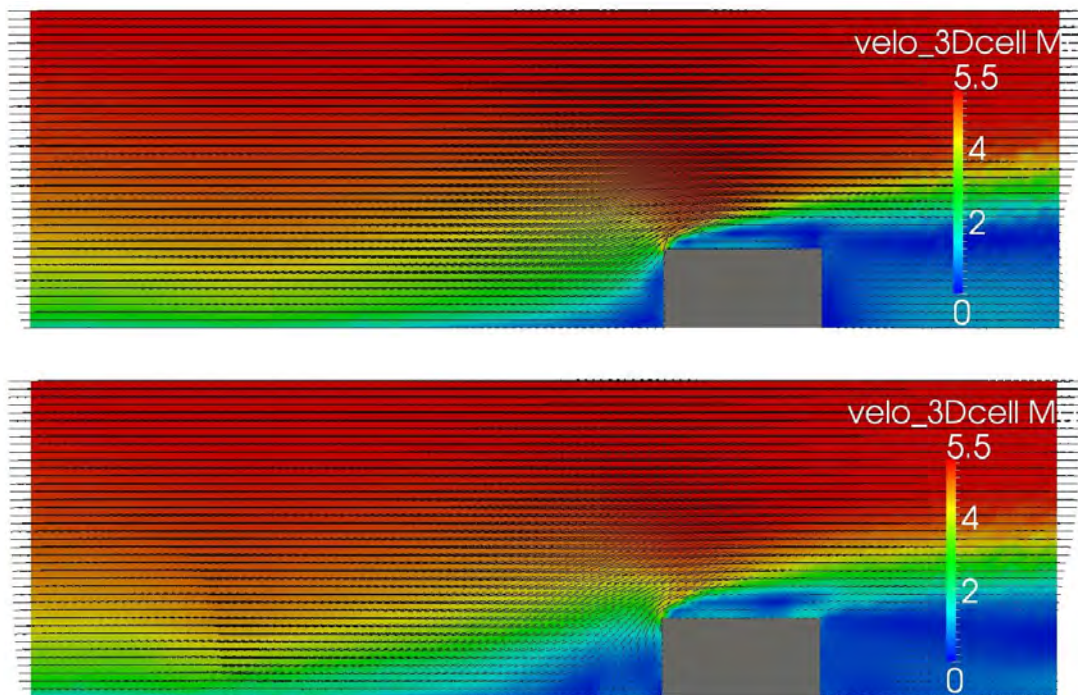


Streamlines (ext):

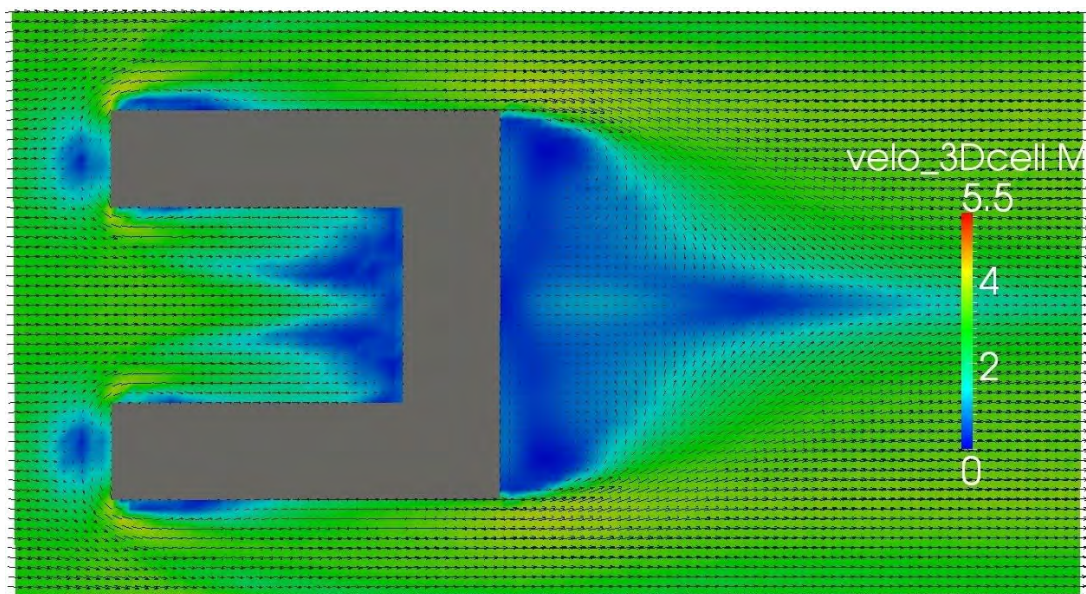




Mean velocity field, planes  $y=0\text{m}$  and  $10\text{m}$ :



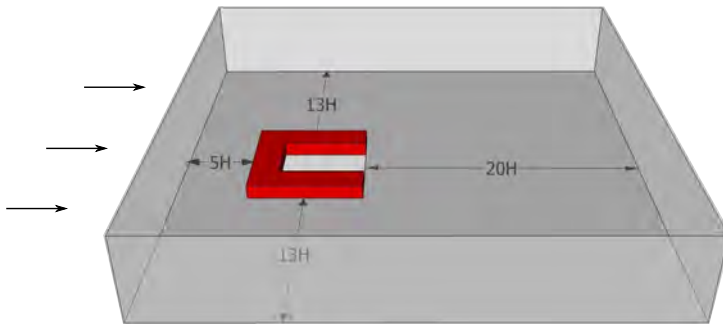
Mean velocity field, plane  $z=2\text{m}$ :











## O.5 The U-block 2

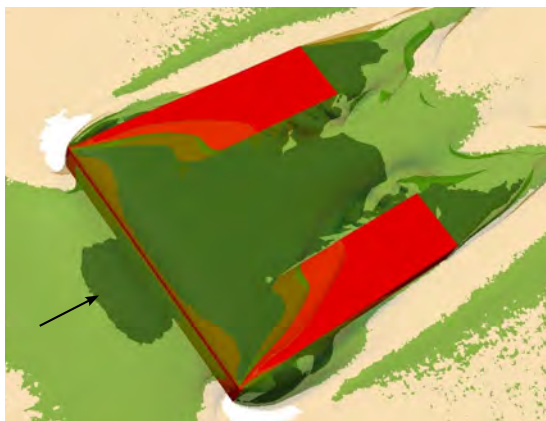
Computational configuration:



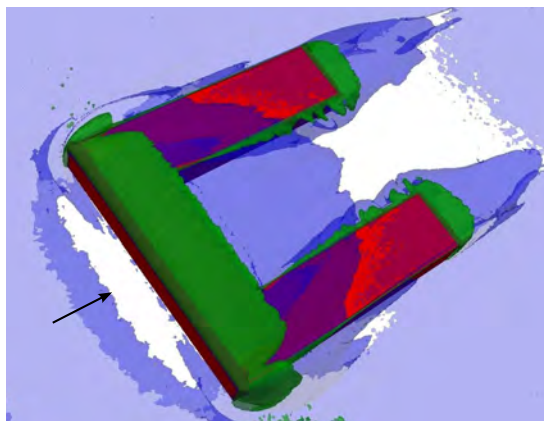
Legend

3D Velocity:		0.5 m/s
		1.5 m/s
		2.5 m/s
3D Vorticity:		0.5 rad/s
		1.5 rad/s
		5.5 rad/s

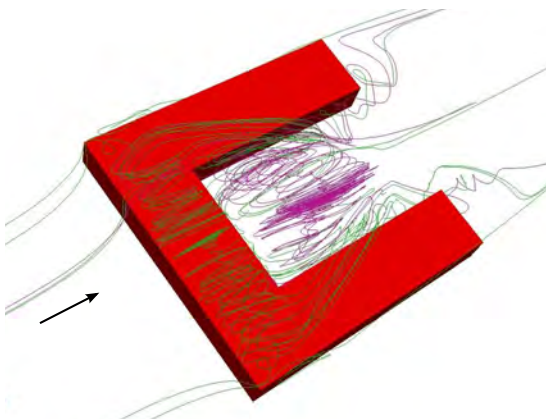
3D mean velocity:



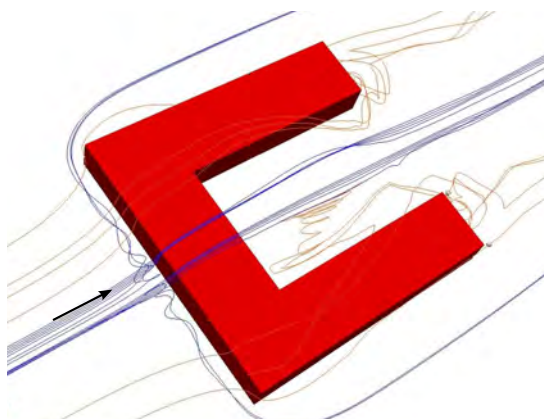
3D vorticity:



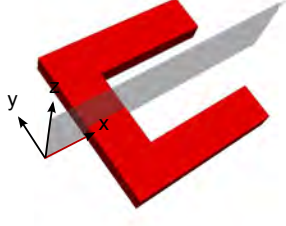
Streamlines (int):



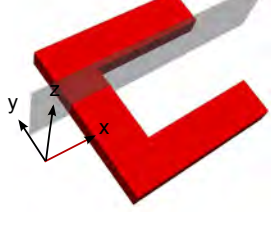
Streamlines (ext):



Plane y=0m:



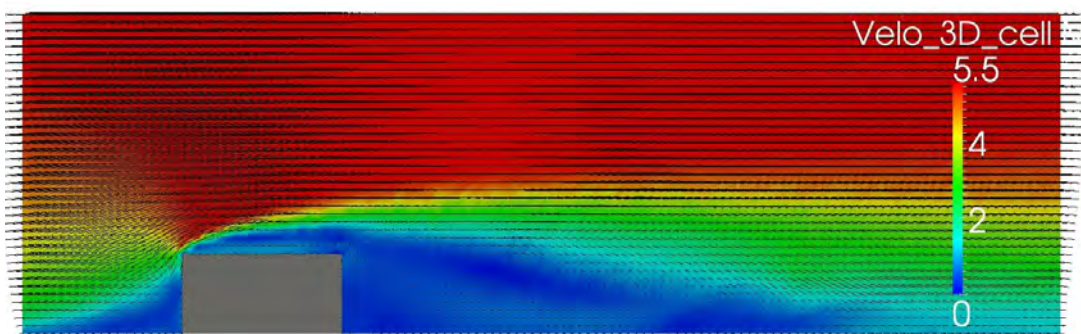
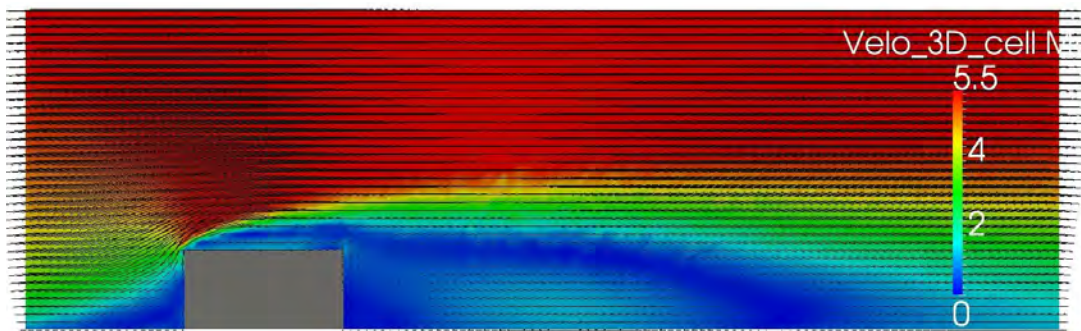
Plane y=10m:



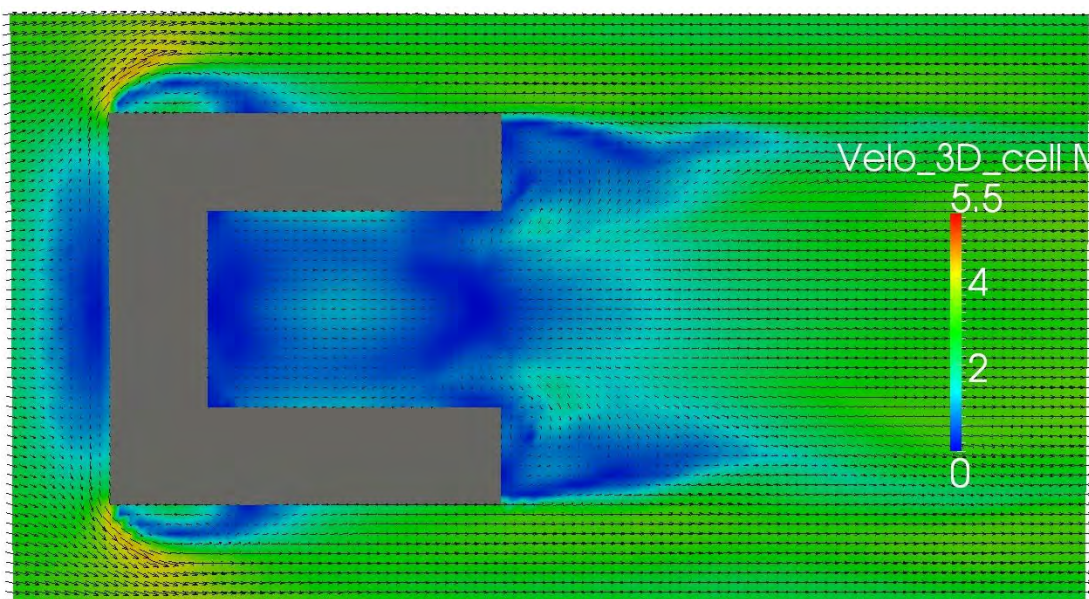
Plane z=2m:



Mean velocity field, planes y=0m and 10m:



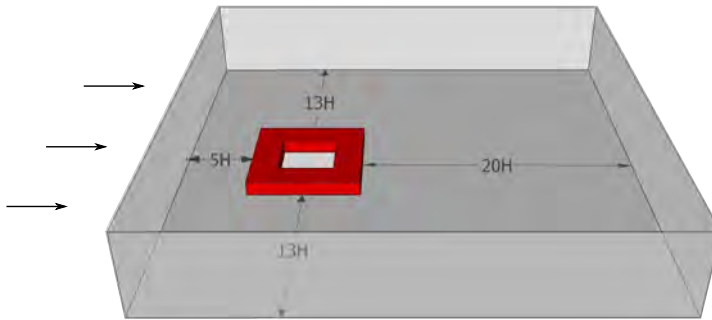
Mean velocity field, plane z=2m:











## O.6 The enclosed block

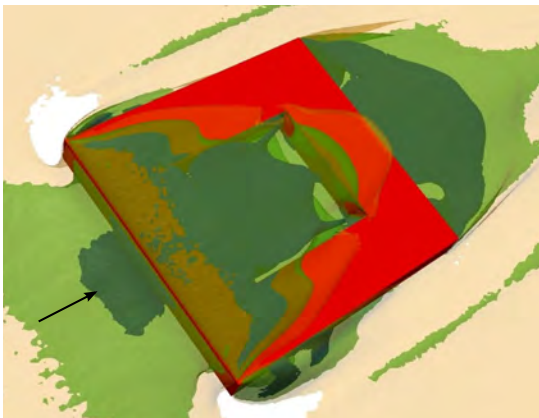
Computational configuration:



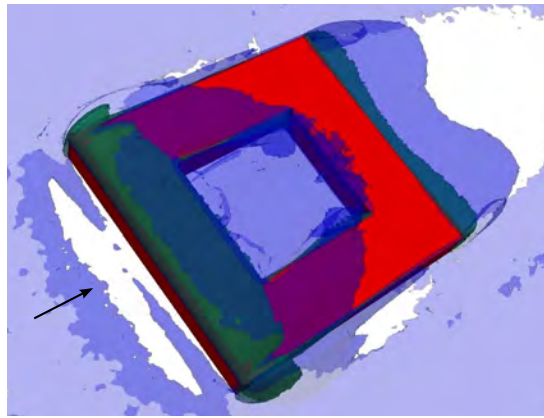
Legend

3D Velocity:		0.5 m/s
		1.5 m/s
		2.5 m/s
3D Vorticity:		0.5 rad/s
		1.5 rad/s
		5.5 rad/s

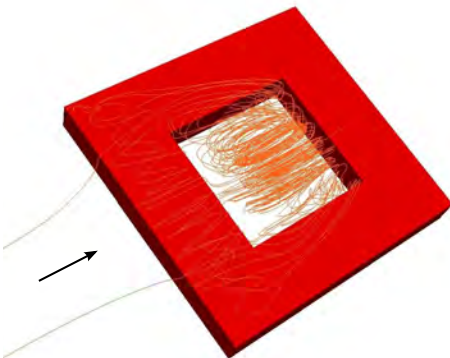
3D mean velocity:



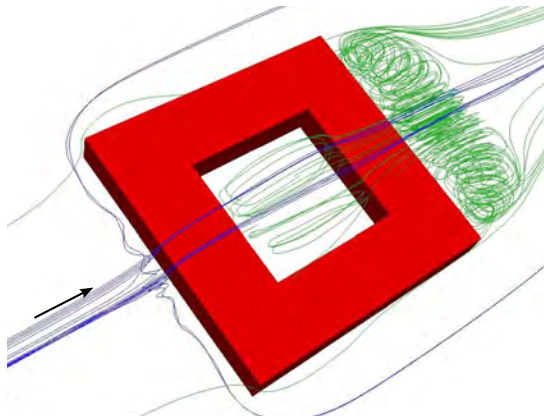
3D vorticity:

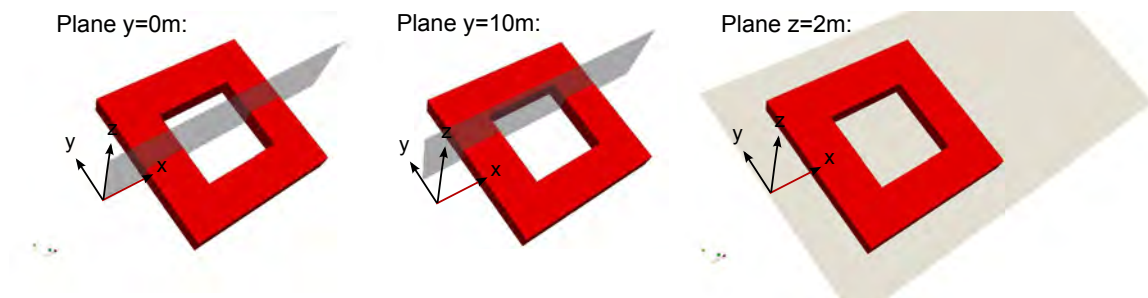


Streamlines (int):

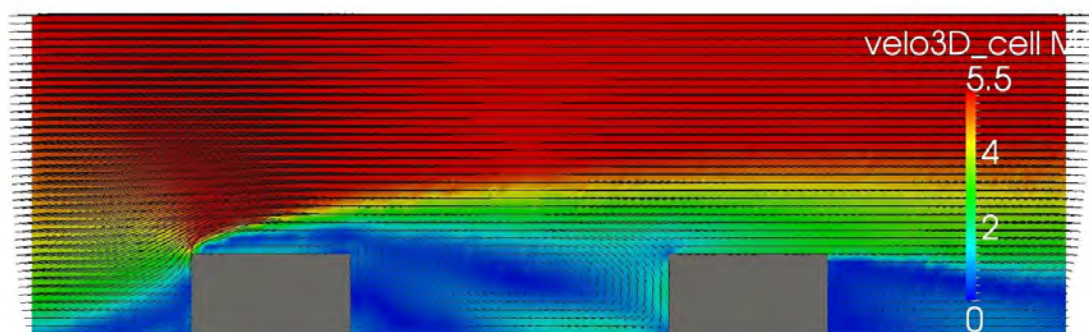
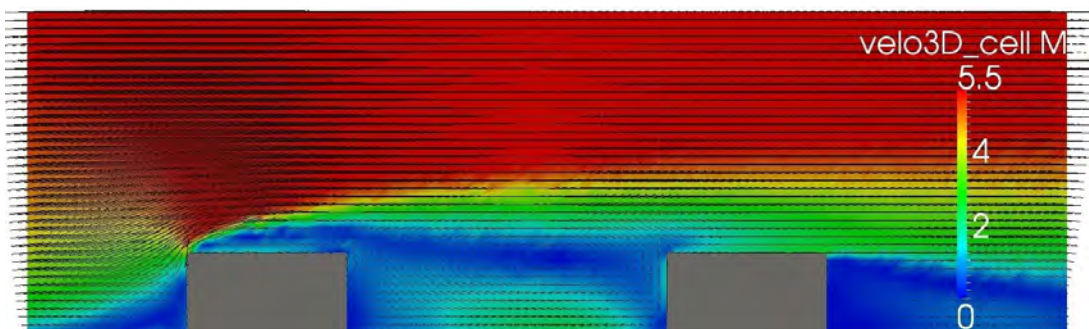


Streamlines (ext):

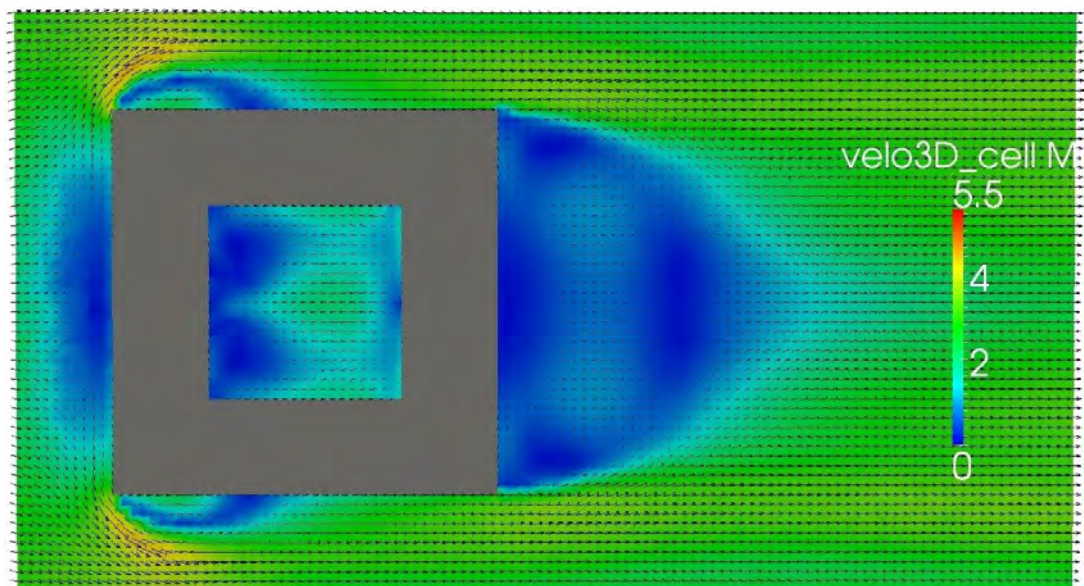




Mean velocity field, planes  $y=0\text{m}$  and  $10\text{m}$ :



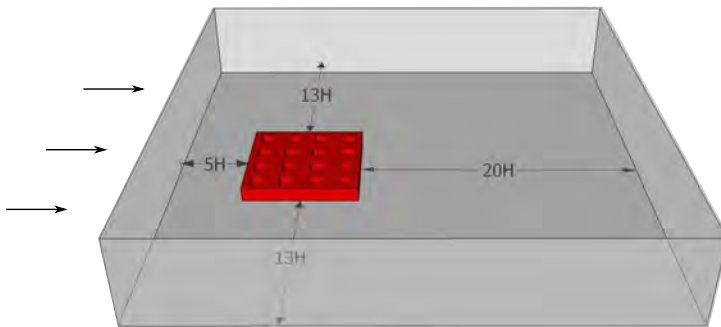
Mean velocity field, plane  $z=2\text{m}$ :











## O.7 The continuous patio array

Computational configuration:



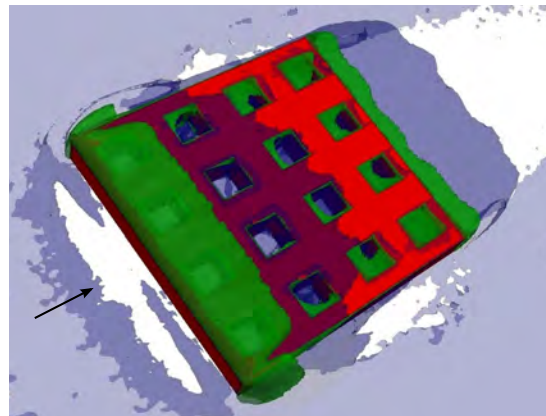
Legend

3D Velocity:		0.5 m/s
		1.5 m/s
		2.5 m/s
3D Vorticity:		0.5 rad/s
		1.5 rad/s
		5.5 rad/s

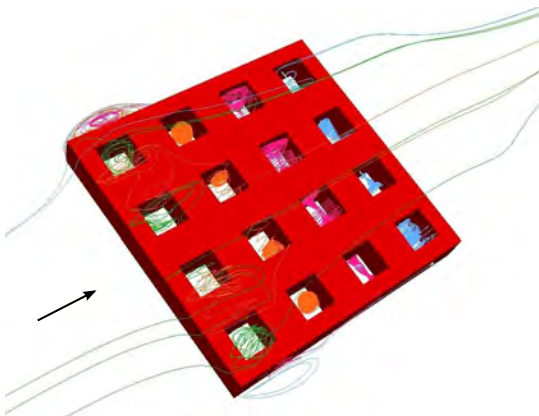
3D mean velocity:



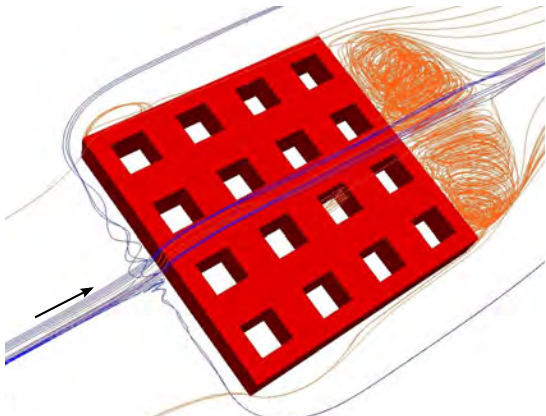
3D vorticity:

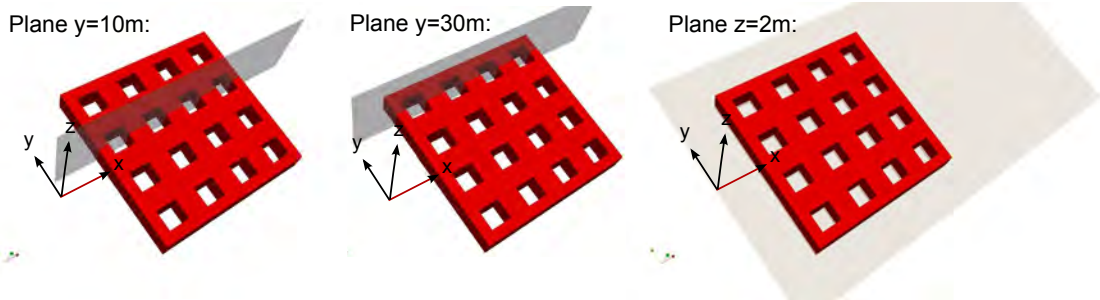


Streamlines (int):

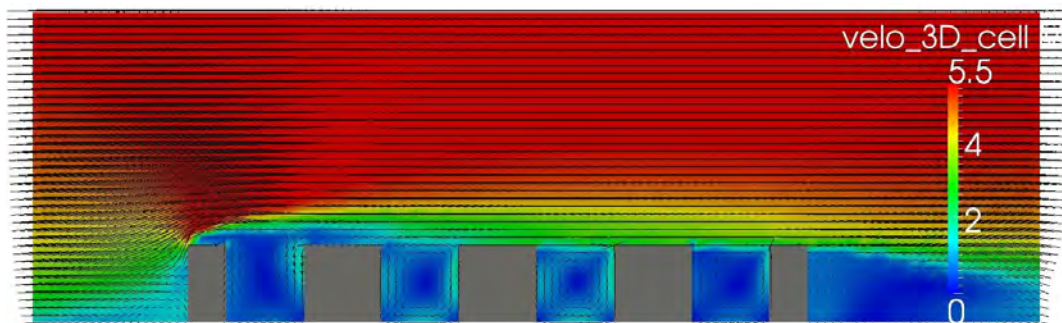
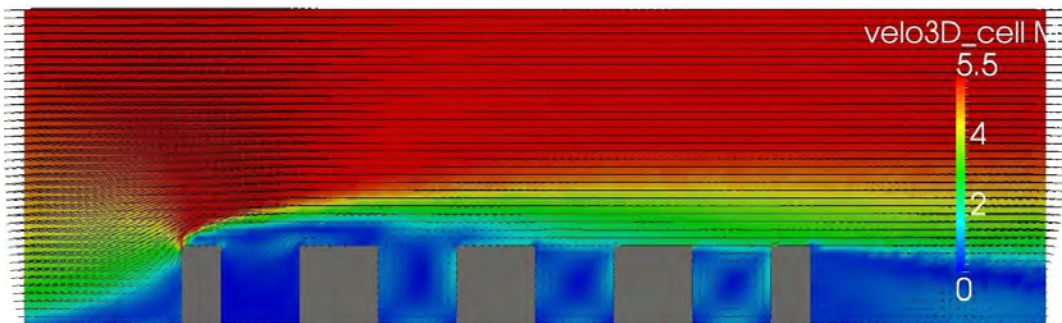


Streamlines (ext):

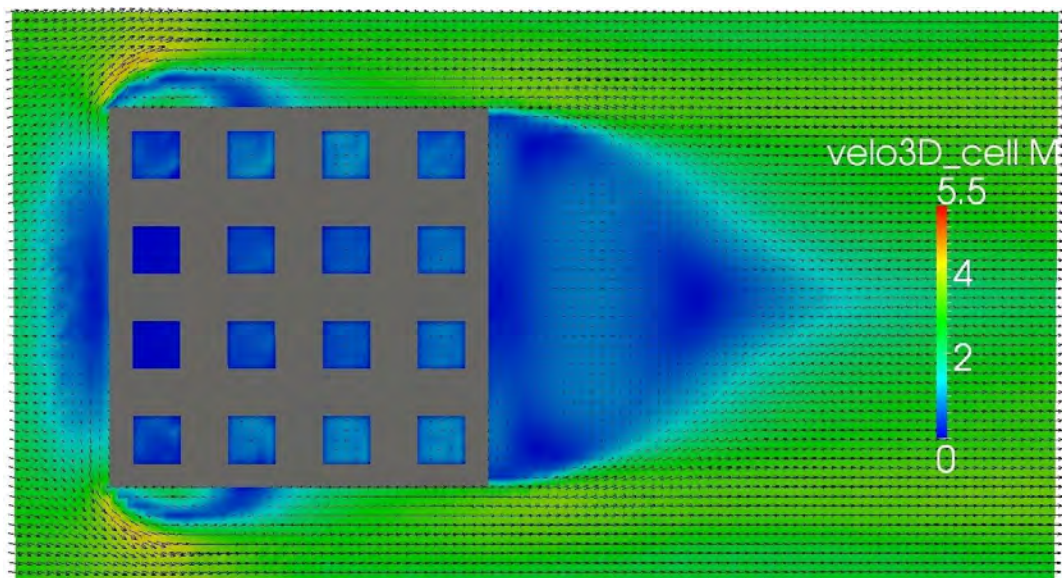




Mean velocity field, planes  $y=10\text{m}$  and  $30\text{m}$ :



Mean velocity field, plane  $z=2\text{m}$ :





## P 2D internal recirculation phenomena for the cube and the continuous patio arrays

The cube array:

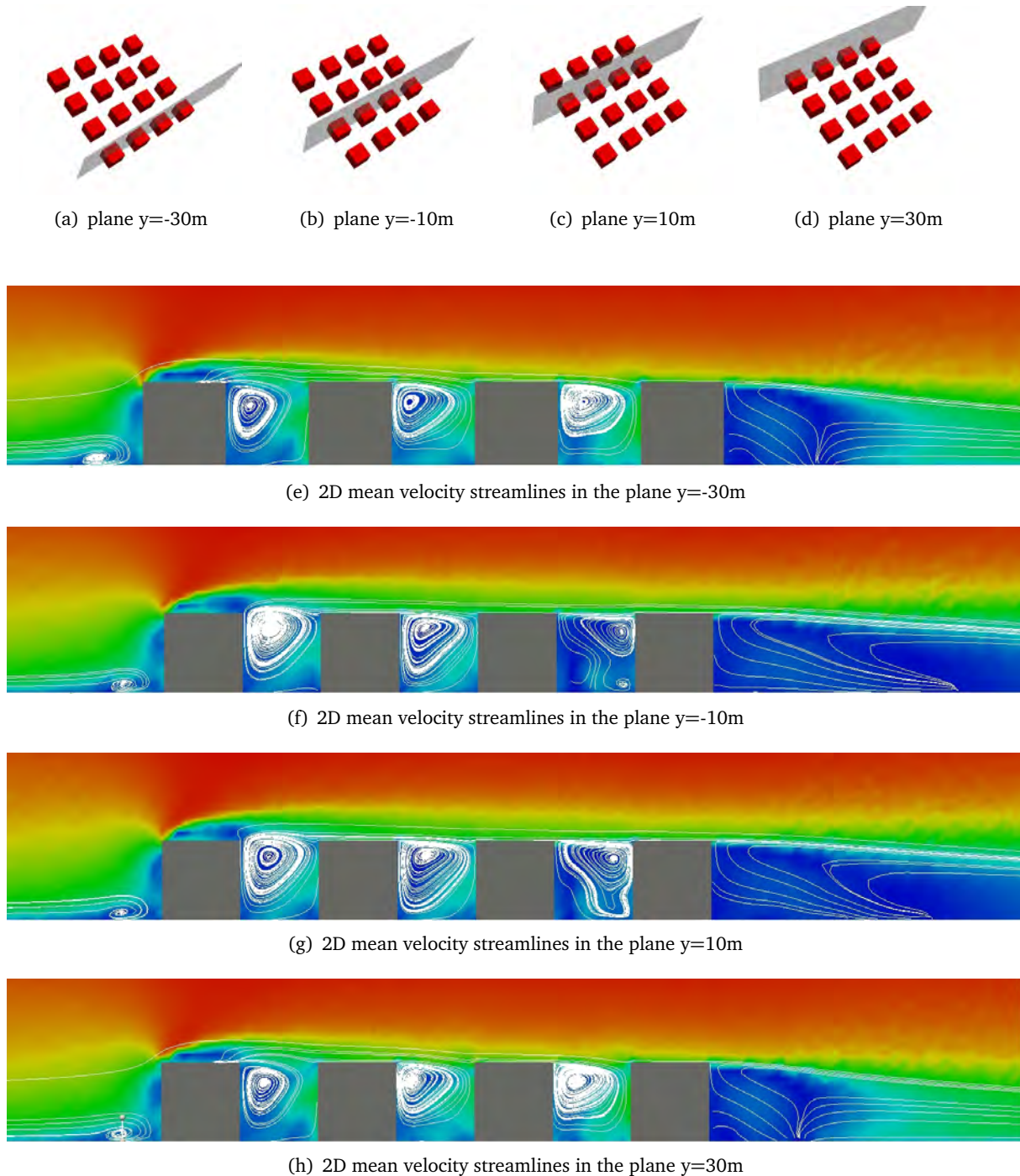


Figure a.14: 2D internal recirculation phenomena developing in each row of the cube array.

### The continuous patio array

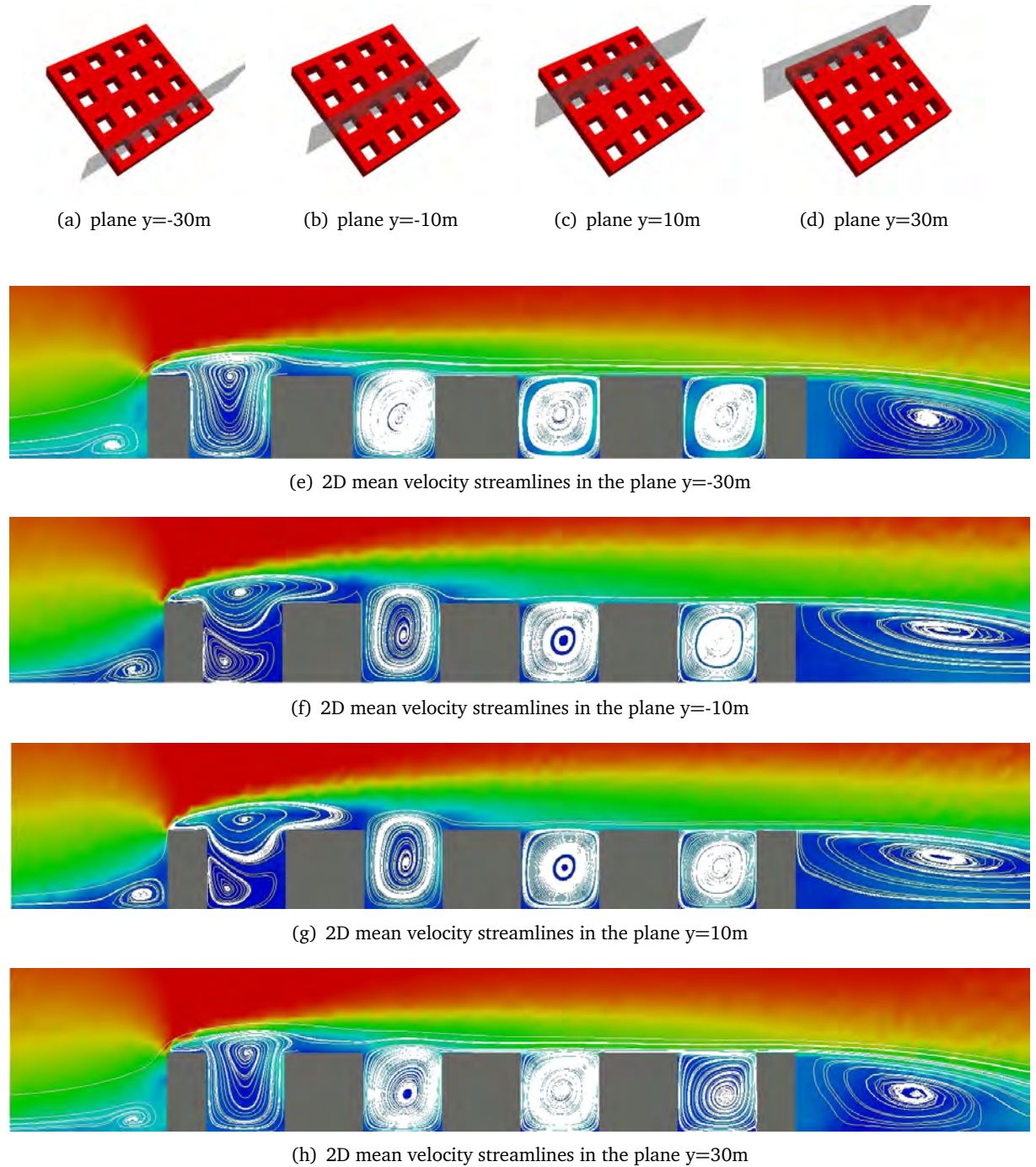


Figure a.15: 2D internal recirculation phenomena developing in each row of the continuous patio array.

## Q Distribution of $C_p$ on the building surfaces

### Q.1 Simulation results: $C_p$ for the cube and the patio

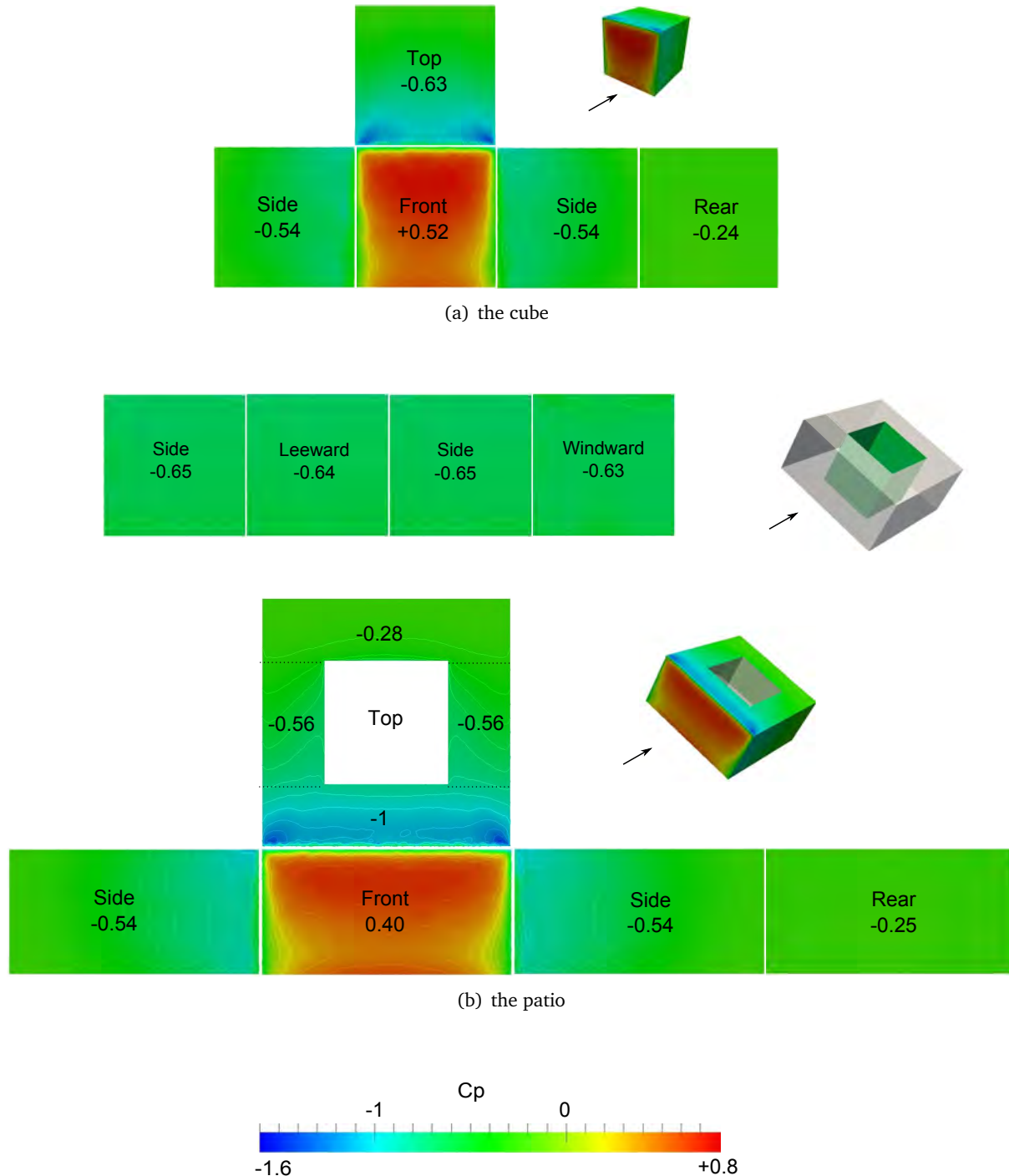


Figure a.16: Distribution of the surface averaged  $C_p$  for the cube and the patio.

## Q.2 Simulation results: $C_p$ for the cube array and the continuous patio array

The cube array:

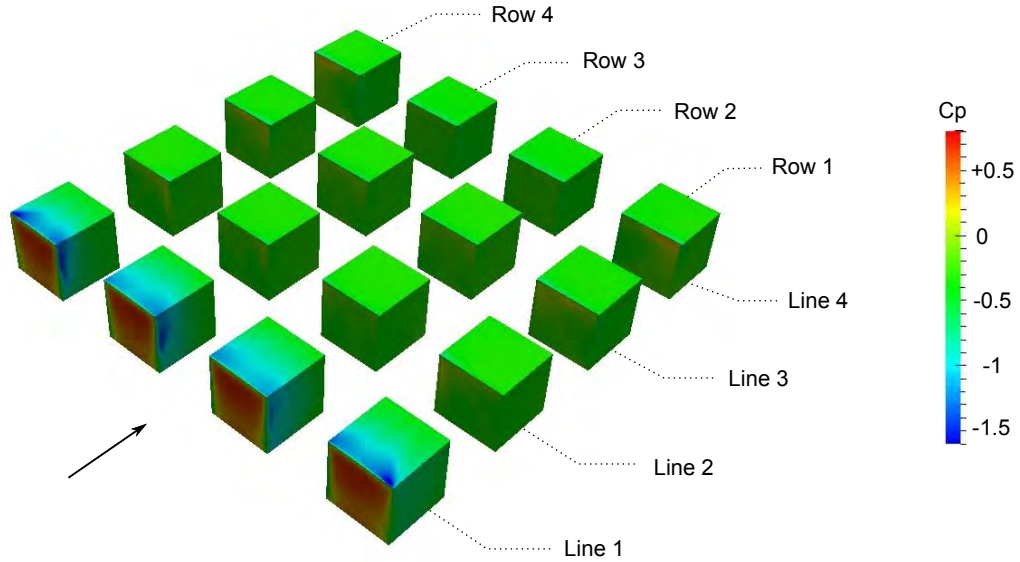


Figure a.17: Specification of the indexes for the cube array.

General		Front	Top	Rear	Side ext.		$\Delta_{F-R}$	
		+ 0.36	- 0.48	- 0.38	- 0.42		+ 0.74	
Line (l)	Row (r)	Front	Top	Rear	Side int.	Side ext.	$\Delta_{F_l-R_l}$	$\Delta_{R_{l-1}-F_l}$
1	1	+ 0.36	- 0.82	- 0.45	- 0.67	- 0.61	+ 0.81	–
1	2	+ 0.36	- 0.82	- 0.39	- 0.72	- 0.73	+ 0.75	–
1	3	+ 0.36	- 0.83	- 0.40	- 0.71	- 0.75	+ 0.76	–
1	4	+ 0.36	- 0.82	- 0.45	- 0.66	- 0.61	+ 0.80	–
2	1	- 0.27	- 0.35	- 0.36	- 0.33	- 0.36	+ 0.09	- 0.18
2	2	- 0.29	- 0.34	- 0.31	- 0.32	- 0.35	+ 0.03	- 0.11
2	3	- 0.29	- 0.34	- 0.32	- 0.32	- 0.34	+ 0.03	- 0.11
2	4	- 0.28	- 0.34	- 0.36	- 0.33	- 0.36	+ 0.08	- 0.17
3	1	- 0.19	- 0.37	- 0.39	- 0.30	- 0.39	+ 0.20	- 0.17
3	2	- 0.23	- 0.34	- 0.31	- 0.31	- 0.29	+ 0.07	- 0.08
3	3	- 0.24	- 0.34	- 0.32	- 0.31	- 0.30	+ 0.09	- 0.08
3	4	- 0.19	- 0.37	- 0.40	- 0.30	- 0.39	+ 0.21	- 0.17
4	1	- 0.19	- 0.37	- 0.40	- 0.41	- 0.32	+ 0.20	- 0.21
4	2	- 0.28	- 0.41	- 0.36	- 0.41	- 0.40	+ 0.08	- 0.02
4	3	- 0.29	- 0.41	- 0.37	- 0.41	- 0.41	+ 0.08	- 0.03
4	4	- 0.19	- 0.37	- 0.40	- 0.42	- 0.32	+ 0.20	- 0.21

Table a.6: Surface averaged  $C_p$  for each face the cube array.



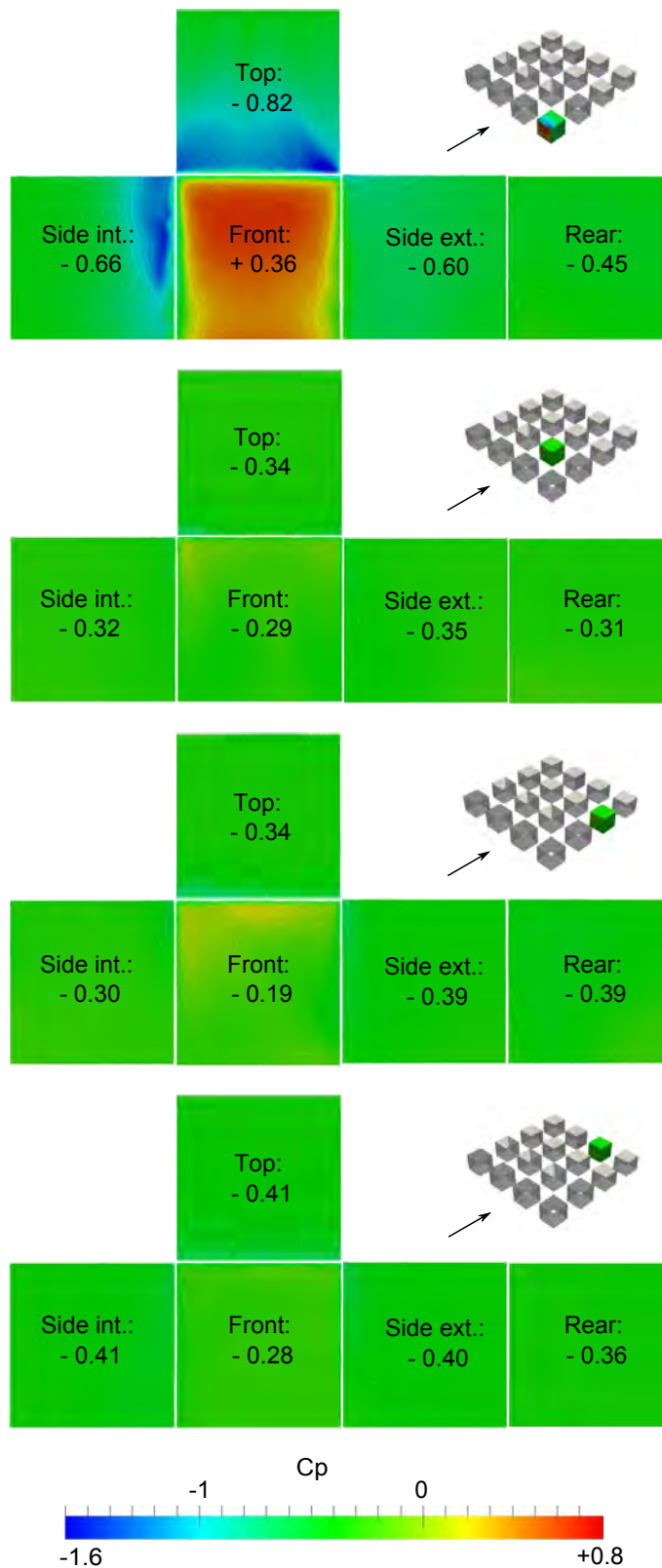


Figure a.18:  $C_p$  distribution and surface averaged mean  $C_p$  by faces for the cubes 1-1, 2-2, 3-1 and 4-2 of the cube array.

The continuous patio array:

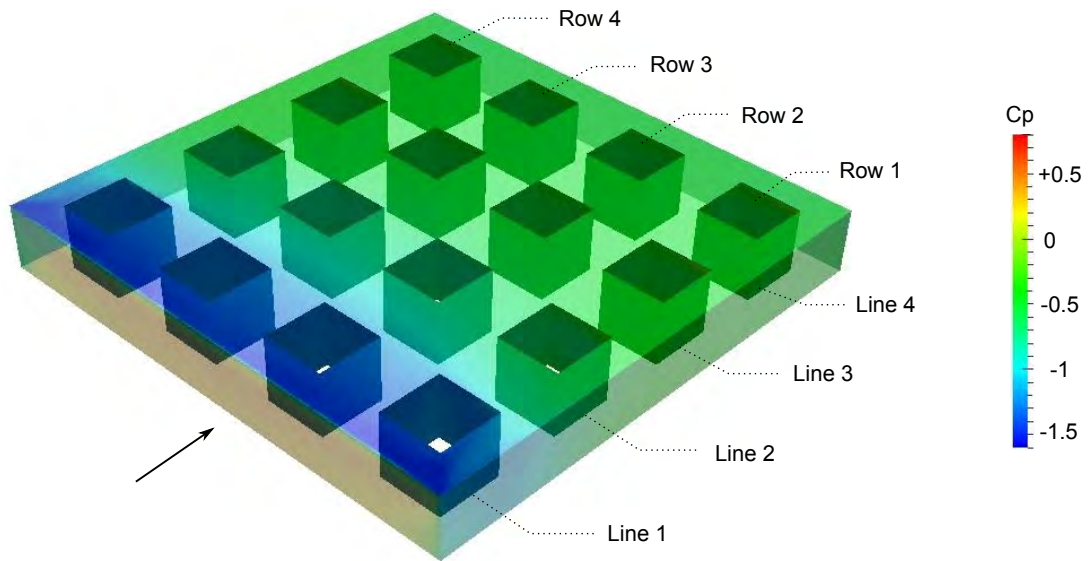


Figure a.19: Specification of the indexes for the continuous patio array.

General		Front	Rear	Sides	Top	$\Delta_{F-R}$	
		+ 0.24	- 0.56	- 0.62	- 0.74	0.80	
Line (l)	Row (r)	Leeward	Windward	Side int.	Side ext.	$\Delta_{W_{l,r}-L_{l,r}}$	$\Delta_{W_{l-1,r}-L_{l,r}}$
1	1	- 1.25	- 1.25	- 1.25	- 1.26	0.01	—
1	2	- 1.25	- 1.26	- 1.25	- 1.26	0.00	—
1	3	- 1.25	- 1.26	- 1.25	- 1.26	0.00	—
1	4	- 1.25	- 1.25	- 1.26	- 1.26	0.00	—
2	1	- 0.63	- 0.61	- 0.65	- 0.65	0.02	- 0.62
2	2	- 0.73	- 0.73	- 0.74	- 0.74	0.01	- 0.52
2	3	- 0.73	- 0.72	- 0.74	- 0.74	0.01	- 0.52
2	4	- 0.63	- 0.61	- 0.65	- 0.65	0.02	- 0.62
3	1	- 0.48	- 0.47	- 0.51	- 0.52	0.02	- 0.13
3	2	- 0.52	- 0.50	- 0.53	- 0.53	0.01	- 0.21
3	3	- 0.52	- 0.50	- 0.53	- 0.53	0.01	- 0.21
3	4	- 0.48	- 0.46	- 0.51	- 0.51	0.02	- 0.13
4	1	- 0.49	- 0.48	- 0.53	- 0.53	0.01	+ 0.02
4	2	- 0.50	- 0.49	- 0.52	- 0.52	0.01	0.00
4	3	- 0.50	- 0.49	- 0.52	- 0.52	0.01	0.00
4	4	- 0.48	- 0.46	- 0.49	- 0.49	0.02	+ 0.02

Table a.7: Surface averaged  $C_p$  for each face the patio array.

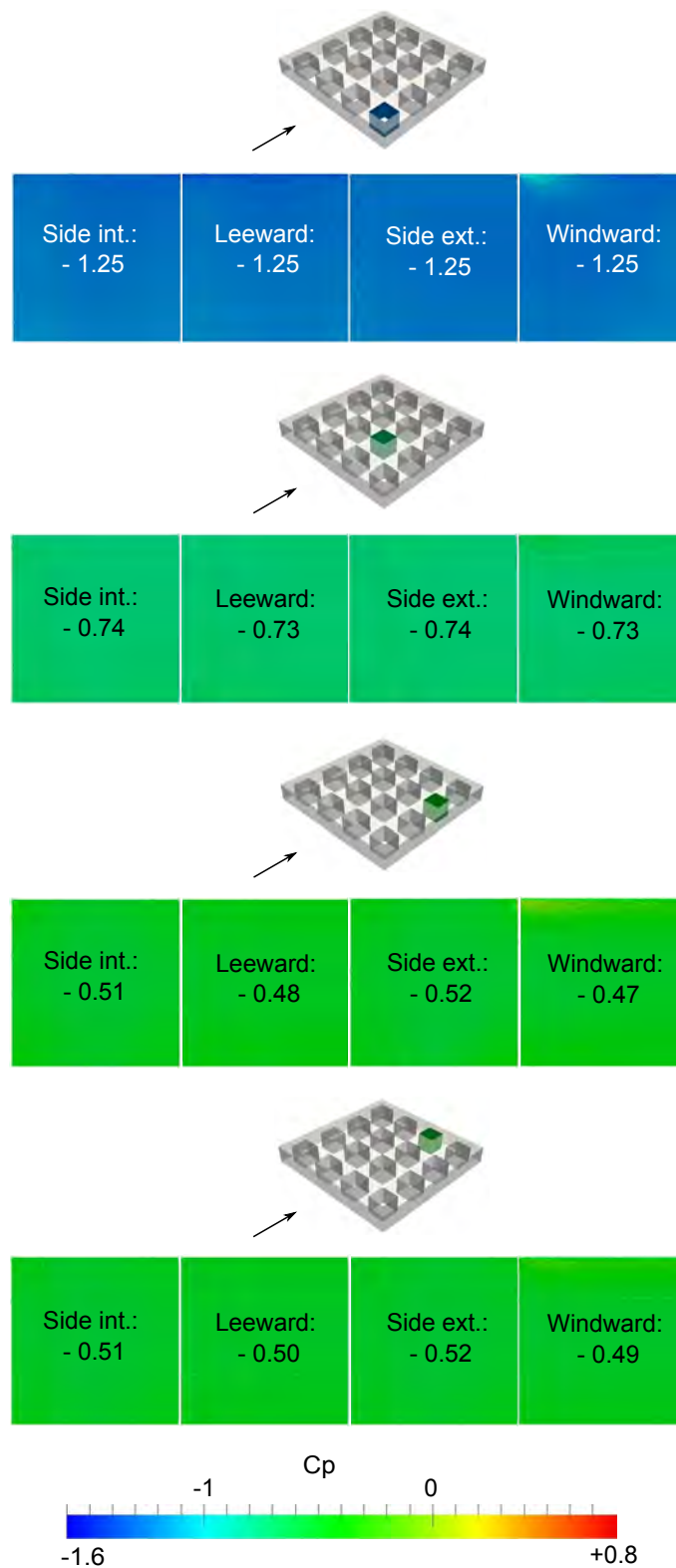


Figure a.20:  $C_p$  distribution and surface averaged mean  $C_p$  by faces for the patios 1-1, 2-2, 3-1 and 4-2 of the continuous patio array.

### Q.3 Wind tunnel data of $C_p$

Wind tunnel data of  $C_p$  are provided by the TPU (2003). Three of the four following cases (cases 1, and 4) are extracted from the isolated low-rise building database, and the other (case 3) is taken from the non-isolated low-rise building database. This database is mainly dedicated to structural purposes but provides mean values for  $C_p$  on the walls of different models. According to the experimental documentation, The wind-tunnel test section is 2.2m wide and 1.8m high. The geometric model scale is 1 : 100 and the velocity scale is 1/3. The approach flow follows a 0.2 power law. At 10 cm high at the model scale, which corresponds to 10 m high full-scale, its velocity is  $7.4 \text{ m} \cdot \text{s}^{-1}$  for isolated building cases. It is  $7.8 \text{ m} \cdot \text{s}^{-1}$  for non-isolated building cases. The turbulence intensity is 0.25.

Fig. a.21 compares the  $U$  profiles of the approach flow used in our simulations with those characterizing the wind-tunnel tests (isolated building cases) and their full-scale equivalents. Following formulas are used:

- Our simulations (RSM):

$$U(z) = \frac{0.3733}{0.418} \times \ln \left[ \frac{z}{0.07968} \right] \quad (.73)$$

as found by the curve fitting. Note that this correspond to a 0.2044 power law ( $R^2 = 0.9968$ ).

$$U(z) = 4.3 \times \left[ \frac{z}{10} \right]^{0.2044} \quad (.74)$$

- Wind tunnel velocity (TPU WT):

$$U(z) = 7.4 \times \left[ \frac{z}{10} \right]^{0.2} \quad (.75)$$

- Wind tunnel velocity (TPU FS):

$$U(z) = 7.8 \times \left[ \frac{z}{10} \right]^{0.2} \quad (.76)$$

Four configurations are selected to discuss our simulation results:

- an isolated cubical obstacle, whose full-scale dimensions are  $W = 16 \text{ m} \times L = 16 \text{ m} \times H = 16 \text{ m}$ , for which  $U_H = 8.13 \text{ m} \cdot \text{s}^{-1}$ . Because of its relative dimensions, this model can be compared to the cube,
- an isolated cuboidal obstacle, whose full-scale dimensions are  $W = 16 \text{ m} \times L = 16 \text{ m} \times H = 8 \text{ m}$ , for which  $U_H = 7.07 \text{ m} \cdot \text{s}^{-1}$ . Because of its relative dimensions, this model can be compared to the patio,
- a non-isolated cuboidal obstacle, whose full-scale dimensions are  $W = 24 \text{ m} \times L = 16 \text{ m} \times H = 12 \text{ m}$ , for which  $U_H = 7.67 \text{ m} \cdot \text{s}^{-1}$ . This obstacle is located in the center of a regular array of identical obstacles with a built density equal to 0.25. Because of its built envi-

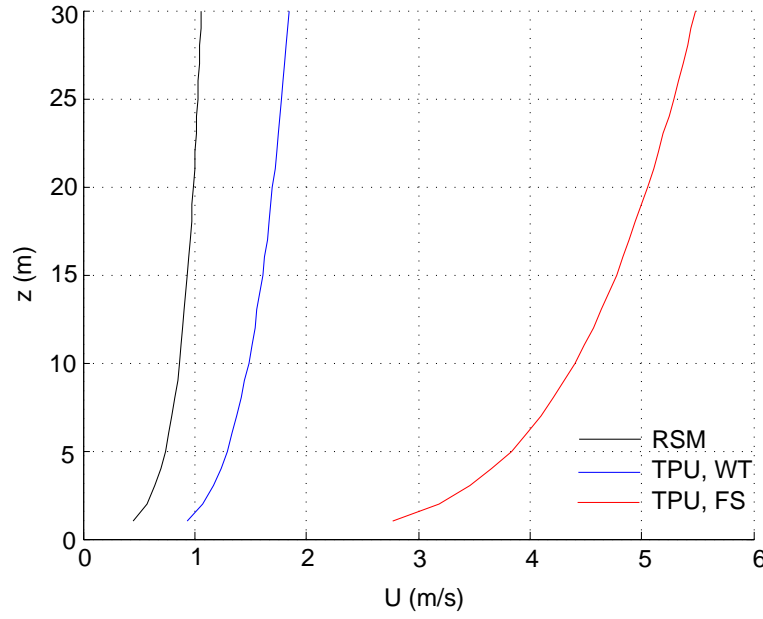


Figure a.21: Comparison of the approach flows used to determine the  $C_p$ .

ronment and rectangular shape, this model can be compared to central cubes of the cube array,

- an isolated cuboidal obstacle, whose full-scale dimensions are  $W = 16 \text{ m} \times L = 16 \text{ m} \times H = 4 \text{ m}$ , for which  $U_H = 6.16 \text{ m} \cdot \text{s}^{-1}$ . Because of its relative dimensions, this model can be compared to the total volume of the continuous patio array.

Wind pressure was measured using pressure taps with a basic spacing of 2 cm but some locations corresponding to low pressure gradient regions were not recorded because of instrumentation constraints. 10 samples were recorded for each case. To compute  $C_p$ , the following formulas were used:

- original wind pressure coefficient:

$$C_{p_{ori}}(i, t) = \frac{p(i, t)}{p_H} \quad (.77)$$

with:  $\begin{cases} C_{p_{ori}}(i, t) : \text{the original wind pressure coefficient at the tap } i \text{ and time } t, \\ p(i, t) : \text{the measured wind pressure at the tap } i \text{ and time } t, \\ p_H = 0.5 \times \rho \times U_H^2 : \text{the reference pressure corresponding to the dynamic pressure of the approach flow at the obstacle height.} \end{cases}$

- mean wind pressure coefficient:

$$\overline{C_{p_n}} = \frac{1}{10} \sum_{i=1}^{10} \overline{C_p(n)} \quad (.78)$$

- surface averaged wind pressure coefficient:

$$C_{p_{surf}}(j, t) = \frac{\sum_{i=1}^{N_j} (C_p(i, t) \times A_i)}{\sum_{i=1}^{N_j} A_i} \quad (.79)$$

with:  $\left\{ \begin{array}{l} C_{p_{surf}}(j, t) : \text{the averaged wind pressure coefficient on surface } j \text{ at time } t, \\ C_p(i, t) : \text{the wind pressure coefficient at point } i \text{ and time } t, \\ N_j : \text{the number of measured points on surface } j, \\ A_i : \text{the effective area of wind pressure at point } i. \end{array} \right.$

Then, the formula given above to compute the mean  $C_p$  applies.

According to the different wind-tunnel and simulation results, Tab. a.8 compares the surface averaged mean  $C_p$  for each case considered. In addition to the case 3, values for the corresponding isolated obstacle are given to distinguish the effects of the surroundings from that of the relative dimensions.  $C_p$  Differences between the front and the rear surfaces ( $\Delta C_{p_{front-rear}}$ ) and between the front and the side surfaces ( $\Delta C_{p_{front-side}}$ ) are precised as  $\Delta C_p$  is more important than the absolute  $C_p$  for ventilation and infiltration purposes.

Experimental data synthesized in Tab. a.8 are taken for a wind incidence of  $0^\circ$ , i.e. perpendicular to the front face, as in our simulations. Following pages give the mean pressure distribution on the different experimental cases considered as well as surface averaged mean  $C_p$ , RMS  $C_p$  and extreme  $C_p$  for the front and rear faces and a wind incidence from  $0^\circ$  to  $90^\circ$ . Despite used to extract the mean values given in Tab. a.8, diagrams for the side and top surfaces are not given. They are available in [TPU \(2003\)](#).

Case		Front face	Side faces	Rear face	Top face	$\Delta_{F-R}$	$\Delta_{F-S}$
Name	Dimensions						
Cube (CFD)	$10 \times 10 \times 10\text{m}^3$	+0.52	-0.54	-0.24	-0.63	0.76	1.02
Case 1 (WT isol)	$16 \times 16 \times 16\text{m}^3$	+0.64	-0.7	-0.32	-0.8	0.96	1.34
Patio (CFD)	$20 \times 20 \times 10\text{m}^3$	+0.4	-0.54	-0.25	-0.61	0.65	0.94
Case 2 (WT isol)	$16 \times 16 \times 8\text{m}^3$	+0.6	-0.5	-0.25	-0.60	0.85	1.08
Cube 3,2 (CFD)	$10 \times 10 \times 10\text{m}^3$	-0.23	-0.31	-0.30	-0.34	0.05	0.06
Case 3 (WT group)	$16 \times 24 \times 12\text{m}^3$	+0.25	-0.23	-0.19	-0.74	0.44	0.48
Case 3b (WT isol)	$16 \times 24 \times 12\text{m}^3$	+0.6	-0.47	-0.25	-0.53	0.85	1.07
Patio array (CFD)	$80 \times 80 \times 10\text{m}^3$	+0.24	-0.62	-0.56	-0.74	0.8	0.86
Case 4 (WT isol)	$16 \times 16 \times 4\text{m}^3$	+0.59	-0.39	-0.26	-0.49	0.86	0.98

Table a.8: Comparison between the numerical and experimental surface averaged  $C_p$  for the four case studies.



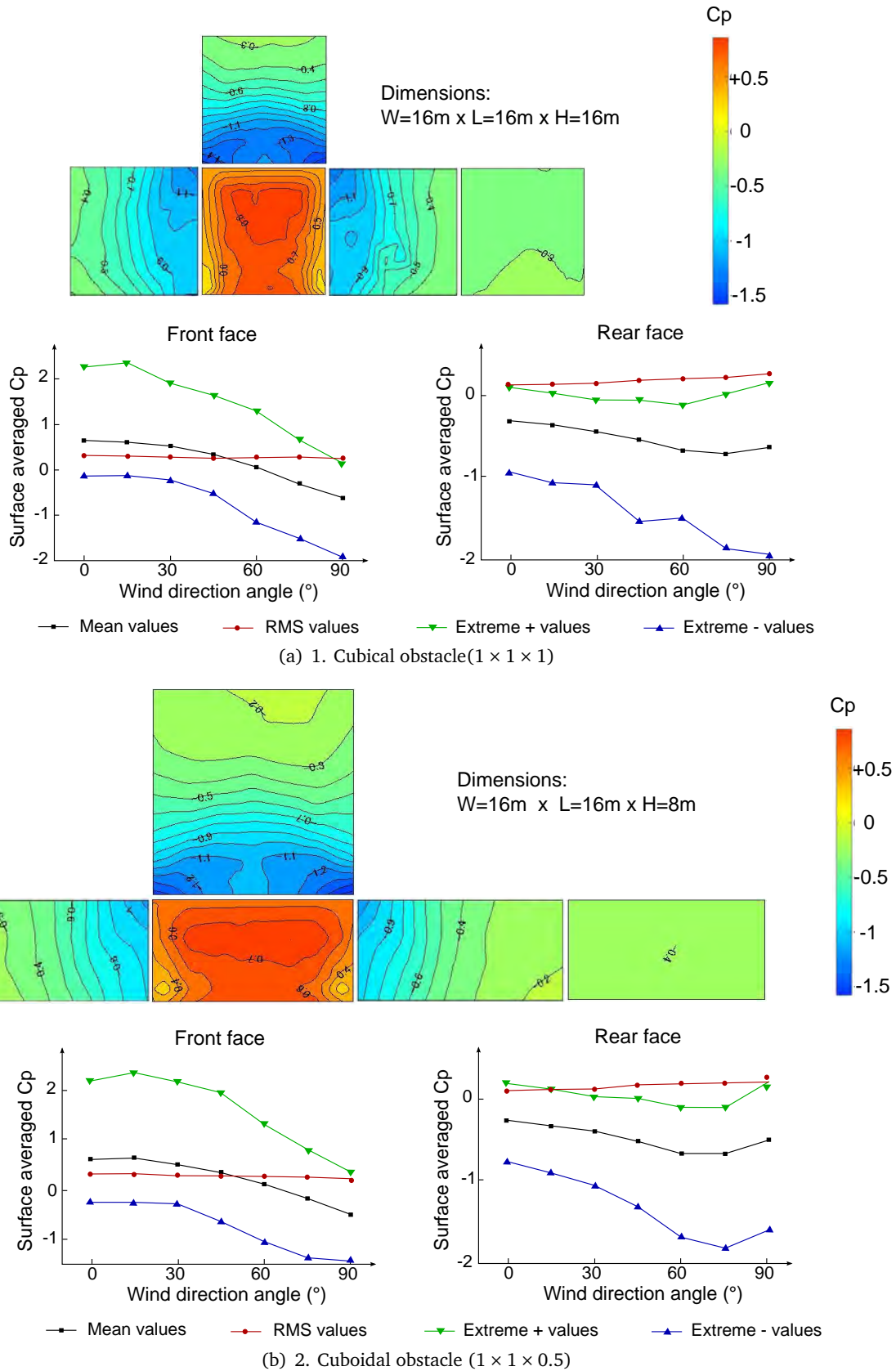
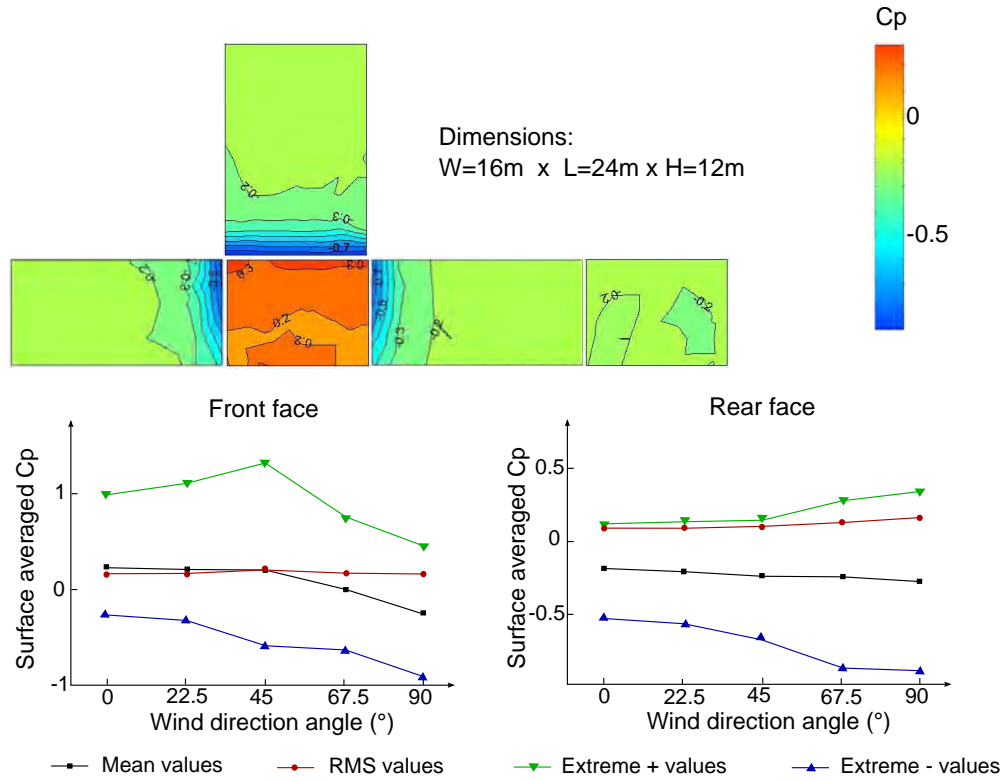
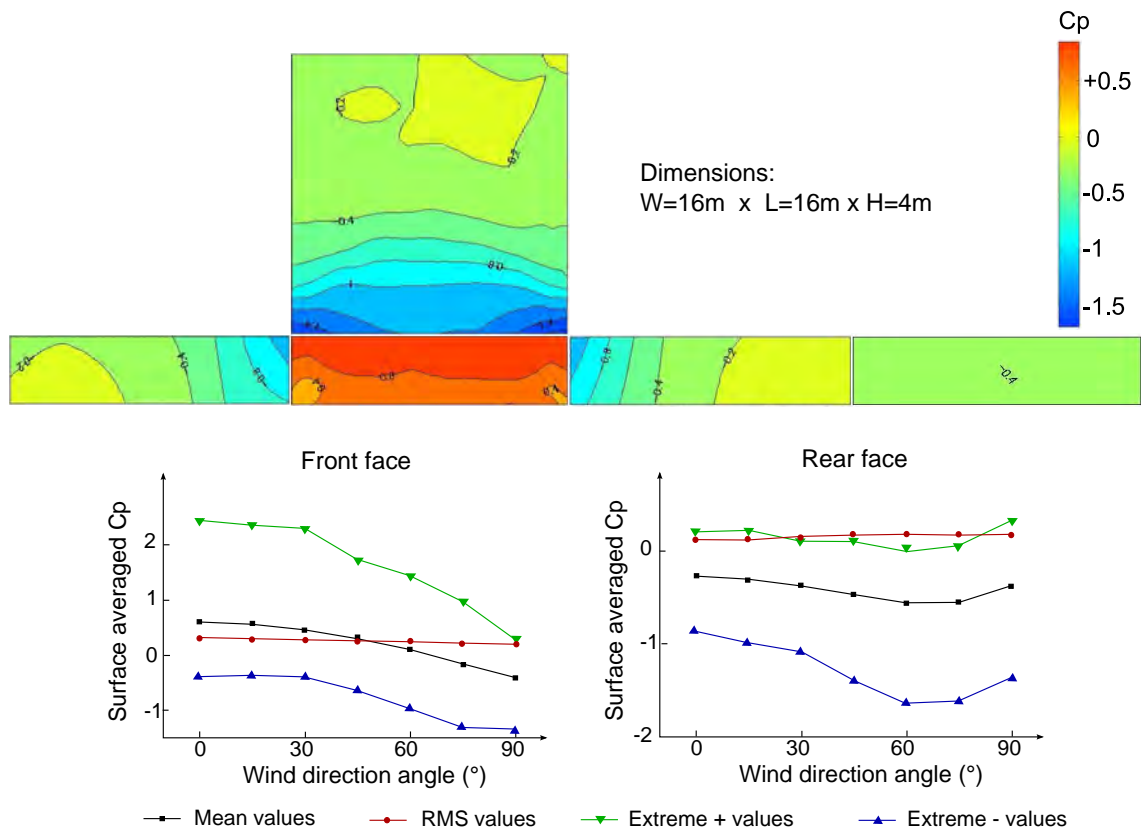


Figure a.22: Wind-tunnel based  $C_p$  distributions and surface averaged values for isolated flat-roofed buildings. (Adapted from (TPU, 2003))



(a) 3. Cuboidal obstacle ( $1 \times 2 \times 0.75$ ) of a regular array



(b) 4. Cuboidal obstacle ( $1 \times 1 \times 0.25$ )

Figure a.23: Wind-tunnel based  $C_p$  distributions and surface averaged values for an element of an array and an isolated flat-roofed buildings. (Adapted from (TPU, 2003))



## Appendices of Part 3

### Contents

<b>R</b>	<b>Comparison of <math>T_w</math> profiles around the small cube . . . . .</b>	<b>A. 99</b>
R.1	Comparison with data of <a href="#">Seeta Ratnam and Vengadesan (2008)</a> . . . . .	A. 99
R.2	Comparison with data of <a href="#">Meinders et al. (1999)</a> and <a href="#">Defraeye et al. (2010)</a> . . . . .	A. 100
<b>S</b>	<b>Optimization of <math>Pr_{t,w}</math> for the RSM . . . . .</b>	<b>A. 101</b>
<b>T</b>	<b>Applicability of the revised customized temperature wall-function for the RSM for high <math>z^*</math> . . . . .</b>	<b>A. 102</b>
T.1	Comparison of $h_{c,w}$ vertical profiles on the cube front and rear faces for $U_{10} = 0.5 \text{ m} \cdot \text{s}^{-1}$ . . . . .	A. 102
T.2	Comparison of $h_{c,w}$ vertical profiles on the cube front and rear faces for $U_{10} = 5 \text{ m} \cdot \text{s}^{-1}$ . . . . .	A. 103
<b>U</b>	<b>Distribution of <math>h_{c,w}</math> on the building surfaces . . . . .</b>	<b>A. 104</b>
U.1	Simulation results: $h_{c,w}$ for the cube and the patio . . . . .	A. 104
U.2	Simulation results: $h_{c,w}$ for the cube array and the continuous patio array . . . . .	A. 105
<b>V</b>	<b>Configurations studied to evaluate the energy needs . . . . .</b>	<b>A. 109</b>
V.1	Schemes of the configurations studied . . . . .	A. 109
V.2	Floor and envelope areas of addressed types . . . . .	A. 109
<b>W</b>	<b>Computation of <math>P_{int}</math> and estimation of <math>E_{inf}</math> . . . . .</b>	<b>A. 110</b>
W.1	Computation of $P_{int}$ for the isolated cube . . . . .	A. 110
W.1.1	Using the $Cp$ values provided by the Th-BCE rules . . . . .	A. 110
W.1.2	Using the simulated $Cp$ values . . . . .	A. 110
W.2	Estimation of $E_{inf}$ for the isolated air tight cube . . . . .	A. 111
W.2.1	According to the $Cp$ values provided by the Th-BCE rules . . . . .	A. 111
W.2.2	According to the simulated $Cp$ values . . . . .	A. 111
W.3	Computation of $P_{int}$ for the different case studies . . . . .	A. 112
<b>X</b>	<b>Comparison of the building energy needs due to air infiltration or heat transmission through the building envelope . . . . .</b>	<b>A. 114</b>
X.1	Infiltration: effects of $Cp$ . . . . .	A. 114
X.2	Thermal transmittivity: effects of $h_{c,w}$ . . . . .	A. 115
X.3	Effects of the built morphology on the building energy loads either due to infiltration or convective heat exchanges . . . . .	A. 116

<b>Y</b>	<b>Comparison of the total building energy needs due to infiltration and heat transmission through the building envelope . . . . .</b>	<b>A. 117</b>
Y.1	The cube . . . . .	A. 117
Y.2	The patio . . . . .	A. 118
Y.3	Effects of the built morphology on the building energy loads both due to infiltration and convective heat exchanges . . . . .	A. 119
Y.3.1	Relative contribution of infiltration and heat transmittivity through the building envelope on the heat exchanges . . . . .	A. 119
Y.3.2	Effects of urban morphology on the building energy loads due to infiltration and convection . . . . .	A. 122

---

## R Comparison of $T_w$ profiles around the small cube

### R.1 Comparison with data of Seeta Ratnam and Vengadesan (2008)

Seeta Ratnam and Vengadesan (2008) used the same experiment as reference but with a lower  $Re$  ( $Re = 2 \times 10^3$  instead of  $Re = 4.4 \times 10^3$ ). Results are only compared for the line A'-B'-C'-D' in terms of  $T_w$  as it seems that the graph reporting  $T_w$  profile for the line A-B-C-D has problems.

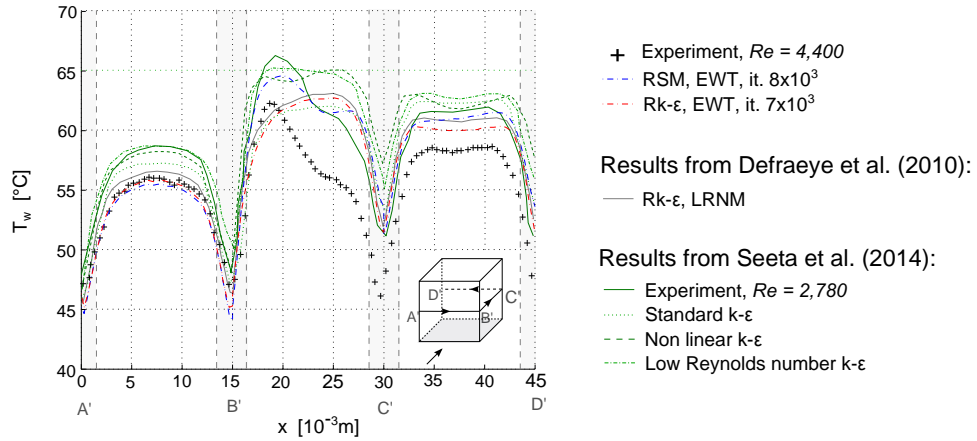


Figure a.24: Comparison of the simulated  $T_w$  profiles with predictions obtained using different  $k-\epsilon$  models by Seeta Ratnam and Vengadesan (2008).

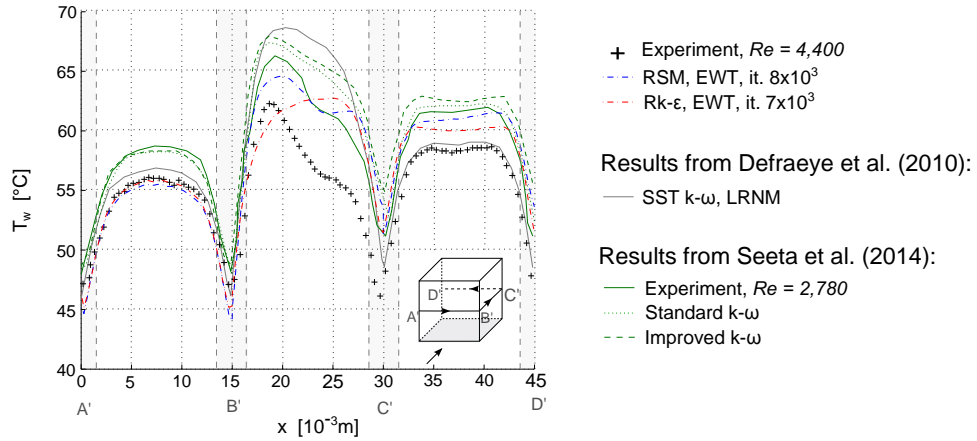


Figure a.25: Comparison of the simulated  $T_w$  profiles with predictions obtained using different  $k-\omega$  models by Seeta Ratnam and Vengadesan (2008).



## R.2 Comparison with data of Meinders et al. (1999) and Defraeye et al. (2010)

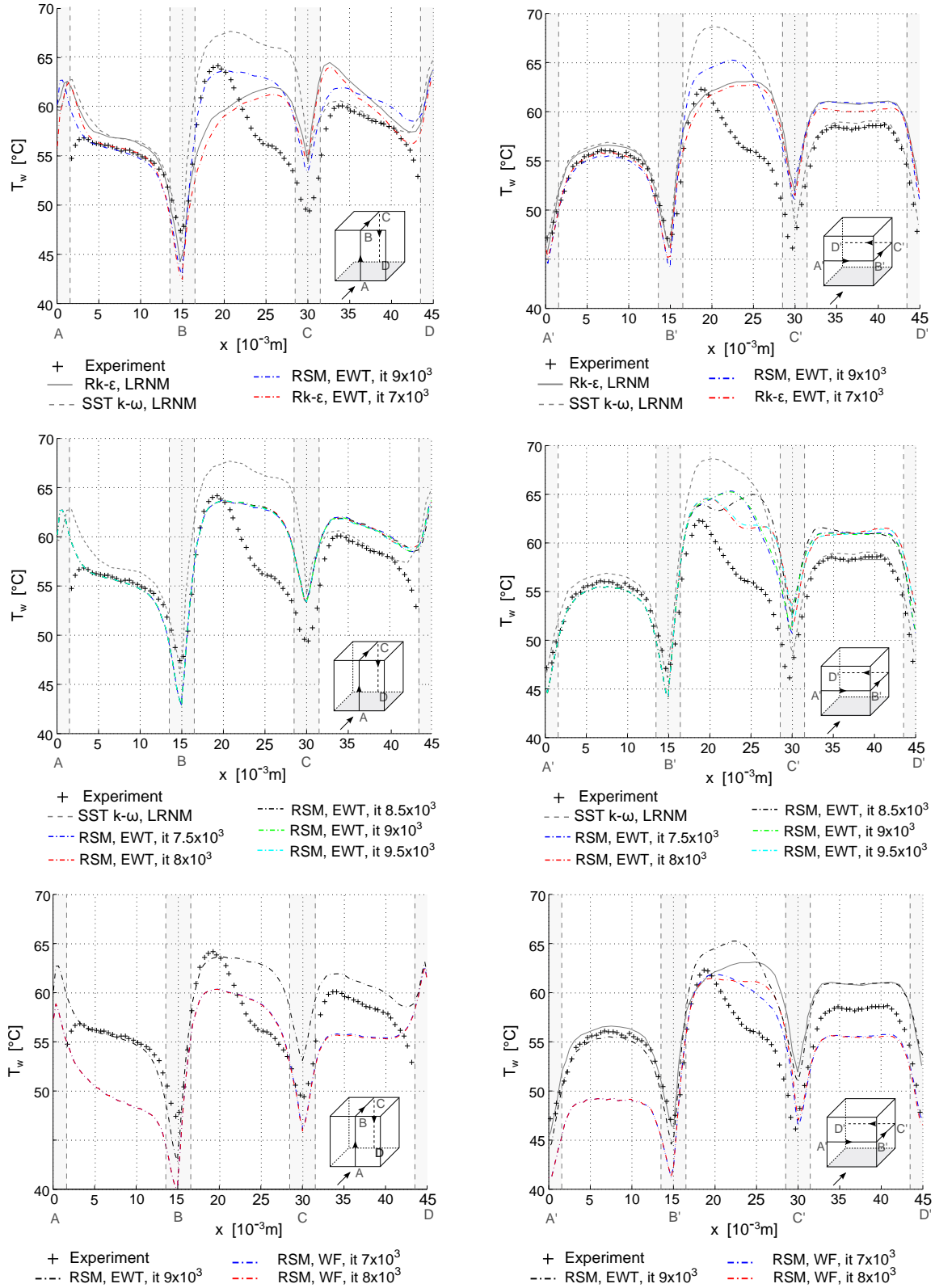
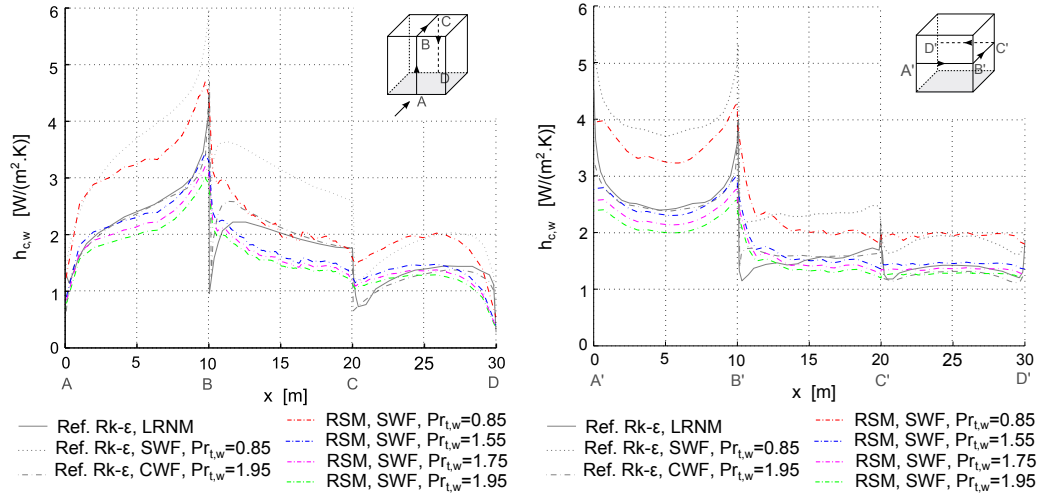
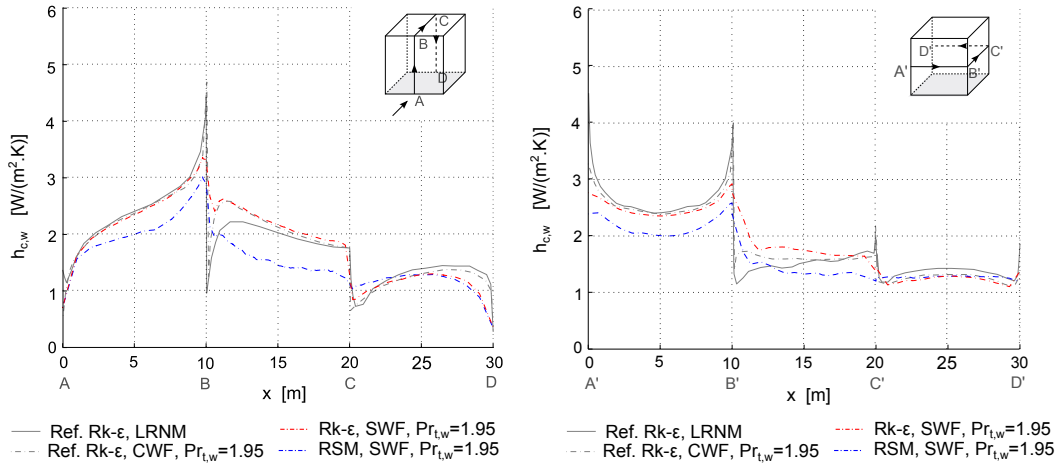
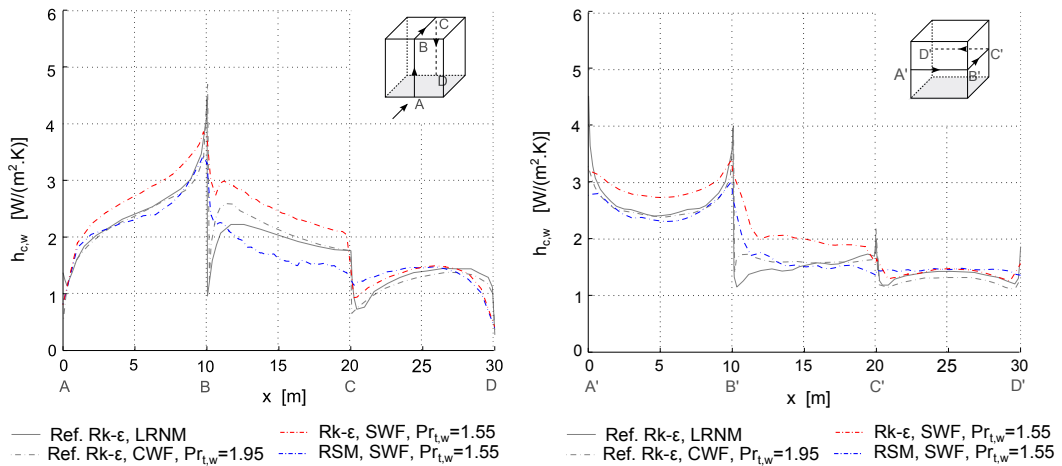


Figure a.26: Comparison of the numerical and experimental  $T_w$  profiles: influence of the turbulence model, convergence study for the RSM and effects of the near wall treatment.

## S Optimization of $Pr_{t,w}$ for the RSM

(a) Test of different  $Pr_{t,w}$  values.(b)  $h_{c,w}$  profiles obtained using either the RSM and or the Rk- $\epsilon$  together with  $Pr_{t,w} = 1.95$ .(c)  $h_{c,w}$  profiles obtained using either the RSM and or the Rk- $\epsilon$  together with  $Pr_{t,w} = 1.55$ .Figure a.27: Optimization of  $Pr_{t,w}$  for RSM-based temperature wall-function.

## T Applicability of the revised customized temperature wall-function for the RSM for high $z^*$

### T.1 Comparison of $h_{c,w}$ vertical profiles on the cube front and rear faces for $U_{10} = 0.5 \text{ m} \cdot \text{s}^{-1}$

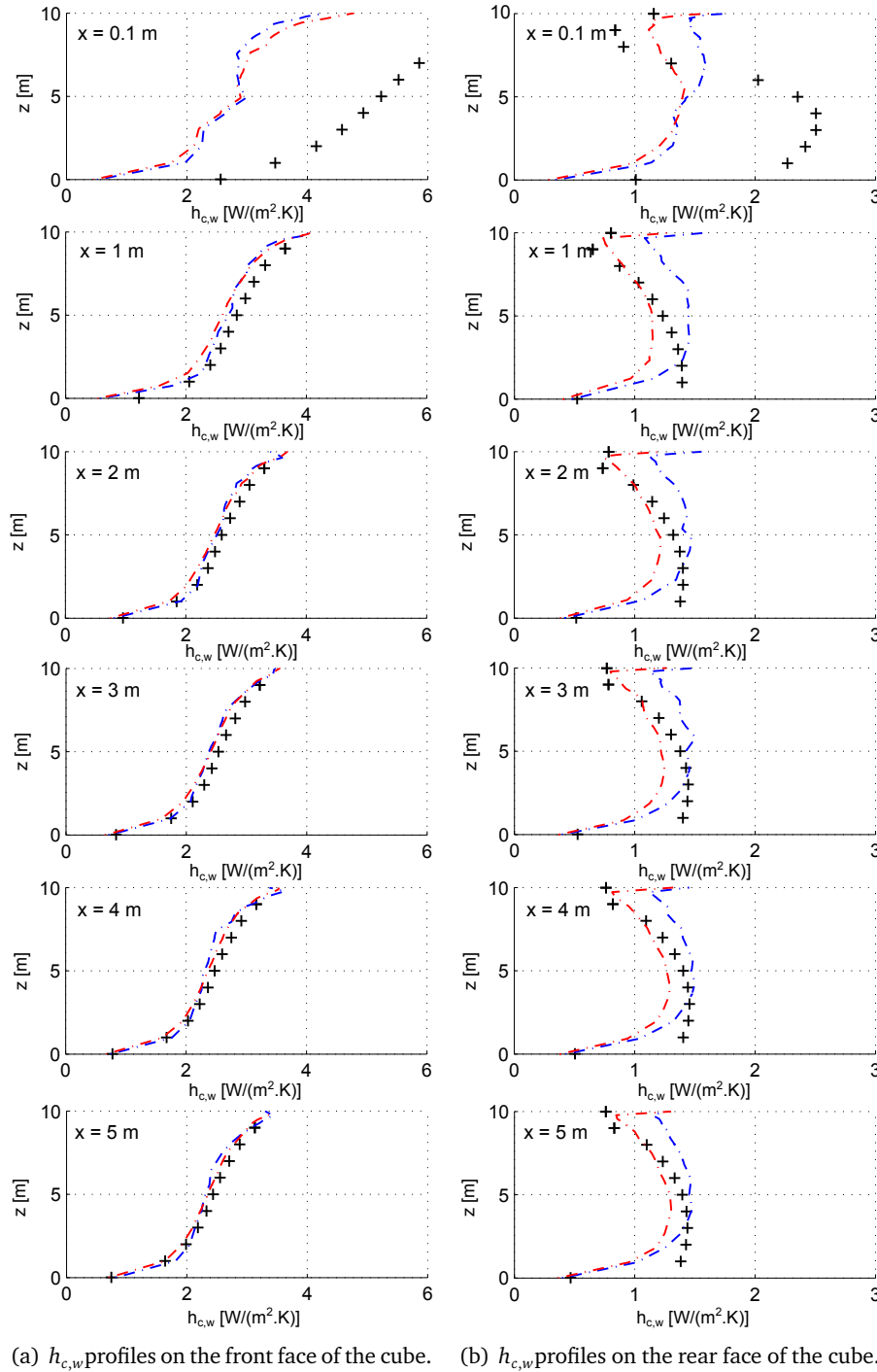


Figure a.28: Comparison of the  $h_{c,w}$  profiles for  $U_{10} = 0.5 \text{ m} \cdot \text{s}^{-1}$ .

**T.2 Comparison of  $h_{c,w}$  vertical profiles on the cube front and rear faces for  $U_{10} = 5 \text{ m} \cdot \text{s}^{-1}$**

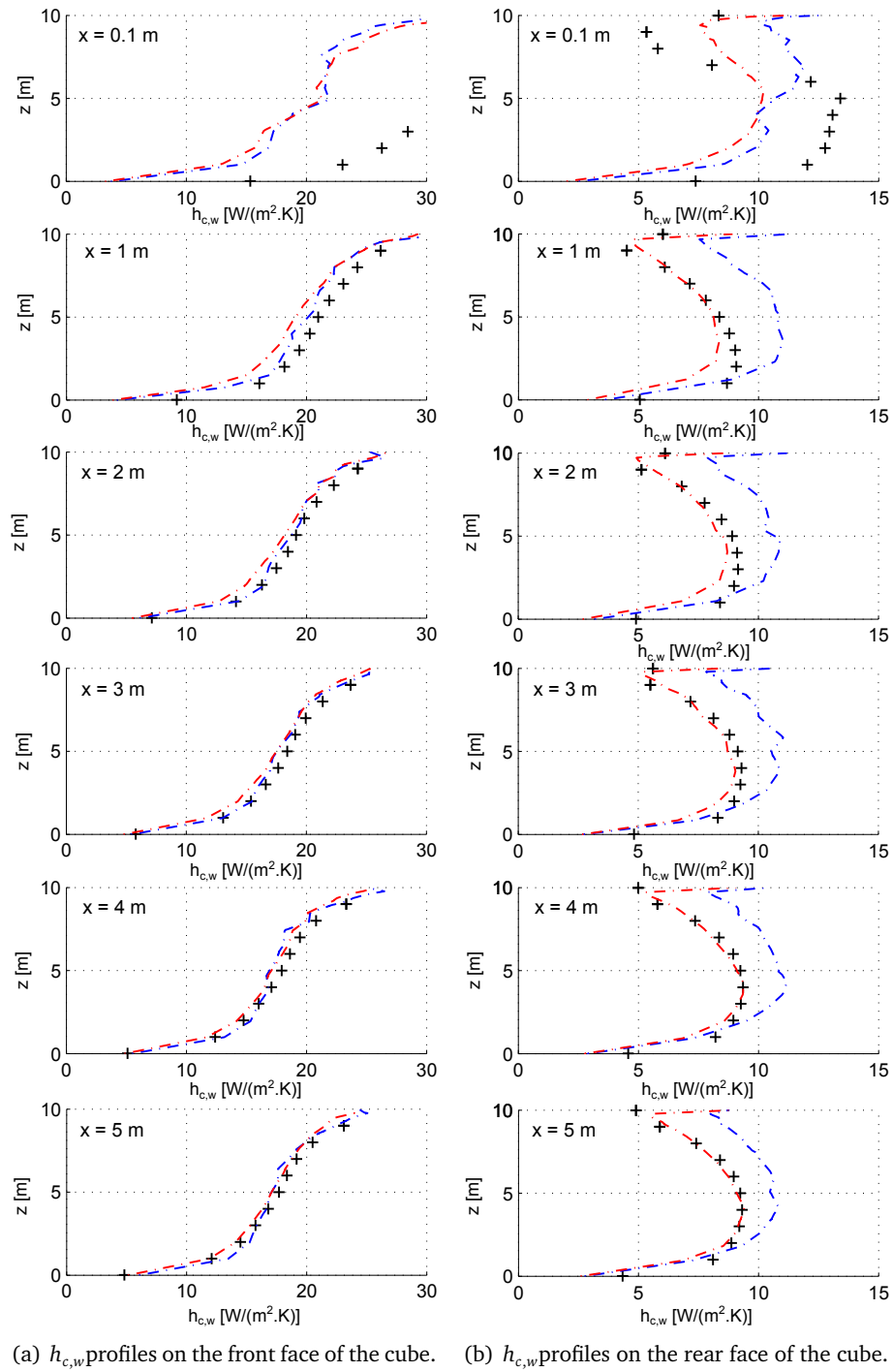


Figure a.29: Comparison of the  $h_{c,w}$  profiles for  $U_{10} = 5 \text{ m} \cdot \text{s}^{-1}$ .

## U Distribution of $h_{c,w}$ on the building surfaces

### U.1 Simulation results: $h_{c,w}$ for the cube and the patio

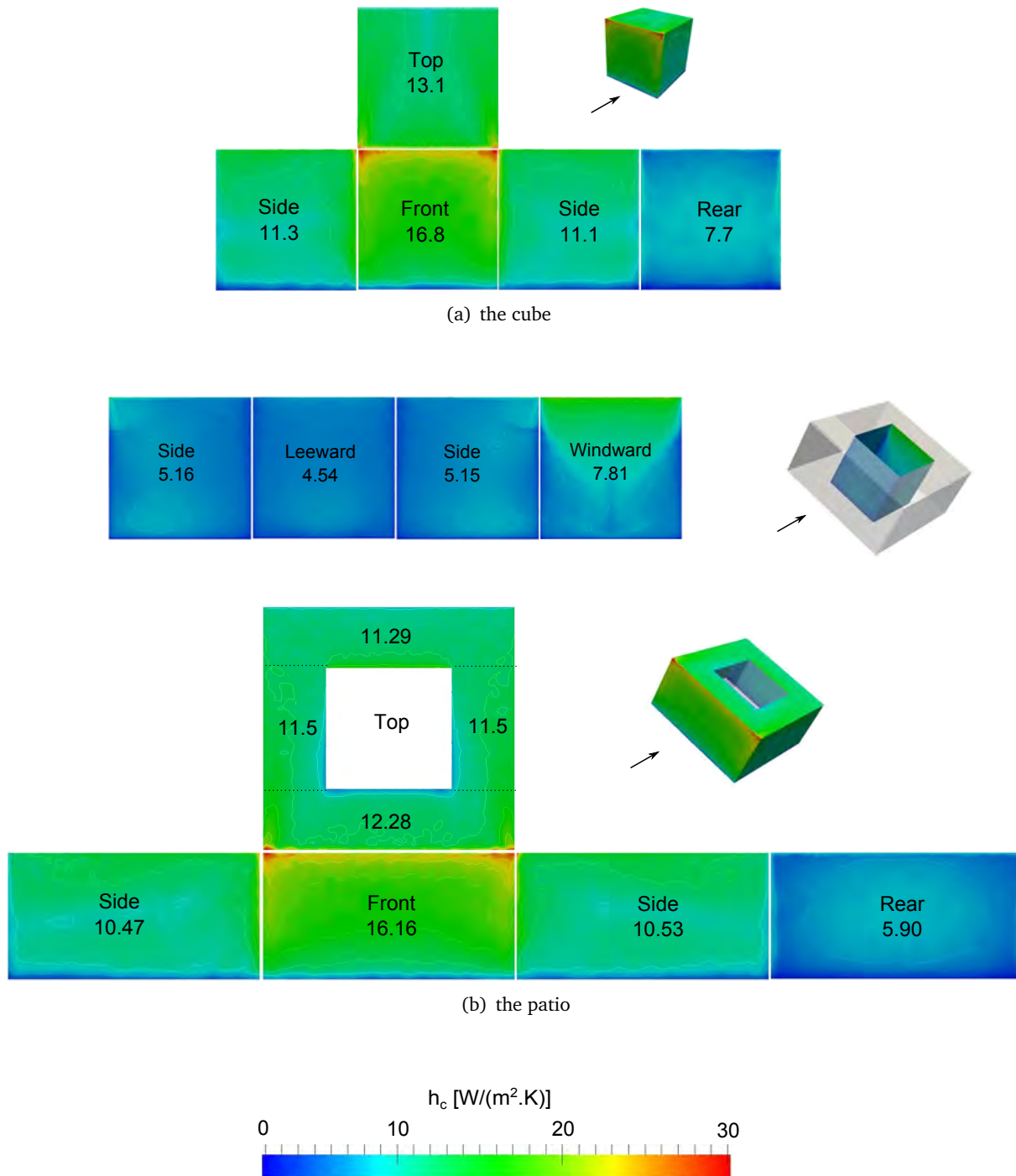


Figure a.30: Distribution of  $h_{c,w}$  for the cube and the patio.

## U.2 Simulation results: $h_{c,w}$ for the cube array and the continuous patio array

The cube array:

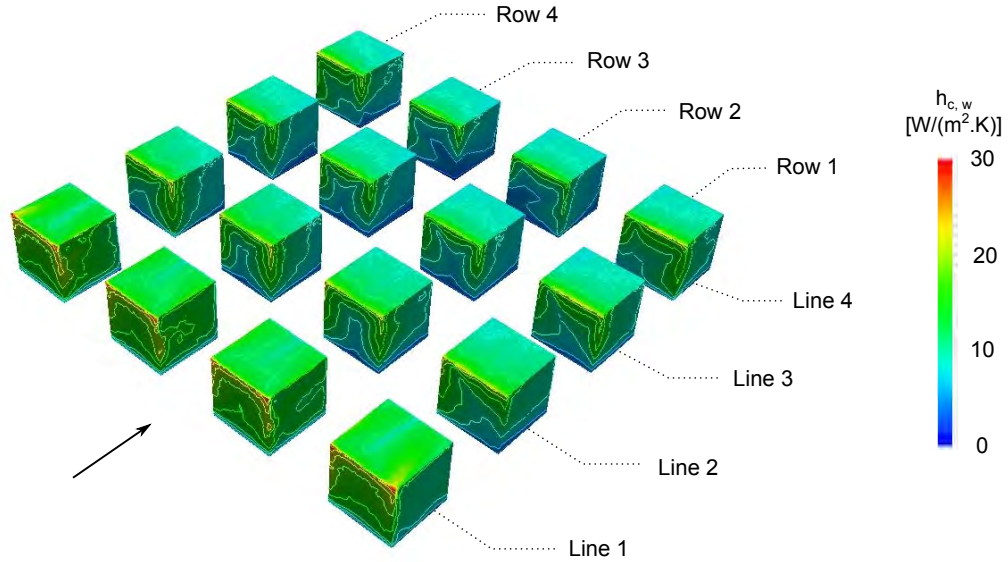


Figure a.31: Specification of the indexes for the cube array.

General		Front	Top	Rear	Side ext.		$\Delta_{F-R}$	Average
		16.49	11.19	4.63	9.81		11.85	9.30
Line	Row	Front	Top	Rear	Side int.	Side ext.	$\Delta_{F-R}$	Average
1	1	16.46	13.66	6.92	14.00	10.24	9.54	11.41
1	2	16.49	12.74	6.96	13.60	12.85	9.53	11.74
1	3	16.52	12.86	6.99	13.53	12.79	9.53	11.74
1	4	16.47	13.62	6.94	14.01	10.28	9.53	11.42
2	1	11.90	11.29	6.81	9.46	9.25	5.09	9.31
2	2	11.33	11.17	5.69	9.88	9.93	5.64	9.25
2	3	11.44	11.27	5.69	9.78	10.16	5.75	9.31
2	4	11.76	11.27	6.84	9.49	9.17	4.92	9.29
3	1	10.96	10.52	7.10	7.90	10.14	3.86	9.00
3	2	9.70	9.87	4.74	7.63	8.30	4.96	7.71
3	3	9.78	10.00	4.92	7.80	8.34	4.86	7.84
3	4	10.90	10.49	7.06	7.96	10.16	3.84	9.00
4	1	11.72	10.46	4.86	8.39	9.97	6.86	8.55
4	2	9.96	9.70	4.43	7.05	7.57	5.53	7.30
4	3	8.24	9.73	4.33	7.08	7.83	3.91	7.28
4	4	11.71	10.45	4.89	8.50	9.95	6.82	8.58

Table a.9: Surface averaged  $h_{c,w}$  for each face of the cube array.



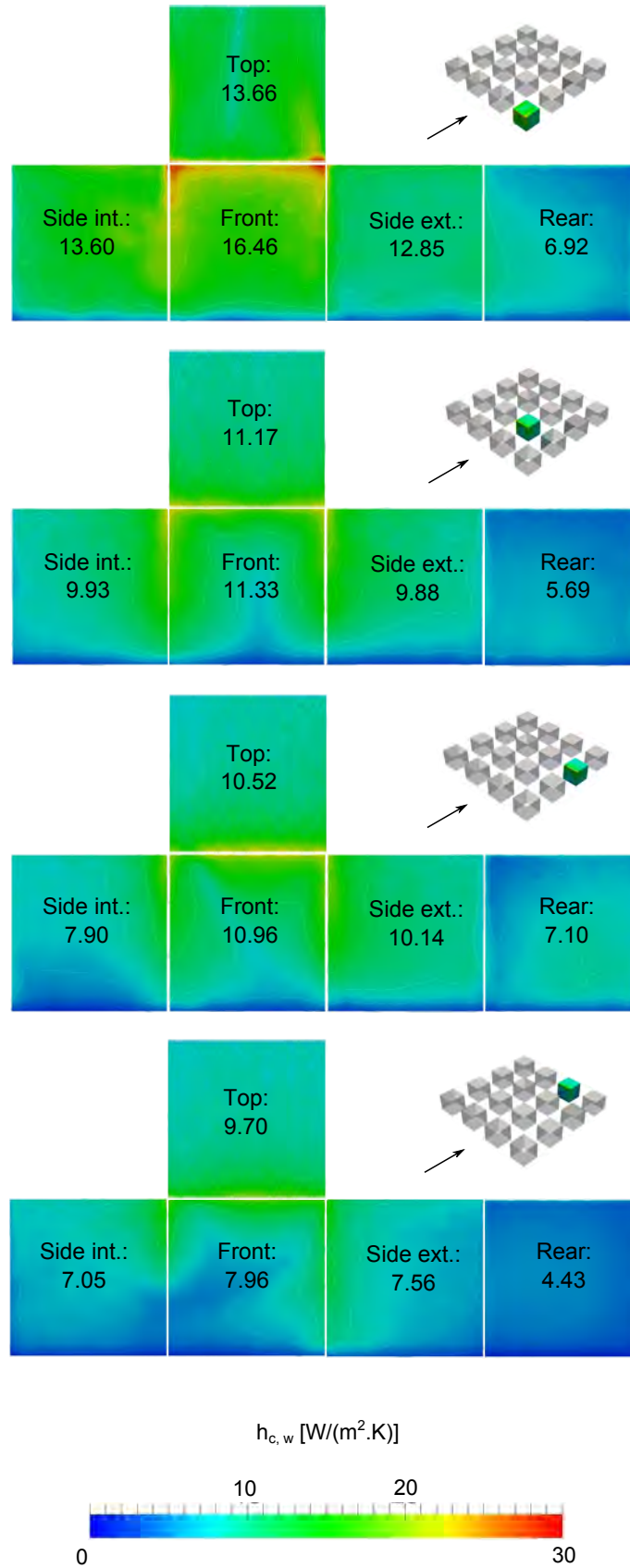


Figure a.32:  $h_{c,w}$  distribution and surface averaged  $h_{c,w}$  by faces for the cubes 1-1, 2-2, 3-1 and 4-2 of the cube array.

The continuous patio array:

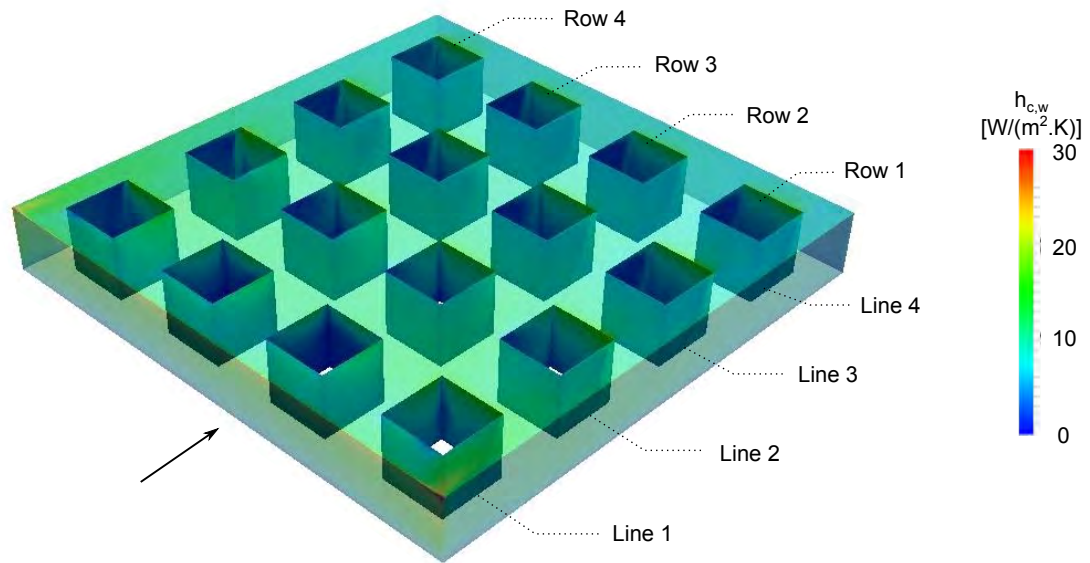


Figure a.33: Specification of the indexes for the continuous patio array.

General		Front	Rear	Sides	Top	$\Delta_{F-R}$	Average
		13.16	4.16	9.07	9.97	9.01	4.49
Line	Row	Leeward	Windward	Side int.	Side ext.	$\Delta_{W-L}$	Average
1	1	4.32	6.97	6.21	3.62	2.65	5.28
1	2	3.79	3.70	3.73	4.03	-0.08	3.81
1	3	3.73	3.77	3.75	4.02	-0.04	3.82
1	4	4.35	6.98	6.24	3.65	2.63	5.30
2	1	4.31	7.67	5.01	4.35	3.36	5.33
2	2	3.66	6.98	4.97	3.83	3.32	4.86
2	3	3.69	7.01	4.99	3.83	3.32	4.88
2	4	4.31	7.66	5.01	4.33	3.36	5.32
3	1	3.59	4.75	3.38	3.70	3.16	4.35
3	2	2.93	6.44	3.60	3.21	3.52	4.04
3	3	2.93	6.43	3.60	3.20	3.50	4.04
3	4	3.71	6.74	3.41	3.67	3.03	4.38
4	1	3.45	6.18	3.03	3.41	2.73	4.02
4	2	3.02	6.07	2.98	3.05	3.05	3.78
4	3	3.00	6.04	3.00	3.03	3.04	3.78
4	4	3.99	6.49	4.47	4.41	2.50	4.84

Table a.10: Surface averaged  $h_{c,w}$  for each face of the continuous patio array.

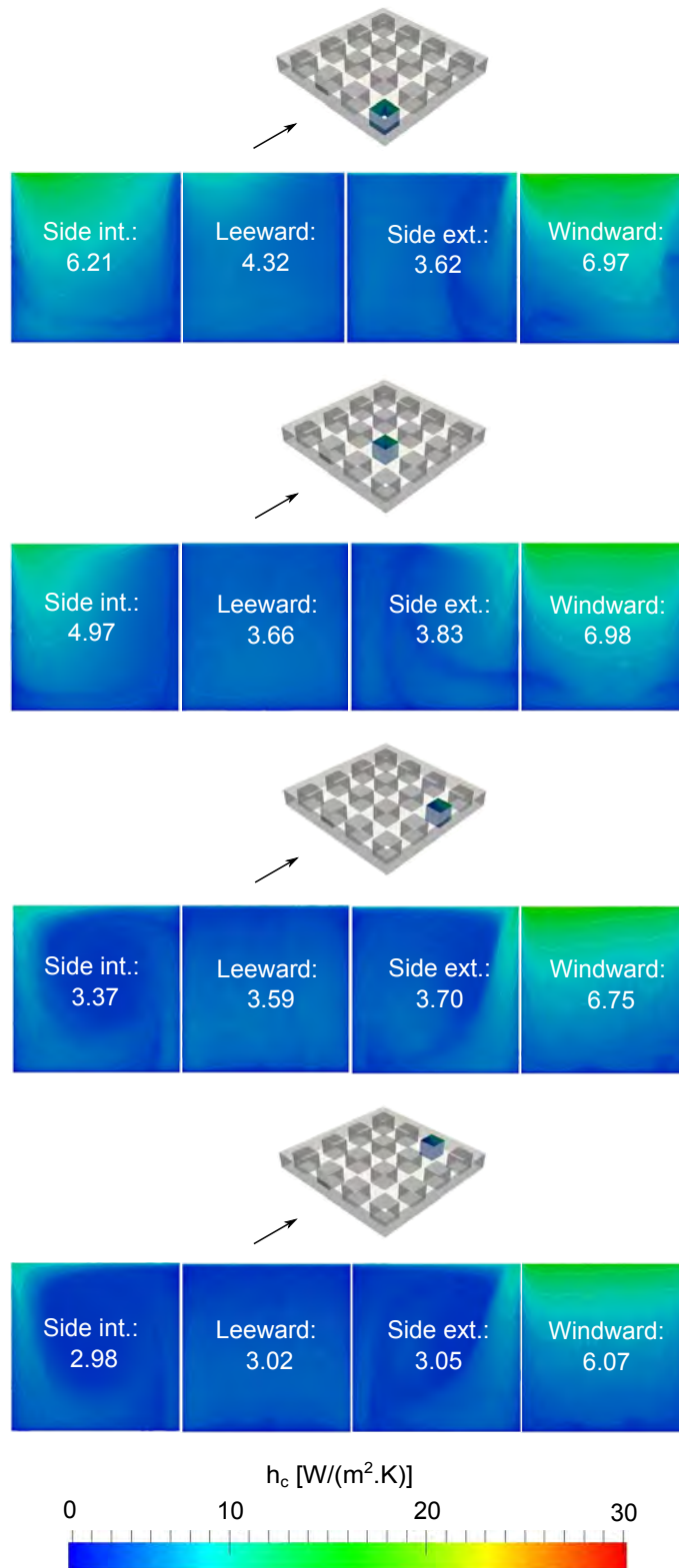


Figure a.34:  $h_{c,w}$  distribution and surface averaged mean  $h_{c,w}$  by faces for the patios 1-1, 2-2, 3-1 and 4-2 of the continuous patio array.

## V Configurations studied to evaluate the energy needs

### V.1 Schemes of the configurations studied

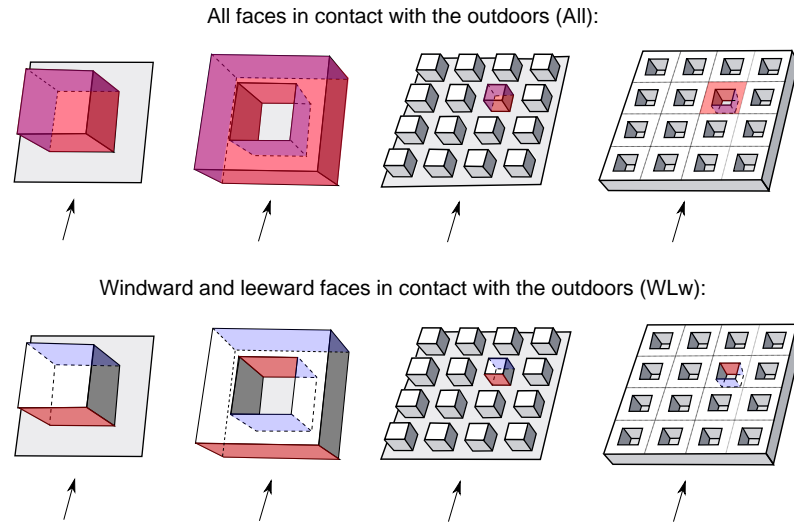


Figure a.35: Isolated and non-isolated cubes and patios, cases “All” and “Lw+Ww”.

### V.2 Floor and envelope areas of addressed types

	Cube		Patio	
Faces/outdoor	All	Ww+Lw	All	Ww+Lw
Isolated				
$A_{env.}$	$5 \times 10^2$	$2 \times 10^2$	$15 \times 10^2$	$6 \times 10^2$
$A_{floor}$	$3 \times 10^2$		$9 \times 10^2$	
Non-isolated				
$A_{env.}$	$5 \times 10^2$	$2 \times 10^2$	$7 \times 10^2$	$2 \times 10^2$
$A_{floor}$	$3 \times 10^2$		$9 \times 10^2$	

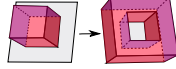
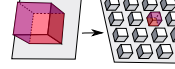
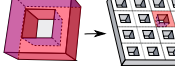
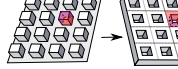
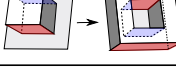
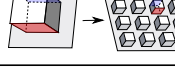
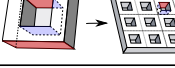
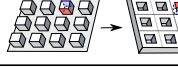
All				
$A_{env.}$	$\times 1$	$\times 1$	$\times 0.47$	$\times 1.4$
$A_{floor}$	$\times 3$	$\times 1$	$\times 1$	$\times 3$
Ww+Lw				
$A_{env.}$	$\times 3$	$\times 1$	$\times 0.33$	$\times 1$
$A_{floor}$	$\times 3$	$\times 1$	$\times 1$	$\times 3$

Table a.11: Comparison of the envelope and floor areas of the isolated and non-isolated cube and patio types.

## W Computation of $P_{int}$ and estimation of $E_{inf}$

### W.1 Computation of $P_{int}$ for the isolated cube

#### W.1.1 Using the $C_p$ values provided by the Th-BCE rules

The Th BCE rules give:

- $C_{p+} = +0.5$  on the (conventional) windward faces;
- $C_{p-} = -0.7$  on the leeward and top faces, considering an horizontal flat roof.

Considering:

- $P_{ext} - P_{int} > 0$  on the windward face of the cube;
- $P_{ext} - P_{int} < 0$  on the other faces of the cube;
- $A_i = 100 \text{ m}^2$  for all the five different faces of the cube;
- $K_{def, facade}^{zone} = K_{def, toit}^{zone} = K_{def}^{zone} = \frac{Q_{4Pa, surf}}{4^{2/3}}$ ;
- $\rho = 1.225 \text{ kg} \cdot \text{m}^{-3}$ ;
- and  $U_{10} = 4.3 \text{ m} \cdot \text{s}^{-1}$ ;

the mass balance of the cube zone is:

$$K_{def}^{zone} \left[ 2 \times |0.5 \times 0.5 \rho U_{10}^2 - P_{int}|^{2/3} - 3 \times |-0.7 \times 0.5 \rho U_{10}^2 - P_{int}|^{2/3} \right] = 0 \quad (.80)$$

This equation has two solutions:  $P_{int} = -24.164 \text{ Pa}$  and  $P_{int} = -3.140 \text{ Pa}$ . As  $P_{int} = -24.16$  is not possible because this value is lower to the external pressure that occurs over the different faces of the cube,  $P_{int} = -3.14 \text{ Pa}$

#### W.1.2 Using the simulated $C_p$ values

According to the simulation results:

- $C_{p_{front}} = +0.52$  on the front face of the cube;
- $C_{p_{side}} = -0.54$  on the side faces of the cube;
- $C_{p_{top}} = -0.63$  on the top face of the cube;
- $C_{p_{rear}} = -0.24$  on the rear face of the cube.

Still considering:

- $P_{ext} - P_{int} > 0$  on the front face of the cube;
- $P_{ext} - P_{int} < 0$  on the other faces of the cube;
- $A_i = 10 \text{ m}$  for all the five different faces of the cube;

- $K_{def, facade}^{zone} = K_{def, toit}^{zone} = K_{def}^{zone} = \frac{Q_{4Pa, surf}}{4^{2/3}};$
- $\rho = 1.225 \text{ kg} \cdot \text{m}^{-3};$
- and  $U_{10} = 4.3 \text{ m} \cdot \text{s}^{-1};$

the mass balance of the cube zone is:

$$K_{def}^{zone} [|0.52 \times 0.5 \rho U_{10}^2 - P_{int}|^{2/3} - 2 \times |-0.54 \times 0.5 \rho U_{10}^2 - P_{int}|^{2/3} - |-0.63 \times 0.5 \rho U_{10}^2 - P_{int}|^{2/3} - |-0.24 \times 0.5 \rho U_{10}^2 - P_{int}|^{2/3}] = 0 \quad (.81)$$

This equation has two solutions:  $P_{int} = -7.416$  and  $P_{int} = -5.370 \text{ Pa}$ . As  $P_{int} = -7.41$  is not possible because this value is lower to the external pressure that occurs over the different faces of the cube, it should be  $P_{int} = -5.36 \text{ Pa}$ . However, this pressure is lower than that occurring at the outer rear face of the cube. Therefore, the initial hypothesis is wrong, and  $P_{ext} - P_{int} > 0$  on the rear face of the cube. Accounting for this modification, the mass balance of the cube zone is:

$$K_{def}^{zone} [|0.52 \times 0.5 \rho U_{10}^2 - P_{int}|^{2/3} - 2 \times |-0.54 \times 0.5 \rho U_{10}^2 - P_{int}|^{2/3} - |-0.63 \times 0.5 \rho U_{10}^2 - P_{int}|^{2/3} + |-0.24 \times 0.5 \rho U_{10}^2 - P_{int}|^{2/3}] = 0 \quad (.82)$$

This equation has two solutions:  $P_{int} = -15.857$  and  $P_{int} = -3.857 \text{ Pa}$ . As  $P_{int} = -15.86$  is not possible because this value is lower to the external pressure that occurs over the different faces of the cube,  $P_{int} = -3.86 \text{ Pa}$ .

## W.2 Estimation of $E_{inf}$ for the isolated air tight cube

### W.2.1 According to the $C_p$ values provided by the Th-BCE rules

Air enters the building through the two windward faces of the building. As a consequence:

$$Q_{inf} = 2 \times 100 \times K_{def}^{zone} |5.66 - 3.14|^{2/3} = 0.056 \text{ m}^3 \cdot \text{s}^{-3} \quad (.83)$$

Considering  $C_{air} = 1.004 \times 10^3 \text{ J} \cdot \text{kg}^{-1} \cdot \text{K}^{-1}$  and  $\Delta T = 10^\circ \text{C}$ , the induced energy loads are:

$$E_{inf} = \rho \times C_{air} \times 0.056 \times 10 = 693.6 \text{ W} \quad (.84)$$

### W.2.2 According to the simulated $C_p$ values

Air enters the building through the front and rear faces of the building. As a consequence:

$$Q_{inf} = 100 \times K_{def}^{zone} |5.89 - 3.86|^{2/3} + 100 \times K_{def}^{zone} |-2.72 - 3.86|^{2/3} = 0.037 \text{ m}^3 \cdot \text{s}^{-3} \quad (.85)$$

Still considering  $C_{air} = 1.004 \times 10^3 \text{ J} \cdot \text{kg}^{-1} \cdot \text{K}^{-1}$  and  $\Delta T = 10^\circ \text{C}$ , the induced energy loads are:

$$E_{inf} = \rho \times C_{air} \times 0.037 \times 10 = 459.9 \text{ W} \quad (.86)$$



### W.3 Computation of $P_{int}$ for the different case studies

#### Isolated cube, case “All”

*According to the standard  $C_p$  values:*

Assuming that air enters the cube through the two windward faces of the building, the resolution of the mass balance gives:  $P_{int} = -24.164$  Pa or  $P_{int} = -3.139$  Pa.  $P_{int} = -24.164$  Pa is not realistic, as a consequence  $P_{int} = -3.139$  Pa.

*According to the simulated  $C_p$  values:*

Assuming that air enters the cube through the front face of the building, the resolution of the mass balance gives:  $P_{int} = -7.415$  Pa or  $P_{int} = -5.369$  Pa. Neither  $P_{int} = -7.415$  Pa nor  $P_{int} = -5.369$  Pa is a realistic value. Assuming that air enters the cube through the front and the rear faces of the building, the resolution of the mass balance gives:  $P_{int} = -15.857$  Pa or  $P_{int} = -3.857$  Pa.  $P_{int} = -15.857$  Pa is not realistic, as a consequence  $P_{int} = -3.857$  Pa.

#### Isolated cube, case “Lw+Ww”

*According to the standard  $C_p$  values:*

Assuming that air enters the cube through the front face of the building, the resolution of the mass balance gives:  $P_{int} = -1.135$  Pa, which is a realistic value.

*According to the simulated  $C_p$  values:*

Assuming that air enters the cube through the front face of the building, the resolution of the mass balance gives:  $P_{int} = 1.585$  Pa, which is a realistic value.

#### Non-isolated cube, case “All”

*According to the standard  $C_p$  values:*

Assuming that air enters the cube through the two windward faces of the building, the resolution of the mass balance gives:  $P_{int} = -16.646$  Pa or  $P_{int} = -2.904$  Pa.  $P_{int} = -16.646$  Pa is not realistic, as a consequence  $P_{int} = -2.904$  Pa.

*According to the simulated  $C_p$  values:*

Assuming that air enters the cube through the front face of the building, the resolution of the mass balance gives:  $P_{int} = -3.405$  Pa. Strictly speaking, this value is not realistic as  $P_{ext} = -3.4$  Pa on the side faces of the cube. However, assuming that the flow also enters the cube through the side faces of the cube yield completely unrealistic values. Therefore and accounting for the uncertainties due to rounds of, it is assumed that  $P_{int} = -3.405$  Pa.

#### Non-isolated cube, case “Lw+Ww”

*According to the standard  $C_p$  values:*

Assuming that air enters the cube through the front face of the building, the resolution of the mass balance gives:  $P_{int} = -1.415$  Pa, which is a realistic value.

*According to the simulated  $C_p$  values:*

Assuming that air enters the cube through the front face of the building, the resolution of the mass balance gives:  $P_{int} = -3.055$  Pa, which is a realistic value.

**Isolated patio, case “All”**

*According to the standard  $C_p$  values:*

Assuming that air enters the patio through the four windward faces of the building, the resolution of the mass balance gives:  $P_{int} = -21.938$  Pa or  $P_{int} = -3.134$  Pa.  $P_{int} = -21.938$  Pa is not realistic, as a consequence  $P_{int} = -3.134$  Pa.

*According to the simulated  $C_p$  values:*

Assuming that air enters the patio through the front face of the building, there is no solution to the mass balance. Assuming that air enters the patio through the front and the rear faces of the building, the resolution of the mass balance gives:  $P_{int} = -8.850$  Pa or  $P_{int} = -5.429$  Pa.  $P_{int} = -8.850$  Pa is not realistic, as a consequence  $P_{int} = -5.429$  Pa.

**Isolated patio, case “Lw+Ww”**

*According to the standard  $C_p$  values:*

Assuming that air enters the patio through the front face of the building, the resolution of the mass balance gives:  $P_{int} = -1.238$  Pa, which is a realistic value.

*According to the simulated  $C_p$  values:*

Assuming that air enters the patio through the front face of the building, the resolution of the mass balance gives:  $P_{int} = -10.462$  Pa or  $P_{int} = -2.259$  Pa.  $P_{int} = -10.462$  Pa is not realistic, as a consequence  $P_{int} = -2.259$  Pa.

**Non-isolated patio, case “All”**

*According to the standard  $C_p$  values:*

Assuming that air enters the patio through the two windward face of the court, the resolution of the mass balance gives:  $P_{int} = -9.472$  Pa or  $P_{int} = -4.468$  Pa.  $P_{int} = -9.472$  Pa is not realistic, as a consequence  $P_{int} = -4.468$  Pa.

*According to the simulated  $C_p$  values:*

Assuming that air enters the patio through the windward face of the court, there is no solution to the mass balance. Assuming that air enters the patio through the windward and the leeward faces of the patio as well as on through the roof, the resolution of the mass balance gives:  $P_{int} = -5.892$  Pa or  $P_{int} = -5.886$  Pa.  $P_{int} = -5.892$  Pa is not realistic, as a consequence  $P_{int} = -5.886$  Pa.

**Non-isolated patio, case “Lw+Ww”**

*According to the standard  $C_p$  values:*

Assuming that air enters the patio through the windward face of the court, the resolution of the mass balance gives:  $P_{int} = -1.415$  Pa, which is a realistic value.

*According to the simulated  $C_p$  values:*

Assuming that air enters the patio through the windward face of the court, the resolution of the mass balance gives:  $P_{int} = -5.775$  Pa, which is a realistic value.

## X Comparison of the building energy needs due to air infiltration or heat transmission through the building envelope

### X.1 Infiltration: effects of $C_p$

Faces in contact with outdoor		Isolated		Non-isolated	
		All	Ww+Lw	All	Ww+Lw
$P_{int}$	Th-BCE	-3.14	-1.14	-2.90	-1.42
	Simu.	-3.86	1.59	-3.41	-3.06
Deviation (%)		+23	-240	+17	116
$Q_{4Pa} : +$					
$Q_{inf}$	Th-BCE	0.06	0.02	0.04	0.02
	Simu.	0.04	0.02	0.01	0.00
$E_{inf}$	Th-BCE	693	291	521	213
	Simu.	460	215	70	48
$Q_{4Pa} : -$					
$Q_{inf}$	Th-BCE	0.28	0.12	0.21	0.09
	Simu.	0.19	0.09	0.03	0.02
$E_{inf}$	Th-BCE	3468	1460	2606	1067
	Simu.	2299	1076	351	239
Deviation (%)		-34	-26	-87	-78

a) The cube

Faces in contact with outdoor		Isolated		Non isolated	
		All	Ww+Lw	All	Ww+Lw
$P_{int}$	Th-BCE	-3.13	-1.24	-4.46	-1.42
	Simu.	-5.43	-2.26	-5.89	-5.78
Deviation (%)		73	82	32	308
$Q_{4Pa} : +$					
$Q_{inf}$	Th-BCE	0.16	0.06	0.05	0.02
	Simu.	0.09	0.02	0.00	0.00
$E_{inf}$	Th-BCE	1922	797	612	213
	Simu.	1061	292	38	19
$Q_{4Pa} : -$					
$Q_{inf}$	Th-BCE	0.78	0.32	0.25	0.09
	Simu.	0.43	0.12	0.02	0.01
$E_{inf}$	Th-BCE	9608	3985	3061	1066
	Simu.	5303	1458	190	95
Deviation (%)		-45	-63	-93	-91

b) The patio

Table a.12: Comparison of  $P_{int}$  [Pa],  $Q_{inf}$  [ $\text{m}^3 \cdot \text{s}^{-1}$ ] and  $E_{inf}$  [W] for patios that are located in different urban configurations.

## X.2 Thermal transmittivity: effects of $h_{c,w}$

Faces in contact with outdoor		Isolated		Non-isolated	
		All	Ww+Lw	All	Ww+Lw
Insul. : +					
$U_{env}$	Th-U	0.36	0.36	0.36	0.36
	Simu.	0.36	0.36	0.36	0.36
$E_{conv}$	Th-U	1815	725	1815	725
	Simu.	1801	718	1789	713
Deviation (%)		-0.8	-0.9	-1.5	-1.7
Insul. : -					
$U_{env}$	Th-U	3.94	3.85	3.94	3.85
	Simu.	3.63	3.53	3.41	3.27
$E_{conv}$	Th-U	19706	7693	19706	7693
	Simu.	18154	7069	17036	6541
Deviation (%)		-7.9	-8.1	-15.6	-15.0

a) The cube

Faces in contact with outdoor		Isolated		Non-isolated	
		All	Ww+Lw	All	Ww+Lw
Insul. : +					
$U_{env}$	Th-U	0.36	0.36	0.36	0.36
	Simu.	0.36	0.36	0.36	0.35
$E_{conv}$	Th-U	5446	2174	2548	725
	Simu.	5379	2144	2498	707
Deviation (%)		-1.2	-1.4	-1.9	-2.4
Insul. : -					
$U_{env}$	Th-U	3.94	3.85	4.05	3.85
	Simu.	3.49	3.37	3.35	3.06
$E_{conv}$	Th-U	59119	23079	28346	7693
	Simu.	52331	20238	23474	6127
Deviation (%)		-11.5	-12.3	-17.2	-20.4

b) The patio

Table a.13: Comparison of the wall thermal transmittivity ( $U_{env} [W \cdot m^{-2} \cdot K^{-1}]$ ) and the related energy needs ( $E_{conv,tot} [W]$ ) for insulated or a non-insulated buildings (cube / patio) located different urban configurations (isolated / in a group of buildings).

### X.3 Effects of the built morphology on the building energy loads either due to infiltration or convective heat exchanges

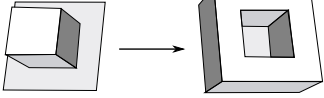
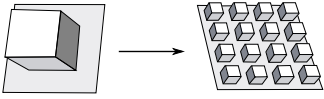
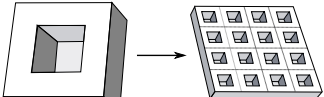
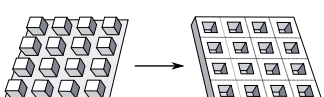
Faces in contact with outdoor			$Q_{4Pa} : +$		$Q_{4Pa} : -$	
			All	Ww+Lw	All	Ww+Lw
	Th-BCE	abs.	1228	505	6140	2526
		rel. (%)	177	173	177	173
	Simu.	abs.	601	76	3004	382
		rel. (%)	131	36	131	36
	Th-BCE	abs.	-172	-79	-862	-393
		rel. (%)	-25	-27	-25	-27
	Simu.	abs.	-390	-167	-1949	-837
		rel. (%)	-85	-78	-85	-78
	Th-BCE	abs.	-1309	-584	-6547	-2919
		rel. (%)	-68	-73	-68	-73
	Simu.	abs.	-1023	-273	-5113	-1364
		rel. (%)	-96	-94	-96	-94
	Th-BCE	abs.	91	0	454	0
		rel. (%)	17	0	17	0
	Simu.	abs.	-32	-29	-161	-144
		rel. (%)	-46	-60	-46	-60

Table a.14: Comparison between  $E_{inf,tot}$  [W] different urban configurations: effects of the building topology and urban morphology.

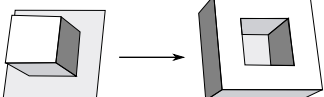
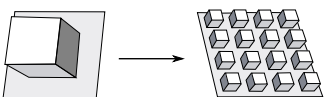
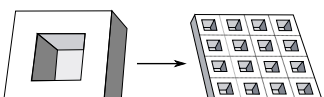
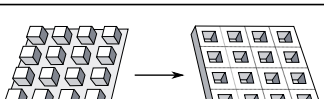
Faces in contact with outdoor			Insul. : +		Insul. : -	
			All	Ww+Lw	All	Ww+Lw
	Th-U	abs.	3631	1449	39412	15386
		rel. (%)	200	200	20	20
	Simu.	abs.	3578	1426	34177	13169
		rel. (%)	199	198	188	186
	Th-U	abs.	0	0	0	0
		rel. (%)	0	0	0	0
	Simu.	abs.	-12	-6	-1118	-529
		rel. (%)	-1	-1	-6	-7
	Th-U	abs.	-2899	-1449	-30772	-15386
		rel. (%)	-53	-67	-52	-67
	Simu.	abs.	-2881	-1437	-28857	-14112
		rel. (%)	-54	-67	-55	-70
	Th-U	abs.	732	0	8640	0
		rel. (%)	40	0	44	0
	Simu.	abs.	709	-5	6438	-414
		rel. (%)	40	-1	38	-6

Table a.15: Comparison between  $E_{conv,tot}$  [W] different urban configurations: effects of the building topology and urban morphology.

## Y Comparison of the total building energy needs due to infiltration and heat transmission through the building envelope

### Y.1 The cube

		Isolated building			Non-isolated building		
Insul.	$Q_{4Pa}$	$E_{inf}$	$E_{conv}$	$E_{i+c}$	$E_{inf}$	$E_{conv}$	$E_{i+c}$
All faces in contact with outdoors							
+	+	693.6	1815.4	2509.0	521.3	1815.4	2336.7
+	—	3468.0	1815.4	5283.4	2606.5	1815.4	4421.9
—	+	693.6	19706.2	20399.8	521.3	19706.2	20227.5
—	—	3468.0	19706.2	23174.2	2606.5	19706.2	22312.6
Windward and leeward faces in contact with outdoors							
+	+	291.9	724.6	1016.6	213.3	724.6	938.0
+	—	1459.5	724.6	2184.2	1066.6	724.6	1791.2
—	+	291.9	7693.1	7985.0	213.3	7693.1	7906.4
—	—	1459.5	7693.1	9152.6	1066.6	7693.1	8759.6

#### a) Regulatory values

		Isolated building			Non-isolated building		
Insul.	$Q_{4Pa}$	$E_{inf}$	$E_{conv}$	$E_{i+c}$	$E_{inf}$	$E_{conv}$	$E_{i+c}$
All faces in contact with outdoors							
+	+	459.9	1800.9	2260.7	70.1	1789.0	1859.1
+	—	2299.3	1800.9	4100.2	350.7	1789.0	2139.7
—	+	459.9	18154.6	18614.4	70.1	17036.2	17106.3
—	—	2299.3	18154.6	20453.9	350.7	17036.2	17386.8
Windward and leeward faces in contact with outdoors							
+	+	215.2	718.5	9323.7	47.8	712.6	760.4
+	—	1076.2	718.5	1794.7	238.9	712.6	951.5
—	+	215.2	7069.2	7284.5	47.8	6540.5	6588.3
—	—	1076.2	7069.2	8145.4	238.9	6540.5	6779.4

#### b) Simulated values

Table a.16: Comparison of  $E_{inf,tot}$ ,  $E_{conv,tot}$  and  $E_{i+c,tot}$  for an isolated and a non-isolated cubes, which present high or low levels of insulation and air tightness.

Insul. +: the building carries a  $1.25 \times 10^{-2}$  m layer of insulation material;

Insul. —: the building is not insulated,

$Q_{4Pa}$  +: the air permeability of the building envelope respects the RT 2012 requirements;

$Q_{4Pa}$  —: the air permeability of the envelope is five times higher than required by the RT 2012.

$E_{inf}$ : energy needs due to infiltration through walls,

$E_{conv}$ : energy needs due to heat losses through walls,

$E_{tot} = E_{inf} + E_{conv}$ : total energy needs.



## Y.2 The patio

		Isolated building			Non-isolated building		
Insul.	$Q_{4Pa}$	$E_{inf}$	$E_{conv}$	$E_{i+c}$	$E_{inf}$	$E_{conv}$	$E_{i+c}$
All faces in contact with outdoors							
+	+	1921.7	5446.2	7367.8	612.2	2547.6	3159.8
+	—	9608.3	5446.2	15054.5	3060.9	2547.6	5608.5
—	+	1921.7	59118.5	61040.2	612.2	28346.2	28958. 4
—	—	9608.3	59118.5	68726.8	3060.9	28346.2	31407.1
Windward and leeward faces in contact with outdoors							
+	+	797.1	2173.9	29871.0	213.3	724.6	938.0
+	—	3985.4	2173.9	6159.3	1066.6	724.6	1791.2
—	+	797.1	23079.2	23876.3	213.3	7693.1	7906.4
—	—	3985.4	23079.2	27064.6	1066.6	7693.1	8759.6

### a) Regulatory values

		Isolated building			Non-isolated building		
Insul.	$Q_{4Pa}$	$E_{inf}$	$E_{conv}$	$E_{i+c}$	$E_{inf}$	$E_{conv}$	$E_{i+c}$
All faces in contact with outdoors							
+	+	1060.6	5379.1	6439.37	38.0	2497.9	2535.9
+	—	5303.0	5379.1	10682.1	189.9	2497.9	2687.8
—	+	1060.6	52331.4	53392.0	38.0	23474.5	23512.5
—	—	5303.0	52331.4	57634.4	189.9	23474.5	23664.3
Windward and leeward faces in contact with outdoors							
+	+	291.7	2144.4	2436.1	18.95	707.4	726.3
+	—	1458.3	2144.4	3602.7	94.75	707.4	802.1
—	+	291.7	20238.6	20529.9	18.95	6126.5	6145.5
—	—	1458.3	20238.6	21696.6	94.75	6126.5	6221.3

### b) Simulated values

Table a.17: Comparison of  $E_{inf,tot}$ ,  $E_{conv,tot}$  and  $E_{i+c,tot}$  for an isolated and a non-isolated patios, which present high or low levels of insulation and air tightness.

Insul. +: the building carries a  $1.25 \times 10^{-2}$  m layer of insulation material;

Insul. —: the building is not insulated,

$Q_{4Pa}+$ : the air permeability of the building envelope respects the RT 2012 requirements;

$Q_{4Pa}-$ : the air permeability of the envelope is five times higher than required by the RT 2012.

$E_{inf}$ : energy needs due to infiltration through walls,

$E_{conv}$ : energy needs due to heat losses through walls,

$E_{tot} = E_{inf} + E_{conv}$ : total energy needs.

### Y.3 Effects of the built morphology on the building energy loads both due to infiltration and convective heat exchanges

#### Y.3.1 Relative contribution of infiltration and heat transmittivity through the building envelope on the heat exchanges

		Isolated building			Non-isolated building		
Insul.	$Q_{4Pa}$	$E_{reg}$	$E_{sim}$	Dev (%)	$E_{reg}$	$E_{sim}$	Dev (%)
All faces in contact with outdoors							
+	+	2509.0	2260.7	−9.9	2336.7	1859.1	−20.4
+	−	5283.4	4100.2	−22.4	4421.9	2139.7	−51.6
−	+	203399.8	18614.4	−8.5	20227.5	17106.3	−15.4
−	−	23174.2	20453.9	.11.73	22312.6	17386.8	−22.1
Windward and leeward faces in contact with outdoors							
+	+	1016.6	933.7	−8.2	938.0	760.4	−18.9
+	−	2184.2	1794.7	−17.8	17891.2	951.5	−46.9
−	+	7985.0	7284.5	−8.8	7906.4	6588.3	−16.7
−	−	9152.6	8145.5	−11.0	8759.6	6779.4	−22.6

a) The cube

		Isolated building			Non-isolated building		
Insul.	$Q_{4Pa}$	$E_{reg}$	$E_{sim}$	Dev (%)	$E_{reg}$	$E_{sim}$	Dev (%)
All faces in contact with outdoors							
+	+	7367.8	6439.7	−12.6	3159.8	2535.9	−19.7
+	−	15054.5	10682.1	−29.0	5608.5	2687.8	−52.1
−	+	61040.1	53392.0	−12.5	28958.4	23512.4	−18.8
−	−	68726.8	57634.4	−16.1	31407.1	23664.3	−24.7
Windward and leeward faces in contact with outdoors							
+	+	2971.0	2436.1	−18.0	938.0	726.3	−22.6
+	−	6159.3	3602.7	−41.5	1971.2	802.1	−55.2
−	+	23876.3	20529.9	−14.0	7906.4	6145.5	−22.3
−	−	27064.6	21696.6	−19.8	8759.6	6221.3	−29.0

b) The patio

Table a.18: Comparison between the  $E_{tot}$  [W] estimated using the standard or simulated values of  $C_p$  and  $h_{c,w}$  in cases of an isolated or a non-isolated building that is insulated and air-tight or not.

Insul. +: the building carries a  $1.25 \times 10^{-2}$  m layer of insulation material;

Insul. −: the building is not insulated,

$Q_{4Pa}+$ : the air permeability of the building envelope respects the RT 2012 requirements;

$Q_{4Pa}-$ : the air permeability of the envelope is five times higher than required by the RT 2012.

$E_{reg}$ : energy needs computed using the regulatory values of  $C_p$  and  $h_{c,w}$ ,

$E_{sim}$ : energy needs computed using the simulated values of  $C_p$  and  $h_{c,w}$ ,

Dev: deviation between the estimates based on the regulatory or simulated  $C_p$  and  $h_{c,w}$  values.

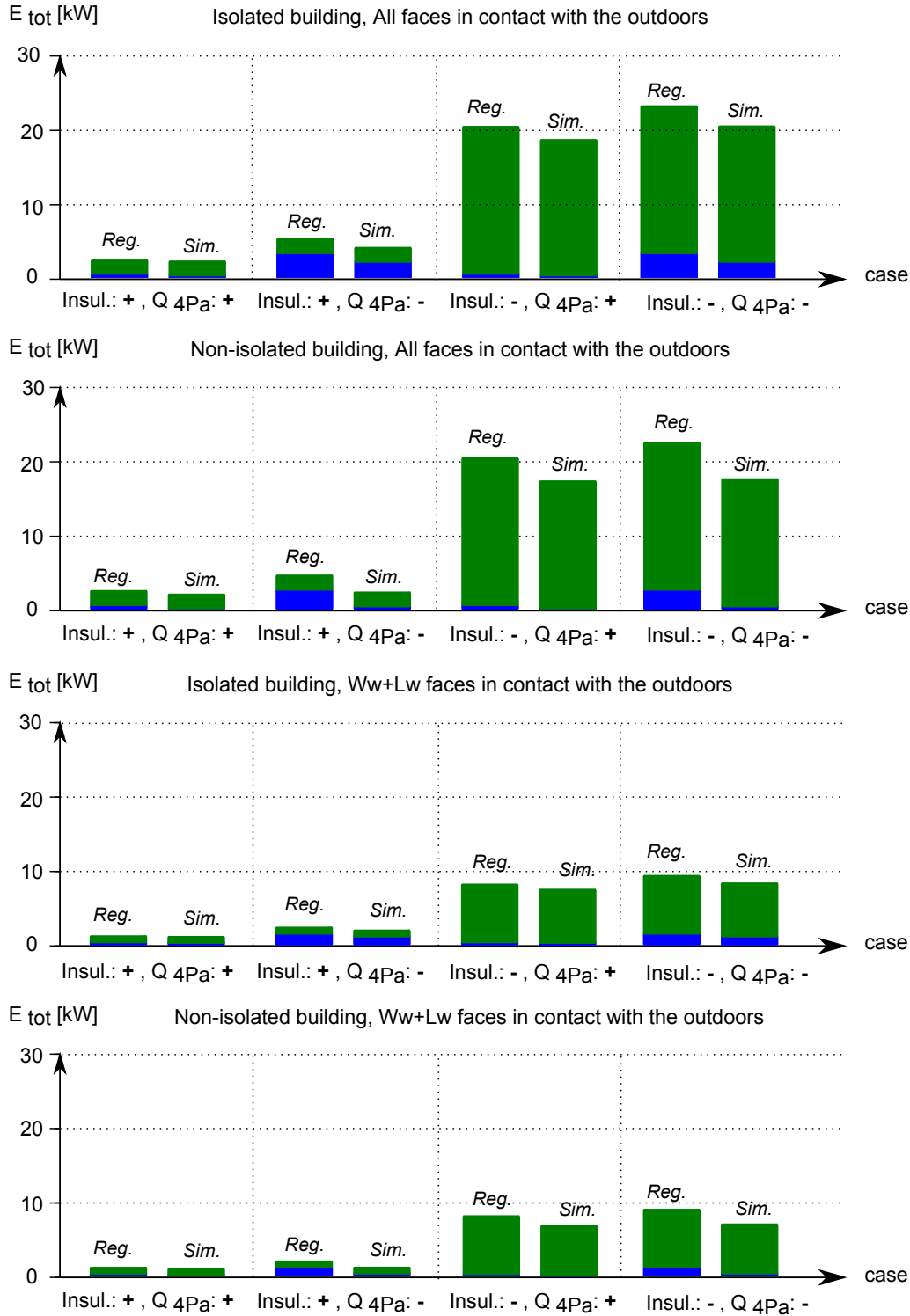


Figure a.36: Comparison of the total energy needs ( $E_{i+c,tot}$ ) differentiated depending on  $E_{inf,tot}$  or  $E_{conv,tot}$  for the cubical building located either in an open terrain or in a theoretical urban environment.

Blue: contribution of  $E_{inf,tot}$ ; Green: contribution of  $E_{conv,tot}$ ;  
 Insul. +: insulated building; Insul. -: non-insulated building;  
 Q<sub>4Pa</sub>+: air tight building; Q<sub>4Pa</sub> -: air permeable building;  
 Reg. (resp. Sim.): estimates based on the standard (respectively simulated)  $C_p$  and  $h_{c,w}$ .

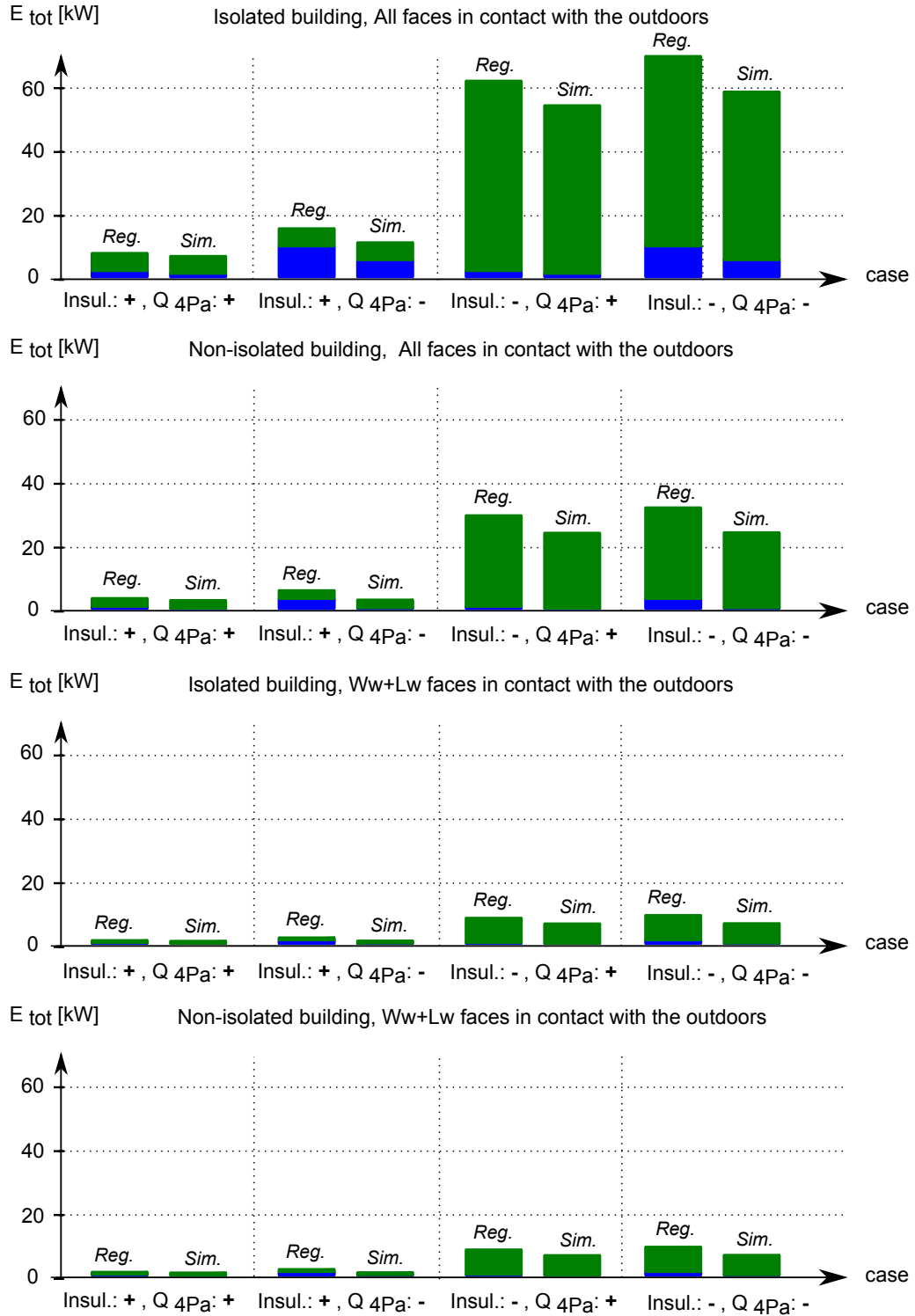


Figure a.37: Comparison of the total energy needs ( $E_{i+c,tot}$ ) differentiated depending on  $E_{inf,tot}$  or  $E_{conv,tot}$  for the patio building located either in an open terrain or in a theoretical urban environment.

Blue: contribution of  $E_{inf,tot}$ ; Green: contribution of  $E_{conv,tot}$ ;

Insul. +: insulated building; Insul. -: non-insulated building;

$Q_{4Pa}+$ : air tight building;  $Q_{4Pa}-$ : air permeable building;

Reg. (resp. Sim.): estimates based on the standard (respectively simulated)  $C_p$  and  $h_{c,w}$ .

### Y.3.2 Effects of urban morphology on the building energy loads due to infiltration and convection

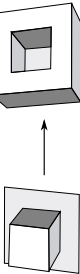
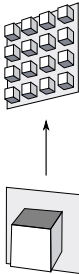
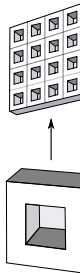
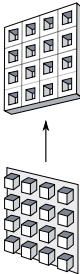
Faces in contact with outdoor		Insul : + $Q_{4Pa} : +$		Insul : + $Q_{4Pa} : -$		Insul : - $Q_{4Pa} : +$		Insul : - $Q_{4Pa} : -$	
		All	W+Lw	All	W+Lw	All	W+Lw	All	W+Lw
	Reg.	abs.	4.86	1.95	9.77	3.98	4.06	15.89	45.56
		rel.(%)	194	192	185	182	199	199	197
	Simu.	abs.	6.44	2.44	6.58	1.81	34.78	13.25	37.18
		rel.(%)	285	261	161	101	200	186	182
	Reg.	abs.	-0.17	-0.08	-0.86	-0.39	-0.17	-0.08	-0.86
		rel.(%)	-7	-8	-16	-18	-4	-5	-4
	Simu.	abs.	-0.40	-0.17	-1.96	-0.84	-1.51	-0.70	-3.07
		rel.(%)	-18	-19	-48	-47	-16	-19	-15
	Reg.	abs.	-4.21	-2.03	-9.45	-4.37	-32.08	-15.97	-37.32
		rel.(%)	-57	-68	-63	-71	-61	-77	-54
	Simu.	abs.	-3.90	-1.71	-7.99	-2.80	-29.89	-14.38	-33.97
		rel.(%)	-61	-70	-75	-78	-64	-75	-59
	Reg.	abs.	0.82	0	1.19	0	8.73	0	9.10
		rel.(%)	35	0	27	0	45	0	41
	Simu.	abs.	0.68	-0.03	0.55	-0.15	6.41	-0.44	6.28
		rel.(%)	36	-4	26	-16	37	-8	36

Table a.19: Comparison between  $E_{i+c,tot}$  [kW] for different built morphologies.









NOM : MERLIER  
Prénoms : Lucie, Tãm-Minh

DATE de SOUTENANCE : 4 septembre 2015

TITRE : On the interactions between urban structures and air flows:  
A numerical study of the effects of urban morphology on the building wind environment and the related building energy loads.

NATURE : Doctorat  
École doctorale : MEGA (Mécanique, Énergétique, Génie Civil, Acoustique)  
Spécialité : Génie Civil

Numéro d'ordre : 2015-ISAL-0070

**RÉSUMÉ :**

Le développement urbain contribue fortement à l'augmentation de la demande énergétique et des émissions de gaz à effet de serre. Dans le même temps, les conditions de vie des citoyens, le réchauffement climatique et la raréfaction des ressources naturelles deviennent problématiques. Les bâtiments consomment 32 % de l'énergie finale mondiale. Ils modifient également le bilan énergétique et les micro-climats urbains. Ces micro-climats affectent en retour les sollicitations thermiques des bâtiments ainsi que les ambiances urbaines. L'approche bioclimatique de la construction apparaît donc être une solution d'avenir pour améliorer la performance énergétique du bâti et favoriser de bonnes conditions de vie en ville. Cependant, une telle approche requiert une connaissance fine des interrelations entre les environnements bâtis, les phénomènes aérodynamiques et les échanges thermiques se développant en milieu urbain.

L'étude exploratoire développée dans cette thèse pose les bases scientifiques et méthodologiques d'une approche transversale visant à étudier l'énergétique urbaine et le bio-climatisme. Elle fait appel à des concepts et des outils empruntés à l'architecture et l'urbanisme d'une part, et à la physique du bâtiment et de la ville d'autre part. Cette thèse étudie plus particulièrement les relations entre la morphologie urbaine et les processus aérodynamiques qui se développent dans la canopée urbaine et leurs effets sur la demande énergétique des bâtiments induite par les infiltrations d'air et les échanges thermiques convectifs.

Cette thèse se compose de trois parties principales. Dans un premier temps, les spécificités de l'aérodynamique et de la physique urbaines sont synthétisées et la morphologie de tissus urbains réels est analysée. Une typologie générique de bâtiments isolés et une autre d'îlots urbains en sont déduites. Dans un second temps et afin d'étudier ensuite les écoulements d'air en milieu bâti, le modèle de mécanique des fluides numérique est validé par comparaison des prédictions du modèle avec des résultats expérimentaux et numériques détaillés. Des expérimentations numériques sont ensuite réalisées sur les différents types morphologiques. Les écoulements moyens sont analysés dans leurs rapports avec la morphologie bâtie, et la distribution des coefficients de pression sur les façades des bâtiments est analysée. Dans un troisième temps, les échanges thermiques sont couplés aux processus aérodynamiques. L'amélioration des estimations des échanges convectifs des bâtiments grâce à la mécanique des fluides numérique est vérifiée par comparaison des résultats de simulation avec des données expérimentales et numériques, ainsi qu'avec les valeurs standard généralement considérées en ingénierie du bâtiment. Une adaptation des fonctions de paroi relatives au transfert thermique est proposée sur la base d'études existantes, et la distribution des échanges convectifs sur les façades de bâtiments est analysée. Enfin, la demande énergétique des bâtiments due aux infiltrations d'air et à la transmission de chaleur au travers de leur enveloppe est estimée pour différents types morphologiques, et comparée avec les valeurs estimées suivant une approche réglementaire.

Les résultats de cette thèse mettent en évidence les effets des propriétés topologiques et métriques des bâtiments et ensembles bâtis sur le développement de recirculations d'air dans la canopée urbaine. Les conditions aérodynamiques en résultant induisent une distribution et intensité hétérogènes des coefficients de pression et d'échange convectif sur les façades des bâtiments. Ces conditions influent notablement sur le comportement thermique des bâtiments non isolés et perméables à l'air. Par ailleurs, l'estimation de leur demande énergétique diffère de façon substantielle suivant si celle-ci est basée sur les valeurs simulées ou standard des coefficients de pression et d'échange convectif. Cependant, si l'on s'intéresse à la contribution relative de la structure bâtie, l'influence des conditions aérodynamiques sur la demande énergétique des bâtiments apparaît plus importante pour les bâtiments isolés thermiquement. Selon les résultats de simulation, la différence entre la demande énergétique, rapportée à l'unité de surface de plancher, due aux infiltrations d'air et pertes thermiques au travers de l'enveloppe peut varier de 18 % à 47 % suivant si le bâtiment est isolé ou non.

Ainsi, la méthodologie développée dans cette thèse intègre différents facteurs de l'environnement urbain (morphologie, vent) pour en étudier leurs effets mutuels dans un souci de développement urbain durable. Les résultats obtenus soulignent l'intérêt de développer une telle approche intégrée et détaillée relevant de la physique urbaine pour mieux comprendre le comportement énergétique des bâtiments. Cependant, la généralisation de cette approche nécessiterait des moyens de calculs très importants. Les méthodes et techniques de calculs nouvellement développées ainsi que des études expérimentales dédiées en site réel apparaissent donc incontournables pour porter cette démarche plus loin.

MOTS-CLÉ : Morphologie urbaine, Aérodynamique urbaine, Physique du bâtiment, Mécanique des fluides numérique (CFD), Infiltrations d'air, Transferts de chaleur convectifs.

Laboratoire de recherche : Centre d'Energétique et de Thermique de Lyon (CETHIL UMR 5008)

Directeur de thèse : Frédéric KUZNIK (CETHIL UMR 5008)

Président de jury : Pierre SAGAUT

Composition du jury : Bert BLOCKEN, Julien HANS, Frédéric KUZNIK, Peter MOONEN, Marjorie MUSY, Christian OBRECHT, Gilles RUSAOUËN, Pierre SAGAUT